ESTABLISHMENT OF THE CENTER FOR ADVANCED SEPARATION TECHNOLOGIES

FINAL TECHNICAL REPORT

Report Period
September 17, 2001 to September 30, 2006

Compiled by

Christopher E. Hull

Issued January 10, 2007

DOE Award Number:
DE-FC26-01NT41091

Center for Advanced Separation Technologies
Virginia Polytechnic Institute & State University
Blacksburg, Virginia 24061-0258

and

National Research Center for Coal and Energy
West Virginia University
Morgantown, WV 26506-6064

DISCLAIMER

ABSTRACT

This Final Technical Report covers the eight sub-projects awarded in the first year and the five projects awarded in the second year of Cooperative Agreement DE-FC26-01NT41091: Establishment of the Center for Advanced Separation Technologies. This work is summarized in the body of the main report: the individual sub-project Technical Progress Reports are attached as Appendices.

Note: SI is an abbreviation for “Le Systeme International d’Unites.”

TABLE OF CONTENTS

INTRODUCTION

The U.S. is the largest producer of mining products in the world. In 1999, U.S. mining operations produced $66.7 billion worth of raw materials that contributed a total of $533 billion to the nation's wealth. Despite these contributions, the mining industry has not been well supported with research and development funds as compared to mining industries in other countries. To overcome this problem, the Center for Advanced Separation Technologies (CAST) was established by Virginia Tech and West Virginia University to develop technologies that can be used by the U.S. mining industry to create new products, reduce production costs, and meet environmental regulations. This endeavor is supported through U.S. DOE Cooperative Agreement No. DE-FC26-01NT41091: Establishment of the Center for Advance Separation Technologies.

Much of the research to be carried out at CAST will be longer-term, high-risk, basic research, and will be carried out in four broad areas:

a) Solid-solid separation
b) Solid-liquid separation
c) Chemical/Biological extraction, and
d) Sensor and control development.

Distribution of funds has been handled via competitive solicitation of research proposals through Site Coordinators at the two universities. Two RFP's have been issued to date. The first of these, referred to as the CAST I – Round 1 RFP, was issued on August 17, 2001 and closed October 15, 2001. A total of 12 proposals were received in response to this first RFP. These were first reviewed and ranked by a group of technical reviewers (selected primarily from industry). Based on these reviews, and an assessment of overall program requirements, the CAST Technical Committee made an initial selection/ranking of proposals and forwarded these proposals to the DOE/NETL Project Officer for final review and approval. This process took some 6 months to complete but 8 projects were in place at the constituent universities (5 at Virginia Tech and three at West Virginia University) by May 17, 2002.

This was followed, on June 1, 2002 with the CAST I – Round 2 RFP, which closed on July 19, 2002. A total of 12 proposals were received in response to this second RFP – five were selected for funding. These were in place at the constituent universities (2 at Virginia Tech and 3 at West Virginia University) by March 1, 2003.

All thirteen of these projects are listed below by category, along with brief abstracts of their aims and objectives.

a) Solid-Solid Separation

1. Improving Coarse Particle Flotation
Principal Investigators: R.-H. Yoon and G.H. Luttrell, (Virginia Tech).
Period of Performance: May 17, 2002-May 31, 2005.

The recovery of coarse particles by flotation is a common problem in the coal and minerals processing industry. The objective of this project is to develop methods of extending the upper particle size limit for flotation. The availability of such a technology will improve processing efficiency and greatly simplify the plant flowsheet. Two different complementary approaches will be used to achieve the project objective. One is to use novel flotation reagents that will help increase the attachment force between air bubbles and coarse particles, and the other is to develop new flotation machines specifically designed to promote coarse particle flotation.

2. Separation of Small Particles due to Density Differences in a CFB Riser System
Principal Investigators: E. Johnson and B. Kang (West Virginia University).
Period of Performance: May 17, 2002-May 31, 2005.

The efficiency of separating small (less than 250 micrometers in diameter) dense particles from small light particles in the internal recirculation flow within a CFB riser is being investigated. Currently, there are many systems for separating fine particles. However, these systems lack the efficiency and/or the economics to be commercially viable in many situations. This research is directed towards removing pyrite from coal fines at a coal cleaning plant. Also, of concern will be the removal of radioactive particles from the desert sand at the Nevada Test Sites.

3. Modeling of Flotation From First Principles
Principal Investigator: R.-H. Yoon (Virginia Tech).
Period of Performance: May 17, 2002-May 31, 2005.

Flotation is widely regarded as the best available technology for separating fine particles. The present form of the technology was invented nearly 100 years ago, yet there is still no reliable model for predicting flotation rate from first principles. It is the purpose of the proposed work to develop a flotation model that can predict flotation performance from both surface chemistry and hydrodynamic parameters.

4. Studies of Froth Stability and Model Development
Principal Investigator: R.-H. Yoon (Virginia Tech).
Period of Performance: May 17, 2002-May 31, 2005.

Froth plays an important role in flotation. It determines the final grade of the product and the maximum carrying capacity (or throughput) of a flotation machine. Also, many operators use stronger frothers to produce smaller air bubbles and, hence, higher recovery and throughput. Despite its importance, little is known of the fundamentals of foam and froth stability. It is, therefore, proposed to study the various factors affecting the stability

of flotation froth. This will be accomplished by using a thin film balance technique and by monitoring the stability of froth in a bubble column using a video camera. The results will be used for developing a froth model and also for developing effective defoamers.

5. Direct Measurement of Forces in Flotation Systems

Principal Investigators: W.A. Ducker and R.-H. Yoon (Virginia Tech).
Period of Performance: May 17, 2002-May 31, 2005.

The objective of this project is to directly measure the force as a function of separation between a particle and a bubble in aqueous solution. This force controls the attachment and detachment of particles to bubbles, which is an essential step in determining the efficiency of the separation of mineral particles in a flotation cell. We are fabricating a device specially designed for these measurements. The device will use a force-detection method from an Atomic Force Microscope and a separation-detection method from a Surface Forces Apparatus. The key advances are to explicitly measure both the separation between the particle and the bubble and the shape of the bubble at all times. Without this separation and shape data, it is not possible to compare the measured forces to theoretical estimates or to the practice of flotation. After fabrication of the device, measurements of the forces acting on hydrophilic, hydrophobic, and charged particles in aqueous solutions of surfactant molecules will be obtained.

6. Novel Surfactants as Collectors for Froth Flotation

Researcher: Richard D. Gandour (Virginia Tech)
Period of Performance: March 1, 2003-May 31, 2005.

Our goals are to synthesize novel, inexpensive surfactants that outperform current collectors in mineral flotation. These surfactants will selectively bind to particles and create a hydrophobic coating on a particle to enable selective separation by froth flotation. We plan to synthesize surfactants that have very hydrophobic, long chains, yet have sufficient water solubility for mineral processing and coal-fines processing. These amphiphiles, which we call "hydra surfactants," will have one tail and three identical functional groups on the head. These novel molecules will be useful for many different separations in mineral processing, but initially will be tested on separation of discoloring impurities (i.e., anatase (TiO2) and iron oxides) from clay.A strategy to make these surfactants from environmentally friendly vegetable oils is outlined.

7. Column Flotation of Fine Dolomitic Phosphate by Selective Fatty Acids

Researcher: F. F. Peng (West Virginia University)
Period of Performance: March 1, 2003-May 31, 2005.

Among the detrimental impurities in phosphate ores, dolomite is considered the most troublesome for down stream operations. Dolomite may cause higher consumption of sulfuric acid, reduce filtration rates and lower P_2O_5 content in fertilizer manufacturing processes. Difficulties in separating dolomite from phosphate arise from the fact that most of the dolomite is disseminated in the phosphate mineral. Both are oxide type minerals and have the same calcium cationic component. They exhibit similar

electrokinetics, adsorption and desorption behavior in physical separation process such as flotation. Several processing schemes have been developed to handle this problem, but none are satisfactory due to high MgO content and/or low overall P_2O_5 recovery in the final phosphate concentrate. In this proposed research project, samples from Florida dolomitic phosphate minerals will be tested in an open flotation column. New selective fatty acid collectors for dolomite particles and appropriate mixtures of phosphoric acid/sulfuric acid depressant for phosphate particles will be selected and used. The aim is to achieve a phosphate concentrate containing as high as 30% P_2O_5 and less than 1.0% MgO contents at high P_2O_5 recovery. Liberation analysis of dolomitic phosphate pebble will be conducted. The selectivity and frothability of the new selective fatty acid collectors will also be characterized by determining dolomitic phosphate flotation. Success in this research project will enable the mineral industry to increase its phosphate reserve base, by recovering phosphate from formerly unusable phosphatic minerals and low grade phosphate reserves.

b) Solid-Liquid Separations

8. Development of a Novel Fine Particle Centrifuge
Researchers: G.H. Luttrell and R-H. Yoon (Virginia Tech)
Period of Performance: March 1, 2003-May 31, 2005.

The solid-solid separation processes employed by modern coal preparation plants require large amounts of process water. After cleaning, the unwanted water must be removed from the surfaces of the particles using mechanical dewatering equipment. Coarse particles can be readily dewatered using simple screening systems, while finer particles require more complicated unit operations such as centrifuges and filters. Unfortunately, the processes used to dewater fine particles are inherently inefficient and expensive to operate and maintain. To overcome these problems, a novel centrifugal filter has been developed by researchers at Virginia Tech. Preliminary test data suggest that this new technology can reduce the moisture content of fine coal products by approximately 30-50% compared to existing dewatering processes. The objective of this project will be to construct a continuous prototype unit and to conduct a detailed experimental investigation of this new technology.

9. New Strategies for Dewatering of Coals
Researchers: M. Seehra, A. Manivannan & M. Bachlechner (West Virginia University)
Period of Performance: March 1, 2003-May 31, 2005.

A two-year innovative research program on the combined experimental-modeling studies of coal-water interactions and coal dewatering is proposed. The experimental program will first focus on determining the relative amounts of "free" and "bound" water in wet coals using analytical techniques of thermogravimetric analysis, heat capacity measurements and 1H nuclear magnetic resonance. Laboratory scale dewatering experiments will then be carried out by vacuum filtration and centrifugation, combined with pulsed heating at microwave or IR (3300 cm-l) frequencies to liberate the "bound" water. These investigations will be complimented with modeling studies of the coal-water

interactions and the effect of centrifugation on dewatering from surface-bound water and coal pores. This integrated experimental-modeling approach is an important component of the proposed research since the results from the molecular-dynamics simulations could provide unique technological insights that will increase the efficiency of dewatering processes. Finally, scale-up of the resulting successful approaches for coal dewatering will be proposed at the conclusion of the two-year program.

c) Chemical/Biological Extraction

10. Novel Bioleaching Technology Assisted by Electrolytic Processes

Principal Investigators: E. Cho and R. Yang (West Virginia University).
Period of Performance: May 17, 2002-May 31, 2005.

Bioleaching of sulfide minerals using bacteria *Thiobacillus ferrooxidans* has been identified as a promising method for heap or dump leaching of low grade mixed sulfide ores containing pyrite (FeS_2), chalcopyrite ($CuFeS_2$), and/or sphalerite (ZnS). However, the major problem with bioleaching is that the rates are too slow for wide commercial utilization. The approach being used in this project focuses on the growth of bacteria under the influence of an applied direct potential and on the utilization of the bacteria to leach sulfide minerals. The objective is to identify the optimum conditions for the bio- and electro- leaching reactions in order to maximize overall leaching rates of the sulfide minerals.

11. Coal Desulfurization Using Hypochlorite and Cupric Ion as a Catalyst – Feasibility Study

Researchers: E. H. Cho & R. Y. K. Yang (West Virginia University)
Period of Performance: March 1, 2003-May 31, 2005.

The utilization of coal as a feedstock to produce carbon materials is very much hampered by the presence of its organic sulfur content. However, the organic sulfur is very difficult to remove. It is generally accepted that only two methods have capability to remove the organic sulfur rather effectively; one is with a melt of sodium hydroxide/potassium hydroxide at high temperatures (Gravimelt Process) and the other is with chlorine chemicals. However, the Gravimelt Process contaminates the coal structure, and its decontamination and the regeneration of the reagents may be insurmountable problems in terms of economic feasibility. Chlorine chemicals also chlorinate the coal structure and the removal of organic sulfur is not high enough to produce a premium coal or feedstock. It is proposed that organic sulfur be leached with hypochlorite using cupric amine as a catalyst. Hypochlorite is the predominant chlorine derivative at high pH's. The catalysis of cupric amine was found during 1990s in leaching of gold with hypochlorite and other oxidants. We will conduct two kinds of consecutive experiments. In the first, coal will be leached in a reactor with a solution containing hypochlorite and cupric amine. In the second, the leached coal will be hydrolyzed in hot sodium carbonate solution, which is believed to cleave the organic sulfur bond from coal and thus further reduce the sulfur content. Leached coal and hydrolyzed coal samples will be analyzed particularly for organic sulfur and chloride content. The data will be analyzed to

determine the desulfurization potential through the two consecutive experiments and also the chlorination/dechlorination of the coal matrix through each of the two experiments.

d) Sensor and Control Development

12. Development of Electrochemical Sensor for On-Site Monitoring of Heavy Metal Ions in Coal Processing And Utilization

Principal Investigators: A. Manivannan and M. Seehra (West Virginia University).
Period of Performance: May 17, 2002-May 31, 2005.

The aim of this research program is to develop a novel electrochemical sensor based on a boron-doped diamond (BDD) electrode for monitoring/controlling heavy metal ions such as Hg, Zn, Cu, Pb, As, Cd, and Fe encountered in the processing and utilization of coals. This research is based on earlier testwork in which ppb levels of Pb and Hg were detected in laboratory prepared solutions. BDD electrodes are superior to other commonly used electrodes (such as glassy carbon) in terms of their ruggedness, chemical stability, wide potential window and lower background current. These advantages are important for the simultaneous detection of a number of elements in solution.

13. Evaluation of Coal Cleaning Efficiency Using Transponder-Based Density Tracers

Principal Investigators: G.H. Luttrell, R.-H. Yoon and C.J. Wood (Virginia Tech).
Period of Performance: May 17, 2002-May 31, 2005.

Density tracers are one of the most powerful diagnostic tools for evaluating the performance of heavy media circuits in coal preparation plants. The objective of this project is to develop a new generation of tracers that can be automatically tracked using recently developed transponder technology. This development also makes it possible for efficiency tests to be performed very rapidly by a single person in an extremely cost-efficient manner. The project will be carried out in two phases. In the first phase of work, the hardware and software required to develop a prototype transponder-based system will be procured and evaluated using a simulated circuit at the Virginia Tech coal laboratory. In the second phase, the monitoring system will be relocated to an industrial coal preparation plant for field-testing.

EXPERIMENTAL

The CAST initiative is comprised of a diverse group of subprojects, most of which are multistage, task-oriented developmental projects that cannot be conveniently categorized by the traditional reporting criteria required by the DOE Uniform Reporting Requirements. For example, several of the projects have required the construction of unique test equipment, others the generation of simulation models, etc., as preliminary tasks in the overall execution of the project. As such, they are more appropriately described and discussed as "Project Tasks" within the context of the individual Technical Progress Reports. These reports are attached to this document as Appendices and should be referred to for this information.

RESULTS AND DISCUSSION

The CAST initiative is comprised of a diverse group of subprojects, most of which are multistage, task-oriented developmental projects that cannot be conveniently categorized by the traditional reporting criteria required by the DOE Uniform Reporting Requirements. For example, several of the projects have required the construction of unique test equipment, others the generation of simulation models, etc., as preliminary tasks in the overall execution of the project. As such, the presentation of results is more appropriately described and discussed within the context of the individual Technical Progress Reports. These reports are attached to this document as Appendices and should be referred to for this information.

ABSTRACTS

This aggregated Final Report covers the third year of operation of Cooperative Agreement DE-FC26-01NT41091: Establishment of the Center for Advanced Separation Technologies. A total of thirteen (13) sub-projects were funded. These reports are attached to this document as Appendices. Abstracts of each project of the sub-projects follows.

a) Solid-Solid Separation

1. VA003 - Improving Coarse Particle Flotation (Appendix 1)
Principal Investigators: R.-H. Yoon and G.H. Luttrell (Virginia Tech)
Period of Performance: May 17, 2002-May 31, 2005

Possibilities for increasing the upper limit of floatable particle sizes in the froth flotation process have been examined since the early beginnings of mineral flotation. The economic implications of such an increase are far ranging; from decreased grinding costs and increased recoveries to simplified flow-sheet design and increased throughput. All leading to increased revenue. Bubble-particle detachment has been identified as the main limiting factor for coarse particle flotation. The detachment process has been studied to better understand the factors influencing the strength of attachment and the energies involved. Direct measurements of bubble particle detachment were performed using a hanging balance apparatus (KSV Sigma 70 tensiometer) and using a submerged hydrophobic plate in water. Three experiments were used; direct force measurement of bubble-particle detachment, detachment force and energy of a bubble from a submerged hydrophobic plate, and detachment force and energy of a cetyltrimethylammonium bromide coated silica sphere from a flat bubble. Octadecyltrichlorosilane was used as a hydrophobic coating in the first two experimental methods. These experiments were recorded with a CCD camera to identify the detachment processes involved. Energies for both methods were calculated and divided into the two main steps of the detachment process: TPC pinning and three phase contact line sliding. The first step represents the energy barrier which must be overcome before detachment can begin. It is directly related to contact angle hysteresis. Detachment occurs during the second step, where the solid-vapor interface is replaced by solid-liquid and liquid-vapor. This step corresponds to the work of adhesion. The effects of surface tension, contact angle and hysteresis were well demonstrated with the three experimental methods. Good correlation was found between theoretical work of adhesion and measured energies.

2. WV002 - Separation of Small Particles due to Density Differences in a CFB Riser System (Appendix 2)
Principal Investigators: E. Johnson and B. Kang (West Virginia University)
Period of Performance: May 17, 2002-May 31, 2005

An exploratory study was conducted to demonstrate that a solid-solid mixture flowing in a riser may be separated in a dry process due to density differences, The results of this study may well lead to the initiation and development of an innovative dry separation

process for solid-solid mixtures. This unique process could easily lend itself to the separation of mixtures of minerals with different densities in arid regions. A more conventional application would be the separation of pyrite from coal or coal fines. The density differences investigated in this study correspond to the density difference between pyrite and clean coal. Another application could be the reclaiming of coal fines currently discarded to settling impoundments due to the inefficiency of current wet separation process techniques. The particle sizes employed in this investigation were of a mean diameter of 350μm for the sand and 450μm for the steel shot. This exploratory study has demonstrated that a dry separation process, based on density difference, is possible in a CFB riser. This study also indicates that a significant effort is required to optimize this separation process due to the fact that many variables enter into the separation process

3. VA001 - Modeling of Flotation From First Principles (Appendix 3)
Principal Investigator: R.-H. Yoon (Virginia Tech)
Period of Performance: May 17, 2002-May 31, 2005

A flotation model has been proposed that is applicable in a turbulent environment. It is the first turbulent model that takes into account hydrodynamics of the flotation cell as well as all relevant surface forces (van der Waals, electrostatic, and hydrophobic) by use of the Extended DLVO theory. The model includes probabilities for attachment, detachment, rising, and froth recovery as well as a collision frequency. A review of the effects fluids have on the flotation process has also been given. This includes collision frequencies, attachment and detachment energies, and how the energies of the turbulent system relate to them. Flotation experiments have been conducted to verify this model. Model predictions were comparable to experimental results with similar trends. Simulations were also run that show trends and values seen in industrial flotation systems. These simulations show the many uses of the model and how it can benefit the industries that use flotation.

4. VA002 - Studies of Froth Stability and Model Development (Appendix 4)
Principal Investigator: R.-H. Yoon (Virginia Tech)
Period of Performance: May 17, 2002-May 31, 2005

This study focuses on developing a methodology to identify the basic factors affecting the stability of foams and froths in flotation. We investigate the stability of aqueous thin films between air bubbles, and then compare film stability to foam stability. The thin film studies indicate that a hydrophobic attractive force exists to destabilize films between air bubbles in dilute aqueous solutions in flotation processes. To better understand the origin of the hydrophobic force in aqueous films between two hydrophobic substrates, we have studied the effects of surfactant type and concentration, and ionic strength on the surface forces in foam films. We have also studied the effect of film elasticity on foam stability. The results show that film elasticities in flotation may be too small to affect foam stability.

5. **VA004 - Direct Measurement of Forces in Flotation Systems (Appendix 5)**
   Principal Investigators: W.A. Ducker and R.-H. Yoon (Virginia Tech)
   Period of Performance: May 17, 2002-May 31, 2005

   The objective of this project is to directly measure the interaction force between a particle and bubbles as a function of separation distance. This force controls the attachment and detachment of particles to bubbles, which is an essential step in determining the efficiency of a flotation process. In the past ten years, one predominant explanation for the long range attraction between hydrophobic surfaces is the nanobubble/gas cavity theory. Firstly, an Atomic Force Microscope was utilized to study the hydrophobic force between solid surfaces to clarify the applicability of nanobubble theory in the solid/surfactant system. The effects of degassing, salt concentration and chain length on the hydrophobic force are systemically studied. The results are beneficial for the understanding of the origin of the hydrophobic force and the particle/bubble interaction in Flotation. Secondly, a specially designed device, wetting film apparatus was fabricated for the direct particle/bubble force measurements. The experiment results show that between hydrophilic substrate/bubble, when the separation decreases, there is a strong repulsive disjoining pressure, which leads to a thick water film between particle/bubble, therefore, a less likely flotation. The wetting film between a hydrophobic substrate and a bubble ruptures in tens of milliseconds drastically, suggesting a possible flotation after the solid particles are hydrophobized. The rupture process is proposed to be studied systemically using a high speed video camera.

6. **VA007 - Novel Surfactants as Collectors for Froth Flotation (Appendix 6)**
   Researcher: Richard D. Gandour (Virginia Tech)
   Period of Performance: March 1, 2003-May 31, 2005

   The three series of triheaded surfactants have been synthesized and characterized. All, including those with 22 carbons in the chain, are quite soluble in triethanolamine solutions. Studies of concentration of surfactant versus contact angle reveal that depending on chain length these surfactants form robust hydrophobic films on TiO2, calcite, apatite, and silver at extremely dilute concentrations.
   .

7. **WV006 - Column Flotation of Fine Dolomitic Phosphate by Selective Fatty Acids (Appendix 7)**
   Researcher: F. F. Peng (West Virginia University)
   Period of Performance: March 1, 2003-May 31, 2005

   A Florida dolomitic phosphate pebble sample was processed in dolomite flotation process using fatty acid FAS-40A as collector. The dolomitic phosphate pebble feed sample contained 26.14% P2O5, 1.3-1.5% MgO and 14.5% acid insoluble. The sample was ground to pass 150μm (100 mesh) for liberation of phosphate from impurities in dolomitic phosphate mineral sample. Dolomite flotation was performed in both Denver D-12 stirred-tank cell and 2-in ID modified packed flotation column. Using stirred-tank cell at 1100 rpm impeller speed, the underflow of dolomite flotation as a rougher phosphate concentrate containing 26.8% P2O5 and 0.8% MgO at the P2O5 recovery of about 93% was obtained. The reagent condition was 2.0 kg/t FAS-40A fatty acid

collector at pH 5.4. Based on the results and conditions of stirred-tank cell flotation, modified packed column flotation tests were conducted using central composite experiment design (CCD). The underflow of the column flotation contained 26.9% P2O5 and 0.95% MgO at the P2O5 recovery of 88.8%. The column flotation operation conditions were pH 5.5, 3.0 kg/t FAS-40A fatty acid collector, 20 cm froth height and 4.5 SCFH air flow rate. In order to achieve a marketable phosphate concentrate product, double reverse flotation technique was employed. The underflow of the column flotation after dolomite removal was further processed in amine flotation to reject silica. The final phosphate concentrate contained over 30% P2O5, about 1% MgO with more than 85% P2O5 recovery.

e) Solid-Liquid Separations

8. VA006 - Development of a Novel Fine Particle Centrifuge (Appendix 8)
Researchers: G.H. Luttrell and R-H. Yoon (Virginia Tech)
Period of Performance: March 1, 2003-May 31, 2005

In order to improve the removal of moisture from fine coal streams, a project was initiated to construct and test a new dewatering technology known as a hyperbaric centrifuge. Previous tests conducted with a batch laboratory unit suggest that this new technology can reduce the moisture content of fine coal products by up to 50% compared to existing mechanical systems. In this project, work focused on the design of a pilot-scale continuous prototype of this technology. The selected design consisted of a two-stage process capable of achieving low product moistures while maintaining nearly complete recoveries of fine coal. To date, several laboratory tests were conducted using a batch fed unit to verify the extent of moisture removal that can be achieved using this approach. However, initial tests showed that several improvements in the design were needed to correct problems with the mechanical seal that allowed water to contaminate the dewatered cake. After correcting this and several other minor mechanical problems, several additional shakedown tests were carried out while operating the prototype unit in continuous mode. This mode of operation required the integration of a thickening unit into the test circuitry. This modification made it possible to improve fines recovery by circulating fines previously lost through the screen back to the circuit feed. Data obtained from these tests indicated that the new technology can indeed achieve extremely good removals of moisture from fine coal. The data also indicate that the moisture reduction was significantly better at higher rotation speeds and with higher gas injection pressures. Future work conducted during the next phase of this project will be performed (i) to demonstrate the capabilities of this new technology at a larger scale and (ii) to obtain scale-up data for the engineering design of a production scale unit.

9. WV004 - New Strategies for Dewatering of Coals (Appendix 9)
Researchers: M. Seehra, A. Manivannan & M. Bachlechner (West Virginia University)
Period of Performance: March 1, 2003-May 31, 2005

In this work, electrochemistry based on boron-doped-diamond (DDD) electrodes was investigated for the quantification of Hg, Cd and Pb in the ppb-ppt range in laboratory prepared solutions. For Hg, the rotating disk electrode technique and the standard

addition method allowed reliable quantification of mercury in the 0.005 – 50 ppb range in practical samples of KCl impinger solutions prepared from flue gas released by a pilot-scale coal-fired combustion facility. For the simultaneous detection of Cd and Pb in laboratory solutions at the ppb range, some mutual interference was detected which could be handled by developing three-dimensional calibration curves. However, testing of Cd and Pb in practical samples has not yet been done. In future work, we will focus on the development of a portable sensor for Hg quantification..

b) Chemical/Biological Extraction

10. WV001 - Novel Bioleaching Technology Assisted by Electrolytic Processes (Appendix 10)

Principal Investigators: E. Cho and R. Yang (West Virginia University)
Period of Performance: May 17, 2002-May 31, 2005

Three sulfide minerals, chalcopyrite, sphalerite, and pyrite, were leached using a bioleaching mode and an electrobioleaching mode. The former mode was used to leach the minerals with the bacterium A. ferrooxidans in a bioreactor. In the latter mode, the leaching of the minerals was performed in a combination of a bioreactor and an electrochemical cell. In this set-up, a solution was drained from the bioreactor by gravity to the cathode compartment where the Fe(III) content was reduced to Fe(II) before the solution was pumped back to the bioreactor. The idea is that an increase in Fe(II) concentration, which is a nutrient of the bacteria, by electrochemical reduction of Fe(III) would increase the bacterial population and in turn would accelerate the leaching of the mineral.

It has been found that the electrobioleaching of chalcopyrite is superior to the bioleaching with respect to the fact that leaching conversion is higher and a high level of Fe(II) can be maintained. However, the electrobioleaching of sphalerite does not show an improvement over bioleaching. The electrobioleaching of pyrite is similar to that of chalcopyrite, and this has potential to be used in applications such as coal desulfurization and pretreatment of refractory gold ore in heap leaching.

11. WV005 - Coal Desulfurization Using Hypochlorite and Cupric Ion as a Catalyst – Feasibility Study (Appendix 11)

Researchers: E. H. Cho & R. Y. K. Yang (West Virginia University)
Period of Performance: March 1, 2003-May 31, 2005

Wet desulfurization of Pittsburgh No. 8 coal and Illinois No. 6 coal were conducted with sodium hypochlorite in the laboratory. Pittsburgh No. 8 coal was leached by hypochlorite at high pHs in one step process. The hypochlorite concentration varied from 0.2 to 0.6 molar; sodium hydroxide concentrations from 0.2 to 0.8 molar; and temperature was at the levels of 80 and 90°C. The desulfurization of Illinois No. 6 coal was conducted in three consecutive steps of pretreatment in concentrated ammonia at room temperature, leaching with hypochlorite at room temperature and hydrolysis in a

sodium hydroxide solution at 90°C. In the leaching step, hypochlorite concentration varied from 0.2 to 0.8 molar.

In the early stages of this project, it was found that cupric ammine and hypochlorite could not be prepared in the same solution because ammonia used to solubilize cupric ions reacts with hypochlorite. Thus, all the subsequent work was conducted with leach solutions containing only hypochlorite without addition of cupric ammonia.

The desulfurization method of Pittsburgh No. 8 coal was found to reduce mainly pyritic sulfur. More than 70% of pyritic sulfur removal was achieved at the optimum conditions of 0.4 molar hypochlorite, 0.4 molar sodium hydroxide and 90°C. The desulfurization method for Illinois No. 6 coal was capable of reducing significant amounts of organic sulfur. The removal of organic sulfur achieved a 37.8% reduction at the optimum operation of leaching at 0.4 molar hypochlorite and room temperature followed by hydrolysis at 0.3 molar sodium hydroxide and 90°C. The chlorine content in the coal produced by the chlorination during leaching was kept below the threshold value of 0.3% at the optimum conditions of the desulfurization method for each coal.

c) Sensor and Control Development

12. WV003 - Development of Electrochemical Sensor for On-Site Monitoring of Heavy Metal Ions in Coal Processing And Utilization (Appendix 12)
Principal Investigators: A. Manivannan and M. Seehra (West Virginia University)
Period of Performance: May 17, 2002-May 31, 2004 (2-Year Project)

In this work, electrochemistry based on boron-doped-diamond (DDD) electrodes was investigated for the quantification of Hg, Cd and Pb in the ppb-ppt range in laboratory prepared solutions. For Hg, the rotating disk electrode technique and the standard addition method allowed reliable quantification of mercury in the 0.005 – 50 ppb range in practical samples of KCl impinger solutions prepared from flue gas released by a pilot-scale coal-fired combustion facility. For the simultaneous detection of Cd and Pb in laboratory solutions at the ppb range, some mutual interference was detected which could be handled by developing three-dimensional calibration curves. However, testing of Cd and Pb in practical samples has not yet been done. In future work, we will focus on the development of a portable sensor for Hg quantification.

13. VA005 - Evaluation of Coal Cleaning Efficiency Using Transponder-Based Density Tracers (Appendix `3)
Principal Investigators: G.H. Luttrell, R.-H. Yoon and C.J. Wood
Period of Performance: May 17, 2002-May 31, 2005

Density tracers are widely regarded as one of the most powerful diagnostic tools for evaluating the performance of heavy medium circuits. Unfortunately, the full capabilities of density tracers are often not realized in practice due to problems that occur during the retrieval step. To overcome this problem, an advanced electronic monitoring system has been developed to automatically identify and count the density tracers as they pass

through a coal cleaning circuit. This technique, which relies on recent technological breakthroughs in transponder technology, improves the reliability of the tracer data by eliminating statistical errors associated with lost tracers. This development also makes it possible for efficiency tests to be performed very rapidly by a single person in an extremely cost-efficient manner. It is estimated that the average U.S. coal preparation plant could easily benefit by $500,000 or more annually by preventing coal losses that are detectable using this new technology.

REFERENCES

References utilized by the individual sub-projects are reported in the relevant Technical Progress Report in the attached Appendices.

Appendix 1: Improving Coarse Particle Flotation

TECHNICAL PROGRESS REPORT

Contract Title and Number:	Period of Performance:
Establishment of the Center for Advanced Separation Technologies (DE-FC26-01NT41091)	Starting Date: 9/17/01 Ending Date: 9/30/06

Sub-Recipient Project Title:	Report Information:
Improving Coarse Particle Flotation	Type: Finall Number: Period:
Principal Investigators:	Date: 05/27/04
Roe-Hoan Yoon and Gerald H. Luttrell Hubert Schimann (MSc Thesis)	Code: VA003
Contact Address:	Contact Information:
146 Holden Hall Virginia Polytechnic Institute & State University Blacksburg, VA 24061	Phone: (540) 231-4508 Fax: (540) 231-3948 E-Mail: cast@vt.edu
Subcontractor Address:	Subcontractor Information:
No subcontracts issued.	Phone: Fax: E-Mail:

DISCLAIMER

The Disclaimer must follow the Title Page and must contain the following paragraph: "This report was prepared as an account of work sponsored by an agency of the United States Government. Neither the United States Government nor any agency thereof, nor any of their employees, make any warranty, express or implied, nor assume any legal liability or responsibility for the accuracy, completeness, or usefulness of any information, apparatus, product, or process disclosed, or represents that its use would not infringe privately owned rights. Reference herein to any specific commercial product, process, or service by trade name, trademark, manufacturer, or otherwise does not necessarily constitute or imply endorsement, recommendation, or favoring by the United States Government or any agency thereof. The views and opinions of authors expressed herein do not necessarily state or reflect those of the United States Government or agency thereof. "

ABSTRACT

Possibilities for increasing the upper limit of floatable particle sizes in the froth flotation process have been examined since the early beginnings of mineral flotation. The economic implications of such an increase are far ranging; from decreased grinding costs and increased recoveries to simplified flow-sheet design and increased throughput. All leading to increased revenue. Bubble-particle detachment has been identified as the main limiting factor for coarse particle flotation. The detachment process has been studied to better understand the factors influencing the strength of attachment and the energies involved. Direct measurements of bubble particle detachment were performed using a hanging balance apparatus (KSV Sigma 70 tensiometer) and using a submerged hydrophobic plate in water. Three experiments were used; direct force measurement of bubble-particle detachment, detachment force and energy of a bubble from a submerged hydrophobic plate, and detachment force and energy of a cetyltrimethylammonium bromide coated silica sphere from a flat bubble. Octadecyltrichlorosilane was used as a hydrophobic coating in the first two experimental methods. These experiments were recorded with a CCD camera to identify the detachment processes involved. Energies for both methods were calculated and divided into the two main steps of the detachment process: TPC pinning and three phase contact line sliding. The first step represents the energy barrier which must be overcome before detachment can begin. It is directly related to contact angle hysteresis. Detachment occurs during the second step, where the solid-vapor interface is replaced by solid-liquid and liquid-vapor. This step corresponds to the work of adhesion. The effects of surface tension, contact angle and hysteresis were well demonstrated with the three experimental methods. Good correlation was found between theoretical work of adhesion and measured energies.

CONTENTS

INTRODUCTION

Coarse particle flotation

Froth flotation is widely used in the mining industry to separate valuable minerals from other materials in their host environment. Minerals are separated by attaching themselves to rising air bubbles in the flotation cell and then recovered at the top of the cell. The ore must be ground small enough so that flotation can proceed (e.g. <.5 mm diameter). Coarse particle flotation provides opportunities for reduced grinding costs, increased recoveries and simplified flow-sheet designs (by eliminating certain classifying and other steps); all leading to increased throughput. However, the limits of coarse particle flotation have been well demonstrated as a severe decrease in recovery above a certain size with plant and laboratory batch tests data (Trahar 1981). A single bubble in a Hallimond tube was also used to demonstrate the dramatic drop in recovery with increasing particle size (Drzymala 1994). While other work identified a flotation domain from the minimum contact angle at which individual particle sizes will float (Crawford and Ralston 1988).

Flotation is a function of the probability of particle collection (Sutherland 1948)

$$P = P_C \cdot P_A \left(1 - P_D\right) \qquad [1]$$

where P_C, P_A, and P_D are the probabilities of collision, adhesion, and detachment respectively. The probability of collision depends on hydrodynamic effects in the flotation cell. The probabilities of adhesion and detachment are a combination of hydrodynamic effects and surface chemistry of the bubble and particle. Since surface chemistry is not affected by particle size, the probability of adhesion does not change much with particle size. Probability of detachment is then the main limiting factor in coarse particle flotation.

Research has focused on characterizing the various factors in flotation in attempts to increase the maximum floatable particle size. Early work identified the work of adhesion

$$W = T_{wa}\left(1 - \cos\theta\right) \qquad [2]$$

as the work done per unit area to create the air-solid interface at the expense of the solid-water interface (Wark 1933). Where T_{wa} is the surface tension of water and θ is the contact angle between the water and solid. Wark (1933) also attempted with limited success to calculate the maximum floatable particle size. The force and work required to remove a particle from the liquid-vapor interface was later measured using a centrifugal force apparatus and calculated as a function of the solid and liquid densities (Nutt 1960). Mathematical models of the flotation process followed taking into account the various sub-processes and physico-chemical properties involved in the system (Mika and Fuerstenau 1968). However, this model still suffered from a lack of proper description of these sub-processes to properly describe flotation. A theoretical evaluations of the upper particle size in flotation was calculated (Schulze 1977). These calculations were used to produce a rough estimation of the energy of rupture of a particle from a bubble. However, the work calculated in this manner does not represent an accurate description of the energy involved in the detachment process. A theoretical detachment force model was developed but disagreed by one order of magnitude when compared to forces measured using the centrifuge method (Nishkov and Pugh 1989).

More recent research on the stability of the bubble-particle aggregate in a flotation column using laboratory batch tests established some qualitative parameters for detachment energy of a particle from an oscillating bubble (Falutsu 1994). A bubble vibration detachment force measurement technique was developed to more closely resemble the conditions in flotation (Cheng and Holtham 1995), which compared favorably with previous theoretical work (Nutt 1960). Attachment and detachment efficiencies have also been described from calculation of the bubble-particle interaction forces in flotation and used to identify a maximum floatable particle size (Ralston et al. 1999).

Turbulent forces in the cell were recently modeled as the cause for bubble-particle detachment (Bloom and Heindel 2002; Pyke et al. 2003). Similarly, the detachment at the pulp-froth interface was described from experimental data by proposing an empirical model of percent apparent detachment during flotation (van Deventer et al. 2004). This later model compared attached and recovered particles to estimate the detachment.

Detachment force measurements

Direct measurements of detachment forces have been studied to better understand the detachment process and its implications for coarse particle flotation. Understanding of the detachment

process holds the key to increasing the upper size limit of floatable particles. The detachment force of a particle from a bubble has been measured to correlate it with contact angle, and interfacial energy values (Janczuk 1983; Janczuk 1985; Janczuk et al. 1990). However, these all use controlled contact areas which prevent the bubble from freely spreading on the particle surface. This may represent some cases encountered in flotation but fails to accurately describe the overall interaction between bubbles and particles. A centrifuge method has also been used to measure the detachment force (Schulze et al. 1989). However, this method does not allow for observation of the detachment process, providing only a force range at which particle detachment occurred.

The atomic force microscope has provided an ideal method for measuring interactions between bubbles and individual colloidal particles(Butt 1994; Butt et al. 1995; Preuss and Butt 1998a; Preuss and Butt 1999). However, they have proved more useful for measuring interactions during the approach cycle than detachment. The amount of bubble deflection during detachment is difficult to accurately measure, thus the detachment cycle cannot by accurately described using this method.

The detachment models proposed above describe the detachment force with varying success, but do not accurately provide the detachment energy process. In the work presented here, detachment forces were obtained using direct measurement methods and recorded by video to map the complete detachment process.

References

Adamson, A. W. (1997). *Physical Chemistry of Surfaces*, J. Wiley, New York.

Bloom, F., and Heindel, T. J. (2002). "On the structure of collision and detachment frequencies in flotation models." *Chemical Engineering Science*, 57(13), 2467-2473.

Butt, H.-J. (1994). "A Technique for Measuring the Force between a Colloidal Particle in Water and a Bubble." *Journal of Colloid and Interface Science*, 166(1), 109-117.

Butt, H.-J., Jaschke, M., and Ducker, W. (1995). "Measuring surface forces in aqueous electrolyte solution with the atomic force microscope." *Bioelectrochemistry and Bioenergetics*, 38(1), 191-201.

Byakova, A. V., Gnyloskurenko, S. V., Nakamura, T., and Raychenko, O. I. (2003). "Influence of wetting conditions on bubble formation at orifice in an inviscid liquid: Mechanism of bubble evolution." *Colloids and Surfaces A: Physicochemical and Engineering Aspects*, 229(1-3), 19-32.

Chatterjee, J. (2002). "Critical Eotvos numbers for buoyancy-induced oil drop detachment based on shape analysis." *Advances in Colloid and Interface Science*, 98, 265-283.

Cheng, T.-W., and Holtham, P. N. (1995). "The particle detachment process in flotation." *Minerals Engineering*, 8(8), 883-891.
Chibowski, E. (2003). "Surface free energy of a solid from contact angle hysteresis." *Advances in Colloid and Interface Science*, 103(2), 149-172.
Churaev, N. V., Ralston, J., Sergeeva, I. P., and Sobolev, V. D. (2002). "Electrokinetic properties of methylated quartz capillaries." *Advances in Colloid and Interface Science*, 96(1-3), 265-278.
Cohen, S. R., Naaman, R., and Sagiv, J. (1986). "Thermally induced disorder in organized organic monolayers on solid substrates." *J. Phys. Chem.*, 90, 3054-3056.
Crawford, R., and Ralston, J. (1988). "The influence of particle size and contact angle in mineral flotation." *International Journal of Mineral Processing*, 23, 1-24.
Datta, R. L., Napier, D. H., and Newitt, D. M. (1950). "The Properties and Behaviour of Gas Bubbles Formed at a Circular Orifice." *Trans. Inst. Chem. Eng.*, 28, 14 - 26.
DePalma, V., and Tillman, N. (1989). "Friction and wear of self-assembled trichlorosilane monolayer films on silicon." *Langmuir*, 5, 868-872.
Drzymala, J. (1994). "Characterization of materials by Hallimond tube flotation. Part 2: maximum size of floating particles and contact angle." *International Journal of Mineral Processing*, 42(3-4), 153-167.
Eckmann, D. M., and Cavanagh, D. P. (2003). "Bubble detachment by diffusion-controlled surfactant adsorption." *Colloids and Surfaces A: Physicochemical and Engineering Aspects*, 227(1-3), 21-33.
Eriksson, L. G. T., Claesson, P. M., Eriksson, J. C., and Yaminsky, V. V. (1996). "Equilibrium wetting studies of cationic surfactant adsorption on mica 1. Mono- and bilayer adsorption of CTAB." *Journal of Colloid and Interface Science*, 181, 476-489.
Eskilsson, K., and Yaminsky, V. V. (1998). "Deposition of monolayers by retraction from solution: Ellipsometric study of cetyltrimethylammonium bromide adsorption at silica-air and silica-water interfaces." *Langmuir*, 14, 2444-2450.
Falutsu, M. (1994). "Column flotation froth characteristics -- stability of the bubble-particle system." *International Journal of Mineral Processing*, 40(3-4), 225-243.
Frank, B., and Garoff, S. (1996). "Surfactant self-assembly near contact lines: control of advancing surfactant solutions." *Colloids and Surfaces A: Physicochemical and Engineering Aspects*, 116(1-2), 31-42.
Gun, J., Iscovici, R., and Sagiv, J. (1984). "On the formation and structure of self-assembling monolayers. II. A comparative study of Langmuir-Blodgett and adsorbed films using ellipsometry and IR reflection-absorption spectroscopy." *Journal of Colloid and Interface Science*, 101, 201-213.
Gun, J., and Sagiv, J. (1986). "On the formation and structure of self-assembling monolayers. III. Time of formation, solvent retention, and release." *Journal of Colloid and Interface Science*, 112, 457-472.
Hughes, R. R., Hanklos, A. E., Evans, H. D., and Maycock, R. L. (1955). "The Formation of Bubbles at Simple Orifices." *Chemical Engineering Progress*, 51(12), 557 - 563.
Huh, C., and Scriven, L. E. (1969). "Shapes of axysimmetric fluid interfaces of unbounded extent." *Journal of Colloid and Interface Science*, 35, 323.
Iimura, K.-i., and Kato, T. (2000). "Robustness of monolayers on the solids; comparative studies on thermal, solvent, pH, and mechanical resistance among 1-layer LB films of cadmium arachidate and alkylchlorosilanes." *Colloids and Surfaces A: Physicochemical and Engineering Aspects*, 171(1-3), 249-264.
Israelachvili, J. (1991). *Intermolecular & Surface Forces*, Elsevier Ltd., London.
James, D. F. (1974). "The meniscus on the outside of a small circular cylinder." *Journal of Fluid Mechanics*, 63(4), 657-664.

Janczuk, B. (1983). "The effect of n-alkanes on the force of air bubble detachment from a quartz surface in water." *Powder Technology*, 34(2), 243-247.
Janczuk, B. (1985). "Force of air bubble detachment from a quartz surface wetted with n-alkane in aqueous solutions of methanol and propanol." *Powder Technology*, 41(2), 106-112.
Janczuk, B., Wojcik, W., and Bialopiotrowicz, T. (1990). "Studies on contact angle and work of adhesion in the system coal/n-alkane film--air bubble--water." *Powder Technology*, 61(3), 211-216.
Janczuk, B., Wojcik, W., and Zdziennicka, A. (1999). "Wettability and surface free energy of glass in the presence of cetyltrimethylammonium bromide." *Materials Chemistry and Physics*, 58(2), 166-171.
Jones, S. F., Evans, G. M., and Galvin, K. P. (1999). "Bubble nucleation from gas cavities -- a review." *Advances in Colloid and Interface Science*, 80(1), 27-50.
Keen, G. S., and Blake, J. R. (1996). "A Note on the Formation and Rise of a Bubble from a Submerged Nozzle, Including Effects of Bulk- and Surface-Dilatational Viscosity." *Journal of Colloid and Interface Science*, 180(2), 625-628.
Li, C., and Somasundaran, P. (1992). "Reversal of Bubble Charge in Multivalent Inorganic Salt Solutions - Effect of Aluminum." *Journal of Colloid and Interface Science*, 148(2), 587-591.
Li, H. C. (1958). "Adsorption of organic and inorganic ions on quartz," PhD, Massachusetts Institute of Technology, Cambridge.
Li, H. Z., Mouline, Y., and Midoux, N. (2002). "Modelling the bubble formation dynamics in non-Newtonian fluids." *Chemical Engineering Science*, 57(3), 339-346.
Li, H. Z., and Quiang, S. (1998). "Formation des bulles dans les fluides newtoniens et non newtoniens." *Fluid Mechanics*, 326, 301-308.
Lin, J. N. (1994). "Role of interfacial tension in the formation and the detachment of air bubbles. 1. A single hole on a horizontal plane immersed in water." *Langmuir*, 10, 936-942.
Liu, J.-F., Min, G., and Ducker, W. (2001). "AFM study of adsorption of cationic surfactants and cationic polyelectrolytes at the silica-water interface." *Langmuir*, 17, 4895-4903.
Maoz, R., and Sagiv, J. (1984). "On the formation and structure of self-assembling monolayers. I. A comparative ATR-wettability study of Langmuir-Blodgett and adsorbed films on flat substrates and glass microbeads." *Journal of Colloid and Interface Science*, 100, 465-496.
Maoz, R., and Sagiv, J. (1987a). "Penetration-controlled reactions in organized monolayer assemblies. 1. Aqueous permanganate interaction with monolayer and multilayer films of long-chain surfactants." *Langmuir*, 3, 1034-1044.
Maoz, R., and Sagiv, J. (1987b). "Penetration-controlled reactions in organized monolayer assemblies. 2. Aqueous permanganate interaction with self-assembling monolayers of long-chain surfactants." *Langmuir*, 3, 1045-1051.
Mika, T. S., and Fuerstenau, D. W. "A microscopic model of the flotation process." *8th International Mineral Processing Congress*, Leningrad, U.S.S.R., 52.
Murray, B. S., Godfrey, J., Griesen, F., Healy, T., Lovelock, B., and Scales, P. (1991). "Spectroscopic and electrokinetic study of pH-dependent ionization of langmuir-blodgett films." *Langmuir*, 7, 3057-3064.
Nahra, H. K., and Kamotani, Y. (2003). "Prediction of bubble diameter at detachment from a wall orifice in liquid cross-flow under reduced and normal gravity conditions." *Chemical Engineering Science*, 58(1), 55-69.
Nishkov, I., and Pugh, R. J. (1989). "The relationship between flotation and adhesion of galena particles to the air-solution interface." *International Journal of Mineral Processing*, 25, 275-288.
Nutt, C. W. (1960). "Froth flotation: The adhesion of solid particles to flat interfaces and bubbles." *Chemical Engineering Science*, 12, 133-141.

Ouz, H., and Zeng, J. (1997). "Axisymmetric and three-dimensional boundary integral simulations of bubble growth from an underwater orifice." *Engineering Analysis with Boundary Elements*, 19(4), 319-330.
Parikh, A. N., Allara, D. L., Ben Azouz, I., and Rondelez, F. (1994). "An Intrinsic Relationship between Molecular Structure in Self-Assembled n-Alkylsiloxane Monolayers and Deposition Temperature." *J. Phys. Chem.*, 98, 7577-7590.
Parikh, A. N., Schivley, M. A., Koo, E., Seshadri, K., Aurentz, D., Mueller, K., and Allara, D. L. (1997). "n-Alkylsiloxanes: From Single Monolayers to Layered Crystals. The Formation of Crystalline Polymers from the Hydrolysis of n-Octadecyltrichlorosilane." *Journal of the American Chemical Society*, 119, 3135-3143.
Preuss, M., and Butt, H.-J. (1998a). "Direct measurement of particle-bubble interactions in aqueous electrolyte: dependence on surfactants." *Langmuir*, 14, 3164-3174.
Preuss, M., and Butt, H.-J. (1998b). "Measuring the Contact Angle of Individual Colloidal Particles." *Journal of Colloid and Interface Science*, 208(2), 468-477.
Preuss, M., and Butt, H.-J. (1999). "Direct measurement of forces between particles and bubbles." *International Journal of Mineral Processing*, 56(1-4), 99-115.
Pyke, B., Fornasiero, D., and Ralston, J. (2003). "Bubble particle heterocoagulation under turbulent conditions." *Journal of Colloid and Interface Science*, 265(1), 141-151.
Ralston, J., Fornasiero, D., and Hayes, R. (1999). "Bubble-particle attachment and detachment in flotation." *International Journal of Mineral Processing*, 56(1-4), 133-164.
Sagiv, J. (1980). "Organized monolayers by adsorption, 1. Formation and structure of oleophobic mixed monolayers on solid surfaces." *Journal of the American Chemical Society*, 102(1), 92-98.
Schulze, H. J. (1977). "New theoretical and experimental investigations on stability of bubble/particle aggregates in flotation: a theory on the upper particle size of floatability." *International Journal of Mineral Processing*, 4, 241-259.
Schulze, H. J., Wahl, B., and Gottschalk, G. (1989). "Determination of adhesive strength of particles within the liquid/gas interface in flotation by means of a centrifuge method." *Journal of Colloid and Interface Science*, 128(1), 57-65.
Shaw, D. J. (1992). *Introduction to colloid and surface chemistry*, Butterworth-Heinemann, Boston.
Silberzan, P., Leger, L., Ausserre, D., and Benattar, J. J. (1991). "Silanation of silica surfaces. A new method of constructing pure or mixed monolayers." *Langmuir*, 7, 1647-1651.
Sutherland, K. L. (1948). "Kinetics of the flotation process." *J. Phys. Chem.*, 52, 394-425.
Trahar, W. J. (1981). "A rational interpretation of the role of particle size in flotation." *International Journal of Mineral Processing*, 8, 289-327.
Tripp, C. P. (1991). "Reaction of chloromethylsilanes with silica: a low-frequency infrared study." *Langmuir*, 7, 923-927.
Tripp, C. P., and Hair, M. L. (1995). "Direct Observation of the Surface Bonds between Self-Assembled Monolayers of Octadecyltrichlorosilane and Silica Surfaces: A Low-Frequency IR Study at the Solid/Liquid Interface." *Langmuir*, 11, 1215-1219.
van Deventer, J. S. J., Feng, D., and Burger, A. J. (2004). "Transport phenomena at the pulp-froth interface in a flotation column: II. Detachment." *International Journal of Mineral Processing*, In Press, Corrected Proof.
van Oss, C. J. (1994). *Interfacial Forces in Aqueous Media*, Marcel Dekker, Inc., New York.
van Oss, C. J., Chaudhury, M. K., and Good, R. J. (1987). "Monopolar surfaces." *Advances in Colloid and Interface Science*, 28, 35-64.
Wark, I. W. (1933). "The physical chemistry of flotation. 1 The significance of contact angle in flotation." *Journal of Physical Chemistry*, 37, 623-644.

Wasserman, S. R., Tao, Y.-T., and Whitesides, G. M. (1989). "Structure and reactivity of alkylsiloxane monolayers formed by reaction of alkyltrichlorosilanes on silicon substrates." *Langmuir*, 5, 1074-1087.

Yaminsky, V. V. (1994). "Thermodynamic Analysis of Solute Effects on Surface Forces. Adhesion between Silicates in Solutions of Cationic Surfactants." *Langmuir*, 10, 2710-2717.

Yaminsky, V. V., and Ninham, B. W. (1999). "Surface forces vs. surface compositions. Colloid science from the Gibbs adsorption perspective." *Advances in Colloid and Interface Science*, 83(1-3 SU -), 227-311.

Yaminsky, V. V., and Yaminskaya, K. B. (1995). "Thermodynamic analysis of solute effects on contact angles. Equilibrium adsorption of cationic surfactants at silica-vapor and silica-water interfaces." *Langmuir*, 11, 936-941.

Yang, Z. L., Dinh, T. N., Nourgaliev, R. R., and Sehgal, B. R. (2001). "Numerical investigation of bubble growth and detachment by the lattice-Boltzmann method." *International Journal of Heat and Mass Transfer*, 44(1), 195-206.

Ye, S., Nihonyanagi, S., and Uosaki, K. (2001). "Sum frequency generation (SFG) study of the pH-dependent water structure on a fused quartz surface modified by an octadecyltrichlorosilane (OTS) monolayer." *Physical Chemistry Chemical Physics*, 3(16), 3643-3469.

Yiantsios S. G., and Karabelas A. J. (1995). "Detachment of Spherical Microparticles Adhering on Flat Surfaces by Hydrodynamic Forces." *Journal of Colloid and Interface Science*, 176(1), 74-85.

Zhao, X., and Kopelman, R. (1996). "Mechanism of organosilane self-assembled monolayer formation on silica studied by second-harmonic generation." *J. Phys. Chem.*, 100, 11014-11018.

Zhuravlev, L. T. (1987). "Concentration of hydroxyl groups on the surface of amorphous silicas." *Langmuir*, 3, 316-318.

CHAPTER 1 - DIRECT FORCE AND ENERGY MEASUREMENT OF BUBBLE-PARTICLE DETACHMENT

Abstract

Bubble-particle detachment is the main limiting factor in coarse particle flotation. Detachment occurs when forces on the bubble-particle aggregate in a flotation cell overcome the strength of adhesion. Strength of adhesion depends on the particle surface roughness, surface chemistry, and surface tension of the liquid media. In the present work, detachment forces between spherical particles of varying hydrophobicity and air bubbles were directly measured using a modified KSV 70 surface tensiometer. The experiment was recorded with a 1 kHz CCD camera to monitor changes in bubble-particle contact area, bubble size and shape, and "neck formation". The detachment energy was found to consist of three parts; bubble stretching, bubble sliding, and bubble necking. The measured energies compared favorably to the work of adhesion.

Introduction

Froth flotation is widely used in the mining industry to separate valuable minerals from other materials in their host environment. Minerals are separated by attaching themselves to rising air bubbles in the flotation cell and then recovered at the top of the cell. The ore must be ground small enough so that flotation can proceed (e.g. <.5 mm diameter). Coarse particle flotation provides opportunities for reduced grinding costs, increased recoveries and simplified flow-sheet designs (by eliminating certain classifying and other steps); all leading to increased throughput.

Flotation is a function of the probability of particle collection (Sutherland 1948);

$$P = P_C \cdot P_A \left(1 - P_D\right) \qquad [3]$$

where P_C, P_A, and P_D are the probabilities of collision, adhesion, and detachment respectively. The probability of collision depends on hydrodynamic effects in the flotation cell. The probabilities of adhesion and detachment are a combination of hydrodynamic effects and surface chemistry of the bubble and particle. Since surface chemistry is not affected by particle size, the probability of adhesion does not change much with particle size. Probability of detachment is then the main limiting factor in coarse particle flotation.

Theory

Flotation efficiency can be described largely in terms of contact angle or particle hydrophobicity. The equilibrium contact angle, θ_{Eq}, is the angle formed between a bubble and solid surface in water once the bubble becomes stable. It is described thermodynamically by Young's equation.

$$\frac{\gamma_{SV} - \gamma_{SL}}{\gamma_{LV}} = \cos\theta_{Eq} \qquad [4]$$

Where, γ_{SV}, γ_{SL}, and γ_{LV} represent the solid-vapor, solid-liquid, and liquid-vapor interfacial tensions respectively. Where the liquid, vapor, and solid phases meet is referred to as the three-phase-contact (TPC) point or line. The interaction between two materials 1 (air) and 2 (solid) immersed in a third liquid 3 is given by (van Oss 1994);

$$\Delta G = \gamma_{SV} - \gamma_{SL} - \gamma_{LV} \qquad [5]$$

Combining equations [4] and [5] leads to the Young-Dupré equation, which gives the free energy change for the attachment of a bubble onto a solid surface.

$$-\Delta G = \gamma_{LV}\left(1 - \cos\theta\right) \qquad [6]$$

This represents the work required to remove liquid from the solid surface and bubble surface and create a new solid-vapor interface. This change in free energy is referred to as the work of adhesion since it represents the work required to form a bubble-particle aggregate. Calculating the actual energy spent requires the addition of an area term to equation [6] to account for the various initial and final interfacial areas. The thermodynamics of the bubble-article aggregate formation are reversible so that work of adhesion can be used to describe the energy required for detachment as well.

Bubble-particle detachment in flotation is mostly caused by turbulence in the cell. Once the forces on the particle are larger than the adhesion force, the particle detaches.

The detachment process depends on contact angle, media surface tension and surface heterogeneity or contact angle hysteresis. Contact angle determines the contact area between bubble and particle, which sets the distance that the TPC line will have to travel on the surface before detachment occurs. Surface tension corresponds to the tensile strength of the bubble.

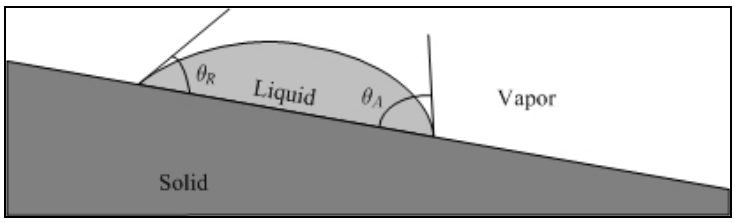

Figure 1 - Advancing and receding contact angle

Contact angle hysteresis has a role in determining the force and energy that must be overcome before the detachment process can begin. Hysteresis is caused by surface roughness (Israelachvili 1991) and on a smaller scale by surface energy of the solid (Chibowski 2003). When a liquid drop moves on a surface, the angle formed at the side of the drop which is advancing on the surface is referred to as the advancing contact angle (see Figure 1). And reversely, the angle formed at the receding end is the receding contact angle. If a bubble is detached from a particle, the TPC will not move until the advancing contact angle is reached. At the higher contact angle the water can advance on the solid surface. The energy spent shifting the TPC from equilibrium to advancing angle represents energy barrier which must be overcome before the detachment process can begin. Alternatively, hysteresis also raises some questions about the reversibility of the work of adhesion. It is believed that during the recession process, the interface may not be retracing its original path, so that the process may not be thermodynamically reversible (Israelachvili 1991). This will be revisited in the results and discussion.

Surface tension is an important determining factor in bubble-particle adhesion and detachment. It determines the strength and elasticity characteristics of the bubble. A lower tension means a less 'stretchable' but stronger bubble. A more 'stretchable' bubble may require more energy, but less force to detach.

Experimental Methods

Forces were measured using a Sigma 70 surface tensiometer (KSV Instruments Ltd.). This equipment was a hanging balance with a resolution of 1μN. The bubble-particle interactions were recorded using a Phantom V4.0 CCD camera (Photo-Sonics Inc.). Interactions were also photographed by a 4.0M pixel S4 digital camera (Canon Inc.) equipped with a reversed 50mm AF NIKKOR (Nikon Corporation) lens (which allows it to act as a macro lens).

All the reagents used in the experiment were at least ACS grade and were obtained from either Fisher Scientific or Alfa Aesar. Soda lime glass spheres with a mean diameter of 2007μm ±40μm (Duke Scientific Corporation) were methylated with octadecyltrichlorosilane (OTS) and butyltrichlorosilane (BTS) to create surfaces with varying hydrophobicity. The methylation procedure consists of washing the samples for 1hr in Piranha solution (30% H_2O_2:70% H_2SO_4) at 60-70°C. The samples are then rinsed in Nanopure water and immersed in a 10^{-5}M silane solution in toluene for 30-90 minutes depending on the target contact angle. The samples are then removed from solution and first rinsed with chloroform to remove any excess toluene from the surface, then acetone to remove any physisorbed silane. Following this, the samples are placed in acetone in an ultrasonic bath for at least 20min. This breaks up any amalgams of polymerized silane which may have accumulated at the silica surface, thereby creating a more uniform silane coating. The samples are stored in Nanopure water in sealed containers until the experiment.

A sphere was fixed to the end of a glass hook, which was manufactured by the Virginia Tech glass shop, using Crystalbond™ 509 glue (Electron Microscopy Sciences). The sphere was then suspended from the tensiometer above the bubble, which sat on the end of a thick glass rod (see Figure 2). The bubble support sat in a glass cell filled with water on top of a mechanical stage that could be moved vertically at 1mm/min to bring the bubble and particle into contact and then detach them.

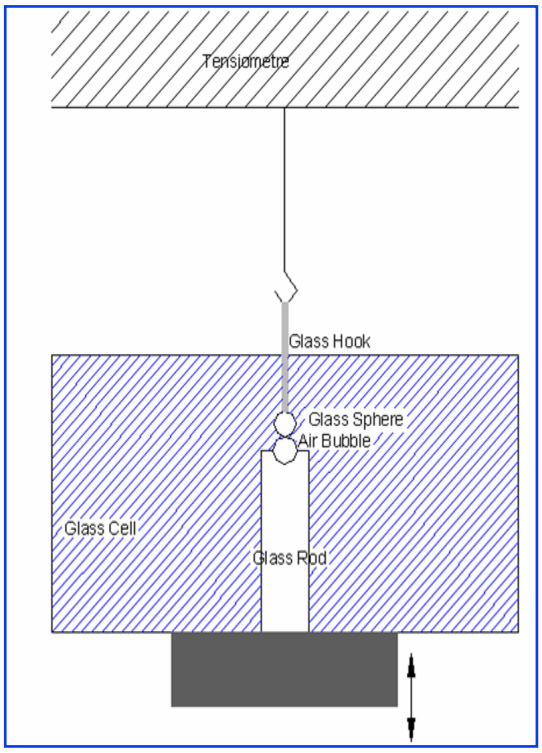

Figure 2 - Experimental apparatus

The tensiometer was connected to a computer to record force and distances every .25s. The reported distance is the relative position of the mechanical stage. Although the actual position is not known, the distance traveled during the detachment process (used for energy calculations) is still recorded.

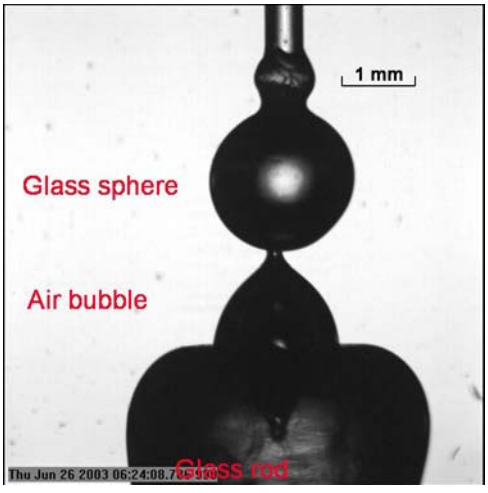

Figure 3 - Bubble-particle interaction

Figure 3 is a picture of the air bubble attached to its support as it is being pulled away from a glass sphere.

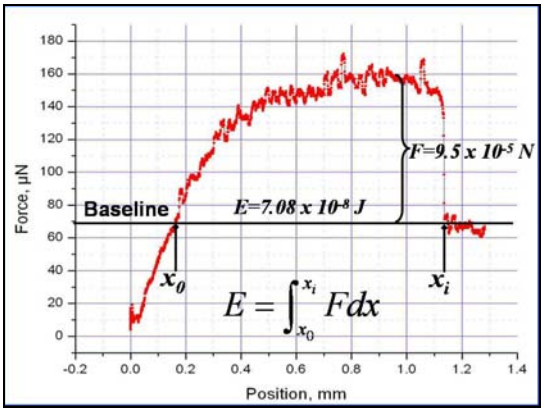

Figure 4 - Detachment force curve

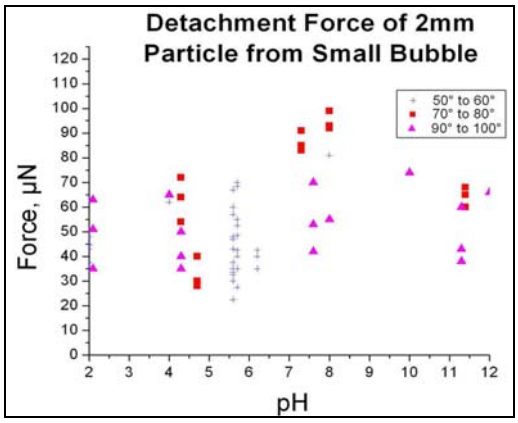

Figure 5 - Round bubble detachment force

A typical output curve from the surface tensiometer is shown in Figure 4. The detachment force is measured as the difference between the maximum and the baseline. The baseline is the force at which the sphere is detached. This is the force exerted on the instrument from the weight of the sphere only. The energy is taken as the integral of the force applied across the distance from equilibrium to detachment. Equilibrium is shown in the figure as x_0. It is the point at which the bubble is neither pushing up nor pulling down on the sphere.

Detachment force measurement between the sphere and bubble were not very reproducible when using a bubble of similar size as the sphere. Figure 5 displays force measurements performed under these conditions at varying contact angles.

In the next series of measurements, the small bubble was replaced by an infinitely large (or flat) bubble. The flat bubble removes the variations in bubble radius. The air bubble was created using a PTFE rod, with a cone bored out in the centre, connected to a syringe that provided the air for the bubble, see Figure 6.

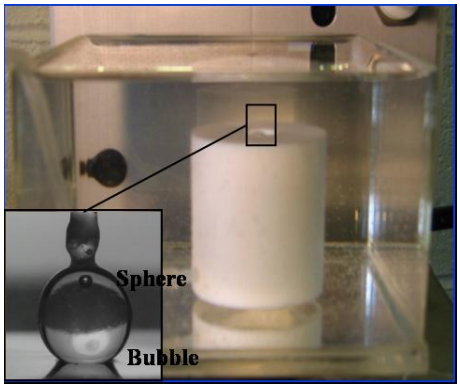

Figure 6 - Flat bubble apparatus

The flat bubble approach produced much more repeatable results as demonstrated in Figure 7. The CCD camera and digital camera were used to record the bubble-particle interactions to better understand the detachment mechanism.

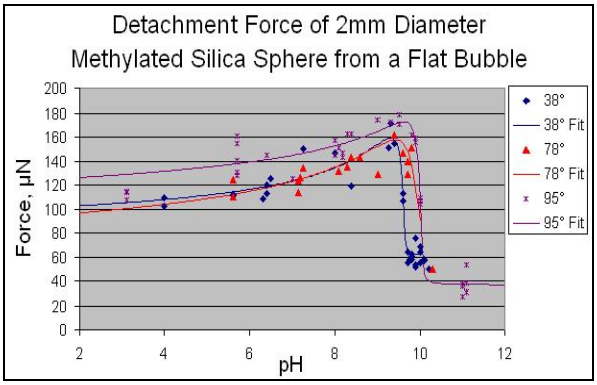

Figure 7 - Flat bubble detachment force

Results and Discussion

Detachment Mechanism

Bubble-particle detachment can be separated into two separate phases; E_1 and E_2; the bubble stretching, and the bubble detaching or sliding (Figure 8). The first phase is dependent on the chemical properties of the bulk solution, namely surface tension, and the second phase is dependent on the hydrophobicity of the particle.

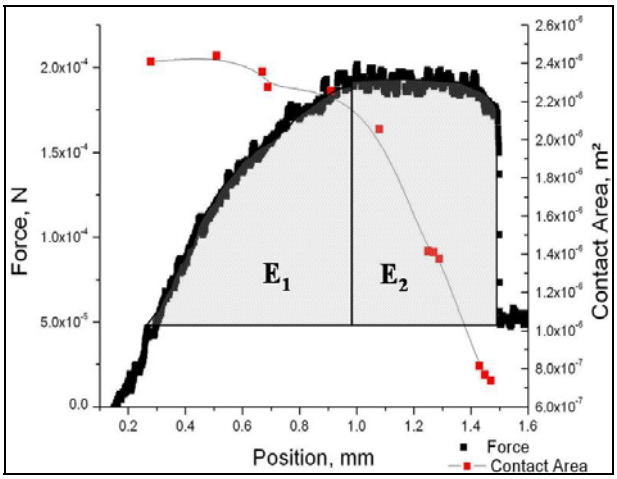

Figure 8 - Detachment force and contact area of methylated sphere from flat bubble (contact angle = 95°)

In the first component, the three-phase-contact (TPC) line is pinned on the silica surface while the bubble is being stretched. The bubble stretches until the advancing contact angle is reached. Surface roughness may cause the bubble to stretch slightly beyond this point. Once the advancing contact angle is reached, the vapor phase retracts from the sphere and the bubble commences detachment. The maximum force reached is dependent on the magnitude of the hysteresis and on surface tension of the media. Figure 8 demonstrates the two stages of the detachment process. Contact area remains constant (E_1) until enough force is applied to move the TPC line and the advancing contact angle has been reached. Once this occurs the force remains constant as the TPC line moves 'down' the sphere until detachment occurs.

The second component of the detachment process is dependent on particle hydrophobicity because this determines the starting contact area between solid and vapor. It also establishes a maximum, the advancing contact angle, which must be reached before movement of the TPC line can begin. Comparison of the different energy components with work of adhesion calculations further demonstrated this relationship.

Table 1 – Sphere-sphere energy of detachment and work of adhesion comparison

θ	48°	95°
E_1	1.824 x 10^{-2} J/m²	1.971 x 10^{-2} J/m²
E_2	1.794 x 10^{-2} J/m²	4.855 x 10^{-2} J/m²
E_{total}	3.618 x 10^{-2} J/m²	6.826 x 10^{-2} J/m²
W_a	1.367 x 10^{-2} J/m²	4.354 x 10^{-2} J/m²

Work of adhesion in the Table 1 was calculated from the differences in surfaces areas of the various interfaces between the initial attached and final detached states.

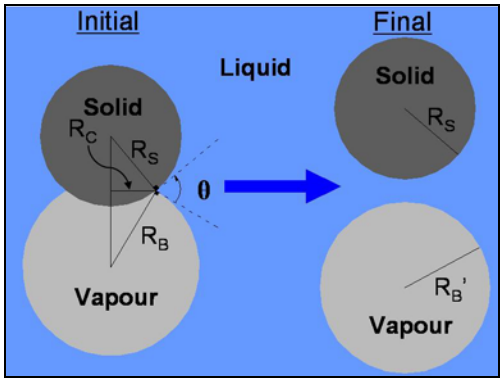

Figure 9 - Sphere-sphere work of adhesion calculation

The relationship is solved by assuming the vapor volume does not change from the initial to the final state. Solving the relationship gives the following equation for work of adhesion.

$$W_A = \frac{\Delta A_{LV}\gamma_{LV} + A_C\left(\gamma_{SL} - \gamma_{SV}\right)}{A_C} \qquad [7]$$

As can be seen from Table 1, the energy E_1, is fairly constant for 48° and 95° surfaces, because this portion of the detachment does not depend on the surface chemistry properties of the sphere. In mineral processing, this part of the detachment energy could be maximized using frother to create stronger bubbles. E_1 can also be regarded as an activation energy for detachment due to surface roughness and the magnitude dependent on the surface tension of the bulk solution in which the process takes place. E_2 shows good correlation with the work of adhesion calculation because it is the actual energy of detachment whereas E_1 is the energy necessary to begin the detachment process.

Detachment Mechanism Model

Sphere and flat bubble detachment measurements provided a better insight into the detachment process, as bubble deformation was much more pronounced with the 'large' radius bubble. Figure 10 describes the bubble deformation geometry as the sphere is pulled away.

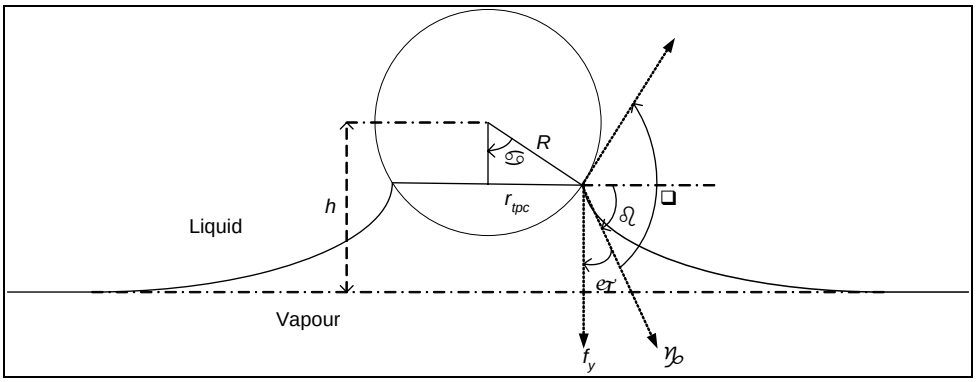

Figure 10 - Flat bubble - sphere detachment geometry

The air-water interface deformation as the sphere is pulled away from the bubble can be described by the following solution (Huh and Scriven 1969) to the Young-Laplace equation for capillarity.

$$\frac{d^2y}{dx^2} = \left[1+\left(\frac{dy}{dx}\right)^2\right]\left[\frac{\rho g}{\gamma}y\sqrt{1+\left(\frac{dy}{dx}\right)^2} - \frac{1}{x}\frac{dy}{dx}\right] \qquad [8]$$

where ρ is the density of the liquid, g is gravity, and γ is the interfacial tension.

Equation [8] can be solved numerically and leads to the following solution describing the height, h, of the TPC line above the flat bubble (James 1974).

$$h = R\sin\alpha\sin\beta\left[\ln\frac{4L}{R\sin\alpha\left(1+\cos\beta\right)} - \sigma\right]$$
$$L \equiv \sqrt{\frac{\gamma}{\rho g}} \qquad [9]$$

R is the radius of the sphere, L is the capillary length and σ is the Euler constant, 0.577. The force exerted by the bubble onto the sphere depends on the contact angle and shape of the bubble as these determine the angle at which the force is applied. The total force F exerted on the sphere in the vertical direction is

$$F = 2\pi R \sin\alpha \cdot \gamma_{LV} \cos\left(\frac{\pi}{2} - \theta + \alpha\right) \qquad [10]$$

When the sphere is at equilibrium position the bubble is not deformed and is not exerting any force on the sphere. The angle between the sphere and bubble at this point is the receding contact angle (Preuss and Butt 1998b), which can easily be calculated from the contact radius. As the sphere is pulled away, the shape of the bubble is defined by equation [8]. The contact angle is then calculated by solving equation [9] at progressing heights of the sphere above the bubble. Once the contact angle is known, and assuming a constant contact radius during the stretching portion of the detachment process, the force is calculated using equation [10] for each sphere height above the flat bubble datum. Force distance curves obtained in this manner were compared to the measured force curves, see Figure 11.

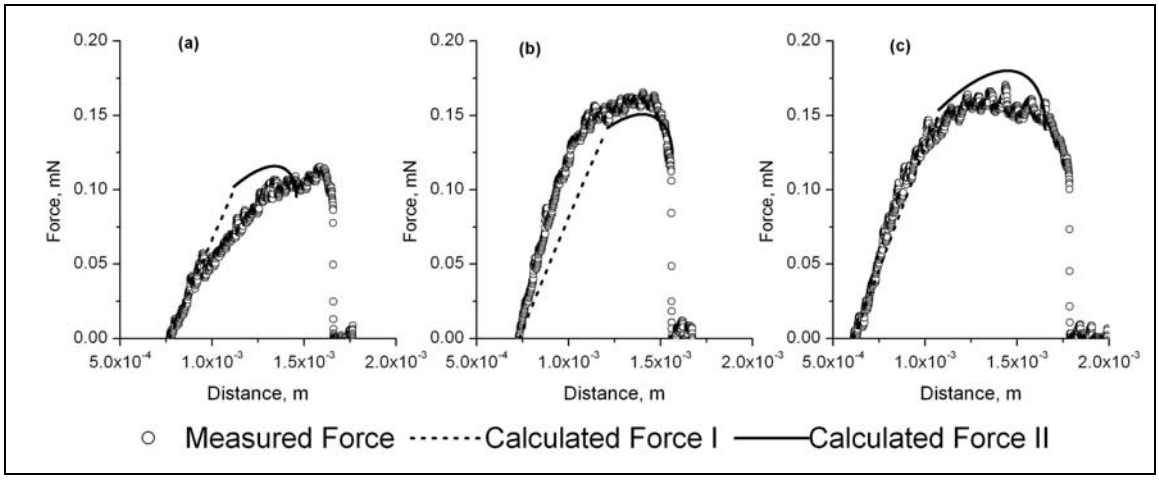

Figure 11 – Detachment force VS sphere center distance from the flat bubble for (a) 38° (b) 78° (c) 95° methylated silica spheres

'Calculated Force I' represents the stretching portion of the force curve calculated as described above. It represents the force exerted by the bubble on the sphere as the contact angle shifts from receding to advancing contact angle. 'Calculated Force I' shows good correlation with the

measured force curve, although, graph (a) demonstrates some of the difficulty in simulating the detachment process. The experimental and calculated forces are in agreement for the first third of the curve, at which point the bubble seems to have 'slipped' on the sphere, causing a change in the slope due to the new contact radius.

Once the advancing contact angle is reached the bubble then begins sliding off the particle. This portion of the detachment curve was modeled by again solving equation [9] at progressing sphere heights, but now assuming that θ stays constant (note that $\theta = \alpha + \beta$). This portion of the detachment process is represented by 'Calculated Force II', which displayed good correlation with the measured force. Variation in this portion of the curve is probably due to the assumption that θ is constant. This is not entirely correct as the bubble will still experience some localized pinning on the sphere surface as it slides off. The calculated force also assumes a clean break instead of the necking behavior of the bubble seen at higher contact angles. Necking was observed during the experiment as contact angle increased, as evidenced by the small bubble often remaining on the sphere after detachment, see Figure 12. This behavior is clearly visible when comparing graphs (a) and (c). In graph (a) there is almost no necking, so the measured force drops off abruptly at the end of the curve. The force curve in graph (c) slowly decreases before finally falling to zero.

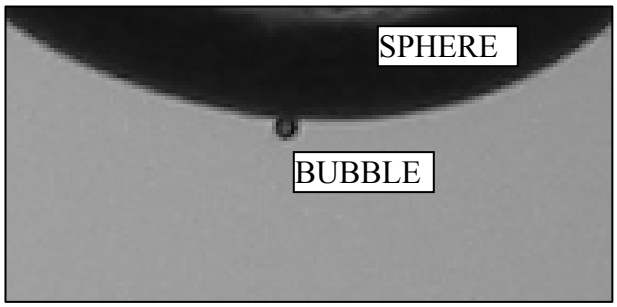

Figure 12 - Bubble on sphere surface after detachment

The measured energy was compared to the calculated work of adhesion for a sphere and flat bubble interaction. Work of adhesion was calculated with the following equation

$$W_A = \gamma_{LV} \pi R^2 \left[\sin^2 \theta_R - 2 \cos \theta_{Eq} \left(1 - \cos \theta_R \right) \right] \qquad [11]$$

where R is the radius of the sphere and θ_R and θ_{Eq} are the receding and equilibrium contact angles respectively. The work of adhesion calculation describes the change in free energies between the initial and final states as described in Figure 13.

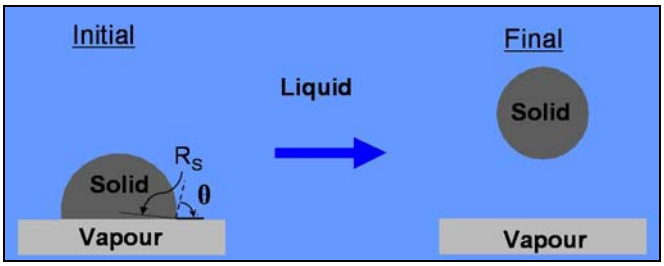

Figure 13 - Sphere - flat bubble work of adhesion calculation

Equation [11] assumes that the initial state is receding contact angle, and the equilibrium contact angle is used to cancel out the solid-liquid and solid-vapor interfacial tension terms by means of Young's equation. If the angle at the initial stage is believed to equal equilibrium contact angle, then equation [11] reduces to the more commonly seen

$$W_A = \gamma_{LV} \pi R^2 \left(1 - \cos\theta\right)^2 \qquad [12]$$

Equation [12] for work of adhesion overestimates the energy of detachment with the difference between experimental and calculated increasing with contact angle. Equation [12] is also valid in the rare case where there is no contact angle hysteresis.

Work of adhesion (equation [11]) was compared to the measured energies of the detachment process. The experimental energy, E_2, was found to be similar to the work of adhesion, see Table 2 below.

Table 2 - Work of adhesion and experimental energy comparison

θ_R	θ_{Eq}	E_2, J	$E_{necking}$, J	E_2 - $E_{necking}$, J	W_A, J	% error
39.688	50.063	3.673E-08	7.771E-09	2.896E-08	2.560E-08	11.6%
43.118	56.588	5.970E-08	1.582E-08	4.387E-08	3.883E-08	11.5%
52.267	64.984	1.002E-07	2.972E-08	7.044E-08	6.800E-08	3.5%

However, if the energy of bubble necking as previously described is subtracted from E_2, then work of adhesion corresponds almost exactly to the measured energy (% error in the table is the

error between W_A and E_2 minus the necking energy). This further supports the previous claim that E_2 represents the energy of detachment and E_1 is simply the energy barrier to detachment.

OTS Layer Modification With pH

The detachment force was measured over a wide pH range to observe its effect. This led to the finding of a pH dependence of the OTS layer on a silica surface. As pH in the bulk solution increases the hydrophobicity of the coating increases (see Figure 7). As the pH further increases, the detachment energy was observed dropping off drastically.

OTS was used because it forms a well ordered hydrophobic layer on the silicon surface (Cohen et al. 1986; Gun et al. 1984; Gun and Sagiv 1986; Maoz and Sagiv 1984; Maoz and Sagiv 1987a; Maoz and Sagiv 1987b). These OTS layers have been shown to be very resilient, resisting change in temperature, bulk solution chemistry, and even physical abrasion (DePalma and Tillman 1989; Iimura and Kato 2000). The adsorption reaction involves the formation of covalent bonds between the polar head group and $SiOH^-$ groups on the surface (Sagiv 1980; Tripp 1991; Tripp and Hair 1995; Zhao and Kopelman 1996). Polymerization between adsorbed sylil groups to form Si-O-Si networks has been reported (Zhao and Kopelman 1996). This seems unlikely due to the large space between ≡Si-OH groups on the surface (Zhuravlev 1987). Rather, the formation of –Si-O-Si- groups between OTS molecules and an adsorbed water layer on the quartz surface is more likely (Parikh et al. 1994; Parikh et al. 1997; Silberzan et al. 1991; Ye et al. 2001; Zhao and Kopelman 1996). This layer begins the ordering of the water molecules at the OTS coated surface, which is the nature of the hydrophobic behavior of the solid.

At acidic pH, the orientation of the water molecules at the substrate is reversed (Ye et al. 2001), which leads to a less ordered molecular structure of the water molecules in the bulk interface, thereby reducing the hydrophobic nature of the overall surface. This explains the slightly lower detachment force seen at acidic pH. As pH increases, detachment force increases until a peak at pH 9.5. The sudden drop following this peak is due to partial etching of the OTS layer at alkaline pH. IN the event of a 'perfect' monolayer, the molecules are packed too tight and prevent the penetration of OH^- ions. But etching can occur at defects in the OTS layer, and continues as more surface is uncovered (Iimura and Kato 2000; Wasserman et al. 1989). This explains the sharp drop in detachment force at alkaline pH.

The possibility of increased energy barrier with increasing pH has been analyzed as another source for the increase in detachment force and energy. OTS coated surfaces have been shown to behave similarly (electrokinetically) to bare silica with changing pH (Murray et al. 1991). In other words, the amorphous nature of silica is conserved on a coated surface.

The electrostatic bubble-particle interaction can be determined using the following relationship (Shaw 1992).

$$V_E = \frac{\pi\varepsilon_0\varepsilon R_1 R_2\left(\psi_1^2+\psi_2^2\right)}{4\left(R_1+R_2\right)}\left[\frac{2\psi_1\psi_2}{\psi_1^2+\psi_2^2}\ln\left(\frac{1+e^{-\kappa H}}{1-e^{-\kappa H}}\right)+\ln\left(1-e^{-2\kappa H}\right)\right] \qquad [13]$$

Where Ψ_1 and Ψ_2 represent the Stern potentials of the particle and air bubble of radii R_1 and R_2, respectively, ε is the dielectric constant of the medium, $1/\kappa$ the Debye length. Surface potential values from literature were used for the calculations (Li and Somasundaran 1992; Li 1958; Yiantsios S. G. and Karabelas A. J. 1995)

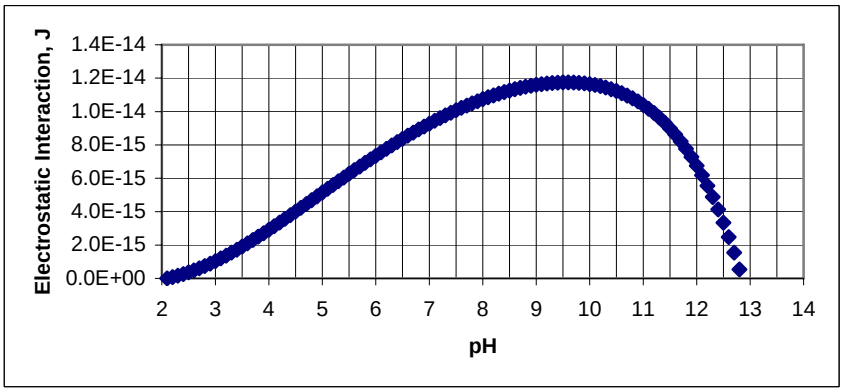

Figure 14 - Electrostatic interaction between a 2mm particle and a flat bubble

As Figure 14 indicates the peak repulsion is at pH 9.5. However, the interaction energy only amounts to 1.2 x 10^{-14} J, which is about 10^7 times lower than the interaction energies associated with these detachment processes. Thus, the energy of detachment variation at pH 9.5 is due to modification of the OTS layer and the water layer at the silica surface.

Summary & Conclusion

The Sigma 70 surface tensiometer was found to provide an accurate and reproducible method of measuring the force and energy of the bubble-sphere detachment process. Much better results were obtained when using a flat bubble, but this could be remedied (in the round bubble experiment) if extreme precaution was taken to ensure that a smaller bubble was the exact same size for each experiment.

Bubble-particle detachment is a three step process. The first step is the bubble stretching, which is directly related to surface tension and contact angle hysteresis. This also represents the energy barrier to detachment. The bubble stretching energy also corresponds to the energy required to move the three-phase-contact line. Once advancing contact angle is reached, the second step of detachment begins. The energy spent as the TPC line 'slides' off the particle is equivalent to the calculated work of adhesion. The third step of detachment is bubble necking. This part of the detachment process occurs as the ratio of contact radius to particle height above the flat bubble datum becomes too small to support a stable interface. Evidence of bubble necking increased with contact angle.

The complete detachment process can be modeled using numerical solutions to the Young-Laplace equation for vapor-liquid interface shape. The stretching portion of detachment is modeled by assuming that contact radius is constant and contact angle increases from receding to advancing. When advancing contact angle is reached the sliding and necking portions of detachment are modeled together assuming that contact angle is constant and contact radius is decreasing.

Silane coating of silica surfaces can be modified by pH. As pH increases, the hydrophobicity of the surface also increases until pH ≈9.5 due to modification of the water layer on the silica surface. Once pH increases past 9.5, the detachment energy decreases dramatically as the OTS layer is etched off the surface.

References

Chibowski, E. (2003). "Surface free energy of a solid from contact angle hysteresis." *Advances in Colloid and Interface Science*, 103(2), 149-172.

Cohen, S. R., Naaman, R., and Sagiv, J. (1986). "Thermally induced disorder in organized organic monolayers on solid substrates." *J. Phys. Chem.*, 90, 3054-3056.

DePalma, V., and Tillman, N. (1989). "Friction and wear of self-assembled trichlorosilane monolayer films on silicon." *Langmuir*, 5, 868-872.

Gun, J., Iscovici, R., and Sagiv, J. (1984). "On the formation and structure of self-assembling monolayers. II. A comparative study of Langmuir-Blodgett and adsorbed films using ellipsometry and IR reflection-absorption spectroscopy." *Journal of Colloid and Interface Science*, 101, 201-213.

Gun, J., and Sagiv, J. (1986). "On the formation and structure of self-assembling monolayers. III. Time of formation, solvent retention, and release." *Journal of Colloid and Interface Science*, 112, 457-472.

Huh, C., and Scriven, L. E. (1969). "Shapes of axysimmetric fluid interfaces of unbounded extent." *Journal of Colloid and Interface Science*, 35, 323.

Iimura, K.-i., and Kato, T. (2000). "Robustness of monolayers on the solids; comparative studies on thermal, solvent, pH, and mechanical resistance among 1-layer LB films of cadmium arachidate and alkylchlorosilanes." *Colloids and Surfaces A: Physicochemical and Engineering Aspects*, 171(1-3), 249-264.

Israelachvili, J. (1991). *Intermolecular & Surface Forces*, Elsevier Ltd., London.

James, D. F. (1974). "The meniscus on the outside of a small circular cylinder." *Journal of Fluid Mechanics*, 63(4), 657-664.

Li, C., and Somasundaran, P. (1992). "Reversal of Bubble Charge in Multivalent Inorganic Salt Solutions - Effect of Aluminum." *Journal of Colloid and Interface Science*, 148(2), 587-591.

Li, H. C. (1958). "Adsorption of organic and inorganic ions on quartz," PhD, Massachusetts Institute of Technology, Cambridge.

Maoz, R., and Sagiv, J. (1984). "On the formation and structure of self-assembling monolayers. I. A comparative ATR-wettability study of Langmuir-Blodgett and adsorbed films on flat substrates and glass microbeads." *Journal of Colloid and Interface Science*, 100, 465-496.

Maoz, R., and Sagiv, J. (1987a). "Penetration-controlled reactions in organized monolayer assemblies. 1. Aqueous permanganate interaction with monolayer and multilayer films of long-chain surfactants." *Langmuir*, 3, 1034-1044.

Maoz, R., and Sagiv, J. (1987b). "Penetration-controlled reactions in organized monolayer assemblies. 2. Aqueous permanganate interaction with self-assembling monolayers of long-chain surfactants." *Langmuir*, 3, 1045-1051.

Murray, B. S., Godfrey, J., Griesen, F., Healy, T., Lovelock, B., and Scales, P. (1991). "Spectroscopic and electrokinetic study of pH-dependent ionization of langmuir-blodgett films." *Langmuir*, 7, 3057-3064.

Parikh, A. N., Allara, D. L., Ben Azouz, I., and Rondelez, F. (1994). "An Intrinsic Relationship between Molecular Structure in Self-Assembled n-Alkylsiloxane Monolayers and Deposition Temperature." *J. Phys. Chem.*, 98, 7577-7590.

Parikh, A. N., Schivley, M. A., Koo, E., Seshadri, K., Aurentz, D., Mueller, K., and Allara, D. L. (1997). "n-Alkylsiloxanes: From Single Monolayers to Layered Crystals. The Formation

of Crystalline Polymers from the Hydrolysis of n-Octadecyltrichlorosilane." *Journal of the American Chemical Society*, 119, 3135-3143.
Preuss, M., and Butt, H.-J. (1998). "Measuring the Contact Angle of Individual Colloidal Particles." *Journal of Colloid and Interface Science*, 208(2), 468-477.
Sagiv, J. (1980). "Organized monolayers by adsorption, 1. Formation and structure of oleophobic mixed monolayers on solid surfaces." *Journal of the American Chemical Society*, 102(1), 92-98.
Shaw, D. J. (1992). *Introduction to colloid and surface chemistry*, Butterworth-Heinemann, Boston.
Silberzan, P., Leger, L., Ausserre, D., and Benattar, J. J. (1991). "Silanation of silica surfaces. A new method of constructing pure or mixed monolayers." *Langmuir*, 7, 1647-1651.
Sutherland, K. L. (1948). "Kinetics of the flotation process." *J. Phys. Chem.*, 52, 394-425.
Tripp, C. P. (1991). "Reaction of chloromethylsilanes with silica: a low-frequency infrared study." *Langmuir*, 7, 923-927.
Tripp, C. P., and Hair, M. L. (1995). "Direct Observation of the Surface Bonds between Self-Assembled Monolayers of Octadecyltrichlorosilane and Silica Surfaces: A Low-Frequency IR Study at the Solid/Liquid Interface." *Langmuir*, 11, 1215-1219.
van Oss, C. J. (1994). *Interfacial Forces in Aqueous Media*, Marcel Dekker, Inc., New York.
Wasserman, S. R., Tao, Y.-T., and Whitesides, G. M. (1989). "Structure and reactivity of alkylsiloxane monolayers formed by reaction of alkyltrichlorosilanes on silicon substrates." *Langmuir*, 5, 1074-1087.
Ye, S., Nihonyanagi, S., and Uosaki, K. (2001). "Sum frequency generation (SFG) study of the pH-dependent water structure on a fused quartz surface modified by an octadecyltrichlorosilane (OTS) monolayer." *Physical Chemistry Chemical Physics*, 3(16), 3643-3469.
Yiantsios S. G., and Karabelas A. J. (1995). "Detachment of Spherical Microparticles Adhering on Flat Surfaces by Hydrodynamic Forces." *Journal of Colloid and Interface Science*, 176(1), 74-85.
Zhao, X., and Kopelman, R. (1996). "Mechanism of organosilane self-assembled monolayer formation on silica studied by second-harmonic generation." *J. Phys. Chem.*, 100, 11014-11018.
Zhuravlev, L. T. (1987). "Concentration of hydroxyl groups on the surface of amorphous silicas." *Langmuir*, 3, 316-318.

CHAPTER 2 - DETACHMENT FORCE AND ENERGY OF A BUBBLE FROM A SUBMERGED HYDROPHOBIC PLATE

Abstract

Bubble particle detachment is the main limiting factor in coarse particle flotation. Detachment occurs when forces on the bubble-particle aggregate in a flotation cell overcome the strength of adhesion. Strength of adhesion depends on the particle contact angle, surface energy and roughness, and surface tension of the liquid media. Surface energy and roughness determine contact angle hysteresis, which causes the activation energy for detachment. Bubble detachment from a flat hydrophobic surface submerged in water was studied using a 1 kHz CCD camera. Images provided the data for thermodynamic and force calculations from the bubble shape size and movement on the plate. The measured energy of detachment was divided into the two parts: activation energy and work of adhesion. The measured work of adhesion compared favorably with calculated values.

Introduction

Froth flotation is widely used in the mining industry to separate valuable minerals from other materials in their host environment. Minerals are separated by attaching themselves to rising air bubbles in the flotation cell and then recovered at the top of the cell. The ore must be ground small enough so that flotation can proceed (e.g. <.5 mm diameter). Coarse particle flotation provides opportunities for reduced grinding costs, increased recoveries and simplified flow-sheet designs (by eliminating certain classifying and other steps); all leading to increased throughput.

Flotation is a function of the probability of particle collection (Sutherland 1948);

$$P = P_C \cdot P_A \left(1 - P_D\right) \qquad [14]$$

where P_C, P_A, and P_D are the probabilities of collision, adhesion, and detachment respectively. The probability of collision depends on hydrodynamic effects in the flotation cell. The probabilities of adhesion and detachment are a combination of hydrodynamic effects and surface chemistry of the bubble and particle. Since surface chemistry is not affected by particle size, the probability of adhesion is mostly a function of hydrodynamics and increases with particle size. Probability of detachment is then the main limiting factor in coarse particle flotation.

Detachment of a bubble from a submerged plate has previously been studied using various methods such as the single hole plate or simply a submerged plate (Byakova et al. 2003; Eckmann and Cavanagh 2003; Jones et al. 1999; Li et al. 2002; Li and Quiang 1998; Nahra and Kamotani 2003). However, these studies do not adequately describe the detachment process with regards to a flotation application. Many others have also observed bubbles at a submerged capillary tip rather than a plate to study formation and detachment (Churaev et al. 2002; Keen and Blake 1996; Ouz and Zeng 1997; Yang et al. 2001). These do not properly describe detachment as seen in flotation as the bubble cannot spread past the boundaries of the capillary tip.

Theory

The detachment of an air bubble from a flat surface submerged in water is dependent on contact angle, surface energy of the solid and water surface tension. Contact angle determines the size of the contact area between bubble and surface. Surface tension may be regarded as a force vector along the bubble wall at the three phase contact (TPC) line. This surface tension multiplied by the contact perimeter represents the tenacity of the bubble adhesion onto the surface.

Surface energy of the solid (Eskilsson and Yaminsky 1998) and roughness determine contact angle hysteresis. Hysteresis is the difference between advancing and receding contact angle. When a water drop slides down a glass window, for example, the bottom part of the drop forms a larger contact angle (taken through the water, between the tangent to the drop wall and the glass surface) then the top part. The bottom portion is advancing on the glass surface and is said to be the advancing contact angle. The top portion is retreating and is said to be the receding contact angle. In the same fashion, when a bubble first attaches to a solid in water, the bubble spreads on the surface at the receding contact angle (water is receding from the surface). As the bubble detaches and the contact area shrinks it does so at the advancing contact angle. When the bubble

is at steady state with the surface, neither spreading nor detaching, it is at equilibrium contact angle, which is the average of receding and advancing angles.

Detachment involves the shrinking of the contact area as the air bubble retreats from the surface. The TPC line must be at advancing contact angle for the initial inward movement to begin. Thus hysteresis plays a determining role along with contact angle in the detachment process.

The bubble contact diameter on a flat surface is dominated by the contact angle (Lin 1994). Subsequently, the final size of the bubble before detachment depends on surface energy of the solid, liquid interfacial tension, and contact angle. The contact angle as reported by (Lin 1994) was always 90° at detachment. However, the angle at detachment should be the advancing angle or slightly larger if the TPC line is moving very rapidly. The plate in this study represents a large smooth hydrophobic particle on which the TPC spreading is not limited by physical characteristics of the solid. The contact area is then controlled strictly by surface energy of the plate and interfacial tension of the media. The role of surface tension was thoroughly explained in experiments with oil drops on a submerged horizontal plate (Chatterjee 2002).

The forces acting on a bubble attached to a horizontal plate submerged in water are the buoyancy force and surface tension force. At high flow rates the bubble momentum also contributes to detachment, but this is not the case here. The buoyant force of the bubble must overcome the interfacial tension for detachment to proceed. Once the interfacial tension force is overcome, the TPC line shifts from equilibrium to advancing angle whence the bubble begins to retract from the surface until complete detachment.

Experimental Methods

All the reagents used in the experiment were at least ACS grade and were obtained from either Fisher Scientific or Alfa Aesar. The plate consisted of a 25.4 mm x 25.4 mm x 1.0 mm silicon wafer donated by the Virginia Tech Materials Science department. Holes (diameter = 0.6mm) were drilled through the center of these plates using an ultrasonic cutting machine. Plate surface roughness was measured to be about 0.5 nm by profiling the surface with an atomic force microscope. These plates were then methylated with octadecyltrichlorosilane (OTS) to create hydrophobic surfaces. The methylation procedure consists of washing the samples for 1hr in

Piranha solution (30% H_2O_2:70% $H2SO_4$) at 60 – 70°C. The samples are then rinsed in Nanopure water and immersed in a 10^{-5}M silane solution in toluene for 30 – 90 minutes depending on the target contact angle. The samples are then removed from the solution and first rinsed with chloroform to remove any excess toluene from the surface, then acetone to remove any physisorbed silane. Following this, the samples are placed in acetone in an ultrasonic bath for at least 20 min. This breaks up any amalgams of polymerized silane which may have accumulated at the silica surface, thereby creating a more uniform silane coating. The samples are stored in Nanopure water in sealed containers until the experiment. The roughness of coated plates was also measured and was found to be less than 1 nm, indicating a consistent silane coating. The above method was used to produce plates with contact angles of 85°, 95°, and 97°. The surface energies of the plates were determined from contact angle measurements of formamide, diiodomethane and water on the surfaces, using the method as outlined by (van Oss et al. 1987).

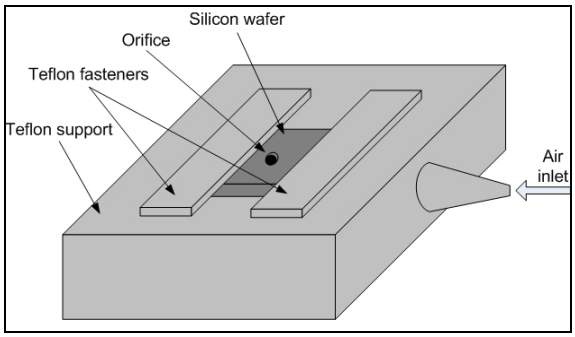

Figure 15 - Silicon plate support

The experiment involved submerging a horizontal plate with a hole drilled through the center in a water filled cell. The plate was attached to a Teflon support as shown in Figure 15, connected to an air source. Bubbles were produced at the orifice as air was fed through the system. The size of the orifice was kept constant, 0.6 mm diameter, as plates of different hydrophobicity were used. The size of the orifice has been shown to not affect the bubble characteristics as long as it is relatively small when compared to the bubble diameter (Datta et al. 1950). The relationship of cell size with bubble shape was also investigated and found to affect the bubble only under specific conditions which satisfy the following equation (Hughes et al. 1955)

$$v_c \approx \frac{A_0 \rho_g c^2}{g \Delta \rho} \qquad [15]$$

where, v_c is the cell volume, A_0 is the area of orifice, ρ_g is the gas density, c is the velocity of sound in the gas, g is the acceleration of gravity, and $\Delta\rho$ is the density difference between air and water. The cell used in this experiment was outside this range.

The experiments were recorded using a Phantom V4.0 CCD camera (Photo-Sonics Inc.) at 1000 frames per second. These digital images were analyzed to measure the bubble-surface contact area, dynamic contact angle, and bubble surface areas for thermodynamic calculations. Using the images, detachment force from buoyancy of the volume of the bubble was measured.

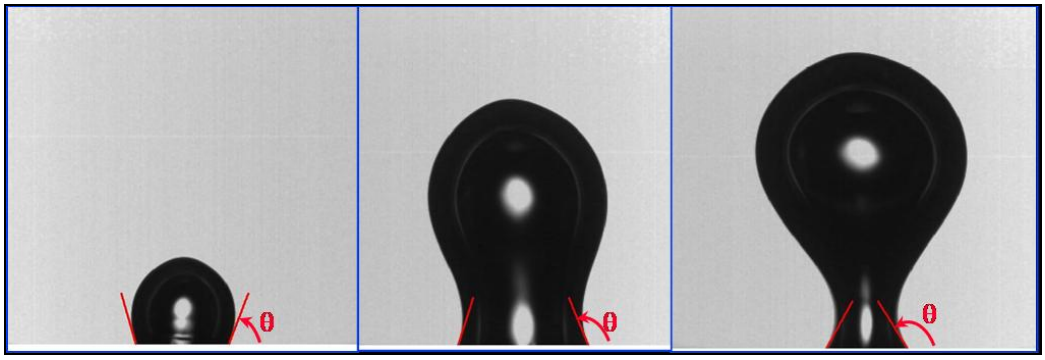

Figure 16 - Bubble at various stages of growth on flat plate

All the bubble measurements were made using MatLab (The MathWorks, Inc.) programs to analyze the images. Figure 16 shows an example of this analysis. The tangent to the bubble was traced at the contact to compute the instantaneous contact angle at each frame.

Results and Discussion

The experiments were limited to surfaces with contact angles larger than 90°, since below this the bubble does not instantaneously spread on the methylated surface. Bubble formation and detachment on the silicon wafer clearly demonstrated the importance of contact angle hysteresis in bubble-particle interactions. Figure 17 demonstrates the various stages of the interaction.

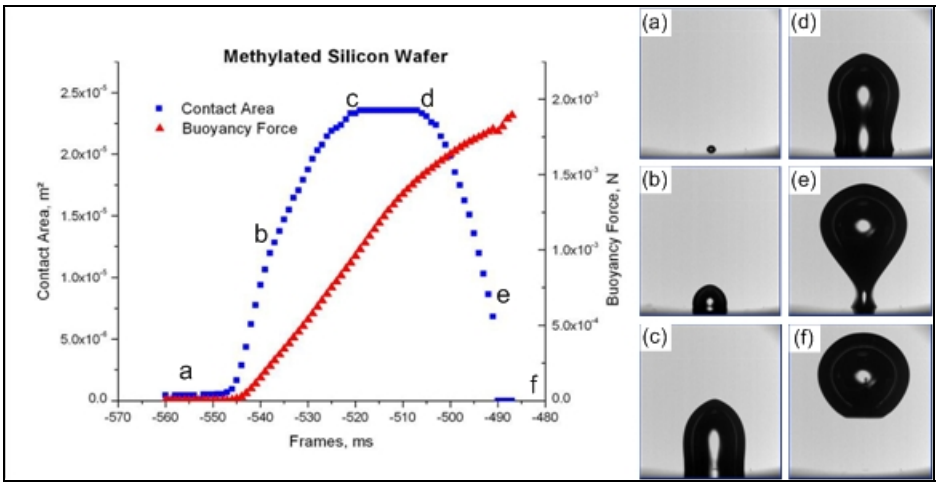

Figure 17 - Stages of bubble growth and detachment on methylated silicon wafer

In Figure 17(a) the bubble is still in the orifice, giving the reader an idea of the relative size of the hole compared to the contact area. As more air is fed through, the bubble wall breaks and attaches to the methylated surface in Figure 17(b). Here, the bubble forms the receding contact angle with the wafer as it spreads across the surface (i.e. water is receding from the surface). In Figure 17(c), the bubble has reached its maximum contact area. From this point on, the contact angle begins to increase until advancing contact angle is reached as shown in Figure 17(d). Once advancing contact angle is reached, water begins to advance on the silica surface. This is the beginning of the detachment process. Figure 17 (e) and (f) show the bubble as it is about to detach and once it has detached.

Between points (c) and (d), the buoyancy force keeps increasing. The energy spent during this time, while the contact area remains constant, is the energy required to shift the contact angle from receding to equilibrium and then advancing.

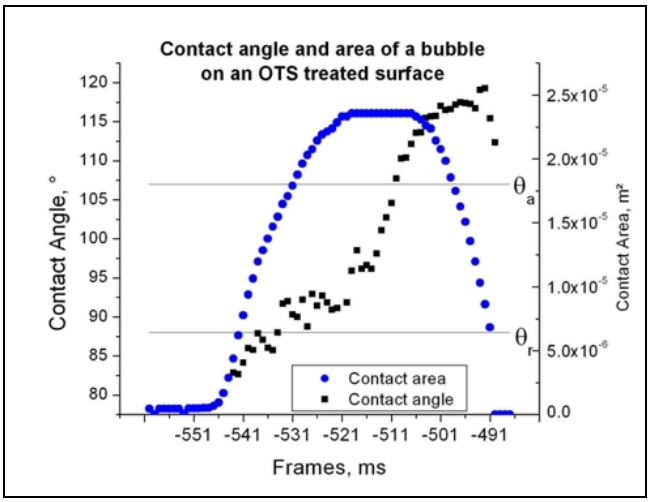

Figure 18 - Contact angle during growth and detachment process

The evolution of contact angle during the bubble spreading on and subsequent detachment from the wafer surface is further demonstrated in Figure 18. The bubble maintains receding contact angle during the contact area expansion. Then contact area decreases once the advancing contact angle has been reached. The energy spent shifting the TPC line from equilibrium angle to advancing to that detachment may begin represents activation energy or energy barrier to detachment. Because of the activation energy, work of adhesion is not a reversible process. The non-reversible nature of work of adhesion has been suggested previously (Israelachvili 1991) but only more recently demonstrated rigorously (Chibowski 2003).

Energy Calculations

Work of adhesion for the plate-sphere system was calculated to see how well it corresponded to the energies measured during the detachment process.

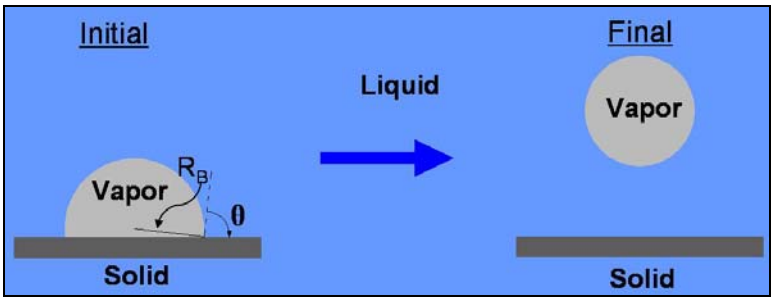

Figure 19 - Initial and final stages of bubble detachment

Figure 19 displays the initial and final energy states used to calculate the work of adhesion. The initial state represents the equilibrium state of the bubble and surface. Thus the bubble is at equilibrium contact angle with the surface. The work of adhesion calculation assumes that the bubble volume doesn't change between initial and final states. From this constant volume, the initial bubble radius, R_B was calculated using the final volume.

$$V = \frac{\pi}{6}\left[3R_C^2 + \left(R_B - \sqrt{R_B^2 - R_C^2}\right)^2\right]\left(R_B - \sqrt{R_B^2 - R_C^2}\right) \quad [16]$$

Equation [16] determines the volume, V, of the bubble where R_B is bubble radius and R_C is the contact radius. The volume is then used in equation [17] to determine the change in liquid-vapor interface. Equation [18] is used to calculate the contact area as is represents the change in solid-vapor and solid-liquid interface.

$$\Delta A_{LV} = 4\pi\left(\frac{3V}{4\pi}\right)^{\frac{2}{3}} - 2\pi R_B\left(R_B - \sqrt{R_B^2 - R_C^2}\right) \quad [17]$$

$$A_C = \pi R_B^2 \sin^2\theta \quad [18]$$

$$W_A = \Delta A_{LV}\gamma_{LV} + A_C\left(\gamma_{SV} - \gamma_{SL}\right) \quad [19]$$

Equation [19] calculates the work of adhesion (in Joules) for the system, where γ_{LV}, γ_{SV} and γ_{SL} are the liquid-vapor, solid-vapor, and solid-liquid interfacial tensions. The volume of the bubble at equilibrium position was used to calculate the work of adhesion, which was compared with experimental detachment energy measurements.

The moving centroid method was used to measure the energy of the detachment. This method involves integrating the force applied by the bubble onto the surface over the distance traveled by the bubble centroid in the vertical direction, as shown in equation [21].

$$F_\gamma = 2\pi R_C\gamma_{LV}\sin\theta \quad [20]$$

$$E = \int_{y_1}^{y_2} F_\gamma dy \quad [21]$$

F_γ is the vertical component of the surface tension multiplied by the contact perimeter as shown in equation [20]. For the detachment process to begin F_B must overcome F_γ. Where, F_B represents the buoyancy force of the bubble.

When these two forces are equal the bubble is at equilibrium position and the bubble forms the equilibrium contact angle with the wafer surface. For the detachment process to begin, the TPC line must be shifted to advancing angle. E_1 is the activation energy required to shift the TPC line, and thereby begin the detachment process. The beginning of the detachment process is marked in Figure 20 by the sudden decrease in contact area. The energy spent from this point on until complete detachment represents the work of adhesion portion of the energy of detachment, E_2.

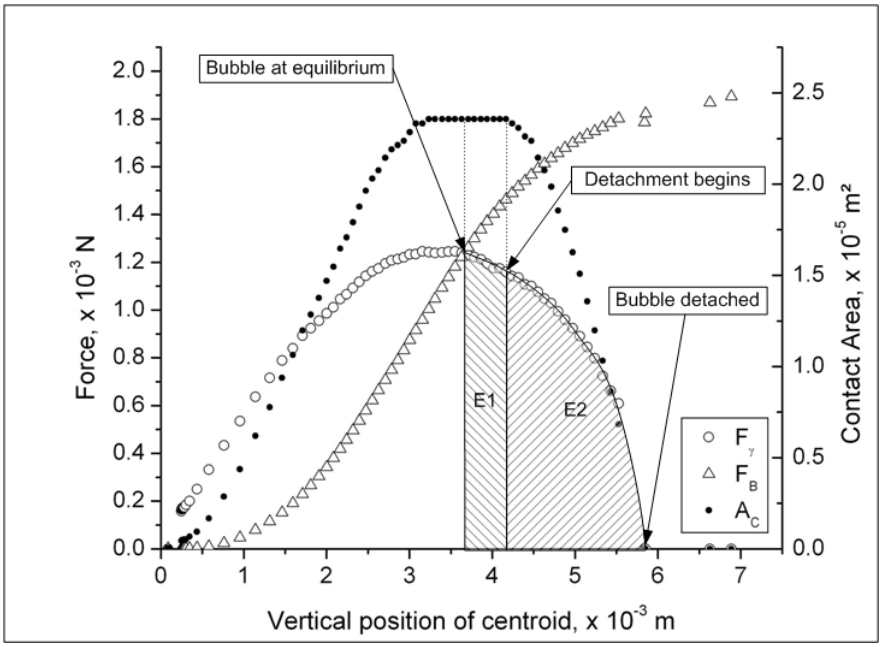

Figure 20 - Moving centroid method of energy of detachment calculation (θ = 97°)

Table 3 shows the energies calculated by the centroid method and how they compare to the work of adhesion calculated for these systems. As demonstrated, E_2 showed good correlation to the theoretical work of adhesion.

Table 3 – Moving centroid detachment energies and theoretical work of adhesion

Sample	I	II
Contact angle (hysteresis)	95° (32°)	97° (18°)
E_1	6.794 x 10^{-7} J	5.435 x 10^{-7} J
E_2	1.034 x 10^{-6} J	1.378 x 10^{-6} J
E_{total}	1.714 x 10^{-6} J	1.922 x 10^{-6} J
Theoretical W_A	1.132 x 10^{-6} J	1.325 x 10^{-6} J
% Error, (W_A vs E_2)	8.66%	4.00%

These measurements clearly demonstrate the importance of contact angle hysteresis. While sample II had a larger equilibrium contact angle, since sample I had more hysteresis, it required much more energy to detach.

Measured surface energies during the experiment provided a third method for energy of detachment determination. This method simply involves calculating the total surface free energy of the system for each frame in the experiment film. The energy difference between equilibrium and complete detachment was then used as the energy of detachment.

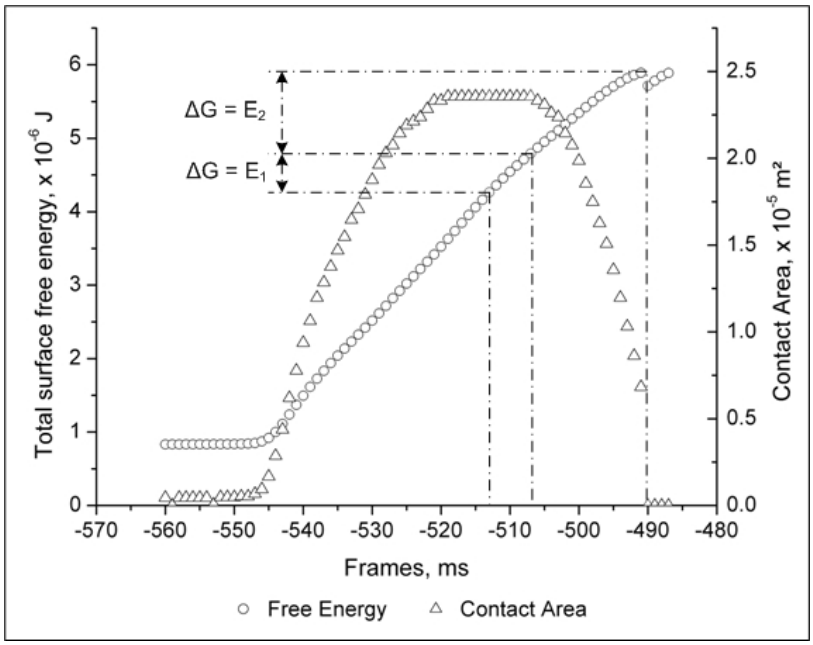

Figure 21 - Surface free energy of bubble and plate system

Figure 21 demonstrates the use of instant surface free energies to measure the energy of detachment. The free energy difference between equilibrium (frame -513) and beginning of detachment (frame -507) is equivalent to the activation energy, E_1. The free energy difference

between beginning of detachment (frame -507) and complete detachment is equivalent to the work of adhesion or E_2. Note that at detachment the free energy dips slightly. This drop represents an exothermic process. Nature constantly seeks to reach lowest energy state. When detachment starts until one frame before detachment the free energy is increasing because an energy input is provided by the extra air being fed to the bubble. The instant before detachment, the bubble has reached its maximum stable size. This means that detaching rather than still growing allows the bubble to reach a lower energy state, thereby creating an instantaneous process.

Table 4 – Surface free energy detachment and theoretical work of adhesion

Sample	I	II
Contact angle (hysteresis)	95° (32°)	97° (18°)
E_1	7.863×10^{-7} J	5.279×10^{-7} J
E_2	9.924×10^{-7} J	1.097×10^{-6} J
E_{total}	1.779×10^{-6} J	1.625×10^{-6} J
Theoretical W_A	1.132×10^{-6} J	1.325×10^{-6} J
% Error, (W_A vs E_2)	12.33%	17.14%

The measured values shown in Table 4 again demonstrate the importance of contact angle hysteresis. Although sample I has a slightly smaller measured work of adhesion, E_2, it benefits from larger hysteresis, leading to larger activation energy, E_1, and ultimately a larger overall energy of detachment.

Summary & Conclusion

A submerged plate with a single orifice was successfully used to measure force and energy of detachment of a single bubble from a hydrophobic surface. The detachment force was obtained from buoyancy of the bubble, which was measured using image analysis of the experiment. Bubble equilibrium with the plate is reached when the buoyant force of the bubble is equivalent to the force due to surface tension.

Detachment energy was successfully measured using both the moving centroid method and surface free energy measurements also from image analysis. These methods clearly outlined the multiphase nature of the bubble detachment process. The first phase of detachment is shifting of the TPC line from equilibrium to advancing contact angle. The energy spent in doing so is

referred to as the activation energy. The second phase occurs when the TPC slides inward until complete detachment. This subsequent component of the detachment process corresponds to the work of adhesion. Thus, if hysteresis is present the bubble-particle interaction is not a reversible process. The measured activation energy showed direct correlation to contact angle hysteresis and subsequent detachment energy corresponded closely to the calculated work of adhesion.

References

Byakova, A. V., Gnyloskurenko, S. V., Nakamura, T., and Raychenko, O. I. (2003). "Influence of wetting conditions on bubble formation at orifice in an inviscid liquid: Mechanism of bubble evolution." Colloids and Surfaces A: Physicochemical and Engineering Aspects, 229(1-3), 19-32.

Chatterjee, J. (2002). "Critical Eotvos numbers for buoyancy-induced oil drop detachment based on shape analysis." Advances in Colloid and Interface Science, 98, 265-283.

Chibowski, E. (2003). "Surface free energy of a solid from contact angle hysteresis." Advances in Colloid and Interface Science, 103(2), 149-172.

Churaev, N. V., Ralston, J., Sergeeva, I. P., and Sobolev, V. D. (2002). "Electrokinetic properties of methylated quartz capillaries." Advances in Colloid and Interface Science, 96(1-3), 265-278.

Datta, R. L., Napier, D. H., and Newitt, D. M. (1950). "The Properties and Behaviour of Gas Bubbles Formed at a Circular Orifice." Trans. Inst. Chem. Eng., 28, 14 - 26.

Eckmann, D. M., and Cavanagh, D. P. (2003). "Bubble detachment by diffusion-controlled surfactant adsorption." Colloids and Surfaces A: Physicochemical and Engineering Aspects, 227(1-3), 21-33.

Eskilsson, K., and Yaminsky, V. V. (1998). "Deposition of monolayers by retraction from solution: Ellipsometric study of cetyltrimethylammonium bromide adsorption at silica-air and silica-water interfaces." Langmuir, 14, 2444-2450.

Hughes, R. R., Hanklos, A. E., Evans, H. D., and Maycock, R. L. (1955). "The Formation of Bubbles at Simple Orifices." Chemical Engineering Progress, 51(12), 557 - 563.

Israelachvili, J. (1991). Intermolecular & Surface Forces, Elsevier Ltd., London.

Jones, S. F., Evans, G. M., and Galvin, K. P. (1999). "Bubble nucleation from gas cavities -- a review." Advances in Colloid and Interface Science, 80(1), 27-50.

Keen, G. S., and Blake, J. R. (1996). "A Note on the Formation and Rise of a Bubble from a Submerged Nozzle, Including Effects of Bulk- and Surface-Dilatational Viscosity." Journal of Colloid and Interface Science, 180(2), 625-628.

Li, H. Z., Mouline, Y., and Midoux, N. (2002). "Modelling the bubble formation dynamics in non-Newtonian fluids." Chemical Engineering Science, 57(3), 339-346.

Li, H. Z., and Quiang, S. (1998). "Formation des bulles dans les fluides newtoniens et non newtoniens." Fluid Mechanics, 326, 301-308.

Lin, J. N. (1994). "Role of interfacial tension in the formation and the detachment of air bubbles. 1. A single hole on a horizontal plane immersed in water." Langmuir, 10, 936-942.

Nahra, H. K., and Kamotani, Y. (2003). "Prediction of bubble diameter at detachment from a wall orifice in liquid cross-flow under reduced and normal gravity conditions." Chemical Engineering Science, 58(1), 55-69.

Ouz, H., and Zeng, J. (1997). "Axisymmetric and three-dimensional boundary integral simulations of bubble growth from an underwater orifice." Engineering Analysis with Boundary Elements, 19(4), 319-330.
Sutherland, K. L. (1948). "Kinetics of the flotation process." J. Phys. Chem., 52, 394-425.
van Oss, C. J., Chaudhury, M. K., and Good, R. J. (1987). "Monopolar surfaces." Advances in Colloid and Interface Science, 28, 35-64.
Yang, Z. L., Dinh, T. N., Nourgaliev, R. R., and Sehgal, B. R. (2001). "Numerical investigation of bubble growth and detachment by the lattice-Boltzmann method." International Journal of Heat and Mass Transfer, 44(1), 195-206.

CHAPTER 3 - DETACHMENT FORCE AND ENERGY OF A CETYLTRIMETHYLAMMONIUM BROMIDE COATED SILICA SPHERE FROM A FLAT BUBBLE

Abstract

Bubble particle detachment is the main limiting factor in coarse particle flotation. Detachment occurs when forces on the bubble-particle aggregate in a flotation cell overcome its adhesive force. The strength of adhesion depends on contact angle, surface tension, and contact angle hysteresis. Detachment forces and energies were measured between a surfactant coated silica sphere and a flat bubble as a function of the surfactant concentration. A digital camera was used to measure the contact radius of the bubble on the sphere, to calculate the receding contact angle. The forces were used to calculate contact angles which were compared to Wilhelmy plate measurements on glass slides. The measured energy was separated into the energy barrier and the detachment energy which was compared to the theoretical work of adhesion.

Introduction

Froth flotation is widely used in the mining industry to separate valuable minerals from other materials in their host environment. Minerals are separated by attaching themselves to rising air bubbles in the flotation cell and then recovered at the top of the cell. The ore must be ground small enough so that flotation can proceed (e.g. <.5 mm diameter). Coarse particle flotation provides opportunities for reduced grinding costs, increased recoveries and simplified flow-sheet designs (by eliminating certain classifying and other steps); all leading to increased throughput.

Flotation is a function of the probability of particle collection (Sutherland 1948).

$$P = P_C \cdot P_A \left(1 - P_D\right) \qquad [22]$$

Where, P_C, P_A, and P_D are the probabilities of collision, adhesion, and detachment respectively. The probability of collision depends on hydrodynamic effects in the flotation cell. The probabilities of adhesion and detachment are a combination of hydrodynamic effects and surface chemistry of the bubble and particle. Since surface chemistry is not affected by particle size, the probability of adhesion is mostly a function of hydrodynamics and increases with particle size. Probability of detachment is then the main limiting factor in coarse particle flotation.

Cationic surfactants such as cetlytrimethylammonium bromide (C_{16}TAB) easily attach to the negatively charged silica surface. The C_{16}TAB molecules attach to the silanol groups at the glass surface which provide the negative sites. The sphere becomes more hydrophobic as more surfactant is adsorbed onto the surface. The density of the silanol groups determines the maximum possible C_{16}TAB density on the surface. As these negative sites are filled the surface is neutralized. The surfactant concentration where this occurs is the point of zero charge (pzc). Further C_{16}TAB adsorption occurs as concentration is increased through attraction between the hydrophobic tails. This creates a densely packed second layer on the sphere with the polar heads pointing toward solution, thereby decreasing the overall hydrophobicity of the sphere. Increasing the C_{16}TAB concentration also decreases the surface tension of the aqueous solution. This is similar to increasing the frother concentration in a flotation cell.

Theory

Detachment force

The total force exerted by the flat bubble onto the sphere is a function of the contact radius and angle formed at the interface. Figure 22 illustrates the geometry involved in the force equation derivation.

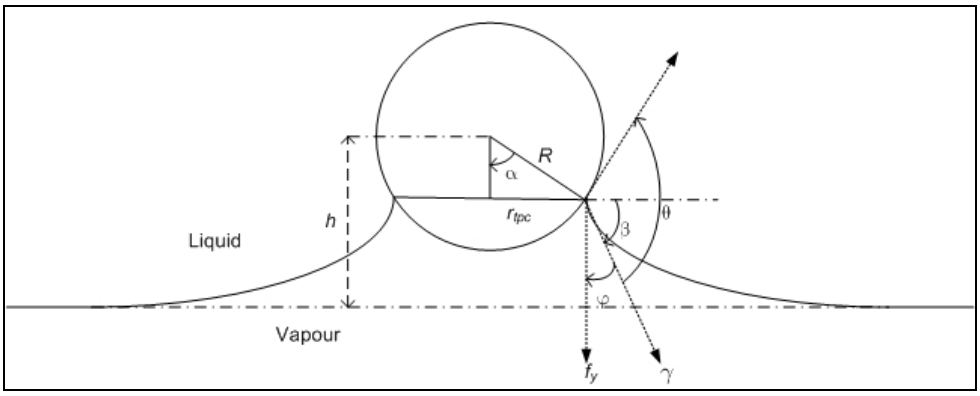

Figure 22 - Flat bubble - sphere detachment geometry

$$F = 2\pi r_{tpc}\gamma_{lv}\cos\varphi \qquad [23]$$

Equation [23] calculates the total force exerted by the bubble onto the sphere in the vertical direction due to surface tension, where γ_{lv} is the surface tension. The contact radius, r_{tpc}, is a function of the receding contact angle, θ_r. When the sphere first penetrates the bubble, water recedes from the solid surface. The TPC spreads on the solid until it is pinned at the radius of contact and settles at receding contact angle (Preuss and Butt 1998b). From Figure 22 it can be seen that the angle between the tangent at the contact line and the horizontal is equal to α. Thus, $r_{tpc} = R\sin\theta_r$. The TPC line stays pinned until advancing contact angle is reached. At advancing contact angle, $\varphi = \pi/2 - \theta_a + \theta_r$. The total force necessary to move the TPC on the sphere surface is then

$$F = 2\pi R\sin\theta_r \cdot \gamma_{lv}\cos\left(\frac{\pi}{2} - \theta_a + \theta_r\right) \qquad [24]$$

Work of adhesion

The measured energy was compared to the calculated work of adhesion for a sphere and flat bubble interaction. Work of adhesion was calculated with the following equation:

$$W_A = \gamma_{LV}\pi R^2\left[\sin^2\theta_R - 2\cos\theta_{Eq}\left(1-\cos\theta_R\right)\right] \qquad [25]$$

where R is the radius of the sphere and θ_R and θ_{Eq} are the receding and equilibrium contact angles respectively. The work of adhesion calculation describes the change in free energies between the initial and final states as described in Figure 13.

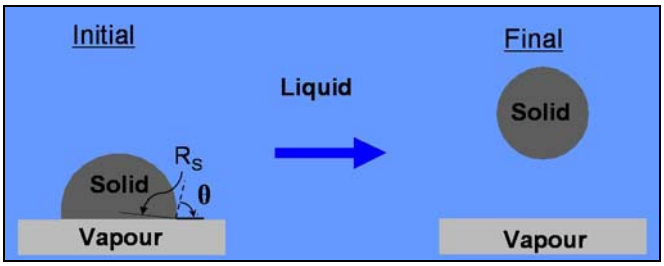

Figure 23 - Sphere - flat bubble work of adhesion calculation

Equation [11] assumes that the initial state is receding contact angle, and the equilibrium contact angle is used to cancel out the solid-liquid and solid-vapor interfacial tension terms by means of Young's equation. If the angle at the initial stage is believed to equal equilibrium contact angle, then equation [11] reduces to the more commonly seen

$$W_A = \gamma_{LV} \pi R^2 \left(1 - \cos\theta\right)^2 \qquad [26]$$

Equation [12] for work of adhesion overestimates the energy of detachment with the difference between experimental and calculated increasing with contact angle. Equation [12] is also valid in the rare case where there is no contact angle hysteresis.

Equations [24] and [11] illustrate the importance of contact angle hysteresis in the detachment process. Hysteresis is caused by surface roughness (Adamson 1997; Israelachvili 1991) and by surface energy of the solid (Chibowski 2003). The C_{16}TAB molecules adsorb onto the silica surface in patches or domains, thereby creating chemically heterogeneous surfaces than can lead to increased hysteresis.

Surfactant adsorption at the solid-liquid-vapor interface during movement of the solid across the liquid vapor interface can also cause hysteresis. During Wilhelmy plate measurements of advancing and receding contact angles, a surfactant coated plate is introduced vertically into aqueous surfactant solution. The liquid vapor boundary depresses as the solid is pushed down

past the water surface. The meniscus created by this depression will form the advancing contact angle with the plate, and remain at that angle as the plate is lowered further into the solution. CTAB molecules in the solution will orient themselves at the TPC so as to have the hydrophobic tail onto the solid to escape the water (Yaminsky and Ninham 1999). This phenomenon leads to increased pinning of the TPC line and consequently larger advancing contact angles.

Experimental Methods

Forces were measured using a Sigma 70 Surface tensiometer (KSV Instruments Ltd.). This equipment was a hanging balance with a resolution of 1 μN. The bubble-particle interactions were photographed by a 4.0M pixel S4 digital camera (Canon Inc.) equipped with a reversed 50 mm AF NIKKOR (Nikon Corporation) lens (which allows it to act as a macro lens).

Soda lime glass spheres with a mean diameter of 2007 μm ± 40 μm (Duke Scientific Corporation) were used in the experiment. The diameter of these spheres was verified with a micrometer as shown in Table 5.

Table 5 - Sample dimensions

Sphere	Diameter, μm
A	1991
B	2008
C	2004

Before treatment, the spheres were washed for 1hr in Piranha solution (30% H_2O_2:70% H_2SO_4) at 60-70°C before treatment. Once washed the spheres were stored in a sealed container filled with Nanopure water. All measurements were done at 20°C ± 0.5°.

A sphere was then fixed to the end of a glass hook, which was manufactured by the Virginia Tech glass shop, using Crytalbond™ 509 glue (Electron Microscopy Sciences). The sphere was then suspended in a solution of cetyltrimethylammonium bromide (C_{16}TAB) for two hours to create a hydrophobic surface.

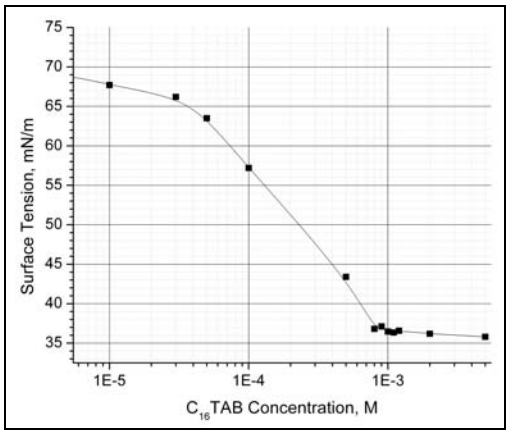

Figure 24 - Surface tension of C_{16}TAB aqueous solutions

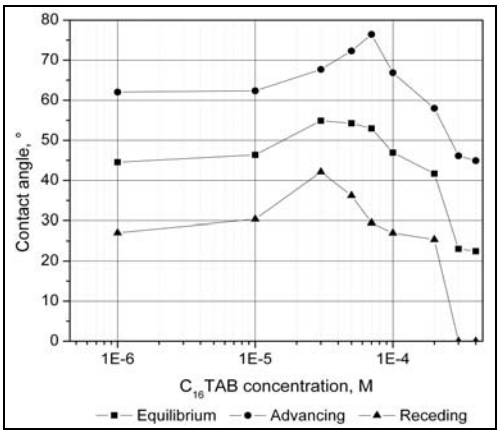

Figure 25 - Contact angle of C_{16}TAB aqueous solutions on glass

C_{16}TAB should reach equilibrium concentration on the glass surface after 1h (Yaminsky and Yaminskaya 1995). Solution concentrations ranged from 10^{-6}M to 10^{-3}M. Samples were first treated with the 10^{-6}M solution and force measurements were taken immediately after. Between measurements the samples were soaked in successively higher concentrations of C_{16}TAB. The purity of the C_{16}TAB (Fluka) was verified by testing the surface tension of a range of concentrations to identify the critical micelle concentration. The surface tension was measured using the same tensiometer equipped with a Du Nouy ring (Pt-Ir-ring made to DIN 53914-80 and ASTM D 971 specifications, also by KSV Instruments Ltd.). Figure 24 indicates a critical micelle concentration (CMC) of 9 x 10^{-4} M, which is in accordance with literature (Frank and Garoff 1996; Liu et al. 2001). The steady surface tension of the aqueous solution above the CMC also indicates an uncontaminated surfactant. The surface tension of pure water was measured at 72.6 mN/m.

Glass plates (Fisher Scientific) were cleaned and treated with C_{16}TAB using the same methods earlier described to obtain contact angle measurements for various concentrations. Advancing and receding contact angles were measured using the Wilhelmy plate principle with the KSV Sigma 70. The contact angles thus obtained can be seen in Figure 25. These measurements were also in agreement with literature (Janczuk et al. 1999).

The measured contact angles were also used to determine the surface free energy, γ_s, of the glass using equation [27] (Chibowski 2003).

$$\gamma_s = \gamma_l \left(\cos\theta_r - \cos\theta_a\right) \frac{\left(1+\cos\theta_a\right)^2}{\left(1+\cos\theta_r\right)^2 - \left(1+\cos\theta_a\right)^2} \qquad [27]$$

Where, γ_l is the surface tension of water, and θ_r and θ_a are the receding and advancing contact angle respectively.

To perform the force measurements, the sphere was suspended from the tensiometer above a flat bubble. The bubble was created using a PTFE rod, with a cone bored out in the center, connected to a syringe that provided the air for the bubble as shown in Figure 6. The bubble support sat in a rectangular glass cell filled with water on top of a mechanical stage that could be moved vertically at 1 mm/min to bring the bubble and particle into contact and then detach them.

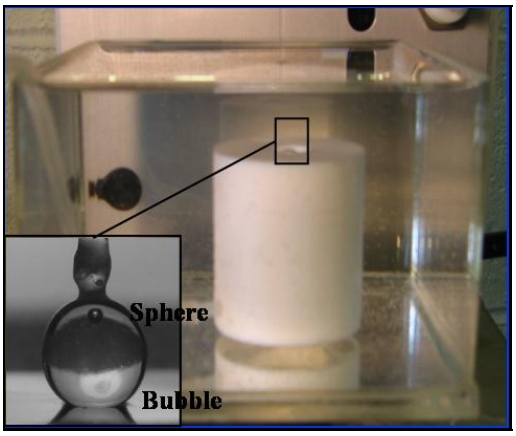

Figure 26 - Flat bubble apparatus

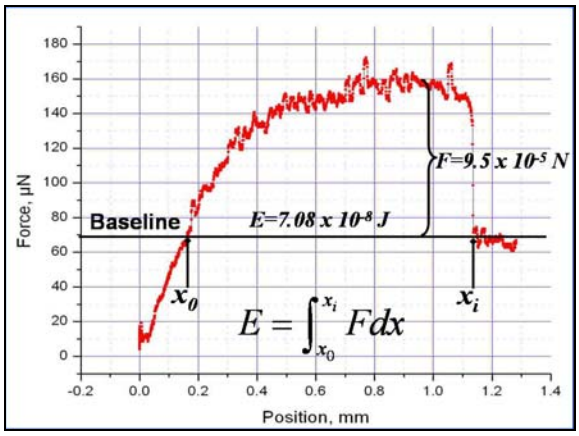

Figure 27- Detachment force curve

The tensiometer was connected to a computer to record force and distances every .25 s. The reported distance is the relative position of the mechanical stage. Although the actual position is not known, the distance traveled during the detachment process (used for energy calculations) is still recorded.

A typical output curve from the surface tensiometer is shown in Figure 27. The detachment force is measured as the difference between the maximum and the baseline. The baseline is the force at which the sphere is detached. This is the force exerted on the instrument from the weight of the sphere only. The energy is taken as the integral of the force applied across the distance

from equilibrium to detachment. Equilibrium is shown in the figure as x_0. It is the point at which the bubble is neither pushing up nor pulling down on the sphere.

Results & Discussion

Detachment forces at increasing surfactant concentration are shown in Figure 28 for the three spheres. Sphere A measurements were stopped at 10^{-4} M because the sphere became unglued from the glass hook.

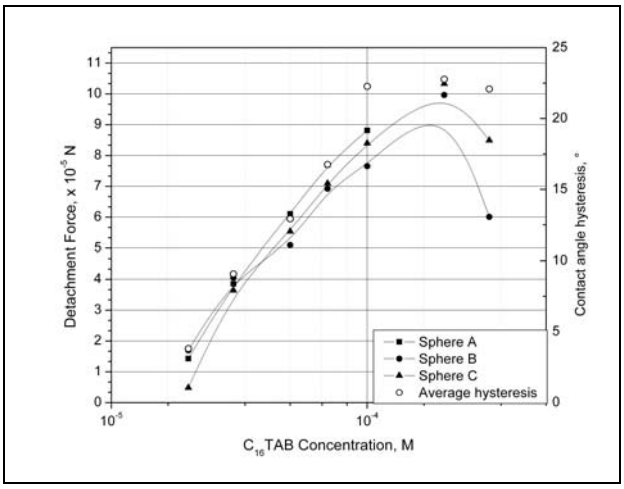

Figure 28 - Detachment force measurements of C_{16}TAB coated silica spheres

As expected, the force measurements showed good correlation between each sphere. The force of detachment was then used with equation [24] to calculate the advancing contact angle. Receding contact angle was calculated separately from radius of contact measurements at the equilibrium point. These measurements were taken from the images of the experiment. Force of detachment is closely related to contact angle hysteresis as shown in Figure 28. While the work of adhesion represents the work necessary to detach the particle once this detachment force has been reached.

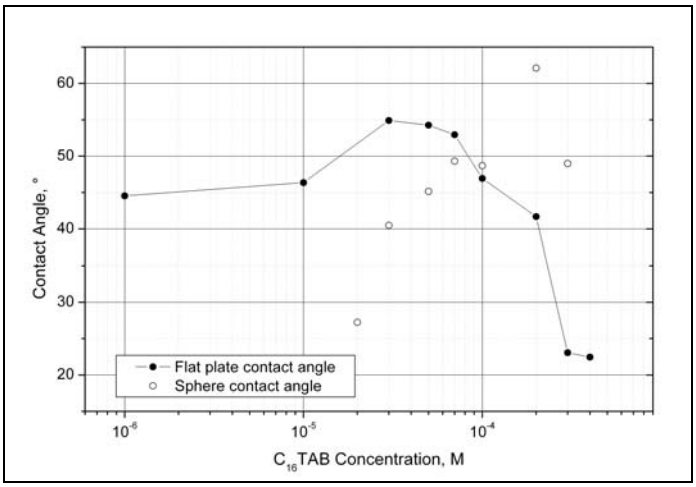

Figure 29 - Flat plate and sphere contact angle

As shown in Figure 29 the calculated contact angles differed considerably from the flat plate measurements. Some differences in contact angle based on the solid shape have been reported before (Preuss and Butt 1998b). The contact angle on a sphere can be 10° smaller for the same surface on a flat plate. This phenomenon was reported for low contact angle surfaces.

The dynamic nature of C_{16}TAB adsorption at the TPC line is also a factor explaining the difference in measurements on the sphere and flat plate. As concentration increases, the dynamic contact angle behavior may be explained by Gibbs' adsorption equation.

$$-\frac{d\gamma}{d\mu} = \Gamma \qquad [28]$$

Where μ is the chemical potential and Γ is the adsorption. The force on a solid partially immersed in water minus the buoyancy can be expressed as the wetting tension (Eriksson et al. 1996).

$$\tau = \gamma_{sv} - \gamma_{sl} \qquad [29]$$

Equation [29] can be substituted into equation [28] to obtain equation [30] (Yaminsky 1994).

$$-\frac{\partial \tau}{\partial \mu} = \Gamma_{sv} - \Gamma_{sl} \qquad [30]$$

Thus, the slope of the wetting tension isotherm represents the competition for adsorption of C_{16}TAB molecules at the solid-liquid and solid-vapor interface.

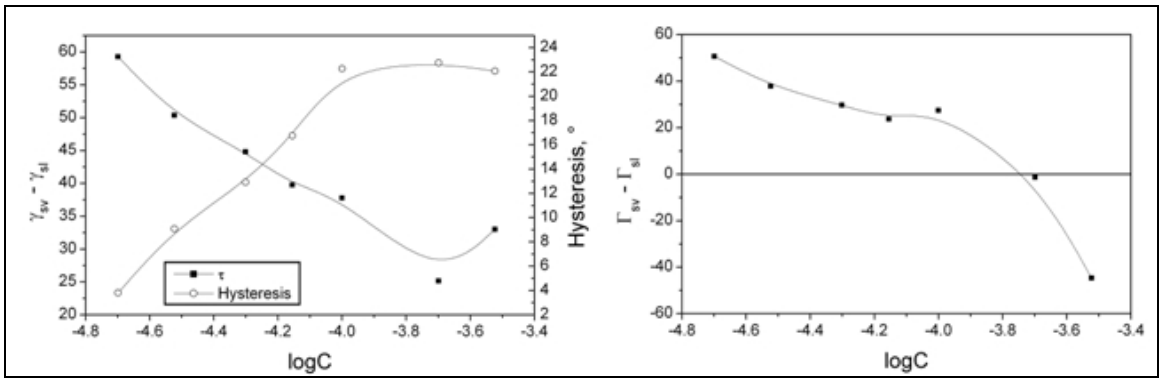

Figure 30 - (a) Wetting tension isotherm and (b) Adsorption difference isotherm

The wetting tension isotherm was graphed as shown in Figure 30(a) to find the slope of the line, which is shown in Figure 30(b). The derivative of the wetting tension isotherm does not produce the adsorption difference isotherm but is still useful as the sign of the derivative and the relative magnitude are still represented. The competition between solid-vapor and solid-liquid interface for C_{16}TAB adsorption explains the variation in contact angle and detachment force with increasing concentration. Hysteresis increases linearly with concentration until about 10^{-4}M. The linear relationship is reflected in the adsorption isotherm as the slope only decreases slightly until about 10^{-4}M. Beyond this point the slope magnitude increases sharply as the solid-vapor interface begins to adsorb less C_{16}TAB compared to the solid-liquid interface. As the adsorption difference approaches zero and becomes negative, the hysteresis plateaus and then begins to decrease.

When the sphere comes into contact with the bubble, and the TPC line spreads over the solid surface the C_{16}TAB molecules migrate out of the water onto the dry surface. This creates a high concentration gradient of surfactant molecules at the dry boundary, allowing the C_{16}TAB hydrophobic tails to escape the water. This accumulation creates a band of increased hydrophobicity on the sphere. These bands then create a surface more prone to pinning for subsequent experiments, thereby increasing hysteresis.

Hysteresis from surface domains

An atomic force microscope was used to produce images of C_{16}TAB coated silica surfaces. Silica wafers were coated with a range of C_{16}TAB concentration using the same procedure previously described. Silica wafers were used because they provide a very smooth surface (mean roughness was ≈ 0.2 nm) on which chemical heterogeneity could be observed. The sphere surface was too rough (50 – 75 nm roughness) to easily see C_{16}TAB molecules, which are only 20Å long. Figure 31 shows the AFM images which provide a qualitative justification for contact angle hysteresis. The patches on these images were about 20Å high which indicated that they were probably the beginning of the C_{16}TAB monolayer formation. As the concentration is increased, the domains seem to grow larger and more frequent. This provides local hysdrophobic sites for the TPC line to get pinned, which in turn leads to increased hysteresis.

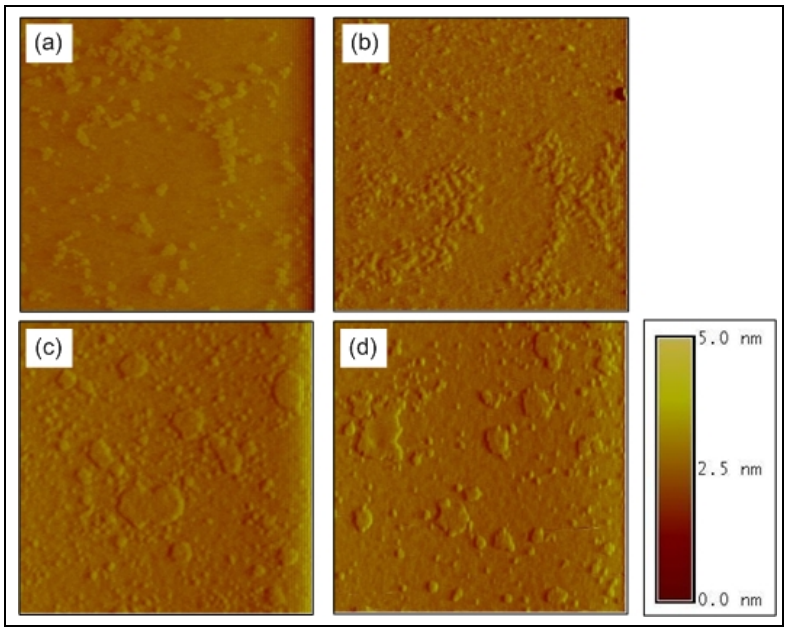

Figure 31 - AFM images of (a) $1x10^{-5}$M, (b) $3x10^{-5}$M, (c) $5x10^{-5}$M, (d) $1x10^{-4}$M C_{16}TAB coated silica wafer. Each square is 5µm x 5µm.

Energy calculations

The energy of detachment was compared with the work of adhesion calculated with equation [11] . The detachment force curve is split into two sections, the stretching or energy barrier, E_1, and the sliding, E_2. E_1 is the energy spent shifting the TPC line from receding to advancing contact

angle. Once the advancing angle is reached, then detachment may begin. E_2 is equivalent to the work of adhesion. The results of these calculations are displayed in Figure 32. The theoretical work of adhesion showed good correlation with measured energy. The difference between total energy of detachment and work of adhesion demonstrates the irreversibility of the bubble particle interaction.

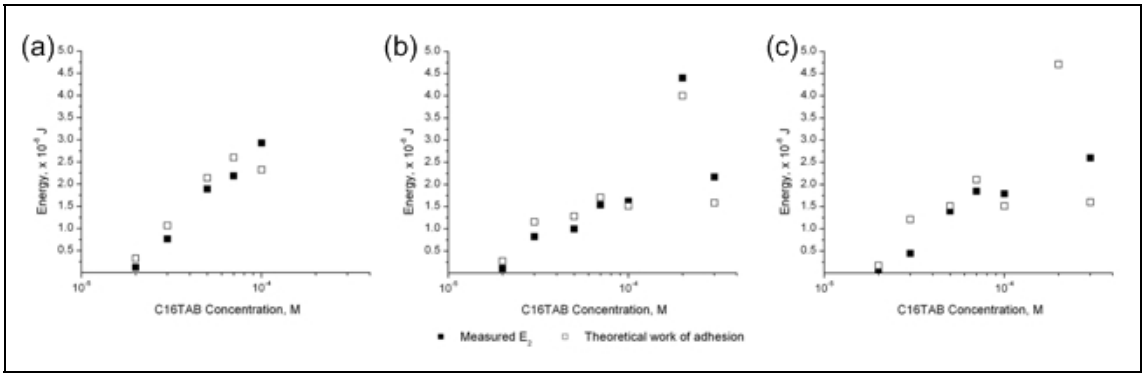

Figure 32 - Measured detachment energy, E_2, and theoretical work of adhesion for (a) Sphere A, (b) Sphere B, (c) Sphere C

Detachment Energy in Flotation

Figure 33 demonstrates the relationship between detachment energy and possible reagent usage in a flotation environment.

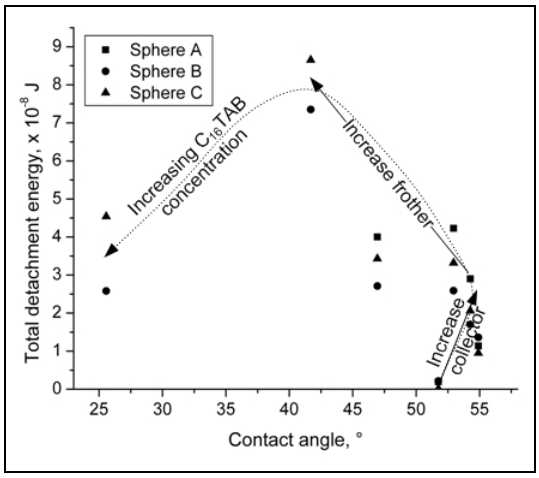

Figure 33 - Total detachment energy VS equilibrium contact angle

Increasing collector dosage increases the contact angle leading to higher detachment energies. Increasing frother decreases contact angle but this is compensated by the increase in bubble tensile strength. However, if surface tension is decreased too much, the bubbles are too strong and do not rupture easily to adhere properly to the hydrophobic particles.

Summary & Conclusion

Bubble-particle detachment energy was successfully measured as indicated by the good correlation with the theoretical work of adhesion. Total detachment energy is larger than the work of adhesion because the energy barrier for movement of the TPC line must be overcome before detachment will begin. The energy barrier is directly related to contact angle hysteresis. It is the energy spent shifting the TPC line from receding to advancing contact angle. The close relation between hysteresis and detachment force was also demonstrated.

Contact angle hysteresis is affected by the dynamic nature of C_{16}TAB adsorption at the solid-liquid-vapor interface. C_{16}TAB adsorption at the solid-vapor interface during sphere-bubble attachment and during Wilhelmy plate measurements created discrepancies between contact angle measurements at the same concentrations.

With increasing C_{16}TAB concentration, the contact angle of the sphere was increased while bulk solution surface tension was decreased. This clearly showed the careful balance between frother and collector dosages that must be optimized in coarse particle flotation.

References

Adamson, A. W. (1997). Physical Chemistry of Surfaces, J. Wiley, New York.

Chibowski, E. (2003). "Surface free energy of a solid from contact angle hysteresis." Advances in Colloid and Interface Science, 103(2), 149-172.

Eriksson, L. G. T., Claesson, P. M., Eriksson, J. C., and Yaminsky, V. V. (1996). "Equilibrium wetting studies of cationic surfactant adsorption on mica 1. Mono- and bilayer adsorption of CTAB." Journal of Colloid and Interface Science, 181, 476-489.

Frank, B., and Garoff, S. (1996). "Surfactant self-assembly near contact lines: control of advancing surfactant solutions." Colloids and Surfaces A: Physicochemical and Engineering Aspects, 116(1-2), 31-42.
Israelachvili, J. (1991). Intermolecular & Surface Forces, Elsevier Ltd., London.
Janczuk, B., Wojcik, W., and Zdziennicka, A. (1999). "Wettability and surface free energy of glass in the presence of cetyltrimethylammonium bromide." Materials Chemistry and Physics, 58(2), 166-171.
Liu, J.-F., Min, G., and Ducker, W. (2001). "AFM study of adsorption of cationic surfactants and cationic polyelectrolytes at the silica-water interface." Langmuir, 17, 4895-4903.
Preuss, M., and Butt, H.-J. (1998). "Measuring the Contact Angle of Individual Colloidal Particles." Journal of Colloid and Interface Science, 208(2), 468-477.
Sutherland, K. L. (1948). "Kinetics of the flotation process." J. Phys. Chem., 52, 394-425.
Yaminsky, V. V. (1994). "Thermodynamic Analysis of Solute Effects on Surface Forces. Adhesion between Silicates in Solutions of Cationic Surfactants." Langmuir, 10, 2710-2717.
Yaminsky, V. V., and Ninham, B. W. (1999). "Surface forces vs. surface compositions. Colloid science from the Gibbs adsorption perspective." Advances in Colloid and Interface Science, 83(1-3 SU -), 227-311.
Yaminsky, V. V., and Yaminskaya, K. B. (1995). "Thermodynamic analysis of solute effects on contact angles. Equilibrium adsorption of cationic surfactants at silica-vapor and silica-water interfaces." Langmuir, 11, 936-941.

Appendix 2: Separation of Small Particles Due to Density Differences in a CFB Riser System

TECHNICAL REPORT

Contract Title and Number:	Period of Performance:
Establishment of the Center for Advanced Separation Technologies (DE-FC26-01NT41091)	Starting Date: 9/17/01 Ending Date: 09/30/06

Sub-Recipient Project Title:
Separation of Small Particles Due to Density Differences in a CFB Riser System

Principal Investigators:
Eric K. Johnson and Bruce Kang

Contact Address:
Mechanical &Aerospace Engineering
P. O. Box 6106
West Virginia University
Morgantown, WV 26506

Subcontractor Address:
No subcontracts issued

Report Information:
Type: Final
Number:
Period: 9/17/01 – 12/31/04
Date: 1/10/2005
Code: WV002-FINAL

Contact Information:
Phone: 304.293.3111 ext.2309
Fax: 304.293.6689
E-Mail: Eric.Johnson@mail.wvu.edu

Subcontractor Information:
Phone:
Fax:
E-Mail:

DISCLAIMER

ABSTRACT

An exploratory study was conducted to demonstrate that a solid-solid mixture flowing in a riser may be separated in a dry process due to density differences, The results of this study may well lead to the initiation and development of an innovative dry separation process for solid-solid mixtures. This unique process could easily lend itself to the separation of mixtures of minerals with different densities in arid regions. A more conventional application would be the separation of pyrite from coal or coal fines. The density differences investigated in this study correspond to the density difference between pyrite and clean coal. Another application could be the reclaiming of coal fines currently discarded to settling impoundments due to the inefficiency of current wet separation process techniques. The particle sizes employed in this investigation were of a mean diameter of 350μm for the sand and 450μm for the steel shot. This exploratory study has demonstrated that a dry separation process, based on density difference, is possible in a CFB riser. This study also indicates that a significant effort is required to optimize this separation process due to the fact that many variables enter into the separation process

TABLE OF CONTENTS

LIST OF FIGURES

EXECUTIVE SUMMARY

The objective of this study was to determine the potential to separate small fines, due to their density difference, in the riser system. The riser system is essentially a vertical duct, usually found in a Circulating Fluidized Bed (CFB) system. The process is dry in that air is used to create the flow of fines through the riser. Experiments in CFB risers indicated that heavy, large, particles moving upward in the gas flow tend to move towards the riser wall, and then flow down the wall. After reaching the lower regions of the riser, the particles are re-entrained in the upward flow and repeat the process until they exit the riser.

This information led to considerations of how this phenomenon may be employed in separating dense particles from lighter particles. Initial consideration was given to the perplexing problem of the separation of plutonium oxide from fused sand. However, this soon gave way to the more regional problem of the separation of pyrite particles from lighter coal. In order to investigate the potential for this dry separation, a feasibility project was proposed to further explore this phenomenon using steel shot and sand in a riser. This proposal was funded in CAST I and the ensuing report describes that work.

A thorough review of the rather large amount of CFB literature produced no information for guidance in this effort. A rather versatile experimental system was designed and constructed. The associated instruments were selected to cover a large range of values for each parameter. A rather lengthy series of initial tests was then conducted to determine the range of operating conditions, which lead to the desired separation process. Subsequently, the following series of exploratory tests was performed to investigate the dry separation process in the experimental system:

1) single particle pass through riser,
2) multiple particle pass through riser,
3) variable heavy particle collection gap,
4) effect of internal riser rings,
5) effect of riser exit geometry,
6) effect of riser height,
7) effect of mixture composition,

Each series of tests consisted of varying the particle mass flux and the average gas velocity in the riser over a series of values selected from the initial tests. These are the common parameters found in the CFB literature.

The performance of the dry separation process was based on two parameters; which are the heavy particle collection efficiency, (η_h), and the heavy particle mass fraction, (ω_h). They are respectively defined as:

$$\eta_h = \frac{mass\ of\ \ heavy\ \ particles\ captured}{mass\ of\ \ heavy\ \ particles\ in\ \ feed}$$

And

$$\omega_h = \frac{mass\ of\ heavy\ particles\ captured}{total\ mass\ of\ the\ particles\ \ captured}$$

For the experimental system employed, the results may be summarized as follows:

1. The initial tests indicated that the flow region, for the riser, showing the greatest potential for separation was the transition zone between the fast-fluidization and dilute flow.

2. The efficiencies were sufficiently high, greater than 75%, for separation in one pass through the riser and that more than one pass produced no significant improvement.

3. The addition of internal rings in the riser to produce flow obstacles produced no significant improvement in separation.

4. Enlarging the collection gap improved the heavy particle collection efficiency but had no effect on the heavy particle mass fraction.

5. The increase in height increased the heavy particle collection efficiency and also increased the heavy particle mass fraction, except at the lowest impractical gas velocity employed.

6. The change in the exit port geometry from a side exit port to a 90^o swept top exit bend increased the heavy particle mass fraction efficiency but decreased the heavy particle collection efficiency.

7. The increase in composition, from 4% steel shot to 34% steel shot showed improved results for separation at higher mass fluxes through the riser.

This exploratory study has demonstrated that a dry separation process, based on density difference, is possible in a CFB riser. This study also indicates that a significant effort is required to optimize this separation process due to the fact that many variables enter into the separation process. A project, also funded by CAST is now in progress to determine the potential for separating coal from pyrite. This activity produced two MSME theses [1,2].

EXPERIMENTAL

The initial literature survey indicated that no attempt to separate small particles due to density difference in a riser system was described in the open literature.

Consequently, a simple versatile experimental system was designed and fabricated. Initially, the particles are loaded into a feed hopper, pneumatically transported to the riser and entrained in the air flow in the riser. Ideally, the heavier particles would exit at the bottom of the riser and the lighter particles would exit at the top of the riser. The riser system was to simulate a circulating fluidized bed riser in that the particles approaching the top of the riser may either be internally re-circulated back towards the bottom of riser or exit the riser, pass down through an external downcomer and re-enter the riser at its bottom. This is defined as continuous recirculation. In addition, after a test run, the particles in the product hopper may be again sent through the riser for a second time. This is defined as batch recirculation. In that case, the product hopper becomes the feed hopper and the feed hopper becomes the product hopper. Afterwards, the air flow could be reversed again and another test with the material (which has now gone through the riser twice) would be performed. Thus as many passes through the riser, for an initial mixture, as desired may be investigated.

In addition to the continuous recirculation and batch operating modes, a third mode of operation may be the partial continuous recirculation mode employed. After the initial results indicated the batch recirculation produced the best results this mode of operation was employed throughout this study.

The instrumentation selected for this exploratory study was based on information relating to CFB systems. The range of variables for each instrument was rather large in order to cover any unexpected magnitudes in measurement. The instrumentation employed is shown in Figure 1. The pressure gauges, the flow meters, and the load cells were all commercial devices. A basic scale was used to measure the weight of the sand and steel shot into the feed hopper. Magnets were used to separate the steel shot from the sand collected in the dense particle bin. The steel shot and sand were then weighed.

Information from the instruments and observations were input data to a dedicated personal computer. Signals from the load cells were sent to an Analog Devices 5B40-3 signal conditioner. The conditioners were mounted in an Analog Devices SB-08 back plane. These signals and those from the differential pressure transducers were sent to a MSTB 009-09 analog termination board. The signals were then sent to a Microstar Laboratories DAP 5200 a/526 data acquisition board. The computer program used to read the sensors was DAPView.

Initial tests were undertaken to establish the conditions for which separation occurred. The controlled variables were the mass flow of solids into the riser and the volumetric flow rate of air through the riser. The conditions selected for further study were those which showed a significant amount of steel shot collected in the dense particle bin. In selecting a range for the test variables, it was decided that an attempt would be made to find the highest value of solids mass flow, with acceptable separation. An unpredictable limiting factor was that for high solid flow rates, the height of the bed of material in the riser would rise to cover the collection gap.

The air flow was established first for each test. The solids flow would then be established. With the flow, system geometry, and test conditions selected, the mass flow rate of solids could not be set accurately. However, once the valves to the feed hopper were opened, a steady flow of solids was quickly established. Consequently, for the usual fifteen minute test run, it is estimated that steady state existed about 95% of the test period. For several tests the load cell on the feed hopper indicated some erratic behavior and that test run data was discarded. The reason for the erratic behavior was traced to the air compressor beginning to malfunction. The air compressor was repaired and a request for a project time extension was made to make up for the lost time.

Tests were conducted for single and multiple passes through the riser. The multiple pass tests showed no significant improvement over the single pass tests; therefore, only single pass tests were employed in the following tests. Because these tests were of an exploratory nature, only sufficient data was obtained for each system modification to determine the corresponding change in separation efficiency. The parameters investigated were:

1) rings (obstructions) in the riser

2) variation in the gap size

3) two different riser heights

4) two different riser exit geometries

5) two different mixtures of steel shot and sand.

The basic geometry for the initial tests was a riser height of 2.44m, a side outlet, a 3.2mm heavy particle collection gap, and a fixed heavy particle mass fraction in the feed. The internal diameter of the riser remained fixed for all tests at 12.7cm. Afterwards, the height of the riser was increased to 4.27m and a side exit port was employed for one test. A 90^0 swept elbow was then attached to the top of the riser as the exit port. The final series of tests was then performed using this configuration

An image acquisition and processing prototype system was designed, assembled, and applied to measuring the size and velocity distribution of moving particles in a gas-solid environment. The prototype system consists of a digital image acquisition module and MATLAB® image-processing module. The goal was to develop a high speed imaging acquisition system for on-line measurement of particle separation in a simulated CFB riser system. Results [2] obtained have demonstrated that the system can capture particles in motion with three cameras and perform online-analysis. We believe the processes developed in the optical system study of particle cluster characteristics constitute a feasible approach to the online monitoring of the particle separation process. Although the methods were only demonstrated with the simulation setup, we believe that similar techniques could be applied to large-scale separation system.

RESULTS AND DISCUSSION

The initial effort in this research was to establish the conditions that appear to have potential for particle separation. The controlled variables during these tests were the solids mass flux and the superficial gas velocity. The geometry of the riser was fixed and the steel shot concentration in the feed was held constant. The conditions for "good" separation are near the boundary between fast fluidization and dilute flow regions. Fast fluidization is defined as flow where particles (clusters) move down along the wall. Dilute flow is defined as containing a bubbling bed in the distribution section. If a fluidized bed formed during a test, the bed height had to be maintained below the location of the gap or the run was discarded. The results of the initial tests are shown in Figure 2.

For selected conditions, solids mass flux and superficial gas velocity, single and multiple pass batch tests were conducted. The results for the multiple pass batch tests are shown in Figure 3. These results indicated that the particle separation in a single pass was sufficient for good performance. The separation in the subsequent passes showed a slight improvement in the collection steel shot which was offset by the increase in the sand captured. Consequently, it was decided that only a single batch test would be used in the remaining work in this study. Single pass batch test results are shown in Figures 4 and 5. The highest separation efficiencies are at solid mass fluxes less than 2 kg/m^2s and relatively low superficial gas (air) velocities, less than 3.35m/s. With these results, it was decided that future exploratory tests would be directed toward higher solids mass fluxes while maintaining acceptable separation rates.

The next variable of concern was the size of the gap for capturing the heavier particles. The gap size was 3.2mm in the basic system and the gap size of 6.4mm was then investigated. The results are shown in Figure 6. For the test conditions indicated, the heavy particle collection efficiency improved, but the heavy particle mass fraction remained essentially the same, with the larger gap size. Since the gap size was relatively easy to change, it was also varied while investigating the other parameters.

The next variable to be investigated was the effect of an obstacle on the separation process in the riser. The obstacle was a ring, whose axis coincided with the axis of the riser, sticking out from the riser wall. The internal diameter of the ring to the internal diameter in the riser was 0.7 and 0.8. The results for the selected conditions are shown in Figures 7 and 8. Although the heavy particle collection efficiency drops slightly with larger obstruction, the heavy particle mass fraction improves significantly. This phenomenon will be investigated more thoroughly in the future.

The effect of increasing the height of the riser on the separation process was then investigated. As the literature search continued, it appeared that a 90^o swept exit port (outlet) at the top of the riser may improve the separation process. Tests were then conducted at a riser height of 4.27 m for a side outlet and a 90^o swept outlet for similar conditions. The results are shown in Figure 9. Also shown on this figure are the results of a higher mass flux through the 90^0 sweep exit port. Although the heavy particle

collection efficiency was reduced, the heavy particle mass fraction result significantly improved. The solids mass flux was then increased and performance for the 90^o outlet was not too different from the original side outlet run, Figure 9. These results were the motivation to continue the exploratory investigation at the increased height and using the 90^0sweep exit port. The gap size for these tests was 6.4mm.

Tests were then conducted to determine the effect of gap size on performance. Figure 10 shows that there is very little difference in performance for the two gap sizes. Consequently, the gap size was no longer considered a significant parameter in this investigation.

Figures 11and 12 illustrate the performance of the 4.27m high riser with a 90^0 swept exit port. The performance (efficiencies) is still acceptable, but the performances at high mass fluxes have improved significantly. Up to this point, all the tests were conducted with an initial mixture with a heavy particle mass fraction of 0.04. The next set of tests was for an initial heavy mass fraction of 0.34, using the same riser configuration. As shown in Figures 13 and 14, the heavy particle mass fraction collected was excellent at higher gas velocities; whereas, the heavy particle collection efficiency was better at lower velocities.

Finally, data was collected to ascertain the effect of the heavy mass fraction of the initial mixture on the performance of the riser. The heavy mass fraction collected as a function of the initial heavy mass fraction is shown in Figure 15. Apparently, there is an improvement in the heavy mass fraction collected as more heavy particles are available to be captured in the riser.

CONCLUSIONS

The prime conclusion of this project is that a solid-solid mixture flowing in a riser may be separated, due to density differences, in a dry process. The results of this exploratory study should initiate the development of a new type of dry separation systems for solid-solid mixtures. Mixtures of minerals with different densities may now be separated in arid regions. An example of an immediate problem is the separation of plutonium oxide from sand in the nuclear weapons test ranges in the Southwest USA. Pulverizing coal to a size with this process has the distinct advantage in that the separation process is dry. Here a large amount of pyrite is liberated and will form a mixture suitable for separation in the riser system. The density differences investigated in this study correspond to the density difference between pyrite and clean coal. Because the waste coal in ponds is rather fine, this separation process is well suited for reclaiming waste coal, after the fines are cleaned. The sizes of the particles employed in this investigation were of a mean diameter of 350μm for the sand and 450μm for the steel shot.

This exploratory study produced the following general conclusions:

1. The separation occurs efficiently, for this riser system, when operating in the transition zone between fast fluidization (core annulus) flow and dilute flow.

2. The taller the riser, the greater the allowed mass flux through the riser with excellent separation characteristics.

3. The overall performance of the riser is improved when employing a 90^0 sweep exit port as opposed to a side exit port.

4. The mass flux through the riser is limited by the formation of a dense bed which will cover the heavy particle exit gap.

Although a general knowledge of separation is now understood, the riser system still requires further study. Optimum design and operating have not been established. The separation of particles less than 100μm, based on density differences, has not been investigated in the riser system. Also, sufficient data has not been produced for a study of the scaling of the riser systems.

In conclusion, this exploratory study has demonstrated the feasibility of a dry separation process, based on density differences, in a riser system. This exploratory work has also drawn attention to what must yet be done to achieve a commercially viable separation process.

REFERENCES

1. Jeremy L. Regester, “Separation of Small Particles Due to Density Differences in a CFB Riser System,” MSME thesis, August 2004.

2. Ming Zhang, “Optical Measurement of Ash Particle Size and Velocity in Gas-Solid Flow,” MSME thesis, May 2004.

Student Endeavors:

The following two students have obtained their Mater of Science in Mechanical Engineering under this project

1. Jeremy L. Regester, “Separation of Small Particles Due to Density Differences in a CFB Riser System,” MSME thesis, August 2004.

2. Ming Zhang, “Optical Measurement of Ash Particle Size and Velocity in Gas-Solid Flow,” MSME thesis, May 2004.

Publications:

Paper has been submitted to SME-Minerals and Metallurgical Procssing Journal in Oct. 2004, "The Fluidized Bed Riser as a Dry Particle Separation System" by E.K. Johnson, J.L. Regester, and B.S.-J. Kang.

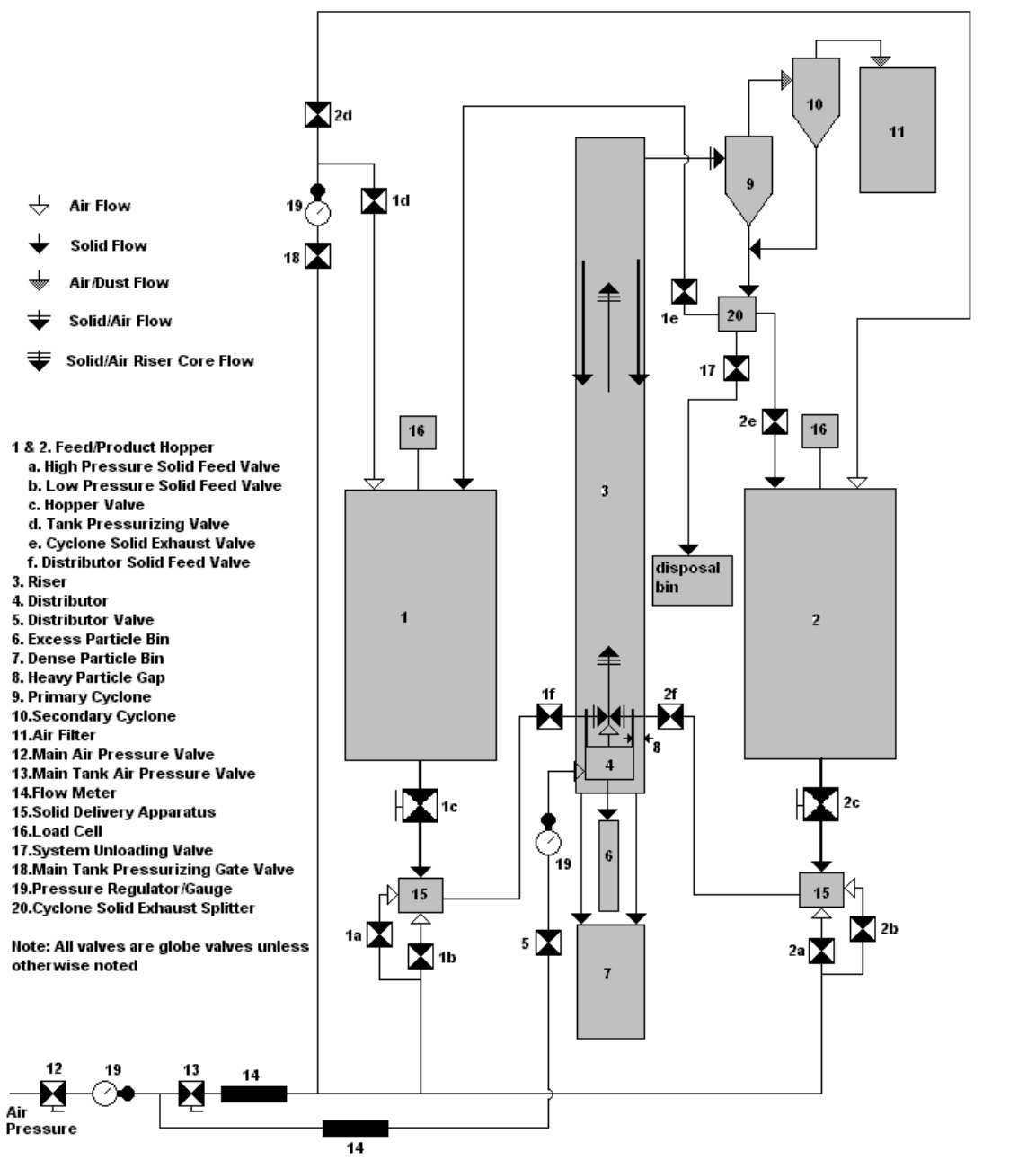

Figure 1: Riser System for the Exploratory Investigation

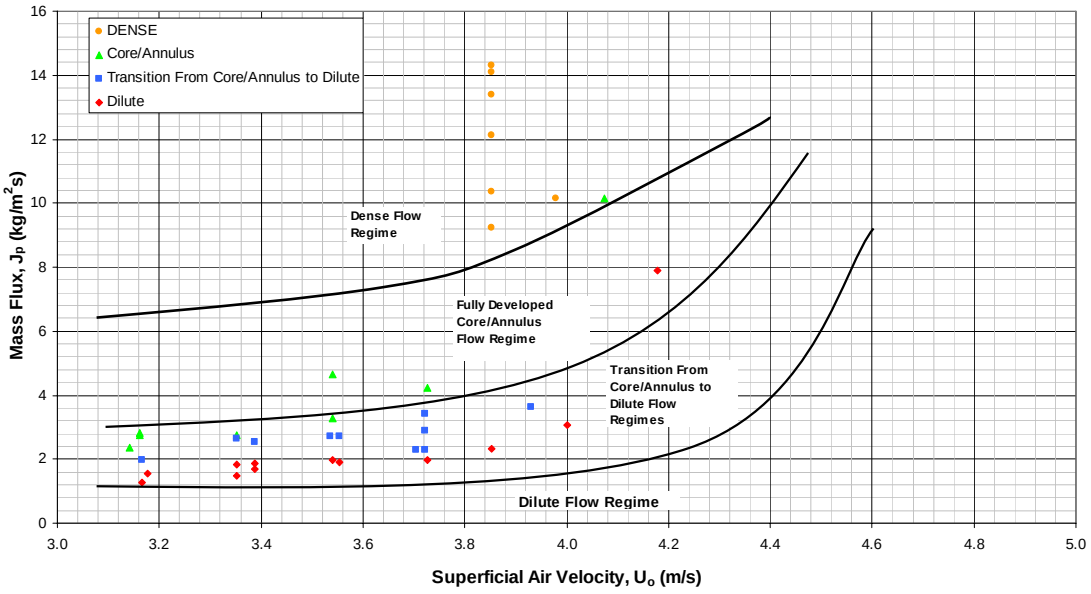

Figure 2: Experimental Flow Regime Diagram for Riser

2.44 meter Riser Height, No Internal Ring, Side Outlet

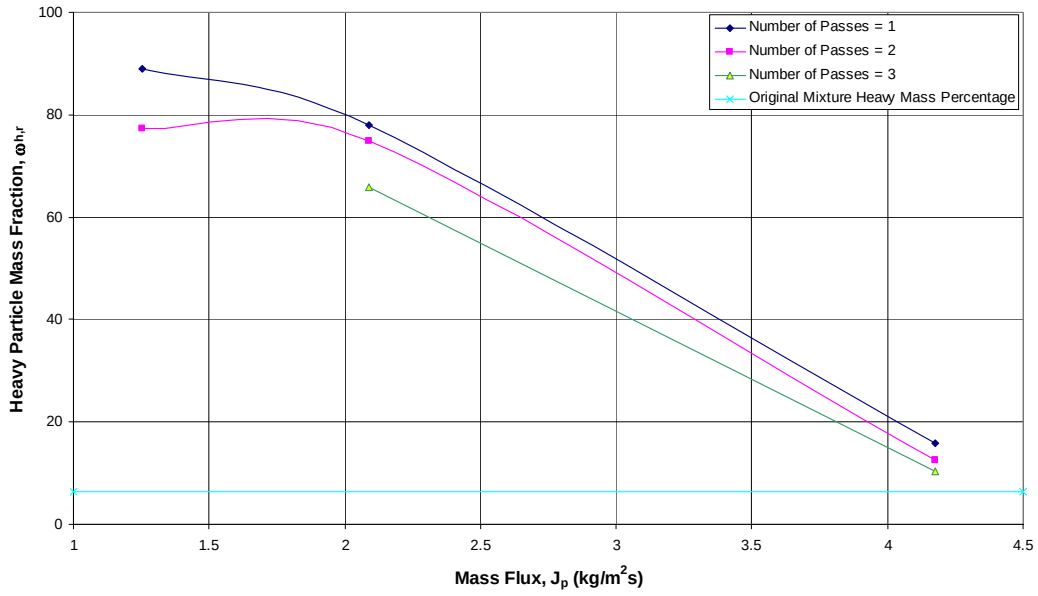

Figure 3: Effect of Number of Passes on Heavy Particle Mass Fraction Collected

U_0 = 3.73 m/s, No Internal Ring, 2.44 meter Riser Height, 3.2 mm Gap, Side Outlet

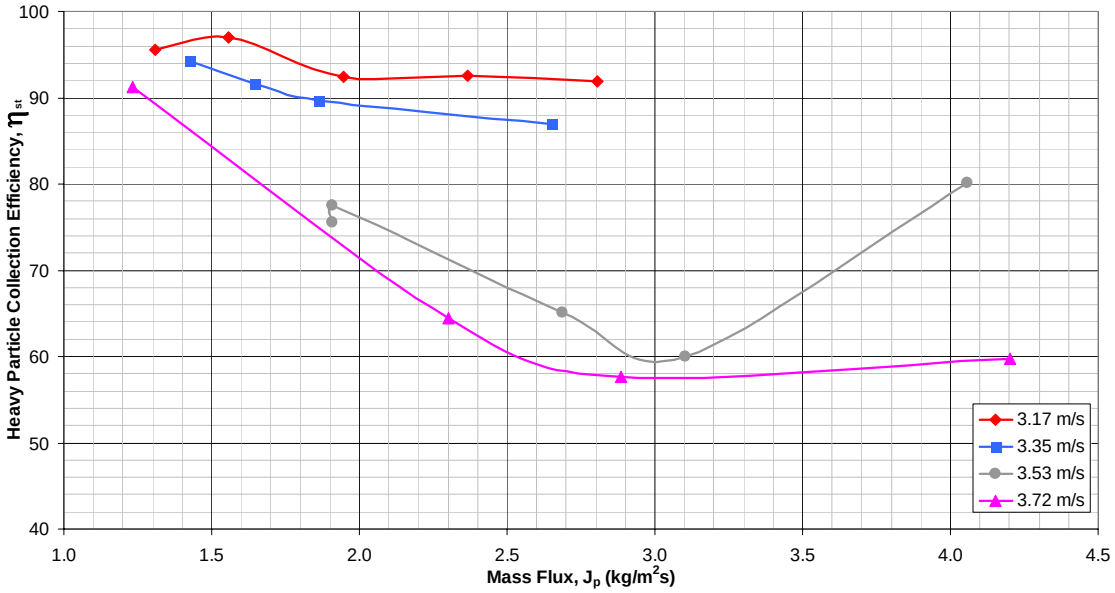

Figure 4: Heavy Particle Collection Efficiency vs. Mass Flux for Single Pass

2.44 meter Riser Height, No Internal Ring, Side Outlet

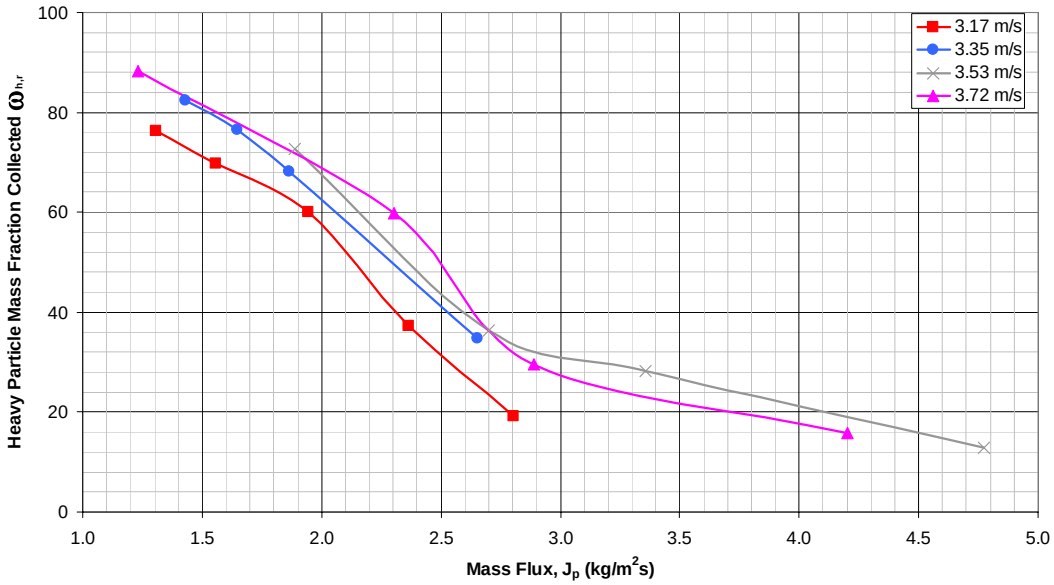

Figure 5: Heavy Particle Mass Fraction vs. Mass Flux for Single Pass

2.44 meter Riser Height, No Internal Ring, Side Outlet

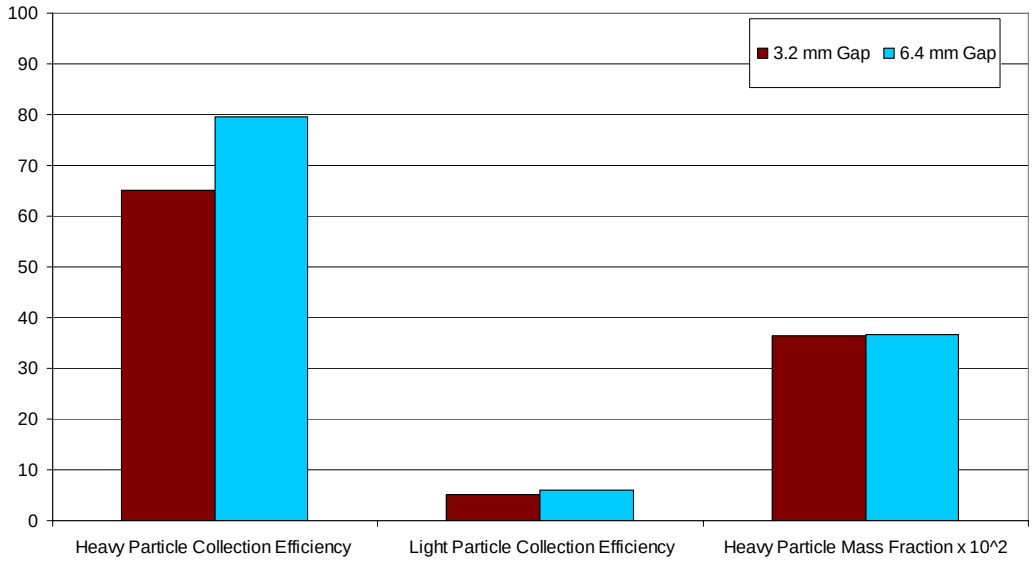

Figure 6: Effects of Gap Variation

Side Outlet, 2.44 meter Riser Height, J_p = 2.68 kg/m2s, U_0 = 3.53 m/s

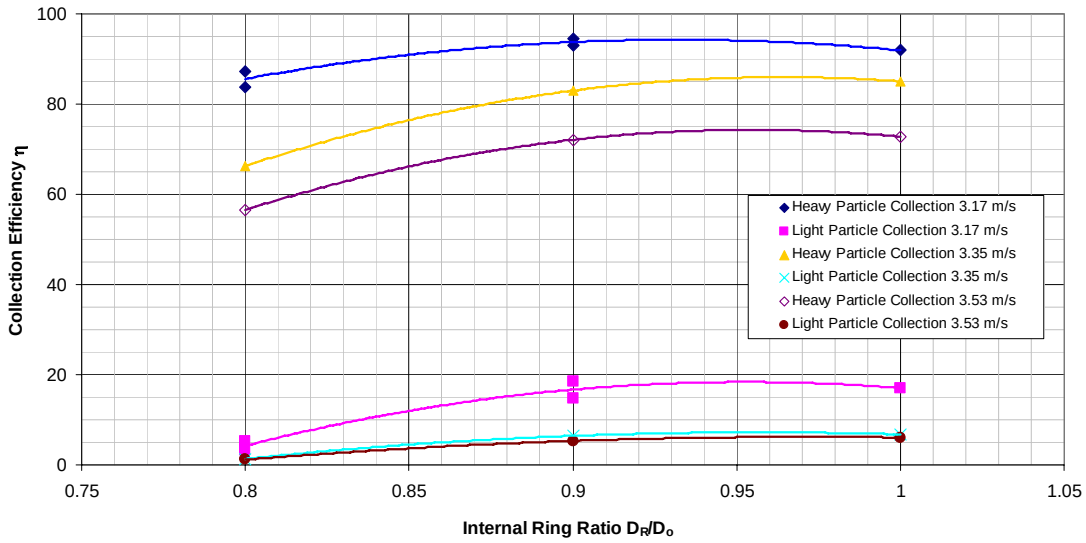

Figure 7: Effect of Internals on Collection Efficiency

3.2 mm Gap, 2.44 meter Riser Height, 0.91 meter Ring Height, Side Outlet, J_p = 2.78 kg/m^{2}s

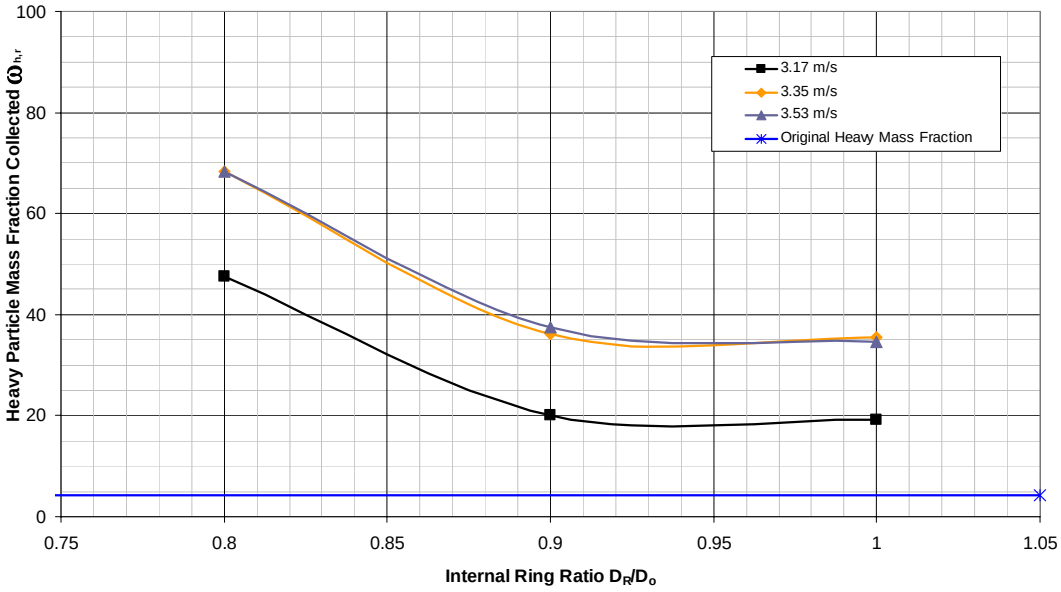

Figure 8: Effect of Internal Ring on Heavy Particle Mass Fraction Collected

3.2 mm Gap, 2.44 meter Riser Height, 0.91 meter Ring Height, Side Outlet, J_p = 2.78 kg/m^{2}s

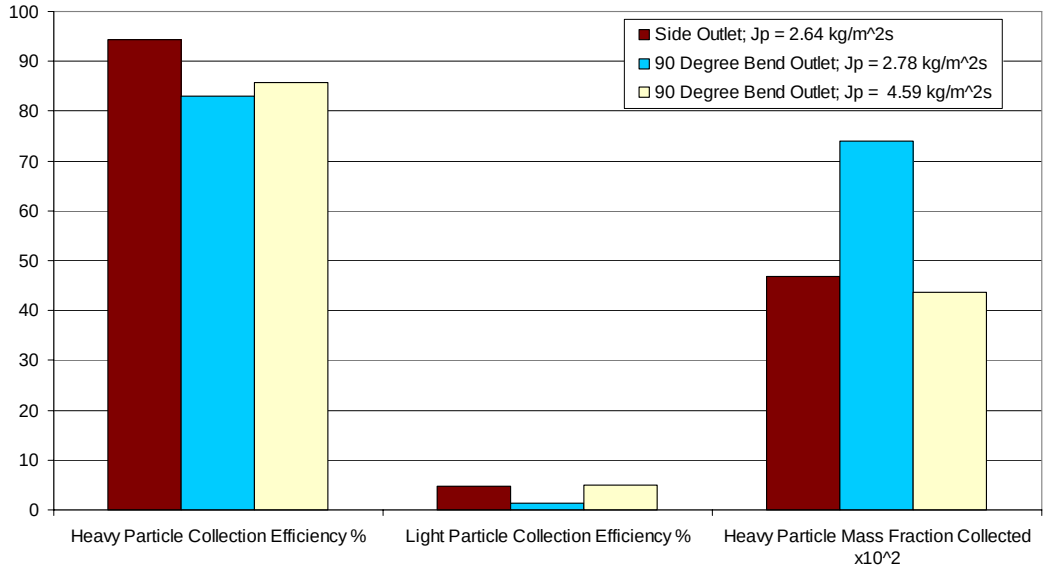

Figure 9: Outlet Comparison

U_0 = 3.53 m/s, 4.27 meter Riser Height, 6.4 mm Gap

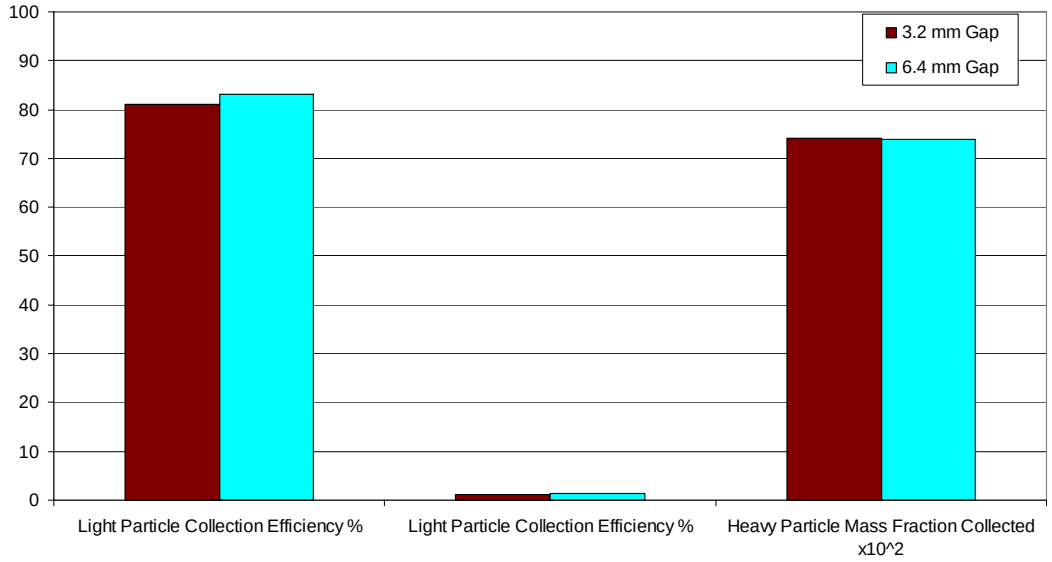

Figure 10: Gap Comparison for 90 Degree Swept Outlet

U_0 = 3.53 m/s, J_p = 2.78 kg/m2s, 4.27 meter Riser Height

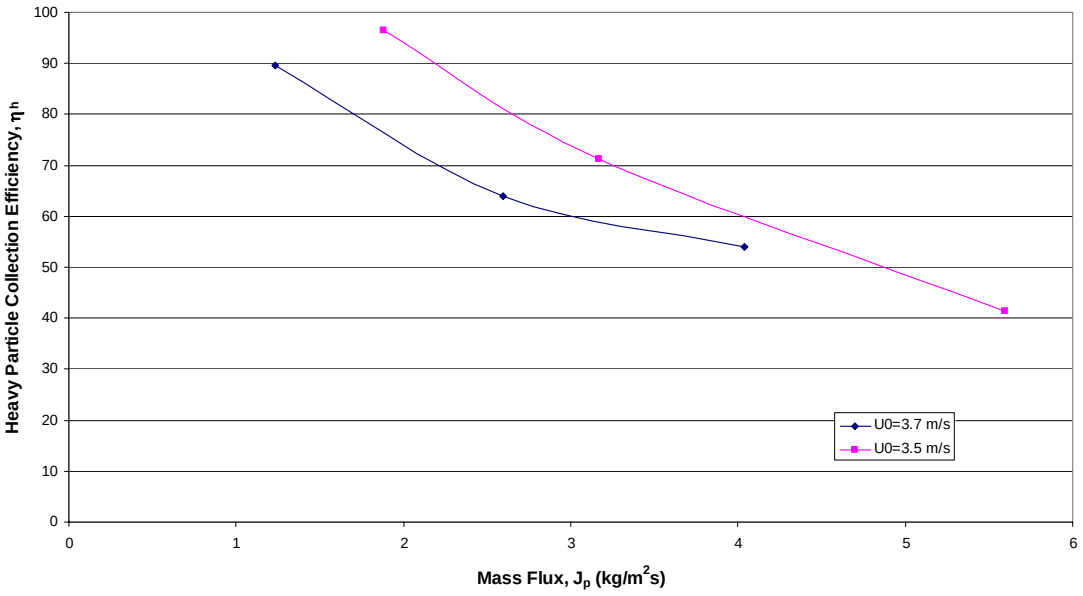

Figure 11: Heavy Particle Collection Efficiency for Swept Outlet

4.27 meter Riser Height, $\omega_{h,g}$ = 0.04

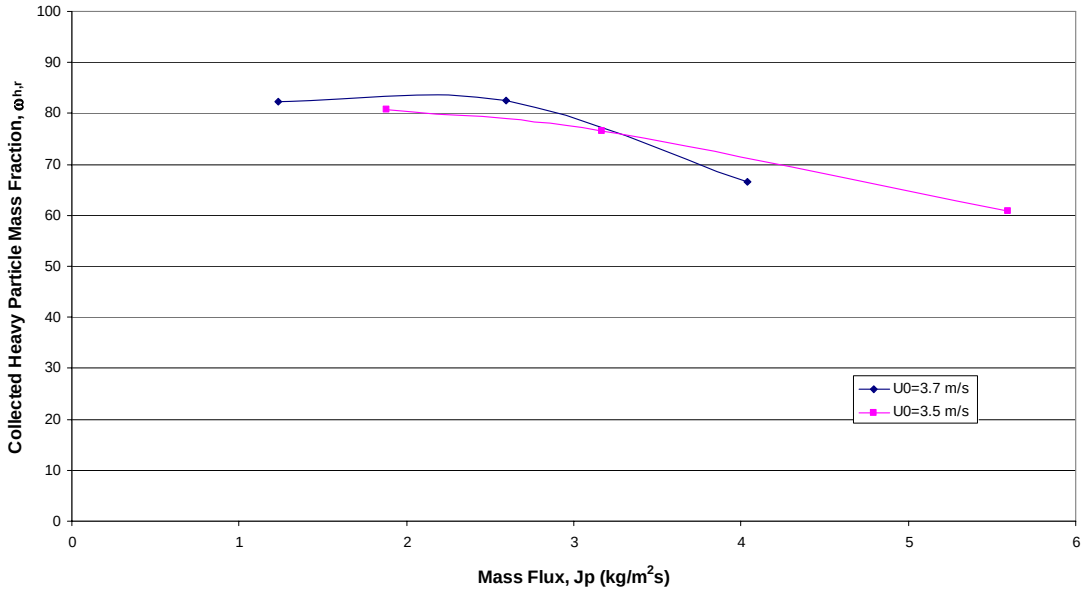

Figure 12: Heavy Particle Mass Fraction Collected for Swept Outlet

4.27 meter Riser Height, $\omega_{h,g}$ = 0.04

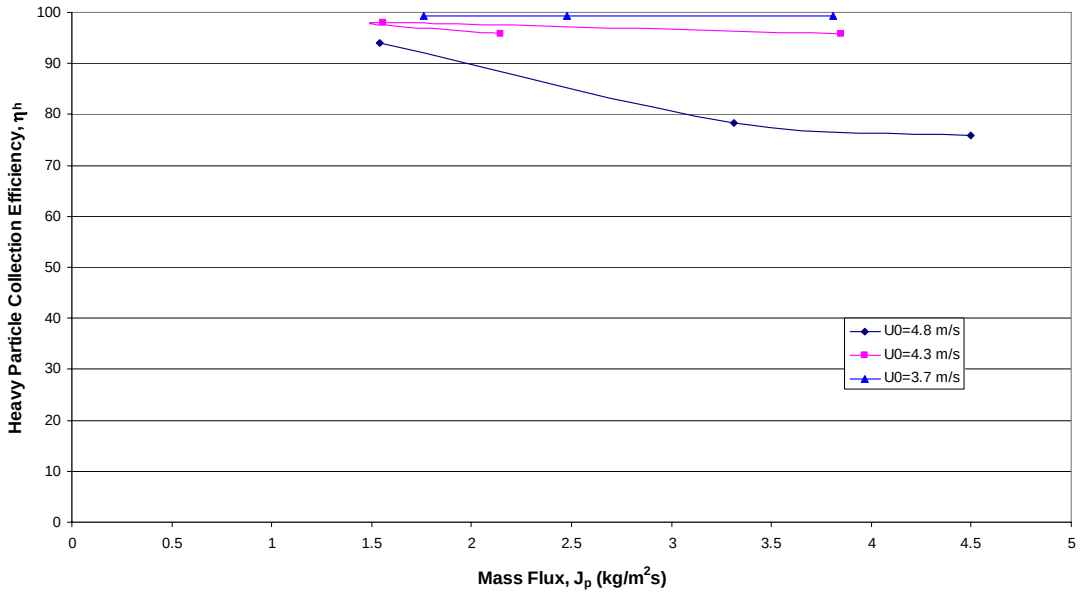

Figure 13: Heavy Particle Collection Efficiency for Swept Outlet

4.27 meter Riser Height, $\omega_{h,g}$ = 0.34

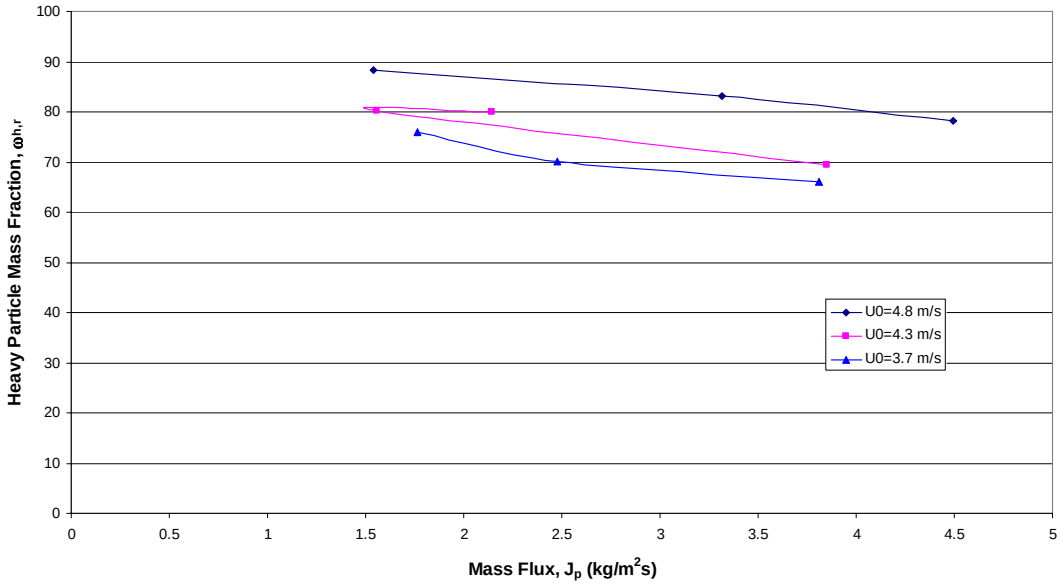

Figure 14: Heavy Particle Mass Fraction for Swept Outlet

4.27 meter Riser Height, $\omega_{h,g}$ = 0.34

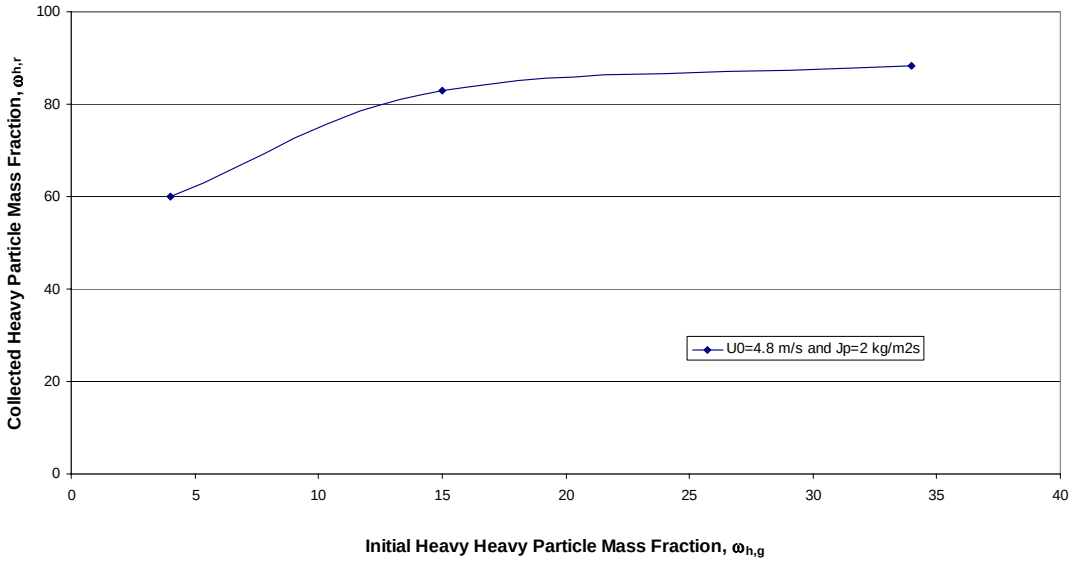

Figure 15: Collected Heavy Particle Mass Fraction as a Function of Initial Heavy Particle Mass Fraction

4.27 meter Riser Height, Swept Outlet

Appendix 3: Modeling of Flotation From First Principles

TECHNICAL PROGRESS REPORT

Contract Title and Number:	Period of Performance:
Establishment of the Center for Advanced Separation Technologies (DE-FC26-01NT41091)	Starting Date: 09/17/01 Ending Date: 09/30/06

Sub-Recipient Project Title:	Report Information:
Modeling of Flotation From First Principles	Type: Final Number: Period:
Principal Investigators:	Date: 9/30/04
Roe-Hoan Yoon	Code: VA001-FINAL
Contact Address:	Contact Information:
146 Holden Hall Virginia Polytechnic Institute & State University	Phone: (540)231-4508 Fax: (540)231-3948 E-Mail: cast@vt.edu
Subcontractor Address:	Subcontractor Information:
No subcontracts issued.	Phone: Fax: E-Mail:

DISCLAIMER

Development of a Flotation Rate Equation from First Principles under Turbulent Flow Conditions

ABSTRACT

A flotation model has been proposed that is applicable in a turbulent environment. It is the first turbulent model that takes into account hydrodynamics of the flotation cell as well as all relevant surface forces (van der Waals, electrostatic, and hydrophobic) by use of the Extended DLVO theory. The model includes probabilities for attachment, detachment, rising, and froth recovery as well as a collision frequency. A review of the effects fluids have on the flotation process has also been given. This includes collision frequencies, attachment and detachment energies, and how the energies of the turbulent system relate to them. Flotation experiments have been conducted to verify this model. Model predictions were comparable to experimental results with similar trends. Simulations were also run that show trends and values seen in industrial flotation systems. These simulations show the many uses of the model and how it can benefit the industries that use flotation.

TABLE OF CONTENTS

List of Figures

List of Tables

PAPER 3

Introduction

Background

Flotation is widely used throughout the mining industry as well as the chemical, and petroleum industries. It can be a highly efficient process for solid-solid separation of minerals. It is now more diverse in its application, with uses such as separation of ink from paper, plastics from each other, radioactive contaminants from soil, and carbon from fly ash. The entire industry is growing along with knowledge of the process and sub-processes. With this increased knowledge, a more reliable flotation model can be derived from first principles. This results in a general flotation model, and allows its use in the mining industry, regardless of machine type and material being recovered.

Generally, flotation is a three-phase process, which uses a medium of water (liquid) to separate various particles (solid) by the addition of air bubbles (gas). Hydrophobic particles attach to the bubbles and rise to the top of the flotation cell where they are extracted while hydrophilic (or less hydrophobic) particles remain in the slurry. The attachment of particles to bubbles is the most important sub process in flotation. Without a selective attachment, no separation would be possible. To enhance this selective attachment, surfactants may be added to alter surface properties. The surfactants control the surface tension and contact angles of the particles in the flotation process.

Flotation occurs within a turbulent environment. Turbulence within a conventional flotation cell is produced by the action of the impeller, which is used for mixing purposes, while turbulence within a column flotation cell is induced by rising air bubbles and settling particles. The combination of the hydrodynamic forces in a turbulent environment and the surface forces controlled by the addition of surfactants makes modeling of the entire flotation process very complex.

Modeling

Modeling of flotation has two major benefits. The main benefit being the control and improvement of the flotation process within an industrial situation. The model will be able to predict a recovery from certain known inputs. If possible, the controller, either

human or computer, may be able to improve the recovery by modifying those inputs. The model has the benefit of instantly knowing what that modification will do. The model can also find the maximum recovery within certain input ranges. The second benefit is that process design can be more easily accomplished. For a typical flotation circuit design within a processing plant, many lab tests are run and scale up of those tests are then performed. A flotation model can bypass the inaccuracy of the scale up process and do away with many of the flotation lab tests. As long as certain input variables are known the flotation recovery can be calculated.

A flotation model is similar to a chemical kinetics model, with one form of that being shown in Equation 1.

$$\frac{dN_1}{dt} = f\left(k, N_i\right) = -k_1 N_1^{f} - k_2 N_2^{g} \qquad 1$$

The model directly predicts the change in particle concentration, N_1, with respect to time, t, as a function of a certain concentration(s), N_i, and rate constant(s), k_i. The negative sign indicates that the concentration is diminishing due to the loss of particles being floated. The exponents f and g signify the order of the process. Most researchers believe that flotation is a first order process and a function of only the particle concentration and a rate constant (Kelsall 1961; Arbiter and Harris 1962; Mao and Yoon 1997).

$$\frac{dN_1}{dt} = -kN_1 \qquad 2$$

The rate constant, k, within this equation conveys how rapidly one species floats. A high rate constant indicates that certain species floats quickly while a low rate constant indicates slow flotation. Knowing the rate constants of two (or more) species within a separation process reveals the efficiency of the process. The greater the difference between the two rate constants, the better the separation is. The recoveries of each individual species, R, can also be calculated knowing the rate constant as well as the residence time within the cell, τ.

$$R = \frac{k\tau}{1 + k\tau} \qquad 3$$

Since recoveries are the desired output from modeling flotation, the rate constant is the useful component of Equation 2. Throughout flotation modeling history, the attempt has been made to produce a general flotation rate constant equation.

The most recent general turbulent flotation rate model was given by Pyke, Fornasiero, and Ralston (2003).

$$k = -2.39 \frac{G_{fr}}{d_2 V_{cell} u_2} \left(\frac{0.33 \varepsilon_d^{4/9} d_2^{7/9}}{\nu^{1/3}} \right) \left(\frac{\Delta \rho_2}{\rho_3} \right)^{2/3} E_C E_A E_S \qquad 4$$

Rate constants are usually modeled as a function of a collision frequency, and probabilities of attachment and detachment (Schulze 1993; Yoon and Mao 1996; Mao and Yoon 1997; Lu 2000; Bloom and Heindel 2002; Pyke, Fornasiero et al. 2003). In Equation 4, the attachment efficiency, E_A, is taken to be the probability of attachment while the stability efficiency, E_S, is an inverse probability of detachment. There is also a collision efficiency, E_C, which takes hydrodynamic effects into account during the collisions of particles and bubbles. The remainder of the equation is the collision frequency. The true number of collisions, that may or may not become attached, results from the combination of the collision efficiency and collision frequency. The collision frequency shown in Equation 4 is a modified equation given by Abrahamson (1975) that is divided by the number density of particles. The turbulent velocity used within Abrahamson's model is given by Liepe and Mockel (1976).

The collision efficiency within Equation 4 takes into account the fact that particles may deviate from the fluid flow and may not collide due to this deviation. Pyke, Fornasiero, and Ralston (2003) use a solution of the BBO equation referred to as the Generalized Sutherland Equation. This takes into account interception and inertial forces.

The attachment efficiency makes use of the angle of collision, which results in a certain maximum sliding time, and relates that to the amount of time needed for the bubble and particle to become attached once collision occurs. When collisions occur, a certain amount of time, referred to as the induction time, is required for the liquid film to be drained between the bubble and particle as well as the three-phase-contact line to spread and become stable. Enough time must be available during the collision process for the attachment to take place.

The stability efficiency is a relationship between the attachment and detachment forces. The attachment forces include capillary and hydrostatic forces. The detachment

forces include buoyancy, gravitational, machine acceleration, and capillary force. Knowing these, the stability of the aggregate can be determined.

Equation 4 provides a model of the flotation process based upon turbulent characteristics of the flow as well as hydrodynamic forces. What the model does not account for is the effects of surface forces. Surface forces are known to have an effect on the outcome of flotation as shown by Mao and Yoon (1997). Without the inclusion of surface forces a model can predict only a certain percentage of cases and is not general in nature. A flotation model has been proposed that accounts for surface forces in a quiescent environment (Yoon and Mao 1996).

$$k = \frac{1}{4} S_b \left[\frac{3}{2} + \frac{4\,\mathrm{Re}^{0.72}}{15} \right] \left(\frac{R_1}{R_2} \right)^2 \exp\left(-\frac{E_1}{E_k} \right) \left[1 - \exp\left(-\frac{W_a + E_1}{E_k^{'}} \right) \right] \qquad 5$$

This model is derived from first principles and is the most rigorous flotation model, to date, dealing with all dominant surface forces found in flotation. These surface forces are the electrostatic, van der Waals, and hydrophobic forces and are modeled based upon the extended DLVO theory. The surface forces are used in calculating the probability of attachment (first exponential term) and the probability of detachment (second exponential term). The energies that must be overcome, by the kinetic energies of the particles and bubbles, for the attachment and detachment processes to occur are related to the surface forces.

The first half of Equation 5 is a combination of the collision frequency ($¼S_b$) and collision efficiency. The collision frequency is derived from the number of particles one bubble would collide with assuming it traveled vertically the entire length of the cell and particles were completely stationary and evenly distributed throughout the cell. This becomes a function of the surface area rate, S_b, of the air. Since particles are not stationary, a collision efficiency is used to take into account hydrodynamic effects. This assumes that particles follow the fluid completely (no inertial effects) and that there is a governing stream function that takes into account the Reynolds number of the bubble.

The problem with this model is that it was derived for a quiescent environment. Due to this, no turbulent effects are present. Since turbulence is found in all flotation situations, this model can not be applied for flotation purposes. It does, on the other

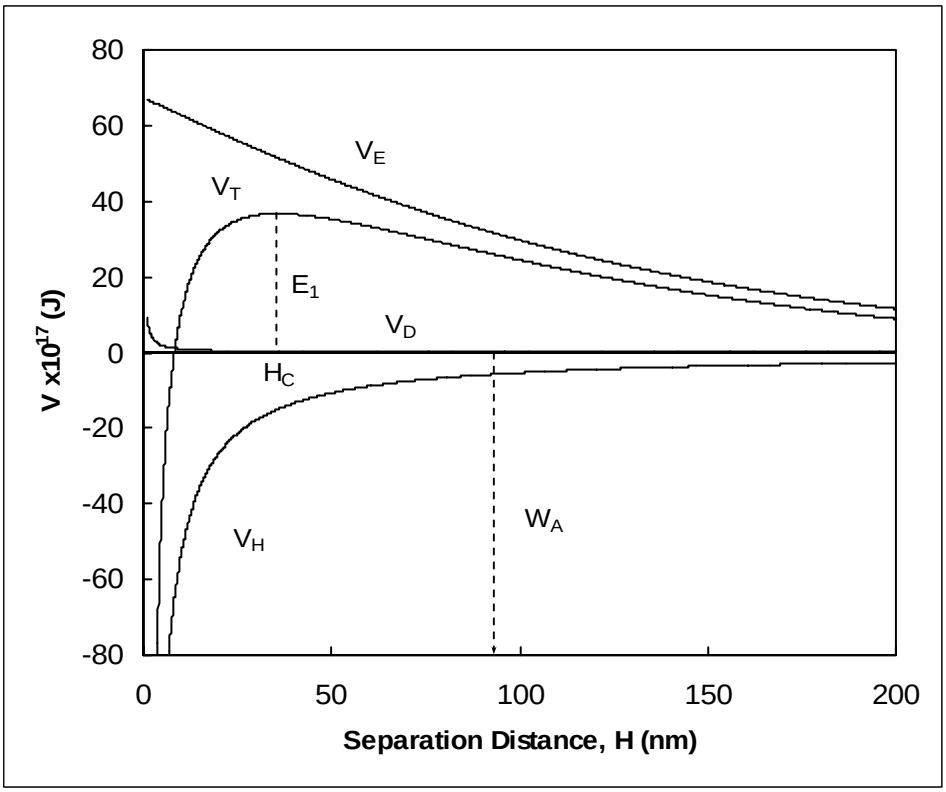

Figure 1. Surface energy vs. distance of separation between two particles (i.e. particle-bubble)

hand, provide a valuable relationship between the hydrodynamics of the system and the surface forces.

Surface Forces (Energies)

Surface forces are interactions between surfaces usually on a scale of less then 100 nanometers. The forces can be converted into energies of interaction based upon the radii of the two interacting surfaces. Surface force modeling in flotation employs the extended DLVO theory. This theory combines the van der Waals (dispersion) energy (force), V_D, electrostatic energy (force), V_E, as well as the hydrophobic energy (force), V_H, into one total surface energy (force), V_T (see Figure 1). These surface energies are additive as shown in Equation 6.

$$V_T = V_E + V_D + V_H \qquad 6$$

All three forces (energies) are either known or shown to have an effect on interactions between particles and bubbles in a water medium (Yoon and Mao 1996; Yoon 2000).

The electrostatic energy is given by Equation 7 (Shaw 1992).

$$V_E = \frac{\pi\varepsilon_0\varepsilon R_1 R_2\left(\Psi_1^2+\Psi_2^2\right)}{\left(R_1+R_2\right)}\left[\frac{2\Psi_1\Psi_2}{\Psi_1^2+\Psi_2^2}\ln\left(\frac{1+e^{-\kappa H}}{1-e^{-\kappa H}}\right)+\ln\left(1-e^{-2\kappa H}\right)\right] \quad 7$$

The Stern potential for the particle and bubble, Ψ_i, is substituted with the zeta-potential, ζ_i, which can be measured.

The dispersion energy is given by Equation 8 (Rabinovich and Churaev 1979)

$$V_D = -\frac{A_{132}R_1R_2}{6H\left(R_1+R_2\right)}\left[1-\frac{1+2bl}{1+bc/H}\right] \quad 8$$

where A_{132} is the Hamaker constant for particle 1 and particle 2 (a bubble in flotation) interacting in a medium (3). The last half of the equation is a correction factor for the retardation effect, where b is a parameter characterizing materials of interacting particles ($3\text{x}10^{-17}$ s for most materials), l is a parameter characterizing the medium ($3.3\text{x}10^{15}$ s^{-1} for water) and c is the speed of light (Yoon and Mao 1996). The retardation effect can usually be omitted due to the small effect that it has on the overall energy of interaction.

The equation for hydrophobic energy is an empirical formula as opposed to Equations 7 and 8 which are theoretical in nature. The most recent proposed form is similar to the dispersion energy equation (Yoon and Mao 1996).

$$V_H = -\frac{R_1R_2K_{132}}{6\left(R_1+R_2\right)H} \quad 9$$

The Hamaker constant, A_{132}, is replaced by the hydrophobic force constant, K_{132}, and there is no retardation effect. The hydrophobic force constant can be found by using Equation 10, which includes the interactions between similar particles in a medium (Yoon, Flinn et al. 1997).

$$K_{132} = \sqrt{K_{131}K_{232}} \quad 10$$

K_{131} and K_{232} are given by Equations 11 & 12, where [F] is the dodecylammonium hydrochloride concentration.

$$K_{131} = a\exp\left(b_k\theta\right) \quad 11$$

for θ<86.89°	a = 2.732E-21,	b_k = 0.04136
for 86.89°<θ<92.28°	a = 4.888E-44,	b_k = 0.6441
for θ>92.28°	a = 6.327E-27,	b_k = 0.2172

$$K_{232} = \exp\left(d + e\sqrt{[F]}\right) \qquad 12$$

for all $[F]$ $\qquad$ d = -39.67, $\qquad$ e = -117.7

Equation 11 was derived from data obtained from Yoon and Ravishankar (1994; 1996), Rabinovich and Yoon (1994), Vivek (1998), and Pazhianur (1999). Equation 12 was derived from data obtained by Yoon and Aksoy (1999).

There is an ongoing debate as to the validity and origin of the hydrophobic force. There has been a tremendous amount of research on this subject, with only a few examples included here. Most, but not all, researchers believe that the force can be measured at long ranges (up to 200 nanometers). Of those, there are varying explanations as to the origin of the force. Attard (1989) proposed that the hydrophobic force is actually a part of the van der Waals force. This can be discredited in flotation due to the fact that the van der Waals force is repulsive between a particle and air bubble in a water medium. This would result in no attractive forces seen in flotation. Another explanation must be given in view of the fact that an attractive force is still seen under these circumstances (Ducker, Xu et al. 1994; Lu 2000; Yoon 2000). The force also might originate from the ordering of water molecules away from the hydrophobic surface (Eriksson, Ljunggren et al. 1989) or from a hydrodynamic fluctuation at the hydrophobic surface and liquid interface that might produce an attractive force (Ruckenstein and Churaev 1991). The most recent explanation is the formation of a microscopic bridging bubble between the two surfaces. The surface tension along the liquid-vapor interface creates the long range hydrophobic force. The bridging bubble can be formed by cavitation of the liquid when the two surfaces approach each other (Berard, Attard et al. 1993; Parker and Claesson 1994) or by stable nano-bubbles that have previously adhered to the hydrophobic surface (Carambassis, Jonker et al. 1998; Ishida, Sakamoto et al. 2000; Ederth, Tamada et al. 2001; Sakamoto, Kanda et al. 2002). Arguments against microscopic bridging bubbles state that they are thermodynamically unstable (Eriksson and Ljunggren 1995; Eriksson and Ljunggren 1999) and too short lived to have a noticeable effect on experimental measurements (Ljunggren and Eriksson 1997). The debate as to the cause of the hydrophobic force will continue until a theoretical model for the interaction can be proposed and verified. Regardless of the origin of the hydrophobic

force, a long range attraction exists between hydrophobic surfaces. Therefore, it is appropriate to use Equation 9 to quantify that attractive force.

Knowing the total surface force energy (Figure 1), there exists a maximum repulsive (positive) energy that must be overcome, E_1. This maximum energy occurs at the critical rupture distance, H_c. At distances smaller than this the free energy continuously drops. This means there is nothing preventing the particle and bubble from coming together. Once this maximum is reached, and overcome, the particle and bubble will spontaneously adhere to each other, and a three-phase contact will occur. Due to vibrations along the liquid-vapor interface, the average critical rupture thickness is greater than the instantaneous critical rupture thickness (Yoon 2000). The vibrations cause the instantaneous distance between the bubble and particle, which is smaller than the average distance, to be equal to the critical rupture thickness. This smaller distance overcomes the energy barrier. These vibrations will result in a higher average critical rupture thickness and a lower energy barrier.

Objectives

The objective of the present research is to derive a general flotation model that takes into account turbulence within a flotation cell as well as all applicable surface forces. The main focus of the model is within the slurry portion of the flotation cell. This model is to be derived, as much as possible, from first principles that relate turbulent parameters of the fluid to physical and chemical properties of the particles, bubbles and fluid. With the addition of a froth recovery model, an entire flotation model will be available.

To accomplish this, a review of flotation fluid dynamics will be performed. Experiments will also be undertaken to verify the model. Simulations using the model will show the applicability to industrial systems. It is hoped that the proposed model will be able to improve upon these systems and be a benefit to the mineral processing industry.

Organization

The body of this thesis has been presented as three independent papers. Paper 1 is titled "Fluid Dynamics of Bubbles and Particles under Turbulent Flotation Conditions: A Review". This paper presents turbulence effects upon flotation. Included within this paper is a review of collision frequencies as well as the proposed attachment and detachment energies imparted by the turbulence. Paper 2 is titled "Developing a Turbulent Flotation Model from First Principles". This paper presents the flotation model that has been derived as well as simulations using this model. Paper 3 is titled "A Comprehensive Model for Flotation under Turbulent Flow Conditions: Verification". This paper demonstrates the validity of the proposed flotation model by experimental verification. The summary of the entire research is presented following these three papers. Recommendations for future work follow the summary.

Nomenclature

1	subscript – refers to particle
2	subscript – refers to bubble
3	subscript – refers to liquid
a	K_{131} parameter [-]
b	material parameter (V_D) [s]
b_k	K_{131} parameter [-]
c	speed of light [$m \cdot s^{-1}$]
d	K_{232} parameter [-]
d_i	diameter of i [m]
e	K_{232} parameter [-]
k	rate constant [s^{-1}]
l	medium parameter (V_D) [s^{-1}]
u_b	bubble velocity [m]
A_{132}	Hamaker constant for 1 interacting with 2 in 3 [-]
E_1	surface energy barrier [J]
E_A	attachment efficiency [-]
E_C	collision efficiency [-]
E_S	stability efficiency [-]

E'_k	kinetic energy of detachment [J]
E_k	kinetic energy of attachment [J]
F	concentration of dodecylammonium hydrochloride [$mol \cdot L^{-1}$]
G_{fr}	gas flow rate through flotation cell [$m^3 \cdot s^{-1}$]
H	distance of separation [m]
H_c	critical rupture thickness [m]
K_{132}	hydrophobic constant for particle 1 interacting with particle 2 in a medium 3 [-]
N_i	number density of i – number per unit volume [m^{-3}]
R	recovery [-]
R_i	radius of i [m]
Re	Reynolds number of a rising bubble [-]
S_b	surface area rate [s^{-1}]
V_{cell}	volume of cell [m^3]
V_D	dispersion free energy of interaction [J]
V_E	electrostatic free energy of interaction [J]
V_H	hydrophobic free energy of interaction [J]
V_T	total free energy of interaction [J]
W_a	work of adhesion [J]
ε	dielectric constant of medium (liquid) [-]
ε_0	permittivity of vacuum [$C^2 \cdot N^{-1} \cdot m^{-2}$]
ε_d	energy dissipation [$m^2 \cdot s^{-3}$]
ζ_i	zeta potential of i [mV]
θ	contact angle [rad] – measured through liquid
κ	inverse Debye length [m^{-1}]
ν	kinematic viscosity [$m^2 \cdot s^{-1}$]
ρ_i	density of i [$kg \cdot m^{-3}$]
τ	retention time within flotation cell [s]
Ψ_i	Stern potential of i [V]

References

Abrahamson, J. (1975). "Collision rates of small particles in a vigorously turbulent fluid." Chemical Engineering Science **30**(11): 1371-9.

Arbiter, N. and C. C. Harris (1962). Flotation Kinetics. Froth flotation - 50th anniversary volume. D. W. Fuerstenau, American Institute of Mining, Metallurgical, and Petroleum Engineers.

Attard, P. (1989). "Long-range attractions between hydrophobic surfaces." Journal of Physical Chemistry **93**: 6441-6444.

Berard, D. R., P. Attard, et al. (1993). "Cavitation of a Lennard-Jones fluid between hard walls, and the possible relevance to the attraction measured between hydrophobic surfaces." J. Chem. Phys. **93**(9): 7236-7244.

Bloom, F. and T. J. Heindel (2002). "On the structure of collision and detachment frequencies in flotation models." Chemical Engineering Science **57**(13): 2467-2473.

Carambassis, A., L. C. Jonker, et al. (1998). "Forces measured between hydrophobic surfaces due to a submicroscopic bridging bubble." Physical Review Letters **80**(24): 5357-5360.

Ducker, W. A., Z. Xu, et al. (1994). "Measurements of hydrophobic and DLVO forces in bubble-surface interactions in aqueous solutions." Langmuir **10**(9): 3279-3289.

Ederth, T., K. Tamada, et al. (2001). "Force measurements between semifluorinated thiolate self-assembled monolayers: long-range hydrophobic interactions and surface charge." Journal of Colloid and Interface Science **235**: 391-397.

Eriksson, J. C. and S. Ljunggren (1995). "Comments on the alleged formation of bridging cavities/bubbles between planar hydrophobic surfaces." Langmuir **11**: 2325-2328.

Eriksson, J. C. and S. Ljunggren (1999). "On the mechanically unstable free energy minimum of a gas bubble which is submerged in water and adheres to a hydrophobic wall." Colloids and Surfaces A: Physicochemical and Engineering Aspects **159**: 159-163.

Eriksson, J. C., S. Ljunggren, et al. (1989). "A phenomenological theory of long-range hydrophobic attraction forces based on a square-gradient variational approach." Journal of the Chemical Society, Faraday Transactions 2 **85**(part 3): 163-176.

Ishida, N., M. Sakamoto, et al. (2000). "Attraction between hydrophobic surfaces with and without gas phase." Langmuir **16**: 5681-5687.

Kelsall, D. F. (1961). "Application of probability in the assessment of flotation systems." Bull. Instn. Min. Metall. **650**: 191-204.

Liepe, F. and H. O. Moeckel (1976). "Studies of the combination of substances in liquid phase. Part 6: The influence of the turbulence on the mass transfer of suspended particles." Chemische Technik (Leipzig, Germany) **28**(4): 205-209.

Ljunggren, S. and J. C. Eriksson (1997). "The lifetime of a colloid-sized gas bubble in water and the cause of the hydrophobic attraction." Colloids and Surfaces A: Physicochemical and Engineering Aspects **129-130**: 151-155.

Lu, S.-c. (2000). "Bubble-particle interaction in flotation cell." Trans. Nonferrous Met. Soc. China **10**(Special Issue): 40-44.

Mao, L. and R.-H. Yoon (1997). "Predicting flotation rates using a rate equation derived from first principles." International Journal of Mineral Processing **51**(1-4): 171-181.

Parker, J. L. and P. M. Claesson (1994). "Bubbles, cavities, and the long-ranged attraction between hydrophobic surfaces." Journal of Physical Chemistry **98**: 8468-8480.

Pazhianur, R. (1999). Hydrophobic force in flotation, Virginia Polytechnic Institute and State University.

Pyke, B., D. Fornasiero, et al. (2003). "Bubble particle heterocoagulation under turbulent conditions." Journal of Colloid and Interface Science **265**(1): 141-151.

Rabinovich, Y. I. and N. V. Churaev (1979). "Effect of electromagnetic delay on the forces of molecular attraction." Kolloidnyi Zhurnal **41**(3): 468-74.

Rabinovich, Y. I. and R. H. Yoon (1994). "Use of atomic force microscope for the measurements of hydrophobic forces." Colloids and Surfaces, A: Physicochemical and Engineering Aspects **93**: 263-73.

Ruckenstein, E. and N. Churaev (1991). "A possible hydrodynamic origin of the forces of hydrophobic attraction." Journal of Colloid and Interface Science **147**(2): 535-538.

Sakamoto, M., Y. Kanda, et al. (2002). "Origin of long-range attractive force between surfaces hydrophobized by surfactant adsorption." Langmuir **18**(5713-5719).

Schulze, H. J. (1993). Flotation as a heterocoagulation process: Possibilities of calculating the probability of flotation. Coagulation and Flocculation. B. Dobias, Marcel Dekker.

Shaw, D. J. (1992). Introduction to colloid and surface chemistry. Boston, Butterworth-Heinemann.

Vivek, S. (1998). Effects of long-chain surfactants, short-chain alcohols and hydrolysable cations on the hydrophobic and hydration forces, Virginia Polytechnic Institute and State University.

Yoon, R. H. (2000). "The role of hydrodynamic and surface forces in bubble-particle interaction." International Journal of Mineral Processing **58**(1-4): 129-143.

Yoon, R. H. and S. B. Aksoy (1999). "Hydrophobic forces in thin water films stabilized by dodecylammonium chloride." Journal of Colloid and Interface Science **211**(1): 1-10.

Yoon, R.-H., D. H. Flinn, et al. (1997). "Hydrophobic interactions between dissimilar surfaces." Journal of Colloid and Interface Science **185**(2): 363-370.

Yoon, R.-H. and L. Mao (1996). "Application of extended DLVO theory, IV. Derivation of flotation rate equation from first principles." Journal of Colloid and Interface Science **181**(2): 613-626.

Yoon, R.-H. and S. A. Ravishankar (1994). "Application of extended DLVO theory III. Effect of octanol on the long-range hydrophobic forces between dodecylamine-coated mica surfaces." Journal of Colloid and Interface Science **166**(1): 215-24.

Yoon, R.-H. and S. A. Ravishankar (1996). "Long-range hydrophobic forces between mica surfaces in alkaline dodecylammonium chloride solutions." Journal of Colloid and Interface Science **179**(2): 403-411.

Fluid Dynamics of Bubbles and Particles under Turbulent Flotation Conditions: a Review

I. M. Sherrell

Abstract

A review and assessment of the current knowledge of the effects of turbulent flow on the flotation process has been undertaken. This includes a review of probabilistic models of collision frequencies with all underlying assumptions. Although there is no model that takes into account all turbulent effects and conditions for the collisions of particles and bubbles, a model proposed by Abrahamson (1975) is the most applicable for flotation purposes. Our review revealed that there are more appropriate models in the literature but modifications are needed to take into account bubble and particle density effects in a liquid. Attachment and detachment energies are also described. Attachment energies are related to the Kolmogorov length scale and the length scales of the particles and bubbles. Detachment energies are related to the system's largest length scale (i.e. the impeller).

Introduction

Fluid effects are seen in all flotation processes. Modeling of the process, therefore, must take this fact into account. Flotation modeling aims at obtaining a rate constant for different components (e.g. minerals, surface chemistry types, particle sizes) of a feed to a flotation circuit. These rate constants are usually modeled as a function of collision frequencies, and probabilities of attachment and detachment (Schulze 1993; Yoon and Mao 1996; Mao and Yoon 1997; Lu 2000; Bloom and Heindel 2002; Pyke, Fornasiero et al. 2003). Since fluid effects are seen in all aspects of flotation, they must be reflected in the collision frequency, attachment and detachment model sections.

To model these processes, assumptions must be made. There are many simplifications in flotation modeling including particle and bubble effects. Shape is assumed to be spherical due to the great difficulty in accounting for non-spherical particles. Particle surface chemistry is assumed to be uniform across the entire surface of the particle. Particle composition (e.g. hydrophobicity) is also assumed to be uniform either throughout the entire flotation cell or component being modeled or divisions of that cell or component. These are only a few of the simplifications encountered in flotation modeling, but the greatest simplification comes from modeling the fluid itself.

Turbulence has always been an extremely complicated subject, and the only way to model it, except under very special circumstances, is to assume that the turbulence is locally homogeneous and isotropic. Although, for certain flow fields, this is not as far-fetched as it may seem, the large scales encountered in flotation modeling do not satisfy this condition and the assumption is needed. This allows statistical modeling of turbulence to be adopted, based mostly

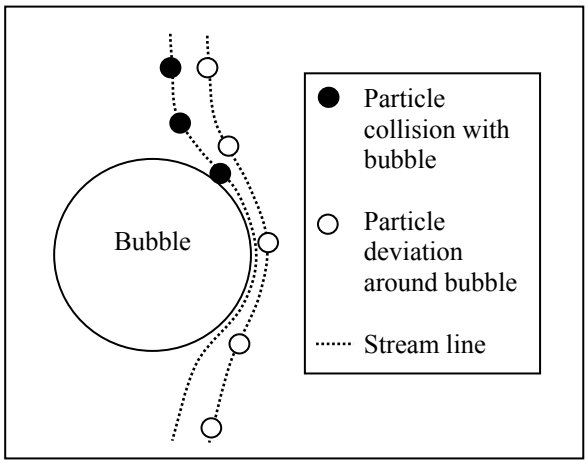

Figure 1. Effects of streamlines for particle collisions with a rising bubble. The assumption is made that particles follow the fluid completely.

on the Kolmogorov theory, which in turn allows the establishment of a relationship between turbulent data such as energy dissipation and root-mean-squared (rms) slip velocity.

Kolmogorov theory is a way of relating scales of turbulence (and in flotation modeling, what those scales are affecting) to their respective energies. Energy is added at the integral scale and from there cascades down through the inertial scales to the dissipative scales where it is lost as heat due to viscous effects. The assumption is that energy is not lost at any scale but the dissipative scale and is only transferred through the intermediate scales. In the flotation process, energy is added by the impeller (integral scale), acts upon the particles and bubbles (inertial scale) and is dissipated from the system at the Kolmogorov microscale (dissipative). Statistical simplification, such as the Kolmogorov theory, allows modeling of turbulent processes, such as flotation, to take place.

Collision Frequencies

Although the Kolmogorov theory is not explicitly used in collision frequency modeling, the assumption that the turbulence is homogeneous and isotropic is still required. Mao and Yoon bypassed this assumption by modeling flotation in a quiescent environment (1996; 1997). This required the use of streamlines and the assumption that particles followed the fluid flow completely.

The total number of collisions was found by multiplying the total possible collisions, Z_C, by a collision efficiency, P_C.

$$Z_{12} = Z_C P_C \qquad [1]$$

The total possible number of collisions was found by multiplying the volume swept by one bubble, assuming that the bubble rises straight up through the entire cell, and the number density of particles to get the number of particle collisions with one bubble. Knowing this and the number of bubbles per unit time through the cell results in the total possible collisions (Equation [2]).

$$Z_C = \frac{3V_g}{4R_2} N_1 = \frac{1}{4} S_b N_1 \qquad [2]$$

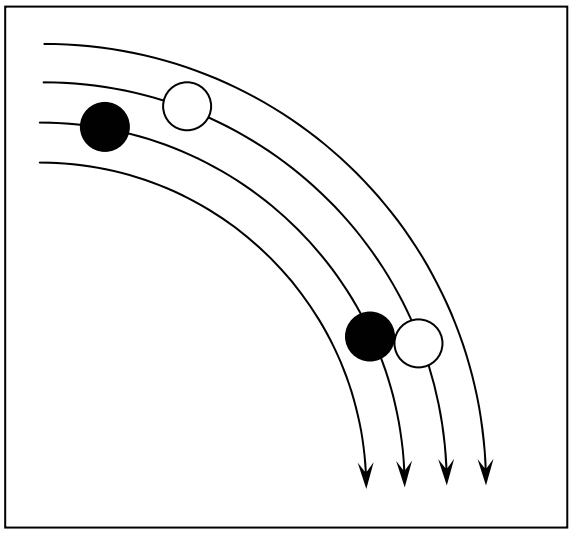

Figure 2. Collision due to shear mechanism.

The collision efficiency, P_C, was obtained by knowing the stream function for the flow around the bubble (Figure 1). Assuming that the particles completely followed the fluid flow (no Brownian or inertial effects) the collision efficiency would then be a function of that stream function and the particle and bubble radii (Luttrell and Yoon 1992; Yoon and Mao 1996; Dai, Fornasiero et al. 2000). There are forms of collision efficiencies that can also take into account, among other things, the inertial effects of particles (Dai, Fornasiero et al. 2000).

When turbulence is encountered, an analysis such as this can not be used. For one, bubbles take meandering paths through the liquid and a total volume that they travel through can not be accounted for. Also, streamlines are not stationary in turbulence. They are constantly changing throughout time and space. A more statistical approach must be taken.

Collision frequencies are all based around one simple model

$$Z_{12} = \beta N_1 N_2 \qquad [3]$$

where β, the collision kernel, is

$$\beta = f\left(C, d_{12}, w\right) \qquad [4]$$

a function of some constant, C, the average diameter of collision, $d_{12} = (R_1+R_2)$, and the relative velocities between the colliding particles, w. A form similar to this was first used by von Smoluchowski (1917) to model coagulation kinetics.

$$Z_{12} = \frac{4}{3} N_1 N_2 d_{12}^3 G \qquad [5]$$

G in Equation [5] is the velocity gradient perpendicular to the direction of particle motion. Only laminar flows with collisions occurring due to shear were considered. In shear flows, particles are able to interact and collide with each other the same way fluid particles can collide with other fluid particles (Figure 2). There is no deviation from the fluid path with this assumption. Camp and Stein (1943) were the first to apply this concept to turbulent collisions.

$$Z_{12} = \frac{4}{3} N_1 N_2 d_{12}^3 \sqrt{\frac{\varepsilon}{\nu}} \qquad [6]$$

They related G to turbulent fluid parameters, ε and ν. In their assumptions, they considered only collisions due to shear fields produced by large eddies. Again, there was the

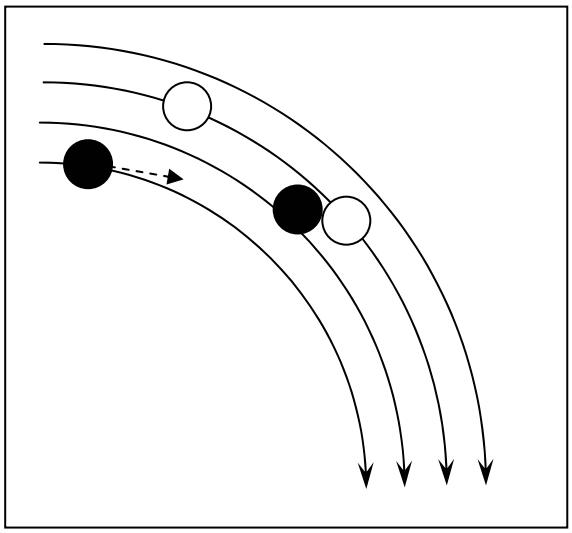

Figure 3. Collision due to acceleration mechanism. Heavy particle deviates from streamline to collide with inertia-less particle.

assumption that particles did not deviate from the fluid path. Saffman and Turner (1956) were later able to refine Camp and Stein's model by a slight modification of the constant *C*.

$$Z_{12} = \sqrt{\frac{8\pi}{15}} N_1 N_2 d_{12}^3 \sqrt{\frac{\varepsilon}{\nu}} \qquad [7]$$

For Equation [7] to be valid the collision diameter (d_{12}) must be small compared to the smallest eddies and the particles and bubbles must follow the fluid completely. In Saffman and Turner's case, Equation [7] was used to model droplet collisions in cloud formations, which followed these assumptions. In flotation these assumptions can not be followed, but Saffman and Turner also produced another model with the addition of an accelerative mechanism of collision.

$$Z_{12} = \sqrt{8\pi} N_1 N_2 d_{12}^2 \left[\left(1 - \frac{\rho_p}{\rho_f} \right)^2 (\tau_1 - \tau_2)^2 \left(\overline{\left(\frac{Du}{Dt} \right)^2} + \frac{1}{3} g^2 \right) + \frac{1}{9} d_{12}^2 \frac{\varepsilon}{\nu} \right]^{1/2} \qquad [8]$$

The accelerative mechanism accounts for inertial effects in turbulent collisions (Figure 3). This indicates that particles do not have to follow the fluid flow and can, therefore, be larger than the smallest eddies. For Equation [8] to be valid particles and bubbles must already be close together (within the same eddy) and must have very similar particle radii ($1 \leq R_1/R_2 \leq 2$).

Abrahamson (1975) then proposed a model for high turbulent energy dissipation, ε. This is shown in equation [9]

$$Z_{12} = \sqrt{8\pi} N_1 N_2 d_{12}^2 \sqrt{\overline{U_1^2} + \overline{U_2^2}} \qquad [9]$$

where the mean squared particle velocity

$$\overline{U_i^2} = \frac{\overline{U_f^2}}{1 + \frac{1.5\tau_i \varepsilon}{\overline{U_f^2}}} \qquad [10]$$

comes from a simplification of a model for particle relative velocity in an oscillating (sinusoidal) fluid given by Levins and Glastonbury (1972). Only the assumptions that very energetic isotropic turbulence was being considered, and that particle velocities were independent and followed some distribution, needed to be made.

Particle size is not an issue in this model. As long as the particle stokes number is high, the model is valid. The Stokes number is a ratio of the particle relaxation (response) time to the smallest fluid relaxation time (for fully developed turbulent flow, this timescale will correspond to the Kolmogorov timescale).

$$St = \frac{\tau_i}{\tau_\eta} = \tau_i \Big/ \left(\frac{\nu}{\varepsilon}\right)^{1/2} \qquad [11]$$

It represents how well a particle follows the fluid flow and is a way to measure this deviation. If a particle's relaxation time is less than the Kolmogorov timescale then the lag time between the fluid movement and the particle movement will be small and the particle will follow the fluid. For particles to accurately follow the flow their Stokes number should be much less than one. Any particles with relaxation times above the Kolmogorov timescale will have some lag in their response to flow fluctuations. Particle and bubble relaxation times are given by various authors throughout the literature (Govan 1989; Ceylan, Altunbas et al. 2001; Bourloutski and Sommerfeld 2002). With a high Stokes number assumption, the retarding effect due to lubrication theory, for particles nearly in contact, can be ignored (Reade and Collins 1998). Therefore, no collision efficiency is needed while using Abrahamson's collision frequency model.

Sundaram and Collins (1997) compared Abrahamson's model with Saffman and Turners' on the basis of particle Stokes numbers. As the Stokes number approached zero, the numerical simulation approached Saffman and Turner's prediction. As the Stokes number increased, Abrahamson's model more closely predicted the true collision frequency. At a Stokes number of, roughly, 1, both models had equal error, with Saffman and Turner under predicting and Abrahamson over predicting. With many flotation particles having Stokes numbers above 1 and with less assumptions being violated, Abrahamson's model is more representative of the flotation process, and, as a result, most flotation models use Equation [9] to determine collision frequency (Schubert 1999; Bloom and Heindel 2002; Pyke, Fornasiero et al. 2003).

Despite its widespread acceptance and use, Abrahamson's model is not the most appropriate for flotation purposes. This stems from the fact that a number of significant assumptions are violated. The greatest assumption being violated is that all colliding particles have an infinite Stokes number. This is not the case in flotation. When the particle Stokes number is above 10, the collision prediction by Equation [9] is fairly accurate, but for Stokes numbers below 10 it will over predict the true number of collisions taking place within the flotation cell.

A more comprehensive model would be one that would account for the full range of Stokes numbers and include both the shear and accelerative mechanisms of collision. Several authors have proposed models for just this scenario (Yuu 1984; Kruis and Kusters 1997). These models also include an added mass term for particle flows in liquid environments. This is very important for flotation modeling since all processes occur within a liquid environment.

One problem with the model proposed by Yuu is its applicability to very small particles (Kruis and Kusters 1997). This is not the case with Kruis and Kusters' model (Equations [12]-[14]).

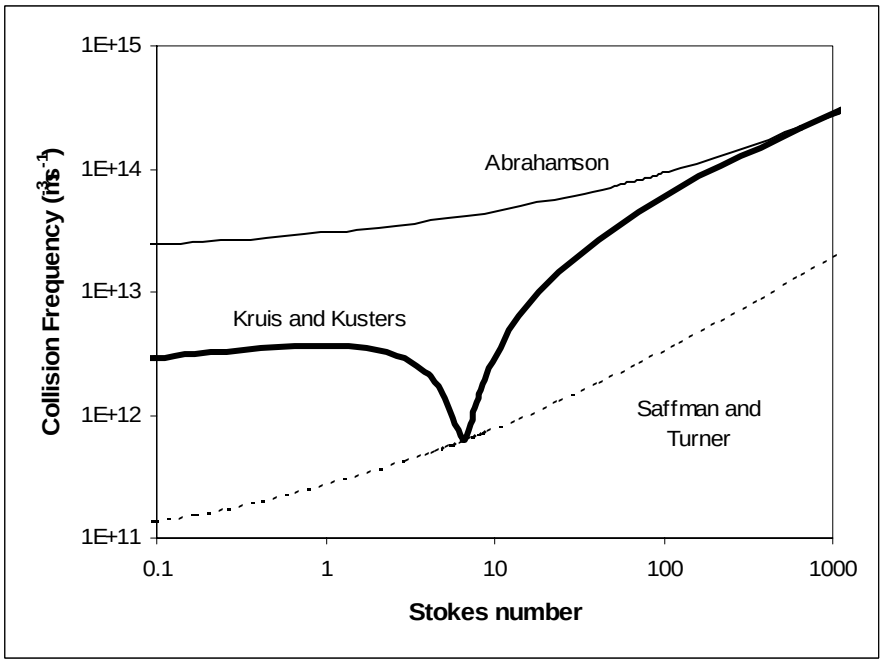

Figure 4. Comparison of collision frequency models. Model predictions are calculated with one colliding particle type's diameter steady at 100 microns, with the other particle type's diameter varying. Both colliding species have the same density.

$$Z_{12} = \sqrt{\frac{8\pi}{3}} N_1 N_2 d_{12}^2 \sqrt{w_{accel}^2 + w_{shear}^2} \qquad [12]$$

$$\frac{w_{shear}^2}{U_f^2} = 0.238b\left(\frac{U_1^2}{U_f^2}\frac{\theta_1}{C_{c,1}} + \frac{U_2^2}{U_f^2}\frac{\theta_2}{C_{c,2}} + \sqrt{\frac{\theta_1\theta_2}{C_{c,1}C_{c,2}}\frac{U_1^2 U_2^2}{U_f^2}} \right) \qquad [13]$$

$$\frac{w_{accel}^2}{U_f^2} = 3(1-b)^2 \frac{\gamma}{\gamma - 1}\left[(\theta_1 + \theta_2) - \frac{4\theta_1\theta_2\sqrt{\frac{1+\theta_1+\theta_2}{(1+\theta_1)(1+\theta_2)}}}{(\theta_1+\theta_2)} \right] \left(\frac{1}{(1+\theta_1)(1+\theta_2)} - \frac{1}{(1+\gamma\theta_1)(1+\gamma\theta_2)} \right) \qquad [14]$$

In Equations [12] - [14] w is the relative velocity between two particles due to either shear or acceleration, U_f is the root-mean-squared fluid velocity, U_i is the root-mean-squared particle velocity, b is the added mass coefficient, γ is the turbulence constant, and θ_i is the dimensionless relaxation time (particle relaxation time with respect to the Lagrangian timescale).

By accounting for intermediate Stokes numbers, Equations [12] - [14] bridge the gap between Equation [7] and Equation [9]. This is shown in Figure 4. Collisions are calculated with one particle type's size being steady while the other varies. Abrahamson's equation over predicts the true collision rate while Saffman and Turner's equation under predicts, with a

difference of approximately 2 orders of magnitude between the two equations. By accounting for intermediate Stokes numbers, as suggested by Kruis and Kusters, an intermediate collision frequency can be calculated between the maximum and minimum predictions given by Abrahamson and Saffman and Turner. Some variations can be noted between Kruis and Kusters and the other two models due to the inclusion of the added mass term. The dip in Kruis and Kusters' prediction, at approximately a Stokes number of 10, is due to the difference in the relaxation time between one species and another. The dip corresponds to the Stokes number of the constant particle size species. When the two relaxation times of the colliding particles are equal, the collisions are minimized. Collisions at this point mostly occur due to the shear mechanism. When the difference between the relaxation times increases, collisions increase. This is shown on either side of the dip in Figure 4.

The current problem with this model is that only one particle density can be given. Flotation collisions, on the other hand, need to account for two different particle densities. This should be taken into account with the added mass coefficient, but Equations [12] - [14] can not properly do this. Since these models can not currently account for bubble-particle collisions, the best model, to date, that can account for different collision densities is Abrahamson's (Equation [9]).

To use Equation [9], the particle and bubble root-mean-squared velocity must be known. This can be determined using Equation [10], with prior knowledge of the fluid rms velocity. Since this velocity is not known in flotation practice, a more suitable equation must be used. Liepe and Moeckel (1976) derived an expression for the slip particle rms velocity from previous researchers experimental data.

$$\sqrt{\overline{U_1^2}} = 0.4 \frac{\varepsilon^{4/9} d_1^{7/9}}{\nu^{1/3}} \left(\frac{\rho_p - \rho_f}{\rho_f} \right)^{2/3} \qquad [15]$$

This equation ([15]) has recently been verified using a digital particle image velocimetry (DPIV) technique (Brady, Telionis et al. 2004). Although this equation is being used in current flotation modeling for bubble velocities (Pyke, Fornasiero et al. 2003) it was never derived for bubbles and should not be used without any experimental verification. For bubbles, a more appropriate velocity is given by Lee et al. (1987) in equation [16].

$$\overline{U_2^2} = C_0 \left(\varepsilon d_2 \right)^{2/3} \qquad [16]$$

C_0 is given by Batchelor (1951) as 2.

Attachment and Detachment Energies

For flotation modeling, the attachment and detachment processes are calculated as probabilities, similar in form to the Arrhenius equation.

$$P_{A/D} = \exp\left(\frac{E_B}{E_K} \right) \qquad [17]$$

A certain probability is given for attachment (P_A) and detachment (P_D) dependent on the energies needed to be overcome, E_B, and the energies available in the system, E_K, to overcome that energy barrier.

The attachment energy barrier, E_1, comes from surface forces, which are modeled using the Extended DLVO theory (see Figure 5) (Yoon and Mao 1996). There are three main surface forces found in flotation; the electrostatic, V_E, dispersion (van der Waals), V_D, and hydrophobic,

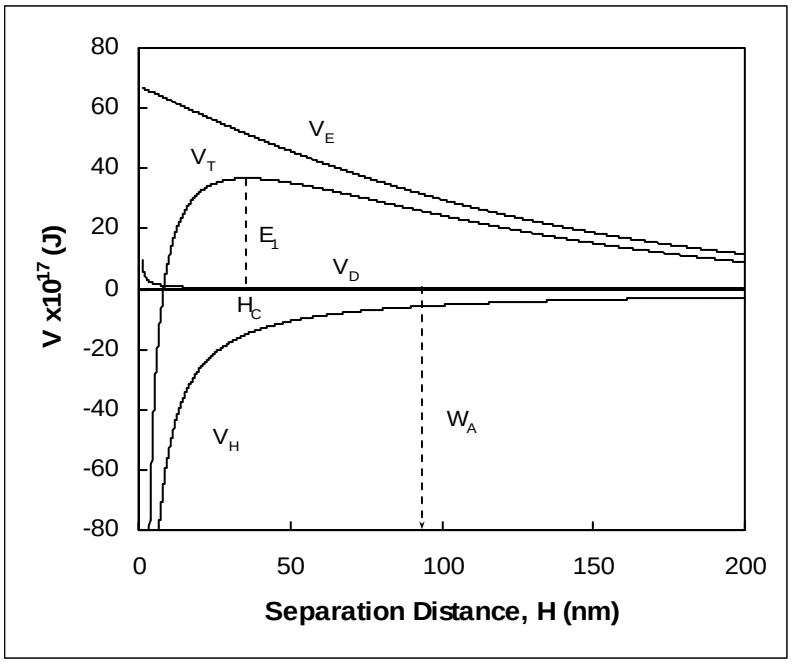

Figure 5. Surface energy vs. distance of separation between two particles (i.e. particle-bubble).

V_H, forces. These are additive and combine to produce the total surface force, V_T. These surface forces can easily be converted into energies. When two particles (e.g. particle/bubble) approach each other, they are initially repulsed (positive surface energy). They must overcome this repulsion to become attached. The repulsion increases until the energy barrier is overcome. Below that separation distance, also called the critical rupture distance, H_C, there is a continuous drop in surface energy. Once this occurs, there is nothing to stop the attachment of the particle and bubble.

The detachment barrier, W_A, comes from the change in surface energies when the detachment process occurs. The loss or gain in surface area of the solid, liquid, or vapor state during the detachment process is multiplied by the respective surface tension to obtain the required energy. The initial state in this process is the combined bubble and particle while the final stage is the separated bubble and particle. Both the attachment and detachment barriers are shown in Figure 5.

To overcome these barriers, a certain amount of energy is required. This energy is provided by the turbulent environment encountered within a flotation cell. The driving force within the cell is the motion of the impeller. The impeller produces the turbulent environment by the creation of eddies. The largest eddy is created by the impeller and is roughly equal to the impeller size. This eddy is where the energy is input into the turbulent environment. According to the Kolmogorov theory, this energy is then transferred through intermediate scales of turbulence to the smallest turbulent scale, the Kolmogorov microscale. This is shown in Figure 6.

The wave number ($\kappa=2\pi/d$) equivalent to the largest eddy size (impeller) corresponds to a kinetic energy equal to the tip-velocity of the impeller squared.

$$U_{T-large}^2 = \left(R_{Imp}\omega\right)^2 \qquad [18]$$

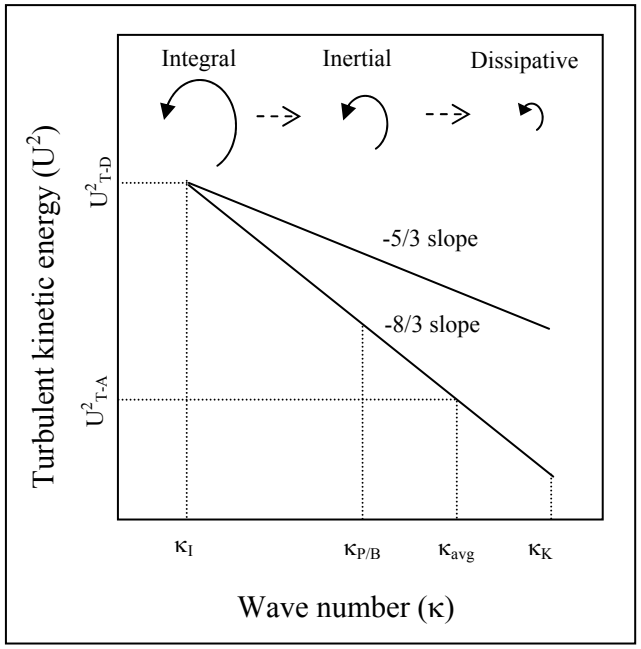

Figure 6. Turbulent kinetic energy spectrum showing attachment and detachment energies.

The cascade of energy on a log-log scale, as stated by the Kolmogorov theory, is represented by a straight line with a slope of -5/3. This is true for a pure liquid system, but with the introduction of bubbles the slope becomes -8/3 (Wang, Lee et al. 1990). With particles the slope is also decreased (Buurman 1990). It is assumed that with a combination of all three phases the slope will follow the -8/3 two-phase prediction. In these dispersed phase systems, the energy is dissipated much more quickly, due to the fact that a portion of the energy is transferred to the particles and bubbles (Gore and Crowe 1991). Because of this, at each wave number there is less energy with particles and bubbles than without. The energy spectrum is shown in Figure 6.

For the attachment and detachment processes, a certain range of these eddy sizes will have an effect on the particles and bubbles and give them their turbulent kinetic energies. For attachment to occur there must be a certain differential movement between the fluid and particle. This allows the particles and bubbles to collide. The attachment energy must, then, overcome the energy barrier, E_1, during this collision. Eddy sizes that allow this differential movement, correspond to the particle/bubble size through the Kolmogorov microscale. The fluid within this range has a different relaxation time than the particles and bubbles, as opposed to large eddies, where bubbles and particles follow their movement. This out of phase motion allows the particles and bubbles to move independent of the fluid and each other. It is assumed that the average amount of this energy over the associated wave numbers ($\kappa_{P/B}$ to κ_K) directly corresponds to the particle and bubble attachment energy, $U^2_{T\text{-}A}$.

$$E_{k-A} = \frac{1}{2}\left(m_1 + m_2\right)\mathrm{U}^2_{T-A} \qquad [19]$$

For the detachment process, bubbles and particles are already combined and do not need a differential relaxation time as they do in the attachment process. It is assumed that detachment comes about from the centrifugal motion of large eddies. When bubbles and particles are subjected to these eddies, they produce differing behavior. Bubbles tend to travel towards the

center of vortices, while particles travel outward (Chahine 1995; Crowe and Trout 1995). If a bubble-particle aggregate were subjected to this, it would tend to pull the aggregate in two which would lead to the detachment of the particle from the bubble. Given this scenario and the fact that all aggregates are subjected to the largest eddy produced by the impeller, which contains the largest available energy within the system, leads to the conclusion that the largest eddy provides the energy for detachment. The turbulent energy corresponding to the largest eddy, $U^2_{T-large}$, is, therefore, equal to the turbulent detachment energy, U^2_{T-D}.

$$E_{k-D} = \frac{1}{2}\left(m_1 + m_2\right)\mathrm{U}^2_{T-D} \qquad [20]$$

Summary

There are many different collision frequency models in the literature to date. All of these models have varying assumptions, with each model having some violation under flotation conditions. The best model for use in flotation modeling is one proposed by Abrahamson (1975). It is assumed that most particles in flotation follow the assumptions used in Abrahamson's derivation of the collision frequency model, which includes infinite (very high) Stokes numbers, independent particle velocities, a particle velocity distribution, and isotropic turbulence.

Newer models that account for the shear and accelerative mechanisms can also account for the entire range of Stokes numbers. These would be better suited for flotation purposes, except for the fact that they can not account for two different particle densities. Therefore, a particle-bubble collision can not be calculated using these models. When these models are updated to allow the use of greater and lesser than the surrounding medium densities, they will be able to account for all particles and bubbles, and their effects, in a turbulent liquid environment within a flotation cell.

Once particles collide, they have a probability of attaching, and once attached, of detaching. The forms of these probabilities are similar to the Arrhenius equation, with energy barriers being overcome by kinetic energies.

For the attachment process, the energy barrier is based upon the Extended DLVO theory and accounts for the electrostatic, dispersion, and hydrophobic surface forces. The energy needed to overcome this barrier is provided by the turbulent environment. For the attachment process to take place, some deviation from the fluid flow is required. The scales of turbulence that allow this are between the Kolmogorov microscale and the particle/bubble scale. It is assumed that the average wave number between these two scales accounts for the attachment energy that is needed to overcome the energy barrier. The Kolmogorov theory is used to calculate this energy. A modification of the theory is needed to account for particle and bubble effects on turbulence. This modification changes the slope of the energy spectrum from -5/3 to -8/3.

For the detachment process, the energy barrier is determined from the change in surface area of the different phases of the particle-bubble aggregate (i.e. solid, liquid, vapor), and the respective surface tensions of those phases. The largest scale of turbulence within the system, the impeller, is used to overcome this barrier. No deviation from the fluid is required for the detachment process. The detachment process follows from the differing effects vortices have on

particles and bubbles, with particles moving outwards, while bubbles move inward. The detachment energy follows from the turbulent energy of the largest scale.

Nomenclature

1,p	subscript – refers to particle
2	subscript – refers to bubble or second particle
b	added mass coefficienct [-]
C	constant within collision kernel [-]
C_0	constant equal to 2.0 [-]
$C_{c,i}$	Cunningham slip correction factor for i [-]
d_{12}	diameter of collision [m]
d_i	diameter of i [m]
E_1	surface energy barrier [J]
E_B	energy barrier [J]
E_K	generic kinetic energy [J]
$E_{k\text{-}D}$	kinetic energy of detachment [J]
$E_{k\text{-}A}$	kinetic energy of attachment [J]
g	gravity [$m \cdot s^{-2}$]
G	velocity gradient [s^{-1}]
H_c	critical rupture thickness [m]
m_i	mass of particle or bubble [kg]
N_i	number density of i – number per unit volume [m^{-3}]
P_A	probability of attachment [-]
P_C	collision efficiency [-]
P_D	probability of detachment [-]
R_i	radius of i [m]
R_{Imp}	radius of impeller [m]
S_b	surface area rate – within slurry [s^{-1}]
St	Stokes number [-]
U_f	fluid velocity [$m \cdot s^{-1}$]
$U^2_{T\text{-large}}$	large scale turbulent kinetic energy [$m^2 \cdot s^{-2}$]
$U^2_{T\text{-}A}$	attachment turbulent kinetic energy [$m^2 \cdot s^{-2}$]
$U^2_{T\text{-}D}$	detachment turbulent kinetic energy [$m^2 \cdot s^{-2}$]
$\sqrt{\overline{U_i}^2}$	root-mean-squared velocity of i – turbulent velocity [$m \cdot s^{-1}$]
V_D	dispersion free energy of interaction [J]
V_E	electrostatic free energy of interaction [J]
V_g	superficial air flow rate [$m \cdot s^{-1}$]
V_H	hydrophobic free energy of interaction [J]
V_T	total free energy of interaction [J]
w	relative velocity between colliding particles – may be due to shear and/or accelerative mechanisms [$m \cdot s^{-1}$]
W_A	work of adhesion [J]
Z_{12}	collision frequency between particle and bubble [$m^{-3} \cdot s^{-1}$]
Z_C	total possible collisions [$m^{-3} \cdot s^{-1}$]

β	collision kernel [$m^3 \cdot s^{-1}$]
ε	average energy dissipation [$m^2 \cdot s^{-3}$]
γ	turbulence constant [-]
κ	wave number [m^{-1}]
κ_{avg}	average attachment wave number [m^{-1}]
κ_I	impeller wave number [m^{-1}]
κ_K	Kolmogorov wave number [m^{-1}]
$\kappa_{P/B}$	particle/bubble wave number [m^{-1}]
θ_i	dimensionless relaxation time [-]
ν	kinematic viscosity [$m^2 \cdot s^{-1}$]
ρ_f	density of fluid [$kg \cdot m^{-3}$]
ρ_p	density of particle [$kg \cdot m^{-3}$]
τ_i	particle/bubble relaxation time [s]
τ_η	Kolmogorov timescale [s]
ω	impeller radial velocity [rpm]

References

Abrahamson, J. (1975). "Collision rates of small particles in a vigorously turbulent fluid." Chemical Engineering Science **30**(11): 1371-9.

Batchelor, G. K. (1951). "Pressure fluctuations in isotropic turbulence." Proc. Cambridge Phil. Soc. **47**: 359-374.

Bloom, F. and T. J. Heindel (2002). "On the structure of collision and detachment frequencies in flotation models." Chemical Engineering Science **57**(13): 2467-2473.

Bourloutski, E. and M. Sommerfeld (2002). "Parameter studies on the effect of boundary conditions in three-dimensional calculations of bubble column." FED (American Society of Mechanical Engineers) **[257-2]**(A, Proceedings of the 2002 ASME Joint U.S.-European Fluids Engineering Conference): 355-364.

Brady, M., D. P. Telionis, et al. (2004). Three-phase, particle image velocimetry measurements in a model flotation cell. 2004 ASME Heat Transfer/Fluids Engineering Summer Conference.

Buurman, C. (1990). "Stirring of concentrated slurries: a semi-empirical model for complete suspension at high solids concentrations and 5 m3 verification experiments." Institution of Chemical Engineers Symposium Series - Fluid Mixing 4 **121**: 343-350.

Camp, T. R. and P. C. Stein (1943). "Velocity gradients and integral work in fluid motion." J. Boston Soc. Civ. Engrs. **30**(4): 219.

Ceylan, K., A. Altunbas, et al. (2001). "A new model for estimation of drag force in the flow of Newtonian fluids around rigid or deformable particles." Powder Technology **119**(2-3): 250-256.

Chahine, G. L. (1995). Bubble interactions with vortices. Fluid Vortices. S. I. Green.

Crowe, C. T. and T. R. Trout (1995). Particle interactions with vortices. Fluid Vortices. S. I. Green.

Dai, Z., D. Fornasiero, et al. (2000). "Particle-bubble collision models -- a review." Advances in Colloid and Interface Science **85**(2-3): 231-256.

Gore, R. A. and C. T. Crowe (1991). "Modulation of turbulence by a dispersed phase." Transactions of the ASME **113**: 304-307.
Govan, A. H. (1989). "A simple equation for the diffusion coefficient of large particles in a turbulent gas flow." International Journal of Multiphase Flow **15**(2): 287-94.
Kruis, F. E. and K. A. Kusters (1997). "The collision rate of particles in turbulent flow." Chemical Engineering Communications **158**: 201-230.
Lee, C. H., L. E. Erickson, et al. (1987). "Bubble breakup and coalescence in turbulent gas-liquid dispersions." Chemical Engineering Communications **59**(1-6): 65-84.
Levins, D. M. and J. R. Glastonbury (1972). "Particle-liquid hydrodynamics and mass transfer in a stirred vessel." Trans. Inst. Chem. Engrs. **50**: 32-41.
Liepe, F. and H. O. Moeckel (1976). "Studies of the combination of substances in liquid phase. Part 6: The influence of the turbulence on the mass transfer of suspended particles." Chemische Technik (Leipzig, Germany) **28**(4): 205-209.
Lu, S.-c. (2000). "Bubble-particle interaction in flotation cell." Trans. Nonferrous Met. Soc. China **10**(Special Issue): 40-44.
Luttrell, G. H. and R. H. Yoon (1992). "A hydrodynamic model for bubble-particle attachment." Journal of Colloid and Interface Science **154**(1): 129-137.
Mao, L. and R.-H. Yoon (1997). "Predicting flotation rates using a rate equation derived from first principles." International Journal of Mineral Processing **51**(1-4): 171-181.
Pyke, B., D. Fornasiero, et al. (2003). "Bubble particle heterocoagulation under turbulent conditions." Journal of Colloid and Interface Science **265**(1): 141-151.
Reade, W. C. and L. R. Collins (1998). "Collision and coagulation in the infinite-stokes number regime." Aerosol Science and Technology **29**: 493-509.
Saffman, P. G. and J. S. Turner (1956). "On the collision of drops in turbulent clouds." Journal of Fluid Mechanics **1**: 16-30.
Schubert, H. (1999). "On the turbulence-controlled microprocesses in flotation machines." International Journal of Mineral Processing **56**: 257-276.
Schulze, H. J. (1993). Flotation as a heterocoagulation process: Possibilities of calculating the probability of flotation. Coagulation and Flocculation. B. Dobias, Marcel Dekker.
Smoluchowski, M. (1917). "Versuch einer mathematischen theorie der koagulations-kinetik kollöider losungen." Z. Phys. Chem **92**: 129.
Sundaram, S. and L. R. Collins (1997). "Collision statistics in an isotropic particle-laden turbulent suspension. Part 1. Direct numerical simulations." Journal of Fluid Mechanics **335**: 75-109.
Wang, S. K., S. J. Lee, et al. (1990). "Statistical analysis of turbulent two-phase pipe flow." Journal of Fluids Engineering **112**(1): 89-95.
Yoon, R.-H. and L. Mao (1996). "Application of extended DLVO theory, IV. Derivation of flotation rate equation from first principles." Journal of Colloid and Interface Science **181**(2): 613-626.
Yuu, S. (1984). "Homogeneous and isotropic turbulence." American Institute of Chemical Engineers Journal **30**(5): 802-807.

Developing a Turbulent Flotation Model from First Principles

I. M. Sherrell

Abstract

A new flotation model has been developed for use in a turbulent environment and is the first proposed to take into account all three surface forces (electrostatic, van der Waals, and hydrophobic). Previous models that account for turbulence do not take into account all surface forces while the one model that does take into account all surface forces (Yoon and Mao 1996) is only applicable in quiescent conditions. Since most flotation occurs in a turbulent environment, these previous models cannot be applied. The new model includes attachment, detachment, and froth recovery probabilities. The effects of each individual process are shown. Simulations using this model show trends seen in industrial flotation systems.

Introduction

Flotation is widely used throughout the mining industry as well as the chemical, petroleum, and recycling industries. It is the most efficient process, to date, for solid-solid separation of minerals. It is now more diverse in its application, with uses such as separation of ink from paper, plastics separation in recycling, soil contamination separation, and separation of carbon from fly ash. The industry is growing along with knowledge of the process and sub-processes. With this increased knowledge, a more reliable flotation model has been derived from first principles. This results in a general flotation model, and allows its use in the mining industry, regardless of machine type and material being recovered.

Flotation is a three-phase process, which uses a medium of water (liquid) to separate various particles (solid) by the addition of air bubbles (gas). Hydrophobic particles attach to the bubbles and rise to the top of the flotation cell where they are extracted while hydrophilic (or less hydrophobic) particles remain in the slurry. All three phases are found in flotation machines, which produce a turbulent environment. To enhance the separation, surfactants may be added that alter surface properties. The combination of a three-phase turbulent environment with a modified surface chemistry makes modeling of the process very complex.

Surface forces play a crucial role in the attachment and detachment processes between a particle and bubble. Proper modeling of these forces is vital to having a general flotation model. The DLVO theory models some of the surface forces seen in flotation. This theory combines the van der Waals force and the electrostatic force into a total surface force. The main problem with the DLVO theory is the lack of any hydrophobic force parameter, which is known to be a major contributor to surface forces between particles and bubbles in a water medium (Yoon and Mao 1996; Yoon 2000). The extended DLVO theory incorporates this third force (hydrophobic) into the DLVO theory.

The most rigorous flotation model, to date, dealing with all three surface forces (electrostatic, van der Waals, and hydrophobic) was proposed by Mao and Yoon (1997).

$$k = \frac{1}{4} S_b \left[\frac{3}{2} + \frac{4 \mathrm{Re}_b^{0.72}}{15} \right] \left(\frac{r_1}{r_2} \right)^2 \exp\left(-\frac{E_1}{E_{k-A}} \right) \left[1 - \exp\left(-\frac{W_A + E_1}{E_{k-D}} \right) \right] \qquad [1]$$

The model is based upon first principles in a quiescent environment and agrees well with experimental data. The problem of this model is its applicability to industrial applications. Turbulence is encountered in almost all flotation systems, including mineral and coal flotation. Since this is a quiescent model, the results predicted do not match industrial flotation systems. This model did provide a key basis for the current model by the use of the extended DLVO theory and its relationship to the energies of the system.

Model

Due to the turbulent environment experienced inside a flotation cell, particle-bubble collisions are modeled far differently than in a quiescent environment. For laminar flows, the collision frequency may be modeled using the volume that the bubble travels through and the percent solids of the slurry (Mao and Yoon 1997). A collision efficiency would then be applied that would account for streamline effects. On the other hand, particles and bubbles in turbulent flows generally do not follow the path of the fluid and are modeled based upon their deviation from the fluid path. The Stokes number, a ratio of the particle relaxation (response) time to the smallest fluid relaxation time (Kolmogorov timescale), represents how well a particle follows the fluid flow and is a way to measure this deviation. If a particle's relaxation time is equal to or less than the Kolmogorov timescale then the lag time between the fluid movement and the particle movement will be zero and the particle will follow the fluid completely. Any particles with relaxation times above the Kolmogorov timescale will have some departure from the fluid path.

$$St = \frac{\tau_i}{\tau_\eta} = \tau_i \Big/ \left(\frac{\nu}{\varepsilon} \right)^{1/2} \qquad [2]$$

Particle and bubble relaxation times are given by various authors throughout the literature (Govan 1989; Ceylan, Altunbas et al. 2001; Bourloutski and Sommerfeld 2002).

There are two mechanisms involved in turbulent collisions. The shear mechanism accounts for relative motions of particles (fluid, solid, or gas) in a shear field. These collisions always occur in a turbulent field, even among fluid particles. Collisions between particles with Stokes numbers less than 1 occur by shear only. The second mechanism, the accelerative mechanism, accounts for inertial effects due to large and/or heavy particles. Collisions due to the accelerative mechanism occur above a Stokes number of 1 where there is some lag between the particle and fluid.

Saffman and Turner (1956) proposed a collision model based upon the shear mechanism, where the Stokes number is zero, while Abrahamson (1975) proposed a model based entirely on the accelerative mechanism, where the Stokes number is infinity. There are collision models that combine the shear and accelerative mechanisms (Williams and Crane 1983; Kruis and Kusters 1997), but nothing to date accounts for bubble-particle collisions in a liquid environment. This is complicated due to the fact that bubbles are lighter than the surrounding fluid, while particles are heavier. Since Abrahamson's model more closely predicts real world collisions when Stokes numbers are greater than 1 (Sundaram and Collins 1997) combined with the fact that most particles in flotation are within this range, leads to the current use of Abrahamson's model.

Abrahamson's model

$$Z_{12} = 2^{3/2}\pi^{1/2}N_1N_2d_{12}^2\sqrt{\left(\overline{U_1^2}+\overline{U_2^2}\right)} \quad [3]$$

incorporates the number densities, N_i, of both the particles (1) and bubbles (2), the average diameter of the collision, d_{12} (= r_1+r_2), and the turbulent root-mean-squared velocities of the particles and bubbles, $\sqrt{\overline{U_i^2}}$. The particle turbulent root-mean-squared velocity is given by Liepe and Moeckel (1976) in Equation [4].

$$\sqrt{\overline{U_1^2}} = 0.4\frac{\varepsilon^{4/9}d_1^{7/9}}{\nu^{1/3}}\left(\frac{\rho_1-\rho_3}{\rho_3}\right)^{2/3} \quad [4]$$

The bubble turbulent mean-squared velocity is given by Lee et al. (1987) in Equation [5].

$$\overline{U_2^2} = C_0\left(\varepsilon d_2\right)^{2/3} \quad [5]$$

Rate Constant

Knowing the collision frequency and the corresponding probability of collection, the change in particle concentration within the entire flotation cell can be calculated as the number of collisions between particles and bubbles that occur (Z_{12}) that lead to attachment (P_A), once attached do not detach (1-P_D), and are able to rise within the froth (R_F).

$$\frac{dN_1}{dt} = -Z_{12}P_A\left(1-P_D\right)R_F \quad [6]$$

Comparing equation [6] with a first order rate equation [7], that most researchers believe model flotation (Kelsall 1961; Arbiter and Harris 1962; Mao and Yoon 1997),

$$\frac{dN_1}{dt} = -kN_1 \quad [7]$$

results in an equation for the rate constant that is dependent on hydrodynamics of the flotation cell as well as surface forces of the particles and bubbles.

$$k = \frac{Z_{12}P_A\left(1-P_D\right)R_F}{N_1} \quad [8]$$

Reducing the collision frequency to its individual components

$$Z_{12} = \beta N_1N_2 \quad [9]$$

produces the final rate constant equation.

$$k = \beta N_2P_A\left(1-P_D\right)R_F \quad [10]$$

Particle Collection

The probability of collection is dependent on the attachment and detachment processes and is a combination of their probabilities. These are both influenced by surface properties of the particles and bubbles as well as hydrodynamics of the system. Surface energies are modeled based upon the Extended DLVO theory. This incorporates the electrostatic, V_E, van der Waals (dispersion), V_D, and hydrophobic, V_H, surface forces (Rabinovich and Churaev 1979; Shaw 1992; Mao and Yoon 1997). V_H is a function of K_{131} and K_{232}, which can be obtained from experimental results (Rabinovich and Yoon 1994; Yoon and Ravishankar 1994; Yoon and Mao 1996; Yoon and Ravishankar 1996; Yoon, Flinn et al. 1997; Vivek 1998; Pazhianur 1999; Yoon

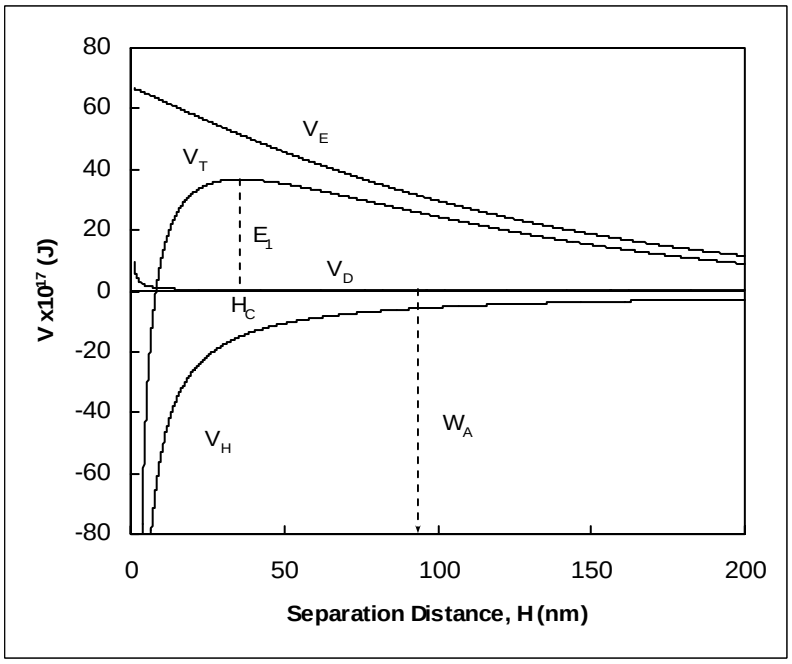

Figure 1. Surface energy vs. distance of separation between two particles (i.e. particle-bubble).

and Aksoy 1999). The surface forces are additive and combine to form the total energy of interaction, V_T, as shown in Figure 1.

For attachment there exists a maximum repulsive (positive) energy, E_1, that must be overcome. This maximum energy occurs at the critical rupture thickness, H_c. For separation distances less than H_c, the free energy continuously drops. Therefore, nothing will prevent the particle and bubble from coming together once H_c is overcome.

The probability of attachment is dependent on the energy barrier that must be overcome and the kinetic energy of attachment, $E_{k\text{-}A}$.

$$P_A = \exp\left(-\frac{E_1}{E_{k-A}}\right) \qquad [11]$$

The probability of detachment is dependent on the kinetic energy of detachment, $E_{k\text{-}D}$, and the work of adhesion, W_A, that must be overcome for detachment to occur (Figure 1).

$$P_D = \exp\left(-\frac{W_A}{E_{k-D}}\right) \qquad [12]$$

The work of adhesion is the energy needed to return the free energy of interaction to a zero value. It is assumed, that when detachment occurs, the equilibrium edge of the bubble will be past the critical rupture thickness. This is due to the small critical rupture thickness (approximately 100 nm) as compared to the deformation that a bubble goes through (tens to hundreds of microns) (Schimann 2004). Since the bubble edge will already be past the critical rupture thickness, E_1 does not need to be overcome and therefore is not used in detachment. The work of adhesion is the energy required to take apart a bubble-particle aggregate into a separate bubble and particle. This energy is obtained by surface tensions (gas-solid, gas-liquid, solid-liquid) and their respective areas. A well known model used by Mao (1997)

$$W_A = \gamma_{lv}\pi r_1^2 \left(1-\cos\theta\right)^2 \qquad [13]$$

assumes that the bubble surface is completely flat. Since the bubble and particle sizes are within two orders of magnitude of each other, a more accurate way to calculate W_A would be to assume a spherical bubble attached to a spherical particle. With simple geometry, this can be easily worked out and the current model uses this approach.

It is known that the contact angle for spherical particles is smaller than flat plate measurements (Preuss and Butt 1998). There can be up to a 10 degree contact angle reduction for colloidal sized particles. The contact angle used in the work of adhesion equation is usually obtained by measurements upon flat plates. Since it is assumed that this reduction is a function of particle size and that particles in flotation are much larger than colloidal sized particles, a constant 5 degree reduction is included in this model.

Energies

The main source of energy within a flotation cell comes from the motion of the impeller. The impeller motion produces the turbulent environment within the flotation cell. The impeller itself creates the largest eddies within the cell, roughly equal to the impeller size. The energy input into the cell (through the impeller) is transferred from the largest turbulent scale (corresponding to the impeller size) to the smallest turbulent scale (Kolmogorov microscale). A certain range of these eddy sizes will have an effect on the particles and give them their turbulent kinetic energies.

The wave number ($\kappa=2\pi/d$) equivalent to the largest eddy size (impeller) gives a kinetic energy equal to the tip-velocity of the impeller squared.

$$U_{T-large}^2 = \left(R_{Imp}\omega\right)^2 \qquad [14]$$

The kinetic energy then cascades, at a slope of -8/3 on a log-log scale, to the Kolmogorov microscale. In a pure liquid system the slope is theoretically -5/3, but with the introduction of bubbles, the slope is reduced to -8/3 (Wang, Lee et al. 1990). Particles are also found to reduce the theoretically predicted single-phase slope (Buurman 1990). In these dispersed phase systems, the energy is dissipated much more quickly, due to the fact that a portion of the energy is transferred to the particles and bubbles (Gore and Crowe 1991). Because of this, at each wave number there is less energy with particles and bubbles than without. It is assumed that with a combination of all three phases the slope will follow the -8/3 two-phase prediction. The energy spectrum is shown in Figure 2.

Eddies corresponding to the particle/bubble size through the Kolmogorov microscale will allow the particle/bubble to deviate from the fluid flow. The fluid within this range will have a different relaxation time than the particles and bubbles, as opposed to large eddies, where bubbles and particles follow their movement. This out of phase motion allows the particles and bubbles to move independent of each other and will produce collisions. It is assumed that the average amount of this energy ($U^2_{T\text{-}A}$) over the associated wave numbers ($\kappa_{P/B}$ to κ_K) directly corresponds to the particle and bubble attachment energy.

$$E_{k-A} = \frac{1}{2}\left(m_1 + m_2\right)\mathrm{U}_{T-A}^2 \qquad [15]$$

Large eddies, on the other hand, provide the energy for detachment. For detachment, bubbles and particles are already combined and, therefore, do not need a corresponding relaxation time as they do in the attachment process. Since all aggregates are subjected to large eddies, and these eddies contain the largest energies within the system, they provide the greatest

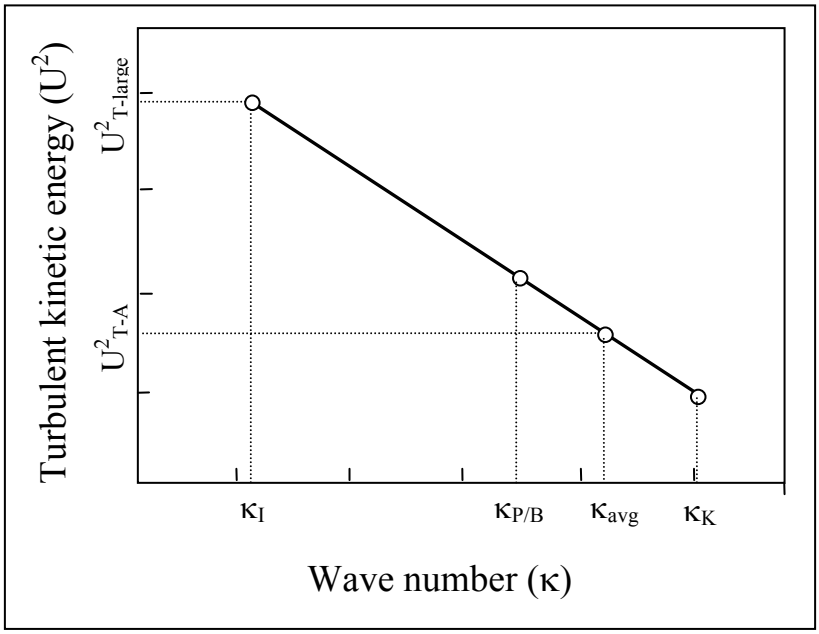

Figure 2. Turbulent kinetic energy spectrum

energy for detachment. Detachment follows from the centrifugal motion of these eddies, in which bubbles travel in towards the center of vortices and particles travel outward (Chahine 1995; Crowe and Trout 1995).

$$E_{k-D} = \frac{1}{2}\left(m_1 + m_2\right)\mathrm{U}_{T-D}^2 \qquad [16]$$

The turbulent energy corresponding to the largest eddy, $U_{T-large}^2$, is equal to the turbulent detachment energy, U_{T-D}^2.

Froth Recovery

Froth behavior can be very complex. The coalescence of bubbles and the subsequent loss of surface area, and the drainage of liquid between bubbles, to name a few, can affect the recovery of particles attached to bubble surfaces and particles entrained within the froth liquid. Froth recovery, R_f, is the percentage of particles which enter the froth, subsequently pass through the froth and are collected. All particles not recovered from the froth are returned to the slurry or never truly enter the froth phase. A simple approach to modeling this is to consider only the particles attached to the bubble surface. The only factor affecting the bubble surface would then be the coalescence of bubbles and loss of surface area. Once bubbles coalesce, a portion of their carrying capacity, for that volume of air, is lost. Once that carrying capacity is lost, it is assumed that those particles that were attached will drain back into the slurry.

This loss of surface area must be calculated with respect to the volume flow rate of air through the cell, which is assumed to be uniform throughout the slurry and froth section. A way to account for the loss of surface area is to calculate the surface area rates at both the initial (S_0) and final (S_f) stages of the froth. The fraction of surface area that is still useful for particle recovery would then be the ratio of these two surface area rates (Equation [17]).

$$R_F = \frac{S_f}{S_0} = \left(\frac{3V_g}{r_{2-f}}\right) \Big/ \left(\frac{3V_g}{r_{2-0}}\right) = \frac{r_{2-0}}{r_{2-f}} \quad [17]$$

V_g is the volumetric air flow rate divided by the cross-sectional area of the flotation cell, and is usually referred to as the superficial air flow rate. The froth recovery then becomes a ratio of the initial to final bubble sizes. This recovery assumes that the same percentage of particles adhere to the bubble surface at the initial and final stages of the froth. This recovery then becomes the maximum recovery allowed for a given froth.

Three-phase froths are highly complex. Aside from liquid and gas effects; particle size, shape, smoothness, hydrophobicity, contact angle, and concentration can affect froth behavior (Harris 1982; Knapp 1990; Johansson and Pugh 1992; Aveyard, Binks et al. 1999). Froth recovery is also thought to be a function of these variables, with particle size having a large effect. An empirical model proposed by Gorain et al. (1998) is thought to give the best results for froth recovery, to date (Equation [18]).

$$R_F = \exp\left(-\alpha \tau_f\right) \quad [18]$$

This model formulates the froth recovery as a function of the froth retention time, τ_f, and a parameter, α, that incorporates both physical and chemical properties of the froth (Mathe, Harris et al. 1998). Froth retention time is usually defined as the ratio of the froth height to superficial air flow rate, V_g. α is an empirical parameter that must be determined by experiments, for each system. α usually ranges, in industrial flotation cells, between 0.1 and 0.5 (Gorain, Harris et al. 1998).

Given the fact that there is a maximum recovery that can not be overcome, a modification of Gorain's model is proposed. All recoveries calculated using Equation [18] must be scaled using the maximum froth recovery. This is shown in Equation [19].

$$R_F = R_{\max} \exp\left(-\alpha \tau_f\right) \quad [19]$$

Assuming that the maximum froth recovery is given by Equation [17], and substituting this into Equation [19], gives the following formula for the froth recovery within a flotation cell.

$$R_F = \frac{r_{2-0}}{r_{2-f}} \exp\left(-\alpha \tau_f\right) \quad [20]$$

It is also known that particles within a flotation froth have varying retention times, due to, in large part, particle size (Mathe, Harris et al. 1998). Average retention time within a froth is given by the following formula (Equation [21]) where h_f is the froth height (Gorain, Harris et al. 1998).

$$\tau_{avg-f} = \frac{h_f}{V_g} \quad [21]$$

Superficial airflow rate is constant throughout the froth, as long as there is no diversion of the froth (secondary product output such as lower froth diversion) and steady state has been reached. Knowing that small particles within a liquid environment follow the flow, small particles are thought to have a froth retention time equal to the average retention time within the froth. It is also known that larger particles have a more difficult time traveling upward in the froth (Bikerman 1973). It is assumed that particles take longer to travel through the froth, due to their density and/or size. Knowing this, a froth retention time model is proposed

$$\tau_f\left(d_p\right)=\frac{h_f}{V_g}P_{fr} \qquad [22]$$

that is a function of particle size, d_p, and takes this into account by the addition of a froth particle effect, P_{fr}.

The particle effect on the retention time is given the functional form

$$P_{fr}=\exp\left(B\frac{d_p}{d_{p-n}}\right) \qquad [23]$$

where B is a constant and $d_{p\text{-}n}$ is the particle diameter whose bubble-particle aggregate mass is equal to the fluid mass as shown in Equation [24].

$$d_{p-n}=\left(\frac{\rho_3-\rho_2}{\rho_1-\rho_3}\right)^{1/3}d_2 \qquad [24]$$

$d_{p\text{-}n}$ takes into account the density of the particle as well as the size of the attached bubble.

A graphical representation of P_{fr} and its effect on froth recovery can be seen in Figure 3. The neutrally buoyant particle, $d_{p\text{-}n}$, affecting Equation [23] is used to take into account the buoyancy of the bubble with an attached particle. Smaller or less dense particles allow the bubble to travel upward within the froth more quickly. The smaller a particle is compared to the neutrally buoyant particle, the closer the particle effect is to 1. Therefore, the closer the particle is to following the fluid flow the closer the particle retention time is to the average retention time within the froth. The larger or more dense the particle is compared to the neutrally buoyant particle, the greater the particle effect becomes. Large particles will take longer to travel through the froth, if at all. Particle effect, using this functional form, must always be greater than 1 and therefore, particle froth retention time must always be equal to or greater than average froth retention time. B is thought to be a function of frother type and cell-dynamics and is found empirically for each system. The effect of B can be seen in Figure 3.

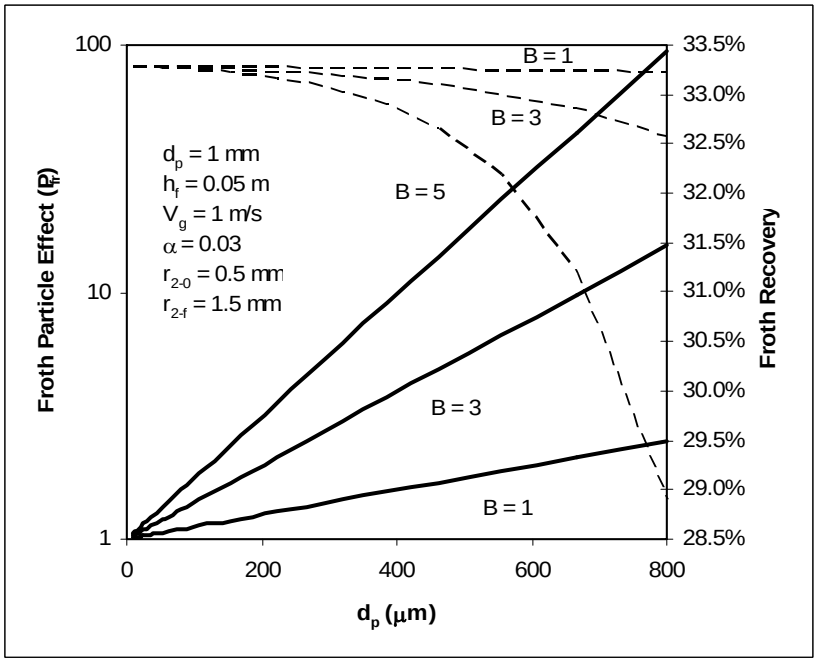

Figure 3. Particle size effect on froth particle effect, P_{fr}, (—) and froth recovery (- -)

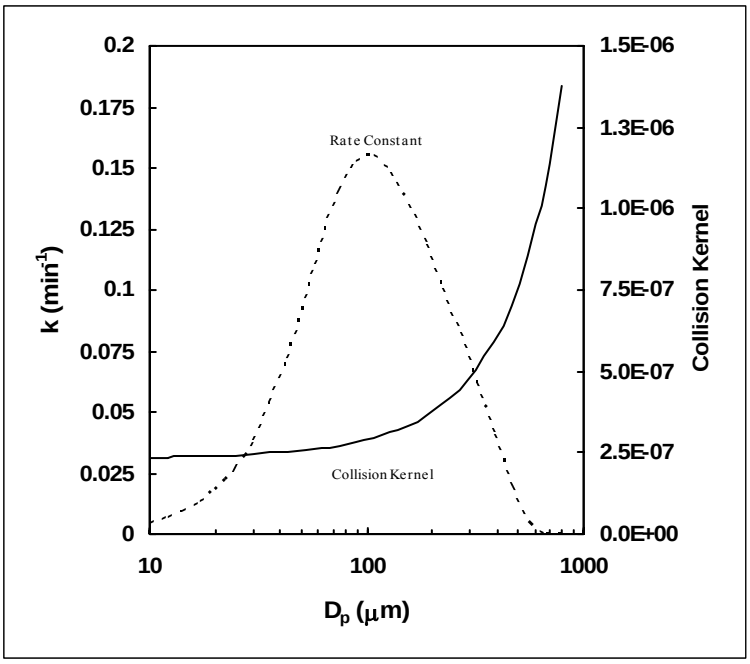

Figure 4. Effect of the collision kernel (—) on the rate constant (- -). Same conditions shown in Figure 9, contact angle 60 degrees.

Results

The effect of the individual components on the theoretical rate constant can be determined using Equation [10]. The importance of each individual process on the overall flotation process can be shown. These processes include the collision frequency, which is a function of the collision kernel (Figure 4), the froth recovery (Figure 5) and the probability of attachment and detachment (Figure 6).

Figure 4 through Figure 6 reveal a great deal of information about the entire flotation process. The overall magnitude of the rate constant is determined by the collision kernel, as well as the number density of the bubbles as shown in Figure 4. As the particle size increases, the collision kernel exponentially increases. This would result in greater and greater rate constants as particle size increases. This is not seen in flotation due to the combined effect of froth recovery and detachment. As shown in Figure 5, as particle size increases, the froth recovery decreases. Depending on the constant *B* being used (Equation [23]), the effect of particle size can be increased or reduced. Therefore, froth is a limiting factor to large particle flotation. Detachment also plays a roll in lowering the rate constant as shown in Figure 6. As particle size increases, detachment increases, until eventually no particle can stay attached to a bubble. The drop in probability of detachment corresponding to the maximum rate constant particle size is due to the combined effect of work of adhesion and turbulent detachment energy. Both increase as particle size increases. Because the relationship between the work of adhesion and turbulent detachment energy to particle size is not linear, initially work of adhesion increases much slower than turbulent detachment energy, until a certain particle size is reached. After this particle size is reached turbulent detachment energy increases more rapidly than work of adhesion which

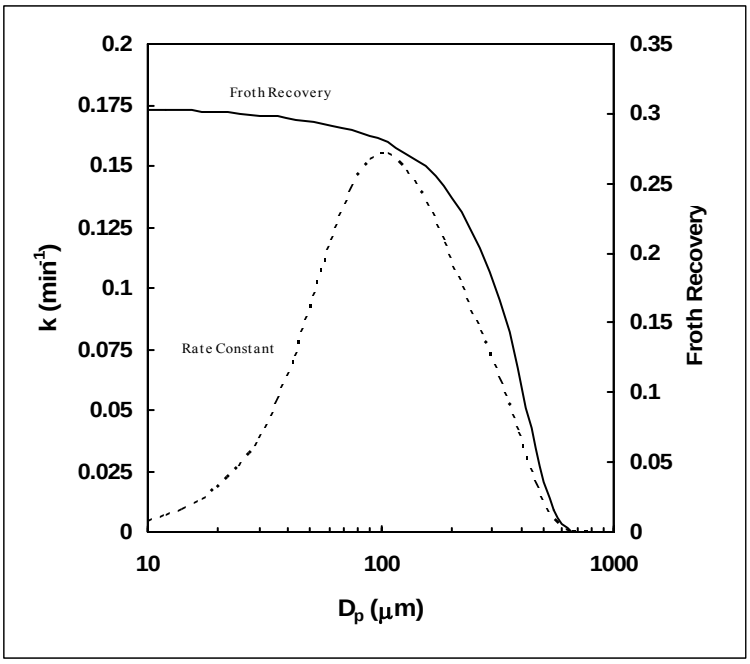

Figure 5. Effect of froth recovery (—) on the rate constant (- -). Same conditions shown in Figure 9, contact angle 60 degrees.

leads to higher detachment probabilities. Attachment does not have an affect on the rate constant due to the fact that everything attaches under the conditions shown.

Simulations were also run to show the effect of individual variables on the flotation rate constant. These variables include the particle diameter, bubble diameter, surface tension, contact

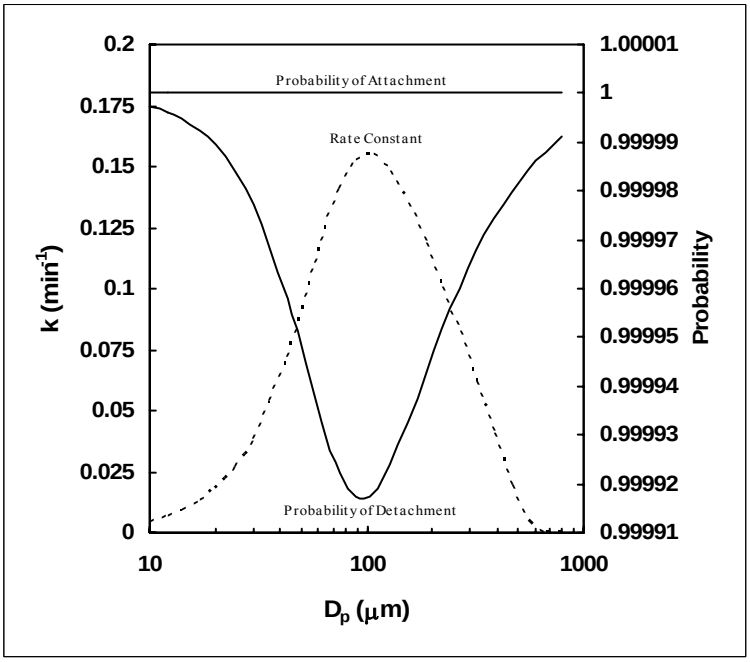

Figure 6. Effect of attachment and detachment probabilities (—) on the rate constant (- -). Same conditions shown in Figure 9, contact angle 60 degrees.

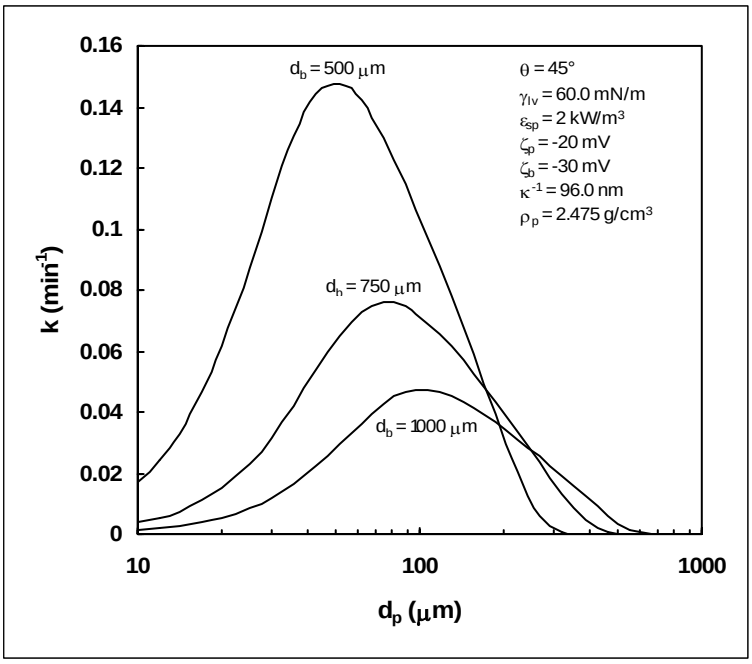

Figure 7. Effect of bubble size on the flotation rate constant. Smaller bubbles are more beneficial to small particle flotation while large particles may benefit more from bigger bubbles. This is due to a combination of specific surface area, kinetic energies, and surface forces.

angle, and specific energy input.

Figure 7 and Figure 8 show the effect of physical variables on the rate constant. The outcome from varying the bubble diameter, along with the particle diameter, can be found in Figure 7. As the bubble diameter decreases, the rate constant increases. In addition, when the bubble diameter is decreased, the particle diameter, where the maximum rate constant occurs, is decreased. This affirms the phenomenon found in column flotation, where smaller bubbles are more beneficial to small particle flotation. The first phenomenon (increased small particle rate constant) is mainly due to the fact that bigger bubbles have lower specific surface area (surface area per unit volume of air flow). This results in a lower amount of sites for potential particles to adhere to. The smaller the bubble, the greater the specific surface area, and therefore the greater potential for particles to become attached. For the same volume of air, smaller bubbles have the potential to float more particles.

The second phenomenon (shift where maximum rate constant occurs) is due, mainly, to kinetic energies, as well as surface forces. As a bubble becomes smaller, its kinetic energy decreases. The energy difference between smaller and larger bubbles is more greatly felt, in interactions, by smaller particles, because of the small particles' already low kinetic energies. Surface forces are also affected by the smaller bubbles but more so in the energy barrier than in the work of adhesion. The energy barrier will decrease, like kinetic energy, when the bubble size is reduced. Since both main variables (energy barrier and attachment kinetic energy) are reduced for the probability of attachment, it is not thought that the attachment process is affecting this movement. Probability of detachment, on the other hand, has only one variable greatly affected by bubble size. It is thought that the detachment process of smaller bubbles will lower the maximum rate constant particle size.

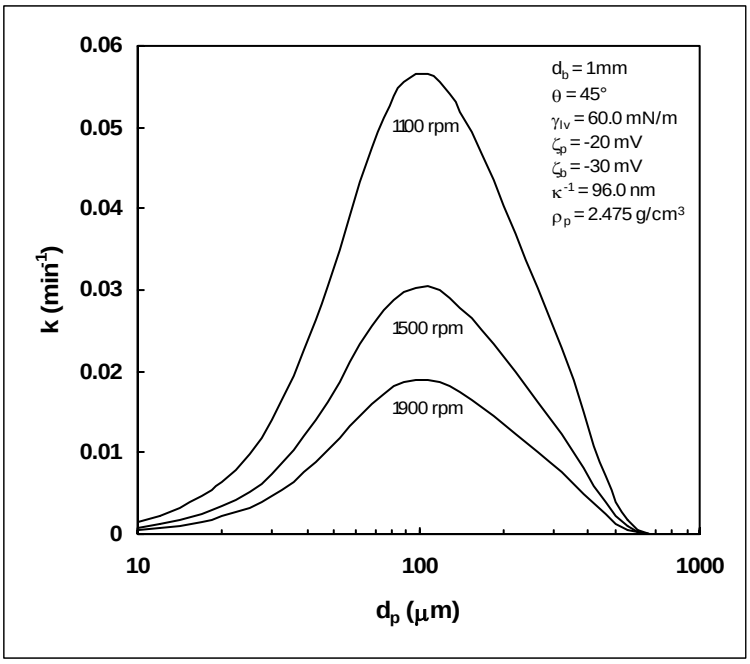

Figure 8. Effect of energy input, in the form of impeller rpm, on the flotation rate constant. Higher energy inputs decrease rate constant due to higher probabilities of detachment from higher kinetic energies of detachment. Bubble size changes due to increased impeller speeds are not taken into account.

It should also be noted that as bubble size decreases, large particles become more difficult to float. This is due to the froth recovery factor, R_F. The neutral density particle size, $d_{p\text{-}n}$, decreases with decreasing bubble size, which makes recovery of large particles more difficult. The smaller the bubble size becomes in the froth, the greater the difficulty large particles have in traveling upward within the froth.

The outcome from varying the energy input, in the form of impeller speed, along with the particle diameter, is shown in Figure 8. Although not much difference is seen in the particle size where the maximum rate constant occurs, there is a meaningful difference in the magnitude of the rate constant. As the specific energy input increases, the rate constant decreases. At first, this seems counter-intuitive, and the opposite effect is seen in industrial machines. It was thought that as the energy input into the system increases the rate constant would also increase. This is true up to a point after which the potential for detachment increases substantially more than the potential for attachment. Lower energy input values, which reverse the effect on the rate constant, are not shown, since most industrial flotation machines are run with much higher impeller speeds. Actual industrial flotation machines see an opposite effect because of the production of bubbles. As the energy input into a system is increased, the bubble size is decreased. The reduced bubble size is what causes the increase in the rate constant. There is no relationship between bubble size and energy input in the present flotation model. The bubble size is constant throughout this simulation. When the bubble production model given by Johansen et al. (1997) is input into the current model, the opposite effect is shown. Higher energy inputs produce higher rate constants because of smaller bubbles. Johansen's model is not used to calculate flotation rate constants due it's applicability to flotation systems. It was derived for bubble formation in a liquid metal environment. It was input here only to state that there can

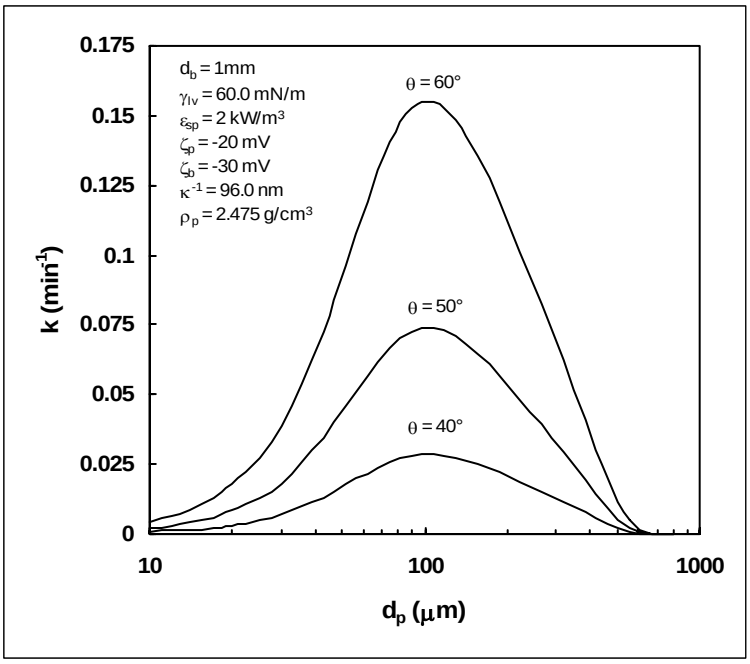

Figure 9. Effect of contact angle on the flotation rate constant. Higher contact angles increase the work of adhesion, which decreases the probability of detachment. This increases the rate constant. It should be noted that contact angles and hydrophobic force constants are directly related. Both increase or decrease the rate constant in tandem.

be a combined effect of bubble size and energy input on the rate constant that shows the same effect as industrial machines.

Figure 9 and Figure 10 show the effects of surface chemistry parameters. The outcome of varying the contact angle, along with the particle diameter, can be found in Figure 9. As the angle increases, the rate constant increases. This is due, mostly, to the work of adhesion. A higher contact angle increases the work of adhesion, which in turn makes a greater "energy barrier" for detachment. This greater "energy barrier" decreases the probability of detachment and increases the rate constant. It should also be noted that the contact angle and hydrophobic force constant are related (Rabinovich and Yoon 1994; Yoon and Ravishankar 1994; Yoon and Ravishankar 1996; Vivek 1998; Pazhianur 1999). The contact angle and hydrophobic force constant, which are directly proportional, will both increase or decrease the rate constant in tandem.

The final surface force parameter that was varied is the surface tension. This is shown in Figure 10, along with the effect of particle diameter. Similar to the contact angle, the effects shown here are entirely due to the work of adhesion. A higher surface tension increases the work of adhesion, which makes it harder for particles to become detached. Therefore, the probability of detachment decreases, with increasing surface tension, and the rate constant increases.

It should be noted that all simulations that were run show a maximum, of the rate constant at, approximately, a particle diameter of 100 microns. This is seen in industrial flotation cells and is a good sign as to the validity of the model and the assumptions used to derive the model.

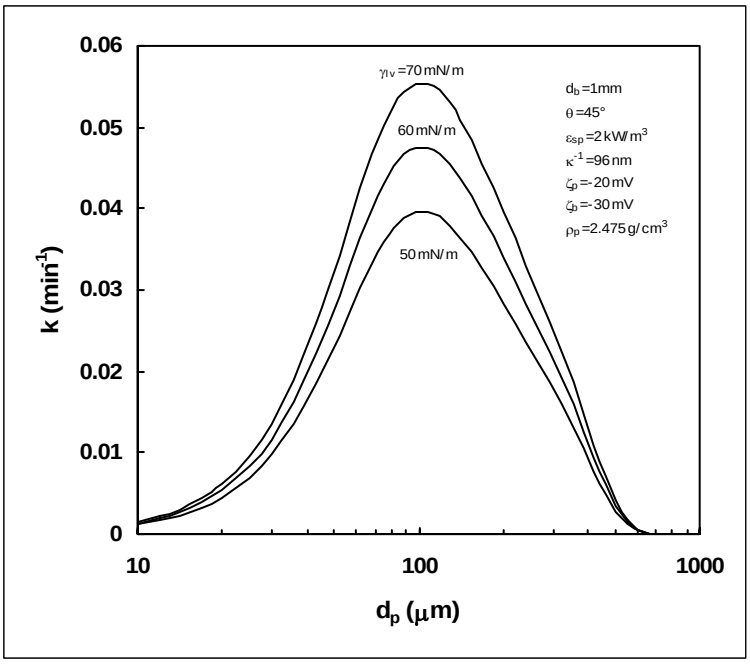

Figure 10. Effect of liquid-vapor surface tension on the flotation rate constant. Higher surface tensions increase the work of adhesion and decrease the probability of detachment. This increases the overall rate constant.

These simulations show that surface chemistry parameters play as important a role in flotation as physical parameters. An analysis of flotation cannot be conducted while only looking at the physical characteristics of the flotation machinery and the feed to that machinery. The chemical interactions between all aspects of flotation must be considered. This includes water chemistry and surface chemistry. A big determining factor in flotation is the hydrophobic force. This manifests itself in the hydrophobic force constant and contact angle. If this force is omitted, a flotation equation cannot be considered universal and will only be valid in a very few situations. The current equation incorporates all current surface chemistry as well as hydrodynamic knowledge. Although the current model does predict trends that are seen in industry, a more precise knowledge of the effect of froth on the rate constant will provide a more robust and applicable model.

Conclusions

A flotation model was developed that can predict trends in the flotation of solid particles. The model incorporates hydrodynamic as well as surface chemistry parameters in a turbulent environment. A collision frequency is used, along with a probability of collection and a froth recovery factor to calculate the rate of particles that are recovered per unit volume per unit time. The collision frequency is calculated using a model proposed by Abrahamson. Both probability of attachment and probability of detachment, which combine to form the probability of collection, compare surface energy values with the kinetic energies of the particles and bubbles to determine their respective probabilities. The kinetic energies of the particles and bubbles come from the turbulent energies of eddies directly affecting the attachment and detachment of the particles and bubbles. The froth recovery factor is calculated using a modification of a model

given by Gorain el al. (1998). The modification takes into account the particle size as well as a maximum froth recovery determined by bubble size.

Simulations were run that found phenomena similar to those found in industrial flotation cells. From these simulations, the surface chemistry parameters were deemed as important as the physical parameters of the flotation system. One of the most important of the surface chemistry parameters was the hydrophobic force. This influences both the hydrophobic force constant, which in turn influences the contact angle; the contact angle having a large impact on the rate constant. Further refinement of the model is necessary to incorporate a better understanding of the froth section of flotation. The current model can predict trends found in the flotation industry.

Nomenclature

1	subscript – refers to particle
2	subscript – refers to bubble
3	subscript – refers to liquid
B	constant
C_0	constant equal to 2.0
d_{12}	diameter of collision [m]
d_i	diameter of i [m]
d_p	diameter of particle [m]
$d_{p\text{-}n}$	diameter of neutrally buoyant particle [m]
E_1	surface energy barrier [J]
$E_{k\text{-}D}$	kinetic energy of detachment [J]
$E_{k\text{-}A}$	kinetic energy of attachment [J]
H_c	critical rupture thickness [m]
h_f	froth height [m]
k	rate constant [min^{-1}]
m_i	mass of particle or bubble [kg]
N_i	number density of i – number per unit volume [m^{-3}]
P_A	probability of attachment [-]
P_D	probability of detachment [-]
P_{fr}	particle effect – retention time [-]
$r_{2\text{-}0}$	radius of bubble – slurry-froth interface [m]
$r_{2\text{-}f}$	radius of bubble – top of froth [m]
Re_b	Reynolds number of bubble [-]
R_F	froth recovery factor [-]
r_i	radius of subscript i [m]
R_{Imp}	radius of impeller [m]
R_{max}	maximum froth recovery [-]
S_0	surface area rate – slurry-froth interface [s^{-1}]
S_b	surface area rate – within slurry [s^{-1}]
S_f	surface area rate – top of froth [s^{-1}]
St	Stokes number [-]
$U^2_{T\text{-large}}$	large scale turbulent kinetic energy [$m^2 \cdot s^{-2}$]
$U^2_{T\text{-}A}$	attachment turbulent kinetic energy [$m^2 \cdot s^{-2}$]

$U^2_{T\text{-}D}$	detachment turbulent kinetic energy [$m^2 \cdot s^{-2}$]
$\sqrt{\overline{U_i^2}}$	root-mean-squared velocity of i – turbulent velocity [$m \cdot s^{-1}$]
V_D	dispersion free energy of interaction [J]
V_E	electrostatic free energy of interaction [J]
V_g	superficial air flow rate [$m \cdot s^{-1}$]
V_H	hydrophobic free energy of interaction [J]
V_T	total free energy of interaction [J]
W_A	work of adhesion [J]
Z_{12}	collision frequency between particle and bubble [$m^{-3} \cdot s^{-1}$]
α	froth recovery parameter [s^{-1}]
β	collision kernel [$m^3 \cdot s^{-1}$]
γ_{lv}	liquid-vapor surface tension [$N \cdot m^{-1}$]
ε	average energy dissipation [$m^2 \cdot s^{-3}$]
κ	wave number [m^{-1}]
κ_{avg}	average attachment wave number [m^{-1}]
κ_I	impeller wave number [m^{-1}]
κ_K	Kolmogorov wave number [m^{-1}]
$\kappa_{P/B}$	particle/bubble wave number [m^{-1}]
θ	contact angle [rad] – measured through liquid
ν	kinematic viscosity [$m^2 \cdot s^{-1}$]
ρ_i	density of i [$kg \cdot m^{-3}$]
$\tau_{avg\text{-}f}$	average froth retention time [s]
τ_f	froth retention time [s]
τ_i	particle/bubble relaxation time [s]
τ_η	Kolmogorov timescale [s]
ω	impeller radial velocity [rpm]

References

Abrahamson, J. (1975). "Collision rates of small particles in a vigorously turbulent fluid." Chemical Engineering Science **30**(11): 1371-9.

Arbiter, N. and C. C. Harris (1962). Flotation Kinetics. Froth flotation - 50th anniversary volume. D. W. Fuerstenau, American Institute of Mining, Metallurgical, and Petroleum Engineers.

Aveyard, R., B. P. Binks, et al. (1999). "Foams and emulsions. Their stability and breakdown by solid particles and liquid droplets. The colloid chemistry of a dog's breakfast." NATO ASI Series, Series E: Applied Sciences **354**(Foams and Emulsions): 21-44.

Bikerman, J. J. (1973). Applied Physics and Engineering, No. 10: Foams. [Physicochemical Aspects].

Bourloutski, E. and M. Sommerfeld (2002). "Parameter studies on the effect of boundary conditions in three-dimensional calculations of bubble column." FED (American Society of Mechanical Engineers) **[257-2]**(A, Proceedings of the 2002 ASME Joint U.S.-European Fluids Engineering Conference): 355-364.

Buurman, C. (1990). "Stirring of concentrated slurries: a semi-empirical model for complete suspension at high solids concentrations and 5 m3 verification experiments." Institution of Chemical Engineers Symposium Series - Fluid Mixing 4 **121**: 343-350.

Ceylan, K., A. Altunbas, et al. (2001). "A new model for estimation of drag force in the flow of Newtonian fluids around rigid or deformable particles." Powder Technology **119**(2-3): 250-256.

Chahine, G. L. (1995). Bubble interactions with vortices. Fluid Vortices. S. I. Green.

Crowe, C. T. and T. R. Trout (1995). Particle interactions with vortices. Fluid Vortices. S. I. Green.

Gorain, B. K., M. C. Harris, et al. (1998). "The effect of froth residence time on the kinetics of flotation." Minerals Engineering **11**(7): 627-638.

Gore, R. A. and C. T. Crowe (1991). "Modulation of turbulence by a dispersed phase." Transactions of the ASME **113**: 304-307.

Govan, A. H. (1989). "A simple equation for the diffusion coefficient of large particles in a turbulent gas flow." International Journal of Multiphase Flow **15**(2): 287-94.

Harris, P. J. (1982). Frothing phenomena and frothers. Principles of Flotation. R. P. King. Johannesburg, South African Institute of Mining and Metallurgy**:** 237-251.

Johansen, S. T., S. Gradahl, et al. (1997). "The bubble size and mass transfer mechanisms in rotor stirred reactors." Light Metals (Warrendale, Pennsylvania): 663-666.

Johansson, G. and R. J. Pugh (1992). "The influence of particle size and hydrophobicity on the stability of mineralized froths." International Journal of Mineral Processing **34**(1-2): 1-21.

Kelsall, D. F. (1961). "Application of probability in the assessment of flotation systems." Bull. Instn. Min. Metall. **650**: 191-204.

Knapp, J. M. S. (1990). A study of flotation froth behavior. Mining and Minerals Engineering, Virginia Polytechnic Institute and State University.

Kruis, F. E. and K. A. Kusters (1997). "The collision rate of particles in turbulent flow." Chemical Engineering Communications **158**: 201-230.

Lee, C. H., L. E. Erickson, et al. (1987). "Bubble breakup and coalescence in turbulent gas-liquid dispersions." Chemical Engineering Communications **59**(1-6): 65-84.

Liepe, F. and H. O. Moeckel (1976). "Studies of the combination of substances in liquid phase. Part 6: The influence of the turbulence on the mass transfer of suspended particles." Chemische Technik (Leipzig, Germany) **28**(4): 205-209.

Mao, L. and R.-H. Yoon (1997). "Predicting flotation rates using a rate equation derived from first principles." International Journal of Mineral Processing **51**(1-4): 171-181.

Mathe, Z. T., M. C. Harris, et al. (1998). "Review of froth modeling in steady state flotation systems." Minerals Engineering **11**(5): 397-421.

Pazhianur, R. (1999). Hydrophobic force in flotation, Virginia Polytechnic Institute and State University.

Preuss, M. and H.-J. Butt (1998). "Measuring the contact angle of individual colloidal particles." Journal of Colloid and Interface Science **208**(2): 468-477.

Rabinovich, Y. I. and N. V. Churaev (1979). "Effect of electromagnetic delay on the forces of molecular attraction." Kolloidnyi Zhurnal **41**(3): 468-74.

Rabinovich, Y. I. and R. H. Yoon (1994). "Use of atomic force microscope for the measurements of hydrophobic forces." Colloids and Surfaces, A: Physicochemical and Engineering Aspects **93**: 263-73.

Saffman, P. G. and J. S. Turner (1956). "On the collision of drops in turbulent clouds." Journal of Fluid Mechanics **1**: 16-30.
Schimann, H. C. R. (2004). "Detachment force and energy of a cetyltrymethylammonium bromide coated silica sphere from a flat bubble." pending publication.
Shaw, D. J. (1992). Introduction to colloid and surface chemistry. Boston, Butterworth-Heinemann.
Sundaram, S. and L. R. Collins (1997). "Collision statistics in an isotropic particle-laden turbulent suspension. Part 1. Direct numerical simulations." Journal of Fluid Mechanics **335**: 75-109.
Vivek, S. (1998). Effects of long-chain surfactants, short-chain alcohols and hydrolysable cations on the hydrophobic and hydration forces, Virginia Polytechnic Institute and State University.
Wang, S. K., S. J. Lee, et al. (1990). "Statistical analysis of turbulent two-phase pipe flow." Journal of Fluids Engineering **112**(1): 89-95.
Williams, J. J. E. and R. I. Crane (1983). "Particle collision rate in turbulent flow." International Journal of Multiphase Flow **9**(4): 421-35.
Yoon, R. H. (2000). "The role of hydrodynamic and surface forces in bubble-particle interaction." International Journal of Mineral Processing **58**(1-4): 129-143.
Yoon, R. H. and S. B. Aksoy (1999). "Hydrophobic forces in thin water films stabilized by dodecylammonium chloride." Journal of Colloid and Interface Science **211**(1): 1-10.
Yoon, R.-H., D. H. Flinn, et al. (1997). "Hydrophobic interactions between dissimilar surfaces." Journal of Colloid and Interface Science **185**(2): 363-370.
Yoon, R.-H. and L. Mao (1996). "Application of extended DLVO theory, IV. Derivation of flotation rate equation from first principles." Journal of Colloid and Interface Science **181**(2): 613-626.
Yoon, R.-H. and S. A. Ravishankar (1994). "Application of extended DLVO theory III. Effect of octanol on the long-range hydrophobic forces between dodecylamine-coated mica surfaces." Journal of Colloid and Interface Science **166**(1): 215-24.
Yoon, R.-H. and S. A. Ravishankar (1996). "Long-range hydrophobic forces between mica surfaces in alkaline dodecylammonium chloride solutions." Journal of Colloid and Interface Science **179**(2): 403-411.

A Comprehensive Model for Flotation under Turbulent Flow Conditions: Verification

I. M. Sherrell

Abstract

A flotation model has been proposed that is applicable in a turbulent environment. The model takes into account hydrodynamics of the flotation cell as well as all relevant surface forces (van der Waals, electrostatic, and hydrophobic) by use of the Extended DLVO theory. The flotation model includes probabilities for attachment, detachment, and froth recovery as well as a collision frequency. Flotation experiments have been conducted to verify this model. Model results are close to experimental values, which lead to the conclusion that the model can predict the flotation rate constant in other circumstances, such as industrial (e.g., coal and mineral) flotation.

Introduction

Industrial flotation is a turbulent process that separates one material from another. In most cases, this includes one solid particle from another solid particle. The process is used, among others, to separate plastics in the recycling industry, decontaminate soil, separate carbon from fly ash, etc. Most importantly, it is used to upgrade minerals in the mining industry.

Flotation begins with the introduction of air into a slurry. Certain particles (hydrophobic) are able to attach to bubbles formed from this air. The bubbles then travel vertically and are collected, while the slurry continues to travel horizontally. The process, essentially, separates material based on its ability to attach to air bubbles. This is the driving factor in flotation.

Modeling of this process, which would be beneficial in the application of flotation as well as the design of the flotation process, is very complex due to the three phases found in the flotation machines as well as the turbulent environment in which flotation occurs. To complicate matters, surface forces must be taken into account. Modification of these forces, by the addition of surfactants, allows the process to be more efficient and in some cases is the only mechanism allowing the process to take place.

Surface forces play a crucial role in the attachment and detachment processes between a particle and bubble. Proper modeling of these forces is vital to having a general flotation model. The DLVO theory models some of the surface forces seen in flotation. This theory combines the van der Waals force and the electrostatic force into a total surface force. The problem with the DLVO theory is the lack of any hydrophobic force parameter, which is known to be a major contributor to surface forces between particles and bubbles in a water medium (Yoon and Mao 1996; Yoon 2000). The extended DLVO theory incorporates this third force (hydrophobic) into the DLVO theory.

The most rigorous flotation model, to date, dealing with all three surface forces (electrostatic, van der Waals, and hydrophobic) was proposed by Mao and Yoon (1997).

$$k = \frac{1}{4} S_b \left[\frac{3}{2} + \frac{4 \mathrm{Re}_b^{0.72}}{15} \right] \left(\frac{r_1}{r_2} \right)^2 \exp\left(-\frac{E_1}{E_{k-A}} \right) \left[1 - \exp\left(-\frac{W_A + E_1}{E_{k-D}} \right) \right] \quad [1]$$

The model is based upon first principles in a quiescent environment and agrees well with experimental data. The problem of this model is its applicability to industrial applications where turbulence is encountered. This model did provide a key basis for the current model by the use of the extended DLVO theory and its relationship to the energies of the system.

Model

The current flotation model was first proposed by Sherrell and Yoon (To be submitted - summer 2004). Assuming that the rate process is first order (Kelsall 1961; Arbiter and Harris 1962; Mao and Yoon 1997) and that the rate is equal to the number of collisions between particles and bubbles ($\beta N_1 N_2$) that lead to attachment (P_A), once attached do not detach ($1\text{-}P_D$), and are able to rise within the froth (R_F), leads to Equation [2].

$$k = \beta N_2 P_A \left(1 - P_D\right) R_F \quad [2]$$

Equation [2] gives the rate constant for the turbulent flotation process and is a function of both the hydrodynamics of the flotation cell and surface forces of the particles and bubbles by the inclusion of the collision frequency kernel, β, probability of attachment, P_A, probability of detachment, P_D, and the froth recovery, R_F.

Collision Frequency

Knowing that the environment within a flotation cell is highly turbulent, collisions that occur within this environment occur for reasons far different than ones that occur in laminar flows. Mao and Yoon (1997) modeled laminar collisions using the volume that the bubble travels through and the percent solids of the slurry. A collision efficiency was then applied that accounted for streamline effects. In turbulent flows, particles and bubbles deviate from the fluid path. This deviation is measured by the Stokes number; a ratio of the particle relaxation (response) time to the smallest fluid relaxation time (Kolmogorov timescale).

Two mechanisms account for turbulent collisions; the shear and accelerative mechanisms. The shear mechanism accounts for relative motions of particles (fluid, solid, or gas) in a shear field. These collisions always occur in a turbulent field, even among fluid particles. Collisions between particles with Stokes numbers less than 1 occur by shear only. The accelerative mechanism accounts for inertial effects due to large and/or heavy particles. Collisions due to the accelerative mechanism occur above a Stokes number of 1 where there is some lag between the particle and fluid.

Sundaram and Collins (1997) ran a numerical simulation of real world collisions and found that for Stokes numbers above 1, a model proposed by Abrahamson (1975) provided more reliable results. Abrahamson's model is based entirely on the accelerative mechanism of collision and assumes a Stokes number of infinity. A combination of shear and accelerative mechanisms (Williams and Crane 1983; Kruis and Kusters 1997) is assumed to provide the best results for flotation collisions, but no current shear/accelerative models can account for both heavier and lighter than the surrounding fluid particle collisions. Since most particles in flotation have a Stokes number greater than 1, Abrahamson's model is currently used (Equation [3]).

$$Z_{12} = 2^{3/2} \pi^{1/2} N_1 N_2 d_{12}^2 \sqrt{\left(\overline{U_1^2} + \overline{U_2^2} \right)} \quad [3]$$

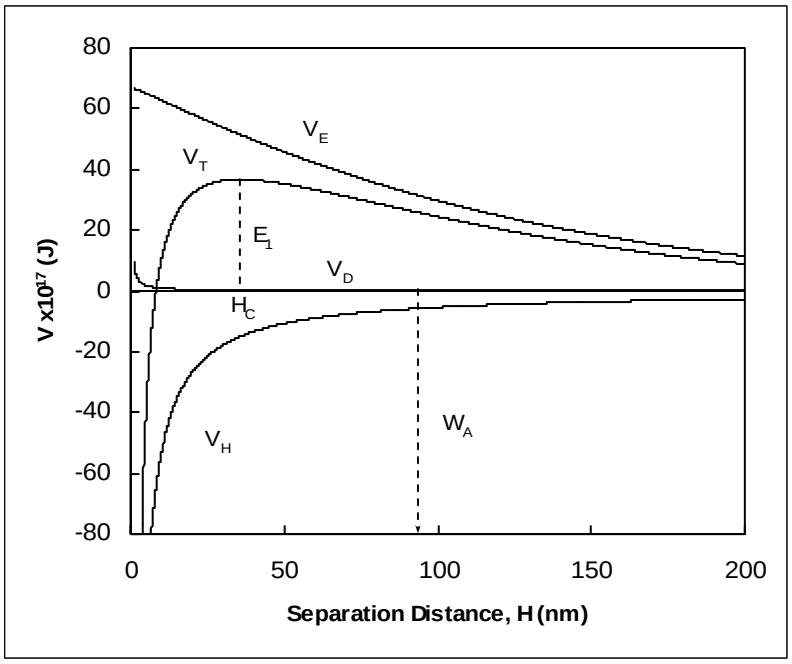

Figure 1. Surface energy vs. distance of separation between two particles (i.e. particle-bubble)

The particle turbulent root-mean-squared velocity, $\sqrt{\overline{U_i^2}}$, within this model is given by Liepe and Moeckel (1976). The bubble turbulent mean-squared velocity is given by Lee et al. (1987).

Particle Collection

The attachment and detachment processes are both influenced by surface properties of the particles and bubbles as well as hydrodynamics of the system. Surface energies are modeled based upon the Extended DLVO theory. This incorporates the electrostatic, V_E, van der Waals (dispersion), V_D, and hydrophobic, V_H, surface forces (Rabinovich and Churaev 1979; Shaw 1992; Mao and Yoon 1997). V_H is a function of hydrophobic force constants (K_{131} and K_{232}), which can be obtained from experimental results (Rabinovich and Yoon 1994; Yoon and Ravishankar 1994; Yoon and Mao 1996; Yoon and Ravishankar 1996; Yoon, Flinn et al. 1997; Vivek 1998; Pazhianur 1999; Yoon and Aksoy 1999). The surface forces are additive and combine to form the total energy of interaction, V_T, as shown in Figure 1.

The probability of attachment is dependent on the energy barrier that must be overcome and the kinetic energy of attachment, $E_{k\text{-}A}$.

$$P_A = \exp\left(-\frac{E_1}{E_{k-A}}\right) \qquad [4]$$

For attachment there exists a maximum repulsive (positive) energy, E_1, that must be overcome. This maximum energy occurs at the critical rupture thickness, H_c. Nothing prevents the particle and bubble from adhering once H_c is overcome due to the continuous drop in surface energy at smaller separation distances.

The probability of detachment is dependent on the kinetic energy of detachment, $E_{k\text{-}D}$, and the work of adhesion, W_A, which must be overcome for detachment to occur (Figure 1).

$$P_D = \exp\left(-\frac{W_A}{E_{k-D}}\right) \quad [5]$$

The work of adhesion is the energy required to return the free energy of interaction to a zero value, which, in turn, is the energy needed to take apart a bubble-particle aggregate into a separate bubble and particle. This energy is obtained thermodynamically by surface tensions (gas-solid, gas-liquid, solid-liquid) and their respective areas. A well known model used by Mao (1997)

$$W_A = \gamma_{lv}\pi r_1^2 \left(1-\cos\theta\right)^2 \quad [6]$$

assumes that the bubble surface is completely flat. Since the bubble and particle sizes are within two orders of magnitude of each other, a more accurate approach to calculate W_A would be to assume a spherical bubble attached to a spherical particle. With simple geometry, this can easily be worked out and the current model uses this approach.

Contact angles, used within Equation [6], are known to be smaller for spherical particles than corresponding flat plate measurements (Preuss and Butt 1998). There can be up to a 10 degree contact angle reduction for colloidal sized particles. The contact angle used in Equation [6] is usually obtained by measurements upon flat plates. Since it is assumed that this reduction is a function of particle size and that particles in flotation are much larger than colloidal sized particles, a constant 5 degree reduction is included in this model.

The energies for the attachment and detachment processes that will overcome these energy barriers are provided by the turbulence within the flotation cell. Energy input into the cell (through the impeller) is transferred from the largest turbulent scale (corresponding to the impeller size) to the smallest turbulent scale (Kolmogorov microscale). A certain range of these eddy sizes will have an effect on the particles and give them their turbulent kinetic energies.

Kolmogorov theory predicts, for homogenous turbulence, that energy will cascade from the largest scales to the smallest scales. The largest scale (impeller) produces the largest energy which then is transferred (at a slope of -5/3 on log-log scale) to the small scale where it is dissipated. With the addition of bubbles the slope is found to be -8/3 (Wang, Lee et al. 1990). Particles are also found to reduce the theoretically predicted slope (Buurman 1990). It is assumed that with a combination of all three phases, the slope will follow the -8/3 prediction for a two-phase flow.

Eddies corresponding to the particle/bubble size through the Kolmogorov microscale will allow the particle and bubble to deviate from the fluid flow. The fluid within this range will have a different relaxation time than the particles and bubbles, as opposed to large eddies, where bubbles and particles follow their movement. This out of phase motion allows the particles and bubbles to move independent of each other and will produce collisions. It is assumed that the average amount of this energy ($U^2_{T\text{-}A}$) over the associated wave numbers directly corresponds to the particle and bubble attachment energy as shown in Equation [7], where m_1 and m_2 are the particle and bubble masses respectively.

$$E_{k-A} = \frac{1}{2}\left(m_1 + m_2\right)\mathrm{U}^2_{T-A} \quad [7]$$

Large eddies, on the other hand, provide the energy for detachment. For detachment, bubbles and particles are already combined and, therefore, do not need a corresponding relaxation time as they do in the attachment process. Since all aggregates are subjected to large eddies, and these eddies contain the largest energies within the system, they provide the greatest energy for detachment. Detachment follows from the centrifugal motion of these eddies, in

which bubbles travel in towards the center of vortices while particles travel outward (Chahine 1995; Crowe and Trout 1995).

$$E_{k-D} = \frac{1}{2}\left(m_1 + m_2\right)\mathrm{U}_{T-D}^2 \qquad [8]$$

The turbulent energy corresponding to the largest eddy is equal to the turbulent detachment kinetic energy, U_{T-D}^2.

Froth Recovery

Froth recovery, R_f, is the percentage of particles that enter the froth and subsequently pass through the froth and are collected. All particles not recovered from the froth are returned to the slurry or never truly enter the froth phase. A simple approach of modeling this is to consider only the particles attached to the bubble surface. The only factor affecting the bubble surface would then be the coalescence of bubbles and loss of surface area. Once bubbles coalesce, a portion of their carrying capacity, for that volume of air, is lost. Once that carrying capacity is lost, it is assumed that those particles that were attached will drain back into the slurry. This provides a maximum froth recovery barrier that can not be overcome. It should be noted that this does not take into account entrainment, but only accounts for attached particles. This loss of surface area is equal to the ratio of the final and initial froth bubble sizes.

$$R_{\max} = \frac{S_f}{S_0} = \left(\frac{3V_g}{r_{2-f}}\right) \Bigg/ \left(\frac{3V_g}{r_{2-0}}\right) = \frac{r_{2-0}}{r_{2-f}} \qquad [9]$$

To theoretically model three-phase froths liquid and gas effects as well as particle size, shape, smoothness, hydrophobicity, contact angle, and concentration must be taken into account (Harris 1982; Knapp 1990; Johansson and Pugh 1992; Aveyard, Binks et al. 1999). Froth recovery is also thought to be a function of these variables, with particle size having a large effect. An empirical model proposed by Gorain et al. (1998) is thought to give the best results for froth recovery, to date.

$$R_F = \exp\left(-\alpha\tau_f\right) \qquad [10]$$

Equation [10] is a function of the froth retention time, τ_f, and a parameter, α, that incorporates both physical and chemical properties of the froth (Mathe, Harris et al. 1998). Froth retention time is usually defined as the ratio of the froth height to superficial air flow rate, V_g. α is an empirical parameter that must be determined by experiments, for each system. α usually ranges, in industrial flotation cells, between 0.1 and 0.5 (Gorain, Harris et al. 1998).

Given the fact that there is a maximum recovery that can not be overcome, a modification of Gorain's model is proposed. All recoveries calculated using equation [10] must then be scaled using the maximum froth recovery (Equation [9]).

$$R_F = \frac{r_{2-0}}{r_{2-f}}\exp\left(-\alpha\tau_f\right) \qquad [11]$$

It is also known that particles within a flotation froth have varying retention times, due to, in large part, particle size (Mathe, Harris et al. 1998). Average retention time within a froth is the ratio of froth height, h_f, to superficial air flow rate (Gorain, Harris et al. 1998). Knowing that small particles within a liquid environment follow the flow, small particles are thought to have a froth retention time equal to the average retention time within the froth. It is also known that larger particles have a more difficult time traveling upward in the froth (Bikerman 1973). It is

proposed that certain particles take longer to travel through the froth due to their size and density. Knowing this, a froth retention time model is proposed

$$\tau_f\left(d_p\right)=\frac{h_f}{V_g}P_{fr} \qquad [12]$$

that is a function of particle size, d_p, and takes this into account by the addition of a froth particle effect, P_{fr}.

The particle effect on the retention time is given the functional form

$$P_{fr}=\exp\left(B\frac{d_p}{d_{p-n}}\right) \qquad [13]$$

where B is a constant and $d_{p\text{-}n}$ is the particle diameter that, when attached to a given bubble size, the bubble-particle aggregate has a neutral buoyancy. The neutrally buoyant particle, $d_{p\text{-}n}$, affecting Equation [13] is used to take into account the buoyancy of the bubble with an attached particle. Smaller or less dense particles allow the bubble to travel upward within the froth more quickly. The smaller a given particle is compared to the neutrally buoyant particle size, the closer the particle effect is to 1. Therefore, the closer the particle is to following the fluid (or bubble) flow the closer the particle retention time is to the average retention time within the froth. The larger or more dense the particle is compared to the neutrally buoyant particle, the greater the particle effect becomes. Large particles will take longer to travel through the froth, if they travel through the froth at all. Particle effect, using this functional form, must always be greater than 1 and therefore, particle froth retention time must always be equal to or greater than the average froth retention time. B is thought to be a function of frother type and cell-dynamics and is found empirically for each system.

Experimental

Sample

Model verification was carried out by continuous flotation experiments. These experiments were performed using samples obtained from Potters Industries Inc. The samples were Ballotini impact beads which are ground soda-lime glass used in sandblasting. These were already sized and at least 80% spherical. Three different sizes were obtained: 40x70 mesh (Potters spec AA), 70x140 mesh (Potters spec AD), and 170x325 mesh (Potters spec AH). No preparation of the sample was required, beyond what the experimental procedure entails.

To measure contact angle of the particles, a flat surface was desired. A representative portion of the glass particles was melted in an oven at 800ºC. These large glass pieces (approximately 12mm x 12mm) were then ground flat on two sides. One side was polished, eventually using a 2400 grit polishing cloth. Contact angles were easily measured using these polished surfaces.

Surfactants

Cetyl (hexadecyl) trimethyl ammonium bromide (C_{16}TAB) was used as a collector due to the wide Ph fluctuations it can encounter and still perform satisfactorily, as well as ease of use. This was obtained from Sigma-Aldrich. Polypropylene glycol with an average molecular weight of 425 (PPG-425) was used as a frother. This was also obtained from Sigma-Aldrich.

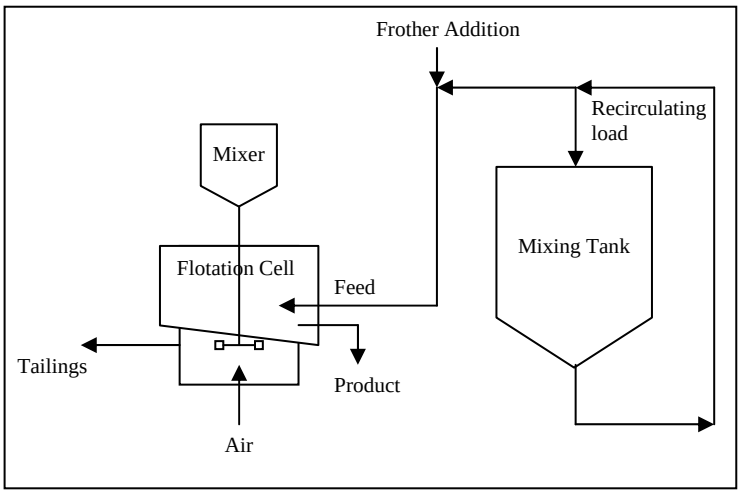

Figure 2. Flotation circuit schematic

Continuous Testing

Testing was run on a continuous flotation circuit. This produces steady-state conditions in which the flotation environment is not constantly changing and a flotation rate constant is not arbitrarily set, as in batch tests (De Bruyn and Modi 1956; Jowett and Safvi 1960; Mehrotra and Padmanabhan 1990). Continuous testing is both more difficult to setup and takes longer than batch testing to perform, but results in more representative and reproducible data. Batch testing data is difficult to collect because it must be collected in a short period of time, with steady state never being reached. This brings into question what conditions are affecting the batch flotation tests. Rate constants are constantly changing, while some believe that the flotation rate order may also change (Brown and Smith 1953-54). This is not the case with a continuous flotation circuit.

Experimental Setup

A diagram of the flotation circuit is shown in Figure 2. All feed to the flotation cell comes from the mixing tank. The contents of the mixing tank are recirculated from the bottom of the tank to the top. The combination of the mixer, within the tank, and the recirculating load provides a well mixed environment in the mixing tank. This allows ideal conditioning, where collector adsorption on particles is as equal as possible, as well as constant feed grade to the flotation cell. A constant feed grade is needed to reach steady state in the continuous cell. The contact angle samples are also placed within the conditioning tank so that they are conditioned along with the sample being tested. They were held in the mixing tank within a perforated plexiglass container which was retrieved after each flotation test was complete.

Feed is pumped out of the recirculating load using a variable speed Masterflex peristaltic pump. This rate is approximately 1.33 L/min, which gives an average residence time (before the introduction of air) within the 2L cell of 1.5 minutes. Before the feed enters the cell, frother is introduced to obtain a dosage of 10ppm.

The flotation cell is modeled after the Rushton flotation cell (Rushton, Costich et al. 1950; Deglon, O'Connor et al. 1997; Armenante, Mazzarotta et al. 1999; Jenne and Reuss 1999) as shown in Figure 3, where $H/D = 1$, $d/D = 1/3$, and $w/D = 1/10$. The height of the impeller off the bottom of the cell, h, was set at 4mm for these tests. The h/D ratio in a typical Rushton cell

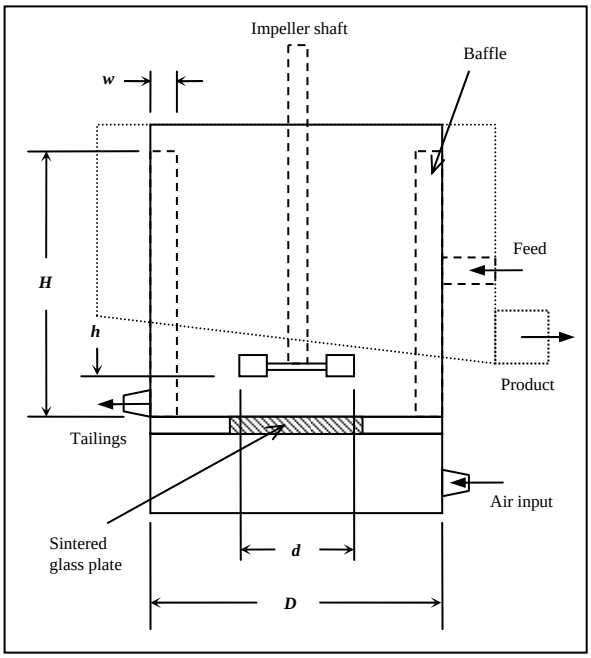

Figure 3. Flotation cell dimensions.

is 1/2, however *h* needed to be smaller than in a typical Rushton cell for the impeller to create small bubbles, from the air coming through the sintered plate, as well as mix large particles, which settle on the bottom of the cell. The height of the impeller still provided excellent mixing as shown by a dye tracer. Four baffles were evenly spaced within the cell, at a height 0.5 inches above the slurry level. A Rushton impeller was used with a diameter of 2.0 inches, which is slightly larger than the desired *d* diameter of 1.83 inches given from the above ratios. The actual dimensions of the flotation cell are as follows; D = 5.5 inches, H = 6.0 inches, d = 2.0 inches, w = 0.55 inches, h = 0.16 inches. H given here is the height of the baffles, while the liquid was kept below this height.

Feed entered the flotation cell mid-way up one side. On the opposite side, tailings were pumped from the bottom of the cell with a variable speed peristaltic pump. The pump speed was adjusted so that froth height was minimized and constant. Air was introduced through the bottom of the cell using compressed gas and a flow meter. All tests were kept at the same constant air rate. Air entered a chamber below the cell which was connected to the main cell by a plexiglass partition which contained a sintered glass plate. The sintered glass plate (porosity C) was obtained from Ace Glass. Air flowed through the plate and was broken up by the plate itself and the action of the impeller situated directly over top of the plate. Mixing within the cell was accomplished by a Lightnin Labmaster L1U10F mixer using a R100 Rushton impeller.

Sampling positions were located as shown in Figure 4 for the feed, product, and tailings. The feed sample was situated where there was a direct drop in the material so that a flow diverter was not needed. Any diversion of a contained flow might cause pressure differences which would lead to different flow rates. The design of the system accommodated this so that correct rates could be measured for the feed as well as the tailings and product. The product was measured at the output of the launder around the cell, which collected the freely overflowing product from the cell. Tailings were collected at the output of the tailings pump.

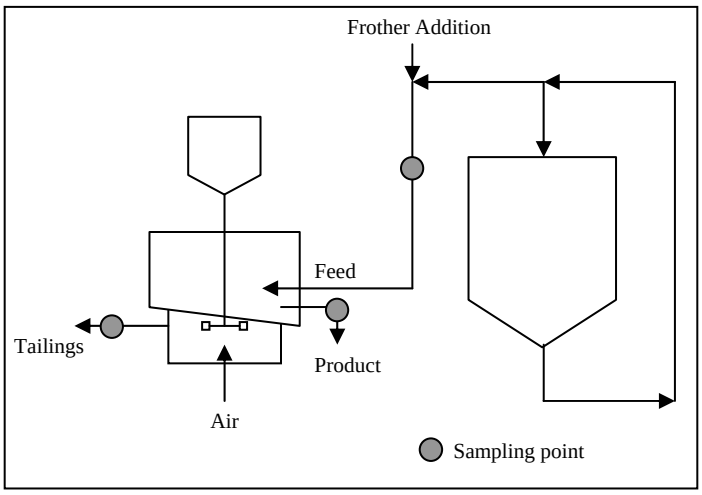

Figure 4. Sampling points around flotation cell.

Experimental Procedure

All samples were reused for subsequent tests so that particle size, as well as particle surface chemistry did not drastically change between tests. This required the cleaning of samples between tests. All glass samples were placed in an H_2SO_4 bath overnight. The acid was then drained using a glass fiber filter and rinsed three times. The sample was then placed in a bucket and filled with water to dilute any leftover acid. The bucket was then drained, making sure particles had settled to the bottom, and the process was repeated until a natural pH reading was obtained (usually 5 repetitions). The glass particles were then placed within the mixing tank and water was added until the correct percent solids (by volume) was reached.

Contact angle samples were rinsed with deionized water, after being cleaned in the acid bath, and a deionized water contact angle was measured to determine if all samples were properly cleaned. The samples were then placed within a plexiglass holder which was subsequently placed within the mixing tank.

Once all samples were within the mixing tank, the mixer and recirculating pump were turned on. C_{16}TAB was then added, at the desired concentration, and left to condition for at least 10 minutes. When conditioning was complete, the feed and frother pump were turned on, airflow was set to the desired flow reading and the Lightnin mixer was turned on to the desired speed setting.

Once steady state was reached, all desired measurements were taken. Torque and rpm measurements, used to calculate energy input, were taken directly from the Lightnin mixer. A pressure differential reading, used for air holdup calculations, was taken between two points within the cell using a Comark C9553 pressure meter. Three full data sets were taken for each test.

Once the test was complete, the contact angle samples were removed from the mixing tank along with a representative sample of the solids and liquid from the tank, for zeta potential and contact angle measurements.

Table 1. Flotation test variables

Test #	Particle Category	Particle Size – approx. (mm)	Contact Angle - approx. (deg)	Impeller RPM	% Solids (by volume)
1	AA	300	25	1200	8.5
2	AD	140	25	1200	8.5
3	AH	65	25	1200	8.5
4	AA	300	33	1200	8.5
5	AD	140	33	1200	8.5
6	AH	65	33	1200	8.5
7	AA	300	40	1200	8.5
8	AD	140	40	1200	8.5
9	AH	65	40	1200	8.5
10	AA	300	33	900	8.5
11	AD	140	33	900	8.5
12	AH	65	33	900	8.5
13	AA	300	33	1500	8.5
14	AD	140	33	1500	8.5
15	AH	65	33	1500	8.5
16	AA	300	33	1200	5
17	AD	140	33	1200	5
18	AH	65	33	1200	5
19	AA	300	33	1200	12
20	AD	140	33	1200	12
21	AH	65	33	1200	12

Sample Analysis

Variables

The effects of 4 different variables were examined during these tests. These include particle size, contact angle, energy input, and feed concentration. A layout of the tests is shown in Table 1. Some tests were run twice due to variations in the measured and desired contact angles. A high, medium and low value for each variable was desired, with a medium baseline comparable for all tests.

Rate Constant

After mass balancing all flow rate data, the rate constant was determined. The typical formula used in flotation is

$$R = \frac{k\tau}{1 + k\tau} \qquad [14]$$

where R is recovery and τ is average retention time within the cell. This formula assumes perfect mixing and can be rewritten by substituting $R=Pp/Ff$ for the recovery.

$$k = \frac{Pp}{\tau(Ff - Pp)} \qquad [15]$$

P and F are the flow rates of the product and feed respectively while p and f are the grades of those flow rates. By assuming that steady state has been reached and substituting in the tailings mass flow rate (Tt), the rate constant is then given by Equation [16].

$$k = \frac{Pp}{\tau Tt} \qquad [16]$$

This formula is valid only for single input and single output processes. Within an industrial flotation process, the flow rate of the froth is much less than the tailings flow rate, and the above

Table 2. Experimental Data

Test #	Part. Size (μm)	Cont. Angle	Imp. RPM	Specific Energy Input (W/m3)	Feed % Solids (by Vol.)	Exp. Rate Constant (min^{-1})	Theo. Rate Constant (min^{-1})
1	294.8	21.7	1200	17615	4.1%	2.2E-3	1.2E-3
				14886	7.7%	1.1E-3	7.6E-3
				13211	7.7%	1.1E-3	3.4E-2
2	139.5	26.4	1200	13534	8.5%	3.0E-2	4.3E-1
				13762	9.3%	1.7E-2	4.2E-1
				13244	8.5%	1.5E-2	3.9E-1
3	63.5	26.8	1200	13980	9.4%	5.1E+0	3.6E+0
				13980	8.9%	3.8E+0	3.5E+0
				12582	9.1%	3.2E+0	1.7E+0
4	297.9	32.4	1200	16514	7.5%	6.5E-3	1.2E-3
				18997	6.9%	5.4E-4	8.6E-4
				22729	7.7%	9.3E-4	7.4E-4
5	140.2	34.3	1200	14591	9.1%	1.5E+0	3.5E+0
				13840	9.0%	1.4E+0	3.8E+0
				13907	8.3%	1.6E+0	4.4E+0
6-a	64.4	32.8	1200	16147	8.9%	3.8E+0	7.1E+0
				16147	9.2%	3.7E+0	7.5E+0
				13550	8.4%	3.7E+0	5.6E+0
6-b	66.4	33.9	1200	13980	8.1%	5.6E+0	8.6E+0
				13980	6.3%	5.4E+0	5.4E+0
				14679	5.9%	5.6E+0	7.9E+0
7-a	295.7	41.2	1200	15378	7.6%	1.0E-2	4.5E-2
				13840	7.1%	7.0E-3	1.9E-1
				15091	7.6%	9.0E-3	2.9E-2
7-b	294.1	50.3	1200	15626	6.8%	1.3E-1	1.0E-1
				15378	7.2%	9.5E-2	3.4E-2
				16147	7.0%	9.3E-2	4.1E-2
8	139.5	40.0	1200	15185	8.9%	4.4E+0	6.8E+0
				13762	8.4%	3.5E+0	4.6E+0
				13426	8.2%	3.2E+0	7.7E+0
9	66.9	38.0	1200	14679	3.4%	7.1E+0	1.7E+1
				16494	3.5%	6.6E+0	1.3E+1
				14928	4.2%	6.9E+0	1.3E+1
10	295.2	37.9	900	11513	6.9%	3.8E-2	1.8E-2
				9813	7.0%	2.3E-2	7.5E-2
				9496	7.1%	2.7E-2	1.7E-1
11	140.2	30.9	900	13294	9.0%	5.1E+0	5.2E+0
				13345	8.7%	3.9E+0	2.8E+0
				12952	8.5%	4.1E+0	3.9E+0
12	66.8	30.5	900	12045	8.4%	7.8E+0	5.7E+0
				12233	7.1%	7.4E+0	5.2E+0
				11627	6.9%	5.8E+0	2.4E+0
13	295.6	39.6	1500	20301	7.3%	3.2E-2	7.1E-3
				20446	7.4%	2.8E-2	5.1E-3
				20668	7.4%	2.8E-2	5.5E-3
14	140.5	32.8	1500	18922	9.4%	2.3E+0	2.8E+0
				17400	9.2%	2.0E+0	1.9E+0
				17809	8.9%	1.7E+0	2.5E+0
15	65.2	31.1	1500	16235	8.6%	4.1E+0	3.9E+0
				14547	7.6%	3.4E+0	2.0E+0
				14769	7.3%	4.2E+0	4.1E+0
16	296.5	43.5	1200	15882	3.7%	5.0E-2	1.7E-2
				14547	4.2%	2.2E-2	7.9E-2
				16533	4.4%	2.4E-2	1.7E-2
17	140.2	39.5	1200	14728	4.9%	4.6E+0	5.9E+0
				14206	4.8%	3.0E+0	4.5E+0
				13892	4.7%	3.5E+0	7.6E+0
18	67.2	32.6	1200	15869	5.0%	6.0E+0	6.7E+0
				15056	4.1%	4.7E+0	6.7E+0
				14534	3.8%	4.8E+0	6.7E+0
19-a	296.1	47.5	1200	13392	12.0%	8.4E-2	2.1E+0
				12024	10.6%	8.0E-2	2.4E+0
				13534	10.1%	5.1E-2	2.3E+0
19-b	293.1	46.7	1200	13696	10.7%	2.2E-2	1.7E+0
				12176	10.4%	3.2E-2	3.3E+0
				13729	9.9%	1.8E-2	5.2E+0
20-a	139.5	33.9	1200	12050	13.3%	1.5E+0	3.4E+0
				12050	11.4%	1.3E+0	4.1E+0
				12485	11.2%	1.4E+0	3.6E+0
20-b	138.8	35.3	1200	16421	12.6%	3.8E+0	5.9E+0
				15728	11.4%	5.0E+0	3.4E+0
				15378	10.4%	5.4E+0	3.5E+0
21	62.6	37.9	1200	17941	13.3%	6.0E+0	1.1E+1
				17941	11.8%	3.9E+0	5.0E+0
				18454	11.5%	3.9E+0	6.6E+0

equation is relatively accurate. Within these flotation experiments, the froth rate is relatively much higher than in industrial flotation practices. The process is actually one input stream with two output streams. Equation [16] is not valid for the current process. A more accurate way of determining the rate constant is to take the mass rate of particle flotation (*Pp*) divided by the mass of that particle within the flotation cell (*Vv*) (Schuhmann 1942; Feteris 1987). If the cell is assumed to be perfectly mixed, the particle concentration within the cell is equal to the particle concentration within the tailings. The rate constant then becomes

$$k = \frac{Pp}{Vv} = \frac{Pp}{Vt} = \frac{Pp}{\tau Ft} \qquad [17]$$

As can be seen, the only difference between Equation [16] and [17] are the flow rates *T* and *F*. If a single output stream at steady state is assumed, Equation [17] reduces to [16]. Since this is not the case for these experiments, the more general form of the equation ([17]) is being used. Rate constants are shown in Table 2.

Air Fraction

Air fraction was determined from the difference between the two pressure differential readings taken during the flotation tests. One reading was obtained with air in the system, while the other was taken without. Knowing the percent solids (*%S*) within the cell (before the addition of air), as well as the densities of the solid (ρ_1), liquid (ρ_3) and air (ρ_2), the air fraction (*%A*) can be calculated using Equation [18].

$$\%A = \frac{\Delta P_A - \Delta P_S}{gh\rho_2\left(\rho_1 \%S + \rho_3\left(1 - \%S\right)\right)} \qquad [18]$$

The percent solids within the cell was assumed to be the tailings percent solids. If the cell is perfectly mixed, the tailings concentration is equal to the cell concentration.

Surface Tension

Surface tension was determined with a KSV Sigma 70 tensiometer using the Du Nouy ring method. Since surface tension is temperature sensitive, the liquid samples were stored in a refrigerator until a measurement could be performed. They were then taken from the refrigerator and allowed to reach their corresponding experimental temperature. A 25 mL sample was placed within a plastic container which was positioned within the machine. C_{16}TAB is surface active on the liquid-vapor interface and therefore affects surface tension. C_{16}TAB also adheres to glass. To keep the amount of C_{16}TAB in solution constant throughout the test and therefore have a constant surface tension, a plastic container was used.

Contact Angle

Contact angle measurements were performed using a Rame-Hart Model 100 goniometer which employs the sessile drop method. The glass samples were rinsed to clear particles from the surface, dried with nitrogen and then placed upon the viewing stage. A sample of the liquid from the mixing tank was used to determine the contact angle. The average of, at least, 5 measurements were obtained for each glass particle. Three glass particles were used per flotation test. All three glass particle values were then averaged together to get one contact angle per test. The average contact angle values can be found in Table 2.

Zeta Potential

The zeta potential of the particles were measured using a Lazer Zee model 501 zeta potential meter. A representative sample from the mixing tank was set within an ultrasonic bath for 10 minutes to break up any particle aggregates. The sample container was then shaken up, let to sit for one minute so that large particles would settle, and a sample was taken near the top of the container. This procedure reduced the particle size being measured, which results in a better measurement from this zeta potential meter. The sample was then measured at least 5 times, with the voltage being applied for, at most, 2 seconds per measurement. This reduced the amount of sample heating which leads to false measurements. One sample was used per test.

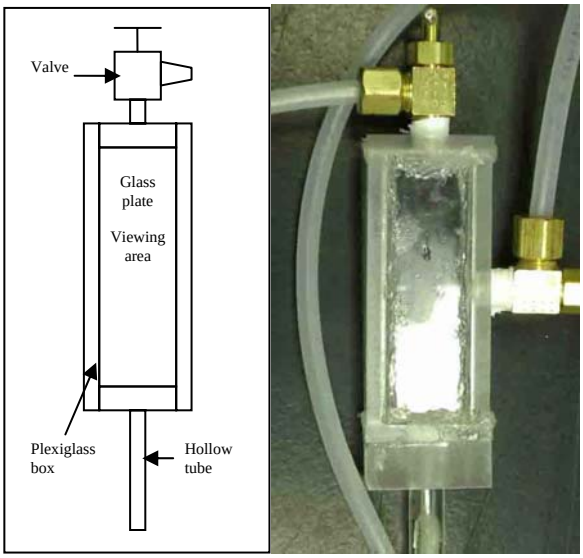

Figure 5. Bubble sampling device.

Particle Size

Particle size is very important for model prediction as well as data representation. This measurement was taken using a Microtrac X100 which employs a laser diffraction analysis and light scattering technique. This technique gives a very reliable measurement for spherical particles and the analyzer measures well within the tested particles' size range.

The sauter mean size was the desired output from this machine. The particle measuring program could not do this automatically, so a number distribution of particle sizes was measured per sample. The number distribution was then converted into the sauter mean size.

The sauter mean size is the particle size that has the same surface area to volume ratio as the entire sample's surface area to volume ratio. This is commonly used in fluid dynamic modeling as well as froth modeling. The sauter particle size for each test can be found in Table 2.

Bubble Size

A representative bubble size was determined for the frother dosage used (10ppm), as well as sintered plate porosity, impeller type and diameter, and air flow rate. This was found by running the flotation setup in exactly the same way as it was in the flotation tests, with the exception of particles. This data was not recorded during the flotation tests because of the time consumed in taking the measurements as well as the fact that particles would have blocked the measuring device. The long time of this test would have resulted in the sample being exhausted mid-way through the bubble size test. A pure water test, with only the addition of frother, could be run continuously, with out a mixing tank. For these reasons, it was thought best to run these tests without particles so that a more reproducible as well as feasible experiment could be performed. The bubble size determined in this test is assumed to be the bubble size within the flotation tests, although it is known that particles can affect the formation of bubbles and therefore bubble size.

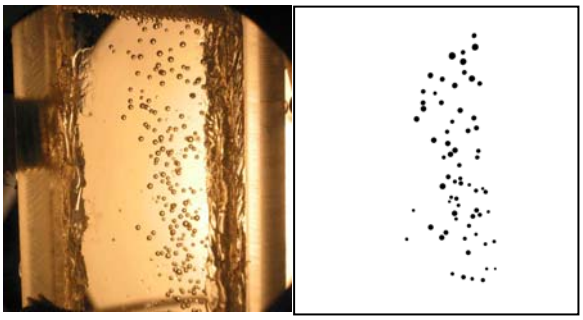

Figure 6. Original and modified bubble pictures.

Once steady state was reached, a sampling device (Figure 5) was lowered into the flotation cell. The device is comprised of two glass plates held in place by a plexiglass box. This provides bubble and liquid containment as well as a viewing area for the bubbles. A hollow plexiglass tube is attached to one end of the box while the other end has a valve. When the valve is opened, and at the bottom of the device, water can be introduced, through the valve end, until water completely fills the device. The valve can then be closed, the device inverted, and the tube can be inserted into the flotation cell. The sealed, liquid-filled container allows bubbles to travel upward, through the plexiglass tubing into the glass-plate viewing area. Pressure measuring positions were made available in the middle of the viewing area and at the bottom of the hollow tube.

Following this procedure, to view bubbles within the flotation cell, digital pictures were taken of those bubbles so that a size analysis could be performed. These digital pictures were imported into Photoshop where they were manipulated into black and white clearly discernible

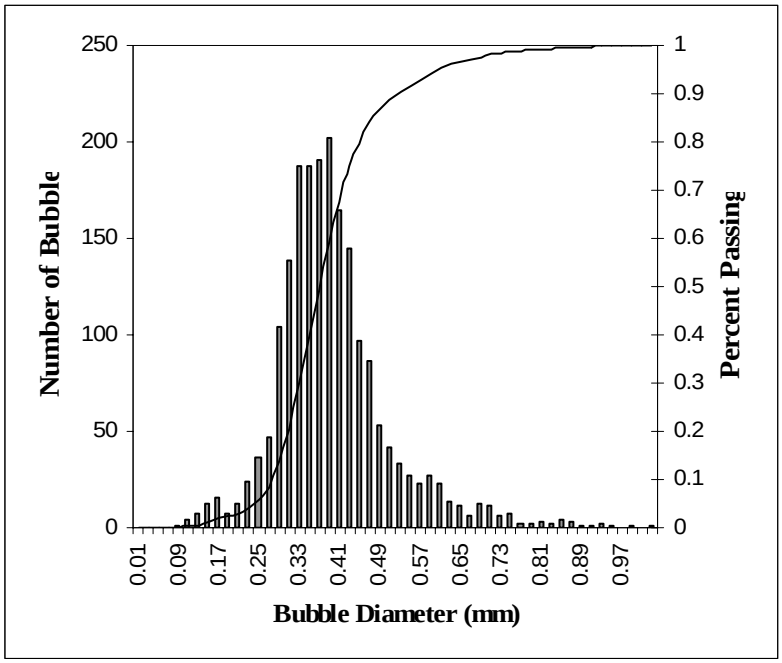

Figure 7. Bubble size population distribution with a Sauter mean size of 467.4 microns

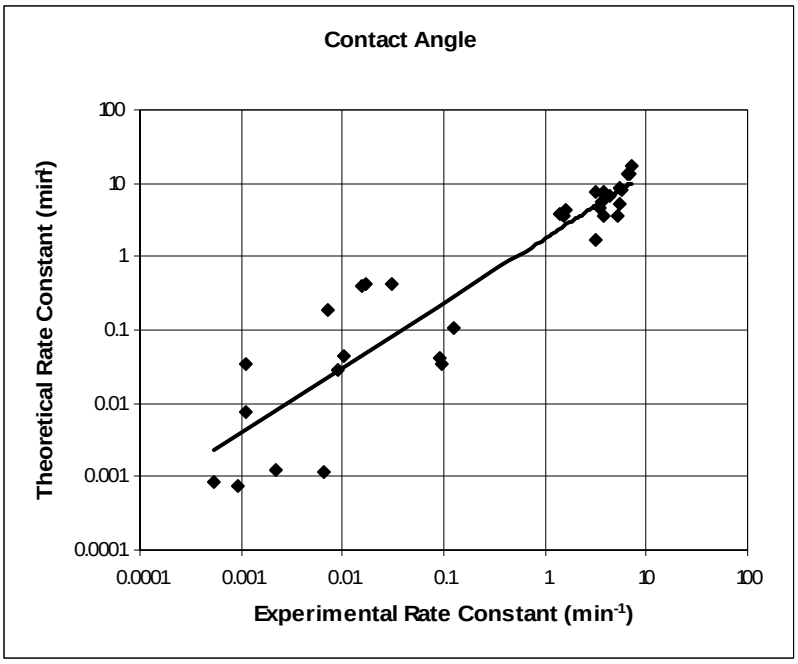

Figure 8. Relationship between experimental and theoretical rate constants with variations in contact angle.

bubble images. An example of this is shown in Figure 6. Bubbles that were indistinct or overlapping were deleted from the picture.

After the clear bubble images were prepared, they were imported into a Matlab program which determined the size of each bubble. Knowing the size of each bubble, under those operating conditions, the sauter size was determined. A graphical representation of the population distribution of the bubble size is shown in Figure 7.

The pressure differential between the inlet of the tube and the viewing area was also recorded. This gives the pressure difference between the measuring area, where the bubble size is now known, and within the cell, where the actual bubble size is desired. The pressure difference was found to be negligible and did not affect the bubble size.

Results

Once all parameters for the model were determined, the rate constants were calculated using Equation [2] and can be found in Table 2. A fit was done for the variable *B* in the froth recovery section of the model. *B* is 4.7 for this machine and frother type. The relationship between experimental and theoretical rate constants is shown in Figure 8 through Figure 11.

Figure 8 shows the relationship between the experimental and theoretical rate constants with variations in contact angle. Overall there is good agreement between the two. As can be seen, as contact angle increases (corresponding to high rate constants) there is excellent agreement between experimental and theoretical rate constants. With lower rate constants, and therefore lower contact angles, more scattering of the data is apparent. This shows the sensitivity of the rate constant to contact angle. With slight variations between measured and actual contact angles, great differences are seen in values of rate constants. These variations may be due to incomplete collector adsorption due to conditioning time or mixing as well as errors in measurement. It should be noted that other input variables will have errors which may cause

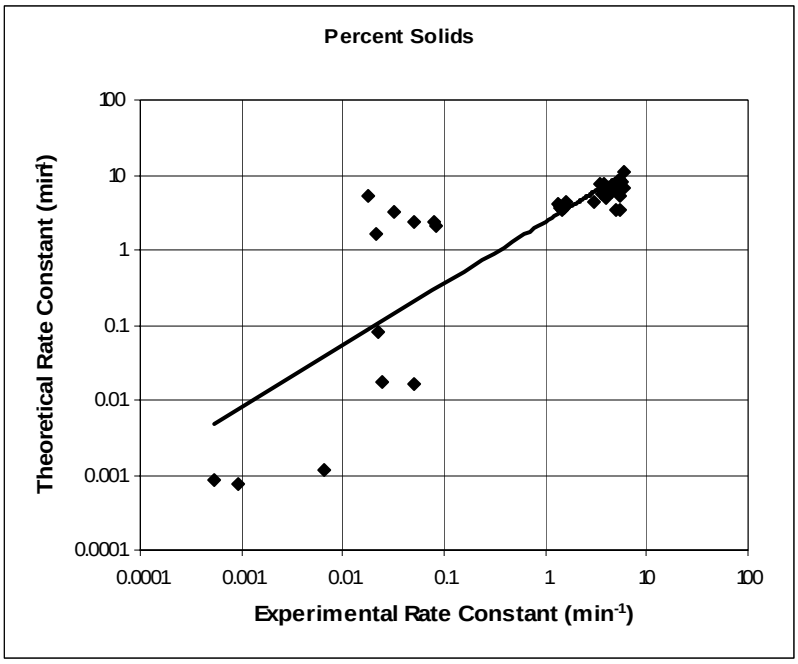

Figure 9. Relationship between experimental and theoretical rate constants with variations in percent solids. Entire data set.

and/or add to this scattering. These errors may only become apparent at low contact angles when particle detachment, in the slurry or froth, becomes an issue. This shows the great importance of reliable input data as well as constant steady state conditions. It was noted that there were fluctuations within the system, while experiments were run, mostly within percent solids. Fluctuations may also have been present for contact angles. The experimental procedure

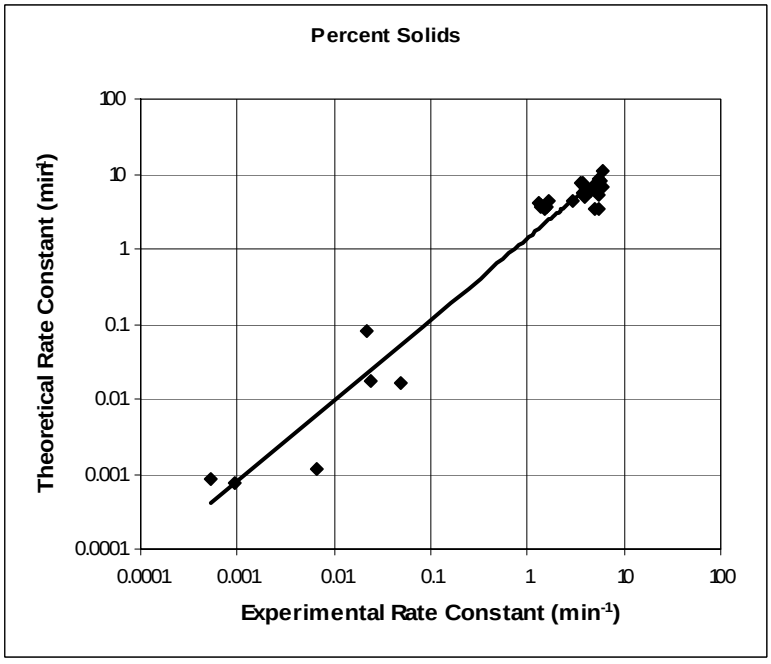

Figure 10. Relationship between experimental and theoretical rate constants with variations in percent solids. Excluding large particle – high percent solids data set.

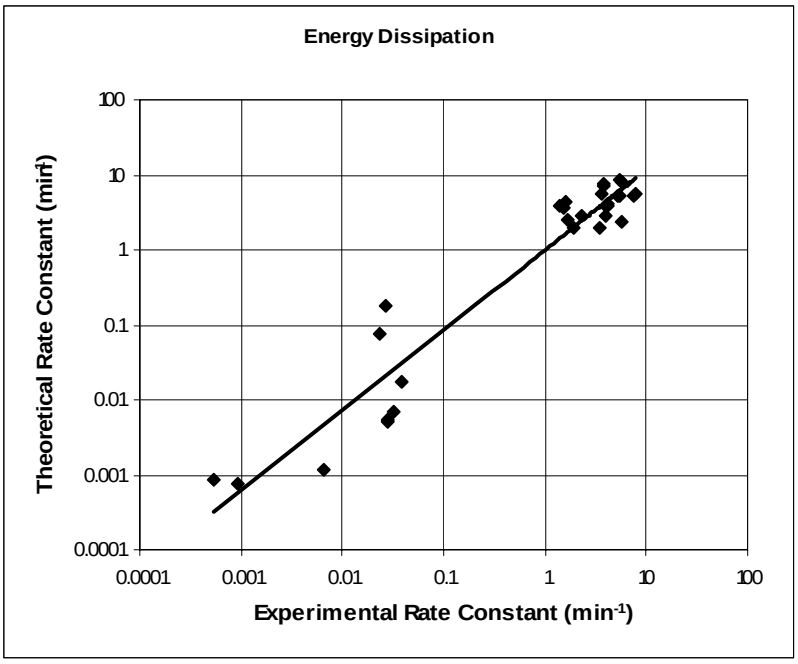

Figure 11. Relationship between experimental and theoretical rate constants with variations in energy dissipation.

available for measuring contact angle would not have perceived these fluctuations.

The effect of percent solids can be seen in Figure 9 and Figure 10. Figure 9 shows wide variations between theoretical and experimental rate constants. This is mostly due to 2 data sets; 19-a and 19-b from Table 2. These data sets are the high percent solids, large particle size tests. Two full tests were run for test number 19 because the particles were difficult to keep in suspension. With this particle size and percent solids, the mixing action of the impeller was inadequate. This is the reason for the discrepancy between the experimental and theoretical rate constants. The model predictions are based upon the assumption that there is complete mixing. Other effects may become noticeable when mixing is not adequate.

Knowing that there was error in these 2 tests, they were removed from the analysis. This is shown in Figure 10, which displays excellent agreement between theoretical and experimental rate constants. Knowing that removal of incomplete mixing data resulted in agreement between experiment and theory tells a great deal about the assumption of mixing for model use. Adequate mixing must be present for the model to predict rate constants accurately.

Figure 11 shows the relationship between theoretical and experimental rate constants while energy input was varied. The energy was varied by increasing or reducing the speed of the mixer within the flotation cell. Overall there is good agreement between the experimental and theoretical values.

Overall, there is good agreement between the experimental and theoretical data, although there are fluctuations within data sets. This is mostly due to errors in measuring input data. Reliable input data is seen to be a problem in these tests, with errors compounding due to the many variables measured. For the model to be useful in real world applications many data sets must be taken, to average out this error, or very reliable input data must be obtained.

Conclusions

A first order turbulent flotation rate equation has been proposed and verified experimentally. The rate model encompasses both hydrodynamic and surface force effects, which are incorporated into the collision frequency, probability of attachment, probability of detachment, and froth recovery sections of the model. The model is semi-empirical in nature due to the inclusion of the froth recovery. No froth recovery model has been proposed that is purely theoretical, so a well known and reliable empirical model has been incorporated into the present rate model.

Experimental verification has been performed with good results. Model calculations are similar to experimental data. A result of the rate calculations was the understanding that input data must be very reliable to use this model. Also, adequate mixing must be observed for the model to be reliable. With this knowledge, the current rate equation can be used to predict output from an industrial flotation process. The model can be very helpful in the optimization of plant performance and flotation equipment design.

Nomenclature

%A	air fraction [-]
%S	percent solids without air - by vol. [-]
1	subscript – refers to particle
2	subscript – refers to bubble
3	subscript – refers to liquid
B	constant [-]
d_{12}	diameter of collision [m]
d_p	diameter of particle [m]
d_{p-n}	diameter of neutrally buoyant particle [m]
E_1	surface energy barrier [J]
E_{k-A}	kinetic energy of attachment [J]
E_{k-D}	kinetic energy of detachment [J]
F	feed flow rate [$m^3 \cdot s^{-1}$]
f	feed grade [-]
g	gravity [$m \cdot s^{-2}$]
h	distance between pressure readings [m]
h_f	froth height [m]
k	rate constant [min^{-1}]
m_i	mass of particle or bubble [kg]
N_i	number density of i – number per unit volume [m^{-3}]
P	product flow rate [$m^3 \cdot s^{-1}$]
p	product grade [-]
P_A	probability of attachment [-]
P_D	probability of detachment [-]
P_{fr}	particle effect – retention time [-]
R	recovery [-]
r_{2-0}	radius of bubble – slurry-froth interface [m]
r_{2-f}	radius of bubble – top of froth [m]

Re_b	Reynolds number of bubble [-]
R_F	froth recovery factor [-]
r_i	radius of subscript i [m]
S_0	surface area rate – slurry-froth interface [s^{-1}]
S_b	surface area rate – within slurry [s^{-1}]
S_f	surface area rate – top of froth [s^{-1}]
T	tailings flow rate [$m^3 \cdot s^{-1}$]
t	tailings grade [-]
$U^2_{T\text{-}A}$	attachment turbulent kinetic energy [$m^2 \cdot s^{-2}$]
$U^2_{T\text{-}D}$	detachment turbulent kinetic energy [$m^2 \cdot s^{-2}$]
$\sqrt{\overline{U_i}^2}$	root-mean-squared velocity of i – turbulent velocity [$m \cdot s^{-1}$]
V	effective volume of cell [m^3]
v	grade within cell [-]
V_g	superficial air flow rate [$m \cdot s^{-1}$]
W_A	work of adhesion [J]
Z_{12}	collision frequency between particle and bubble [$m^{-3} \cdot s^{-1}$]
α	froth recovery parameter [s^{-1}]
β	collision kernel [$m^3 \cdot s^{-1}$]
γ_{lv}	liquid-vapor surface tension [$N \cdot m^{-1}$]
ΔP_A	pressure differential – with air [Pa]
ΔP_S	pressure differential – without air [Pa]
θ	contact angle [rad] – measured through liquid
ρ_i	density of i [$kg \cdot m^{-3}$]
τ	average retention time [s]
τ_f	froth retention time [s]

References

Abrahamson, J. (1975). "Collision rates of small particles in a vigorously turbulent fluid." Chemical Engineering Science **30**(11): 1371-9.

Arbiter, N. and C. C. Harris (1962). Flotation Kinetics. Froth flotation - 50th anniversary volume. D. W. Fuerstenau, American Institute of Mining, Metallurgical, and Petroleum Engineers.

Armenante, P. M., B. Mazzarotta, et al. (1999). "Power Consumption in Stirred Tanks Provided with Multiple Pitched-Blade Turbines." Industrial & Engineering Chemistry Research **38**(7): 2809-2816.

Aveyard, R., B. P. Binks, et al. (1999). "Foams and emulsions. Their stability and breakdown by solid particles and liquid droplets. The colloid chemistry of a dog's breakfast." NATO ASI Series, Series E: Applied Sciences **354**(Foams and Emulsions): 21-44.

Bikerman, J. J. (1973). Applied Physics and Engineering, No. 10: Foams. [Physicochemical Aspects].

Brown, D. J. and H. G. Smith (1953-54). "The flotation of coal as a rate process." Transactions - the Insitution of Mining Engineers **113**: 1001-1020.

Buurman, C. (1990). "Stirring of concentrated slurries: a semi-empirical model for complete suspension at high solids concentrations and 5 m3 verification experiments." Institution of Chemical Engineers Symposium Series - Fluid Mixing 4 **121**: 343-350.

Chahine, G. L. (1995). Bubble interactions with vortices. Fluid Vortices. S. I. Green.

Crowe, C. T. and T. R. Trout (1995). Particle interactions with vortices. Fluid Vortices. S. I. Green.

De Bruyn, P. L. and H. J. Modi (1956). "Particle size and flotation rate of quartz." Transactions of the American Institute of Mining, Metallurgical and Petroleum Engineers **205**(Tech. Publ. 4210-B).

Deglon, D. A., C. T. O'Connor, et al. (1997). "Efficacy of a spinning disk as a bubble break-up devices." Chemical Engineering Science **53**(1): 59-70.

Feteris, S. M. F., J.A.; Jowett, A. (1987). "Modelling the effect of froth detph in flotation." International Journal of Mineral Processing **20**: 121-135.

Gorain, B. K., M. C. Harris, et al. (1998). "The effect of froth residence time on the kinetics of flotation." Minerals Engineering **11**(7): 627-638.

Harris, P. J. (1982). Frothing phenomena and frothers. Principles of Flotation. R. P. King. Johannesburg, South African Institute of Mining and Metallurgy**:** 237-251.

Jenne, M. and M. Reuss (1999). "A critical assessment on the use of k-e turbulence models for simulation of the turbulent liquid flow induced by a Rushton-turbine in baffled stirred-tank reactors." Chemical Engineering Science **54**(17): 3921-3941.

Johansson, G. and R. J. Pugh (1992). "The influence of particle size and hydrophobicity on the stability of mineralized froths." International Journal of Mineral Processing **34**(1-2): 1-21.

Jowett, A. and S. M. M. Safvi (1960). "Refinements in methods of determining flotation rates." Transactions of the American Institute of Mining, Metallurgical and Petroleum Engineers **217**(Tech. Publ. 59B244): 351-7.

Kelsall, D. F. (1961). "Application of probability in the assessment of flotation systems." Bull. Instn. Min. Metall. **650**: 191-204.

Knapp, J. M. S. (1990). A study of flotation froth behavior. Mining and Minerals Engineering, Virginia Polytechnic Institute and State University.

Kruis, F. E. and K. A. Kusters (1997). "The collision rate of particles in turbulent flow." Chemical Engineering Communications **158**: 201-230.

Lee, C. H., L. E. Erickson, et al. (1987). "Bubble breakup and coalescence in turbulent gas-liquid dispersions." Chemical Engineering Communications **59**(1-6): 65-84.

Liepe, F. and H. O. Moeckel (1976). "Studies of the combination of substances in liquid phase. Part 6: The influence of the turbulence on the mass transfer of suspended particles." Chemische Technik (Leipzig, Germany) **28**(4): 205-209.

Mao, L. and R.-H. Yoon (1997). "Predicting flotation rates using a rate equation derived from first principles." International Journal of Mineral Processing **51**(1-4): 171-181.

Mathe, Z. T., M. C. Harris, et al. (1998). "Review of froth modeling in steady state flotation systems." Minerals Engineering **11**(5): 397-421.

Mehrotra, S. P. and N. P. H. Padmanabhan (1990). "Flotation kinetics - a review." Transactions of the Indian Institute of Metals **43**(1): 9-21.

Pazhianur, R. (1999). Hydrophobic force in flotation, Virginia Polytechnic Institute and State University.

Preuss, M. and H.-J. Butt (1998). "Measuring the contact angle of individual colloidal particles." Journal of Colloid and Interface Science **208**(2): 468-477.
Rabinovich, Y. I. and N. V. Churaev (1979). "Effect of electromagnetic delay on the forces of molecular attraction." Kolloidnyi Zhurnal **41**(3): 468-74.
Rabinovich, Y. I. and R. H. Yoon (1994). "Use of atomic force microscope for the measurements of hydrophobic forces." Colloids and Surfaces, A: Physicochemical and Engineering Aspects **93**: 263-73.
Rushton, J. H., E. W. Costich, et al. (1950). "Power characteristics of mixing impellers. I." Chem. Eng. Progress **46**: 395-404.
Schuhmann, R. J. (1942). "Flotation Kinetics: I. Methods for steady state study of flotation problems." Journal of Physical Chemistry **46**: 891-902.
Shaw, D. J. (1992). Introduction to colloid and surface chemistry. Boston, Butterworth-Heinemann.
Sherrell, I. M. and R. H. Yoon (To be submitted - summer 2004). "Developing a turbulent flotation model from first principles." Journal of Colloid and Interface Science.
Sundaram, S. and L. R. Collins (1997). "Collision statistics in an isotropic particle-laden turbulent suspension. Part 1. Direct numerical simulations." Journal of Fluid Mechanics **335**: 75-109.
Vivek, S. (1998). Effects of long-chain surfactants, short-chain alcohols and hydrolysable cations on the hydrophobic and hydration forces, Virginia Polytechnic Institute and State University.
Wang, S. K., S. J. Lee, et al. (1990). "Statistical analysis of turbulent two-phase pipe flow." Journal of Fluids Engineering **112**(1): 89-95.
Williams, J. J. E. and R. I. Crane (1983). "Particle collision rate in turbulent flow." International Journal of Multiphase Flow **9**(4): 421-35.
Yoon, R. H. (2000). "The role of hydrodynamic and surface forces in bubble-particle interaction." International Journal of Mineral Processing **58**(1-4): 129-143.
Yoon, R. H. and S. B. Aksoy (1999). "Hydrophobic forces in thin water films stabilized by dodecylammonium chloride." Journal of Colloid and Interface Science **211**(1): 1-10.
Yoon, R.-H., D. H. Flinn, et al. (1997). "Hydrophobic interactions between dissimilar surfaces." Journal of Colloid and Interface Science **185**(2): 363-370.
Yoon, R.-H. and L. Mao (1996). "Application of extended DLVO theory, IV. Derivation of flotation rate equation from first principles." Journal of Colloid and Interface Science **181**(2): 613-626.
Yoon, R.-H. and S. A. Ravishankar (1994). "Application of extended DLVO theory III. Effect of octanol on the long-range hydrophobic forces between dodecylamine-coated mica surfaces." Journal of Colloid and Interface Science **166**(1): 215-24.
Yoon, R.-H. and S. A. Ravishankar (1996). "Long-range hydrophobic forces between mica surfaces in alkaline dodecylammonium chloride solutions." Journal of Colloid and Interface Science **179**(2): 403-411.

Summary

The primary objective of this research was to derive a generic turbulent flotation model based as much as possible upon first principles. This was accomplished by incorporating models of the collision frequency, probability of attachment, probability of detachment, and froth recovery into one model for the rate constant of the entire flotation process.

Collision frequency - The collision frequency model used is typical to other flotation models in existence. It assumes a Stokes number of infinity, which is not true in flotation for either particles or bubbles, but has been shown to be close to real world situations for much lower Stokes numbers. This was based upon numerical simulations performed by previous researchers.

A review of the collision frequency models relating to flotation, existing in the literature to date, was also given. The most relevant, current model available for flotation was presented with all applicable assumptions. An area that has not been studied within the fluid mechanics profession was pointed out. This included the collision of particles and bubbles within a liquid environment. No present model can account for the differing densities between these three phases.

Probability of attachment - The probability of attachment related the surface forces of interaction, based upon the extended DLVO theory, to the turbulent energy of attachment. The energy of attachment was assumed to be that of an average vortex between the kolmogorov microscale and the particle/bubble scale.

Probability of detachment – The probability of detachment relates the work of adhesion to the maximum turbulent energy available within the system for detachment. The work of adhesion was calculated by the thermodynamic change in energy based upon the change in area between the final and initial conditions of detachment and the respective surface tensions of those areas. The maximum scale for the detachment turbulent energy was given as the impeller size with the detachment energy equal to the turbulent energy at this scale.

Froth recovery - Once the particle has intersected the froth, there is a certain probability that the particle will travel through the froth and exit into the product as

opposed to re-entering the slurry or never truly entering the froth. A form of a well known empirical model was used for this probability which is a function of average residence time within the froth. A function of the particle residence time was proposed as well as a maximum froth recovery.

The flotation model was verified by experiments performed in an idealized flotation cell. The cell was based upon a typical Rushton flotation cell with slight modifications to dimensional ratios due to mixing effects. Ground silica particles were floated using cetyl trimethyl ammonium bromide as the collector and polypropylene glycol (M_N = 425) as the frother. Once the froth recovery parameter was fit to the experimental data, there was good agreement between the theoretical and experimental rate constants across the entire range of variables tested, which includes particle diameter, contact angle, percent solids, and energy input.

Theoretical trends were predicted using the derived flotation rate equation. The effects of particle size, bubble size, energy input, contact angle, and liquid-vapor surface tension were shown. Trends and values predicted by the model were similar to those seen in industrial situations. This shows the usefulness of the model with control and prediction capabilities for running industrial processes as well as the design of those processes.

Recommendations for Future Work

Based upon the knowledge gained from this investigation, the following are considered excellent areas for further research.

(1) **Froth recovery (particle froth residence time)** – The development of a non-empirical froth recovery model will greatly benefit the proposed flotation equation. The current equation is empirical with no theoretical basis. Also, the one parameter that must be fit in the current flotation equation is included within the froth recovery model. This parameter is used to calculate the particle residence time within the forth. When this parameter can be replaced by known input variables and a theoretical froth recovery model can be derived, a truly universal slurry and froth flotation model will be available. The current model is only universal within the slurry.

(2) **Collision frequencies of particles and bubbles** – The derivation of a collision frequency that can account for particles and bubbles is needed for future flotation models. Currently, only two phases are accounted for in collision frequencies. This is not the case in flotation, where three phases are encountered. The effect of all three phases on the collision frequency must be accounted for, as well as the full range of Stokes numbers encountered in flotation.

(3) **Combined effect of particles and bubbles on turbulence** – The individual effects of particles and bubbles on the turbulent energy spectrum have been previously predicted and verified. The combined effect of two phases on a third has not. Since a similar relationship exists between air and water and solid and water, the assumption was made that the combined air-solid effects on water are equal. This may not be the case. Further research into this will verify or disprove this assumption.

(4) **Attachment and detachment energies** – The proposed attachment and detachment energies are based upon the turbulent energy spectrum and what that spectrum can affect. Although the scales given can affect the particles and bubbles, the exact magnitude of the energy imparted to them might vary from the

assumed magnitude. Further research and verification into this should be performed.

(5) **Bubble turbulent velocity** – The bubble turbulent slip velocity used within the current flotation model has not been found to be verified within the literature. It was input into the current model solely on the basis of its stated prediction for bubble turbulent slip velocity. No other bubble turbulent slip velocity has been found within the literature. Verification of the current velocity should be performed.

Appendix A

Experimental Data and Model Predictions

Date performed	2/19/2004
Test number	1

Constants

solids density	2475	kg/m3
pressure differential distance	0.0994	m
cell diameter	13.97	cm

Experimental

		Run			
		1	2	3	units
experimental data	tailings wet weight - total	124.4	112.1	133.3	g
	tailings wet tare	26.077	25.982	26.387	g
	tailings dry weight - total	47.8	59.0	68.6	g
	tailings dry tare	8.3	8.3	8.3	g
	tailings time	30.21	11.43	13.71	sec
	product wet weight - total	148.8	133.3	147.7	g
	product wet tare	25.387	25.422	25.035	g
	product dry weight - total	8.6	8.3	8.4	g
	product dry tare	8.4	8.2	8.2	g
	product time	7.02	6.55	7.03	sec
	feed wet weight - total	146.9	147.9	127.2	g
	feed wet tare	18.871	18.429	18.360	g
	feed dry weight - total	30.3	29.7	26.8	g
	feed dry tare	8.3	8.3	8.2	g
	feed time	5.10	5.17	4.24	sec
	pressure differential - no air	0.129	0.139	0.176	psi
		0.125	0.140	0.172	psi
		0.123	0.139	0.171	psi
	pressure differential - with air	0.103	0.143	0.143	psi
		0.102	0.142	0.145	psi
		0.103	0.149	0.145	psi
	liquid height	10.0	12.0	13.2	cm
		0.0	11.5	13.5	cm
		0.0	12.0	13.3	cm
calculated	avg pressure dif. - no air	0.126	0.139	0.173	psi
	avg pressure dif. - with air	0.103	0.145	0.144	psi
	avg liquid height	10.0	11.8	13.3	cm
	air fraction	0.118	-0.025	0.135	-
	active volume	1352	1585	1769	ml
	retention time	72.0	72.1	77.5	sec
mass balanced	feed percent solids	0.041	0.077	0.077	by vol
	feed flow rate	18.77	21.99	22.83	ml/sec
	tailings percent solids	0.257	0.352	0.341	by vol
	tailings flow rate	2.95	4.77	5.15	ml/sec
	product percent solids	0.001	0.001	0.001	by vol
	product flow rate	15.83	17.21	17.68	ml/sec
	exp. rate constant	**2.17E-03**	**1.10E-03**	**1.09E-03**	**min^{-1}**

Misc experimental data

	Run			
	1	2	3	units
temp	42	44	46	F
pH	4.15	4.24	4.38	

Particle Size Data

particle size passing - (μm)	percent in channel - by number		
704	0.13	0.09	0.06
592	0.73	0.55	0.34
497.8	3.16	2.74	1.90
418.6	10.96	10.79	8.71
352	27.11	28.81	26.88
296	36.26	38.28	39.92
248.9	18.43	16.67	19.40
209.3	3.22	2.07	2.79
176	0.00	0.00	0.00
148	0.00	0.00	0.00
124.5	0.00	0.00	0.00
104.7	0.00	0.00	0.00
88	0.00	0.00	0.00
74	0.00	0.00	0.00
62.23	0.00	0.00	0.00
52.33	0.00	0.00	0.00
44	0.00	0.00	0.00
37	0.00	0.00	0.00
31.11	0.00	0.00	0.00
26.16	0.00	0.00	0.00
22	0.00	0.00	0.00

Model

		Run			
		1	2	3	units
additional experimental data	torque	12	12	12	in-lb
	impeller speed	1200			rpm
	contact angle	23	16	20	deg
	contact angle	21	20	19	deg
	contact angle	21	25	21	deg
	contact angle	26	21	21	deg
	contact angle	28	23	21	deg
	contact angle	-	-	-	deg
	contact angle	-	-	-	deg
	contact angle	-	-	-	deg
	surface tension	59.06	59.83	60.08	N/m
	zeta potential	6.1			mV
calculated data	power	27.12	27.12	27.12	Watt
	avg contact angle	23.80	21.00	20.40	deg
	overall contact angle	21.73			deg
	overall surface tension	59.66			N/m
	sauter particle diameter	296.6	297.5	290.2	μm
	avg sauter part diameter	294.8			μm
	avg bub. sauter diameter	467.4			μm
	model rate constant	**1.24E-03**	**7.51E-03**	**3.40E-02**	**min^{-1}**

Date performed	2/24/2004
Test number	2

Constants

solids density	2475	kg/m3
pressure differential distance	0.0994	m
cell diameter	13.97	cm

Experimental

		Run			
		1	2	3	units
experimental data	tailings wet weight - total	128.9	163.2	131.7	g
	tailings wet tare	25.455	25.843	25.663	g
	tailings dry weight - total	39.7	53.2	40.3	g
	tailings dry tare	8.3	8.2	8.2	g
	tailings time	8.67	8.78	6.88	sec
	product wet weight - total	177.3	146.4	131.7	g
	product wet tare	26.396	25.840	25.814	g
	product dry weight - total	13.6	10.7	9.9	g
	product dry tare	8.3	8.2	8.1	g
	product time	12.89	10.99	9.49	sec
	feed wet weight - total	145.4	164.3	165.7	g
	feed wet tare	18.676	18.623	18.825	g
	feed dry weight - total	34.4	37.6	36.9	g
	feed dry tare	8.4	8.1	8.8	g
	feed time	4.95	5.70	5.84	sec
	pressure differential - no air	0.132	0.129	0.141	psi
		0.133	0.130	0.142	psi
		0.131	0.132	0.139	psi
	pressure differential - with air	0.129	0.130	0.129	psi
		0.130	0.129	0.131	psi
		0.129	0.130	0.127	psi
	liquid height	14.0	13.8	13.2	cm
		14.1	13.8	13.3	cm
		14.2	14.0	13.4	cm
calculated	avg pressure dif. - no air	0.132	0.130	0.141	psi
	avg pressure dif. - with air	0.129	0.130	0.129	psi
	avg liquid height	14.1	13.9	13.3	cm
	air fraction	0.015	0.004	0.067	-
	active volume	2016	1983	1902	ml
	retention time	93.5	85.9	82.1	sec
mass balanced	feed percent solids	0.085	0.093	0.085	by vol
	feed flow rate	21.55	23.09	23.18	ml/sec
	tailings percent solids	0.161	0.165	0.153	by vol
	tailings flow rate	10.32	12.41	12.46	ml/sec
	product percent solids	0.015	0.009	0.007	by vol
	product flow rate	11.23	10.67	10.71	ml/sec
	exp. rate constant	**3.02E-02**	**1.69E-02**	**1.54E-02**	**min^{-1}**

Misc experimental data

	Run			
	1	2	3	units
temp	42	44	44	F
pH	3.4	3.43	3.49	

Particle Size Data

particle size passing - (μm)	percent in channel - by number		
704	0.00		0.00
592	0.00		0.00
497.8	0.00		0.00
418.6	0.01		0.00
352	0.06		0.06
296	0.30		0.28
248.9	1.50		1.41
209.3	6.92		6.55
176	22.45		21.64
148	37.60		37.43
124.5	24.79		25.75
104.7	6.37		6.88
88	0.00		0.00
74	0.00		0.00
62.23	0.00		0.00
52.33	0.00		0.00
44	0.00		0.00
37	0.00		0.00
31.11	0.00		0.00
26.16	0.00		0.00
22	0.00		0.00

Model

		Run			
		1	2	3	units
additional experimental data	torque	13	13	12	in-lb
	impeller speed	1200			rpm
	contact angle	23	27	27	deg
	contact angle	25	28	25	deg
	contact angle	25	27	27	deg
	contact angle	27	29	26	deg
	contact angle	-	28	-	deg
	contact angle	-	-	-	deg
	contact angle	-	-	-	deg
	contact angle	-	-	-	deg
	surface tension	60.07	60.77	60.62	N/m
	zeta potential	17.0			mV
calculated data	power	29.38	29.38	27.12	Watt
	avg contact angle	25.00	27.80	26.25	deg
	overall contact angle	26.35			deg
	overall surface tension	60.49			N/m
	sauter particle diameter	140.0		139.0	μm
	avg sauter part diameter	139.5			μm
	avg bub. sauter diameter	467.4			μm
	model rate constant	**4.27E-01**	**4.15E-01**	**3.84E-01**	**min^{-1}**

Date performed	2/25/2004
Test number	3

Constants

solids density	2475	kg/m3
pressure differential distance	0.0994	m
cell diameter	13.97	cm

Experimental

		Run			
		1	2	3	units
experimental data	tailings wet weight - total	98.3	114.2	128.0	g
	tailings wet tare	26.733	25.830	26.569	g
	tailings dry weight - total	12.1	13.8	14.6	g
	tailings dry tare	8.3	8.1	8.2	g
	tailings time	13.57	12.62	14.56	sec
	product wet weight - total	146.0	156.0	140.0	g
	product wet tare	26.455	26.544	25.937	g
	product dry weight - total	37.0	39.4	36.8	g
	product dry tare	8.2	8.4	8.1	g
	product time	5.60	6.95	6.35	sec
	feed wet weight - total	154.6	149.5	160.6	g
	feed wet tare	18.574	18.685	18.806	g
	feed dry weight - total	36.1	34.4	36.5	g
	feed dry tare	8.3	8.2	8.3	g
	feed time	5.28	5.16	5.44	sec
	pressure differential - no air	0.127	0.125	0.122	psi
		0.124	0.125	0.121	psi
		0.125	0.127	0.121	psi
	pressure differential - with air	0.078	0.078	0.099	psi
		0.076	0.077	0.095	psi
		0.076	0.077	0.093	psi
	liquid height	11.0	10.0	10.0	cm
		10.0	10.5	11.0	cm
		0.0	11.0	0.0	cm
calculated	avg pressure dif. - no air	0.125	0.126	0.121	psi
	avg pressure dif. - with air	0.077	0.077	0.096	psi
	avg liquid height	10.5	10.5	10.5	cm
	air fraction	0.332	0.328	0.174	-
	active volume	1074	1082	1329	ml
	retention time	46.5	47.9	59.6	sec
mass balanced	feed percent solids	0.094	0.089	0.091	by vol
	feed flow rate	23.08	22.60	22.31	ml/sec
	tailings percent solids	0.022	0.027	0.026	by vol
	tailings flow rate	5.08	6.67	6.76	ml/sec
	product percent solids	0.114	0.116	0.120	by vol
	product flow rate	18.00	15.92	15.55	ml/sec
	exp. rate constant	**5.14E+00**	**3.79E+00**	**3.17E+00**	**min^{-1}**

Misc experimental data

	Run			
	1	2	3	units
temp	42	42	44	F
pH	7.29	7.37	7.42	

Particle Size Data

particle size passing - (μm)	percent in channel - by number		
704	0.00	0.00	0.00
592	0.00	0.00	0.00
497.8	0.00	0.00	0.00
418.6	0.00	0.00	0.00
352	0.00	0.00	0.00
296	0.00	0.00	0.00
248.9	0.00	0.00	0.00
209.3	0.02	0.01	0.02
176	0.06	0.05	0.06
148	0.23	0.21	0.26
124.5	0.94	0.90	1.12
104.7	3.81	3.71	4.61
88	12.55	12.35	14.90
74	27.25	27.00	30.12
62.23	31.43	31.41	30.47
52.33	17.88	18.21	14.50
44	5.83	6.15	3.94
37	0.00	0.00	0.00
31.11	0.00	0.00	0.00
26.16	0.00	0.00	0.00
22	0.00	0.00	0.00

Model

		Run			
		1	2	3	units
additional experimental data	torque	10	10	9	in-lb
	impeller speed	1200			rpm
	contact angle	24	26	27	deg
	contact angle	28	21	25	deg
	contact angle	29	25	28	deg
	contact angle	32	27	31	deg
	contact angle	27	-	#REF!	deg
	contact angle	-	-	#REF!	deg
	contact angle	-	-	#REF!	deg
	contact angle	-	-	#REF!	deg
	surface tension	59.4	60.69	60.6	N/m
	zeta potential	-20.5			mV
calculated data	power	22.60	22.60	20.34	Watt
	avg contact angle	28.00	24.75	27.75	deg
	overall contact angle	26.83			deg
	overall surface tension	60.23			N/m
	sauter particle diameter	62.9	62.6	64.8	μm
	avg sauter part diameter	63.5			μm
	avg bub. sauter diameter	467.4			μm
	model rate constant	**3.54E+00**	**3.48E+00**	**1.67E+00**	**min^{-1}**

Date performed	2/26/2004
Test number	4

Constants

solids density	2475	kg/m3
pressure differential distance	0.0994	m
cell diameter	13.97	cm

Experimental

		Run			
		1	2	3	units
experimental data	tailings wet weight - total	181.1	142.9	167.1	g
	tailings wet tare	26.077	25.982	26.387	g
	tailings dry weight - total	58.0	66.5	87.3	g
	tailings dry tare	8.3	8.3	8.2	g
	tailings time	13.30	18.11	19.00	sec
	product wet weight - total	103.4	127.6	114.6	g
	product wet tare	25.387	25.422	25.035	g
	product dry weight - total	8.6	8.2	8.2	g
	product dry tare	8.3	8.2	8.1	g
	product time	6.42	5.53	5.01	sec
	feed wet weight - total	207.7	168.6	159.4	g
	feed wet tare	18.871	18.429	18.360	g
	feed dry weight - total	40.9	34.2	32.4	g
	feed dry tare	8.3	8.3	8.2	g
	feed time	8.10	6.26	6.00	sec
	pressure differential - no air	0.108	0.120	0.128	psi
		0.112	0.121	0.130	psi
		0.108	0.122	0.133	psi
	pressure differential - with air	0.079	0.103	0.105	psi
		0.077	0.105	0.100	psi
		0.076	0.106	0.100	psi
	liquid height	8.0	8.5	7.5	cm
		0.0	0.0	8.0	cm
		0.0	0.0	0.0	cm
calculated	avg pressure dif. - no air	0.109	0.121	0.130	psi
	avg pressure dif. - with air	0.077	0.105	0.102	psi
	avg liquid height	8.0	8.5	7.8	cm
	air fraction	0.181	0.079	0.134	-
	active volume	1004	1200	1028	ml
	retention time	47.1	55.3	46.7	sec
mass balanced	feed percent solids	0.075	0.069	0.077	by vol
	feed flow rate	21.29	21.71	22.02	ml/sec
	tailings percent solids	0.165	0.310	0.343	by vol
	tailings flow rate	9.53	4.85	4.90	ml/sec
	product percent solids	0.002	0.000	0.000	by vol
	product flow rate	11.76	16.86	17.13	ml/sec
	exp. rate constant	**6.53E-03**	**5.37E-04**	**9.33E-04**	**min^{-1}**

Misc experimental data

	Run			
	1	2	3	units
temp	41	42	44	F
pH	3.94	3.97	4.03	

Particle Size Data

particle size passing - (μm)	percent in channel - by number		
704	0.15		0.12
592	0.81		0.67
497.8	3.37		3.06
418.6	11.25		11.14
352	27.20		28.13
296	36.05		36.87
248.9	18.07		17.36
209.3	3.10		2.65
176	0.00		0.00
148	0.00		0.00
124.5	0.00		0.00
104.7	0.00		0.00
88	0.00		0.00
74	0.00		0.00
62.23	0.00		0.00
52.33	0.00		0.00
44	0.00		0.00
37	0.00		0.00
31.11	0.00		0.00
26.16	0.00		0.00
22	0.00		0.00

Model

		Run			
		1	2	3	units
additional experimental data	torque	9	11	12	in-lb
	impeller speed	1200			rpm
	contact angle	30	31	30	deg
	contact angle	33	32	34	deg
	contact angle	38	34	31	deg
	contact angle	34	32	33	deg
	contact angle	27	32	35	deg
	contact angle	-	-	33	deg
	contact angle	-	-	-	deg
	contact angle	-	-	-	deg
	surface tension	51.65	56.29	51.31	N/m
	zeta potential	26.5			mV
calculated data	power	20.34	24.86	27.12	Watt
	avg contact angle	32.40	32.20	32.67	deg
	overall contact angle	32.42			deg
	overall surface tension	53.08			N/m
	sauter particle diameter	297.9		297.8	μm
	avg sauter part diameter	297.9			μm
	avg bub. sauter diameter	467.4			μm
	model rate constant	**1.14E-03**	**8.53E-04**	**7.30E-04**	**min^{-1}**

Date performed	2/20/2004
Test number	5

Constants

solids density	2475	kg/m3
pressure differential distance	0.0994	m
cell diameter	13.97	cm

Experimental

		Run			
		1	2	3	units
experimental data	tailings wet weight - total	126.0	125.0	130.1	g
	tailings wet tare	26.733	25.830	7.667	g
	tailings dry weight - total	20.0	20.7	20.0	g
	tailings dry tare	8.3	8.2	8.2	g
	tailings time	15.90	15.24	15.66	sec
	product wet weight - total	146.0	129.1	140.5	g
	product wet tare	26.455	26.544	25.937	g
	product dry weight - total	35.2	30.7	31.8	g
	product dry tare	8.4	8.3	8.2	g
	product time	6.31	5.13	5.68	sec
	feed wet weight - total	143.1	151.1	142.9	g
	feed wet tare	18.574	18.713	18.778	g
	feed dry weight - total	33.2	34.7	32.6	g
	feed dry tare	8.3	8.3	8.2	g
	feed time	4.77	4.98	4.83	sec
	pressure differential - no air	0.126	0.123	0.121	psi
		0.125	0.122	0.119	psi
		0.124	0.124	0.119	psi
	pressure differential - with air	0.095	0.088	0.087	psi
		0.091	0.090	0.085	psi
		0.089	0.088	0.085	psi
	liquid height	11.0	11.2	12.5	cm
		11.0	12.0	12.7	cm
		11.2	11.8	12.8	cm
calculated	avg pressure dif. - no air	0.125	0.123	0.120	psi
	avg pressure dif. - with air	0.092	0.089	0.086	psi
	avg liquid height	11.1	11.7	12.7	cm
	air fraction	0.219	0.224	0.226	-
	active volume	1325	1388	1503	ml
	retention time	58.9	59.3	62.3	sec
mass balanced	feed percent solids	0.091	0.090	0.083	by vol
	feed flow rate	22.50	23.41	24.12	ml/sec
	tailings percent solids	0.051	0.055	0.042	by vol
	tailings flow rate	5.83	6.01	7.14	ml/sec
	product percent solids	0.105	0.102	0.100	by vol
	product flow rate	16.67	17.40	16.98	ml/sec
	exp. rate constant	**1.55E+00**	**1.40E+00**	**1.63E+00**	**min^{-1}**

Misc experimental data

	Run			
	1	2	3	units
temp	41	41	42	F
pH	5.98	6.09	6.28	

Particle Size Data

particle size passing - (μm)	percent in channel - by number		
704	0.00		0.00
592	0.00		0.00
497.8	0.00		0.00
418.6	0.01		0.00
352	0.08		0.07
296	0.36		0.31
248.9	1.71		1.54
209.3	7.33		6.90
176	22.62		22.04
148	37.14		37.25
124.5	24.47		25.24
104.7	6.28		6.65
88	0.00		0.00
74	0.00		0.00
62.23	0.00		0.00
52.33	0.00		0.00
44	0.00		0.00
37	0.00		0.00
31.11	0.00		0.00
26.16	0.00		0.00
22	0.00		0.00

Model

		Run			
		1	2	3	units
additional experimental data	torque	11	11	12	in-lb
	impeller speed	1200			rpm
	contact angle	31	39	30	deg
	contact angle	30	37	34	deg
	contact angle	32	36	33	deg
	contact angle	33	38	34	deg
	contact angle	37	41	31	deg
	contact angle	33	-	31	deg
	contact angle	-	-	-	deg
	contact angle	-	-	-	deg
	surface tension	60.72	55.05	60.45	N/m
	zeta potential	-13.6			mV
calculated data	power	24.86	24.86	27.12	Watt
	avg contact angle	32.67	38.20	32.17	deg
	overall contact angle	34.34			deg
	overall surface tension	58.74			N/m
	sauter particle diameter	140.7		139.7	μm
	avg sauter part diameter	140.2			μm
	avg bub. sauter diameter	467.4			μm
	model rate constant	**3.51E+00**	**3.80E+00**	**4.35E+00**	**min^{-1}**

Date performed	2/21/2004
Test number	6-a

Constants

solids density	2475	kg/m3
pressure differential distance	0.0994	m
cell diameter	13.97	cm

Experimental

		Run			
		1	2	3	units
experimental data	tailings wet weight - total	111.6	139.5	153.6	g
	tailings wet tare	26.733	25.830	26.569	g
	tailings dry weight - total	13.4	15.2	14.8	g
	tailings dry tare	8.2	8.2	8.2	g
	tailings time	15.24	17.46	16.29	sec
	product wet weight - total	136.9	134.6	137.5	g
	product wet tare	26.455	26.544	25.937	g
	product dry weight - total	34.0	36.4	34.6	g
	product dry tare	8.3	8.1	8.2	g
	product time	5.80	6.15	6.26	sec
	feed wet weight - total	156.9	136.2	148.2	g
	feed wet tare	18.574	18.713	18.778	g
	feed dry weight - total	35.6	30.9	32.5	g
	feed dry tare	8.2	8.2	8.1	g
	feed time	5.63	4.79	5.16	sec
	pressure differential - no air	0.140	0.124	0.101	psi
		0.131	0.131	0.099	psi
		0.124	0.126	0.104	psi
	pressure differential - with air	0.095	0.088	0.070	psi
		0.093	0.087	0.069	psi
		0.000	0.087	0.072	psi
	liquid height	10.0	10.0	10.5	cm
		0.0	0.0	11.0	cm
		0.0	0.0	11.0	cm
calculated	avg pressure dif. - no air	0.132	0.127	0.101	psi
	avg pressure dif. - with air	0.094	0.087	0.070	psi
	avg liquid height	10.0	10.0	10.8	cm
	air fraction	0.256	0.270	0.212	-
	active volume	1140	1119	1309	ml
	retention time	52.4	52.6	57.7	sec
mass balanced	feed percent solids	0.089	0.092	0.084	by vol
	feed flow rate	21.75	21.27	22.67	ml/sec
	tailings percent solids	0.025	0.026	0.022	by vol
	tailings flow rate	5.35	6.36	7.46	ml/sec
	product percent solids	0.110	0.120	0.114	by vol
	product flow rate	16.39	14.90	15.21	ml/sec
	exp. rate constant	**3.75E+00**	**3.73E+00**	**3.65E+00**	**min^{-1}**

Misc experimental data

	Run			
	1	2	3	units
temp	42	42	44	F
pH	5.91	6.18	6.28	

Particle Size Data

particle size passing - (μm)	percent in channel - by number		
704	0.00	0.00	0.00
592	0.00	0.00	0.00
497.8	0.00	0.00	0.00
418.6	0.00	0.00	0.00
352	0.00	0.00	0.00
296	0.00	0.00	0.00
248.9	0.00	0.00	0.00
209.3	0.02	0.00	0.01
176	0.09	0.00	0.04
148	0.35	0.10	0.18
124.5	1.47	0.77	0.76
104.7	5.78	4.37	3.17
88	17.44	15.78	10.98
74	31.92	31.61	25.74
62.23	28.31	30.21	32.49
52.33	11.73	13.65	19.94
44	2.89	3.51	6.69
37	0.00	0.00	0.00
31.11	0.00	0.00	0.00
26.16	0.00	0.00	0.00
22	0.00	0.00	0.00

Model

		Run			
		1	2	3	units
additional experimental data	torque	11	11	10	in-lb
	impeller speed	1200			rpm
	contact angle	36	34	22	deg
	contact angle	36	31	34	deg
	contact angle	34	35	30	deg
	contact angle	37	34	30	deg
	contact angle	35	31	33	deg
	contact angle	-	-	-	deg
	contact angle	-	-	-	deg
	contact angle	-	-	-	deg
	surface tension	60.43	61.2	61.05	N/m
	zeta potential	-15.8			mV
calculated data	power	24.86	24.86	22.60	Watt
	avg contact angle	35.60	33.00	29.80	deg
	overall contact angle	32.80			deg
	overall surface tension	60.89			N/m
	sauter particle diameter	66.8	64.8	61.6	μm
	avg sauter part diameter	64.4			μm
	avg bub. sauter diameter	467.4			μm
	model rate constant	**7.01E+00**	**7.40E+00**	**5.55E+00**	**min^{-1}**

Date performed	3/5/2004
Test number	6-b

Constants

solids density	2475	kg/m3
pressure differential distance	0.0994	m
cell diameter	13.97	cm

Experimental

		Run			
		1	2	3	units
experimental data	tailings wet weight - total	118.6	89.3	104.7	g
	tailings wet tare	26.077	25.982	26.387	g
	tailings dry weight - total	6.9	5.1	5.5	g
	tailings dry tare	3.3	3.3	3.3	g
	tailings time	15.18	13.37	16.49	sec
	product wet weight - total	130.1	146.9	130.1	g
	product wet tare	25.387	25.422	25.035	g
	product dry weight - total	26.6	24.0	19.9	g
	product dry tare	3.3	3.3	3.3	g
	product time	5.45	6.01	5.56	sec
	feed wet weight - total	184.5	161.0	161.8	g
	feed wet tare	18.871	18.429	18.360	g
	feed dry weight - total	33.0	23.7	22.7	g
	feed dry tare	3.3	3.3	3.3	g
	feed time	6.59	5.72	6.09	sec
	pressure differential - no air	0.119	0.117	0.122	psi
		0.121	0.116	0.128	psi
		0.118	0.113	0.125	psi
	pressure differential - with air	0.078	0.090	0.090	psi
		0.079	0.089	0.087	psi
		0.080	0.089	0.086	psi
	liquid height	10.5	10.5	10.0	cm
		0.0	0.0	0.0	cm
		0.0	0.0	0.0	cm
calculated	avg pressure dif. - no air	0.119	0.115	0.125	psi
	avg pressure dif. - with air	0.079	0.089	0.088	psi
	avg liquid height	10.5	10.5	10.0	cm
	air fraction	0.278	0.180	0.259	-
	active volume	1162	1319	1136	ml
	retention time	51.5	57.9	52.2	sec
mass balanced	feed percent solids	0.081	0.063	0.059	by vol
	feed flow rate	22.55	22.80	21.74	ml/sec
	tailings percent solids	0.016	0.012	0.012	by vol
	tailings flow rate	5.94	4.66	4.66	ml/sec
	product percent solids	0.104	0.077	0.072	by vol
	product flow rate	16.61	18.15	17.09	ml/sec
	exp. rate constant	**5.58E+00**	**5.37E+00**	**5.62E+00**	**min^{-1}**

Misc experimental data

	Run			
	1	2	3	units
temp	46	51	55	F
pH	7.25	7.42	7.48	

Particle Size Data

particle size passing - (μm)	percent in channel - by number		
704	0.00		0.00
592	0.00		0.00
497.8	0.00		0.00
418.6	0.00		0.00
352	0.00		0.00
296	0.00		0.00
248.9	0.00		0.00
209.3	0.02		0.02
176	0.09		0.07
148	0.37		0.31
124.5	1.54		1.37
104.7	5.89		5.51
88	17.19		16.70
74	31.02		31.15
62.23	28.20		28.94
52.33	12.43		12.71
44	3.25		3.22
37	0.00		0.00
31.11	0.00		0.00
26.16	0.00		0.00
22	0.00		0.00

Model

		Run			
		1	2	3	units
additional experimental data	torque	10	10	10	in-lb
	impeller speed	1200			rpm
	contact angle	35	32	31	deg
	contact angle	41	29	32	deg
	contact angle	36	32	34	deg
	contact angle	37	32	34	deg
	contact angle	38	31	35	deg
	contact angle	-	30	-	deg
	contact angle	-	-	-	deg
	contact angle	-	-	-	deg
	surface tension	60.73	60.88	59.7	N/m
	zeta potential	-15.6			mV
calculated data	power	22.60	22.60	22.60	Watt
	avg contact angle	37.40	31.00	33.20	deg
	overall contact angle	33.87			deg
	overall surface tension	60.44			N/m
	sauter particle diameter	66.6		66.2	μm
	avg sauter part diameter	66.4			μm
	avg bub. sauter diameter	467.4			μm
	model rate constant	**8.47E+00**	**5.33E+00**	**7.88E+00**	**min^{-1}**

Date performed	2/23/2004
Test number	7-a

Constants

solids density	2475	kg/m3
pressure differential distance	0.0994	m
cell diameter	13.97	cm

Experimental

		Run			
		1	2	3	units
experimental data	tailings wet weight - total	151.8	167.3	178.9	g
	tailings wet tare	25.455	25.843	25.663	g
	tailings dry weight - total	58.0	58.0	67.1	g
	tailings dry tare	8.3	8.3	8.2	g
	tailings time	11.41	14.00	14.54	sec
	product wet weight - total	150.7	138.2	132.3	g
	product wet tare	26.396	25.840	25.814	g
	product dry weight - total	9.4	8.9	9.1	g
	product dry tare	8.4	8.3	8.3	g
	product time	8.02	6.73	7.17	sec
	feed wet weight - total	151.0	179.6	157.4	g
	feed wet tare	18.676	18.623	18.825	g
	feed dry weight - total	30.7	36.3	32.2	g
	feed dry tare	8.4	8.3	8.2	g
	feed time	5.59	6.77	5.77	sec
	pressure differential - no air	0.123	0.115	0.121	psi
		0.127	0.114	0.121	psi
		0.119	0.115	0.123	psi
	pressure differential - with air	0.097	0.079	0.108	psi
		0.096	0.080	0.107	psi
		0.095	0.081	0.106	psi
	liquid height	10.5	12.0	10.8	cm
		10.4	11.5	10.8	cm
		10.6	11.5	10.5	cm
calculated	avg pressure dif. - no air	0.123	0.115	0.122	psi
	avg pressure dif. - with air	0.096	0.080	0.107	psi
	avg liquid height	10.5	11.7	10.7	cm
	air fraction	0.146	0.190	0.079	-
	active volume	1374	1448	1510	ml
	retention time	60.0	63.2	68.1	sec
mass balanced	feed percent solids	0.076	0.071	0.076	by vol
	feed flow rate	22.91	22.93	22.19	ml/sec
	tailings percent solids	0.206	0.194	0.206	by vol
	tailings flow rate	8.27	8.17	8.00	ml/sec
	product percent solids	0.003	0.002	0.003	by vol
	product flow rate	14.64	14.76	14.19	ml/sec
	exp. rate constant	**1.02E-02**	**7.04E-03**	**9.01E-03**	**min^{-1}**

Misc experimental data

	Run			
	1	2	3	units
temp	42	42	44	F
pH	5.19	5.4	5.65	

Particle Size Data

particle size passing - (μm)	percent in channel - by number		
704	0.08		0.07
592	0.46		0.41
497.8	2.48		2.23
418.6	10.80		9.95
352	29.65		28.67
296	37.74		38.65
248.9	16.37		17.46
209.3	2.42		2.56
176	0.00		0.00
148	0.00		0.00
124.5	0.00		0.00
104.7	0.00		0.00
88	0.00		0.00
74	0.00		0.00
62.23	0.00		0.00
52.33	0.00		0.00
44	0.00		0.00
37	0.00		0.00
31.11	0.00		0.00
26.16	0.00		0.00
22	0.00		0.00

Model

		Run			
		1	2	3	units
additional experimental data	torque	11	11	11	in-lb
	impeller speed	1200			rpm
	contact angle	37	39	41	deg
	contact angle	42	41	41	deg
	contact angle	40	40	42	deg
	contact angle	38	49	42	deg
	contact angle	37	48	40	deg
	contact angle	41	45	-	deg
	contact angle	-	41	-	deg
	contact angle	-	-	-	deg
	surface tension	58.78	59.92	59.63	N/m
	zeta potential	-7.9			mV
calculated data	power	24.86	24.86	24.86	Watt
	avg contact angle	39.17	43.29	41.20	deg
	overall contact angle	41.22			deg
	overall surface tension	59.44			N/m
	sauter particle diameter	297.1		294.4	μm
	avg sauter part diameter	295.7			μm
	avg bub. sauter diameter	467.4			μm
	model rate constant	**4.46E-02**	**1.83E-01**	**2.87E-02**	**min^{-1}**

Date performed	3/1/2004
Test number	7-b

Constants

solids density	2475	kg/m3
pressure differential distance	0.0994	m
cell diameter	13.97	cm

Experimental

		Run			
		1	2	3	units
experimental data	tailings wet weight - total	111.0	122.6	132.9	g
	tailings wet tare	25.455	25.843	25.663	g
	tailings dry weight - total	32.8	40.6	42.6	g
	tailings dry tare	3.3	3.3	3.3	g
	tailings time	14.35	15.68	15.32	sec
	product wet weight - total	142.1	132.9	135.5	g
	product wet tare	26.396	25.840	25.814	g
	product dry weight - total	11.8	11.0	10.2	g
	product dry tare	3.3	3.3	3.3	g
	product time	6.58	6.17	6.63	sec
	feed wet weight - total	146.5	169.5	149.3	g
	feed wet tare	18.676	18.623	18.825	g
	feed dry weight - total	24.9	28.7	24.2	g
	feed dry tare	3.3	3.3	3.3	g
	feed time	5.29	6.28	5.55	sec
	pressure differential - no air	0.117	0.107	0.123	psi
		0.119	0.110	0.123	psi
		0.118	0.110	0.117	psi
	pressure differential - with air	0.088	0.101	0.106	psi
		0.090	0.100	0.106	psi
		0.091	0.000	0.104	psi
	liquid height	11.0	10.5	10.0	cm
		10.0	10.7	10.0	cm
		10.0	10.3	10.0	cm
calculated	avg pressure dif. - no air	0.118	0.109	0.121	psi
	avg pressure dif. - with air	0.090	0.101	0.105	psi
	avg liquid height	10.3	10.5	10.0	cm
	air fraction	0.157	0.046	0.086	-
	active volume	1335	1536	1401	ml
	retention time	62.6	72.1	65.9	sec
mass balanced	feed percent solids	0.068	0.072	0.070	by vol
	feed flow rate	21.32	21.29	21.25	ml/sec
	tailings percent solids	0.185	0.209	0.193	by vol
	tailings flow rate	4.94	4.87	5.53	ml/sec
	product percent solids	0.032	0.031	0.027	by vol
	product flow rate	16.38	16.42	15.72	ml/sec
	exp. rate constant	**1.28E-01**	**9.52E-02**	**9.33E-02**	**min^{-1}**

Misc experimental data

	Run			
	1	2	3	units
temp	42	42	44	F
pH	7.05	7.15	7.21	

Particle Size Data

particle size passing - (μm)	percent in channel - by number		
704	0.13	0.03	0.03
592	0.69	0.24	0.23
497.8	3.16	1.58	1.57
418.6	11.49	8.66	8.78
352	28.68	28.69	29.41
296	36.59	40.47	40.85
248.9	16.71	17.86	16.98
209.3	2.55	2.47	2.15
176	0.00	0.00	0.00
148	0.00	0.00	0.00
124.5	0.00	0.00	0.00
104.7	0.00	0.00	0.00
88	0.00	0.00	0.00
74	0.00	0.00	0.00
62.23	0.00	0.00	0.00
52.33	0.00	0.00	0.00
44	0.00	0.00	0.00
37	0.00	0.00	0.00
31.11	0.00	0.00	0.00
26.16	0.00	0.00	0.00
22	0.00	0.00	0.00

Model

		Run			
		1	2	3	units
additional experimental data	torque	11	11	11	in-lb
	impeller speed	1200			rpm
	contact angle	54	46	48	deg
	contact angle	53	51	46	deg
	contact angle	54	50	49	deg
	contact angle	48	51	49	deg
	contact angle	49	52	47	deg
	contact angle	52	53	49	deg
	contact angle	54	-	51	deg
	contact angle	-	-	-	deg
	surface tension	58.87	52.46	59.31	N/m
	zeta potential	-8.1			mV
calculated data	power	24.86	24.86	24.86	Watt
	avg contact angle	52.00	50.50	48.43	deg
	overall contact angle	50.31			deg
	overall surface tension	56.88			N/m
	sauter particle diameter	299.2	291.0	292.1	μm
	avg sauter part diameter	294.1			μm
	avg bub. sauter diameter	467.4			μm
	model rate constant	**1.04E-01**	**3.38E-02**	**4.03E-02**	**min^{-1}**

Date performed	2/27/2004
Test number	8

Constants

solids density	2475	kg/m3
pressure differential distance	0.0994	m
cell diameter	13.97	cm

Experimental

		Run			
		1	2	3	units
experimental data	tailings wet weight - total	125.4	111.6	140.6	g
	tailings wet tare	25.455	25.843	25.663	g
	tailings dry weight - total	13.4	12.4	15.0	g
	tailings dry tare	8.1	8.1	8.2	g
	tailings time	18.47	16.03	17.90	sec
	product wet weight - total	143.0	135.9	135.6	g
	product wet tare	26.396	25.840	25.814	g
	product dry weight - total	36.3	32.5	33.3	g
	product dry tare	8.2	8.1	8.2	g
	product time	6.20	5.92	5.97	sec
	feed wet weight - total	168.9	161.1	160.4	g
	feed wet tare	18.676	18.623	18.825	g
	feed dry weight - total	36.8	34.6	33.2	g
	feed dry tare	8.2	8.2	8.2	g
	feed time	6.15	5.84	5.81	sec
	pressure differential - no air	0.127	0.121	0.130	psi
		0.121	0.123	0.130	psi
		0.126	0.126	0.127	psi
	pressure differential - with air	0.090	0.100	0.093	psi
		0.088	0.102	0.093	psi
		0.088	0.099	0.091	psi
	liquid height	9.0	11.0	11.0	cm
		10.0	10.5	11.0	cm
		10.0	10.5	10.8	cm
calculated	avg pressure dif. - no air	0.125	0.123	0.129	psi
	avg pressure dif. - with air	0.089	0.100	0.092	psi
	avg liquid height	9.7	10.7	10.9	cm
	air fraction	0.246	0.157	0.250	-
	active volume	1117	1378	1257	ml
	retention time	52.1	64.2	57.3	sec
mass balanced	feed percent solids	0.089	0.084	0.082	by vol
	feed flow rate	21.43	21.47	21.95	ml/sec
	tailings percent solids	0.022	0.021	0.025	by vol
	tailings flow rate	5.28	5.20	6.21	ml/sec
	product percent solids	0.111	0.104	0.104	by vol
	product flow rate	16.15	16.27	15.74	ml/sec
	exp. rate constant	**4.37E+00**	**3.52E+00**	**3.18E+00**	**min^{-1}**

Misc experimental data

	Run			
	1	2	3	units
temp	41	42	42	F
pH	7.1	7.15	7.12	

Particle Size Data

particle size passing - (μm)	percent in channel - by number		
704	0.00		0.00
592	0.00		0.00
497.8	0.00		0.00
418.6	0.00		0.00
352	0.06		0.06
296	0.31		0.29
248.9	1.56		1.42
209.3	7.17		6.40
176	22.87		21.14
148	37.57		37.39
124.5	24.34		26.30
104.7	6.12		7.00
88	0.00		0.00
74	0.00		0.00
62.23	0.00		0.00
52.33	0.00		0.00
44	0.00		0.00
37	0.00		0.00
31.11	0.00		0.00
26.16	0.00		0.00
22	0.00		0.00

Model

		Run			
		1	2	3	units
additional experimental data	torque	10	10	10	in-lb
	impeller speed	1200			rpm
	contact angle	38	36	38	deg
	contact angle	39	38	41	deg
	contact angle	45	39	40	deg
	contact angle	46	41	39	deg
	contact angle	41	-	39	deg
	contact angle	43	-	40	deg
	contact angle	-	-	-	deg
	contact angle	-	-	-	deg
	surface tension	60.29	60.08	54.53	N/m
	zeta potential	-14.9			mV
calculated data	power	22.60	22.60	22.60	Watt
	avg contact angle	42.00	38.50	39.50	deg
	overall contact angle	40.00			deg
	overall surface tension	58.30			N/m
	sauter particle diameter	140.5		138.6	μm
	avg sauter part diameter	139.5			μm
	avg bub. sauter diameter	467.4			μm
	model rate constant	**6.76E+00**	**4.54E+00**	**7.66E+00**	**min^{-1}**

Date performed	3/17/2004
Test number	9

Constants

solids density	2475	kg/m3
pressure differential distance	0.0994	m
cell diameter	13.97	cm

Experimental

		Run			
		1	2	3	units
experimental data	tailings wet weight - total	102.2	99.3	100.8	g
	tailings wet tare	26.733	25.830	26.575	g
	tailings dry weight - total	5.4	5.4	5.6	g
	tailings dry tare	4.1	4.2	4.2	g
	tailings time	15.05	14.53	14.71	sec
	product wet weight - total	119.6	130.7	129.7	g
	product wet tare	26.455	26.544	25.937	g
	product dry weight - total	13.6	14.0	15.6	g
	product dry tare	4.2	4.2	4.2	g
	product time	5.17	5.40	5.96	sec
	feed wet weight - total	147.0	157.1	158.4	g
	feed wet tare	18.574	18.713	18.778	g
	feed dry weight - total	14.4	16.3	19.3	g
	feed dry tare	4.1	4.2	4.2	g
	feed time	5.63	6.07	6.11	sec
	pressure differential - no air	0.122	0.129	0.130	psi
		0.123	0.128	0.129	psi
		0.122	0.127	0.131	psi
	pressure differential - with air	0.072	0.091	0.089	psi
		0.072	0.090	0.090	psi
		0.071	0.087	0.089	psi
	liquid height	9.0	9.0	8.9	cm
		0.0	8.8	8.8	cm
		0.0	0.0	0.0	cm
calculated	avg pressure dif. - no air	0.122	0.128	0.130	psi
	avg pressure dif. - with air	0.072	0.089	0.089	psi
	avg liquid height	9.0	8.9	8.9	cm
	air fraction	0.354	0.270	0.284	-
	active volume	891	996	972	ml
	retention time	40.9	44.1	45.4	sec
mass balanced	feed percent solids	0.034	0.035	0.042	by vol
	feed flow rate	21.82	22.60	21.42	ml/sec
	tailings percent solids	0.007	0.007	0.008	by vol
	tailings flow rate	4.97	4.90	4.90	ml/sec
	product percent solids	0.043	0.043	0.052	by vol
	product flow rate	16.85	17.71	16.52	ml/sec
	exp. rate constant	**7.09E+00**	**6.62E+00**	**6.87E+00**	**min^{-1}**

Misc experimental data

	Run			
	1	2	3	units
temp	48	48	50	F
pH	7.4	7.53	7.62	

Particle Size Data

particle size passing - (μm)	percent in channel - by number		
704	0.00		0.00
592	0.00		0.00
497.8	0.00		0.00
418.6	0.00		0.00
352	0.00		0.00
296	0.00		0.00
248.9	0.00		0.00
209.3	0.02		0.00
176	0.06		0.03
148	0.28		0.21
124.5	1.29		1.30
104.7	5.40		6.16
88	16.94		19.24
74	31.85		33.42
62.23	28.99		27.17
52.33	12.21		10.24
44	2.96		2.23
37	0.00		0.00
31.11	0.00		0.00
26.16	0.00		0.00
22	0.00		0.00

Model

		Run			
		1	2	3	units
additional experimental data	torque	9	10	9	in-lb
	impeller speed	1200			rpm
	contact angle	39	38	35	deg
	contact angle	39	40	37	deg
	contact angle	40	37	36	deg
	contact angle	39	39	37	deg
	contact angle	41	36	-	deg
	contact angle	40	-	-	deg
	contact angle	41	-	-	deg
	contact angle	-	-	-	deg
	surface tension	59.34	56.55	55.34	N/m
	zeta potential	-16.3			mV
calculated data	power	20.34	22.60	20.34	Watt
	avg contact angle	39.86	38.00	36.25	deg
	overall contact angle	38.04			deg
	overall surface tension	57.08			N/m
	sauter particle diameter	66.3		67.5	μm
	avg sauter part diameter	66.9			μm
	avg bub. sauter diameter	467.4			μm
	model rate constant	**1.72E+01**	**1.31E+01**	**1.33E+01**	**min^{-1}**

Date performed	3/10/2004
Test number	10

Constants

solids density	2475	kg/m3
pressure differential distance	0.0994	m
cell diameter	13.97	cm

Experimental

		Run			
		1	2	3	units
experimental data	tailings wet weight - total	136.9	132.3	127.2	g
	tailings wet tare	25.455	25.843	25.663	g
	tailings dry weight - total	45.0	45.5	43.6	g
	tailings dry tare	4.3	4.2	4.3	g
	tailings time	13.82	11.87	12.45	sec
	product wet weight - total	165.3	149.7	148.5	g
	product wet tare	26.396	25.840	25.814	g
	product dry weight - total	8.2	6.9	7.4	g
	product dry tare	4.2	4.2	4.2	g
	product time	8.64	7.47	7.41	sec
	feed wet weight - total	150.6	153.7	160.3	g
	feed wet tare	18.676	18.623	18.825	g
	feed dry weight - total	26.2	25.9	28.2	g
	feed dry tare	4.3	4.2	4.2	g
	feed time	5.33	5.50	5.79	sec
	pressure differential - no air	0.133	0.132	0.142	psi
		0.129	0.132	0.143	psi
		0.131	0.133	0.136	psi
	pressure differential - with air	0.117	0.120	0.125	psi
		0.117	0.121	0.124	psi
		0.119	0.125	0.123	psi
	liquid height	10.2	12.0	12.4	cm
		10.1	12.0	12.4	cm
		10.3	11.9	12.3	cm
calculated	avg pressure dif. - no air	0.131	0.132	0.140	psi
	avg pressure dif. - with air	0.118	0.122	0.124	psi
	avg liquid height	10.2	12.0	12.4	cm
	air fraction	0.073	0.056	0.088	-
	active volume	1450	1732	1730	ml
	retention time	66.2	76.1	78.3	sec
mass balanced	feed percent solids	0.069	0.070	0.071	by vol
	feed flow rate	21.91	22.76	22.08	ml/sec
	tailings percent solids	0.200	0.208	0.215	by vol
	tailings flow rate	6.59	6.95	6.50	ml/sec
	product percent solids	0.012	0.009	0.011	by vol
	product flow rate	15.32	15.81	15.58	ml/sec
	exp. rate constant	**3.81E-02**	**2.34E-02**	**2.71E-02**	**min^{-1}**

Misc experimental data

	Run			
	1	2	3	units
temp	44	46	46	F
pH	6.56	6.75	7	

Particle Size Data

particle size passing - (μm)	percent in channel - by number		
704	0.07		0.09
592	0.38		0.51
497.8	2.09		2.67
418.6	9.62		11.02
352	28.44		29.08
296	38.93		36.94
248.9	17.79		16.92
209.3	2.68		2.77
176	0.00		0.00
148	0.00		0.00
124.5	0.00		0.00
104.7	0.00		0.00
88	0.00		0.00
74	0.00		0.00
62.23	0.00		0.00
52.33	0.00		0.00
44	0.00		0.00
37	0.00		0.00
31.11	0.00		0.00
26.16	0.00		0.00
22	0.00		0.00

Model

		Run			
		1	2	3	units
additional experimental data	torque	8	8	8	in-lb
	impeller speed	1200			rpm
	contact angle	34	40	37	deg
	contact angle	35	37	39	deg
	contact angle	36	36	41	deg
	contact angle	37	37	40	deg
	contact angle	36	37	38	deg
	contact angle	42	-	38	deg
	contact angle	42	-	-	deg
	contact angle	-	-	-	deg
	surface tension	59.78	59.73	53.9	N/m
	zeta potential	-14.0			mV
calculated data	power	18.08	18.08	18.08	Watt
	avg contact angle	37.43	37.40	38.83	deg
	overall contact angle	37.89			deg
	overall surface tension	57.80			N/m
	sauter particle diameter	293.3		297.0	μm
	avg sauter part diameter	295.2			μm
	avg bub. sauter diameter	467.4			μm
	model rate constant	**1.78E-02**	**7.41E-02**	**1.73E-01**	**min^{-1}**

Date performed	3/12/2004
Test number	11

Constants

solids density	2475	kg/m3
pressure differential distance	0.0994	m
cell diameter	13.97	cm

Experimental

		Run			
		1	2	3	units
experimental data	tailings wet weight - total	108.8	118.2	101.8	g
	tailings wet tare	25.455	25.843	25.663	g
	tailings dry weight - total	9.3	9.8	9.0	g
	tailings dry tare	4.2	4.1	4.2	g
	tailings time	15.01	15.97	14.46	sec
	product wet weight - total	152.6	146.3	143.0	g
	product wet tare	26.396	25.840	25.814	g
	product dry weight - total	33.9	31.4	29.5	g
	product dry tare	4.1	4.2	4.2	g
	product time	6.43	6.26	5.94	sec
	feed wet weight - total	166.9	175.2	163.6	g
	feed wet tare	18.676	18.623	18.825	g
	feed dry weight - total	33.2	34.7	32.0	g
	feed dry tare	4.2	4.1	4.2	g
	feed time	5.68	6.08	5.61	sec
	pressure differential - no air	0.140	0.128	0.138	psi
		0.139	0.133	0.138	psi
		0.135	0.129	0.139	psi
	pressure differential - with air	0.088	0.100	0.097	psi
		0.081	0.096	0.097	psi
		0.083	0.100	0.097	psi
	liquid height	9.0	9.0	9.0	cm
		9.0	8.6	9.2	cm
		8.5	8.8	9.0	cm
calculated	avg pressure dif. - no air	0.138	0.130	0.138	psi
	avg pressure dif. - with air	0.084	0.099	0.097	psi
	avg liquid height	8.8	8.8	9.1	cm
	air fraction	0.366	0.213	0.281	-
	active volume	858	1062	1000	ml
	retention time	38.1	47.3	44.4	sec
mass balanced	feed percent solids	0.090	0.087	0.085	by vol
	feed flow rate	22.52	22.45	22.51	ml/sec
	tailings percent solids	0.026	0.026	0.026	by vol
	tailings flow rate	5.39	5.57	5.07	ml/sec
	product percent solids	0.110	0.107	0.102	by vol
	product flow rate	17.13	16.88	17.45	ml/sec
	exp. rate constant	**5.11E+00**	**3.94E+00**	**4.06E+00**	**min^{-1}**

Misc experimental data

	Run			
	1	2	3	units
temp	46	48	48	F
pH	7.42	7.62	7.64	

Particle Size Data

particle size passing - (μm)	percent in channel - by number		
704	0.00		0.00
592	0.00		0.00
497.8	0.00		0.00
418.6	0.00		0.01
352	0.06		0.07
296	0.31		0.35
248.9	1.56		1.70
209.3	7.05		7.35
176	22.26		22.63
148	37.02		37.01
124.5	24.99		24.50
104.7	6.75		6.38
88	0.00		0.00
74	0.00		0.00
62.23	0.00		0.00
52.33	0.00		0.00
44	0.00		0.00
37	0.00		0.00
31.11	0.00		0.00
26.16	0.00		0.00
22	0.00		0.00

Model

		Run			
		1	2	3	units
additional experimental data	torque	8	8	8	in-lb
	impeller speed	1200			rpm
	contact angle	27	29	29	deg
	contact angle	36	31	32	deg
	contact angle	27	35	29	deg
	contact angle	32	29	30	deg
	contact angle	35	30	31	deg
	contact angle	31	32	31	deg
	contact angle	-	-	-	deg
	contact angle	-	-	-	deg
	surface tension	54.83	61.31	61.32	N/m
	zeta potential	-19.7			mV
calculated data	power	18.08	18.08	18.08	Watt
	avg contact angle	31.33	31.00	30.33	deg
	overall contact angle	30.89			deg
	overall surface tension	59.15			N/m
	sauter particle diameter	139.8		140.6	μm
	avg sauter part diameter	140.2			μm
	avg bub. sauter diameter	467.4			μm
	model rate constant	**5.12E+00**	**2.77E+00**	**3.85E+00**	**min^{-1}**

Date performed	3/11/2004
Test number	12

Constants

solids density	2475	kg/m3
pressure differential distance	0.0994	m
cell diameter	13.97	cm

Experimental

		Run			
		1	2	3	units
experimental data	tailings wet weight - total	110.1	118.2	147.3	g
	tailings wet tare	26.733	25.830	26.569	g
	tailings dry weight - total	6.6	6.6	7.4	g
	tailings dry tare	4.2	4.2	4.2	g
	tailings time	14.66	15.06	20.37	sec
	product wet weight - total	133.6	143.2	127.7	g
	product wet tare	26.455	26.544	25.937	g
	product dry weight - total	29.5	27.2	23.6	g
	product dry tare	4.2	4.1	4.2	g
	product time	5.42	6.00	5.31	sec
	feed wet weight - total	173.0	150.7	165.5	g
	feed wet tare	18.574	18.713	18.778	g
	feed dry weight - total	32.3	25.8	27.7	g
	feed dry tare	4.1	4.2	4.1	g
	feed time	6.09	5.19	5.82	sec
	pressure differential - no air	0.131	0.132	0.119	psi
		0.133	0.132	0.120	psi
		0.134	0.133	0.119	psi
	pressure differential - with air	0.105	0.106	0.107	psi
		0.105	0.107	0.107	psi
		0.104	0.107	0.108	psi
	liquid height	9.5	9.7	10.0	cm
		10.0	9.5	10.2	cm
		0.0	0.0	0.0	cm
calculated	avg pressure dif. - no air	0.133	0.132	0.119	psi
	avg pressure dif. - with air	0.105	0.107	0.107	psi
	avg liquid height	9.8	9.6	10.1	cm
	air fraction	0.194	0.178	0.083	-
	active volume	1204	1209	1419	ml
	retention time	53.4	52.3	62.1	sec
mass balanced	feed percent solids	0.084	0.071	0.069	by vol
	feed flow rate	22.56	23.13	22.85	ml/sec
	tailings percent solids	0.012	0.011	0.011	by vol
	tailings flow rate	5.62	6.00	5.79	ml/sec
	product percent solids	0.109	0.093	0.089	by vol
	product flow rate	16.94	17.14	17.06	ml/sec
	exp. rate constant	**7.84E+00**	**7.39E+00**	**5.84E+00**	**min^{-1}**

Misc experimental data

	Run			
	1	2	3	units
temp	46	46	48	F
pH	7.38	7.52	7.53	

Particle Size Data

particle size passing - (μm)	percent in channel - by number		
704	0.00		0.00
592	0.00		0.00
497.8	0.00		0.00
418.6	0.00		0.00
352	0.00		0.00
296	0.00		0.00
248.9	0.00		0.00
209.3	0.02		0.03
176	0.08		0.09
148	0.32		0.39
124.5	1.37		1.62
104.7	5.51		6.21
88	16.82		17.97
74	31.44		31.64
62.23	28.90		27.56
52.33	12.45		11.53
44	3.09		2.96
37	0.00		0.00
31.11	0.00		0.00
26.16	0.00		0.00
22	0.00		0.00

Model

		Run			
		1	2	3	units
additional experimental data	torque	8	8	8	in-lb
	impeller speed	1200			rpm
	contact angle	27	32	29	deg
	contact angle	30	30	30	deg
	contact angle	26	29	31	deg
	contact angle	30	34	31	deg
	contact angle	33	30	30	deg
	contact angle	31	36	30	deg
	contact angle	-	-	-	deg
	contact angle	-	-	-	deg
	surface tension	57.28	60.98	59.76	N/m
	zeta potential	-18.8			mV
calculated data	power	18.08	18.08	18.08	Watt
	avg contact angle	29.50	31.83	30.17	deg
	overall contact angle	30.50			deg
	overall surface tension	59.34			N/m
	sauter particle diameter	66.3		67.2	μm
	avg sauter part diameter	66.8			μm
	avg bub. sauter diameter	467.4			μm
	model rate constant	**5.63E+00**	**5.16E+00**	**2.34E+00**	**min^{-1}**

Date performed	3/8/2004
Test number	13

Constants

solids density	2475	kg/m3
pressure differential distance	0.0994	m
cell diameter	13.97	cm

Experimental

		Run			
		1	2	3	units
experimental data	tailings wet weight - total	131.2	142.9	143.2	g
	tailings wet tare	26.077	26.182	26.387	g
	tailings dry weight - total	46.8	53.5	53.5	g
	tailings dry tare	3.3	3.3	3.3	g
	tailings time	13.03	14.27	14.17	sec
	product wet weight - total	158.5	163.9	163.2	g
	product wet tare	25.387	25.422	25.035	g
	product dry weight - total	6.5	6.3	6.2	g
	product dry tare	3.3	3.3	3.2	g
	product time	8.26	8.58	8.66	sec
	feed wet weight - total	151.9	159.6	164.8	g
	feed wet tare	18.871	18.429	18.360	g
	feed dry weight - total	25.8	26.9	27.9	g
	feed dry tare	3.3	3.3	3.3	g
	feed time	5.35	5.78	5.93	sec
	pressure differential - no air	0.116	0.117	0.122	psi
		0.118	0.117	0.120	psi
		0.117	0.115	0.121	psi
	pressure differential - with air	0.094	0.099	0.099	psi
		0.095	0.099	0.104	psi
		0.094	0.098	0.097	psi
	liquid height	9.0	9.0	9.2	cm
		9.7	9.5	9.4	cm
		9.5	9.5	9.1	cm
calculated	avg pressure dif. - no air	0.117	0.116	0.121	psi
	avg pressure dif. - with air	0.094	0.099	0.100	psi
	avg liquid height	9.4	9.3	9.2	cm
	air fraction	0.119	0.092	0.110	-
	active volume	1269	1299	1260	ml
	retention time	57.8	59.3	57.5	sec
mass balanced	feed percent solids	0.073	0.074	0.074	by vol
	feed flow rate	21.94	21.92	21.92	ml/sec
	tailings percent solids	0.230	0.238	0.238	by vol
	tailings flow rate	6.26	6.16	6.23	ml/sec
	product percent solids	0.010	0.009	0.009	by vol
	product flow rate	15.68	15.76	15.69	ml/sec
	exp. rate constant	**3.21E-02**	**2.77E-02**	**2.78E-02**	**min^{-1}**

Misc experimental data

	Run			
	1	2	3	units
temp	46	46	48	F
pH	7.18	7.34	7.39	

Particle Size Data

particle size passing - (μm)	percent in channel - by number		
704	0.17		0.07
592	0.89		0.42
497.8	3.53		2.21
418.6	11.21		9.82
352	26.51		28.28
296	35.74		38.26
248.9	18.67		18.00
209.3	3.28		2.94
176	0.00		0.00
148	0.00		0.00
124.5	0.00		0.00
104.7	0.00		0.00
88	0.00		0.00
74	0.00		0.00
62.23	0.00		0.00
52.33	0.00		0.00
44	0.00		0.00
37	0.00		0.00
31.11	0.00		0.00
26.16	0.00		0.00
22	0.00		0.00

Model

		Run			
		1	2	3	units
additional experimental data	torque	13	13	13	in-lb
	impeller speed	1200			rpm
	contact angle	37	39	39	deg
	contact angle	37	38	39	deg
	contact angle	41	39	39	deg
	contact angle	41	40	40	deg
	contact angle	42	43	40	deg
	contact angle	-	-	-	deg
	contact angle	-	-	-	deg
	contact angle	-	-	-	deg
	surface tension	60.44	54.52	57.64	N/m
	zeta potential	-11.3			mV
calculated data	power	29.38	29.38	29.38	Watt
	avg contact angle	39.60	39.80	39.40	deg
	overall contact angle	39.60			deg
	overall surface tension	57.53			N/m
	sauter particle diameter	297.7		293.5	μm
	avg sauter part diameter	295.6			μm
	avg bub. sauter diameter	467.4			μm
	model rate constant	**7.05E-03**	**5.05E-03**	**5.49E-03**	**min^{-1}**

Date performed	3/4/2004
Test number	14

Constants

solids density	2475	kg/m3
pressure differential distance	0.0994	m
cell diameter	13.97	cm

Experimental

		Run			
		1	2	3	units
experimental data	tailings wet weight - total	95.0	101.8	101.2	g
	tailings wet tare	25.455	25.843	25.663	g
	tailings dry weight - total	10.3	10.7	11.7	g
	tailings dry tare	3.2	3.3	3.2	g
	tailings time	14.07	14.68	15.04	sec
	product wet weight - total	157.6	159.2	159.1	g
	product wet tare	26.396	25.840	25.814	g
	product dry weight - total	33.4	33.3	32.1	g
	product dry tare	3.3	3.2	3.3	g
	product time	6.24	6.18	6.36	sec
	feed wet weight - total	159.3	170.1	168.9	g
	feed wet tare	18.676	18.623	18.825	g
	feed dry weight - total	32.1	33.7	32.1	g
	feed dry tare	3.2	3.3	3.3	g
	feed time	5.36	5.75	5.90	sec
	pressure differential - no air	0.124	0.110	0.116	psi
		0.125	0.109	0.117	psi
		0.129	0.111	0.120	psi
	pressure differential - with air	0.084	0.081	0.079	psi
		0.080	0.081	0.080	psi
		0.082	0.080	0.078	psi
	liquid height	11.0	12.0	11.5	cm
		10.5	11.8	11.3	cm
		10.5	11.0	11.2	cm
calculated	avg pressure dif. - no air	0.126	0.110	0.118	psi
	avg pressure dif. - with air	0.082	0.081	0.079	psi
	avg liquid height	10.7	11.6	11.3	cm
	air fraction	0.292	0.195	0.255	-
	active volume	1158	1431	1295	ml
	retention time	50.6	61.2	56.9	sec
mass balanced	feed percent solids	0.094	0.092	0.089	by vol
	feed flow rate	22.89	23.41	22.76	ml/sec
	tailings percent solids	0.043	0.042	0.048	by vol
	tailings flow rate	4.65	4.86	4.68	ml/sec
	product percent solids	0.107	0.105	0.099	by vol
	product flow rate	18.24	18.54	18.08	ml/sec
	exp. rate constant	**2.34E+00**	**1.96E+00**	**1.71E+00**	**min^{-1}**

Misc experimental data

	Run			
	1	2	3	units
temp	46	46	48	F
pH	7.57	7.67	7.56	

Particle Size Data

particle size passing - (μm)	percent in channel - by number		
704	0.00		0.00
592	0.00		0.00
497.8	0.00		0.00
418.6	0.01		0.00
352	0.07		0.06
296	0.35		0.30
248.9	1.73		1.51
209.3	7.60		6.89
176	23.24		22.23
148	37.09		37.52
124.5	23.84		25.08
104.7	6.07		6.41
88	0.00		0.00
74	0.00		0.00
62.23	0.00		0.00
52.33	0.00		0.00
44	0.00		0.00
37	0.00		0.00
31.11	0.00		0.00
26.16	0.00		0.00
22	0.00		0.00

Model

		Run			
		1	2	3	units
additional experimental data	torque	11	11	11	in-lb
	impeller speed	1500			rpm
	contact angle	28	35	33	deg
	contact angle	28	32	34	deg
	contact angle	28	33	34	deg
	contact angle	35	32	36	deg
	contact angle	32	-	38	deg
	contact angle	-	-	37	deg
	contact angle	-	-	-	deg
	contact angle	-	-	-	deg
	surface tension	60.84	60.65	61.59	N/m
	zeta potential	-15.8			mV
calculated data	power	31.07	31.07	31.07	Watt
	avg contact angle	30.20	33.00	35.33	deg
	overall contact angle	32.84			deg
	overall surface tension	61.03			N/m
	sauter particle diameter	141.2		139.8	μm
	avg sauter part diameter	140.5			μm
	avg bub. sauter diameter	467.4			μm
	model rate constant	**2.75E+00**	**1.91E+00**	**2.51E+00**	**min^{-1}**

Date performed	3/9/2004
Test number	15

Constants

solids density	2475	kg/m3
pressure differential distance	0.0994	m
cell diameter	13.97	cm

Experimental

		Run			
		1	2	3	units
experimental data	tailings wet weight - total	111.0	107.1	114.2	g
	tailings wet tare	26.733	25.830	26.569	g
	tailings dry weight - total	7.7	8.0	8.1	g
	tailings dry tare	3.3	4.2	4.2	g
	tailings time	16.98	14.74	15.73	sec
	product wet weight - total	139.1	137.0	156.6	g
	product wet tare	26.455	26.544	25.937	g
	product dry weight - total	29.1	26.3	29.7	g
	product dry tare	4.2	4.2	4.2	g
	product time	5.71	5.72	6.66	sec
	feed wet weight - total	156.5	166.3	169.6	g
	feed wet tare	18.574	18.713	18.778	g
	feed dry weight - total	30.3	29.6	29.0	g
	feed dry tare	4.3	4.3	4.2	g
	feed time	5.35	5.88	6.04	sec
	pressure differential - no air	0.123	0.106	0.121	psi
		0.125	0.104	0.124	psi
		0.000	0.101	0.124	psi
	pressure differential - with air	0.083	0.082	0.082	psi
		0.084	0.082	0.082	psi
		0.084	0.082	0.078	psi
	liquid height	11.0	11.0	11.5	cm
		10.7	11.2	10.5	cm
		0.0	0.0	10.8	cm
calculated	avg pressure dif. - no air	0.124	0.104	0.123	psi
	avg pressure dif. - with air	0.084	0.082	0.081	psi
	avg liquid height	10.9	11.1	10.9	cm
	air fraction	0.276	0.149	0.291	-
	active volume	1205	1449	1189	ml
	retention time	54.0	64.5	52.4	sec
mass balanced	feed percent solids	0.086	0.076	0.073	by vol
	feed flow rate	22.30	22.45	22.68	ml/sec
	tailings percent solids	0.022	0.019	0.019	by vol
	tailings flow rate	4.83	5.35	5.40	ml/sec
	product percent solids	0.103	0.094	0.090	by vol
	product flow rate	17.47	17.10	17.28	ml/sec
	exp. rate constant	**4.10E+00**	**3.41E+00**	**4.24E+00**	**min^{-1}**

Misc experimental data

	Run			
	1	2	3	units
temp	46	46	48	F
pH	7.63	7.61	7.68	

Particle Size Data

particle size passing - (μm)	percent in channel - by number		
704	0.00		0.00
592	0.00		0.00
497.8	0.00		0.00
418.6	0.00		0.00
352	0.00		0.00
296	0.00		0.00
248.9	0.00		0.00
209.3	0.02		0.02
176	0.07		0.07
148	0.29		0.27
124.5	1.26		1.19
104.7	4.99		4.82
88	15.40		15.21
74	30.05		30.08
62.23	29.83		30.06
52.33	14.21		14.34
44	3.88		3.94
37	0.00		0.00
31.11	0.00		0.00
26.16	0.00		0.00
22	0.00		0.00

Model

		Run			
		1	2	3	units
additional experimental data	torque	12	11	11	in-lb
	impeller speed	1200			rpm
	contact angle	32	32	33	deg
	contact angle	29	29	32	deg
	contact angle	31	29	30	deg
	contact angle	32	28	33	deg
	contact angle	30	30	32	deg
	contact angle	30	34	33	deg
	contact angle	-	-	-	deg
	contact angle	-	-	-	deg
	surface tension	61.08	60.65	60.3	N/m
	zeta potential	-17.6			mV
calculated data	power	27.12	24.86	24.86	Watt
	avg contact angle	30.67	30.33	32.17	deg
	overall contact angle	31.06			deg
	overall surface tension	60.68			N/m
	sauter particle diameter	65.2		65.1	μm
	avg sauter part diameter	65.2			μm
	avg bub. sauter diameter	467.4			μm
	model rate constant	**3.91E+00**	**1.95E+00**	**4.05E+00**	**min^{-1}**

Date performed	3/2/2004
Test number	16

Constants

solids density	2475	kg/m3
pressure differential distance	0.0994	m
cell diameter	13.97	cm

Experimental

		Run			
		1	2	3	units
experimental data	tailings wet weight - total	117.8	117.6	123.9	g
	tailings wet tare	26.077	25.982	26.387	g
	tailings dry weight - total	26.1	31.9	35.2	g
	tailings dry tare	3.3	3.3	3.3	g
	tailings time	14.82	14.95	15.60	sec
	product wet weight - total	160.0	151.9	141.7	g
	product wet tare	25.387	25.422	25.035	g
	product dry weight - total	6.2	4.9	4.8	g
	product dry tare	3.3	3.3	3.3	g
	product time	7.61	7.03	6.61	sec
	feed wet weight - total	154.9	149.5	162.2	g
	feed wet tare	18.871	18.429	18.360	g
	feed dry weight - total	16.2	16.9	18.7	g
	feed dry tare	3.3	3.3	3.3	g
	feed time	5.65	5.44	6.00	sec
	pressure differential - no air	0.110	0.124	0.123	psi
		0.106	0.125	0.126	psi
		0.109	0.119	0.124	psi
	pressure differential - with air	0.097	0.101	0.108	psi
		0.097	0.101	0.106	psi
		0.098	0.102	0.106	psi
	liquid height	10.0	11.5	10.0	cm
		10.0	11.0	9.8	cm
		10.5	10.8	9.5	cm
calculated	avg pressure dif. - no air	0.108	0.123	0.124	psi
	avg pressure dif. - with air	0.097	0.101	0.107	psi
	avg liquid height	10.2	11.1	9.8	cm
	air fraction	0.066	0.121	0.100	-
	active volume	1456	1495	1348	ml
	retention time	65.0	66.7	60.5	sec
mass balanced	feed percent solids	0.037	0.042	0.044	by vol
	feed flow rate	22.39	22.42	22.27	ml/sec
	tailings percent solids	0.124	0.163	0.171	by vol
	tailings flow rate	5.51	5.19	5.19	ml/sec
	product percent solids	0.009	0.005	0.005	by vol
	product flow rate	16.88	17.24	17.08	ml/sec
	exp. rate constant	**4.96E-02**	**2.18E-02**	**2.43E-02**	**min^{-1}**

Misc experimental data

	Run			
	1	2	3	units
temp	44	46	46	F
pH	7.22	7.36	7.45	

Particle Size Data

particle size passing - (μm)	percent in channel - by number		
704	0.10		0.08
592	0.53		0.47
497.8	2.54		2.58
418.6	10.06		11.13
352	27.45		30.50
296	37.89		38.02
248.9	18.49		15.26
209.3	2.94		1.96
176	0.00		0.00
148	0.00		0.00
124.5	0.00		0.00
104.7	0.00		0.00
88	0.00		0.00
74	0.00		0.00
62.23	0.00		0.00
52.33	0.00		0.00
44	0.00		0.00
37	0.00		0.00
31.11	0.00		0.00
26.16	0.00		0.00
22	0.00		0.00

Model

		Run			
		1	2	3	units
additional experimental data	torque	11	11	11	in-lb
	impeller speed	1200			rpm
	contact angle	42	44	48	deg
	contact angle	42	43	44	deg
	contact angle	43	39	44	deg
	contact angle	48	42	44	deg
	contact angle	43	43	43	deg
	contact angle	-	43	45	deg
	contact angle	-	-	44	deg
	contact angle	-	-	-	deg
	surface tension	57.22	57.35	58.88	N/m
	zeta potential	-8.9			mV
calculated data	power	24.86	24.86	24.86	Watt
	avg contact angle	43.60	42.33	44.57	deg
	overall contact angle	43.50			deg
	overall surface tension	57.82			N/m
	sauter particle diameter	294.1		298.9	μm
	avg sauter part diameter	296.5			μm
	avg bub. sauter diameter	467.4			μm
	model rate constant	**1.66E-02**	**7.84E-02**	**1.73E-02**	**min^{-1}**

Date performed	3/3/2004
Test number	17

Constants

solids density	2475	kg/m3
pressure differential distance	0.0994	m
cell diameter	13.97	cm

Experimental

		Run			
		1	2	3	units
experimental data	tailings wet weight - total	103.2	120.9	97.3	g
	tailings wet tare	26.733	25.830	26.570	g
	tailings dry weight - total	5.4	6.7	5.8	g
	tailings dry tare	3.3	3.3	3.3	g
	tailings time	14.69	13.64	13.62	sec
	product wet weight - total	143.7	131.7	137.6	g
	product wet tare	26.455	26.544	25.937	g
	product dry weight - total	19.0	18.1	17.4	g
	product dry tare	3.3	3.3	3.2	g
	product time	5.96	6.13	5.82	sec
	feed wet weight - total	169.0	143.7	138.0	g
	feed wet tare	18.574	18.713	18.778	g
	feed dry weight - total	20.6	16.9	16.6	g
	feed dry tare	3.2	3.2	3.2	g
	feed time	6.06	5.11	4.90	sec
	pressure differential - no air	0.116	0.110	0.122	psi
		0.117	0.115	0.124	psi
		0.116	0.110	0.125	psi
	pressure differential - with air	0.088	0.088	0.088	psi
		0.085	0.088	0.086	psi
		0.083	0.088	0.085	psi
	liquid height	10.0	10.2	10.5	cm
		9.9	10.4	10.4	cm
		10.0	10.4	10.8	cm
calculated	avg pressure dif. - no air	0.116	0.112	0.124	psi
	avg pressure dif. - with air	0.085	0.088	0.086	psi
	avg liquid height	10.0	10.3	10.6	cm
	air fraction	0.215	0.163	0.258	-
	active volume	1199	1325	1202	ml
	retention time	51.7	58.5	52.7	sec
mass balanced	feed percent solids	0.049	0.048	0.047	by vol
	feed flow rate	23.20	22.64	22.80	ml/sec
	tailings percent solids	0.012	0.015	0.014	by vol
	tailings flow rate	5.10	6.86	5.06	ml/sec
	product percent solids	0.060	0.062	0.057	by vol
	product flow rate	18.10	15.78	17.74	ml/sec
	exp. rate constant	**4.62E+00**	**2.99E+00**	**3.49E+00**	**min^{-1}**

Misc experimental data

	Run			
	1	2	3	units
temp	42	44	46	F
pH	7.37	7.4	7.43	

Particle Size Data

particle size passing - (μm)	percent in channel - by number		
704	0.00		0.00
592	0.00		0.00
497.8	0.00		0.00
418.6	0.00		0.00
352	0.00		0.05
296	0.05		0.27
248.9	0.58		1.39
209.3	5.25		6.66
176	25.28		22.44
148	44.44		38.52
124.5	21.34		24.83
104.7	3.06		5.84
88	0.00		0.00
74	0.00		0.00
62.23	0.00		0.00
52.33	0.00		0.00
44	0.00		0.00
37	0.00		0.00
31.11	0.00		0.00
26.16	0.00		0.00
22	0.00		0.00

Model

		Run			
		1	2	3	units
additional experimental data	torque	10	10	10	in-lb
	impeller speed	1200			rpm
	contact angle	41	40	38	deg
	contact angle	39	40	36	deg
	contact angle	40	43	36	deg
	contact angle	39	41	38	deg
	contact angle	39	41	39	deg
	contact angle	42	-	38	deg
	contact angle	-	-	-	deg
	contact angle	-	-	-	deg
	surface tension	59.11	59.29	59.59	N/m
	zeta potential	-16.0			mV
calculated data	power	22.60	22.60	22.60	Watt
	avg contact angle	40.00	41.00	37.50	deg
	overall contact angle	39.50			deg
	overall surface tension	59.33			N/m
	sauter particle diameter	140.5		139.8	μm
	avg sauter part diameter	140.2			μm
	avg bub. sauter diameter	467.4			μm
	model rate constant	**5.83E+00**	**4.46E+00**	**7.51E+00**	**min^{-1}**

Date performed	3/15/2004
Test number	18

Constants

solids density	2475	kg/m3
pressure differential distance	0.0994	m
cell diameter	13.97	cm

Experimental

		Run			
		1	2	3	units
experimental data	tailings wet weight - total	111.5	97.9	100.5	g
	tailings wet tare	26.077	25.982	26.387	g
	tailings dry weight - total	6.3	6.0	5.8	g
	tailings dry tare	4.2	4.1	4.2	g
	tailings time	16.23	13.71	14.40	sec
	product wet weight - total	123.6	123.6	143.6	g
	product wet tare	25.387	25.422	25.035	g
	product dry weight - total	16.8	15.4	16.1	g
	product dry tare	4.1	4.2	4.1	g
	product time	5.25	5.05	6.40	sec
	feed wet weight - total	136.9	139.4	161.6	g
	feed wet tare	18.871	18.429	18.360	g
	feed dry weight - total	17.8	15.1	17.0	g
	feed dry tare	4.2	4.1	4.2	g
	feed time	4.76	4.97	6.04	sec
	pressure differential - no air	0.127	0.125	0.119	psi
		0.120	0.120	0.123	psi
		0.123	0.122	0.124	psi
	pressure differential - with air	0.087	0.086	0.087	psi
		0.087	0.084	0.085	psi
		0.084	0.085	0.083	psi
	liquid height	9.0	9.5	10.0	cm
		9.5	10.0	10.2	cm
		0.0	0.0	0.0	cm
calculated	avg pressure dif. - no air	0.123	0.122	0.122	psi
	avg pressure dif. - with air	0.086	0.085	0.085	psi
	avg liquid height	9.3	9.8	10.1	cm
	air fraction	0.259	0.259	0.258	-
	active volume	1050	1107	1149	ml
	retention time	46.3	47.7	51.1	sec
mass balanced	feed percent solids	0.050	0.041	0.038	by vol
	feed flow rate	22.70	23.18	22.47	ml/sec
	tailings percent solids	0.010	0.010	0.009	by vol
	tailings flow rate	5.20	5.16	5.08	ml/sec
	product percent solids	0.062	0.050	0.047	by vol
	product flow rate	17.49	18.02	17.40	ml/sec
	exp. rate constant	**6.00E+00**	**4.70E+00**	**4.80E+00**	**min^{-1}**

Misc experimental data

	Run			
	1	2	3	units
temp	46	48	48	F
pH	7.65	7.68	7.71	

Particle Size Data

particle size passing - (μm)	percent in channel - by number		
704	0.00	0.00	0.00
592	0.00	0.00	0.00
497.8	0.00	0.00	0.00
418.6	0.00	0.00	0.00
352	0.00	0.00	0.00
296	0.00	0.00	0.00
248.9	0.00	0.01	0.00
209.3	0.03	0.03	0.00
176	0.10	0.10	0.00
148	0.38	0.37	0.20
124.5	1.53	1.51	1.39
104.7	5.75	5.72	6.89
88	16.80	16.85	21.08
74	30.89	30.91	34.21
62.23	28.63	28.54	25.48
52.33	12.65	12.66	8.87
44	3.24	3.30	1.88
37	0.00	0.00	0.00
31.11	0.00	0.00	0.00
26.16	0.00	0.00	0.00
22	0.00	0.00	0.00

Model

		Run			
		1	2	3	units
additional experimental data	torque	10	10	10	in-lb
	impeller speed	1200			rpm
	contact angle	30	35	27	deg
	contact angle	29	40	31	deg
	contact angle	36	30	29	deg
	contact angle	32	36	31	deg
	contact angle	31	37	33	deg
	contact angle	-	40	-	deg
	contact angle	-	35	-	deg
	contact angle	-	-	-	deg
	surface tension	60.8	60.43	60.26	N/m
	zeta potential	-13.2			mV
calculated data	power	22.60	22.60	22.60	Watt
	avg contact angle	31.60	36.14	30.20	deg
	overall contact angle	32.65			deg
	overall surface tension	60.50			N/m
	sauter particle diameter	66.5	66.5	68.5	μm
	avg sauter part diameter	67.2			μm
	avg bub. sauter diameter	467.4			μm
	model rate constant	**6.63E+00**	**6.68E+00**	**6.66E+00**	**min^{-1}**

Date performed	2/2/2004
Test number	19-a

Constants

solids density	2475	kg/m3
pressure differential distance	0.0994	m
cell diameter	13.97	cm

Experimental

		Run			
		1	2	3	units
experimental data	tailings wet weight - total	255.7	245.5	256.2	g
	tailings wet tare	26.077	25.982	26.387	g
	tailings dry weight - total	89.7	64.5	65.7	g
	tailings dry tare	8.4	8.6	8.5	g
	tailings time	14.43	11.76	11.72	sec
	product wet weight - total	148.6	158.4	134.2	g
	product wet tare	18.412	18.308	18.102	g
	product dry weight - total	25.3	27.9	19.8	g
	product dry tare	8.5	8.8	8.9	g
	product time	15.42	22.95	22.68	sec
	feed wet weight - total	215.3	231.5	243.6	g
	feed wet tare	25.846	25.543	25.293	g
	feed dry weight - total	52.4	55.3	56.0	g
	feed dry tare	8.6	8.6	8.6	g
	feed time	7.74	8.11	9.09	sec
	pressure differential - no air	0.179	0.171	0.178	psi
		-	0.176	0.181	psi
		-	0.168	0.177	psi
	pressure differential - with air	0.169	0.159	0.160	psi
		0.157	0.162	0.160	psi
		0.161	0.157	0.158	psi
	liquid height	14.3	14.6	14.0	cm
		14.2	14.7	14.2	cm
		-	-	-	cm
calculated	avg pressure dif. - no air	0.179	0.172	0.179	psi
	avg pressure dif. - with air	0.162	0.159	0.159	psi
	avg liquid height	14.3	14.7	14.1	cm
	air fraction	0.095	0.074	0.116	-
	active volume	1977	2080	1910	ml
	retention time	96.4	96.1	89.8	sec
mass balanced	feed percent solids	0.120	0.106	0.101	by vol
	feed flow rate	20.51	21.64	21.28	ml/sec
	tailings percent solids	0.162	0.122	0.118	by vol
	tailings flow rate	12.45	16.01	16.47	ml/sec
	product percent solids	0.055	0.060	0.040	by vol
	product flow rate	8.06	5.63	4.81	ml/sec
	exp. rate constant	**8.36E-02**	**8.01E-02**	**5.14E-02**	**min^{-1}**

Misc experimental data

	Run			
	1	2	3	units
temp	46	48	48	F
pH	6.91	7.21	7.53	

Particle Size Data

particle size passing - (μm)	percent in channel - by number		
704	0.11		0.16
592	0.60		0.82
497.8	2.83		3.28
418.6	10.75		10.68
352	27.89		26.14
296	37.02		36.39
248.9	17.87		19.23
209.3	2.93		3.30
176	0.00		0.00
148	0.00		0.00
124.5	0.00		0.00
104.7	0.00		0.00
88	0.00		0.00
74	0.00		0.00
62.23	0.00		0.00
52.33	0.00		0.00
44	0.00		0.00
37	0.00		0.00
31.11	0.00		0.00
26.16	0.00		0.00
22	0.00		0.00

Model

		Run			
		1	2	3	units
additional experimental data	torque	13	12	13	in-lb
	impeller speed	1200			rpm
	contact angle	45	50	50	deg
	contact angle	48	46	49	deg
	contact angle	47	42	50	deg
	contact angle	47	48	48	deg
	contact angle	-	-	52	deg
	contact angle	-	-	46	deg
	contact angle	-	-	-	deg
	contact angle	-	-	-	deg
	surface tension	60.4	60.6	60.39	N/m
	zeta potential	-15.0			mV
calculated data	power	29.38	27.12	29.38	Watt
	avg contact angle	46.75	46.50	49.17	deg
	overall contact angle	47.47			deg
	overall surface tension	60.46			N/m
	sauter particle diameter	296.2		295.9	μm
	avg sauter part diameter	296.1			μm
	avg bub. sauter diameter	467.4			μm
	model rate constant	**2.10E+00**	**2.33E+00**	**2.24E+00**	**min^{-1}**

Date performed	2/16/2004
Test number	19-b

Constants

solids density	2475	kg/m3
pressure differential distance	0.0994	m
cell diameter	13.97	cm

Experimental

		Run			
		1	2	3	units
experimental data	tailings wet weight - total	266.8	205.2	181.7	g
	tailings wet tare	26.733	25.830	26.569	g
	tailings dry weight - total	74.9	70.3	62.4	g
	tailings dry tare	8.7	8.4	8.4	g
	tailings time	12.26	16.54	14.86	sec
	product wet weight - total	126.3	94.9	84.7	g
	product wet tare	18.860	18.683	18.741	g
	product dry weight - total	12.8	12.2	9.7	g
	product dry tare	8.3	8.3	8.2	g
	product time	18.90	8.03	6.77	sec
	feed wet weight - total	232.1	230.2	215.6	g
	feed wet tare	26.169	26.574	25.974	g
	feed dry weight - total	56.8	57.6	53.6	g
	feed dry tare	8.3	8.5	8.4	g
	feed time	8.67	8.50	8.06	sec
	pressure differential - no air	0.134	0.132	0.175	psi
		0.132	0.127	0.171	psi
		0.133	0.130	0.172	psi
	pressure differential - with air	0.117	0.107	0.100	psi
		0.114	0.106	0.127	psi
		0.115	0.108	0.127	psi
	liquid height	13.8	14.2	13.7	cm
		14.0	14.5	14.0	cm
		14.0	14.7	14.0	cm
calculated	avg pressure dif. - no air	0.133	0.130	0.173	psi
	avg pressure dif. - with air	0.115	0.107	0.118	psi
	avg liquid height	13.9	14.5	13.9	cm
	air fraction	0.104	0.125	0.300	-
	active volume	1914	1940	1492	ml
	retention time	89.7	104.6	80.8	sec
mass balanced	feed percent solids	0.107	0.104	0.099	by vol
	feed flow rate	21.33	18.54	18.47	ml/sec
	tailings percent solids	0.137	0.187	0.194	by vol
	tailings flow rate	15.90	9.22	8.94	ml/sec
	product percent solids	0.017	0.021	0.009	by vol
	product flow rate	5.44	9.31	9.52	ml/sec
	exp. rate constant	**2.16E-02**	**3.24E-02**	**1.81E-02**	**min^{-1}**

Misc experimental data

	Run			
	1	2	3	units
temp	44	44	46	F
pH	6.99	7.19	7.24	

Particle Size Data

particle size passing - (μm)	percent in channel - by number		
704	0.08		0.10
592	0.46		0.57
497.8	2.25		2.70
418.6	9.11		10.37
352	26.39		27.50
296	39.20		37.53
248.9	19.63		18.34
209.3	2.88		2.89
176	0.00		0.00
148	0.00		0.00
124.5	0.00		0.00
104.7	0.00		0.00
88	0.00		0.00
74	0.00		0.00
62.23	0.00		0.00
52.33	0.00		0.00
44	0.00		0.00
37	0.00		0.00
31.11	0.00		0.00
26.16	0.00		0.00
22	0.00		0.00

Model

		Run			
		1	2	3	units
additional experimental data	torque	13	12	13	in-lb
	impeller speed	1200			rpm
	contact angle	49	42	47	deg
	contact angle	50	44	48	deg
	contact angle	47	44	47	deg
	contact angle	49	44	48	deg
	contact angle	-	46	46	deg
	contact angle	-	-	48	deg
	contact angle	-	-	-	deg
	contact angle	-	-	-	deg
	surface tension	59.93	55.48	60.81	N/m
	zeta potential	-4.4			mV
calculated data	power	29.38	27.12	29.38	Watt
	avg contact angle	48.75	44.00	47.33	deg
	overall contact angle	46.69			deg
	overall surface tension	58.74			N/m
	sauter particle diameter	291.3		295.0	μm
	avg sauter part diameter	293.1			μm
	avg bub. sauter diameter	467.4			μm
	model rate constant	**1.63E+00**	**3.21E+00**	**4.98E+00**	**min^{-1}**

Date performed	2/3/2004
Test number	20-a

Constants

solids density	2475	kg/m3
pressure differential distance	0.0994	m
cell diameter	13.97	cm

Experimental

		Run			
		1	2	3	units
experimental data	tailings wet weight - total	197.4	240.8	202.7	g
	tailings wet tare	25.455	25.843	25.663	g
	tailings dry weight - total	32.8	38.2	31.6	g
	tailings dry tare	8.5	8.5	8.4	g
	tailings time	21.71	19.43	27.22	sec
	product wet weight - total	89.6	81.8	86.0	g
	product wet tare	18.661	18.460	18.597	g
	product dry weight - total	32.4	27.0	26.7	g
	product dry tare	8.3	8.6	8.5	g
	product time	3.39	3.15	3.29	sec
	feed wet weight - total	185.1	198.2	143.3	g
	feed wet tare	26.411	26.003	26.042	g
	feed dry weight - total	50.6	51.4	36.3	g
	feed dry tare	8.3	8.3	8.0	g
	feed time	6.29	6.77	4.92	sec
	pressure differential - no air	0.171	0.157	0.130	psi
		0.165	0.162	0.133	psi
		0.171	0.157	0.134	psi
	pressure differential - with air	0.145	0.127	0.136	psi
		0.137	0.125	0.136	psi
		0.142	0.125	0.137	psi
	liquid height	13.4	13.2	12.8	cm
		13.3	13.4	13.0	cm
		13.5	13.6	13.0	cm
calculated	avg pressure dif. - no air	0.169	0.159	0.132	psi
	avg pressure dif. - with air	0.141	0.126	0.136	psi
	avg liquid height	13.4	13.4	12.9	cm
	air fraction	0.179	0.214	-0.026	-
	active volume	1687	1615	1593	ml
	retention time	74.1	65.9	72.5	sec
mass balanced	feed percent solids	0.133	0.114	0.112	by vol
	feed flow rate	22.75	24.50	21.98	ml/sec
	tailings percent solids	0.062	0.061	0.058	by vol
	tailings flow rate	7.13	9.44	5.85	ml/sec
	product percent solids	0.166	0.147	0.131	by vol
	product flow rate	15.62	15.06	16.13	ml/sec
	exp. rate constant	**1.49E+00**	**1.34E+00**	**1.38E+00**	**min^{-1}**

Misc experimental data

	Run			
	1	2	3	units
temp	48	46	48	F
pH	7.02	7.38	7.4	

Particle Size Data

particle size passing - (μm)	percent in channel - by number		
704	0.00		0.00
592	0.00		0.00
497.8	0.00		0.00
418.6	0.00		0.00
352	0.06		0.06
296	0.29		0.28
248.9	1.46		1.45
209.3	6.79		6.67
176	22.36		21.78
148	37.92		37.37
124.5	24.89		25.61
104.7	6.23		6.78
88	0.00		0.00
74	0.00		0.00
62.23	0.00		0.00
52.33	0.00		0.00
44	0.00		0.00
37	0.00		0.00
31.11	0.00		0.00
26.16	0.00		0.00
22	0.00		0.00

Model

		Run			
		1	2	3	units
additional experimental data	torque	11	11	11	in-lb
	impeller speed	1200			rpm
	contact angle	30	39	34	deg
	contact angle	32	37	35	deg
	contact angle	31	35	33	deg
	contact angle	31	36	34	deg
	contact angle	31	37	36	deg
	contact angle	-	34	-	deg
	contact angle	-	-	-	deg
	contact angle	-	-	-	deg
	surface tension	59.22	61.4	60.61	N/m
	zeta potential	-18.4			mV
calculated data	power	24.86	24.86	24.86	Watt
	avg contact angle	31.00	36.33	34.40	deg
	overall contact angle	33.91			deg
	overall surface tension	60.41			N/m
	sauter particle diameter	139.8		139.2	μm
	avg sauter part diameter	139.5			μm
	avg bub. sauter diameter	467.4			μm
	model rate constant	**3.34E+00**	**4.06E+00**	**3.57E+00**	**min^{-1}**

Date performed	2/17/2004
Test number	20-b

Constants

solids density	2475	kg/m3
pressure differential distance	0.0994	m
cell diameter	13.97	cm

Experimental

		Run			
		1	2	3	units
experimental data	tailings wet weight - total	146.5	131.1	147.2	g
	tailings wet tare	26.077	25.982	26.387	g
	tailings dry weight - total	18.2	13.3	13.1	g
	tailings dry tare	8.2	8.2	8.2	g
	tailings time	18.62	15.33	17.82	sec
	product wet weight - total	139.8	151.0	146.7	g
	product wet tare	25.387	25.422	25.035	g
	product dry weight - total	45.4	45.7	42.3	g
	product dry tare	8.2	8.2	8.1	g
	product time	6.77	7.39	7.35	sec
	feed wet weight - total	160.9	175.4	181.9	g
	feed wet tare	18.871	18.429	18.360	g
	feed dry weight - total	46.6	49.0	47.5	g
	feed dry tare	8.2	8.2	8.2	g
	feed time	6.07	6.84	7.34	sec
	pressure differential - no air	0.137	0.118	0.118	psi
		0.132	0.119	0.124	psi
		0.131	0.117	0.125	psi
	pressure differential - with air	0.089	0.093	0.094	psi
		0.082	0.088	0.093	psi
		0.081	0.087	0.095	psi
	liquid height	10.0	10.2	10.4	cm
		9.5	10.3	10.5	cm
		10.0	10.3	10.6	cm
calculated	avg pressure dif. - no air	0.133	0.118	0.122	psi
	avg pressure dif. - with air	0.084	0.089	0.094	psi
	avg liquid height	9.8	10.3	10.5	cm
	air fraction	0.331	0.196	0.195	-
	active volume	1009	1265	1295	ml
	retention time	51.1	62.5	64.9	sec
mass balanced	feed percent solids	0.126	0.114	0.104	by vol
	feed flow rate	19.74	20.24	19.97	ml/sec
	tailings percent solids	0.035	0.020	0.017	by vol
	tailings flow rate	6.10	6.42	6.37	ml/sec
	product percent solids	0.167	0.157	0.145	by vol
	product flow rate	13.65	13.82	13.59	ml/sec
	exp. rate constant	**3.83E+00**	**5.03E+00**	**5.42E+00**	**min^{-1}**

Misc experimental data

	Run			
	1	2	3	units
temp	41	42	42	F
pH	6.67	6.73	6.87	

Particle Size Data

particle size passing - (μm)	percent in channel - by number		
704	0.00		0.00
592	0.00		0.00
497.8	0.00		0.00
418.6	0.00		0.00
352	0.05		0.05
296	0.26		0.24
248.9	1.35		1.26
209.3	6.56		6.09
176	22.13		21.14
148	38.04		38.10
124.5	25.28		26.41
104.7	6.33		6.71
88	0.00		0.00
74	0.00		0.00
62.23	0.00		0.00
52.33	0.00		0.00
44	0.00		0.00
37	0.00		0.00
31.11	0.00		0.00
26.16	0.00		0.00
22	0.00		0.00

Model

		Run			
		1	2	3	units
additional experimental data	torque	11	11	11	in-lb
	impeller speed	1200			rpm
	contact angle	37	35	37	deg
	contact angle	35	35	36	deg
	contact angle	34	33	34	deg
	contact angle	36	34	36	deg
	contact angle	-	35	37	deg
	contact angle	-	-	-	deg
	contact angle	-	-	-	deg
	contact angle	-	-	-	deg
	surface tension	60.11	60.34	61.09	N/m
	zeta potential	-20.3			mV
calculated data	power	24.86	24.86	24.86	Watt
	avg contact angle	35.50	34.40	36.00	deg
	overall contact angle	35.30			deg
	overall surface tension	60.51			N/m
	sauter particle diameter	139.4		138.3	μm
	avg sauter part diameter	138.8			μm
	avg bub. sauter diameter	467.4			μm
	model rate constant	**5.86E+00**	**3.41E+00**	**3.47E+00**	**min^{-1}**

Date performed	2/18/2004
Test number	21

Constants

solids density	2475	kg/m3
pressure differential distance	0.0994	m
cell diameter	13.97	cm

Experimental

		Run			
		1	2	3	units
experimental data	tailings wet weight - total	75.0	154.5	119.1	g
	tailings wet tare	25.455	25.843	25.663	g
	tailings dry weight - total	10.8	16.1	14.1	g
	tailings dry tare	8.3	8.3	8.2	g
	tailings time	27.22	20.72	12.58	sec
	product wet weight - total	139.7	152.0	136.3	g
	product wet tare	26.396	25.840	25.814	g
	product dry weight - total	43.0	47.2	44.3	g
	product dry tare	8.2	8.2	8.3	g
	product time	5.82	7.70	7.36	sec
	feed wet weight - total	137.8	139.6	124.5	g
	feed wet tare	18.676	18.623	18.825	g
	feed dry weight - total	39.9	39.5	34.5	g
	feed dry tare	8.2	8.2	8.1	g
	feed time	5.37	5.81	4.71	sec
	pressure differential - no air	0.124	0.124	0.113	psi
		0.125	0.124	0.114	psi
		0.127	0.126	0.112	psi
	pressure differential - with air	0.093	0.110	0.094	psi
		0.095	0.109	0.095	psi
		0.096	0.110	0.091	psi
	liquid height	9.0	9.0	8.5	cm
		0.0	0.0	9.0	cm
		0.0	0.0	0.0	cm
calculated	avg pressure dif. - no air	0.125	0.125	0.113	psi
	avg pressure dif. - with air	0.095	0.110	0.093	psi
	avg liquid height	9.0	9.0	8.8	cm
	air fraction	0.210	0.102	0.134	-
	active volume	1090	1239	1162	ml
	retention time	60.4	66.3	60.5	sec
mass balanced	feed percent solids	0.133	0.118	0.115	by vol
	feed flow rate	18.06	18.68	19.22	ml/sec
	tailings percent solids	0.022	0.026	0.027	by vol
	tailings flow rate	1.78	5.79	7.08	ml/sec
	product percent solids	0.145	0.159	0.167	by vol
	product flow rate	16.28	12.89	12.14	ml/sec
	exp. rate constant	**6.02E+00**	**3.88E+00**	**3.95E+00**	**min^{-1}**

Misc experimental data

	Run			
	1	2	3	units
temp	41	42	42	F
pH	7.27	7.31	7.35	

Particle Size Data

particle size passing - (μm)	percent in channel - by number		
704	0.00	0.00	0.00
592	0.00	0.00	0.00
497.8	0.00	0.00	0.00
418.6	0.00	0.00	0.00
352	0.00	0.00	0.00
296	0.00	0.00	0.00
248.9	0.00	0.00	0.00
209.3	0.01	0.00	0.02
176	0.05	0.04	0.07
148	0.18	0.17	0.30
124.5	0.74	0.77	1.28
104.7	3.04	3.36	5.03
88	10.41	11.83	15.23
74	24.26	27.09	29.27
62.23	31.10	32.30	29.37
52.33	20.23	18.51	14.84
44	7.57	5.93	4.59
37	2.41	0.00	0.00
31.11	0.00	0.00	0.00
26.16	0.00	0.00	0.00
22	0.00	0.00	0.00

Model

		Run			
		1	2	3	units
additional experimental data	torque	11	11	11	in-lb
	impeller speed	1200			rpm
	contact angle	34	37	36	deg
	contact angle	37	38	37	deg
	contact angle	39	39	37	deg
	contact angle	37	42	38	deg
	contact angle	40	37	38	deg
	contact angle	-	-	40	deg
	contact angle	-	-	-	deg
	contact angle	-	-	-	deg
	surface tension	60.26	60.3	61.04	N/m
	zeta potential	-12.5			mV
calculated data	power	24.86	24.86	24.86	Watt
	avg contact angle	37.40	38.60	37.67	deg
	overall contact angle	37.89			deg
	overall surface tension	60.53			N/m
	sauter particle diameter	60.5	62.3	65.0	μm
	avg sauter part diameter	62.6			μm
	avg bub. sauter diameter	467.4			μm
	model rate constant	**1.06E+01**	**4.97E+00**	**6.58E+00**	**min^{-1}**

Appendix 4: Studies of Froth Stability and Model Development

FINAL TECHNICAL REPORT

Contract Title and Number:	Period of Performance:
Establishment of the Center for Advanced Separation Technologies (DE-FC26-01NT41607)	Starting Date: 9/17/01 Ending Date: 3/31/05

Sub-Recipient Project Title: Studies of Froth Stability and Model Development	Report Information: Type: Final Number: Period: 9/17/01-3/31/05
Principal Investigators: Roe-Hoan Yoon	Date: Code: VA002-FINAL
Contact Address: 146 Holden Hall Virginia Polytechnic Institute & State University Blacksburg, VA 24061	Contact Information: Phone: (540)231-4508 Fax: (540)231-3948 E-Mail: cast@vt.edu
Subcontractor Address: No subcontracts issued.	Subcontractor Information: Phone: Fax: E-Mail:

DISCLAIMER

ABSTRACT

This study focuses on developing a methodology to identify the basic factors affecting the stability of foams and froths in flotation. We investigate the stability of aqueous thin films between air bubbles, and then compare film stability to foam stability. The thin film studies indicate that a hydrophobic attractive force exists to destabilize films between air bubbles in dilute aqueous solutions in flotation processes. To better understand the origin of the hydrophobic force in aqueous films between two hydrophobic substrates, we have studied the effects of surfactant type and concentration, and ionic strength on the surface forces in foam films. We have also studied the effect of film elasticity on foam stability. The results show that film elasticities in flotation may be too small to affect foam stability.

TABLE OF CONTENTS

LIST OF GRAPHICAL MATERIALS

EXECUTIVE SUMMARY

Froth plays an important role in flotation as it determines the final grade of the product and the maximum carrying capacity (or throughput). It is known that flotation rate increases with decreasing bubble size. It is, therefore, proposed to study the various factors affecting the stability of flotation froths.

Current literature suggests that the coalescence of air bubble may be affected by the elasticity of thin aqueous films between them. Elasticity is a measure of the property of returning to an initial form or state following deformation. It is sometimes referred to the "self-healing" capacity against external disturbance. To peer into the effect of film elasticity on foam stability at low surfactant concentrations, particularly at the concentrations where some nonionic surfactants are used for chemical separation processes of coal and minerals, we have developed an analytical model to calculate film elasticity from surface tension. Compared to other models, our model has no additional restrictions and no oversimplifications in its derivation, and it is applicable to a broad surfactant concentration range. By using our model, we have found that the film elasticities at very low surfactant concentrations are nearly unchanged. It is, therefore, suggested that foam stability in flotation may *not* be controlled by film elasticity.

Hydrophobic particles suspended in water attract with each other due to forces that are larger than the van der Waals force, a process generally referred to as hydrophobic interaction. Recent studies showed that air bubbles may be hydrophobic and, hence, attract with each other in water, which may be a driving force for bubble coalescence and foam collapse. In the present work, the thin film pressure balance (TFPB) technique of Scheludko-Exerowa type (1959) was used to determine the surface forces acting in foam films stabilized by sodium dodecylsulfate (SDS) and various frothers, such as pentanol and methylisobutyl carbinol (MIBC). The contribution from hydrophobic force to film pressure was estimated by subtracting the electrostatic double-layer and van der Waals forces from the total force (or pressure) measured. For the bubbles stabilized by the ionic surfactant (SDS), the double-layer forces were calculated using the adsorption densities of the surfactants and the counter ions at the air/water interface, while the van der Waals forces were calculated using the Hamaker constants from literature. In the presence of a nonioinic surfactant, for which it is difficult to evaluate the surface potentials, we measure the equilibrium film thickness to qualitatively evaluate the contributions from the hydrophobic force. The results obtained in the present work showed that the hydrophobic force reaches a maximum in the absence of surfactant, and that it decreases with increasing surfactant concentration. Further, the results correlated well with the stabilities of the three-dimensional foams. We have also studied the effect of pH on the stability of foams in the presence of pentanol. The results show that foam stability increases with increasing pH. The methodology of quantifying surface forces and film elasticity to elucidate foam stability is expected to be useful for characterizing various frothers used in flotation.

INTRODUCTION

Better understanding of the mechanisms involved in the stability of bubbles and foams is of crucial importance in many scientific and technological fields. In flotation, for example, bubbles laden with hydrophobic particles rise to the surface of a pulp, forming a three-phase froth, which is subsequently removed mechanically or by displacement. The importance in controlling the froth stability in flotation is widely recognized in recent years (Neethling and Ciliers, 2003; Ata *et al.*, 2003; Mathe *et al.*, 1998).

Froth is a three-phase foam in which particles are dispersed, and its stability is largely dependent on the stability of the foam. Foam is a dispersion of gas bubbles in a liquid. When the gas fraction is high, the bubbles contact with each other and deform, creating lamellae and Plateau boarders between the bubbles in contact. The large surface area of the bubbles (or lamellae) in a foam represents high surface free energy, which makes foams thermodynamically unstable. Various surfactants are used to produce and stabilize aqueous foams. Surfactant adsorption at the air/water interface lowers the energy of the system, which in turn reduces the energy required to produce foam and increases thermodynamic stability. When using an ionic surfactant, the surfactant adsorption also increases kinetic stability by increasing the electrostatic repulsion between the two air/water interfaces of a lamella (or foam film) and, thereby, retards film thinning. As a foam film thins further, it undergoes either a spontaneous rupture or reaches a final equilibrium state.

Foam stability is largely determined by the disjoining pressure of the thin liquid films between air bubbles in contact. A positive pressure stabilizes the foam, while negative pressure destabilizes it. In general, the positive disjoining pressure arises from repulsive double-layer force, while the negative pressure arises from attractive van der Waals forces and possibly from hydrophobic force (Tchaliovska *et al*., 1994; Yoon and Aksoy, 1999; Angarska *et al.*, 2004).

In the present work, the thin film pressure balance (TFPB) technique was used to measure film thickness and disjoining pressure isotherm for single foam films stabilized by an ionic surfactant, i.e., sodium dodecyl sulfate (SDS). The contribution from hydrophobic force to film pressure was estimated by subtracting the electrostatic double-layer and van der Waals forces from the total force (or pressure) measured. For the bubbles stabilized by the ionic surfactant, the double-layer forces were calculated using the adsorption densities of the surfactants and the counter ions at the air/water interface, while the van der Waals forces were calculated using the Hamaker constants from literature. In the presence of the nonioinic surfactants, for which it is difficult to evaluate the surface potentials, we measure the equilibrium film thickness to qualitatively evaluate the contributions from the hydrophobic force. The stability of three-dimensional foams/froths was studied by the shake tests and the pressure decay method. The main goal of this work is to explain the stability of foams and froths in view of surface forces in foam films. In a more comprehensive manner, however, we have expanded our research to the effect of film elasticity on foam stability.

EXPERIMENTAL

Materials

Specially pure sodium dodecyl sulfate (SDS) was obtained from BDH and recrystallized from ethanol. Its surface tension isotherm showed no minimum near cmc, indicating that the surfactant has no significant impurities. Methyl isobutyl carbinol, MIBC (99%) from Research Chemicals Ltd., and n-pentanol from Sigma Chemical Co., were used as received. A high-purity sodium chloride (99.99%) from Alfa Aesar was used as an electrolyte. All the solutions were prepared using double-distilled and deionized water with a conductivity of 18.2 $M\Omega cm^{-1}$.

Surface Tension

The surface tensions were determined by the pendant drop method, utilizing a surface tension/contact angle meter, FTÅ 125, from First Ten Ångstroms.

Film Thickness and Disjoining Pressure

The TFPB technique was used to measure the rate of film thinning in a Scheludko cell (Scheludko and Exerowa, 1959; Scheludko, 1967; Exerowa and Kruglyakov, 1998). The inner radius of the film holder (r_c) was 2.0 mm. Following the recommendation by Exerowa *et al.* (1979), the inner wall of the film holder was scratched with a sharpening stone to improve wettability. A PC-based data acquisition system was used to record the intensities of the reflected lights, from which film thicknesses were obtained using the microinterferometric technique (Scheludko, 1967). We used a rather strong surfactant, SDS, to obtain very small foam films, which may be deemed as tangentially immobile (Exerowa and Kruglyakov, 1998). In the present work, the film radii (R_f) were controlled within the 0.060-0.070 mm range. On the other hand, according to Radoev *et al*.(1983) the inhomogeneity of film thickness across the film (H_{max}-H_{min}) approaches zero when film radius is below 0.1 mm. These conditions were necessary to minimize the influence from hydrodynamic or thermal fluctuations.

The disjoining pressure isotherms were probed by measuring the equilibrium thickness of a film under varying gas pressure in the TFPB vessel, in which a film holder was placed. Two types of film holders were used. One is the Scheludko cells with 1.0 and 2.0 mm radii, which were used to measure the disjoining pressures below 150 Pa. The other is a bike-wheel microcell (Cascão Pereira *et al*., 2001) with a hole diameter of 0.75 mm, which was used to measure the disjoining pressure above 150 Pa. The bike-wheel film holder is reusable, has a uniform liquid drainage inside, and exhibits an air/water entry pressure of about 10 KPa. A nanomover was used to drive a 20 ml gas-tight syringe and change the gas pressure in the vessel.

Foam stability

The stability of three-dimensional foams was measured by the shake tests (Waltermo *et al*., 1996). The tests were conducted using 50 ml volumetric flasks, each containing 25 ml of a surfactant solution. In each test, a flask was hand-shaken 20 times at a fixed frequency and then left to stand for observation. After a period of time, a clear water surface began to appear at the center of the foam. As the time elapses, the clear surface expanded toward the wall of the flask, forming a ring of bubbles, which subsequently broke into clusters of bubbles. The size of clusters was reduced with time, some of which eventually becoming isolated bubbles. The time it took until only the isolated bubbles became visible was taken as a measure of foam stability.

The pressure decay method (PDM) was used to assess the stability of three-dimensional foams/froths in a more reproducible manner. The principle of this method is based on monitoring the increase in pressure in a froth chamber when bubbles rupture. In a closed foam column, the pressure inside rises as bubbles collapse as a result of bursting, coalescence, and/or diffusion. The change in pressure (ΔP) is directly related to the decrease in the bubble surface area (ΔA) as follows (Nishioka and Ross, 1981):

$$3V \cdot \Delta P + 2\gamma \cdot \Delta A = 0 \qquad [1]$$

where V is the total volume of the foam and the vapor space external to the foam, and γ is the surface tension.

A dimensionless fractional interfacial area at any given time t during foam decay was calculated by using the equation (Yu and Damodaran, 1991),

$$A / A_0 = (\Delta P_\infty - \Delta P_t) / \Delta P_\infty \qquad [2]$$

where A and A_0 are the instant and initial interfacial area of the foam, respectively, ΔP_t and ΔP_∞ are the instant and the final net pressure change, respectively. The rate of decrease in A/A_0 indicates the rate of collapse of the foam, thus the foam stability.

Similar to the device described by Murray and Liang (1999), a reference chamber identical to the sample chamber was used to minimize the effect of temperature fluctuation on the differential pressure measurements. Nitrogen gas saturated with water was used to produce the foam, with a constant flow rate of 0.6 liter per minute. Nitrogen was bubbled through the sample solution via 12 stainless steel needles (inner diameter 0.1 mm) for 30±1 seconds before valves were closed and the pressure difference between the sample and reference chambers was subsequently monitored.

RESULTS AND DISCUSSION

Surfactant- free

Preliminary TFPB experiments were conducted at the Max Planck Institute of Colloids and Interfaces at Golm, Germany. Horizontal thin films were formed using Scheludko cells with inner radii of 1.0 and 2.0 mm. The results showed that thin films made from pure water are unstable; rupture occurs instantaneously. It is feasible, however, to make meta-stable thin films at low concentrations of an inorganic electrolyte (*e.g.*, from 10^{-6} to $5x10^{-5}$ M NaCl) in the absence of any surfactant. When the NaCl concentration is increased further, the films become unstable. Figure 1 shows the lifetimes of films, formed using a Scheludko cell with an inner radius of 1.0 mm. As seen, the lifetimes decrease with increasing NaCl concentration from 10^{-6} to 0.1 M. The decrease in the film lifetime at high NaCl concentration is mostly likely related with the decrease in electrostatic disjoining pressure as a result of double-layer compression.

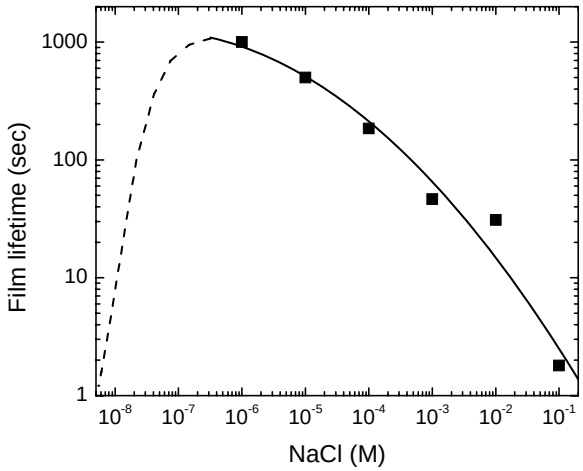

Figure 1. Effect of the NaCl concentration on the lifetime of thin films formed in a Scheludko cell with inner radius of 1.0 mm. The dotted line is hypothesized on the basis of the observation that the lifetime of a thin film formed from pure water is less than 1 second.

Ionic Surfactants

Figure 2 shows the surface tension isotherms for the SDS solutions at various concentrations of NaCl. As predicted by the Gouy-Chapman theory, added salt systematically decreases surface tension by promoting surfactant adsorption since salt can decrease the free energy of forming a charged monolayer with increasing ionic strength (Persson et al. 2003).

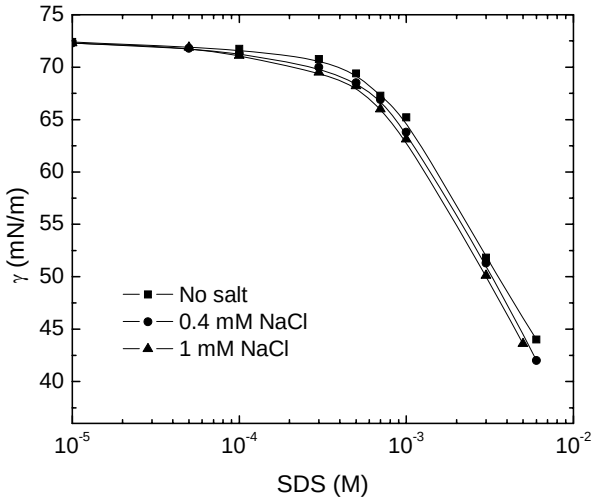

Figure 2. Surface tensions of SDS solutions in presence and absence of NaCl.

The double-layer potential (ψ_s) was calculated by first calculating the adsorption density (Γ_s) of the ionic surfactant at the air/water interface, which in turn was used to calculate the *apparent* surface potential (ψ_0) using the Gouy-Chapman theory. The *apparent* surface potential was then corrected for the adsorption of counter ions at the air/water interface using a counter-ion binding model (Wang and Yoon, 2004):

$$\frac{\delta}{\varepsilon_0 \varepsilon_s}\sqrt{8kT\varepsilon_0\varepsilon_r n_0}\sinh\left(\frac{ze\psi_s}{2kT}\right)+\psi_s-\psi_0=0 \qquad [3]$$

where δ is the distance between the polar head of a surfactant and the counter ion in the Stern layer, ε_s the local dielectric constant in the Stern layer, ε_0 and ε_r the permittivity of vacuum and the dielectric constant of water, respectively, k the Boltzmann's constant, T the absolute temperature, z the ionic valency, e the electronic charge, and n_0 is the number density of the counter ions in solution. This relation can be used to obtain the values of ψ_s from ψ_0. The *apparent* surface potential (ψ_0) can be calculated from Γ_s, the surface excess of the surfactant ions (DS^-) using the method reported by Tchaliovska *et al*. (1994) and Yoon and Aksoy (1999), assuming that SDS molecules are fully dissociated at the interface.

The double-layer potential (ψ_s) at the air/water interface were calculated using Eq. [3] where T=25°C, $\varepsilon_s = 32$ (Adamson, 1990), and δ=0.5 nm (Wang and Yoon, 2004). The results are given in Figure 3. As shown, the Stern potentials (ψ_s) decreased systematically with increasing NaCl concentration, mainly due to the increase in the ionic strength.

At low concentrations of NaCl, where SDS concentration became higher than the fixed NaCl concentrations, the three curves tend to overlap with each other. This can be attributed to the fact that the ionic strengths employed in the three sets of experiments were close to each other at relatively high SDS concentrations. Likewise, the sharp decrease in ψ_s above 10^{-3} M SDS can be attributed to the increase in ionic strength (Kralchevsky *et al*. 1999). At 0.3 M NaCl, the increase in SDS concentration has little impact on the ionic strength; therefore, the magnitude of the Stern potential increased monotonically with increasing SDS concentration due to surfactant ion adsorption.

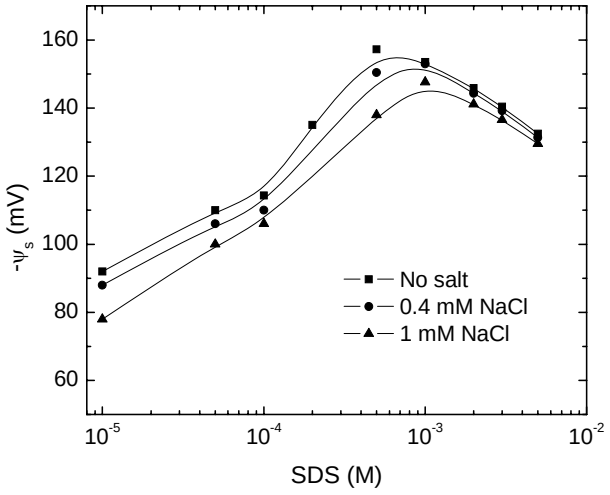

Figure 3. The Stern potential at the air-water interface as calculated using the counterion binding model (Eq.[1]).

Figure 4 shows the equilibrium film thicknesses (H_e) measured at varying SDS concentrations both in the presence and absence of NaCl. As shown, H_e decreased sharply with increasing electrolyte concentration due to double layer compression. Note, however, that H_e increased slightly as the SDS concentration increased from 10^{-6} to 4×10^{-6} M in the absence of NaCl. Likewise, H_e increased slightly as SDS concentration increased in the presence of NaCl. These increases were observed only at low surfactant concentrations before ionic strength became an overriding factor. This phenomenon may possibly be caused by a decrease in hydrophobic force with increasing SDS concentration. The presence of an attractive hydrophobic force should cause H_e to decrease. As will be shown later, the hydrophobic force decreases with increasing SDS concentration, which should cause H_e to increase.

From the data presented heretofore, we can estimate the contributions from the hydrophobic force in the same manner as described by Yoon and Aksoy (1999). When using the TFPB technique to measure the thickness of a film, the disjoining pressure of a soap film should be equal to the capillary pressure (P_c) at equilibrium. Thus,

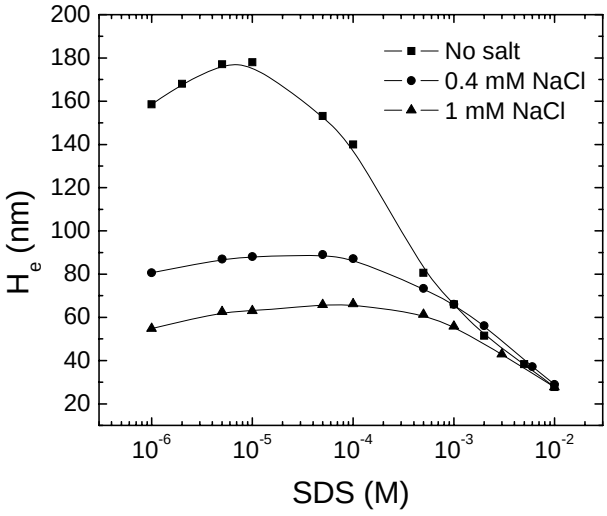

Figure 4. Equilibrium film thicknesses as a function of SDS concentration at 0, 0.4 and 1 mM NaCl; pH 5.7-6.0; and 25±0.1°C.

$$\Pi = P_c \ , \qquad [4]$$

where P_c is the capillary pressure at the meniscus of a horizontal film (Scheludko, 1967; Exerowa and Kruglyakov, 1998), given by

$$P_c = \frac{2\gamma}{R_c} \ , \qquad [5]$$

where γ is surface tension, and R_c is the inner radius of the capillary tube holding a foam film. By using a film holder with R_c = 2 mm, the value of P_c and hence Π in units of N/m^2 should be numerically equal to the surface tension in units of mN/m.

According to the DLVO theory, the disjoining pressure in a soap film can be expressed as the sum of the double-layer force (Π_{el}) and van der Waals force (Π_{vw}):

$$\Pi = \Pi_{el} + \Pi_{vw} \qquad [6]$$

where the contribution from the double-layer force is usually given by,

$$\Pi_{el} = 64 C_{el} RT \tanh^2\left(\frac{ze\psi_s}{4kT}\right)\exp(-\kappa H), \qquad [7]$$

and the contribution from the van der Waals force is given by,

$$\Pi_{vw} = -\frac{A_{232}}{6\pi H^3}. \qquad [8]$$

In Eq. [7], C_{el} is electrolyte concentration, R the gas constant, κ the inverse Debye length, and H is the distance between two charged surfaces (film thickness). In Eq. [8], A_{232} is the Hamaker constant for the air **2** in water **3**, which is usually in the order of 10^{-20} J.

As discussed in the forgoing section, hydrophobic force may play a role in foam films, in which case Eq. [6] may be extended as follows:

$$\Pi = \Pi_{el} + \Pi_{vw} + \Pi_{hb} \qquad [9]$$

to include contributions from hydrophobic force (Π_{hb}), which may be expressed as a power law (Claesson *et al.*, 1986; Rabinovich and Derjaguin, 1988; Yoon and Aksoy, 1999):

$$\Pi_{hb} = -\frac{K_{232}}{6\pi H^3} \qquad [10]$$

where K_{232} is a hydrophobic force constant. An advantage of using Eq. [10] rather than an exponential form (Israelachvil and Pashley, 1982; Tsao *et al.*, 1991; Eriksson *et al.*, 1989) is that it is of the same form as the van der Waals force (Eq. [8]). This will allow the magnitudes of the hydrophobic force to be compared directly with those of the van der Waals force by means of the two force constants, *i.e.*, K_{232} and A_{232}.

Substituting Eqs. [5, 7-9] into Eq. [4], one obtains,

$$64C_{el}RT\tanh^2\left(\frac{ze\psi_s}{4kT}\right)\exp(-\kappa H_e) - \frac{A_{232}}{6\pi H_e^3} - \frac{K_{232}}{6\pi H_e^3} - \frac{2\gamma}{R_c} = 0, \qquad [11]$$

in which H_e is the equilibrium thickness.

Eq. [11] can be solved for K_{232} using the values of γ presented in Figure 2, ψ_s illustrated in Figure 3, H_e shown in Figure 4 and the Hamaker constant (A_{232}) from literature. Israelachvili (1992), for example, gave the value of A_{232}=3.7x10^{-20} J for two air phases interacting across water.

Figure 5 shows the K_{232} values obtained using Eq. [11] for the SDS-stabilized films. In general, hydrophobic force decreases with increasing SDS and NaCl concentrations. Thus, air bubbles appear to be most hydrophobic in pure water. As the SDS concentration increased, K_{232} decreased steadily. Note that at 5x10^{-3} M SDS and above, K_{232} became negative, indicating possibly the appearance of a repulsive force. This force may arise from the hydrated counterions adsorbed on the polar heads of the DS^- ions.

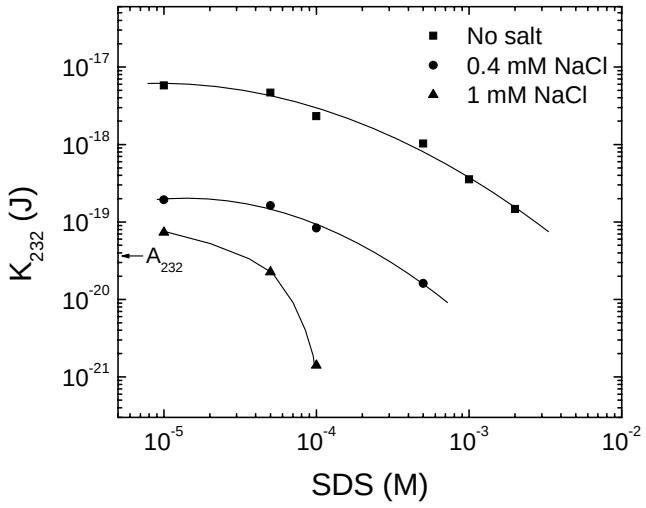

Figure 5. K_{232} of Eq. [11] as a function of SDS concentration at 0, 0.4 and 1 mM NaCl.

By extrapolating the K_{232} vs. SDS concentration plots shown in Figure 5 to the lower concentration region, one can estimate the magnitude of K_{232} in the absence of surfactant, and find that the hydrophobic force constant is larger than A_{232} by more than two-orders of magnitude. This finding is consistent with a thermodynamic consideration based on the changes in interfacial tensions at the air/water interface, which may be used as a measure of hydrophobicity. In the absence of surfactant, the interfacial tension is the largest (72.6 mN/m) and hence air/water interface should be most hydrophobic. It decreases with increasing surfactant concentration, indicating a decrease in hydrophobicity. In this regard, an air bubble in water is most hydrophobic in pristine water, and becomes less hydrophobic with increasing surfactant concentration. Thus, the role of surfactant is to dampen the hydrophobicity of air bubbles, and to dampen the hydrophobic force.

One should note here that at low surfactant concentrations, the choice of A_{232} does not make a big difference in the calculation of K_{232} using Eq. [11] because the latter is much larger than the former. On the other hand, the Stern potentials calculated using Eq. [1] is comparable to those obtained using other counter-ion binding models (Kalinin and Radke, 1996; Kralchevsky *et al.*, 1999; Warszynski *et al.*, 1998). It has been shown recently that the surface charge densities calculated using a counter-ion binding model are close to those measured using a film conductance technique (Yaros *et al.*, 2003).

Although it is possible to determine K_{232} from equilibrium film thickness measurements, as shown in the foregoing paragraph, its accuracy depends critically on the validity of double-layer potential (ψ_s). Unfortunately, there are no reliable methods of directly measuring ψ_s at the air-water interface. Thus, K_{232} by itself may not serve as a direct evidence for the existence of the long-range hydrophobic force. As suggested by Tchaliovska *et al.,* (1994), there is a need to measure surface forces (or disjoining pressures) as a function

of film thickness (H), *i.e.*, to obtain disjoining pressure isotherms. A challenge, however, is that it is difficult to measure disjoining pressures at low surfactant concentrations (due to instability) where hydrophobic forces are discernable. This problem can be minimized by increasing the film stability by adding a small amount of an inorganic electrolyte. Further, the use of a bike-wheel film holder (Cascão Pereira *et al.*, 2001) may stabilize the films during disjoining pressure measurement using the TFPB technique.

Figure 6 shows the disjoining pressure isotherms for the thin aqueous films stabilized in the presence of 10^{-4} M SDS and varying concentrations of NaCl. A bike-wheel film holder, with the air/water entry pressure of approximately 10 kPa, was used to measure the disjoining pressures above 150 Pa, while the lower pressures were measured using the Scheludko cells with 1.0 and 2.0 mm radii. In the absence of NaCl, the measured disjoining pressure isotherm (squares) deviates significantly from the DLVO theory (Eq. [6]) (dotted line) due to the presence of the hydrophobic force. The experimental data can be fitted to the extended DLVO theory (solid line, Eq. [9]), with ψ_s = -114.3 mV, $A_{232} = 3.7\text{x}10^{-20}$ J, $K_{232} = 2.33\times10^{-18}$ J, and κ^{-1} = 30.4 nm. The DLVO curve was obtained using the same set of parameters except that K_{232} was set to be zero. The value of ψ_s was obtained using the counter-ion binding model (Wang and Yoon, 2004), and the value of K_{232} that was used to fit the experimental data was from Figure 4. That the K_{232} value obtained from one method (equilibrium film thickness measurement under one capillary pressure) can be used to fit the experimental data (disjoining pressure isotherm) obtained using a different method is significant.

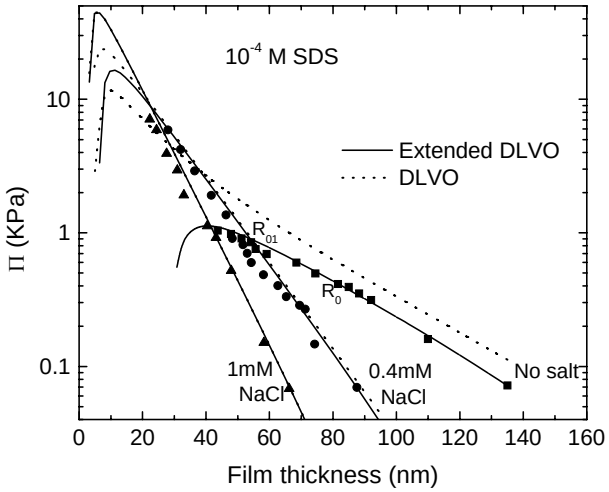

Figure 6. Disjoining pressure isotherms obtained in 10^{-4} M SDS solutions at different NaCl additions.

The isotherm obtained at 10^{-4} M SDS and in the absence of NaCl shows that the film ruptures at H = 43 nm and Π = 1.1 kPa. It should be noted here that this isotherm is the most typical of the many duplicate isotherms. In some cases, the rupture occurs at larger thicknesses and lower pressures. The lowest rupture pressure recorded is denoted as R_0 on

the isotherm. The measured rupture thicknesses are much larger than predicted by the DLVO theory as shown. Also, the measured disjoining pressures were considerably lower than predicted by the theory, indicating the presence of hydrophobic force. Furthermore, the DLVO theory predicted the primary maximum to occur at 15 nm, while it was observed at 40 nm in experiment. That the experiment agrees well with the primary maximum predicted by the extended DLVO theory indicates the presence of a strong attractive force not considered in the DLVO theory.

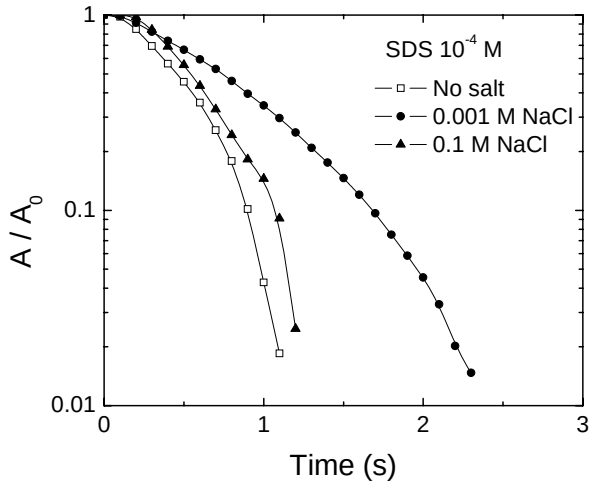

Figure 7. Surface area decay of SDS foams containing various concentrations of NaCl.

It may be of interest to note here that these deviations from the DLVO theory are much larger than observed in the surface force measurements conducted with the mica surfaces coated with dodecylamonium hydrochloride (Yoon and Ravishankar, 1996). Furthermore, the experimental disjoining pressure isotherm begins to deviate from the DLVO theory at much larger separations (H) than observed in the force measurements conducted between macroscopic solid surfaces. These findings suggest that the hydrophobic forces operating in soap films are much longer-ranged than observed with the amine-coated mica surfaces.

Note in Figure 6 that the disjoining pressure isotherms deviate progressively less from the DLVO theory with increasing NaCl concentration. The isotherm obtained at 10^{-4} M SDS and 0.4 mM NaCl shows that the film ruptures at 6.0 kPa. In repeat measurements conducted at the same NaCl and SDS concentrations, the film ruptures at a pressure as low as 0.9 kPa, as indicated by R_{01}. At 1 mM NaCl, no rupture occurs at a pressure as high as 8.5 kPa, which is the highest pressure attainable with the apparatus used for the measurements. With a better instrument, it may be possible to observe films rupturing at a pressure predicted by the DLVO theory. It seems that at 1 mM NaCl the classical DLVO theory can perfectly predict the disjoining pressure isotherm obtained, indicating that hydrophobic force disappears completely at such a high electrolyte concentration.

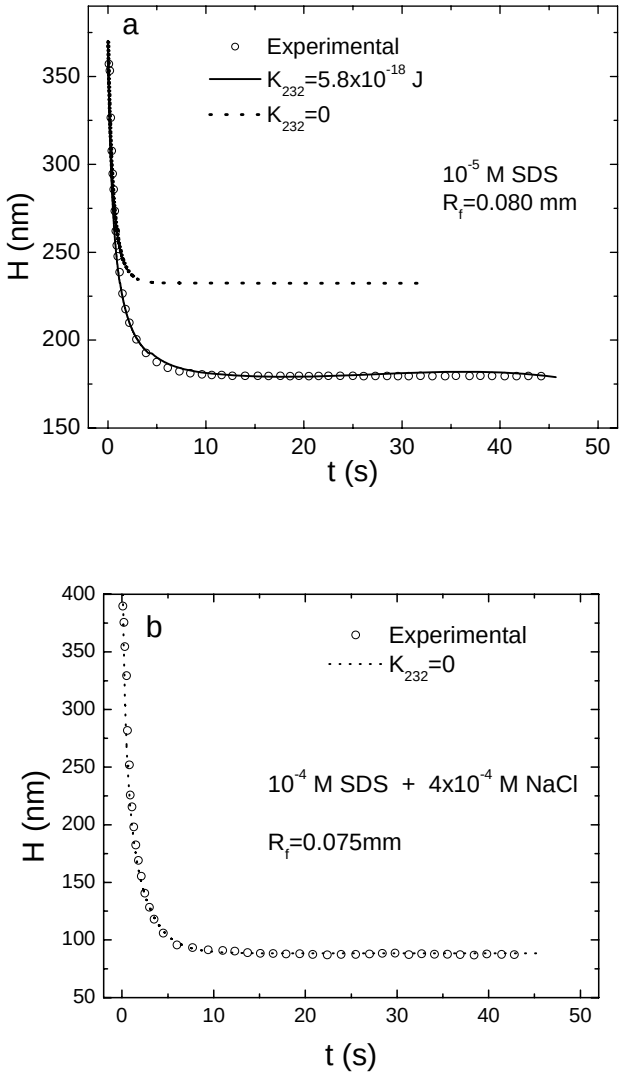

Figure 8. Kinetics of film thinning at a) 10^{-5} M SDS; b) 10^{-4} M SDS and 4×10^{-4} M NaCl. The solid line represents the Reynolds equation (Eq.[12]) with the extended-DLVO theory, while the dotted line represents the Reynolds equation with the DLVO theory (Wang and Yoon, 2005).

The isotherms given in this figure show the classical behavior of colloidal systems; the films become thinner with increasing electrolyte concentration, which is of course due to double-layer compression. As the NaCl concentration is increased from 0, 0.4 and 1 mM, the Debye length decreases from 30.4, 13.6 and 9.2 nm, respectively.

From the disjoining pressure isotherm (Figure 6), it would be natural to think that foam stability is related to the rupture pressure of foam films. Foam stability is frequently measured by simple shaking tests. As the NaCl concentration was increased from 0, 0.4 and 1

mM NaCl, τ^I increased from 32, 89, and 162 s, respectively. In contrast, K_{232} values decreased remarkably with increasing NaCl concentration. Thus, it is our belief that the increase in foam stability with increasing NaCl concentration is at least partially due to the rapid decrease in hydrophobic force in foam films.

The pressure decay method was employed to assess foam stability more exactly and reproducibly. Figure 7 shows that the foam produced at 10^{-4} M SDS with no added NaCl was unstable and its stability decayed in several seconds. When 0.001 M NaCl was added, the rate of decay in interfacial area of the foam was much lower, indicating that the stability of the foam is improved by adding moderate amount of electrolyte. At 0.1 M NaCl, however, the decay curve shifted back to the left and became steeper, indicating that addition of high concentration electrolyte destabilizes the foam.

The lifetime of a foam film is controlled by drainage and rupture. For a horizontal foam film, the driving force for the drainage process is the capillary pressure, which is determined by the curvature at the Plateau boarder and the surface tension. The drainage would stop when the capillary pressure becomes equal to the disjoining pressure of the film, which in turn gives rise to an equilibrium film thickness. Thus, the initial process of film thinning is controlled by capillary pressure, while the subsequent process is controlled by surface forces. It would, therefore, be of interest to monitor the process of film thinning, which may shed light on the existence of hydrophobic force in thin aqueous films. Of particular interest would be to see if the later stages of a film thinning process is described by the classical (Eq. [6]) or the extended DLVO theory (Eq. [9]).

The rate of film thinning can be described by the Reynolds equation (Scheludko and Platikanov, 1961; Scheludko, 1967):

$$-\frac{dH}{dt} = \frac{2H^3 \Delta P}{3\mu {R_f}^2} \qquad [12]$$

where t is drainage time, μ dynamic viscosity, R_f film radius, and ΔP is the driving force for film thinning. In view of the discussions above, the driving force may be represented by the following relation:

$$\Delta P = P_c - \Pi \qquad [13]$$

where P_c is the capillary pressure represented by Eq. [5], and Π is the disjoining pressure represented by Eq. [6] or [9].

The Reynolds equation was derived originally for film thinning that takes place under no-slip conditions. Therefore, it is applicable to the foam films with tangentially immobile surfaces. It has been shown that this condition is met by using very small films stabilized by a surfactant (Exerowa and Kruglyakov, 1998; Langevin, 2000; Coons *et al.*, 2005). It has also been shown that Eq. [12] can be used even at low surfactant concentrations (Ivanov *et al.*, 2005; Angarska *et al.*, 2004).

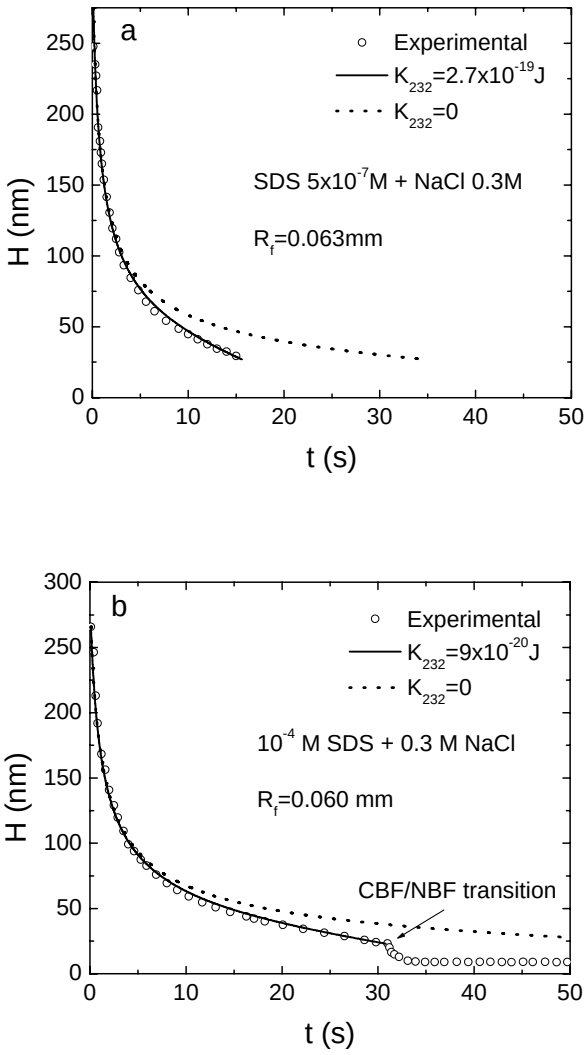

Figure 9. Kinetics of film thinning at a) 5×10^{-7} M SDS and 0.3 M NaCl; b) 1×10^{-4} M SDS and 0.3 M NaCl. The solid line represents the Reynolds equation (Eq.[12]) with the extended DLVO theory, while the dotted line represents the Reynolds equation with the DLVO theory (Wang and Yoon, 2005).

Figure 8 shows the results of the film thinning kinetics measurements conducted on two horizontal foam films stabilized at two different concentrations of SDS in the presence and absence of NaCl (Wang and Yoon, 2005). In both cases, the initial film thinning is fast and can be described by the Reynolds equation with its driving force (ΔP) represented by Eq. [13] with $\Pi = 0$, that is, the process is controlled solely by capillary force (Eq. [5]). This is fully anticipated as the initial film thickness is too large for surface forces to affect the process. As the film thickness (H) is reduced to below approximately 250 nm, however, surface forces begin to influence the film thinning process. The film thinning kinetics curve obtained at a relatively low SDS (10^{-5} M) concentration and in the absence of NaCl cannot be

described by the Reynolds equation without considering the contribution from the hydrophobic force to ΔP, *i.e.*, Eq. [13] in which Π is given by the DLVO theory (Eq. [6]). The experimental data (empty circles) can be fitted to the Reynolds equation when Π of Eq. [13] is represented by the extended DLVO theory (Eq. [9]) with $K_{232} = 5.8\times10^{-18}$ J, ψ_s = -92 mV, and $A_{232} = 3.7\text{x}10^{-20}$ J. Not surprisingly, the K_{232} value is the same as obtained using the equilibrium film thickness technique and given in Figure 4. (Note here that equilibrium film thickness is reached during the later stage of the film thinning process.) On the other hand, the kinetics curve obtained at 10^{-4} M SDS in the presence of 4×10^{-4} M NaCl can be fitted to the Reynolds equation with the classical DLVO theory (Eq. [1]) with $K_{232} = 0$, ψ_s = 110 mV, and $A_{232} = 3.7\text{x}10^{-20}$ J. The ψ_s value used for the fitting procedure has been obtained using the counter-ion binding model. Note here that the hydrophobic force constant becomes zero due to the presence of 0.4 mM of NaCl. In the absence of NaCl, $K_{232} = 5.8\times10^{-18}$ J at 10^{-4} SDS (see Figure 5). Thus, hydrophobic force is dampened by both surfactant and inorganic electrolyte. More importantly, the hydrophobic force constants determined using the static methods, *i.e.*, the equilibrium film thickness and disjoining pressure isotherm methods, can be used to fit the dynamic film thinning data.

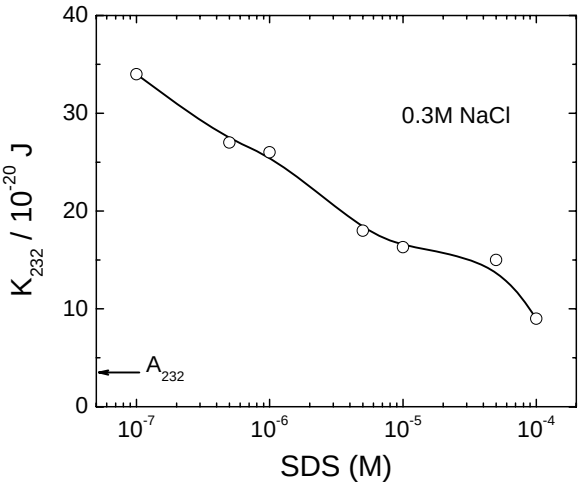

Figure 10. Effect of SDS concentration on K_{232} at 0.3 M NaCl. The results were obtained by fitted using the film thinning data to the Reynolds equation (Eq.[12]) (Wang and Yoon, 2005). The arrow represents the non-retarded Hamaker constant (=$3.7\text{x}10^{-20}$ J) (Israelachvili, 1992).

As has already been noted, the accuracy of determining the magnitudes of hydrophobic force depends critically on the double-layer potentials. Therefore, it would be of interest to study the kinetics of film thinning under conditions of $\Pi_{el} \approx 0$, in which case the extended DLVO theory (Eq. [9]) is reduced to:

$$\Pi = \Pi_{vw} + \Pi_{hb} \qquad [14]$$

By substituting this into Eq. [13] and then to Eq. [12], one can predict the kinetics of film thinning using the Reynolds equation without the possible ambiguity associated in determining double-layer potentials.

Figure 9 shows the results obtained in the kinetics studies conducted at $5x10^{-7}$ and 10^{-4} M SDS in the presence of 0.3 M NaCl. At the lower SDS concentration, the kinetics of film thinning is considerably faster than predicted (dotted line) without considering the hydrophobic force, *i.e.*, $K_{232} = 0$. The experimental data can be fitted to the Reynolds equation (solid line) with $K_{232} = 2.7\times10^{-19}$ J, and with the A_{232} values determined by considering the retardation effects (Russel *et al.*, 1989). The film is shown to rupture at 28.2 nm in 15.7 s. At 10^{-4} M SDS and 0.3 M NaCl, the film becomes more stable owing to the higher surfactant concentration, and ruptures at 23.3 nm in 30.9 s before the common black film (CBF) is transformed to a Newton black film (NBF). The kinetics curve can be fitted to the Reynolds equation with $K_{232} = 9.0\times10^{-20}$ J before the CBF/NBF transition occurs.

The kinetics of film thinning was also studied at other SDS concentrations in the presence of 0.3 M NaCl, and the K_{232} values determined in the manner described in the foregoing paragraph have been plotted as a function of SDS concentration in Figure 10. At 10^{-7} M SDS, K_{232} is $3.4x10^{-19}$ J, which is 9.2 times larger than the non-retarded Hamaker constant ($3.7x10^{-20}$ J). At 10^{-4} M SDS, K_{232} is $9x10^{-20}$ J, which is 2.4 times larger than the Hamaker constant. Thus, the hydrophobic forces are still observed under conditions of $\Pi_{el} \approx 0$, demonstrating that hydrophobic forces in thin aqueous films are real. The difference between K_{232} and A_{232} are not as large as obtained in the absence of an inorganic electrolyte (see Figure 1). The reason is that hydrophobic force is also dampened by NaCl.

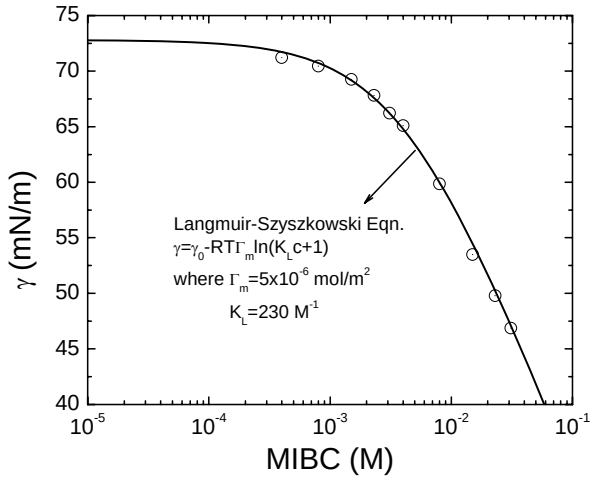

Figure 11. Static surface tension of MIBC solutions as a function of concentration (Comley et al., 2002).

Nonionic Surfactant

Figure 11 shows the static surface tension of MIBC solutions as a function of concentration, adapted from Comley et al. (2002). Also plotted in the figure is the best fit of the Langmuir-Szyszkowski equation:

$$\gamma = \gamma_0 - RT\Gamma_m \ln(1 + K_L c) \qquad [15]$$

where γ_0 is the surface tension of pure water, Γ_m a maximum adsorption density, K_L the Langmuir equilibrium adsorption constant, and c the bulk concentration of MIBC. It gives $5\text{x}10^{-6}$ mol/m^2 for Γ_m, and 230 M^{-1} for K_L. The surface excess of MIBC at the air/water interface was then plotted in Figure 12 as a function of the bulk concentration using the Langmuir isotherm:

$$\Gamma = \frac{\Gamma_m K_L c}{1 + K_L c} \qquad [16]$$

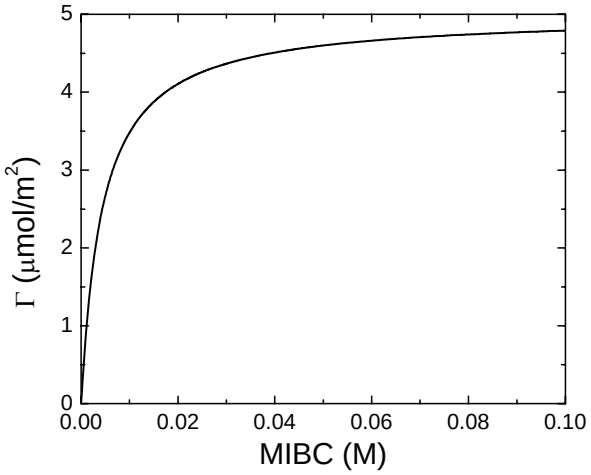

Figure 12. Surface excess for MIBC as a function of bulk concentration.

The film elasticity was calculated using the method developed by Wang and Yoon (2006), where a constant volume was assumed for a completely closed film being stretched, and the most commonly used Gibbs elasticity for a film is defined as (Christenson and Yaminsky (1995):

$$E = 2\frac{d\gamma}{d\ln A} = 2A\frac{d\gamma}{dA} = 2A\frac{d\gamma}{dc}\frac{dc}{dA} \qquad [17]$$

where c is the bulk surfactant concentration. For a closed system, the volume of a foam film, $V = AH$, is constant, *i.e.*, dV=0, where H is film thickness. Also, the total number of the surfactant molecules is constant in a closed system. Therefore,

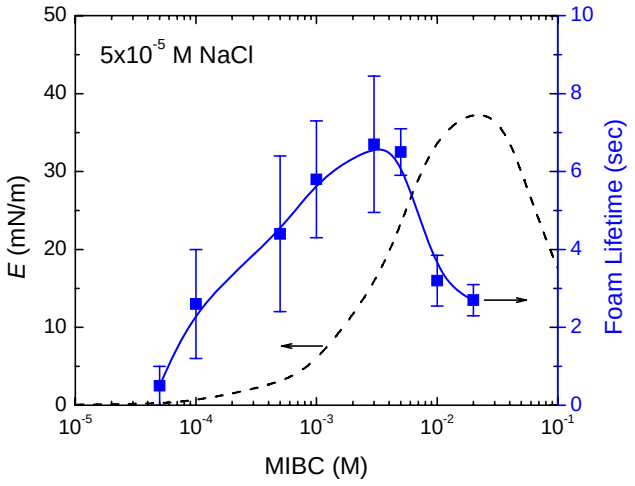

Figure 13. The effects of MIBC concentration on film elasticity (E) and lifetime of three-dimensional foams.

$$d(2A\Gamma + Vc) = 0 \qquad [19]$$

which gives

$$dc = -\frac{2(\Gamma dA + Ad\Gamma)}{AH} \qquad [20]$$

under conditions of constant volume. Eq. [20] is similar to Christenson and Yaminsky's model (1995), except that these authors ignored the $Ad\Gamma$ term, which makes their model applicable only at very high concentrations of surfactant (or electrolyte).

Equation [20] can be rewritten as

$$\frac{dc}{dA} = -\frac{2\Gamma}{A(H + 2\frac{d\Gamma}{dc})} \qquad [21]$$

while Gibbs equation gives:

$$\frac{d\gamma}{dc} = -\frac{RT\Gamma}{c} \qquad [22]$$

Substituting Eqs. [21] and [22] into Eq.[17] and rearranging it, one obtains an expression for the Gibbs elasticity as follows:

$$E = -\frac{4RT\Gamma^2}{c(H + 2\frac{d\Gamma}{dc})} \qquad [23]$$

Equation [23] can be transformed into a more useful form by combining it with the Langmuir isotherm (Eq. [16]), which can be differentiated to obtain:

$$\frac{d\Gamma}{dc} = \frac{\Gamma_m K_L}{(1 + K_L c)^2} \qquad [24]$$

Substituting Eqs. [16] and [24] into Eq.[23] gives a useful expression for Gibbs elasticity:

$$E = \frac{4cRT\Gamma_m{}^2 K_L{}^2}{H(1 + K_L c)^2 + 2\Gamma_m K_L} \qquad [25]$$

In the present work, the values of Gibbs elasticities (E) have been calculated using Eq. [25], in which H was set equal to the measured equilibrium film thicknesses (H_e) and the values of Γ_m and K_L were obtained by fitting the surface tension data to the Langmuir-Szyszkowski equation (Eq.[15]). The results are shown in Figure 13 (as a dashed line) along with the foam lifetimes measured by the shake tests. As shown, the film elasticity increases with increasing MIBC concentration, reaching a maximum at 4×10^{-2} M. The foam lifetime also increase accordingly. In the presence of 5×10^{-5} M NaCl, foam lifetime increased with increasing surfactant concentration, reached a maximum at 3×10^{-3} M, and then decreased with further increasing surfactant concentration. At either very low or very high surfactant concentrations the foams were unstable. At low concentrations (below 10^{-3} M), however, the increase in film elasticity is relatively small. Therefore, the increase in foam stability in this concentration region may be due to the change in other factors, such as surface forces.

We also investigated the effect of pH on the stability of foam film in the presence of 1×10^{-4} M pentanol, and 5×10^{-4} M NaCl. Table 1 shows that film stability increases with increasing pH from 4 to 8. Specifically, the film is not stable at pH 4, probably because of low charge density at the air/water interfaces. A low charge density is normally associated with weak double-layer repulsion, therefore the equilibrium film thickness is also small.

Table 1. Effect of pH on equilibrium film thickness and film stability.

pH	4	5.7	8	10
τ (sec)	22.1	993	1485	>1800
H_e (nm)	42.0*	61.0	64.1	62.3

* Unstable film

CONCLUSION

We developed a methodology of studying the basic factors affecting the stabilities of the two-phase froths produced in the presence of surfactants or in the absence of surfactants. We

investigated the stability of aqueous thin films between air bubbles, and then compared film stability to foam stability. The thin film studies indicate that surface forces play a critical role in determining film stability, and therefore foam stability. A case in point is that surfactant-free aqueous films are stable at low inorganic electrolyte concentrations, despite exceedingly low film elasticity. Therefore, more efforts should go toward surface force studies in flotation where surfactant concentrations are very low.

The thin film studies also indicate that a hydrophobic attractive force exists to destabilize films between air bubbles in dilute aqueous solutions in flotation processes. To identify the origin of the hydrophobic force in aqueous films between two hydrophobic substrates, we study the effects of surfactant type and concentration, and ionic strength on the surface forces in foam films. The improved understanding of hydrophobic force and hydrophobicity gives insights into froth stability in flotation.

We have developed an analytical model to calculate film elasticity from surface tension. Combining with surface forces in thin aqueous films, this work has demonstrated that by balancing the interfacial interactions of air bubbles and the elasticities of foam films, we can control the foam stability properly. This methodology is promising in characterizing various frothers used in flotation.

REFERENCES

Angarska, J. K., Dimitrova, B. S., Danov, K. D., Kralchevsky, P. A., Ananthapadmanabhan, K. P., and Lips, A., 2004. *Langmuir* 20: 1799.

Ata, S., Ahmed, N., and Jameson, G. J., 2003. *Int. J. Miner. Process*. 72: 255.

Cascão Pereira, L. G., Johansson, C., Blanch, H. W., Radke, C. J., 2001. *Colloids and Surfaces A: Physicochem Eng Aspects* 186: 103.

Christenson, H. K. and Yaminsky, V. V., 1995. *J. Phys. Chem*. 99: 10420.

Claesson, P. M., Blom, C. E., Herder, P. C., Ninham, B. W., 1986. *J. Colloid Interface Sci.* 114: 234.

Comley, B. A., Harris, P. J., Bradshaw, D. J., and Harris, M. C., 2002. *Int. J. Miner. Process.* 64: 81.

Coons, J. E., Halley, P. J, McGlashan, S. A., Tran-Cong T., 2005. *Colloids and Surfaces A: Physicochem. Eng. Aspects* 263: 197.

Eriksson, J. C., Ljunggren S., Claesson, P. M., 1989. *J. Chem. Soc., Faraday Trans*. 2, 85: 163.

Exerowa, D, Zacharieva, M, Cohen, R, and Platikanov, D, 1979. *Colloid and Polymer Sci,* 257:1089.

Exerowa, D. and Kruglyakov, P. M., 1998. Foam and Foam Films, Elsevier.

Israelachvili, J. N., 1992. *Intermolecular and surface forces*, (Academic press: London).

Israelachvili, J. N., Pashley, R.M., 1982. *Nature* 300: 341.

Ivanov, I. B., Danov, K. D., Ananthapadmanabhan, K. P., Lips, A., 2005. *Adv. Colloid Interface Sci.* 114– 115: 61.

Kalinin, V. V., Radke, C. J., 1996. *Colloids Surf. A: Physicochem. Eng. Aspects* 114: 337.

Kralchevsky, P. A., Danov, K. D., Broze, G., Mehreteab, A.,1999. *Langmuir* 15: 2351.

Langevin, D., 2000. *Adv. Colloid and Interface Sci*. 88: 209.

Mathe, Z. T., Harris, M. C., O'Connor, C. T., and Franzidis, J.-P., 1998. *Minerals Engineering* 11: 397.

Murray, B S, and Liang, H –J, 1999. *J Agric Food Chem,* 47: 4984.

Neethling, S. J. and Cilliers, J. J., 2003. *Int. J. Miner. Process*. 72: 267.

Nishioka, G, and Ross, S, 1981. *J Colloid Interface Sci*, 81: 1.

Persson, C, Jonsson, A, Bergström, M, and Eriksson, J C, 2003. *J Colloid and Interface Sci,* 267:151.

Rabinovich, Y. I., Derjaguin, B. V., 1988. In: Proceed. 5th Hungarian Conference on Colloid Chemistry, Loránd Eötvös University, Budapest, Hungary, 1988.

Radoev, B. P., Scheludko, A. D., Manev, E. D., 1983. *J. Colloid Interface Sci*. 95: 255.

Scheludko, A. and Exerowa, D., 1959. *Comm. Dept. Chem., Bul. Acad. Sci*. 7: 123.

Scheludko, A., 1967. *Adv. Colloid and Interface Sci*. 1: 391.

Scheludko, A., and Platikanov, D., 1961. *Kolloid Z*. 175: 150.

Tchaliovska, S., Manev, E., Radoev, B., Eriksson, J. C., and Claesson, P. M., 1994. *J Colloid Interface Sci.* 168: 190.

Tsao, Y., Yang, S.X., Evans, D.F., Wennerström, H.,1991. *Langmuir* 7: 3154.

Waltermo, Å., Claesson, P. M., Simonsson, S., Manev, E., Johansson, I., and Bergeron, V., 1996. *Langmuir* 12: 5271.

Wang, L. and Yoon, R.-H., 2004. *Langmuir* 20: 11457.

Wang, L., Yoon, R.-H., 2005. *Colloids Surfaces A: Physicochem. Eng. Aspects* 263: 267.

Warszynski, P., Barzyk, W., Lunkenheimer, K., Fruhner, H., 1998. *J. Phys. Chem. B* 102: 10948.

Yaros, H. D., Newman, J., and Radke, C. J., 2003. *J. Colloid Interface Sci*. 262: 442.

Yoon R.-H. and Mao, L., 1996. *J. Colloid Interface Sci*. 181: 613.

Yoon, R.-H., and Aksoy, B. S., 1999. *J Colloid Interface Sci*. 211: 1.

Yoon, R.-H., Ravishankar, S. A., 1996. *J. Colloid Interface Sci*. 179: 403.

Yu, M –A, and Damodaran, S, 1991. *J Agric Food Chem,* 39: 1555.

Appendix 5: Direct Measurement of Forces in Flotation Systems

TECHNICAL REPORT

Contract Title and Number:	Period of Performance:
Establishment of the Center for Advanced Separation Technologies ((DE-FC26-01NT41091)	Starting Date: 9/17/01 Ending Date: 5/31/05

Sub-Recipient Project Title: Direct Measurement of Forces in Flotation Systems	Report Information: Type: Final Number: Period: 9/17/01-5/31/05 Date: Code: VA004
Principal Investigators: Roe-Hoan Yoon and William Ducker	
Contact Address: 146 Holden Hall and 304 Davidson Hall Virginia Polytechnic Institute & State University Blacksburg, VA 24061	Contact Information: Phone: (540)231-4508 Fax: (540)231-3948 E-Mail: cast@vt.edu
Subcontractor Address: No subcontracts issued.	Subcontractor Information: Phone: Fax: E-Mail:

Abstract

The objective of this project is to directly measure the interaction force between a particle and bubbles as a function of separation distance. This force controls the attachment and detachment of particles to bubbles, which is an essential step in determining the efficiency of a flotation process. In the past ten years, one predominant explanation for the long range attraction between hydrophobic surfaces is the nanobubble/gas cavity theory. Firstly, an Atomic Force Microscope was utilized to study the hydrophobic force between solid surfaces to clarify the applicability of nanobubble theory in the solid/surfactant system. The effects of degassing, salt concentration and chain length on the hydrophobic force are systemically studied. The results are beneficial for the understanding of the origin of the hydrophobic force and the particle/bubble interaction in Flotation. Secondly, a specially designed device, wetting film apparatus was fabricated for the direct particle/bubble force measurements. The experiment results show that between hydrophilic substrate/bubble, when the separation decreases, there is a strong repulsive disjoining pressure, which leads to a thick water film between particle/bubble, therefore, a less likely flotation. The wetting film between a hydrophobic substrate and a bubble ruptures in tens of milliseconds drastically, suggesting a possible flotation after the solid particles are hydrophobized. The rupture process is proposed to be studied systemically using a high speed video camera.

Table of contents

List(s) of graphical materials

List(s) of Tables

Executive Summary

Sakamoto *et al*. (2002) conducted AFM force measurements between silica sphere and fused-silica plate in aqueous octadecyltrimethylammonium chloride (C_{18}TACl) solutions, and concluded that long-range attractive force is not observed in carefully degassed solutions. In the present work, AFM force measurements were conducted by following the procedures described by Sakamoto *et al.* The results showed the presence of the long-range attractive force both in air-saturated and degassed solutions. It was most attractive at $5x10^{-6}$ M C_{18}TACl, where the surface was most hydrophobic. At this concentration, which is close to the point of charge neutralization (p.c.n.) of the glass sphere, the long-range decay lengths (D_2) were 34 and 38 nm in air-saturated and degassed solutions, respectively. At 10^{-5} M, the decay length decreased from 30 to 4 nm upon degassing, which is explicable by simple pH change associated with the changes in the concentration of dissolved CO_2. The attractive force was screened by an added electrolyte (NaCl), indicating that the attractive force may be of electrostatic origin. Therefore, the very long decay lengths observed in the absence of electrolyte may be ascribed to the fact that the p.c.n. occurs at a very low surfactant concentration.

Surface forces were measured using an AFM with silica surfaces immersed in C_nTACl (n = 12-18) solutions in the absence of added salt. The results showed long-range attractive forces that cannot be explained by the DLVO theory. The long-range attractions increased with increasing surfactant concentration, reaching a maximum at the point of charge neutralization (p.c.n.) and then decreased. The long-range forces decayed exponentially, with the decay lengths increasing from 3 to 32 nm as the chain length of the surfactants increased from C-12 to C-18. The measured forces can be fitted to the charged-patch model of Miklavic *et al.* (1994) by assuming patch sizes that are much larger than the values reported in the literature.

It was found that the decay length decreases linearly with the effective concentration of the CH_2/CH_3 groups of the C_nTACl homologues raised to the power of -1/2, which is in line with the Eriksson *et al.'s* (1989) hydrophobic force model derived using a mean-field approach. It appears, therefore, that the long-range attractions observed in the present work are hydrophobic forces originating from changes in water structure across the thin surfactant solution film between the silica surfaces. It is conceivable that hydrocarbon chains in solution disrupt the surface-induced water structure and cause a decrease in hydrophobic force.

The film thicknesses of a wetting film in different NaCl solutions on oxidized hydrophilic silicon wafer surface show that equilibrium film thickness decreases with salt concentration increasing, which is the same as predicted by the DLVO theory. The experiment results also suggest that there is an equilibrated thick water film between a hydrophilic solid and a bubble, therefore, a less likely flotation. However, the wetting film between a hydrophobic substrate and a bubble ruptures in tens of milliseconds drastically, suggesting a possible flotation after the solid particles are hydrophobized. The rupture process is proposed to be studied systemically using a high speed video camera.

Introduction

Of the many variables affecting flotation, particle hydrophobicity plays the most decisive role. In general, the hydrophobicity determines both selectivity and recovery. Various collectors are used to control the hydrophobicity, and many investigators studied ways to increase the hydrophobicity and hence improve the separation process.

In colloid chemistry, it is recognized that the kinetics of particle coagulation is controlled by the surface forces. In general, coagulation is *slow* when the surface forces create an energy barrier and the coagulation is *fast* when the energy barrier becomes zero. Derjaguin and Dukhin (1961) were the first to model flotation (or bubble-particle interaction) using the surface forces that are known to be present in colloidal systems; namely, the electrostatic force due to double-layer interaction and the van der Waals dispersion force. However, both of these forces are repulsive in most of the conditions encountered in flotation, which makes it difficult to model flotation using the DLVO theory. Blake and Kitchener (1972) showed later that the thin film of water (wetting film) between a hydrophobic solid and air bubble ruptures spontaneously and that it does so at much larger separation distances than predicted by the classical DLVO theory. These investigators suggested, therefore, the presence of '*hydrophobic force*' in wetting films. In fact, the presence of the third force (i.e., hydrophobic force) had been suggested by Laskowski and Kichener (1969) three years prior to the Blake and Kitchener's work. The former discovered that methylated and pure silica particles exhibited practically the same ζ-potentials and yet the former floated while the latter did not, which led to their suggestion that a long-range '*hydrophobic influence*' caused by the instability of the water structure in the vicinity of a hydrophobic surface may be responsible for the flotation.

It was not until 1982 when Israelachvili and Pashley (1982) actually measured the hydrophobic force using the surface force apparatus (SFA). Since then, numerous investigators conducted follow-up experiments, many of which confirmed the existence of the hydrophobic force while others did not.

Tsao and Evans (1993) observed long-range attractive forces with mica surfaces coated with double-chain cationic surfactants. They found that the forces were screened by electrolyte and, therefore, concluded that they are electrostatic in origin. Further, long-chain surfactants self-assembled at interfaces/surfaces form domains and the hydrocarbon chains are tilted relative to the interface. The tilted structure generates in-plane dipole moment, which creates electric fields extending large distances. More recently, we developed a mathematical model relating attractive forces to the dipole moments of the domains (or patches) that are formed during self-assembly processes. (Pazhianur and Yoon, 2003) Miklavic et al. (1994) also suggested that net-neutral surfaces consisting of charged patches can create attractive double-layer forces, provided that the charged species are free to migrate.

The strongest opposition came from those who observed nano-bubbles on hydrophobic surfaces during measurement. It was suggested that the so-called

hydrophobic force is due to the capillary force caused by the coalescence of preexisting nano-bubbles when two hydrophobic surface approach each other. (Sakamoto *et al.*, 2002; Attard, 1996; Ishida *et al.*, 2000a, 2000b; Tyrrell and Attard, 2002) Recent work from the group of Higashitani (Ishida *et al.*, 2000a, 2000b) offered support for the preexisiting adsorbed bubble hypothesis, which may be acceptable for the surfaces whose water angles (θ) were greater than 90^o due to hydrophobization with silanes Thermodynamically, cavitation should occur at $\theta>90^o$. However, Sakamoto, *et al*. (2002) reported that air bubbles are also the cause for the hydrophobic forces observed with surfaces coated with a water-soluble surfactant (octadecyltrimethylammonium chloride, C_{18}TACl). They observed long-range (60-250 nm) attractive forces between silica surfaces in $1\text{-}3\times10^{-5}$ M C_{18}TACl when the solution was equilibrated with air. The force *vs*. distance curves exhibited discontinuities (or steps), as were also reported by other investigators. (Parker, *et al*. 1994; Nuyen *et al*. 2003) When the measurement was conducted in a degassed solution, both the steps and the long-range attraction disappeared, which lead to the conclusion that the long-range attraction is caused by the gas bridges formed between two hydrophobic surfaces interacting with each other. They stated further that long-range attraction never appears in completely air-free C_{18}TACl solutions.

In the present work, the AFM force measurements conducted by Sakamoto *et al*. (2002) in C_{18}TACl solutions were repeated by exactly following their procedure in order to help clarify the origin of the long range attraction. What is more, systematic studies on the effect of chain length on hydrophobic force were carried out by measuring the hydrophobic forces between silica surfaces in solutions of alkylammoniumtrimetyl chloride (C_nTACl) homologues. The results are also used to discuss the role of hydrocarbon chain length on the mechanisms of adsorption of the long-chain surfactants and to discuss the possible origins of hydrophobic force

Finally, we performed direct measurements of the interaction between solid substrates of different surface hydrophobicity and an air bubble using a wetting film apparatus. The obtained information is utilized to analyze the effect of surface hydrophobicity of solid on the solid/bubble interaction, which is important in flotation practice.

Experimental

Materials

Nanopure water was obtained by using the Nanopure III (Barnstead IA) water system. The conductivity of the water was 18.2 MΩ/cm at 25°C and the surface tension was 72.5 mN/m at 22°C. The water and surfactant solutions were used without purging with ultra pure nitrogen to exclude atmospheric CO_2. Thus, the pH of the solutions was in the range of 5.6-5.8. NaOH (99%, Mallinckrodt Baker) was used without further purification. Liquid reagents, such as chloroform (99.9%, Burdick & Jackson), H_2SO_4 (98%, VMR International) and H_2O_2 (30%, VMR International) were used as received without further purification. The surfactants used in the present work included dodecyltrimetyl-ammonium chloride (C_{12}TACl), tetradecyltrimetylammonium chloride

(C_{14}TACl), hexadecyltrimetylammonium chloride (C_{16}TACl) and octadecyltrimetylammonium chloride (C_{18}TACl) all from TCI and of greater than 97% purity. They were used without further purification.

Quartz plates (Hereaus Amersil, Inc.) and silicon wafers (100 oriented, Polished Wafer, Sumco, Oregon) were boiled in a H_2SO_4/H_2O_2 solution (7:3 by volume) at 120^{o}C for 60 minutes. The plates were rinsed thoroughly with a large amount of Nanopure water, equilibrated with the water in a sealed vial for at least 20 minutes, removed and dried by blowing pure nitrogen gas over the surface, and then used for experiments.

Degassing procedure

To conduct AFM force measurements under air-free conditions, surfactant solutions were degassed by following the procedure described by Sakamoto *et al.* (2002) Nanopure water was boiled for one hour, frozen in a vessel with liquid nitrogen, evacuated for two hours with a final air pressure at 20mbar, and then melted under reduced pressure. This procedure was repeated three times. During the third degassing step, a known amount of surfactant was placed on the ice and evacuated for two hours. The vessel containing the ice and surfactant powder was then allowed to reach thermal equilibrium with ambient temperature before use. According to Sakamoto *et al.* (2002), this procedure "guarantees that the solution is completely free from dissolved gas".

When the target surfactant concentration was very low, i.e., 10^{-6} M, it was difficult to add accurately a desired amount of dry surfactant to frozen water unless a very large amount solution was boiled, frozen, and degassed. Therefore, we prepared a 1 mL of 10^{-4} M C_{18}TACl solution and 125 mL of water, degassed them in the manner described above, mixed the two, and boiled the mixture for 1 hour. During the boiling, only about 25 mg of water evaporated so that the surfactant concentration remained close to 10^{-6} M. The boiled solution was frozen by liquid nitrogen, degassed, melted under vacuum, and allowed to reach a thermal equilibrium with the ambient before use. For comparison purpose, we prepared higher concentrations of C_{18}TACl solutions using this modified procedure and Sakamoto *el al*.'s, and conducted AFM force measurements. We found no significant differences between the two methods of obtaining air-free solutions.

Air-equilibrated solutions

Air-equilibrated C_{18}TACl solutions were prepared in a vessel such that the amount of air above the liquid was greater than the amount of air in the equilibrated solution. This was easily accomplished because the concentration of gas molecules in air (~40 mM) at STP is about 40 times that in water. In each experiment, a solution vessel was thoroughly shaken to speed equilibration, and then was left sealed for 30 minutes. At the end of this period, the seal was broken to allow mixing with ambient air for a few minutes. This procedure was repeated 4 times.

Surface Force Measurement

Surface forces were measured using a Digital Instrument Nanoscope IIIa AFM at room temperature (~22°C) using the colloidal probe technique. (Ducker *et al.*, 1991, 1992) The separation distance (H) between the probe (glass sphere) and the substrate

(slica plate) was measured by monitoring the deflection of the cantilever on which the probe was attached. Silicon-nitride NP-20 cantilevers were obtained from Veeco, CA. Triangular cantilevers with spring constant of 0.58 N/m were used. The spring constants were determined using the resonant frequency technique. (Cleveland *et al.*, 1993) The error associated with this technique was ±7%. The glass spheres (12-20μm in diameter) were obtained from Polysciences Inc. Warrington, PA. They were soaked in chloroform for 30 minutes and UV-irradiated for 30 minutes to remove possible organic contaminants. In each experiment, a glass sphere was glued onto a cantilever with EPON 1004 resin (Shell Chemical Co.). The diameter of the glass sphere was measured using an Olympus BH-2 light microscope with a video caliper with an error of ±0.5 μm. Combined error between the measurements of the spring constants and the sphere diameters was about ±12% in force/diameter (F/R) calculations.

Surface forces were measured for a series of surfactant concentrations. For a given series of measurements, the surfactant solutions were injected into an AFM liquid cell starting from the lowest concentration and continuing to the highest one. For each new concentration, the glass sphere and silica plate were exposed to the surfactant solution for a period of 20 minutes before force measurements were commenced. Forces reported in this paper were recorded about 1 hour after exposure of the solids to a new solution. Although the forces measured during the periods of 20 minutes to 1 hour were reproducible, we found that the forces varied slowly with time after 1 hour, presumably because of slow adsorption kinetics and possible rearrangement of the surfactant molecules on the surface. Thus, we have no evidence that the forces reported here were at adsorption equilibrium.

All reported forces, F, are normalized by the particle radius, R. For measurements at equilibrium, when R is much greater than the range of the force, $F/2\pi R$ is equal to the energy of interaction per unit area for an infinite flat plate interacting with another infinite flat plate of the same material. (Derjaguin, 1934)

AFM Imaging

All AFM images reported in this communication are height (constant force) images captured at 22±1°C with integral and proportional gains of about 2. Silicon nitride cantilevers with nominal k=0.12 Nm^{-1} were used. The images are of the same type of silica plate as used in the force measurements. The images were captured after a substrate was soaked in an aqueous solution for about 1 hour using the soft contact-mode imaging technique. Minimum contact forces were used in order not to disturb the adsorbed surfactant layer.

ζ-Potential Measurement

The silica plates and glass spheres that were used for the AFM force measurements were subjected to ζ-potential measurements. The glass spheres were suspended in water, and the coarser spheres were allowed to settle. The finer spheres (<3 μm) left in suspension were used for the ζ-potential measurements. For silica plates, the measurements were conducted after pulverizing the plates by means of an agate mortar and pestle and isolating the finer particles by sedimentation. The ζ-potential

measurements were conducted in both air-equilibrated and degassed C_{18}TACl solutions using a Lazer Zee meter, Model 501 (Pen Kem, Inc, NY). The ζ-potentials were calculated from the mobilities using the Smoluchowski equation. Reported results represent arithmetic averages of six measurements.

Contact Angle Measurement

A silica plate was immersed in a surfactant solution for a desired period of time, removed from the solution, and dried by blowing nitrogen gas over the surface. A drop of the surfactant solution was then placed on the surface and the contact angles were measured by means of a contact angle goniometer. The contact angles were also measured using the captive bubble technique, in which silica plates were kept in solution while air bubbles were brought to contact. A total of six contact angles were measured at a given experimental condition and averaged.

Film thickness measurement

The thickness of wetting film on a silicon wafer has been obtained in NaCl solutions at different electrolyte concentrations from the measurement of light intensity. The value was compared to that calculated from the disjoining pressure using classical DLVO theory. The capillary radius is about 0.75mm. Hydrophilic substrate is obtained by oxidizing the silicon wafer in H_2SO_4/H_2O_2 solution (7:3 by volume) at 100°C for 60 minutes. Hydrophobic surface is obtained by hydrophobizing silicon wafer using dilute OTS solution with a resulting contact angle about 30~50 degrees.

Results and Discussion

Contact Angle Measurement

Figure 1 shows the equilibrium contact angles of the fused silica plates immersed in 10^{-5} M C_{18}TACl solutions. The contact angles measured with the captive bubble technique reached a maximum after approximately 2 hours, which was shorter than

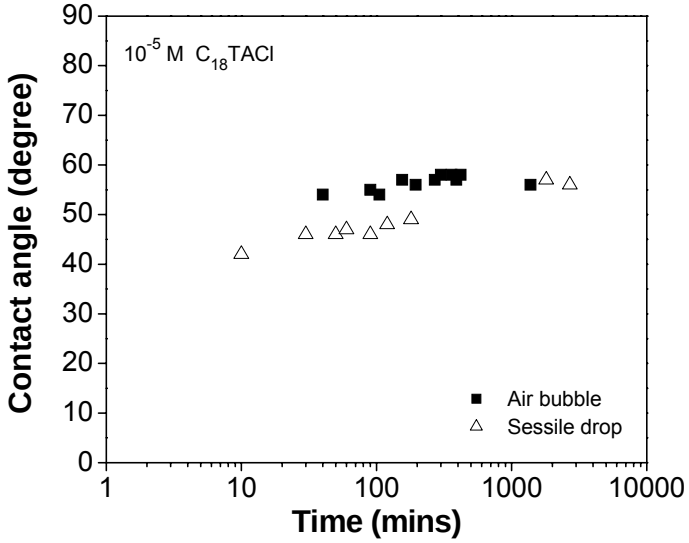

Figure 1. Sessile drop and captive bubble contact angles of the fused silica plates as a function of the time that the plate was exposed to 10^{-5} M C_{18}TACl solutions.

suggested by ellipsometry. The maximum contact angles were less than 60^{o} despite the long chain length of the surfactant, which may be attributed to the possibility that some of the surfactant molecules adsorb with the head group facing toward the solution, that is, the inverse (or flip-flop) orientation.

Forces in Air-Equilibrated Solution

Figure 2 shows the results of the AFM force measurements conducted as a function of the C_{18}TACl concentration in air-equilibrated solutions. It shows the same general trend as the forces measured previously in cationic surfactant solutions. (Subramanian and Ducker, 2001; Lokar and Ducker, 2002, 2004) Addition of a small amount of the cationic surfactant reduces the repulsive force between the negatively charged surfaces, and a further increase in concentration lead to a repulsive force. In the present work, however, the changes in force were observed at lower concentrations of C_{18}TACl than of C_{12}TABr or C_{16}TABr, as expected of a longer chain surfactant. Also, the range of the forces was much greater. This can be attributed to the fact that the changes in forces was brought about at substantially lower surfactant concentrations than with C_{12}TABr. It is important to note here that a) the most attractive force is much greater

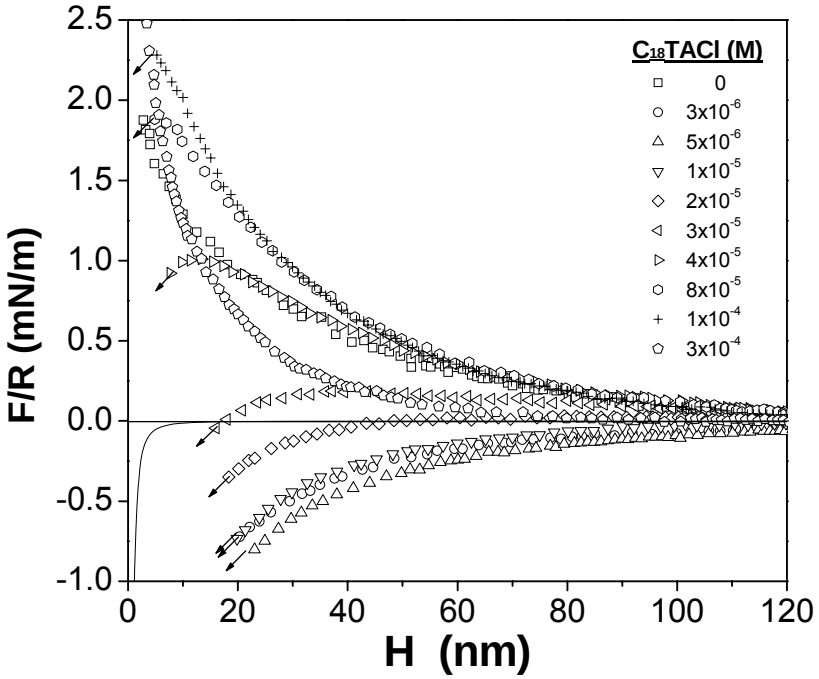

Figure 2. Forces (F) normalized by the radius (R) of the sphere in air-equilibrated C_{18}TACl solutions. The solid line represents the theoretical van der Waals force calculated using a Hamaker constant of 8x10^{-21} J. The measured forces were repulsive in 0 – 3x10^{-4} M C_{18}TACl solutions. At 0 M, the surface potential obtained from a fit to Poisson-Boltzman theory was -85 mV. The arrows represent the point where the cantilever undergoes a mechanical instability. Forces at smaller separations were measured, but are not reproduced here because the deflection of the spring does not give the surface force when it is not in mechanical equilibrium. Forces were measured in the order of increasing surfactant concentrations with the same sphere-plate combination. The forces were measured ~60 minutes after injection of each new reagent addition.

than the van der Waals force between either silica solids or hydrocarbon solids, and that b) there is a very large gradient in the force as a function of concentration near the minimum (most attractive) force. The measured force was most attractive at $5x10^{-6}$ M and became progressively weaker at higher concentrations.The force became net repulsive above $3x10^{-5}$ M. The concentration at which the measured force became most attractive was close to the p.c.n. of the glass sphere and silica plate, as will be shown later. Other investigators also showed that long-range force is most attractive near p.c.n. (Kerkicheff and Spalla, 1995; Parker *et al.* 1993)

The decrease in attractive force above the p.c.n. ($5x10^{-6}$ M) is due to the adsorption of the cationic surfactant in excess of the negative charge sites available on silica. The ability of the cationic surfactant to adsorb above p.c.n. is due to net attraction between the hydrocarbon chains, which is known as "hydrophobic effect". According to Somasundaran *et al.* (1964) the standard free energy change (ΔG^o) associated with this process is given by $\Delta G^o = -0.85n$ kcal/mole, where n is the number of CH_2 groups of a hydrocarbon chain that are in contact with the CH_2 groups of the neighboring hydrocarbon chains. This value is comparable to the free energy of transferring hydrocarbon chain to water, 0.88 kcal per mole of CH_2 group. (Tanford, 1980)

It is possible that $C_{18}TA^+$ ions adsorbing above p.c.n. may do so with inverse (or

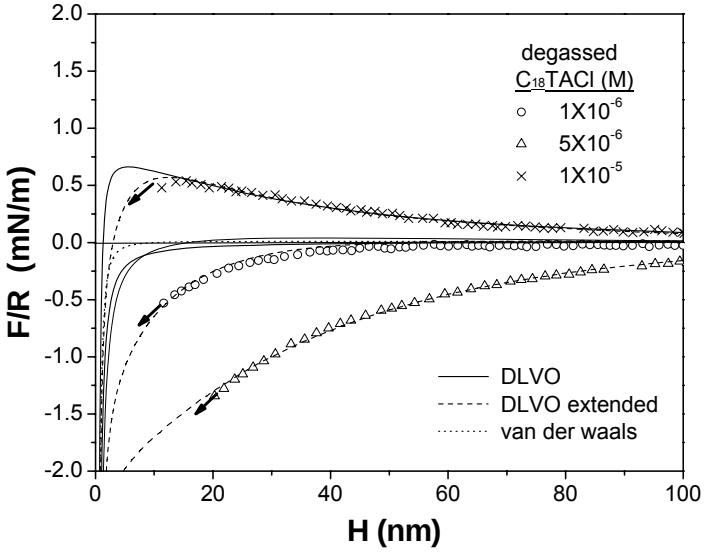

Figure 3. Forces (F) normalized by the radius (R) of sphere in degassed $C_{18}TACl$ solutions. The magnitudes of the forces are similar to those measured in air-equilibrated solutions shown in Figure 2. The force in $1x10^{-5}$ M solution fits well to DLVO theory that was calculated using an exact numerical solution of the Poisson Boltzmann equation at separations great than ~15 nm, which is shown as a line though the points. The addition of an exponential force term improves the fit as shown by the dashed line. The forces at $1x10^{-6}$ and 5×10^{-6} M are much more attractive than the van der Waals force alone, which is shown as a dotted line.

flip-flop) orientation, i.e., with the head groups pointing toward the solution. The inverse orientation may occur after the surface has become hydrophobic by virtue of the normal mode of orientation, i.e., the head group in touch of the surface and the tails pointing to the solution. The possible inverse orientation may provide an explanation for the relatively low contact angles observed in C_{18}TACl solutions (Figure 1).

The forces measured by Sakamoto *et al*. in air-equilibrated C_{18}TACl solutions are about 30-100 times larger than shown in Figure 2. Furthermore, we did not observe the steps that were observed by these investigators and attributed to bridging air bubbles. Other investigators also observed the steps and attributed them to bridging bubbles. (Parker, *et al*. 1994; Nuyen *et al*. 2003)

Effect of Degassing on AFM Force Measurement

Figure 3 shows the forces between glass sphere and fused silica plate in solutions that were degassed. Overall, the forces in degassed and air-equilibrated solutions show the same trends. The measured forces in degassed solutions were attractive at a concentration as low as 10^{-6} M. The strongest attractive force was observed at $5\text{x}10^{-6}$ M, as was the case with the measurements conducted in air-equilibrated solutions (Figure 2). In fact, the force measured in degassed solution was slightly more attractive than in the air-saturated solution (Figure 4a). As the concentration was increased to 10^{-5} M, the measured force in degassed solution became repulsive while the force measured in air-saturated solution remained attractive (Figure 4b). Below we explain these differences without using the theory of bridging air bubbles.

The measured forces were fitted to an exponential function,

$$\frac{F}{R} = C\exp\left(-\frac{H}{D}\right) \tag{1}$$

where F is the surface force, R the radius of the glass sphere used for the force measurements, H the closest separation distance between the sphere and plate, and C, and D are fitting parameters. It was assumed that the electrical potentials of the silica plates and glass spheres were zero and that C=-1.4 mN/m. Also, the fitting was carried out after subtracting the forces due to van der Waals interaction from the measured forces.

Note here that the glass sphere and the fused silica plate jumped into contact in the degassed 10^{-5} M C_{18}TACl solution at a separation distance of 12 nm, suggesting the presence of an attractive force not considered in the DLVO theory. The solid line of Figure 3 represents the DLVO fit of the data obtained in 10^{-5} M degassed solution. The dashed lines represent the extended DLVO theory, which considers the contributions from non-DLVO attractive force whatever its origin is. Details of the fitting procedures will be discussed later.

The results given in Figures 2 and 3 show that, although the effect of degassing was quite dramatic at some individual concentrations of surfactant, degassing the solution

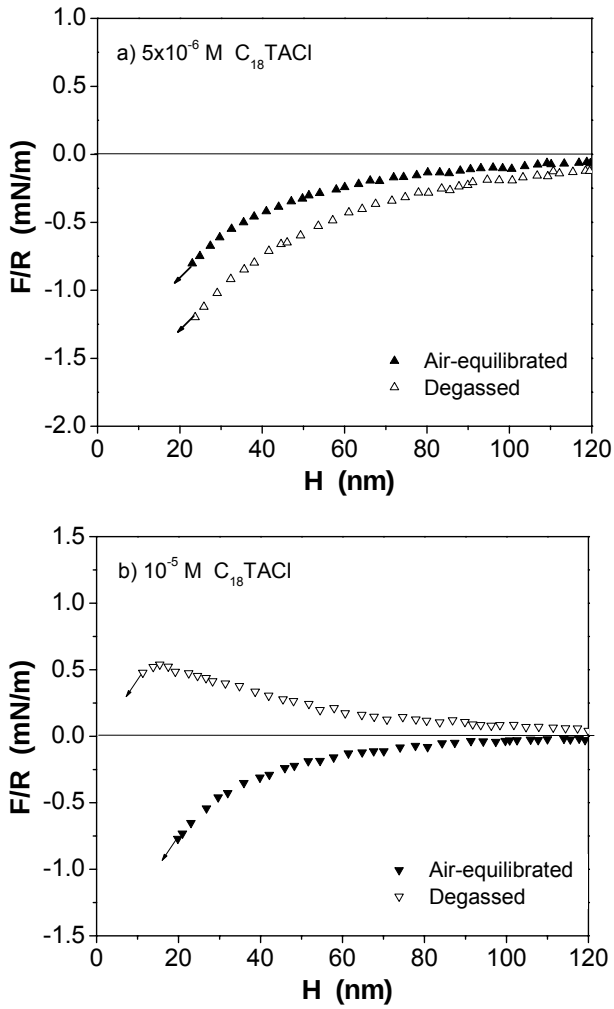

Figure 4. Comparison of the forces measured in degassed and air-equilibrated $5x10^{-6}$ and $1x10^{-5}$ M $C_{18}TACl$ solutions. The data were taken from Figures 2 and 3. At $5x10^{-6}$ M, D_2 is 38 and 34 nm in degassed and air-equilibrated solutions, respectively. At $1x10^{-5}$ M, D_2 is 30 and 4 nm in air-equilibrated and degassed solutions, respectively. The decrease in decay lengths by degassing can be attributed to pH change upon degassing.

did not change the overall trends, and caused only a small change in magnitude particularly at the concentration of maximum attractive force. In the remainder of this communication, we will discuss 1) our hypothesis for the mechanism of the changes in force upon degassing surfactant solutions, and 2) further experiments to reveal the nature of the attractive force.

Our hypothesis is that the primary effect of degassing the solution in our experiments was to raise the pH. As the pH increases, the surface charge becomes more negative, which in turn causes an increase in the adsorption of the $C_{18}TA^+$ ions and, hence, a change in surface force. We found that the pH of the air-equilibrated solutions was 5.7, which increased to 6.6 when the solution was degassed. Degassing removes CO_2 from the solution, causing shift in the following set of equilibria to the left: (Stumm and Morgan, 1996)

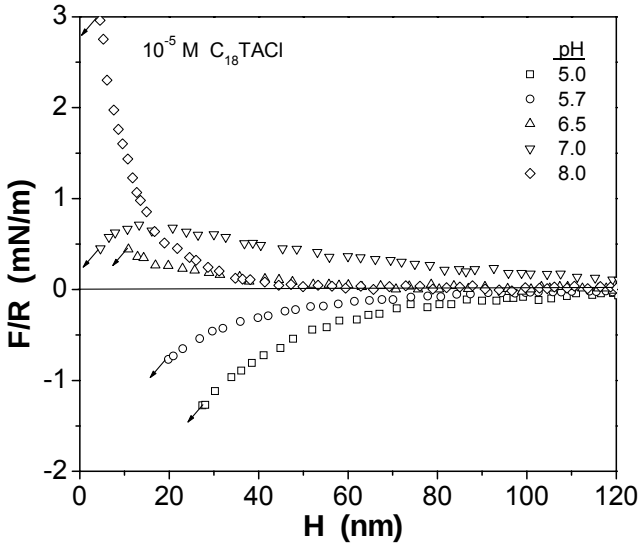

Figure 5. Effect of pH on forces in air-equilibrated 10^{-5} M C_{18}TACl solutions. The data for pH=5.7 were taken from Figure 6; all other data were for the same particle/plate combination

$$H_2O + CO_2(aq) \rightleftharpoons H_2CO_3(aq) \rightleftharpoons H^+(aq) + HCO_3^-(aq) \qquad (2)$$

The fact that the solution remained at pH 6.6 rather than 7.0 suggests that we had not completely degassed the solution, or that some CO_2 had returned on the timescale of our pH measurement. Using the known equilibrium constant for the composite reaction above ($K = 4.47\times10^{-7}$), (Stumm and Morgan, 1996) we can calculate that our degassing

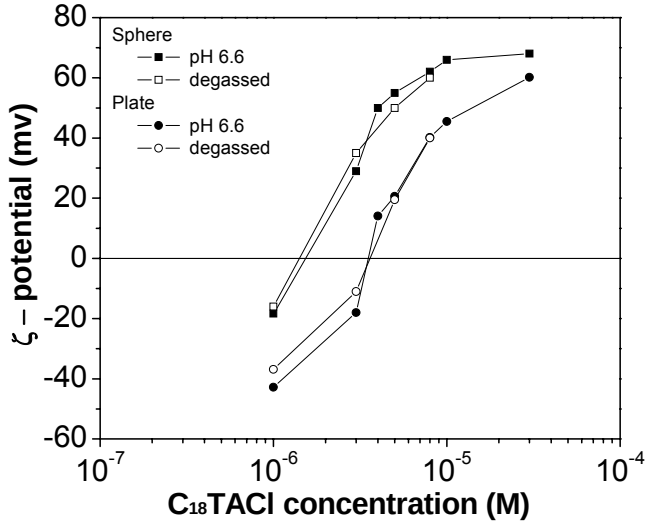

Figure 6. Comparison of the ζ-potentials measured in degassed C_{18}TACl solutions with those measured in air-equilibrated solutions whose pH have been adjusted to the same pH (=6.6) as the degassed solutions.

procedure decreased the concentration of dissolved carbon dioxide from 8.9×10^{-6} to 1.2×10^{-7} M, i.e. we removed about 99% of the CO_2.

Figure 5 shows the forces measured in air-equilibrated 10^{-5} M $C_{18}TACl$ solutions by changing the pH with NaOH or HCl. The effect of increasing the pH was very similar to the effect of degassing (compare Figure 5 with Figure 4). As the pH increases, the surface becomes more negative, which should cause an increase in the adsorption of the $C_{18}TA^+$ ions and render the surface more hydrophobic. As the surface becomes more hydrophobic, additional $C_{18}TA^+$ ions adsorb on the surface, the adsorption mechanism being hydrophobic effect between the hydrocarbon chains. The additional adsorption of the cationic surfactant should lead to an increased surface charge and, hence, an increased repulsive surface force, as shown in Figures 4 and 5.

To examine the above mechanism, we have measured the ζ-potentials of the glass particles and the pulverized plate. Figure 6 shows the ζ-potentials as a function of the $C_{18}TACl$ concentration. The measurements were conducted both in degassed and air-equilibrated solutions. The pH of the degassed solutions was 6.6, and the pH of the air-equilibrated solutions was adjusted to 6.6 with NaOH. Clearly, the effect of degassing on the ζ-potential was reproduced by increasing the pH of the air-saturated solution.

Figure 7 compares the ζ-potentials of the silica plate and glass sphere measured at pH 5.7 and pH 6.6. As the pH was increased from 5.7 to that of the degassed solution, i.e., pH 6.6, the ζ-potentials became considerably more positive, indicating that $C_{18}TA^+$ ions adsorb more readily at the higher pH. The increased adsorption of the cationic surfactant at the higher pH (and hence the higher surface potential) may be responsible

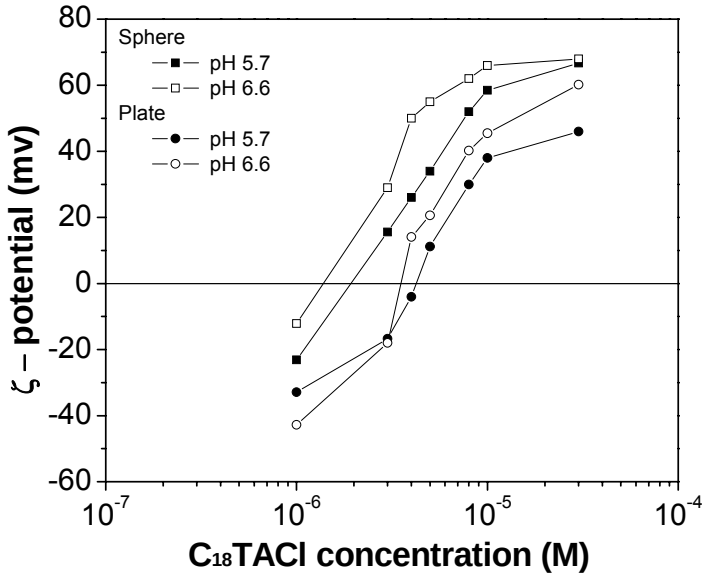

Figure 7. Comparison of the ζ-potentials measured in air-equilibrated $C_{18}TACl$ solutions of pH~5.7 with those measured in solutions whose pH was adjusted to pH 6.6.

for the transition of the measured forces from the long-range attraction to long-range repulsion when a 10^{-5} M C_{18}TACl solution was degassed (see Figure 4b). That the measured force became net repulsive does not mean that the surface became hydrophilic. It simply indicates that the repulsive force was greater than the attractive force. In the degassed solution, the two surfaces jumped into contact at 12 nm, which was much larger than predicted by the DLVO theory. It can be stated, therefore, that the long-range attractive force still existed in the degassed 10^{-5} M C_{18}TACl solution.

The ζ-potential measurements also show that the potentials of the glass sphere

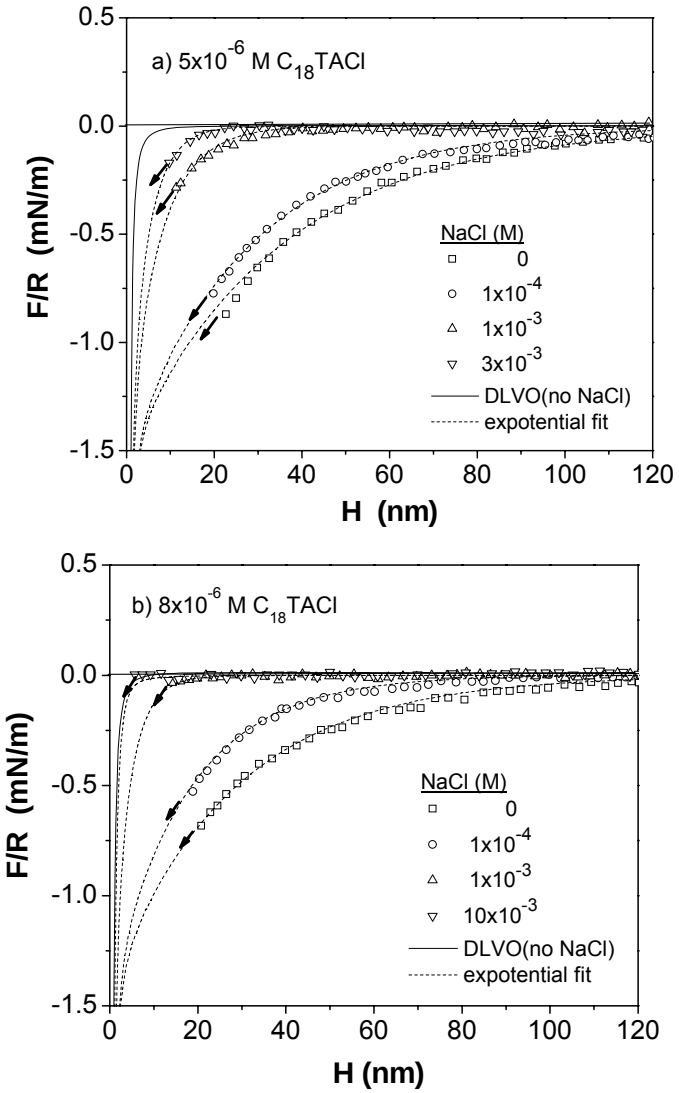

Figure 8. Effect of NaCl on the forces measured in air-equilibrated solutions of a) $5x10^{-6}$ M and b) $8x10^{-6}$ M C_{18}TACl solutions. The solid lines represent the DLVO fit, and the dashed lines represent the extended DLVO theory with a double-exponential force term (Eq. [3]). The fitting parameters are given in Table 1. The decrease in the long-range attractive force suggests that it may be of electrostatic origin.

Table 1. Effects of NaCl on Debye Lengths (κ^{-1}) and Decay Lengths (D_2) in C_{18}TACl Solutions.

NaCl (mM)	κ^{-1} (nm)	D_2 (nm)	
		C_{18}TAC Concentration (M)	
		$5x10^{-6}$	$8x10^{-6}$
0	136	33	28
0.1	30	26	18
1	9.6	7.5	4
3	5.6	3	-
10	3	-	1

were different from those of the ground silica plate. This finding suggests that we should consider the possibility that the long-range attractive forces measured in the present work could be attributed to attractive double-layer interactions.

Effect of Salt Concentration on the Forces in C_{18}TACl Solutions

One possible explanation for the attractive forces measured in air-equilibrated and degassed C_{18}TACl solutions and given in Figures 2 and 3, respectively, is that the force is of electrical origin. In this case, the magnitude of the force should decrease with an increase in salt concentration. Figure 8 shows the effect of added salt (NaCl) on the forces measured in 5×10^{-6} and 8×10^{-6} M C_{18}TACl solutions. Attractive forces decreased with increasing NaCl concentration. In all cases, the forces were approximately exponential. It is not likely that the decrease in force was caused by desorption of surfactant. Goloub, *et al.* (1997) showed that the addition of salt near a p.c.n. does not change the amount of adsorbed surfactant.

The measured forces were fitted to a double-exponential function,

$$\frac{F}{R} = C_1 \exp\left(-\frac{H}{D_1}\right) + C_2 \exp\left(-\frac{H}{D_2}\right) \tag{3}$$

where F is the surface force, R the radius of the glass sphere used for the force measurements, H the closest separation distance between the sphere and plate, and C_1, C_2, D_1 and D_2 are fitting parameters. It was assumed that the electrical potentials of the silica plates and glass spheres were zero, and that C_1=-50 mN/m, D_1=1.0 nm, and C_2=-1.4 mN/m. Also, the fitting was carried out after subtracting the forces due to van der Waals interaction from the measured forces.

The decay lengths (D_2) obtained from the fitting procedure described above are given in Table 1. Also shown in the table are the Debye lengths (κ^{-1}) calculated from the NaCl concentrations used. The values of D_2 obtained from the force curves obtained in 5×10^{-6} and 8×10^{-6} M C_{18}TACl solutions show the same trends although the values are not

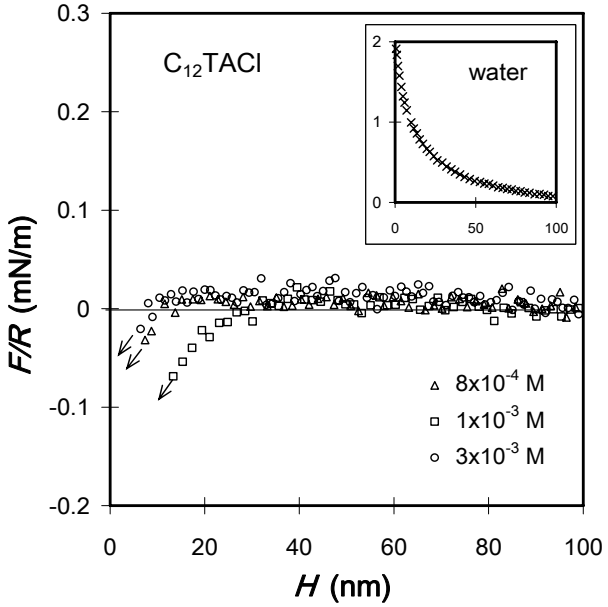

Figure 9. The AFM force curves obtained with the glass sphere and silica plate immersed in C_{12}TACl solutions at pH≈6. The repulsive forces measured in the presence of the surfactant are much lower than that obtained in pure water (inset). The arrows represent the distance where the two surfaces jumped into contact due to attractive forces. The attraction was strongest at 10^{-3} M C_{12}TACl.

identical. Unfortunately, the slow equilibration of the solution complicated the analysis of these results. Nevertheless, the decrease in the attractive force with NaCl suggests that the long-range attractive force may be of electrical origin and, therefore, is screened by the salt.

Force Measurements in C_nTACl Surfactant Solutions

Figure 9 shows the surface forces (F/R) measured between a glass sphere of radius R and a flat silica plate in C_{12}TACl solutions as a function of the closest distance (H) separating the two macroscopic surfaces. The inset, which represents the force curve obtained in pure water, shows a strong repulsive force due to the electrostatic repulsion between two negatively charged surfaces. All of the force curves shown in Figures 9-12 were smooth, without showing steps or kinks, indicating that the adsorption systems were relatively free of contamination or air bubbles.

In the presence of the cationic surfactant, the repulsive force disappeared almost completely due to charge neutralization. The force curve obtained at 8×10^{-4} M C_{12}TACl showed a weakly attractive force at H<10 nm. At 10^{-3} M C_{12}TACl, the attractive force became stronger and considerably longer ranged, the net attractive force being detectable at H≈25 nm. As the surfactant concentration was further increased to 3×10^{-3} M, the attractive force was significantly reduced.

Several investigators (Rutland and Parker, 1994; Christenson and Claesson, 2001) showed that the attractive forces measured between hydrophobic surfaces became the

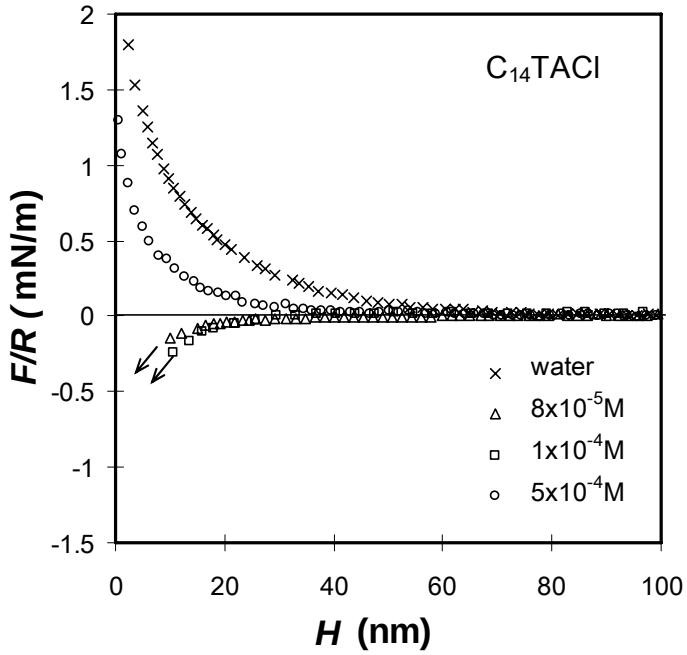

Figure 10. The AFM force curves obtained with the glass sphere and silica plate immersed in $C_{14}TACl$ solutions.

strongest at the surfactant concentrations close to the points of charge neutralization (p.c.n.), which is defined as the concentrations where the surface charge of the substrate is neutralized by the adsorption of an ionic surfactant. The *F*/*R* vs. *H* curves given in Figure 9 show the p.c.n. for the silica-$C_{12}TAC$ system is approximately 10^{-3} M, as the attractive force was the strongest at this concentration. At the p.c.n., most of the negative sites are occupied by the $C_{12}TA^+$ ions, forming hemimicelles in which the hydrocarbon tails of the adsorbed surfactant molecules are closely packed. (Somasundaran *et al*. 1964)

At 3×10^{-3} M $C_{12}TACl$, additional $C_{12}TA^+$ ions adsorb on silica, but most probably with inverse (or flip-flop) orientation. Such an orientation would be favored as it would cost less energy to insert additional surfactant molecules into the adsorption layer with their polar heads farthest apart from each other. The inverse orientation exposes the head groups toward the aqueous phase and, hence, causes the surface to be less hydrophobic. Therefore, the decrease in attractive force at the higher concentration can be attributed to the inverse orientation.

Figure 10 shows the surface forces measured between a glass sphere and a silica plate in the presence of a longer-chain ($C_{14}TACl$) homologue. The trend is the same as observed with $C_{12}TACl$. At 8×10^{-5} M $C_{14}TACl$, the repulsive double layer force that was observed in pure water was completely suppressed by charge neutralization, and a net-attractive force was observed. At 10^{-4} M $C_{14}TACl$, the net-attractive force became stronger. As the surfactant concentration was further increased to 5×10^{-4} M $C_{14}TACl$, the measured force became totally repulsive. It appears, therefore, that the p.c.n. is close to 10^{-4} M $C_{14}TACl$. At concentrations above the p.c.n., additional $C_{14}TA^+$ ions adsorbed,

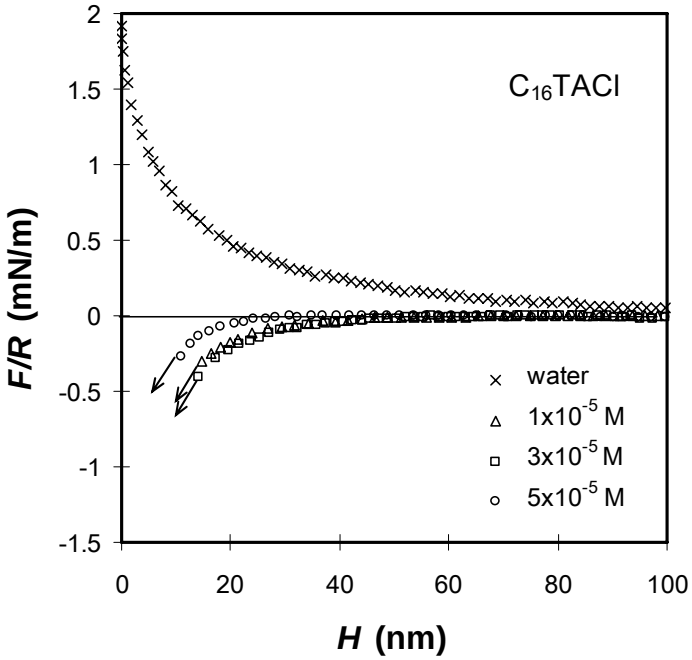

Figure 11. The AFM force curves obtained with the glass sphere and silica plate immersed in C_{16}TACl solutions. The measured forces are most attractive at $3x10^{-5}$ M C_{16}TACl. The long-range forces become less negative at the higher concentration possibly due to inverse orientation.

causing the observed force totally repulsive. It is likely that additional surfactant ions adsorbed with inverse orientation, rendering the surface hydrophilic. It is interesting to note here that an increase in the number of ethylene groups by two caused a ten-fold decrease in the concentration (p.c.n.) at which the strongest attractive force was observed. This observation is a powerful message that longer-chain surfactants be used to increase the attractive force between hydrophobic surfaces.

Figure 11 shows the results obtained with an even longer-chain (C_{16}TACl) homologue. At 10^{-5} M C_{16}TACl, the repulsive force disappeared completely and a net-attractive force appeared. At 3×10^{-5} M, the measured force became most attractive, indicating that the p.c.n. for the silica-C_{16}TACl was close to this concentration. At 5×10^{-5} M, the attractive force was somewhat reduced, most probably due to the inverse orientation of the $C_{16}TA^+$ ions. It is interesting to note here that the attractive forces observed with the C-16 cationic surfactant were substantially longer ranged than those observed with shorter-chain (*i.e.*, C-12 and C-14) homologues.

The results obtained with C_{18}TACl are presented in Figure 12. At 3×10^{-6} M C_{18}TACl, a very long-ranged and net-attractive force was observed. When the concentration was raised to 5×10^{-6} M, the attractive force was strongest. At 10^{-5} M, the attractive force was reduced a little. Thus, the p.c.n. of the silica-C_{18}TACl system was approximately 3×10^{-5} M, which was significantly lower than observed for the shorter chain homologues. The most interesting aspect of the data shown in Figure 4 was that the

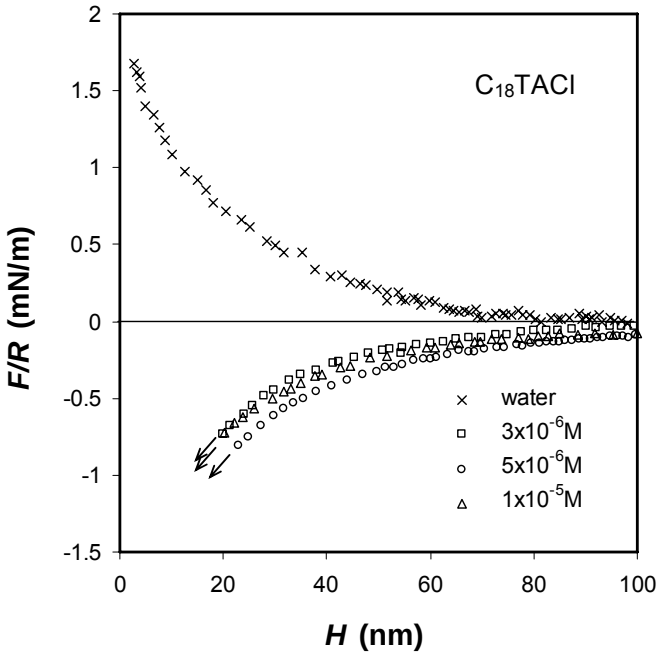

Figure 12. The AFM force curves measured with the glass sphere/silica plate immersed in $C_{18}TACl$ solutions. The long-range forces measured are most attractive at $5x10^{-6}$ M $C_{18}TACl$, which is close to the p.c.n.

C-18 surfactant gave much stronger and longer-range attractive forces than observed for the shorter-chain homologues. With the $C_{18}TACl$, net attractive forces were observed at separations as large as 100 nm.

The strongest attractive force curves shown in each of Figures 9-12 are redrawn in Figure 13, and were fitted to a single-exponential force law, *viz*. eq[1]. Table 2 gives the values of these parameters as well as the Debye length (κ^{-1}). From Figure 5, it is clearly seen that the maximum attractive force that can be created by the adsorption of a C_nTACl on silica increases with increasing hydrocarbon chain length. As shown in Table 2, the decay length (D) of the attractive force increases with chain length. It was only 3 nm at n=12. As n was increased to 14, 16, and 18, D was increased to 6, 14, and 32 nm, respectively. While D was very sensitive to chain length, the values of C stayed practically the same, 1.3-1.4 mN/m. It is important to note here that the surfactant concentration at which surface charge is neutralized and the maximum hydrophobic force observed decreases substantially with increasing chain length.

AFM Images

Figure 14 shows the contact mode AFM images of a fused quartz plate immersed in water. It shows that the surface is smooth with a roughness of less than 2 nm on a 100×100 nm scale. The AFM images show boundaries between fused silica particles of approximately 100 nm.

The presence of the grain boundaries on the fused silica surfaces can make it difficult to see the surfactant molecules adsorbing on the surface. Therefore, the images of surfactant

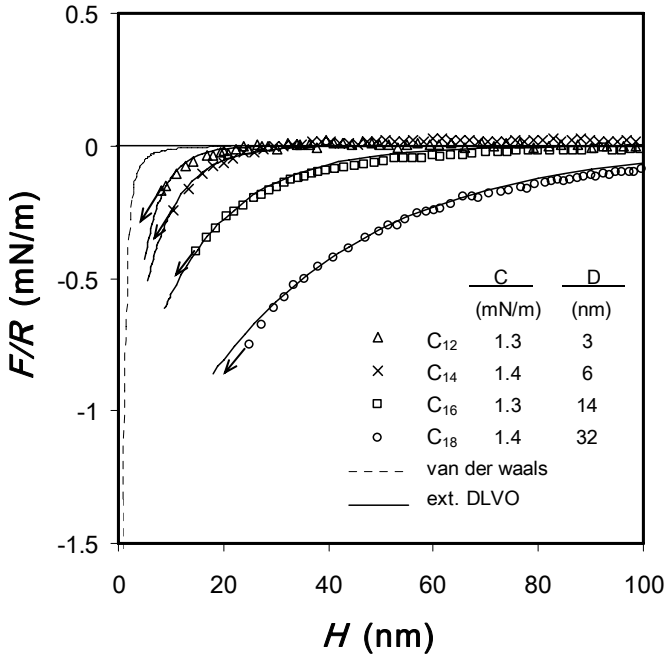

Figure 13. The AFM force curves obtained with glass sphere and silica plate at the p.c.n.'s of the C_nTACl homologues (n = 12, 14, 16, 18). The dashed line represents the van der Waals force with the Hamaker constant $A = 0.8x10^{-20}$ J. The solid lines represent the extended DLVO theory which includes contributions from the van der Waals force and the hydrophobic force. (The double layer force is considered to be zero.) The hydrophobic force is represented by the single-exponential force law (Eq. (1)) with a pre-exponential parameter C and the decay length D as fitting parameters. It is shown that the hydrophobic force increases with increasing chain length.

molecules adsorbing on SiO_2 surfaces were taken using silicon wafers as substrates. Figure 15a shows an AFM image of a silicon wafer surface immersed in Nanopure water. Before taking the images, the substrate had been boiled in a H_2SO_4/H_2O_2 solution (7:3 by volume) at 120°C for 1 hour to remove possible organic contaminants and to generate a "clean" oxide surface. The 10×10 μm image shows that the substrate surface is smooth with 0.2 nm roughness. No lumps or scratches were seen, indicating that the surface was clean and free of contaminants. Figure 15b shows an image of a silicon wafer surface that had been immersed in 10^{-5} M $C_{18}TACl$ solution for 1 hour. It shows that the surfactant molecules cover most of the surface with some areas unoccupied, suggesting the formation of patches or hemi-micelles. The height of the adsorption layer is approximately 2.2 nm, which is a little less than the length (2.3 nm) of a fully extended C_{18} hydrocarbon chain.

Figure 15c and d show the AFM images of a silicon wafer immersed in a 3×10^{-5} M $C_{18}TACl$ solution which was above its p.c.n. The images obtained at this concentration show that the adsorption occurs in patches. The heights of some of the patches are higher than 2.3 nm, indicating bilayer formation. Some of the patches are of 20-30 nm in dimension, while others are larger.

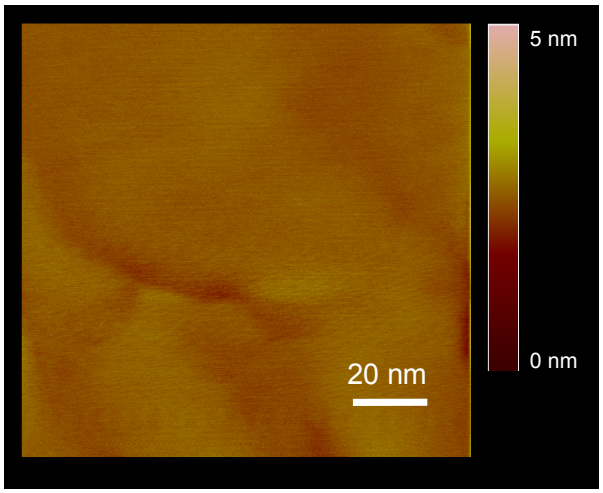

Figure 14. A soft contact mode AFM image of the fused silica plate immersed in water. The dimension of the scanning area is given by a scale bar. Height data for the surface were obtained using the scale bar to the right.

Adsorption Mechanism

When a glass or silica substrate is immersed in water, its surface becomes eclectically charged by the following mechanism:

$$-\overset{|}{\underset{|}{Si}}-OH_2^+ \overset{H^+}{\Leftrightarrow} -\overset{|}{\underset{|}{Si}}-OH \overset{OH^-}{\Leftrightarrow} -\overset{|}{\underset{|}{Si}}-O^- + H_2O \qquad (4)$$

in which silanol (Si-OH) groups are protonated to become positive ($Si\text{-}OH_2^+$) sites or are hydroxylated to become negative ($Si\text{-}OH_2^-$) sites depending on pH. The point of zero charge (p.z.c.) of silica is approximately pH 2. (Parks, 1965; Papirer, 2000) Thus, silica surfaces are negatively charged at pHs above 2. It has been shown, however, that the negative charge density is low until the pH increases above 6 (Zajac *et al*., 1996; Goloub *et al*., 1996) In the present work, direct force measurements were conducted at pH≈5.7, where surface charge densities are relatively low. Under this condition, the adsorption of cationic surfactants may occur in patches. (Rutland, J.L. Parker, 1994; Wong *et al*. 1989)

In 1955, Gaudin and Fuerstenau (1955) studied the adsorption of dodecylammonium hydrochloride (DAH) on quartz, and introduced the concept of "hemi-micelle" formation (Fuerstenau, 1970). More detailed studies conducted by Somasundaran and Fuerstenau (1966) and Wakamatsu and Fuerstenau (1968) showed that the onset of the hemi-micelle formation is indicated by a sharp decrease in ζ-potential. Below this concentration, which is referred to as the critical hemi-micelle concentration (c.h.c.), the surfactant molecules adsorb individually by displacing the counter-ions, causing no changes in the ζ-potentials. Above the c.h.c., however, the hydrocarbon chains of the surfactant molecules associate with each other, causing a sharp increase in adsorption density and, hence, a sharp decrease in ζ-potentials. When the surfactant concentration is increased further, the surface charge can be neutralized. Above this concentration, which is referred to as point of charge neutralization (p.c.n.), the surfactant molecules adsorb with inverse (or flip-flop) orientation, causing a decrease

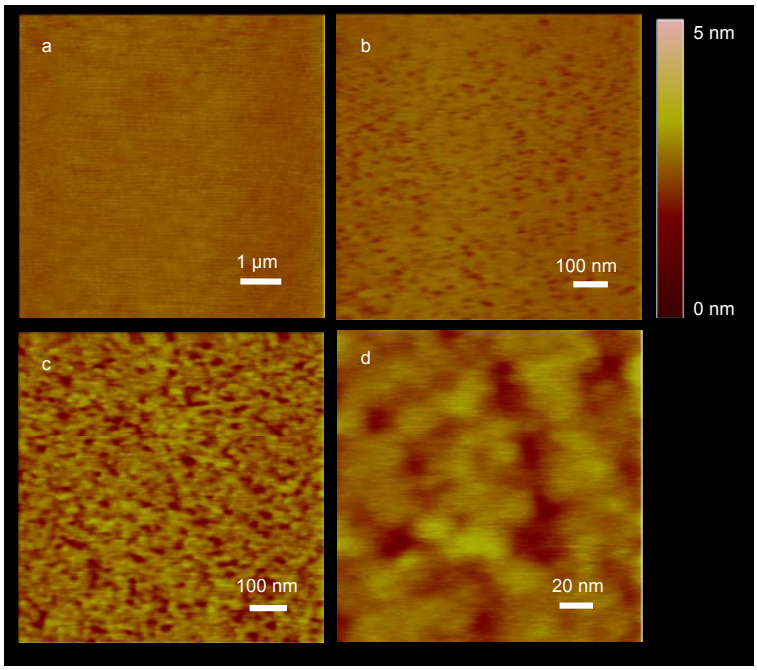

Figure 15. The soft contact mode AFM images of the silicon wafer surfaces immersed in C_{18}TACl solutions at different concentrations and scale. The scale of the image is given in each image. The scale bar on the side gives height information. All of the images were taken 1 hour after the solution had been injected into the AFM cell. a) 10×10 μm image in water; b) 1×1 μm image in a 10^{-5} M C_{18}TACl solution; c) 1 × 1 μm image in a 3×10^{-5} M C_{18}TACl solution; d) 200×200 nm image in a $3\text{x}10^{-5}$ M C_{18}TACl solution.

in hydrophobicity. Thermodynamically, the inverse orientation is favored as it is not necessary to remove some of the hydrated water molecules from polar heads.

It was shown by Herder (1990) that the details concerning the formation of an adsorption layer of an ionic surfactant (DAH) onto an ion-exchanging solid surface (mica) are surprisingly complex. Upon raising the surfactant concentration, a localized (site-wise) adsorption mechanism is gradually being replaced by an adsorption mechanism that in the end involves migrating (mobile) surfactant ions. Simultaneously, hemi-micelles are formed, first as immobile patches at low surfactant concentrations (typically two to three orders of magnitude below the c.m.c.) and possibly also as mobile surfactant aggregates at higher surfactant concentrations (typically one order of magnitude below the c.m.c.) which are more closely related to ordinary surfactant micelles in bulk solution. A full bilayer is as a rule finally formed in the c.m.c. concentration range. Reaching equilibrium for an adsorption layer of this kind is an amazingly slow process (many hours), especially for surfactants with a long hydrocarbon tail.

The AFM images of the silicon wafers immersed in surfactant solutions support the adsorption mechanism discussed above. Figure 15b, which was obtained at 10^{-5} M C_{18}TACl, which was close to the p.c.n. ($=5\times10^{-6}$ M), shows patches (or hemi-micelles) of

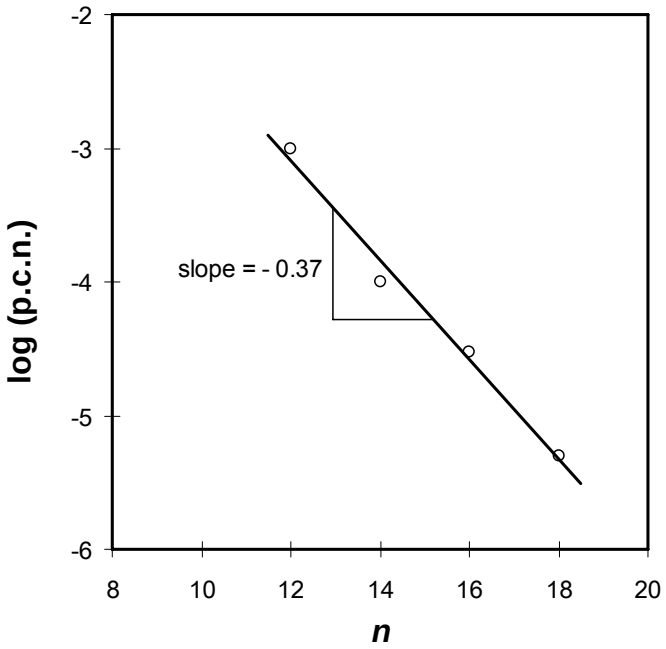

Figure 16. A relationship between the p.c.n.'s for the silica-C_nTACl system and the number of carbons in the hydrocarbon chains. According to the Stern-Graham equation (Eq. 5), the slope of -0.37 gives ϕ = -0.85 kT per CH_2 group.

the $C_{18}TA^+$ ions adsorbed on the silica substrate. Many of the patches have coalesced to form a self-assembled monolayer with parts of the surface unoccupied. At this concentration, it appears that the surfactants have the normal mode of orientation with their head groups in contact with the surface and the hydrocarbon tail stretching out toward water. An evidence for this is that the thickness of the adsorption layer is close to the length of the fully-extended C-18 hydrocarbon chains. At 3×10^{-5} M, which is well above the p.c.n, the adsorption layer was non-uniform and the heights of the clusters are much larger than the hydrocarbon chain length, indicating that additional surfactant molecules adsorb on top of the monolayer most probably with inverse orientation.

It has been suggested that the attractive hydrophobic force becomes the strongest at the p.c.n. of a surfactant. Thus, one can determine the p.c.n. from a set of force curves obtained at different concentrations of a given surfactant. Table 2 gives the values of the p.c.n.'s determined from the data obtained for the C_nTACl-silica systems studied in the present work. Also shown in the table for comparison are the points of zeta-potential reversal (p.z.r.) obtained by Somasundaran *et al*. (1964) for the quatz-alkylammonium acetate system. In Figure 16, the p.c.n. values given in Table 2 have been plotted *vs*. the number of hydrocarbons (n) in the alkyl chains of the C_nTACl homologues. This plot represents the Stern-Grahame equation (Grahame, 1947):

$$\ln C_0 = -n_c(\phi / kT) - \ln\left(\Gamma_\delta^+\right)_0 - \ln(2r) \qquad (5)$$

Table 2. The parameters of Eq. (1) obtained for the force curves measured at the p.c.n's of the silica-C_nTACl system

Surfactant	p.c.n. (M)	p.z.r.[1] (M)	C (mN/m)	D (nm)	κ^{-1} (nm)
C_{12}TACl	$1x10^{-3}$	$2x10^{-3}$	1.3	3	9.5
C_{14}TACl	$1x10^{-4}$	$4x10^{-4}$	1.4	6	30
C_{16}TACl	$3x10^{-5}$	$7x10^{-5}$	1.3	14	54.8
C_{18}TACl	$5x10^{-6}$	$8x10^{-6}$	1.4	32	134

*point of zeta-potential reversal, from Somasundaran *et al*. [30].

in which C_0 is the., ϕ is the standard adsorption free energy per mole of CH_2 or CH_3 group and $\left(\Gamma_{\delta}^{+}\right)_0$ is the adsorption density of the cationic surfactant at ζ=0, r is the radius of the polar head of the surfactant, and k is the Boltzmann constant. If the product of $\left(\Gamma_{\delta}^{+}\right)_0$ and $2r$ remain relatively constant for the C_nTACl homologues studied in the present work, a plot of log (p.c.n) *vs*. n should give a slope of $-\phi/2.3kT$, from which one can obtain the value of ϕ = -0.85 kT (-0.50 kcal per mole). This value is pretty close to the value of -0.97 kT obtained from a plot of log (p.z.r.) vs. n for the quartz-primary amine system (Somasundaran *et al*., 1964; Somasundaran and Huang, 2000). For the ordinary micelles forming in solutions of ionic surfactants, the corresponding figure is about -0.75 kT per CH_2 group.

The above discussion shows that a major driving force for adsorption of a long-chain surfactant is the hydrocarbon chain association, which is commonly recognized as hydrophobic effect. (Tanford, 1980) Therefore, the longer the hydrocarbon chain length is, the larger the hydrophobic effect becomes, which in turn causes a decrease in the p.c.n.

Possible Origin(s) of Hydrophobic Force

We see little merit in attributing the long-range attractive forces observed in present work to the effects of adsorbed bubbles because: 1) the effects of degassing are minor, and can be explained by the effect of a small pH change, 2) the observed changes in AFM images on addition of surfactant could be explained simply by the adsorption of surfactant, rather than by the adsorption of bubbles, and 3) we did not observe steps (small discontinuities) in force curves that could be attributed to bridging bubbles. Therefore, for the remainder of this paper, we will consider three alternate hypotheses for the long-range attractive forces: a) attractive double-layer forces; b) a long-range hydrophobic force, and c) attractive forces due to correlations between charged patches.

Figure 13 and Table 2 show that the long-range attraction becomes stronger and longer ranged with increasing hydrocarbon chain length. Further, the concentration at which the strongest attractive force was observed increased with increasing carbon number (n) in a chain.

It has been more than twenty years since Israelachvilli and Pashley (1982, 1984) observed long-range attractive forces between two mica surfaces hydrophobized with hexadecyltrimethylammonium bromide (C_{16}TABr). Numerous other investigators observed similar results, (Christenson and Claesson, 1988; Rabinovich and Derjaguin, 1988; Wood and Sharma, 1995; Hato, 1996; Yoon and Ravishankar, 1996) and proposed possible causes for the long-range attraction. (Claesson and Christenson, 1988; Eriksson *et al.*, 1989; Miklavic *et al.*, 1994; Sakamoto *et al*., 2002) However, its origin is not yet fully understood. In the following, we discuss the possible origin(s) of the long-range attraction between hydrophobic surfaces. Discussing the effect of the chain length may shed light from a different angle on this complex and continually perplexing issue.

It was shown that the long-range attractive force deceases in the presence of inorganic electrolyte, which may be taken as evidence that the non-DLVO force is of electrostatic origin. In this regard, it is of interest to analyze the force data obtained in the present work in terms of the charged-patch model developed by Miklavic *et al*. (1994). Their model suggests that the long-range attraction may originate from the electrostatic correlation attraction between the patches of surfactant molecules formed on surfaces. It was necessary to assume, of course, that the patches are electrically charged. The charged-patch model was based on the recognition that long-chain surfactants adsorb in patches (or hemi-micelles) at a relatively low concentration. According to Fuerstenau and Pradip (2005), hemi-micelles begin to form at concentrations 2-3 orders of magnitude below the c.m.c. The AFM (Zhang *et al.*, 2005) and SEM (Delamarche, *et al.*, 1994) images of the surfactant-coated surfaces indeed showed patches, as is also shown in Figure 15. Further, the aggregation numbers of the hemi-micelles (or 'soloids') determined using the electron spin resonance (ESR) and fluorescence spectroscopic techniques showed the patch-wise adsorption mechanism (Fan *et al.*, 1997; Ström *et al.*, 2000).

1) Attractive Double-layer Forces?

The possibility of explaining the long-range attractive forces observed in the present work as due to double-layer interaction was considered in an earlier publication of one of us.[33] An appeal for this approach was that it is a known interaction, and the measured forces have the appropriate functional form (exponential). In the present work, however, we are immediately in trouble with the assumptions of DLVO theory. Not only do we have the usual problems with additivity of the double-layer and van der Waals forces, but also the fact that C_{18}TACl ions are not point-sized, that there are significant interactions between them, and that the charge regulation is unknown. Furthermore, we have good evidence that the surfaces were inhomogeneous on the length scale of the forces, and the adsorption was not at equilibrium. Nevertheless, we went ahead and estimated the values of the surface potentials (ψ_0) that are required to fit the measured

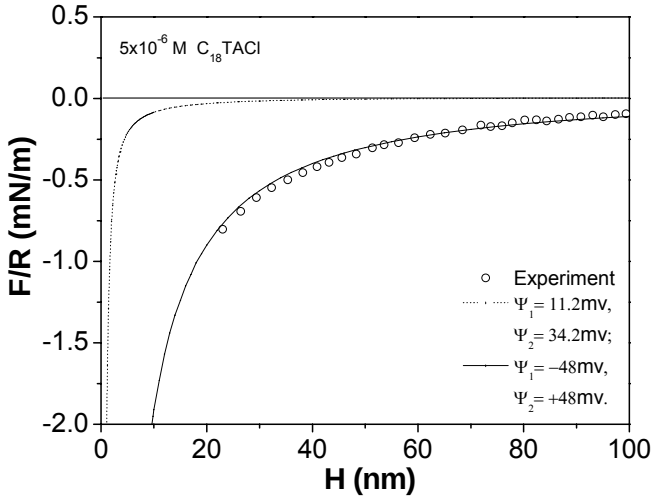

Figure 17. Force curves for the silica plate-glass sphere interaction in an air-equilibrated $5x10^{-6}$ M $C_{18}TAC$ solution. The dotted line represents the DLVO fit with Ψ_1=+11.2 mV and Ψ_2=+34.2 mV, which were taken from the ζ-potential measurements. To fit the long-range attractive force, it was necessary to assume that Ψ_1=+48 mv and Ψ_2=-48mv, which is unreasonable.

forces assuming that that Poisson-Boltzmann theory applies. We used the constant potential boundary condition.

Figure 17 shows the force curve obtained in an air-equilibrated 5×10^{-6} M $C_{18}TACl$ solution. The measured force can be reproduced by assuming that one surface has ψ_1=+48 mV and the other has ψ_2=-48 mV with κ^{-1}=130 nm. However, these potentials were very different to the zeta potential measurements. As shown in Figures 6 and 7, the ζ-potentials of the silica plate and glass sphere were +34 and +11 mV, respectively, in air-saturated solutions of pH 5.7. The force curve obtained with these values as ψ_1 and ψ_2, and κ^{-1}=130.4 nm became weakly attractive. Clearly, the agreement was not good. Although the long-range attractive force observed in the air-saturated $5x10^{-6}$ M $C_{18}TACl$ solution decayed exponentially, it was definitely not due to double-layer force.

2) Charged Patches Model

Miklavic *et al*. (1994) considered that the patches are charged but the surface as a whole is neutral. The model implies that the interaction between the two surfaces covered with patches of positive and negative charges is always attractive when the patches are sufficiently mobile and free to correlate with each other. At an infinite separation, the patches may be distributed randomly. As the separation decreases, the patches migrate laterally on the surface in order for the system to minimize the free energy. Assuming that the patches are distributed in a square lattice with a dimension of *a*, the free energy of interaction per unit area ($G(H)$) is given as follows:

$$G(H) = -\frac{A}{kT}\Omega^2 \exp\left(-2q_{\min}H\right) \tag{6}$$

Table 3. The parameters of Miklavic *et al.*'s charged-patch model as obtained by fitting the decay lengths obtained at the p.c.n.'s of the silica/C_nTACl system

	p.c.n. (mM)	D (nm)	q_{min}	κ^2	$(\pi/a)^2$	a (nm)	b (nm)
C_{12}TACl	1	3	0.167	0.011	0.0168	24	18
C_{14}TACl	0.1	6	0.083	0.0011	0.0058	41	31
C_{16}TACl	0.03	14	0.036	0.00033	0.00097	101	76
C_{18}TACl	0.005	32	0.0156	0.000056	0.000188	229	172

b=0.75a

where A is the area of the unit cell, Ω is a constant which varies with surface property (surface potential or charge), reciprocal lattice vector, and lateral displacement. As shown, the interaction energy decays exponentially, with a decay length of $(2q_{\min})^{-1}$, in which $q_{\min}$ is given as follows:

$$q_{\min} = \left[(\pi / a)^2 + \kappa^2\right]^{1/2} \tag{7}$$

where κ is the reciprocal Debye length. At a high electrolyte concentration, $q_{\min} \approx \kappa$; therefore, the interaction energy should decay as $(2\kappa)^{-1}$. At a low electrolyte concentration, κ is small; therefore, $q_{\min}$ should vary inversely with a.

From the decay lengths, D ($=(2q_{\min})^{-1}$), measured in the present work, one can obtain the values of $q_{\min}$, which can then be used to obtain the values of a using Eq. (7). In this exercise, the κ values have been calculated from the concentrations of the ionic surfactants used in force measurements. As shown in Table 3, the lattice patch size b, which may be roughly estimated from the value of a by multiplying it with a factor 0.75 used by Miklavic *et al.*, increases with chain length. This finding is in agreement with the results obtained by Fan *et al*. (1997) and Strom *et al*.. (2000), who showed that the aggregation numbers of the hem-micelles increased with increasing chain length. These investigators studied the adsorption of C_{12}TABr, C_{14}TABr, and C_{16}TABr on silica and alumina.

Eq. (7) suggests that decay length (or $q_{\min}$) is mainly controlled by two parameters, *i.e.*, a and κ. The data presented in Table 3 show that the contribution from a is more significant than from κ in determining the range of attraction, but κ still plays an important role, particularly with the shorter chain surfactant, *e.g.*, C_{12}TACl. These findings may be anticipated from the fact that all of the force data presented in Table 3

were obtained in the absence of supporting electrolyte. Under this condition, the residual concentrations of the ionic surfactants act as electrolytes that can dampen the hydrophobic force.

It has been shown in the present work that the long-range attraction was strongest at p.c.n., and that the adsorption of the C_nTACl on silica is likely to occur as patches. Both of these observations provide a basis for discussing the origin of the long-range attraction in view of the model developed by Miklavic *et al*.. A question remains, however, as to whether it is physically possible for the patches to be positively charged, while unoccupied silica surface remains negatively charged. This would undoubtedly be the case if the adsorption occurs as micelles (Gu and Huang, 1989), or as bilayers (Yeskie and Harwell, 1988). In both of these cases, the number of the surfactant molecules adsorbing in each patch (aggregation number) can exceed the negative charge sites underneath, causing it net positively charged. However, the micellar or bilayer adsorption should render the surface hydrophilic due to the orientation of the polar heads toward the aqueous phase. Therefore, such adsorption mechanisms cannot explain the experimental observations that both the long-range attraction and contact angle reached the maxima at a p.c.n..

Somasundaran and Fuerstenau (1966) showed, on the other hand, that long-chain surfactants adsorb as hemi-micelles, in which the head groups of the surfactant molecules are in touch with substrates and the hydrocarbon tails point toward the aqueous phase.

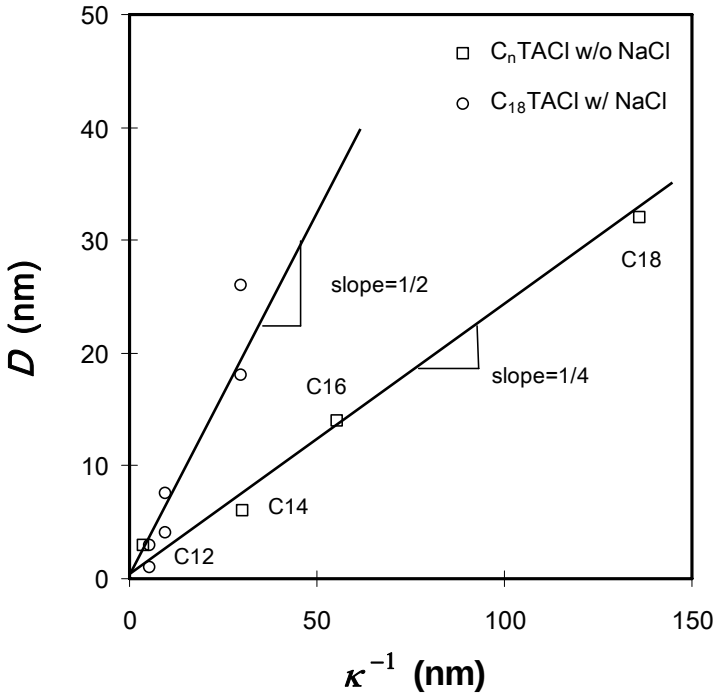

Figure 18. Decay length *vs.* the Debye length plots for the data obtained with $C_{18}TACl$ with NaCl and for the data obtained in C_nTACl solutions at the p.c.n.'s in the absence of electrolyte. The former fits the charged patch model of Miklavic *et al.*, while the latter cannot be explained with any available theory.

Such orientation renders the surface hydrophobic. Once the surface has been neutralized, the surfactant molecules begin to adsorb with inverse orientation, rendering the surface hydrophilic. Thus, the surface should become most hydrophobic at a p.c.n, as has been demonstrated by Fan *et al*. (1997) with a series of vacuum flotation experiments.

For the case of C_nTA^+ ions adsorbing on silica, the hemi-micelles formed at a p.c.n. must be positively charged in order for the surface, which includes the patches of unoccupied negative charge sites, to be neutral as a whole. The positive charges associated with the hemi-micelles should come from the surfactant molecules co-adsorbing into the hemi-micelles along with those that adsorb on negatively charged sites. Fuerstenau and Pradip (2005) showed that at p.c.r. the co-adsorption occurs with the head groups in contact with the surface which gives rise to optimal flotation. Beyond the p.c.r., the co-adsorption occurs with the head groups oriented toward the water phase.

It appears, therefore, that the charged patch model of Miklavic *et al*. (1994) requires substantially larger patches than observed experimentally with self-assembled monolayers to predict the long-range attractive forces measured in the present work. Moreover, it seems unlikely that the hemi-micelles (patches) formed at or slightly below the p.c.n. can migrate on the surfaces rapidly enough to actually generate an attractive correlation force.

3) Eriksson et al.'s theory

Figure 18 shows a plot of D *vs*. κ^{-1} for the data obtained with C_nTACl homologues. Also shown is a plot of the D values obtained with $C_{18}TACl$ in the presence of varying concentrations of NaCl. The latter has a slope of ½ as predicted by Eq. (7). The former, on the other hand, has a slope of ¼, for which there is so far no adequate theoretical explanation.

Figure 19 shows a plot of D *vs*. $(C_0 n)^{-1/2}$, where C_0 is the concentration of C_nTACl in bulk solution and n is the number of carbons in a hydrocarbon chain. The linear relationship suggests that the range of hydrophobic force is simply a function $C_0 n$, which is the molar concentration of the CH_2 and CH_3 groups in solution. In effect, the results presented in Figure 18 shows that the long-range attraction decreases with increasing concentration of the species that can disrupt the structure of water, *i.e.*, hydrocarbons. That the long-range attraction decreases in the presence of NaCl may be given the same explanation, that is, the long-range attraction decreases with increasing concentration of the species, *i.e.*, Na^+ and Cl^- ions in this case, that can disrupt the water structure. Thus, the results presented in Figures 8 and 13 show that the long-range attraction is strongest when water is in its pristine state. Any foreign species added to water causes a decrease in D.

According to the Derjaguin approximation (Derjaguin, 1934), the surface force (F) normalized by the diameter of the sphere (R) can be given as follows:

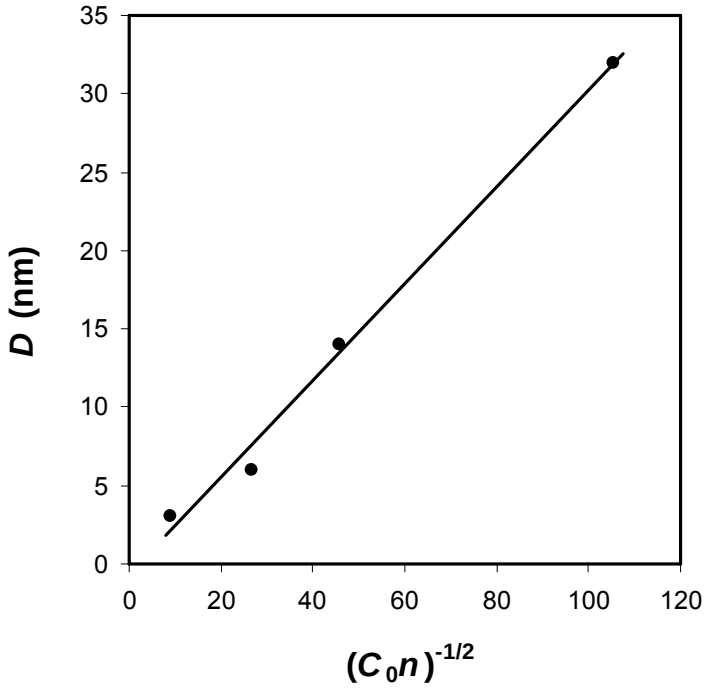

Figure 19. A decay length (D) *vs*. $(C_0 n)^{-1/2}$ plot for the data obtained in C_nTACl solutions in the absence of electrolyte. C_0 represents the surfactant concentration, and D is equivalent to b^{-1} of Eriksson *et al*.'s hydrophobic force model (Eq. [11]) derived from the mean-field theory. $C_0 n$ represents the effective concentration of CH_2/CH_3 species in solution.

$$F / R = 2\pi\left(\gamma^{\mathrm{f}} - \gamma_{\infty}^{\mathrm{f}}\right) \tag{8}$$

Eriksson *et al*. (1989) derived theoretical expressions for γ^{f} and $\gamma_{\infty}^{\mathrm{f}}$ using a mean field approach based on the 'square-gradient approximation'. By substituting those into Eq. (8), they obtained the following expression for the hydrophobic force:

$$F / R = -B\left[\coth(bH / 2) - 1\right] \tag{9}$$

which can be simplified to:

$$F / R = -2B\exp(-bH) \tag{10}$$

for large enough separations. Eq. (10) shows that b^{-1} can be identified with D and that $2B$ is equivalent to C of Eq. (1). Furthermore, according to Eriksson *et al*.,

$$b^{-1} = \sqrt{c_3 / 2c_2} \tag{11}$$

where c_2 and c_3 are constants which account for the free energy costs of structuring the water and forming order parameter gradients, respectively. From Figure 18, it is seen that the decay length D (or b^{-1}) varies as $(C_0 n)^{-1/2}$. According to Eq. 11, such a relationship can be generated if we assume that c_2 is proportional to $(C_0 n)^{1/2}$ and c_3 is inversely proportional to $(C_0 n)^{1/2}$. In other words, the presence of surfactant ions would make it more costly free-energy-wise to obtain a certain ordered water state, whereas it would be less costly with the gradients in the order parameter function in the vicinity of a hydrophobic surface. Although these assumptions seem reasonable, they are nevertheless in need of further justification.

Based on the data obtained in the present work, two possible origins for the long-range attractions have been discussed. The charged-patch model of Miklavi**c** *et al.* seems to provide an explanation at high electrolyte concentration. At low electrolyte concentrations, however, it is necessary to assume that the patch sizes are much larger than known from experimental work. A basic premise of the model is that the patches have lateral mobility. Otherwise, the model predictions are too small to predict the long-range forces measured between hydrophobic surfaces. A question arises then as to whether the charged patches are indeed mobile enough to give rise to long-range attractions. It is conceivable that *physically* adsorbing surfactant molecules might possess the necessary molecular and micellar mobility that is a prerequisite for the applicability of the theory of Miklavic *et al.*. However, ionic surfactants adsorb primarily on oppositely charged surface sites rather than being evenly distributed across the surface. For a surfactant molecule to be mobile, it may have to jump from one site to another, which is likely to be a slow process when the surfactant-site bond is fairly strong. Needless to say, the corresponding aggregate mobility should be exceedingly slow. Thus, correlation attraction might possibly arise in the concentration range well above the p.c.n., where, however, electrostatic repulsion as a rule predominates. Further, the charged-patch model does not explain the long-range forces observed with silylated surfaces and Langmuir-Blodgett-deposited surfaces. The surfactants in neither of these two surfaces are likely to be mobile. It should also be noted here that long-range attractions have been observed with thiolated gold surfaces, which is a well-known chemisorbing system.

The third possibility discussed above is related to water structure. It suggests that surfactant monomers and inorganic electrolytes break the hydrogen bond network present in thin watery films between hydrophobic surfaces, thereby reducing the long-range attraction. A short-chain surfactant requires a higher monomer concentration in solution to obtain a given surface coverage, which would be the reason that it gives a relatively short-range attraction. Chemisorbing surfactants such as thiols would leave very few monomers in solution, which may be conducive to creating long-range attractions. The very long-range attractions observed with silylated and LB-deposited surfaces may be explained in the same vein. The circumstance that the experimental data support Eriksson *et al.*'s theoretical model (Eriksson *et al.* 1989), which is based on the changes in water

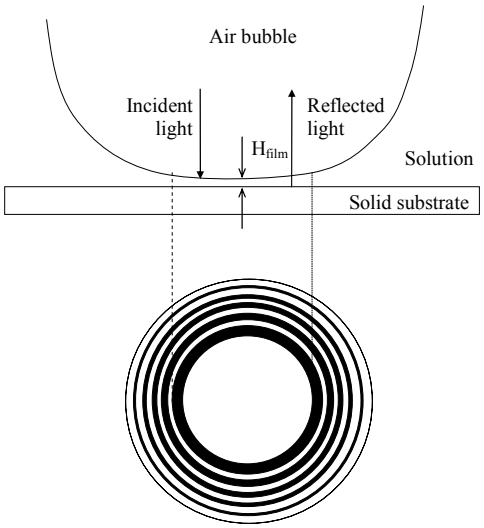

$$H_{film} = \frac{\lambda}{2n}\left(\frac{1}{2} - \frac{1}{\pi}\arcsin\sqrt{\frac{I_t - I_{\min}}{I_{\max} - I_{\min}}}\right) \quad (12)$$

Figure 20. Film Thickness Measured Using a Micro-interference Technique

structure across a hydrophobic surface-solution interface, is yet another reason to further explore the possibility of the hydrophobic force actually being a structural force.

Measurement of wetting film thickness

The thickness of wetting film at different NaCl solution has been carried out on oxidized hydrophilic and hydrophobic Silicon wafer to study the effect of surface hydrophobicity on the wetting film thickness. Also, the kinetics of film thinning in certain salt solution was studied. However, due to the formation of the "dimple" at the time of film thinning, the kinetics of film thinning does not apply to the theoretical Reynold equation. However, on hydrophilic substrate, the equilibrium film thickness was finally obtained after 30 seconds thinning and the values were compared to those calculated from classical DLVO theory. (Schulze *et al.*, 2001)

The theoretical disjoining pressure at different salt concentrations can be calculated using the following equations from Eq. (13) to Eq. (17) and plotted as Fig. 21. The theoretical equilibrium film thickness can be obtained by picking up the point at which the disjoining pressure is 194 Pa, which equals the capillary pressure, P_c in present wetting film system, on the disjoining pressure-distance curves for each salt concentration; thus the obtained distance, H gives the equilibrium film thickness, H_e from the DLVO theory.

$$\Pi = \Pi_{el} + \Pi_{vdw} \quad (13)$$

$$\Pi - P_c = 0 \quad (14)$$

$$P_c = \frac{2\gamma}{R_c} \quad (15)$$

$$\Pi_{vdw} = -\frac{A_{slv}}{6\pi h^3} \quad (16)$$

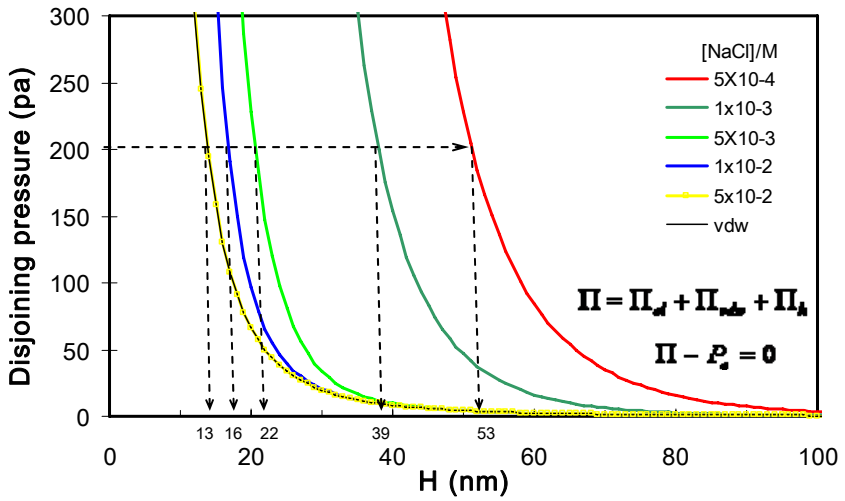

Figure 21 Theoretical equilibrium film thickness at different salt concentrations.

$$\Pi_{el} = -\frac{1}{2}\left[\kappa\left(\frac{\sigma_2^2}{\varepsilon_0\varepsilon\kappa} - \varepsilon_0\varepsilon\kappa\Psi_1^2\right)\frac{1}{\cosh^2(\kappa h)} - 2\kappa\Psi_1\sigma_2\frac{\sinh(\kappa h)}{\cosh^2(\kappa h)}\right] \quad (17)$$

in which,

- κ : Debye-Huckel Parameter;
- ε_0 : absolute dielectric constant;
- ε : relative dielectric constant;
- σ_2: charge density of silica surface;
- ψ_1: surface potential of gas bubble;
- h : film thickness;
- γ : surface tension of liquid.
- R_c: radius of capillary tube;
- A_{slv}: Hamaker constant for wetting film(silica/water/air system), ~$1x10^{-20}$J.

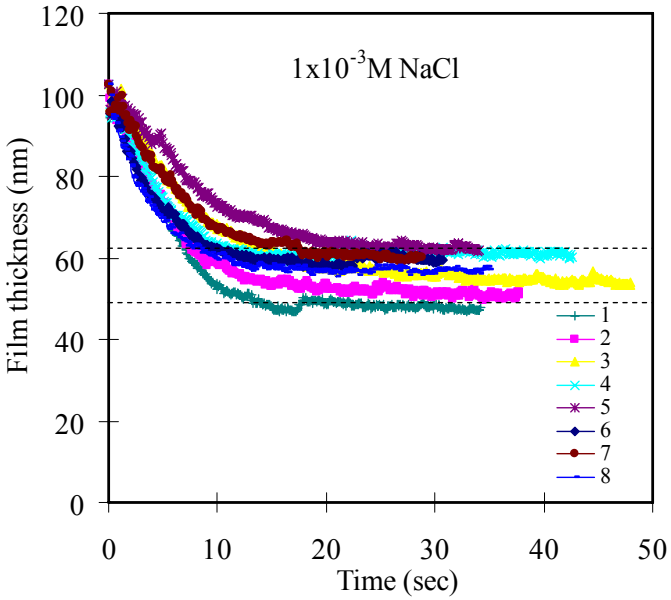

Figure 23. Experimental equilibrium film thickness at $1x10^{-3}$M NaCl concentration.

For example, as shown in Figure 21, the equilibrium film thickness, H_e, in $1x10^{-3}$M NaCl solutions should be 39 nm at a capillary pressure of 194 pa and the film thickness is 22 nm accordingly in $5x10^{-3}$M salt solutions.

Figure 22 and 23 shows the kinetic thinning of wetting film on an oxidized silicon wafer in $1x10^{-3}$M NaCl solutions. The initial film thickness was set at 102 nm; then the water film keeps on thinning until the strong repulsive disjoining pressure makes the two interfaces apart, as which is predicted by the classical DLVO theory. After nearly 15 seconds, an equilibrium film thickness is obtained and the value is read directly from the curve shown in Figure 23. Due to the formation of dimple at the time of film forming, the experiment results show some variations. It is shown in the figure that the equilibrium film thickness varies from 45 nm to 65 nm. This experiment error in present investigation

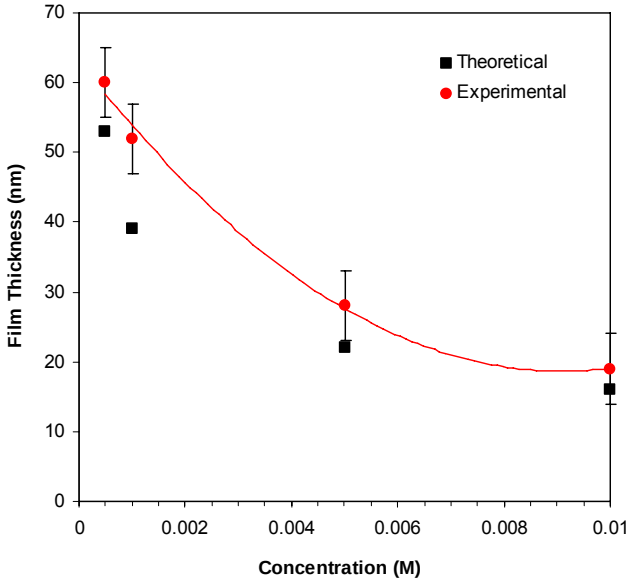

Figure 24. Experimental and theoretical equilibrium film thickness at different NaCl concentration.

Table 4. Experimental and Theoretical Equilibrium Film Thickness at different NaCl Concentration.

Concentration (M)	Equilibrium Film Thickness Theoretical (nm)	Equilibrium Film Thickness Experimental(nm)
0.0005	53	60
0.001	39	52
0.005	22	28
0.01	16	20

therefore is much higher than that obtained in foam film thickness measurement because of the less pronounced dimple formation in the latter.

The experimental equilibrium film thicknesses measured in NaCl solutions at different salt concentrations are listed in Figure 24. In addition, the theoretical values of film thicknesses are also shown in Figure 24 for comparison. The figure shows that, both from theoretical and experimental data, the equilibrium film thickness decreases with salt concentration increasing. This is mainly due to the depression of repulsive double layer disjoining pressure with ionic strength increasing in solution, while the van der waals force doesn't change much at large surface separation. Table 4 also shows that the experiment film thickness generally has larger value than that calculated from theory. This may be partially due to the fact that experimental equilibrium film thickness is obtained within 30 seconds, which is not yet at a full equilibrium. It may origin from the underestimate of the capillary diameter, which accordingly decreases the theoretical equilibrium film thickness. In another possibility, the surface charge density on oxidized silicon wafer may be higher than the one used in theoretical calculation, of which the value is taken from silica substrate

The experiment results of kinetic thinning and equilibrium film thickness show that between hydrophilic substrate/bubble, when the separation decreases, there is a strong repulsive disjoining pressure, which leads to a thick water film between particle/bubble. The water film doesn't rupture even when the film thickness is as thin as 20 nm; therefore, flotation is very less likely to occur.

The wetting film between a hydrophobic substrate, with contact angle varying from 30-50 degree, and a bubble ruptures in tens of milliseconds drastically. No kinetic film thinning data was obtained in the present investigation due to the extremely short film life time. Of course, no equilibrium film thickness was obtained because the film ruptured, which suggested a possible flotation after the solid particles are hydrophobized. This phenomenon is the same as what has been observed by Blake and Kitchener (1972). The wetting film ruptures are a very long surface separation, which is far beyond the range of the attractive van der waal force. That is, there must be attractive hydrophobic force acting between hydrophobic solid and a bubble. It is this additional non-DLVO

hydrophobic attraction that introduces the rupture of wetting film on hydrophobic substrate. The rupture process is proposed to be studied systemically using a high speed video camera.

Conclusions

In the present work, AFM force measurements were conducted by following the procedures described by Sakamoto *et al.* The results showed the presence of the long-range attractive force both in air-saturated and degassed solutions. It was most attractive at $5x10^{-6}$ M $C_{18}TACl$, where the surface was most hydrophobic. At this concentration, which is close to the point of charge neutralization (p.c.n.) of the glass sphere, the long-range decay lengths (D_2) were 34 and 38 nm in air-saturated and degassed solutions, respectively. At 10^{-5} M, the decay length decreased from 30 to 4 nm upon degassing, which is explicable by simple pH change associated with the changes in the concentration of dissolved CO_2. The attractive force was screened by an added electrolyte (NaCl), indicating that the attractive force may be of electrostatic origin. Therefore, the very long decay lengths observed in the absence of electrolyte may be ascribed to the fact that the p.c.n. occurs at a very low surfactant concentration.

A series of surface force measurements were measured with silica surfaces coated *in situ* with C_nTACl homologues with n = 12-18 using an AFM. The measured forces decayed exponentially with separation, with the decay lengths varying in the range of 3-32 nm. With a given surfactant, the strongest attractions were observed at the p.c.n. Both the maximum decay lengths measured at the p.c.n.'s and the adhesion forces increased with increasing chain length. The adhesion forces can be predicted from the solid-liquid interfacial tensions, with appropriate corrections for surface roughness. It was found that the roughness increased with increasing chain length.

The long-range forces measured in the present work were analyzed in terms of the migrating charged-patch model, which might explain the forces measured in high electrolyte concentrations. For the long-range attractions measured in the absence of added salt, however, it was necessary to assume that the patch sizes were substantially larger than those measured experimentally and reported in the literature. Furthermore, there is no evidence that hemimicelles are mobile in the p.c.n. concentration range.

A plot of the maximum decay lengths measured at p.c.n.'s *vs.* the concentration of the CH_2 and CH_3 groups in solution shows a linear relationship, which supports the formalism derived by Eriksson *et al.* from the mean-field theory by considering the structural changes across the thin water solution film between the silica surfaces. It is possible that the residual surfactant monomers in solution break the structure of the water and cause the long-range force to decrease.

The film thicknesses of a wetting film in different NaCl solutions on oxidized hydrophilic silicon wafer surface show that equilibrium film thickness decreases with salt concentration increasing, which is the same as predicted by the DLVO theory. The experiment results also suggest that there is an equilibrated thick water film between a

hydrophilic solid and a bubble, therefore, a less likely flotation. However, the wetting film between a hydrophobic substrate and a bubble ruptures in tens of milliseconds drastically, suggesting a possible flotation after the solid particles are hydrophobized. The results also suggest that, between hydrophobic solid and a bubble, there must be an additional non-DLVO attractive hydrophobic force, which introduces the rupture of wetting film on hydrophobic substrate. The rupture process is proposed to be studied systemically using a high speed video camera.

Bibliography

Attard, P., Langmuir 1996, 12, 1693-1695.

Blake, T. D.; Kitchener, J. A., J. Chem. Soc Faraday Trans. 1972, 68, 1435-1442.

Christenson, H. K.; Claesson, P. M., Adv. Colloid Interface Sci., 2001, 91, 391- 436.

Christenson, H.K.; Claesson, P..M., Science, 1988, 239, 390.

Claesson, P. M.; Christenson, H. K., J. Phys. Chem. 1988, 92, 1650-1655.

Cleveland, J. P.; Manne, S.; Bocek, D.; Hansma, P. K., Rev. Sci. Instrum. 1993, 64, 403-406.

Delamarche, E. ; Michel, B.; Gerber, Ch.; Anselmetti, D.; Guntherodt, H.-J.; Wolf, H.; Ringsdorf, H., Langmuir 1994,10, 2869-2871.

Derjaguin, B. V., Duhkin, S. S., Trans. Inst. Min. Metall. 1961, 70, 221.

Derjaguin, B.V., Kolloid Z. 1934, 69, 155.

Ducker, W. A.; Senden, T. J.; Pashley, R. M., Langmuir 1992, 8, 1831-1836.

Ducker, W. A.; Senden, T. J.; Pashley, R. M., Nature 1991, 353, 239-241.

Eriksson, J. C.; Ljunggren, S.; Claesson, P. M., J. Chem. Soc., Faraday Trans. 2, 1989, 85, 163-176.

Fan, P. Somasundaran, N.J. Turro, Langmuir, 1997, 13, 506.

Fuerstenau, D. W., Pure Appl Chem 1970, 24, 135.

Fuerstenau, D.W.; Pradip, T., Adv. Colloid Interface Sci., 2005, 114–115, 9-26.

Gaudin, M.; Fuerstenau, D. W., Trans. AIME, 1955, 202,958.

Goloub, T. P.; Koopal, L. K. *Langmuir* 1997, 13, 673-681.

Goloub, T. P.; Koopal, L. K.; Bijsterbosch, B. H., Langmuir, 1996, 12, 3188-3194.

Grahame, D. C., Chem. Rev., 1947, 40, 441.

Gu, T.; Huang, Z., Colloids Surf., 40, 1989, 71.

Hato, M., J. Phys. Chem. 1996, 100, 18530-18538.

Herder, P. C., J. Colloid and Interface Sci., 1990, 134, 2, 346-356.

Ishida, N.; Inoue, T.; Miyahara, M.; Higashitani, K., Langmuir, 2000, 16, 6377-6380

Ishida, N.; Sakamoto, M.; Miyahara, M.; Higashitani, K., Langmuir, 2000, 16*,* 5681-5687.

Israelachvili, J. N.; Pashley, R. M., J. Colloid Interface Sci., 1984, 98, 500.

Israelachvili, J. N.; Pashley, R. M., Nature, 1982, 300, 341.

Kerkicheff, P. and Spalla, O., 1995, *Phys. Rev. Lett.* 75, 1851.

Laskowski, J.; Kitchener, J.A., J. Colloid Interface Sci. 1969, 30, 391.

Lokar, W. J.; Ducker, W. A. *Langmuir* 2002, 18, 3167-3175.

Lokar, W. J.; Ducker, W. A. *Langmuir* 2004, 20, 378-388.

Miklavic, S. J.; Chan, D. Y. C.; White, L. R.; Healy, T. W., J. Phys. Chem. 1994, 98, 9022-9032.
Nuyen, A.V.; Nalaskowski, Miller. J.; Butt, H.-J. *Int. J. Miner. Process.,* 2003, 72, 215-225.
Papirer, E.(ed), 'Adsorption on Silica Surface', Surfactant Science Series, Vol. 90, New York, Marcel Dekker, Inc. 2000.
Parker, J. L.; Claesson, P.; Attar, P. *J. Phys. Chem.* 1994, 98, 8468
Parker, J.L.;Yaminsky, V.V.; Claesson, P.M., *J. Phys. Chem.* 1993, 97, 7706.
Parks, G. A., Chem. Rev., 1965, 65(2), 177-198.
Pazhianur, R. and Yoon, R.-H., *Minerals & Metallurgical Processing,* 2003, 20, 178-184.
Rabinovich, Ya. I.; Derjaguin, B.V., Colloids Surf., 1988, 30, 243.
Rutland, M.W.; Parker, J.L., Langmuir 10, 1994, 1110-1121.
Sakamoto, M.; Kanda, Y.; Miyahara, M.; Higashitani, K., Langmuir 2002, 18, 5713-5719.
Schulze, H.J.; Stockelhuber, K.W.; Wenger, A., J. Colloids and Surfaces A 192 (2001) 61–74.
Somasundaran, P.; Fuerstenau, D. W., J Phys Chem 1966;70:90.
Somasundaran, P.; Healy, T. W.; Fuerstenau, D. W., J. Phys. Chem. 1964, 68, 3562-3566.
Somasundaran, P.; Huang, L., Adv. Colloid Interface Sci., 2000, 88, 179-208
Ström, P. Hansson, B. Jönsson, O. Söderman, Langmuir, 2000, 16, 2469.
Stumm, W.; Morgan, J. J. *Aquatic Chemistry: Chemical Equilibria and Rates in Natural Waters Environmental Science and Technology*; John Wiley & Sons: New York, 1996.
Subramanian, V.; Ducker, W. *J. Phys. Chem. B* 2001, 105, 1389-1402.
Tanford, C., "The Hydrophobic Effect," 1980, 2nd ed. Wiley, New York.
Tanford, C., 1980, *"The Hydrophobic Effect,"* 2nd ed.. Wiley, New York, p.9.
Tsao, Y. H.; Evans, D. F.; Wennerström, H., Science 1993, 262, 547-550.
Tyrrell, J. W. G. ; Attard, P., Langmuir, 2002, 18, 160-167.
Wakamatsu, T.; Fuerstenau, D. W., Adv Chem Ser 1968;79:161.
Wong, K.; Cabane, B.; Duplessix, R.; Somasundaran, P., Langmuir, 1989, 5, 1346-1350.
Wood, J.; Sharma, R., Langmuir 1995, 11, 4797-4802
Yeskie, M. A.; Harwell, J. H., J. Phys. Chem., 1988, 92, 8, 2346-2352.
Yoon, R.-H.; Ravishankar, S. A., J. Colloid and Interface Sci., 1996, 179, 403-411
Zajac, J.; Trompette, J. L.; Partyka, S., Langmuir, 1996, 12, 1357-1367.
Zhang, J.; Yoon, R.-H.; Mao, M.; Ducker, W. A., Langmuir, 2005; 21, 5831-5841.

List of Acronyms and Abbreviations

None

Appendices (if necessary)

None

Appendix 6: Novel Surfactants as Collectors for Froth Flotation

TECHNICAL PROGRESS REPORT

Contract Title and Number:	Period of Performance:
Establishment of the Center for Advanced Separation Technologies (DE-FC26-01NT41091)	Starting Date: Sep 17, 2001 Ending Date: May 31, 2005

Sub-Recipient Project Title: NOVEL SURFACTANTS AS COLLECTORS FOR FROTH FLOTATION.	Report Information: Type: Final Number: Period:
Principal Investigators: Richard D. Gandour	Date: December 23, 2006 Code: VA007-Final
Contact Address: Department of Chemistry, MC 0212 Virginia Tech Blacksburg, VA 24061	Contact Information: Phone: 540-231-3731 Fax: 540-231-3255 E-Mail: gandour@vt.edu
Subcontractor Address: Insert address of subcontractor. If none awarded, insert "No subcontracts issued."	Subcontractor Information: Phone: Fax: E-Mail:

DISCLAIMER

ABSTRACT

The three series of triheaded surfactants have been synthesized and characterized. All, including those with 22 carbons in the chain, are quite soluble in triethanolamine solutions. Studies of concentration of surfactant versus contact angle reveal that depending on chain length these surfactants form robust hydrophobic films on TiO_2, calcite, apatite, and silver at extremely dilute concentrations.

TABLE OF CONTENTS

LIST OF GRAPHICAL MATERIALS

EXECUTIVE SUMMARY

Froth flotation involves separating finely divided solid particulates suspended in water. Many mining companies worldwide employ froth flotation to enhance the concentration of desired mineral and coal fines. Processing occurs on the scale of billions of tons of ore annually and consumes millions of kilograms of reagents—collectors, depressants, activators, modifiers, and frothers.(Fuerstenau and Herrera-Urbina, 1989) The proposed triheaded amphiphiles will function as collectors. The goal is to find a collector that will operate at very low concentrations such that the amount of reagent needed is drastically reduced. This reduction will lead to energy savings and lessen the environmental impact of reagent disposal.

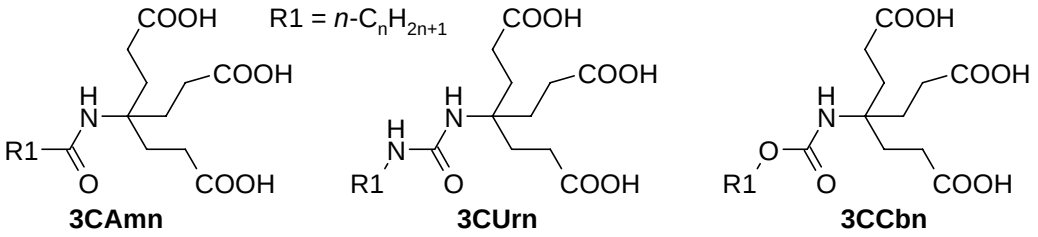

We synthesized 17 new surfactants in three different series—**3CAmn**, **3CUrn**, and **3CCbn**; the shorthand terms are 3C = three carboxyl groups, Am = amide linker, Ur = ureido linker, Cb = carbamate linker, and n = the number of carbons in the fatty chain. These surfactants were water soluble in basic aqueous solutions, especially those comprised of triethanolamine as the base, up to 20 mM for the longest chains.

Although they were quite water soluble, they bound to mineral surfaces to create hyrdophobic coatings. We measured the contact angles of **3CUr16**, **3CCb16**, and **3CAm17** absorbed on TiO_2. These three showed a maximum contact angle of 80° at a concentration of 10^{-5} M. We then measured the contact angles for a complete series, **3CAmn**, absorbed on calcite and apatite surfaces. The best amphiphile varied by surface. Absorption of **3CAm21** on an apatite surface gave a maximum contact angle of 94° at a concentration of 5×10^{-7} M. Absorption of **3CAm14** on calcite gave a contact angle of 92° ad 5×10^{-6} M. We also studied the absorption of the **3CAmn** series on silver using RAIRS (reflection absorption infrared spectroscopy). These homologous amphiphiles formed homologous thin films that were not highly ordered. These thin films on silver could serve as models for thin films on mineral oxides.

EXPERIMENTAL

Chemical Synthesis of Surfactants.

*General Comments***.** Unless specified, solvents and reagents were used as received. Pentadecanoyl chloride and heptadecanoyl choride were synthesized via a reaction of the corresponding carboxylic acid in refluxing thionyl chloride and a few drops of DMF for 24 h. The products were purified by bulb-to-bulb distillation until a clear, colourless liquid was obtained. Behera's amine(Newkome et al., 1991) and Weisocyanate^{TM}(Newkome et al., 1997) were prepared as described. Analytical thin layer chromatography was performed on aluminum-coated silica gel 60 Å and detected by dipping in a solution of 10% ethanolic phosphomolybdic acid reagent (20 wt. % solution in ethanol) and then heated with a heat gun. The R_f for **3ECbn** in hexane:THF (6:1 v:v) was 0.32–0.41. Flash column chromatography was carried out on silica gel (60 Å). The samples were introduced as concentrated solutions in hexane:THF (6:1 v:v). After eluting the solvent mixture (100 mL), fractions (25 mL) were collected. The flow rate (~64 mL/min) was controlled by compressed air. The product appeared in fractions 3 to 12. Solutions were concentrated by rotary evaporation. Melting points were determined in open capillary tubes at 1°C/min and uncorrected. NMR spectra of **3CCbn** series were recorded at 400 and 100 MHz for ^{1}H and ^{13}C, respectively, and reported in ppm. References in ^{1}H and ^{13}C spectra were TMS and DMSO-d_6, respectively. NMR spectra of **3CAm14** and **3CAm16** were recorded at 500 and 125 MHz for ^{1}H and ^{13}C, respectively, and reported in ppm. References in ^{1}H and ^{13}C spectra were CD_3OD and DMSO-d_6, respectively. IR spectra were recorded on neat samples with an FTIR equipped with a diamond ATR system, and reported in cm^{-1}. HRMS data were obtained on a dual-sector mass spectrometer in FAB mode with 2-nitrobenzylalcohol as the proton donor. Elemental analyses were performed by a commercial vendor.

General procedure A for long chain tri tert-butylesters, **3EAmn***: Procedure A.* Behera's amine was dissolved in dry benzene. Triethylamine and the appropriate acid halide were added to the flask. Addition of the acid halide resulted in an immediate cloudy solution. The solution was stirred for 48 h. The reaction mixture was washed with sat. $NaHCO_3$, water, cold 10% aqueous HCl, and brine. The solution was dried with Na_2SO_4. The solvent was concentration yielding an off-white solid which was crystallized with $EtOH/H_2O$ which yielded a white needles or white solid (61-83%).

Procedure B. A mixture of the appropriate carboxylic acid, DCC, and 1-hydroxybenzotriazole was dissolved in dry THF and stirred at room temperature. A white precipitate crashed out of solution after approximately 1 h. The solution is stirred for 3 d. The precipitate was filtered and the filtrate was concentrated in vacuo. The slightly yellow solid was dissolved in CH_2Cl_2. The solution was placed in the freezer overnight. The resulting precipitate was again removed by filtration. The filtrate was washed with cold 10% aqueous HCl, water, sat. $NaHCO_3$, and brine. The solution was dried with Na_2SO_4. The solvent was concentration yielding an off-white solid which was crystallized with $EtOH/H_2O$ which yielded a white solid (30-49%).

Di-tert-butyl 4-(2-(tert-butoxycabonyl)ethyl)-4-tetradecanoylaminoheptanedioate, **3EAm13.** The general procedure (B) described above afforded a white solid; mp 72.8-73.7 °C; ^{1}H NMR ($CDCl_3$) δ 0.87 (t, CH_3, 3H), 1.20-1.30 (bm, CH_2, 20H), 1.42 (s, CH_3, 27H), 1.57 (t,

CH_2, 2H), 1.95 (t, CH_2, 6H), 2.08 (t, CH_2, 2H), 2.21 (t, CH_2, 6H), 5.7, (s, NH, 1H); FAB HRMS: 626.4981 (M+, cald for $C_{38}H_{71}NO_7$), 626.4996.

Di-tert-butyl 4-(2-tert-butoxycarbonyl)ethyl)-4-pentadecanoylaminoheptanedioate, **3EAm14:** The general procedure (A) afforded a white solid (5.94 g, 76%) ; mp 66.4–67.2°C; ^{1}H NMR ($CDCl_3$): δ 0.87 (t, 3H), 1.2~1.30 (bm, 22H), 1.43 (s, 27H), 1.58 (bm, 2H), 1.96 (m, 6H), 2.08 (t, 2H), 2.21 (m, 6H), 5.77 (s, 1 H); ^{13}C NMR ($CDCl_3$) δ 14.2, 22.7, 25.9, 28.1, 29.39, 29.42, 29.44, 29.58, 29.71, 29.76, 29.89, 30.06, 37.7, 57.3, 80.7, 172.7, 173.0; IR 3362, 2918, 2851, 1718, 1708, 1676, 1536, 1149 cm^{-1}; HRMS: for $C_{37}H_{69}NO_7$ calcd 640.5152, found 640.5160. Anal. Calcd for $C_{37}H_{69}NO_7$: C, 69.44; H, 10.87; N, 2.19. Found: C, 69.42; H, 10.87; N, 2.21.

Di-tert-butyl 4-(2-(tert-butoxycabonyl)ethyl)-4-hexadecanoylaminoheptanedioate, **3EAm15***:* The general procedure (A) described above afforded a white solid; mp 66.6-67.2 °C ^{1}H NMR ($CDCl_3$) δ 0.87 (t, CH_3, 3H), 1.31-1.1.30 (bm, CH_2, 28H), 1.42 (s, CH_3, 27H), 1.95 (t, CH_2, 6H), 2.08 (t, CH_2, 2H), 2.21 (t, CH_2, 6H). ^{13}C NMR δ 14.18 , 22.76, 25.89, 28.14, 29.40, 29.43, 29.59, 29.72, 29.72, 29.76, 29.90, 30.08, 31.99, 37.71, 57.33), 80.03, 173.01, 172.68; FAB HRMS: 654.5309 (M+, cald for $C_{38}H_{71}NO_7$, 654.5269. IR 3395, 2914, 1730, 1725, 1713, 1669, 1526; Anal. Calcd for $C_{38}H_{71}NO_7$: C, 69.79; H, 10.94; N, 2.14; O, 17.12. Found: C, 69.76; H, 10.96; N, 2.21; O, 17.14.

Di-tert-butyl 4-(2-tert-butoxycarbonyl)ethyl)-4-heptadecanoylaminoheptanedioate, **3EAm16**. The general procedure (A) afforded a yellow solid (7.47 g). During the recrystallization of the yellow solid in EtOH/water, a yellow solid formed. The clear, colorless liquid was decanted and left sitting at room temperature. The resulting white solid, 2.74 g, was removed via filtration. The filtrate was placed in a fridge overnight, which yielded a yellow solid (3.76 g). Additional material could possibly be attained from this yellow solid by further purification. The white solid was recrystallized again in EtOH/water, yielding white needles (2.02 g, 25%). This material was used in the subsequent formolysis reactions; mp 64.5–65.3°C; ^{1}H NMR ($CDCl_3$) δ 0.87 (t, 3H), 1.25–1.28 (bm, 26H), 1.43 (s, 27H), 1.96 (m, 6H), 2.09 (m, 2H), 2.21 (m, 6H), 5.78 (s, 1H); ^{13}C NMR ($CDCl_3$) δ 14.2, 22.7, 25.9, 28,1, 29.37, 29.42, 29.57, 29.71, 29.75, 29.87, 30.0, 32.0, 37.7, 57.3, 80.7, 172.7, 173.0; IR 3381, 2915, 1729, 1727, 1712, 1671, 1529, 1146 cm^{-1}; HRMS: for $C_{39}H_{73}NO_7$ calcd 668.5465, found 668.5461. Anal. Calcd for $C_{39}H_{73}NO_7$: C, 70.12; H, 11.01; N, 2.10. Found: C, 69.77; H, 10.92; N, 2.09.

Di-tert-butyl 4-(2-tert-butoxycabonyl)ethyl)-4-octadecanoylaminoheptanedioate, **3EAm17**. The general procedure (A) described above afforded a white solid; mp 66.6-67.2°C; ^{1}H NMR ($CDCl_3$) δ 0.87 (t, CH_3, 3H), 1.21-1.30 (bm, CH_2, 32H), 1.42 (s, CH_3, 27H), 1.57, (t, CH_2, 2H), 1.95 (t, CH_2, 6H), 2.08 (t, CH_2, 2H), 2.21 (t, CH_2, 6H); ^{13}C NMR CH_3 28.14, 29.40, 2943, 29.59, 29.73, 29.78, 29.90, 30.07, 32.00, 57.33, 80.70, 172.68, 173.01; IR 3397, 2915, 1730, 1725, 1714, 1670, 1528, 1148

Di-tert-butyl 4-(2-tert-butoxycabonyl)ethyl)-4-icosanoylaminoheptanedioate, **3EAm1**. The general procedure (B) described above afforded a white solid; mp 70.6-71.3°C; ^{1}H NMR ($CDCl_3$) δ 0.87 (t, CH_3, 3H), 1.21-1.31(bm, CH_2, 32H), 1.42 (s, CH_3, 27H), 1.57, (t, CH_2,

2H), 1.95 (t, CH_2, 6H), 2.08 (t, CH_2, 2H), 2.21 (t, CH_2, 6H), 5.77 (s, NH, 1H); IR 3336, 2914, 1731, 1724, 1713, 1669, 1526, 1147

Di-tert-butyl 4-(2-tert-butoxycabonyl)ethyl)-4-docosanoylaminoheptanedioate, **3EAm21**. The general procedure (B) described above afforded a white solid; mp 74.7-75.0°C; ^{1}H NMR ($CDCl_3$) δ 0.87 (t, CH_3, 3H), 1.21-1.30 (bm, CH_2, 36H), 1.42 (s, CH_3, 27H), 1.57, (t, CH_2, 2H), 1.95 (t, CH_2, 6H), 2.08 (t, CH_2, 2H), 2.21 (t, CH_2, 6H); FAB HRMS: 738.6212 (M+, cald for $C_{38}H_{71}NO_7$), 738.6248.

General synthesis of long chain triacid, **3CAmn***:* Triester was dissolved in 96% formic acid and stirred overnight. The milky white solution was concentrated in vacuo. The white solid was crystallized in either ethyl acetate or glacial acetic acid/hexane which yielded a white solid (55-80%).

4-(2-Carboxyethyl)-4-tetradecanoylaminoheptanedioic acid, **3CAm13**. The general procedure described above afforded a white solid; mp 162.7-163.1°C; ^{1}H NMR (CD_3OD) δ 0.89 (t, CH_3, 3H), 1.20-1.35 (bm, CH_2, 20H), 1.58 (t, CH_2, 2H), 2.00 (t, CH_2, 6H), 2.16 (t, CH_2, 2H), 2.26 (t, CH_2, 6H); ^{13}C NMR δ13.12, 22.41, 25.89, 27.91, 29.11, 29.34, 29.45, 31.75, 36.36, 57.19, 174.68, 175.80, 186.68

4-(2-Carboxyethyl)-4-pentadecanoylaminoheptanedioic acid, **3CAm14**. The general procedure described in the manuscript afforded a white solid (0.42 g, 74 %); mp 164.5–164.8°C; ^{1}H NMR (CD_3OD) δ 0.89 (t, 3H), 1.26–1.32 (bm, 22H), 1.58 (bm, 2H), 2.02 (m, 6H), 2.16 (m, 2H), 2.26 (m, 6H); ^{13}C NMR (DMSO-d_6) δ 14.5, 22.7, 26.0, 28.6, 29.16, 29.28, 29.36, 29.54, 29.58, 29.61, 31.9, 36.4, 56.8, 172.6, 175.0; IR 3413, 3070, 2915, 2847, 1725, 1694, 1628, 1517, 1175 cm^{-1}; HRMS: for $C_{25}H_{45}NO_7$ calcd 472.3274, found 472.3247. Anal. Calcd for $C_{25}H_{45}NO_7$: C, 63.67; H, 9.62; N, 2.97. Found: C, 63.68; H, 9.67; N, 2.98.

4-(2-Carboxyethyl)-4-hexadecanoylaminoheptanedioic acid, **3CAm15**. The general procedure described above afforded a white solid; mp 164.5-165.1°C; ^{1}H NMR (CD_3OD) δ 0.89 (t, CH_3, 3H), 1.26–1.32 (bm, CH_2, 24H), 1.58 (t, CH_2, 2H), 2.00 (t, CH_2, 2H), 2.16 (t, CH_2, 6H), 2.26 (t, CH2, 2H); IR 3417, 3100, 2915, 1723, 1694,1636, 1520.

4-(2-Carboxyethyl)-4-heptadecanoylaminoheptanedioic acid, **3CAm16**. The general procedure described above afforded a white solid (0.57 g, 80%); mp 168.1–168.7 °C; ^{1}H NMR (CD_3OD) δ 0.89 (t, 3H), 1.26–1.32 (bm, 26H), 1.58 (bm, 2H), 2.01 (m, 6H), 2.16 (t, 2H), 2.26 (m, 6H); ^{13}C NMR (DMSO-d_6) δ 14.5, 22.7, 26.0, 28.59, 29.16, 29.27, 29.36, 29.54, 29.61, 31.9, 36.4, 56.8, 172.6, 175.0; IR 3412, 3103, 2915, 1724, 1694, 1628, 1518, 1175 cm^{-1}; HRMS: calcd for $C_{27}H_{49}NO_7$ 500.3587, found 500.3583. Anal. Calcd for $C_{27}H_{49}NO_7$: C, 64.90; H, 9.88; N, 2.80. Found: C, 64.65; H, 9.71; N, 2.80.

4-(2-Carboxyethyl)-4-octadecanoylaminoheptanedioic acid, **3CAm17**. The general procedure described above afforded a white solid; mp 165.9-166.9°C; ^{1}H NMR (CD_3OD) δ 0.89(t, CH_3, 3H), 1.21–1.37 (bm, CH_2, 28H), 1.58 (t, CH_2, 2H), 2.00 (t, CH_2, 6H), 2.16 (t, CH_2, 2H), 2.26 (t, CH_2, 6H). IR 3358, 2918, 1721, 1707, 1677, 1150 IR 3417, 3100, 2916, 1722, 1694, 1636, 1521, 1175

4-(2-Carboxyethyl)-4-icosanoylaminoheptanedioic acid, **3CAm19**. The general procedure described above afforded a white solid; mp162.5-163.8°C; ^{1}H NMR (CD_3OD) δ 0.89(t, CH_3, 3H), 1.25–1.35 (bm, CH_2, 32H), 1.58 (t, CH_2, 2H), 2.00 (t, CH_2, 6H), 2.16 (t, CH_2, 2H), 2.26 (t, CH_2, 6H). FAB HRMS: 738.6212 (M+, cald for $C_{44}H_{84}NO_7$) 738.6248. IR 3418, 3100, 2916, 1720, 1694, 1652, 1521, 1175

4-(2-Carboxyethyl)-4-docosanoylaminoheptanedioic acid, **3CAm21**. The general procedure described above afforded a white solid; mp 165.0-165.9°C; ^{1}H NMR (CD_3OD) δ 0.89 (t, CH_3, 3H), 1.24–1.35 (bm, CH_2, 36H), 1.58 (t, CH_2, 2H), 2.00 (t, CH_2, 6H), 2.16 (t, CH_2, 2H), 2.26 (t, CH_2, 6H).

General procedures for long-chain carbamate tri tert-butyl esters, **3ECbn**. Alkan-1-ol (3.4 mmol), Weisocyanate™ (3.2 mmol), and Et_3N (3.2 mL) were combined in a 50-mL round bottom flask and stirred at 95 °C for 4 h. The mixture was allowed to cool to room temperature, and diluted with Et_2O (40 mL). The resulting solution was washed with 2-*M* HCl (3×5 mL), then saturated $NaHCO_3$ (3×5 mL), and finally saturated NaCl (1×5 mL). The solution was dried with $MgSO_4$, filtered, and concentrated to a white solid (92%). The resulting solid was purified via flash column chromatography with 6:1 hexane:EtOAc to give a white solid (63–84 % yield).

Di-tert-butyl 4-(2-(tert-butoxycarbonyl)ethyl)-4-(3-tetradecoxycarbonylamino)heptanedioate, **3ECb14.** Following the general procedure, tetradecan-1-ol (0.73 g, 3.40 mmol), Weisocyanate™ (1.42 g, 3.22 mmol) gave, after flash column chromatography with 6:1 hexane/EtOAc, a white solid (1.77 g, 84 % yield); mp 54.3–54.9 °C; ^{1}H NMR ($CDCl_3$) δ 0.88 (t, 3H), 1.25 (m, 22H), 1.42 (s, 27H), 1.57 (broad p, 2H), 1.91 (t, 6H), 2.21 (t, 6H), 3.96 (broad t, 2H), 4.69 (broad s, 1H); ^{13}C NMR ($CDCl_3$) δ 14.1, 22.7, 25.9, 28.08, 28.99, 29.35, 29.37, 29.58, 29.62, 29.67, 29.69, 29.72, 30.2, 31.9, 56.4, 64.6, 80.6, 154.6, 172.6; IR 3371, 2916, 1727, 1703, 1363, 1142, 1075; HRMS (FAB+) calcd for $C_{37}H_{69}NO_8$ (MH^+) 656.5101, found 656.5105. Anal. Calcd. for $C_{37}H_{69}NO_8$: C, 67.75; H, 10.60; N, 2.14. Found: C, 67.75; H, 10.84; N, 2.27.

Di-tert-butyl 4-(2-(tert-butoxycarbonyl)ethyl)-4-(3-hexadecoxycarbonylamino)heptanedioate, **3ECb16**. Following the general procedure, hexadecan-1-ol (0.789 g, 3.25 mmol) and Weisocyanate™ (1.44 g, 3.26 mmol) gave, after flash column chromatography with 6:1 hexane/EtOAc, a white solid (1.8781 g, 84 %); mp 60.8–61.4 °C; ^{1}H NMR ($CDCl_3$) δ 0.89 (t, 3H), 1.27 (m, 26H), 1.45 (s, 27H), 1.59 (broad p, 2H), 1.92 (t, 3H), 2.23 (t, 3H), 3.99 (broad t, 2H), 4.70 (broad s, 1H); ^{13}C NMR ($CDCl_3$) δ 14.1, 22.7, 25.9, 28.08, 28.99, 29.33, 29.37, 29.56, 29.62, 29.66, 29.70, 30.2, 31.9, 56.4, 64.6, 80.6, 154.6, 172.6; IR 3357, 2921, 1727, 1708, 1530, 1363, 1257, 1142; HRMS (FAB+) calcd for $C_{39}H_{73}NO_8$ (MH^+) 684.5414, found 684.5427. Anal. Calcd for $C_{39}H_{73}NO_8$: C, 68.48; H, 10.76; N, 2.05. Found: C, 68.37; H, 10.83; N, 2.18.

Di-tert-butyl 4-(2-(tert-butoxycarbonyl)ethyl)-4-(3-octadecoxycarbonylamino)heptanedioate, **3ECb18**. Following the general procedure, octadecan-1-ol (0.907 g, 3.35 mmol) and Weisocyanate™ (1.41 g, 3.20 mmol) gave, after flash column chromatography with 6:1

hexane/EtOAc, a white solid (1.80 g, 79 %); mp 58.6–59.1 °C; ^{1}H NMR ($CDCl_3$) δ 0.88 (t, 3H), 1.26 (m, 30H), 1.44 (s, 27H), 1.58 (broad p, 2H), 1.91 (t, 3H), 2.22 (t, 3H), 3.98 (broad t, 2H), 4.70 (broad s, 1H); ^{13}C NMR ($CDCl_3$) δ 14.1, 22.7, 25.9, 28.1, 28.99, 29.34, 29.36, 29.57, 29.61, 29.67, 29.71, 30.2, 31.9, 56.4, 64.6, 80.6, 154.6, 172.6; IR 3357, 2921, 1727, 1708, 1531, 1363, 1253, 1142; HRMS (FAB+) calcd for $C_{41}H_{77}NO_8$ (MH^+) 712.5727, found 712.5710. Anal. Calcd for $C_{41}H_{77}NO_8$: C, 69.16; H, 10.90; N, 1.97. Found: C, 69.10; H, 11.10; N, 2.13.

Di-tert-butyl 4-(2-(tert-butoxycarbonyl)ethyl)-4-(3-icosoxycarbonylamino)heptanedioate, **3ECb20**. Following the general procedure, icosan-1-ol (1.02 g, 3.40 mmol) and Weisocyanate™ (1.51 g, 3.21 mmol) gave, after flash column chromatography with 6:1 hexane/EtOAc, a white solid (1.51 g, 63 %); mp 59.0–59.6 °C; ^{1}H NMR ($CDCl_3$) δ 0.88 (t, 3H), 1.25 (m, 34H), 1.44 (s, 27H), 1.57 (broad p, 2H), 1.90 (t, 3H), 2.21 (t, 3H), 3.97 (broad t, 2H), 4.69 (broad s, 1H); ^{13}C NMR ($CDCl_3$) δ 14.2, 22.8, 26.0, 28.2, 29.11, 29.46, 29.48, 29.69, 29.75, 29.83, 30.3, 32.0, 56.5, 64.7, 80.7, 154.7, 172.7; IR 3338, 2916, 1727, 1703, 1526, 1363, 1142; HRMS (FAB+) calcd for $C_{43}H_{81}NO_8$ (MH^+) 740.6040, found 740.6021. Anal. Calcd for $C_{43}H_{81}NO_8$: C, 69.78; H, 11.03; N, 1.89. Found: C, 69.73; H, 11.27; N, 2.05.

Di-tert-butyl 4-(2-(tert-butoxycarbonyl)ethyl)-4-(3-docosoxycarbonylamino)heptanedioate, **3ECb22**. Following the general procedure described in the manuscript, docosan-1-ol (1.11 g, 3.39 mmol) and Weisocyanate™ (1.42 g, 3.22 mmol) gave, after flash column chromatography with 6:1 hexane/EtOAc, a white solid (1.70 g, 69 %); mp 65.8–66.3 °C; ^{1}H NMR ($CDCl_3$) δ 0.88 (t, 3H), 1.25 (m, 38H), 1.44 (s, 27H), 1.59 (broad p, 2H), 1.90 (t, 3H), 2.21 (t, 3H), 3.98 (broad t, 2H), 4.69 (broad s, 1H); ^{13}C NMR ($CDCl_3$) δ 14.3, 22.9, 26.1, 28.3, 29.17, 29.51, 29.54, 29.75, 29.80, 29.89, 30.3, 32.1, 56.5, 64.8, 80.8, 154.8, 172.8; IR 3338, 2916, 1727, 1703, 1531, 1464, 1363, 1142, HRMS (FAB+) calcd for $C_{45}H_{85}NO_8$ (MH^+) 768.6353, found 768.6356; Anal. Calcd for $C_{45}H_{85}NO_8$: C, 70.36; H, 11.15; N, 1.82. Found: C, 70.33; H, 11.25; N, 1.89.

General procedures for preparation of long-chain carbamate triacids, **3CCbn**. The tri *tert*-butyl ester (5.02 mmol) was added to formic acid (20 mL). The resulting mixture was stirred to give a transparent solution. For some compounds, it was necessary to warm the solution to get the ester to dissolve. The transparent solution was stirred at rt for 9 h; the complete reaction was identified by the formation of milky solution. The solution was concentrated to yield a white solid, which was recrystallized with acetic acid and hexane to give a white solid (74–85%).

4-(2-Carboxyethyl)-4-(3-tetradecoxycarbonylamino)heptanedioic acid, **3CCb14**. Following the general procedure described in the manuscript, **3ECb14** (3.42 g, 5.21 mmol) gave upon recrystallization from acetonitrile a white powder (1.96 g, 77%); mp 121.4–121.9 °C; ^{1}H NMR (DMSO-d_6) δ 0.80 (t, 3H), 1.19 (broad m, 22H), 1.43 (broad p, 2H), 1.65 (t, 6H), 2.05 (t, 6H), 3.81 (t, 2H), 6.62 (broad s, 1H), 11.98 (broad s, 3H); ^{13}C NMR (DMSO-d_6) δ 13.9, 22.1, 25.3, 28.1, 28.68, 28.69, 28.96, 28.98, 29.02, 29.20, 31.3, 55.6, 63.1, 154.5, 174.3; IR 3429, 3165, 2916, 1725, 1678, 1570, 1237, 1090; HRMS (FAB+) calcd for $C_{25}H_{45}NO_8$ (MH^+) 488.3223, found 488.3234 Anal. Calcd for $C_{25}H_{45}NO_8$: C, 61.58; H, 9.30; N, 2.87. Found: C, 61.58; H, 9.51; N, 2.84.

4-(2-Carboxyethyl)-4-(3-hexadecoxycarbonylamino)heptanedioic acid, **3CCb16**. Following the general procedure described in the manuscript, **3ECb16** (4.11 g, 6.01 mmol) gave upon recrystallization from acetonitrile a white powder(2.79 g, 90%); mp 123.9–124.7 °C; ^{1}H NMR (DMSO-d_6) δ 0.85 (t, 3H), 1.23 (broad m, 26H), 1.50 (broad p, 2H), 1.76 (t, 6H), 2.10 (t, 6H), 3.88 (t, 2H), 6.72 (broad s, 1H), 11.98 (broad s, 3H); ^{13}C NMR (DMSO-d_6) δ 13.9, 22.1, 25.4, 28.07, 28.70, 28.71, 28.98, 28.99, 29.03, 29.19, 31.3, 55.6, 63.1, 154.5, 174.3; IR 3429, 3156, 2916, 1723, 1675, 1521, 1234, 1090; HRMS (FAB+) calcd for $C_{27}H_{49}NO_8$ (MH^+) 516.3536, found 516.3521. Anal. Calcd for $C_{27}H_{49}NO_8$: C, 62.89; H, 9.58; N, 2.72. Found: C, 62.67; H, 9.79; N, 2.76.

4-(2-Carboxyethyl)-4-(3-octadecoxycarbonylamino)heptanedioic acid, **3CCb18**. Following the general procedure described in the manuscript, **3ECb18** (2.93 g, 4.11 mmol) gave upon recrystallization from acetonitrile as a white powder(1.68 g, 75%); mp 125.3–126.3 °C; ^{1}H NMR (DMSO-d_6) δ 0.85 (t, 3H), 1.23 (broad m, 30H), 1.50 (broad p, 2H), 1.76 (t, 6H), 2.10 (t, 6H), 3.88 (t, 2H), 6.71 (broad s, 1H), 12.05 (broad s, 3H); ^{13}C NMR (DMSO-d_6) δ 13.9, 22.1, 25.4, 28.05, 28.69, 28.71, 29.02, 29.17, 31.3, 55.5, 63.1, 154.5, 174.3; IR 3431, 3159, 2918, 1725, 1677, 1523, 1236, 1030; HRMS (FAB+) calcd for $C_{29}H_{53}NO_8$ (MH^+) 544.3849, found 544.3855. Anal. Calcd for $C_{29}H_{53}NO_8$: C, 64.06; H, 9.82; N, 2.58. Found: C, 64.02; H, 10.06; N, 2.54.

4-(2-Carboxyethyl)-4-(3-icosoxycarbonylamino)heptanedioic acid, **3CCb20**. Following the general procedure described in the manuscript, **3ECb20** (2.68 g, 3.62 mmol) gave upon recrystallization from MeOH/water a white powder (2.00 g, 96%); mp 124.1–124.8 °C; ^{1}H NMR (DMSO-d_6) δ 0.85 (t, 3H), 1.23 (broad m, 34H), 1.50 (broad p, 2H), 1.76 (t, 6H), 2.10 (t, 6H), 3.87 (t, 2H), 6.71 (broad s, 1H), 12.06 (broad s, 3H); ^{13}C NMR (DMSO-d_6) δ 13.9, 22.1, 25.4, 28.06, 28.68, 28.71, 29.00, 29.17, 31.3, 55.6, 63.1, 154.5, 174.3; IR 3429, 3165, 2916, 1723, 1675, 1521, 1238, 1028; HRMS (FAB+) calcd for $C_{31}H_{57}NO_8$ (MH^+) 572.4162, found 572.4153. Anal. Calcd for $C_{31}H_{57}NO_8$: C, 65.12; H, 10.05; N, 2.45. Found: C, 64.82; H, 10.16; N, 2.49.

4-(2-Carboxyethyl)-4-(3-docosoxycarbonylamino)heptanedioic acid, **3CCb22**. Following the general procedure described in the manuscript, **3ECb22** (1.52 g, 1.98 mmol) gave upon recrystallization from MeOH/water a white powder (1.17, 86%); mp 125.9–126.6 °C; ^{1}H NMR (DMSO-d_6) δ 0.85 (t, 3H), 1.23 (broad m, 38H), 1.50 (broad p, 2H), 1.76 (t, 6H), 2.10 (t, 6H), 3.87 (t, 2H), 6.71 (broad s, 1H), 12.06 (broad s, 3H); ^{13}C NMR (DMSO-d_6) δ 13.9, 22.1, 25.4, 28.07, 28.71, 28.74, 29.01, 29.18, 31.3, 55.6, 63.1, 154.5, 174.3; IR 3429, 3161, 2916, 1723, 1680, 1521, 1239, 1028; HRMS (FAB+) calcd for $C_{33}H_{61}NO_8$ (MH^+) 600.4475, found 600.4476. Anal. Calcd for $C_{33}H_{61}NO_8$: C, 66.08; H, 10.25; N, 2.34. Found: C, 65.96; H, 10.49; N, 2.37.

General procedures for long-chain ureido tri tert-butyl esters, **3EUrn.** Alkan-1-amine (5.43 mmol) was added slowly to a solution of Weisocyanate™ (5.43 mmol) in CH_2Cl_2 (45 mL). The resulting transparent solution was stirred at rt. After stirring overnight, the solvent was removed to leave a crude yellow oil (n = 14) and a crude white solid (n = 16, 18, 20, 22). The crude yellow oil was purified by flash chromatography (hexane:ethyl acetate = 5:1),

while the crude white solid was purified by recrystalization with EtOH–H_2O. Both purification methods gave a pure white solid (69–92%).

Di-tert-butyl 4-(2-(tert-butoxycarbonyl)ethyl)-4-(3-tetradecylureido)heptanedioate, **3EUr14**. The general procedure described above afforded a white solid; mp 55.0–55.6 °C; ^{1}H NMR ($CDCl_3$): δ 0.88 (t, 3H), 1.20–1.35 (bm, 22H), 1.35–1.50 (bm, 29H), 1.94 (t, 6H), 2.24 (t, 6H), 3.14 (q, 2H), 4.08 (m, 1H), 4.57 (s, 1H). ^{13}C NMR ($CDCl_3$): δ 14.1, 22.7, 26.9, 28.1, 29.3, 29.57, 29.58, 29.62 29.65, 29.9, 30.2, 30.6, 31.9, 40.6, 56.4, 80.5, 156.8, 173.1 cm^{-1}. IR: 3327, 2919, 2850, 1721, 1673, 1646, 1559, 1148. HRMS: for $C_{37}H_{70}N_2O_7$ calcd 655.5246, found 655.5261. Anal. Calcd for $C_{37}H_{70}N_2O_7$: C, 67.85; H, 10.77; N, 4.28. Found: C, 68.01; H, 10.92; N, 4.27.

Di-tert-butyl 4-(2-(tert-butoxycarbonyl)ethyl)-4-(3-hexadecylureido)heptanedioate, **3EUr16**. The general procedure described above afforded a white solid; mp 59.1–59.8 °C. ^{1}H NMR ($CDCl_3$): δ 0.88 (t, 3H), 1.20–1.35 (bm, 26H), 1.35–1.50 (bm, 29H), 1.94 (t, 6H), 2.24 (t, 6H), 3.07 (q, 2H), 4.10 (m, 1H), 4.59 (s, 1H). ^{13}C NMR ($CDCl_3$): δ 14.1, 22.7, 26.9, 28.05, 28.07, 28.13, 29.3, 29.58, 29.60, 29.64, 29.7, 29.9, 30.2, 30.6, 31.9, 40.6, 56.5, 80.5, 156.8, 173.1. IR: 3310, 2917, 2851, 1719, 1700, 1645, 1563, 1147 cm^{-1}. HRMS: for $C_{39}H_{74}N_2O_7$ calcd 683.5574, found 683.5540. Anal. Calcd for $C_{39}H_{74}N_2O_7 \cdot ½H_2O$: C, 67.69; H, 10.92; N, 4.05. Found: C, 67.92; H, 11.03; N, 4.04. Thermogravimetric analysis: 1.3 % weight loss from 40–80 °C corresponds to loss of ½H_2O.

Di-tert-butyl 4-(2-(tert-butoxycarbonyl)ethyl)-4-(3-octadecylureido)heptanedioate, **3EUr18**. The general procedure described above afforded a white solid; mp 65.0–65.8 °C. ^{1}H NMR ($CDCl_3$): δ 0.88 (t, 3H), 1.20–1.35 (bm, 30H), 1.35–1.50 (bm, 29H), 1.94 (t, 6H), 2.24 (t, 6H), 3.14 (q, 2H), 4.03 (m, 1H), 4.55 (s, 1H). ^{13}C NMR ($CDCl_3$): δ 14.1, 22.7, 26.9, 28.0, 29.32, 29.33, 29.57, 29.58, 29.62, 29.7, 29.9, 30.2, 30.6, 31.9, 40.5, 56.4, 80.5, 156.9, 173.1. IR: 3310, 2917, 2850, 1721, 1700, 1646, 1565, 1149 cm^{-1}. HRMS: for $C_{41}H_{78}N_2O_7$ calcd 711.5887, found 711.5893. Anal. Calcd for $C_{41}H_{78}N_2O_7 \cdot ½H_2O$: C, 68.39; H, 11.06; N, 3.89. Found: C, 68.46; H, 11.03; N, 3.89.

Di-tert-butyl 4-(2-(tert-butoxycarbonyl)ethyl)-4-(3-icosylureido)heptanedioate, **3EUr20**. The general procedure described above afforded a white solid; mp 66.5–67.3 °C. ^{1}H NMR ($CDCl_3$): δ 0.88 (t, 3H), 1.20–1.35 (bm, 34H), 1.35–1.50 (bm, 29H), 1.94 (t, 6H), 2.23 (t, 6H), 3.07 (q, 2H), 4.01 (br t, 1H), 4.54 (s, 1H). ^{13}C NMR ($CDCl_3$): δ 14.2, 22.7, 27.0, 28.1, 29.4, 29.6, 29.65, 29.69, 29.73, 29.9, 30.2, 30.7, 32.0, 40.6, 56.5, 80.5, 156.8, 173.2. IR: 3310, 2917, 2851, 1721, 1701, 1646, 1567, 1150 cm^{-1}. HRMS: for $C_{43}H_{82}N_2O_7$ calcd 739.6200, found 739.6199. Anal. Calcd for $C_{43}H_{82}N_2O_7 \cdot ½H_2O$: C, 69.03; H, 11.18; N, 3.74. Found: C, 69.07; H, 11.26; N, 3.73.

Di-tert-butyl 4-(2-(tert-butoxycarbonyl)ethyl)-4-(3-docosylureido)heptanedioate, **3EUr22**. The general procedure described above afforded a white solid; mp 67.9–68.8 °C. ^{1}H NMR ($CDCl_3$): δ 0.88 (t, 3H), 1.20–1.35 (bm, 38H), 1.35–1.50 (bm, 29H), 1.94 (t, 6H), 2.24 (t, 6H), 3.07 (q, 2H), 4.12 (m, 1H), 4.60 (s, 1H). ^{13}C NMR ($CDCl_3$): δ 14.1, 22.7, 26.9, 28.1, 29.4, 29.59, 29.61, 29.7, 29.9, 30.2, 30.6, 31.9, 40.6, 56.5, 80.5, 156.8, 173.1. IR: 3310, 2916, 2850, 1723, 1701, 1646, 1565, 1152 cm^{-1}. HRMS: for $C_{45}H_{86}N_2O_7$ calcd 767.6513,

found 767.6532. Anal. Calcd for $C_{45}H_{86}N_2O_7 \cdot ½H_2O$: C, 69.63; H, 11.30; N, 3.61. Found: C, 69.99; H, 11.56; N, 3.60.

General procedures for preparation of long-chain ureido triacids, **3CUrn**. The tri *tert*-butyl ester (5.02 mmol) was added to formic acid (20 mL). The resulting mixture was stirred to give a transparent solution. For some compounds, it was necessary to warm the solution to get the ester to dissolve. The transparent solution was stirred at rt for 9 h; the complete reaction was identified by the formation of milky solution. The solution was concentrated to yield a white solid, which was recrystallized with acetic acid and hexane to give a white solid (74–85%).

4-(2-Carboxyethyl)-4-(3-tetradecylureido)heptanedioic acid, **3CUr14.** The general procedure described above afforded a white solid; mp 159.0–159.5 °C; ^{1}H NMR (CD_3OD): 0.90 (t, 3H), 1.25–1.35 (bm, 22H), 1.44 (bm, 2H), 1.95 (t, 6H), 2.27 (t, 6H), 3.05 (t, 2H). ^{13}C NMR (DMSO): 14.0, 22.1, 26.4, 28.2, 28.7, 28.8, 29.0, 29.1, 30.0, 31.3, 38.8, 55.0, 157.0, 174.5. IR: 3395, 3352, 2916, 2849, 1709, 1693, 1610, 1559 cm^{-1}. HRMS: for $C_{25}H_{46}N_2O_7$ calcd 487.3383, found 487.3384. Anal. Calcd for $C_{25}H_{46}N_2O_7$: C, 61.70; H, 9.53; N, 5.76. Found: C, 61.94; H, 9.55; N, 5.70.

4-(2-Carboxyethyl)-4-(3-hexadecylureido)heptanedioic acid, **3CUr16**. The general procedure described above afforded a white solid; mp 162.4–162.8 °C; ^{1}H NMR (CD_3OD): δ 0.90 (t, 3H), 1.25–1.35 (bm, 26H), 1.44 (bm, 2H), 1.95 (t, 6H), 2.27 (t, 6H), 3.05 (t, 2H). ^{13}C NMR (DMSO): δ 14.4, 22.6, 26.9, 28.6, 29.2, 29.3, 29.5, 30.47, 30.54, 31.8, 39.3, 55.5, 157.5, 175.0. IR: 3395, 3355, 2916, 2849, 1701, 1692, 1610, 1560 cm^{-1}. HRMS: for $C_{27}H_{50}N_2O_7$ calcd 515.3696, found 515.3669. Anal. Calcd for $C_{27}H_{50}N_2O_7$: C, 63.01; H, 9.79; N, 5.44. Found: C, 62.91; H, 9.79; N, 5.33.

4-(2-Carboxyethyl)-4-(3-octadecylureido)heptanedioic acid, **3CUr18**. The general procedure described above afforded a white solid; mp 160.7–161.5 °C; ^{1}H NMR (CD_3OD): δ 0.90 (t, 3H), 1.25–1.35 (bm, 30H), 1.44 (bm, 2H), 1.95 (t, 6H), 2.27 (t, 6H), 3.05 (t, 2H). ^{13}C NMR (DMSO): δ 14.6, 22.8, 27.1, 28.8, 29.4, 29.5, 29.71, 29.74, 30.7, 32.0, 39.5, 55.7, 157.7, 175.2. IR: 3396, 3348, 2914, 2849, 1709, 1692, 1607, 1558 cm^{-1}. HRMS: for $C_{29}H_{54}N_2O_7$ calcd 543.4009, found 487.3384. Anal. Calcd for $C_{29}H_{54}N_2O_7$: C, 64.18; H, 10.03; N, 5.16. Found: C, 64.17; H, 10.12; N, 5.12.

4-(2-Carboxyethyl)-4-(3-icosylureido)heptanedioic acid, **3CUr20**. The general procedure described above afforded a white solid; mp 160.3–161.2 °C; ^{1}H NMR (CD_3OD): ^{1}H NMR (CD_3OD): δ 0.90 (t, 3H), 1.25–1.35 (bm 34H), 1.44 (bm, 2H), 1.95 (t, 6H), 2.28 (t, 6H), 3.05 (t, 2H). ^{13}C NMR (DMSO): δ 14.4, 22.6, 26.9, 28.7, 29.2, 29.3, 29.5, 30.48, 30.54, 31.8, 39.3, 55.5, 157.5, 176.0. IR: 3394, 3348, 2914, 2848, 1708, 1691, 1608, 1560 cm^{-1}. HRMS: for $C_{31}H_{58}N_2O_7$ calcd 571.4322, found 571.4290. Anal. Calcd for $C_{31}H_{58}N_2O_7$: C, 65.23; H, 10.24; N, 4.91. Found: C, 65.08; H, 10.28; N, 4.80.

4-(2-Carboxyethyl)-4-(3-docosylureido)heptanedioic acid, **3CUr22**. The general procedure described above afforded a white solid; mp 157.3–158.3 °C; ^{1}H NMR (CD_3OD): ^{1}H NMR (CD_3OD): δ 0.90 (t, 3H), 1.25–1.35 (bm, 38H), 1.44 (bm, 2H), 1.95 (t, 6H), 2.27 (t, 6H), 3.05

(t, 2H). ^{13}C NMR (DMSO): δ 13.9, 22.1, 26.4, 27.7, 28.1, 28.7, 28.8, 29.0, 30.0, 31.3, 38.8, 55.0, 157.0, 174.5. IR: 3395, 3347, 2914, 2849, 1708, 16921, 1609, 1560 cm^{-1}. HRMS: for $C_{33}H_{62}N_2O_7$ calcd 599.4635, found 599.4636. Anal. Calcd for $C_{33}H_{62}N_2O_7$: C, 66.19; H, 10.44; N, 4.68. Found: C, 66.44; H, 10.60; N, 4.57.

Absorption of Surfactants on Mineral Surfaces.

Materials. Nanopure water was obtained by Nanopure III (Barnstead, IA) water system. The conductivity of the water was 18.1 MΩ/cm at 22°C. A stock solution (5% wt) was made for each surfactant. Calcite, apatite, and TiO_2 plates were obtained from MTI Corporation, CA.

Preparation. Solutions were diluted to specific surfactant concentration by using the stock solution. All the solutions were prepared one day before contact angle measurement. Plates were cleaned in hot H_2SO_4/H_2O_2 solution (7:3 by volume) for 30 min. The plates were rinsed thoroughly with nanopure water, equilibrated with the nanopure water in a sealed vial for at least 20 minutes, and then used for experiments.

Contact angle measurement. Cleaned plates were soaked in surfactant solution of a specific concentration for 1 h. Then the surfactant coated plate was removed from the solution and dried by passing a stream of N_2 over the plate. A small drop of water was then dipped onto the dried solid substrate by using a syringe; the contact angle was measured by means of a contact angle goniometer. The results reported here are the averages over three measurements for each surfactant concentration. Experimental error was in a range of ±3°.

RESULTS AND DISCUSSION

Description of Synthesis. Our research team of three graduate students, one laboratory specialist, and two undergraduate synthesized 17 surfactants (Figure 1). The **3CCbn** series required a fatty alcohol (A = O) and Weisocyante™ as starting materials. The **3CUrn** series required a fatty amine (A = NH) and Weisocyante™ as starting materials. High yields of the

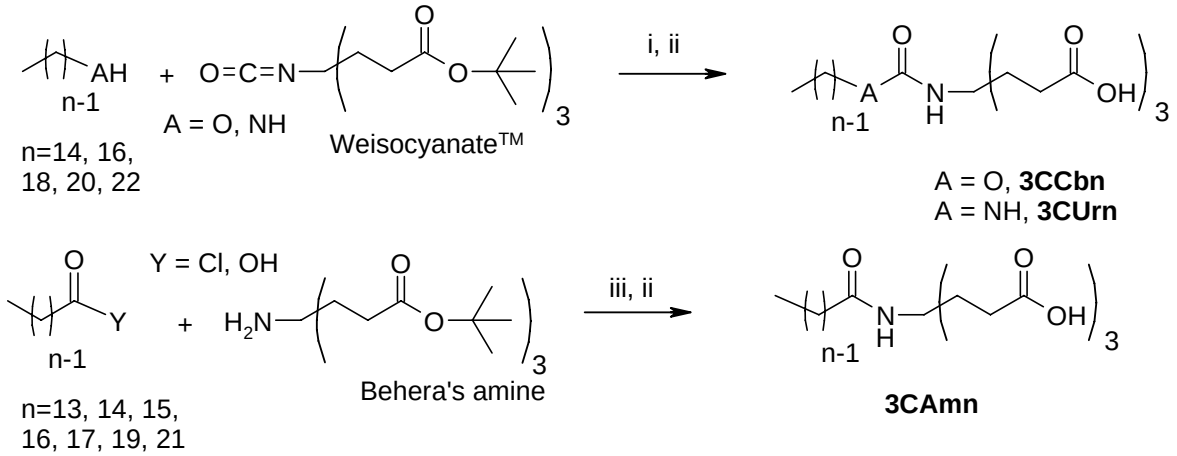

Figure 1. Synthesis of surfactants. i. A=O triethylamine, 95 °C, 4 h; A=NH rt, 18 h; ii. HCOOH, rt, 9 h; iii. Y=Cl Ph, rt, 48 h; Y=OH dicyclohexylcarbodiimide, 1-hydroxybenztriazole, rt, 72 h.

desired surfactants. The **3CAmn** series required a fatty acid chloride and Behera's amine as starting materials. High yields of the desired surfactants resulted after removal of the *tert*-butyl groups with formic acid.

Solubility Studies. We measured the solubility of these amphiphiles in aqueous triethanolamine solutions. As shown for *N*-lauroyl-L-glutamate/water, triethanolammononium salts can be dissolved in a much greater concentration than potassium salts.(Kaneko et al., 2002) All surfactants readily dissolved to form 2.0×10^{-2}-*M* solutions in water with 6 equivalents of triethanolamine, which neutralizes the carboxyl groups (Figure 2). The pH of these solutions ranged from 8 to 9. These concentrations would be well above those needed for an efficient collector for flotation.

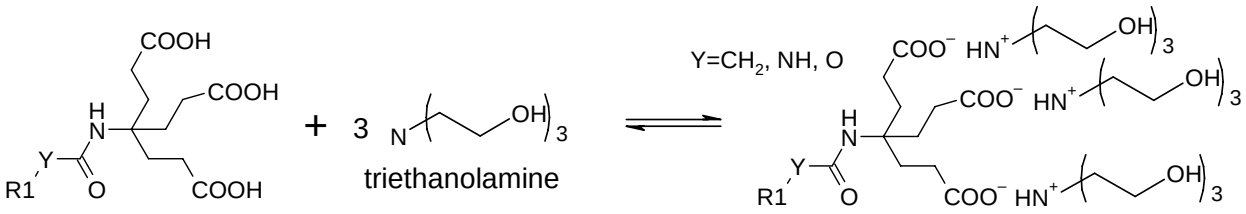

Figure 2. Equilibrium for the neutralization of triheaded surfactants with triethanolamine.

Contact Angle Measurements on Mineral Surfaces. Three surfactants (**3CUr16**, **3CCb16**, and **3CAm17**) from the three different series were compared as to hydrophobization of TiO_2 (Figure 3). All the three surfactants increased the hydrophobicity of TiO_2 surface around 72–80 degree; the maximum contact angle (80°) occurred at a concentration of 1×10^{-5} M for **3CUr16** and **3CAm17**. The maximum contact angle (78°) for **3CCb16** occurred at 5×10^{-5} M. Because the contact angle–concentration curves were very similar, the adsorption mechanism onto the TiO_2 surface for all the three surfactants was very likely the same.

That the contact angles are not very high (>90°) may be explained by the relatively low charge density of TiO_2 surface in pH 6 solution, which results in a loosely packed surfactant layer. The presence of triethanolamine in all the three surfactant solutions should decrease the surface tension of water. Triethanoamine, a known "frother", makes an excellent companion to the long-chain hydra surfactants, which should be excellent "collectors".

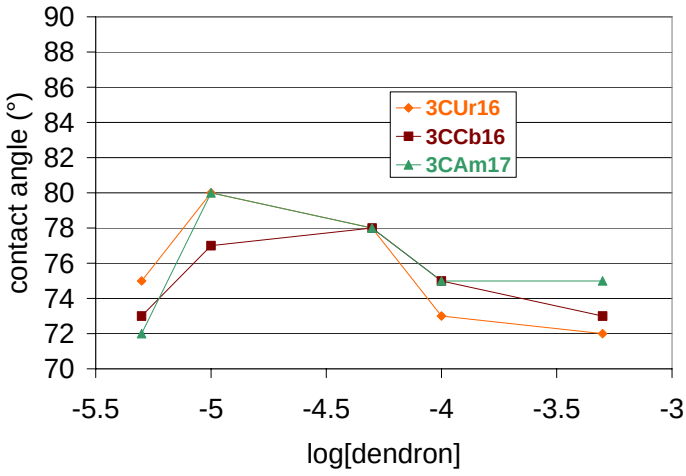

Figure 3. Water contact angles (°) on TiO_2. Plate soaked in different surfactant solutions (**3Cxxn**:triethanolamine, 1:6) at specific concentrations for 1 hour.

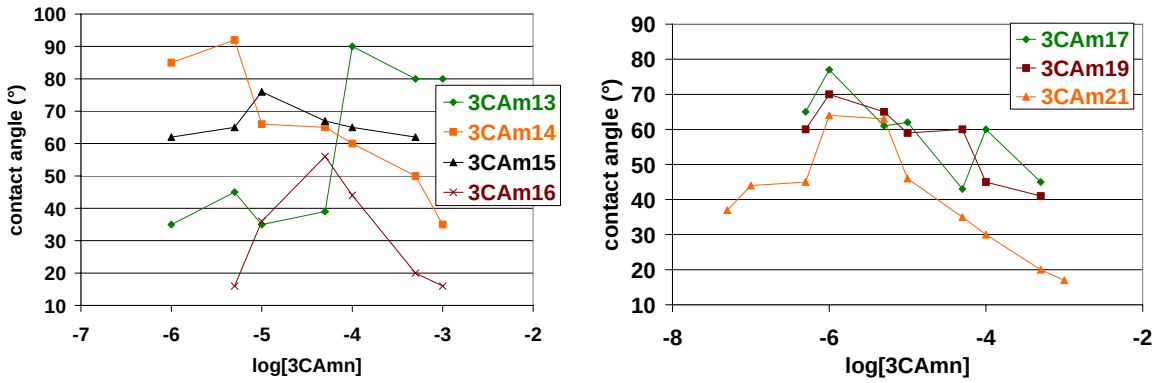

Figure 4. Water contact angles (°) on a calcite. Plate was soaked in different surfactant solutions (**3CAmn**:triethanolamine, 1:6) at specific concentrations for 1 hour.

The shorter chain surfactants showed the best contact angles for the hydrophobization of calcite (Figure 4). Surfactant **3CAm13** gave a maximum contact angle of 90° at 1×10^{-4} M; this is the minimum concentration that gives the highest contact angle. Surfactant **3CAm14** gave a contact angle of 92° at 5×10^{-6} M. Surfactant **3CAm15** showed a maximum contact angle of 76° at 1×10^{-5} M; surfactant **3CAm16**, 56° at 5×10^{-5} M. The next two surfactants in the series, **3CAm17** and **3CAm19**, showed maximum contact angles of 77° and 70°, respectively at 1×10^{-6} M. The longest member of the series, **3CAm21**, showed a maximum contact angle of 64° at 1×10^{-6} M. The data clearly supported the finding that **3CAm14** is the best hydrophobizing agent for calcite in this series.

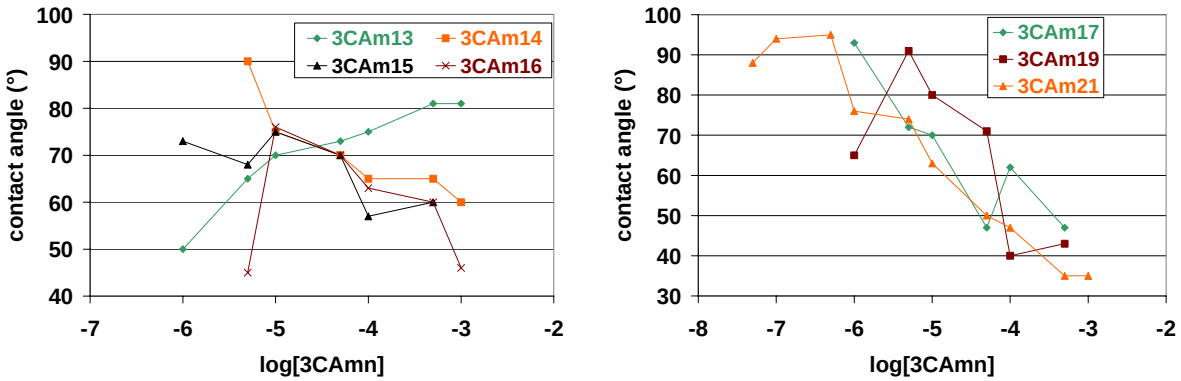

Figure 5. Water contact angles (°) on a apatite. Plate was soaked in different surfactant solutions (**3CAmn**:triethanolamine, 1:6) at specific concentrations for 1 hour.

Figure 5 presents the data for the hydrophobization of apatite. The longer chain surfactants show the best contact angles. Surfactant **3CAm21** gives a maximum contact angle of 94° at 5×10^{-7} M, which is a extremely dilute solution. The contact angles of 93° and 88° at concentrations of 1×10^{-7} M and 5×10^{-8} M are exceptionally dilute. Surfactant **3CAm19** gives a contact angle of 91° at 5×10^{-6} M. Surfactant **3CAm17** gives a contact angle of 93° at 5×10^{-6} M; lower concentrations need to be tested to confirm that this is the maximum. (Given the results with **3CAm21**, we should also test **3CAm19** at lower concentrations to confirm that the maximum contact angle does occur at a concentration higher than **3CAm17**.) Surfactant **3CAm16** shows a maximum contact angle of 63° at 1×10^{-4} M;

however, the data are missing at concentrations of 5×10^{-5} M and 1×10^{-5} M. Surfactant **3CAm15** gives a maximum contact angle of 75° at 1×10^{-5} M. However, **3CAm14**, which is the best surfactant for calcite, shows a maximum contact angle of 90° at 5×10^{-5} M; this may not be the maximum contact angle or minimum concentration because lower concentrations were not tested. Surfactant **3CAm13** shows a maximum contact angle of 81° at 5×10^{-4} M and 1×10^{-3} M. The results suggest that the longer the chain the lower the concentration needed to produce a contact angle that will be useful for hydrophobization.

Characterization of hydrophobic, thin films on silver surfaces. Thin films formed the by the deposition of **3CAmn** on silver oxide, which is a surface that enables the measurement of reflection absorption infrared spectra (RAIRS), were prepared and characterized.(Williams et al., 2005) We knew that long-chain fatty acids often form well-ordered, densely-packed SAMs on the native oxide surface of silver.(Allara and Nuzzo, 1985a; Allara and Nuzzo, 1985b; Chau and Porter, 1990; Tao, 1993)

RAIRS, recorded for a series of adsorbed acids (**3CAmn**, where **n** = 13, 15, 17, 19 and 21) showed narrow, intense peaks for the CH_2 symmetric and asymmetric stretches located at 2856 cm^{-1} and 2928 cm^{-1} (Figure 4a), which resembled those for alkanes in liquids.(Porter et al., 1987) The intensities of the methylene peaks were consistent with those expected for a uniform layer, or layers, of alkane chains on the surface.(Laibinis et al., 1991; Porter et al., 1987) However, these thin films lacked the highly ordered structure often observed for long chain fatty acids on silver. Ordered SAMs were evident from a red-shifted methylene asymmetric stretch(Porter et al., 1987) below about 2920 cm^{-1} and clearly resolved methyl stretches at 2965 cm^{-1} and 2885 cm^{-1}. The lack of order in these systems was attributed to the large footprint of the bulky head groups and competition between surface adsorption and

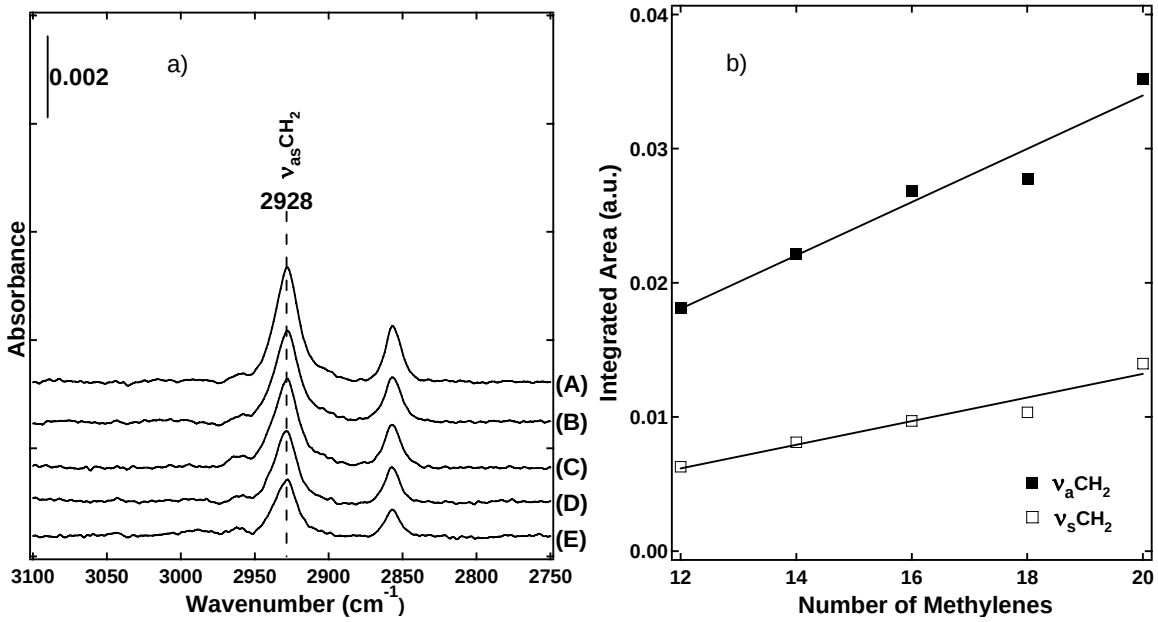

Figure 6. RAIRS analysis of a silver surface covered with **3CAmn**. (a) Spectra of **3CAm21** (A), **3CAm19** (B), **3CAm17** (C), **3CAm15** (D) and **3CAm13** (E) from 2750–3100 cm^{-1}. Vertical bar in top-left corner indicates the scale in absorbance units. (b) Integrated intensities of two methylene signals *vs.* the number of methylenes. The number of methylenes in a chain = **n** – 1.

chain–chain hydrogen bonding interactions of neighboring carboxylic acids. Despite the disordered nature of the system, the molecules did resist extensive rinsing with ethanol and appeared to form a stable thin film. Figure 4b demonstrated that the methylene stretching intensity was directly proportional to the number of methylenes in the triacid used to make the film. The linear dependence of the methylene peak intensity on chain length demonstrated that the overall coverage and density of acids adsorbed on each surface is constant, a characteristic of uniform molecular adsorption on a surface. This uniform absorption could be a monolayer, bilayer or multilayer thin film.

CONCLUSIONS

We have developed procedures for making triheaded surfactants. These versatile procedures can be used for reactions with inexpensive hydrophobic materials and mixtures thereof to create inexpensive surfactants, which could serve as collectors for froth flotation. These surfactants, even the ultra-long chain members of the series, are soluble in aqueous triethanolamine. One series forms hydrophobic films on calcite and apatite. The longest member of the series, **3CAm21**, gives a contact angle >90° on an apatite surface at concentrations of 1×10^{-7} M. This concentration is 100 times more dilute than that for sodium oleate.(Sis and Chander, 2003)

The data presented confirm that the triheaded surfactants can hydrophobize mineral surfaces. Although these surfactants are quite water soluble, they can absorb readily onto these surfaces. The results with calcite and apatite certainly confirm our goals developing surface-selective surfactants. The shorter chain surfactants are more effective for calcite than apatite; the longer chain surfactants are effective at extremely low concentrations for apatite. These results suggest that the hydra surfactants have considerable potential to fulfill our goal of developing efficient froth flotation agents.

REFERENCES

Allara, D.L. and Nuzzo, R.G., 1985a. Spontaneously Organized Molecular Assemblies .1. Formation, Dynamics, and Physical-Properties of Normal-Alkanoic Acids Adsorbed from Solution on an Oxidized Aluminum Surface. Langmuir, 1(1): 45–52.

Allara, D.L. and Nuzzo, R.G., 1985b. Spontaneously Organized Molecular Assemblies .2. Quantitative Infrared Spectroscopic Determination of Equilibrium Structures of Solution-Adsorbed Normal-Alkanoic Acids on an Oxidized Aluminum Surface. Langmuir, 1(1): 52–66.

Chau, L.K. and Porter, M.D., 1990. Composition and Structure of Spontaneously Adsorbed Monolayers of Normal-Perfluorocarboxylic Acids on Silver. Chem. Phys. Lett., 167(3): 198–204.

Fuerstenau, D.W. and Herrera-Urbina, R., 1989. Flotation Reagents. In: S. Chander and R.R. Klimpel (Editors), Advances in Coal and Mineral Processing Using Flotation. Society for Mining, Metallurgy, and Exploration, Inc., Littleton, Colorado, pp. 3–18.

Kaneko, D., Olsson, U. and Sakamoto, K., 2002. Self-assembly in some *N*-lauroyl-L-glutamate/water systems. Langmuir, 18(12): 4699–4703.

Laibinis, P.E. et al., 1991. Comparison of the Structures and Wetting Properties of Self-Assembled Monolayers of Normal-Alkanethiols on the Coinage Metal-Surfaces, Cu, Ag, Au. J. Am. Chem. Soc., 113(19): 7152–7167.

Newkome, G.R., Behera, R.K., Moorefield, C.N. and Baker, G.R., 1991. Chemistry of micelles. 18. Cascade polymers: syntheses and characterization of one-directional arborols based on adamantane. J. Org. Chem., 56(25): 7162–7167.

Newkome, G.R., Weis, C.D., Moorefield, C.N. and Fronczek, F.R., 1997. Chemistry of micelles series .66. A useful dendritic building block: Di-*tert*-butyl 4-[(2-*tert*-butoxycarbonyl)ethyl]-4-isocyanato-1,7-heptanedicarboxylate. Tetrahedron Lett., 38(40): 7053–7056.

Porter, M.D., Bright, T.B., Allara, D.L. and Chidsey, C.E.D., 1987. Spontaneously Organized Molecular Assemblies .4. Structural Characterization of Normal-Alkyl Thiol Monolayers on Gold by Optical Ellipsometry, Infrared-Spectroscopy, and Electrochemistry. J. Am. Chem. Soc., 109(12): 3559–3568.

Sis, H. and Chander, S., 2003. Adsorption and contact angle of single and binary mixtures of surfactants on apatite. Minerals Eng., 16(9): 839–848.

Tao, Y.T., 1993. Structural comparison of self-assembled monolayers of n-alkanoic acids on the surfaces of silver, copper, and aluminum. J. Am. Chem. Soc., 115(10): 4350–4358.

Williams, A.A. et al., 2005. Homologous, long-chain alkyl dendrons form homologous thin films on silver oxide surfaces. Chem. Commun.(40): 5053–5055.

BIBLIOGRAPHY

Williams, A. A.; Day, B. S.; Kite, B. L.; McPherson, M. K.; Slebodnick, C.; Morris, J. R.; Gandour, R. D. Homologous, Long-chain Alkyl Dendrons Form Homologous Thin Films on Silver Oxide Surfaces. *Chem. Commun.* **2005**, 5053–5055.

Macri, R. V.; Gandour, R. D. Synthesis, characterization, and physicochemical properties of novel multi-headed anionic surfactants. *Abstracts of Papers, 230th ACS National Meeting,* Washington, DC, United States, August 28–September 1, 2005; COLL-131.

Appendix 7: Column Flotation of Fine Dolomitic Phosphate by Selective Fatty Acids

TECHNICAL REPORT

Contract Title and Number:	Period of Performance:
Establishment of the Center for Advanced Separation Technologies. (DE-FC26-01NT41091)	Starting Date: 04/01/02 Ending Date: 5/31/2006

Sub-Recipient Project Title: Column Flotation of Fine Dolomitic Phosphate Using Selective Fatty Acid Collectors	Report Information: Type: Final Number: Period: 04/01/02-05/31/2005 Date: 12/30/2005 Code: WV006-Final
Principal Investigators: Felicia F. Peng	
Contact Address: 356 Mineral Resources Building Mining Engineering Department West Virginia Universty Morgantown, WV 26506-6070	Contact Information: Phone: (304) 293-7680 Fax: (304) 293-5708 E-Mail: ffpeng@mail.wvu.edu
Subcontractor Address: Insert address of subcontractor. No subcontracts issued.	Subcontractor Information: Phone: Fax: E-Mail:

Disclaimer

TABLEOF CONTENTS

Page

ABSTRACT

A Florida dolomitic phosphate pebble sample was processed in dolomite flotation process using fatty acid FAS-40A as collector. The dolomitic phosphate pebble feed sample contained 26.14% P_2O_5, 1.3-1.5% MgO and 14.5% acid insoluble. The sample was ground to pass 150µm (100 mesh) for liberation of phosphate from impurities in dolomitic phosphate mineral sample. Dolomite flotation was performed in both Denver D-12 stirred-tank cell and 2-in ID modified packed flotation column. Using stirred-tank cell at 1100 rpm impeller speed, the underflow of dolomite flotation as a rougher phosphate concentrate containing 26.8% P_2O_5 and 0.8% MgO at the P_2O_5 recovery of about 93% was obtained. The reagent condition was 2.0 kg/t FAS-40A fatty acid collector at pH 5.4. Based on the results and conditions of stirred-tank cell flotation, modified packed column flotation tests were conducted using central composite experiment design (CCD). The underflow of the column flotation contained 26.9% P_2O_5 and 0.95% MgO at the P_2O_5 recovery of 88.8%. The column flotation operation conditions were pH 5.5, 3.0 kg/t FAS-40A fatty acid collector, 20 cm froth height and 4.5 SCFH air flow rate. In order to achieve a marketable phosphate concentrate product, double reverse flotation technique was employed. The underflow of the column flotation after dolomite removal was further processed in amine flotation to reject silica. The final phosphate concentrate contained over 30% P_2O_5, about 1% MgO with more than 85% P_2O_5 recovery.

INTRODUCTION

Phosphate rock, as a primary source of phosphorous in inorganic fertilizers, represents a vital non-renewable resource. This commodity is neither substitutable nor recyclable in agricultural applications. Hence, total demand must be met through the mining, beneficiation and processing of naturally derived materials. Approximately, 138 million tons of phosphate concentrate is produced each year worldwide with 37 million tons from United States (Stephen, 2005). Among this phosphate production, about 90% is applied for manufacturing phosphate-bearing fertilizers, 4% for feed supplements, 4% for detergent and remaining part for other applications.

Florida is rich in phosphate resources. Its annual phosphate production accounts for one third of the total output of the world. The easily-beneficiated and high grade siliceous phosphate ore from the Bone Valley Formation is being depleted rapidly. It is estimated that the Florida phosphate reserve that could be economically processed with the available phosphate beneficiation technology could last only about 20 years at the current mining rate. As the phosphate mining operation is moving south and southeast of Florida, the phosphate matrix becomes leaner in phosphate grade and higher in dolomite mineral.

In order that the dolomitic phosphate resource can be mined and utilized in the near future to meet the demands on the phosphate products, the studies have been carried out on recovering phosphate from Florida dolomitic phosphate ores since 1970's. Some encouraging results have been achieved. The most typical processes include International Mineral & Chemical-Agrico Company (IMCA) cationic process, Tennessee Valley Authority (TVA) diphosphonic acid process, University of Florida (UF) two-stage conditioning process, University of Alabama (UA) no conditioning process, US Bureau of Mine (USBM) scrubbing and flotation process, etc. In 1990's, Florida Institute of Phosphate Research (FIPR) organized an in-house research project to conduct a comprehensive evaluation on the typical flowsheets available for processing dolomitic phosphate rocks with the results summarized in the following table (El-Shall, 1996). Table 1 shows that most processes could not produce an acceptable phosphate concentrate with more than 30% P_2O_5 and less than 1% MgO except IMCA cationic process. All other processes gave either very low P_2O_5 recovery and/or high MgO in concentrate. It can also be noted that the feed for most of those process was deslimed at 150 μm (100 mesh) prior to flotation which should be one of the reasons leading to low P_2O_5 recovery of final phosphate concentrate.

Table 1 Summary of process developed for dolomitic phosphate beneficiation

Feed Size, μm (Tyler mesh)	Process	Concentrate, %		
		P_2O_5	MgO	P_2O_5 Recovery
-420+106 μm (-35+150 mesh)	IMCA	31.66	0.84	58.4
-600+106 μm (-28+150 mesh)	USBM	31.73	1.22	27.4
-420+106 μm (-35+150 mesh)	UF	28.97	0.97	27.7
-300+44 μm (-48+325 mesh)	TVA	30.73	1.51	66.0
-420+106 μm (-35+150 mesh)	UA	26.20	1.19	87.1

In this study, a typical Florida dolomitic phosphate pebble sample was processed with Denver 1.2-liter flotation cell and 2" ID modified packed flotation column with the aim to produce an industrially acceptable phosphate concentrate. There will be no desliming operation in preparing flotation feed in order to achieve high overall P_2O_5 recovery.

The objectives of the this research are to study the effect of grinding on the liberation of impurities from phosphate and to determine the effect of operation conditions of modified packed flotation column, including pH value, collector dosage, airflow rate, and froth height.

EXECUTIVE SUMMARY

The United States is one of the world's largest phosphate producers. Its phosphate production represents one third of the world's total and 70% of the U.S. phosphate production comes from Florida. Unfortunately, the high grade siliceous phosphate ore from the Bone Valley Formation is being depleted rapidly. In order to extend the phosphate resources to meet the future demands one phosphate products, low quality and high impurity phosphate deposits must be exploited. Among the deleterious impurities in phosphate rock, dolomite is the most troublesome because it causes high consumption of sulfuric acid, reduce filtration capacity and lowers P_2O_5 recovery in the fertilizer manufacturing process. Almost 50% of future phosphate reserves in Florida are contaminated with dolomite impurity. Therefore, the removal of dolomite from phosphate rock has been a high priority for investigations in phosphate industry.

Since 1970s, much of research work has been conducted and different processes have been developed. Most of those processes have used flotation approach, either dolomite flotation, phosphate flotation or silica flotation, or combination of them. As mentioned earlier, most of those processes generated a phosphate concentrate with P_2O_5 grade lower than 30%, or MgO content higher than 1%, or lower P_2O_5 recovery due to the desliming of flotation feed or inefficiency of the flotation reagents. IMC cationic flotation process is considered the most effective one in which cationic amine type collectors were used for both silica flotation and phosphate flotation (El-Shall et al, 1996). In recent years, a CLDRI fine particle flotation process was developed for processing Florida dolomitic phosphate pebble. In this process, the sample was ground to minus 100 mesh for liberating impurities from phosphate. The ground material was used as flotation feed without desliming. However, a fatty acid type collector PA-31 made of local raw materials was used (Gu, et al. 1999). Although a pilot plant test was conducted in Florida in 2000, the collector was manufactured in China and shipped to test site (Gruber, et al. 2001). In this study, a U.S. fatty acid type collector is used to separate dolomite from phosphate. The project includes two steps, one is stirred-tank cell flotation test and another is modified packed column flotation test.

The dolomitic phosphate pebble sample was provided by IMC-Phosphate, FL. The sample contains 26.1% P_2O_5, 1.3 to 1.5% MgO and 14.5% acid insoluble. In stirred-tank cell flotation test, the sample was ground to 98.5% passing 150 μm (100 mesh) for liberation of phosphate from the impurity such as dolomite, silica, etc. from dolomitic phosphate mineral sample. The ground slurry was conditioned with phosphoric acid as pH modifier and phosphate depressant for one minute, then with FAS-40A as collector for two minutes. The optimum flotation result was achieved under the conditions of pH 5.4, 2.0 kg/t FAS-40A and 1100 rpm impeller speed. The underflow of dolomite flotation contains 26.8% P_2O_5, 0.8% MgO with about 93% P_2O_5 recovery. To adjust the pH value

of the slurry, phosphoric acid was used as pH modifier as well as depressant for phosphate particles.

Based on the results of stirred-tank cell flotation, a central composite experiment design (CCD) was applied to run modified packed column flotation tests. The central composite experiment design was made by the statistics software JMP 4.0 (SAS Institute, Inc., Cary, NC). A total of 26 runs was performed with the test order and conditions arranged by the experiment design. During the test, it was found that it was difficult to produce a stable froth layer at the top of the original packed column. It may be due to the low content of dolomitic mineral particles in the phosphate ore sample used for this study and in the froth layer. A ceramic sparger was installed at the bottom of the flotation column to generate fine size bubbles for stabilizing the froth layer. After completion of all the tests, the selectivity index was computed for each run as the response of the test. The experiment data of Selectivity Index, SI, was input into JMP program. Experiment designed flotation test results were analyzed statistically by JMP. According to JMP output, a reduced model was established. The model includes pH, collector dosage and air flow rate and their interaction. The best selectivity index was achieved at the conditions of pH 5.5, 3.0 kg/t collector and 4.5 SCFH air flow rate. The underflow of dolomite flotation contains 26.9% P_2O_5, 0.95% MgO at 88.8% P_2O_5 recovery. Double reverse flotation technology was applied. The underflow of dolomite flotation was collected for further amine flotation to reject silica which was performed in Denver D-12 stirred- tank cell. The final phosphate concentrate of 30.35% P_2O_5, 1.03% MgO, 4.88% acid insoluble was obtained at the overall P_2O_5 recovery of 87.14%.

EXPERIMENTAL

Dolomitic phosphate pebble sample

The dolomitic phosphate pebble (DPP) sample A for this study was collected supplied by IMC Phosphate, Lakeland, Pork County, Florida. For phosphate production in Florida, the phosphate matrix is mined by high capacity dragline. The matrix mined is made into slurry using high pressure water jet and then pumped to the phosphate beneficiation plant for washing operation using spiral classifier. After washing, the matrix was split by screens and cyclones into three streams, usually +1 mm, -1+0.106 mm and –0.106 mm size fractions. The minus 0.106 mm (minus 150 Tyler mesh) fines is treated as phosphatic slime. This slime is transported in tailings pond for storage due to its high impurities and low P_2O_5 content. The size fraction of –1+0.1 mm is fed to conventional two stage "Crago" flotation process to recover phosphate concentrate. "Crago" process involves a rougher phosphate flotation using fatty acid collector. The rougher phosphate concentrate is washed with dilute sulfuric acid to remove fatty acid from surface of mineral particles, which is called "deoiling". The deolied material is subjected to silica flotation using amine collector. The plus 1 mm coarse size fraction is known as phosphate pebble. This fraction is usually blended with flotation concentrate to make up a composite product for downstream phosphoric acid production, if the MgO content in the composite product is lower than 1%. If the MgO content is higher than the limit, it is considered as dolomitic phosphate pebble (DPP) and will be discarded as waste. Usually, one third of the phosphate mineral is bound with slimes, one third is recovered with the "Crago" flotation process and another one third is contained in dolomitic phosphate pebble in a typical phosphate production practice in Florida.

The chemical analysis result of the as-received sample A is given in Table 2. The overall dolomitic phosphate pebble sample has 26.14% P_2O_5 and 14.58% acid insoluble. The MgO content is about 1.5 % which is lower than expected. This sample is used as feed for the column flotation tests.

Table 2 Chemical analysis of as-received dolomitic phosphate pebble sample

Components	P_2O_5	MgO	Insol	Fe_2O_3	Al_2O_3	CaO
Analysis, %	26.14	1.52	14.58	0.96	1.22	39.23

The size distribution of the dolomitic phosphate pebble sample and chemical analysis of each size fraction are presented in Table 3. The analysis results show that plus 4 mm coarse fractions contain much higher MgO content, and the MgO grade in size range between 2 mm and minus 0.15 mm is less than 1%.

After the dolomitic phosphate pebble sample was received, it was air dried to expel the surface moisture. The dried sample was crushed to pass 1.18mm (14 mesh) using a double roll-crusher. Prior to flotation, the crushed sample was further ground to finer size using a lab size rod mill.

Reagents

In dolomite phosphate flotation experiment, following reagents are used:

FAS-40A fatty acid collector: A mixture of C-16 to C-20 fatty acid is supplied by ARR-MAZ Products (Winter Haven, FL). The reagent is brownish and insoluble in water. This reagent is causticized with NaOH which weighs about 14% of total fatty acid and prepared into 2% wt. solution for application.

Amine collector: Fatty acid amine, provided by ARR-MAZ Products, is used as quartz collector for separating silica from phosphate. The product is a light brownish liquid and has a good solubility in water. The solution of 2% wt. concentration is prepared.

Phosphoric acid: H_3PO_4 is as chemical analysis grade with the purity of 85% P_2O_5 from Fisher Scientific (Pittsburgh, PA). Phosphoric is prepared into 5% wt. solution for application. It is used as both pH modifier and depressant of phosphate minerals in dolomitic phosphate flotation.

Kerosene: Kerosene is obtained from Fisher Scientific (Pittsburgh, PA). This reagent is used as a collector aid in amine flotation to float silica from phosphate.

Apparatus and procedures

Grinding

As demonstrated in Table 3, the dolomitic phosphate pebble sample must be ground to smaller size particles to well liberate phosphate particles from impurities such as dolomite, silica, etc. in the dolomitic phosphate ore sample prior to flotation. In this study, a laboratory rod mill was used to grind the sample. The dimension of the rod mill is 200 mm ID and 250 mm length. The size, quantity, weight and percentage of the stainless steel rods used as grinding media are given in Table 4. A series of milling tests were conducted to determine the grinding time to achieve sufficient phosphate liberation using 300 g and 1000 g sample size for each batch. Five batches of 1000 g ground sample, i.e. 5 kg, were then combined for one batch of column flotation tests.

Table 3 Size distribution and chemical analysis of as-received dolomitic phosphate pebble sample

Particle size	Wt.%	Analysis, %						Distribution, %					
		P_2O_5	MgO	Insol	Fe_2O_3	Al_2O_3	CaO	P_2O_5	MgO	Inso	Fe_2O_3	Al_2O_3	CaO%
+6.3 mm (0.25-in)	5.45	15.26	7.57	15.52	1.33	0.87	33.47	3.16	24.66	6.01	7.79	4.73	4.74
-6.3mm+4.0 mm (-0.25-in +5 mesh)	8.35	22.74	4.37	11.14	0.86	0.95	39.05	7.22	21.83	6.62	7.72	7.93	8.48
-4.0+2.0 mm (-5+2 mesh)	36.91	28.11	1.29	10.69	0.84	0.99	41.57	39.43	28.48	28.07	33.33	36.51	39.90
-2.0+1.18 mm (-9+14 mesh)	28.88	27.13	0.87	15.73	0.97	0.92	39.53	29.77	15.03	32.31	30.11	26.54	29.68
-1.18 mm+600 μm (-14+28 mesh)	10.80	24.85	0.80	22.65	0.89	0.95	26.02	10.20	5.17	17.40	10.33	10.25	7.31
-600+300 μm (-28+48 mesh)	3.71	28.10	0.61	15.02	1.05	1.10	39.96	3.96	1.35	3.97	4.19	4.08	3.86
-300+150 μm (-48+100 mesh)	2.72	29.40	0.41	12.86	0.95	1.04	40.92	3.04	0.67	2.49	2.78	2.83	2.90
-150 μm (100 mesh)	3.17	26.60	1.48	13.87	1.10	2.25	38.08	3.21	2.81	3.13	3.75	7.13	3.14
Computed feed	100.00	26.31	1.67	14.06	0.93	1.00	38.46	100.00	100.00	100.00	100.00	100.00	100.00

Table 4 Stainless steel rods as grinding media for the grinding tests in a laboratory scale rod mill

Rod diameter (mm)	Quantity (No. of rods)	Weight (g)	Weight (%)
16	17	8175	49.34
12	16	5710	32.33
10	14	3238	18.33
Total	47	17663	100.00

Stirred-tank cell Flotation

Dolomite flotation of DDP sample was carried out in Denver stirred-tank cell to determine the appropriate flotation pH and collector dosage. The impeller speed of flotation machine was set up at 1100 rpm and the air flowrate was 0.75 L/min. The ground DDP slurry was transferred into flotation cell. It was first conditioned with phosphoric acid as pH modifier and phosphate depressant for 1 min., and with fatty acid collector, FAS-40A, for 2 min. After conditioning with collector, the slurry was aerated for another one min. Then, the float was skimmed to a froth container. Both float and sink were filtered, dried, weighed and analyzed.

Modified packed column Flotation

The dolomitic phosphate pebble (DPP) flotation tests using fatty acid collector, FAS-40A, were carried out in a 2 in. ID and 6 ft. height modified packed column. The packing material was made of 0.002" thickness structured corrugated plates. Each plate has 3/4" pitch running diagonally at about 50^{o} angles. The modified packed column flotation system was schematically presented in Fig. 1. The packed flotation column was designed to incorporate steel plates packed inside an open column to provide narrow, small and long torturous flow passages to provide sufficient time for particle/bubble contact. The packing structures were stacked up in column as shown in the Fig. 1.

The structured plate packed flotation column has a feed slurry inlet at the intermediate location, a water inlet at the top for spraying wash water into the column to resin the froth, and an inlet at the bottom of the column for introducing compressed air into the column to generate bubbles. Washing water goes down through a maze of flow passages confined by the packing structures. As air passes upward through the winding flow passages, the bubbles continuously carry the hydrophobic particles into a froth zone in the upper portion of the column, while the hydrophilic particles as sink product is discharged through the outlet at the bottom of the column. Capillary effects between the structure plates support a controllable froth height. This effect makes a deep froth column flotation achievable, when the high number of hydrophobic particles is presented in the pulp. Washing water drains off entrapped and detaches the entrained mineral particles in the froth. The slurry level or the froth interface in the modified packed column is

controlled by adjusting the height of the discharging tubing for the underflow discharge.

To prepare feed slurry for column flotation, at least five batches of 1000 grams milled sample were combined and added into the conditioning tank. The slurry was diluted to a desired solid percentage. The slurry was continuously stirred in the tank to maintain the particles in suspension and was circulated through a circulation loop with a pump to achieve the homogeneity of the suspension. Phosphoric acid is added to the circulation loop to modify the pH of the flotation slurry and depress phosphate particles. The fatty acid soap, FAS-40A was also added into the circulation loop after the pH adjustment. The reagentized DPP slurry is fed at about 3 ft from the bottom of the packed flotation column.

The sink discharge was collected from the fine DDP flotation in modified packed flotation column. The sink sample was sized at 38 μm or 20 μm (400 mesh or 630 mesh). Plus 38 μm or plus 20 μm fraction was subjected to fatty acid amine flotation to separate silica from phosphate. The silica was collected as froth product, while the phosphate product was remained in the cell as sink. Amine flotation tests were conducted using the Denver D-12 stirred-tank type flotation machine and a 1.2 liter flotation cell.

Preliminary packed column flotation test results showed that it was difficult to maintain a stable froth layer at the top of the original packed flotation column due to the low content of dolomitic mineral particles in the feed and thus in the froth layer. Therefore, a ceramic sparger (CPT Inc., British Columbia, Canada) was installed at the bottom of the column a shown in Fig. 1 to generate fine size bubbles to stabilize the froth layer.

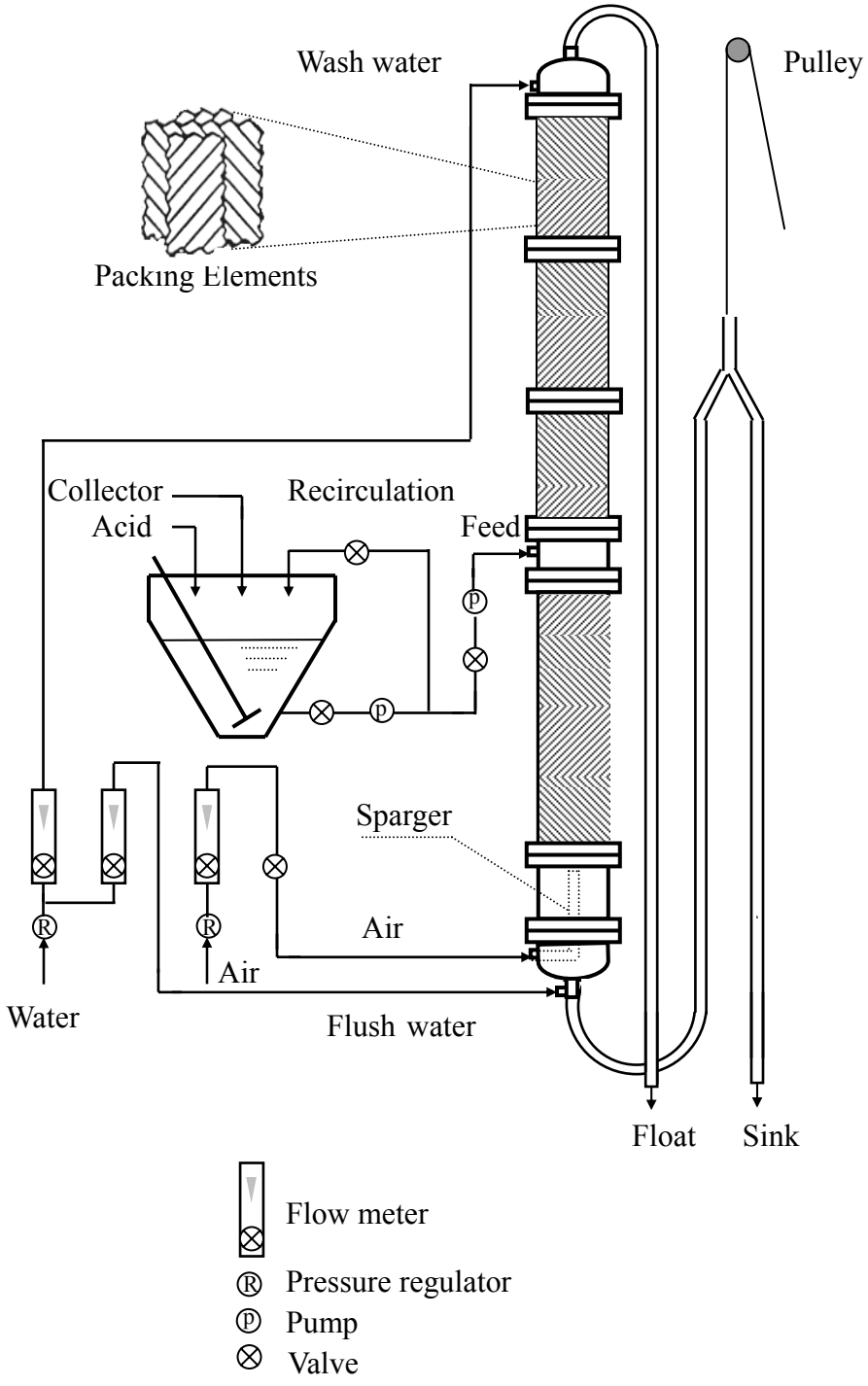

Figure 1 Schematic diagram of 2-in ID packed flotation column system

Experiment design

Based on previous experience on the original packed column flotation of Florida dolomitic phosphate samples (Gu, 2002) as well as fine dolomitic phosphate pebble flotation using stirred-tank cell in this study, the control parameters considered in the experiment design included collector pH, dosage, slurry/froth interface level (froth height) and air flowrate. According to the results of modified packed column flotation and stirred-tank cell flotation on dolomitic phosphate pebble samples, the operation conditions for the modified packed column flotation in this study were determined and listed in Table 5.

Table 5 Conditions for the modified packed column flotation

Factors	-1	0	+1
pH	4.5	5	5.5
Collector (kg/t)	2	2.5	3
Interface (cm)	10	15	20
Air rate (SCFH)	3.5	4	4.5

Central composite design (CCD) is applied for the experiment. The distance from the center of the design space to a factorial point is ± 1 unit for each factor. The distance from the center of the design space to a star point is $\pm\alpha$. In this case, α value is 1, then the design is called face centered composite design. According to the output of the JMP software, standard CCD requires 26 runs with 2 center points needed for the experiment design analysis. The coded conditions and natural conditions are arranged as shown in Table 6.

Separation efficiency

The yield of the concentrate, Y_c is calculated by the following equation:

$$Y_c\% = \frac{P_f - P_t}{P_c - P_t} \times 100\% \quad (1)$$

where Y_c is yield of concentrate; P_f is P_2O_5 grade in feed; P_c is P_2O_5 grade in concentrate and P_t is P_2O_5 grade in tailings.

The phosphate recovery is defined as

$$R_{cp}\% = \frac{Y_c P_c}{P_f}(\%) \quad (2)$$

Table 6 Experiment design of column flotation tests

Run	Coded conditions				Natural conditions			
	pH[1]	CL[2]	IF[3]	AR[4]	pH	CL	IF	AR
1	-1	-1	-1	-1	4.5	2	10	3.5
2	1	-1	-1	-1	5.5	2	10	3.5
3	-1	1	-1	-1	4.5	3	10	3.5
4	-1	-1	1	-1	4.5	2	20	3.5
5	-1	-1	-1	1	4.5	2	10	4.5
6	1	1	-1	-1	5.5	3	10	3.5
7	-1	1	1	-1	4.5	3	20	3.5
8	-1	-1	1	1	4.5	2	20	4.5
9	-1	1	-1	1	4.5	3	10	4.5
10	1	-1	1	-1	5.5	2	20	3.5
11	1	-1	-1	1	5.5	2	10	4.5
12	1	1	1	-1	5.5	3	20	3.5
13	-1	1	1	1	4.5	3	20	4.5
14	1	-1	1	1	5.5	2	20	4.5
15	1	1	-1	1	5.5	3	10	4.5
16	1	1	1	1	5.5	3	20	4.5
17	1	0	0	0	5.5	2.5	15	4
18	-1	0	0	0	4.5	2.5	15	4
19	0	1	0	0	5	3	15	4
20	0	-1	0	0	5	2	15	4
21	0	0	1	0	5	2.5	20	4
22	0	0	-1	0	5	2.5	15	4
23	0	0	0	1	5	2.5	20	4.5
24	0	0	0	-1	5	2.5	20	3.5
25	0	0	0	0	5	2	20	4
26	0	0	0	0	5	2	20	4

1. pH: pH value of flotation slurry adjusted with phosphoric acid;
2. CL: Dosage of FAS-40A as dolomite collector, kg/t;
3. IF: Froth height, cm;
4. AR: Air flowrate, SCFH.

where R_{cp} is recovery of phosphate in concentrate.

Similarly, the dolomite (as MgO) recovery is defined as

$$R_{cd}\% = \frac{Y_c M_c}{M_f}(\%) \tag{3}$$

where R_{cd} is the recovery of dolomite in concentrate; M_f is the MgO grade in feed and M_c is MgO grade in concentrate.

In order to evaluate the performance of the dolomite flotation, the Selectivity Index (SI) of separating dolomite from phosphate is defined as an evaluation criterion. This selectivity index, SI is defined as

$$SI = \sqrt{R_{cp} \times (R_{cp} - R_{cd}) \times P_c / P_{max}} \tag{4}$$

where P_{max} is theoretical P_2O_5 grade of the phosphate mineral in the sample. The mineralogical study (Gu, 2002) determined the value of P_{max}= 36% for the dolomitic phosphate pebble sample.

In Eq. 4, when more phosphate is recovered and more dolomite is rejected, SI value becomes larger. Higher P_2O_5 grade in concentrate also increases the value of SI. The value of SI ranges from 0 to 100. The value of SI is zero if there is no selective separation of dolomite from phosphate, i.e., in case of no flotation. If the value of SI is 100, that means all phosphate mineral is recovered at a theoretical grade and all impurities are removed. Eq. 4 will be invalid if the value of R_{cp} becomes smaller than that of R_{cd}. In such a case, the process is phosphate flotation rather than dolomite flotation. SI is as a criterion specifically defined for evaluating the performance of separating dolomite from dolomitic phosphate pebble by dolomite flotation.

RESULTS AND DISCUSSION

Grinding tests

To determine the grinding time for achieving sufficient liberation, a series of grinding tests were conducted using 300 or 1000 gram sample for each batch respectively. For 300 g batch, 300 g sample in particle size of minus 1.18mm (14 mesh) was mixed with 200 ml water inside the mill, and ground for the given time period of 4, 6, 8 and 10 minutes. For 1000 batch, 1000 gram sample was mixed with 650 ml water in rod mill and ground for a pre-set time period of 8, 12, 16 and 20 minutes respectively. The solid percent for grinding is about 60%. After the grinding time reached the pre-set time interval, the slurry was dumped into a container. The slurry was sized at 150μm (100 mesh), 74μm (200 mesh) and 38μm (400 mesh) to determine the size distribution for different grinding time period. The size distribution and chemical analysis for 300 g batch is given in Table 7 and plotted in Fig. 2. Fig. 3 shows the size distribution after grinding the sample of 1000 g batch.

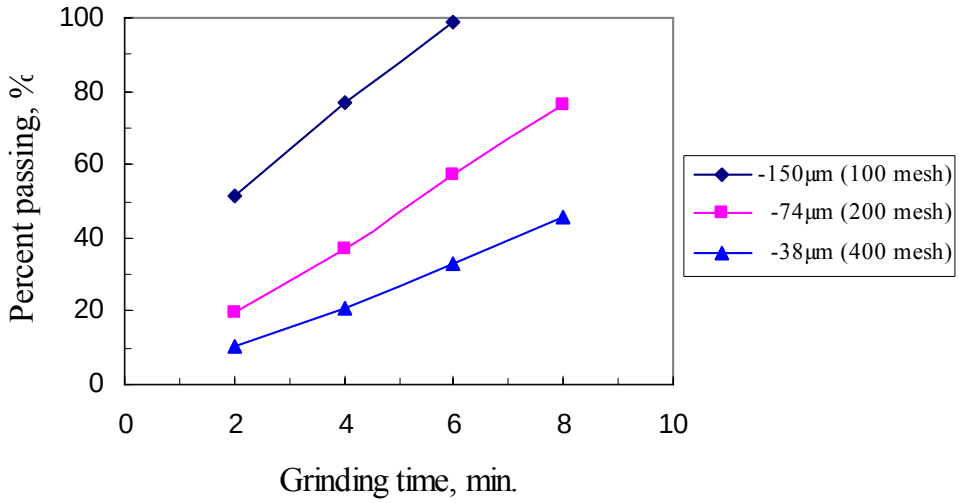

Figure 2 Size distribution as a function of grinding time for 300 g batch

It can be seen that the particle size becomes finer with the increase of grinding time. After grinding, there is no much difference in P_2O_5 grade in different size fractions as demonstrated in Table 7. However, fine fractions contain much higher MgO content because carbonate minerals are softer than phosphate and silica. When the grinding time is 8 minutes, about 98.5% of the particles in the slurry pass 150μm (100 mesh) and about 38.5% pass 38μm (400 mesh).

Table 7 Size distribution and chemical analysis after dolomitic phosphate sample was ground for various time period (300 g batch)

Grinding time	Size range	Wt.%	Grade, %			Distribution, %		
			P_2O_5	MgO	Acid insol.	P_2O_5	MgO	Acid insol.
4'	+250μm (+60 mesh)	5.53	26.40	0.78	19.60	5.30	3.11	8.34
	-250+150μm (-60+100 mesh)	26.98	27.20	1.00	16.07	26.66	19.54	33.35
	-150+74μm (-100+200mesh)	30.33	28.20	1.08	13.33	31.07	23.78	31.10
	-74+38μm (-200+400 mesh)	13.81	28.80	1.19	11.96	14.45	11.87	12.70
	-38+25μm (-400+635 mesh)	7.24	27.10	1.98	10.59	7.13	10.38	5.90
	-25μm (-635 mesh)	16.12	26.30	2.68	6.94	15.40	31.33	8.61
	Head	100.00	27.53	1.38	13.00	100.00	100.00	100.00
6'	+150μm (+100 mesh)	10.60	24.00	0.63	17.41	9.33	5.15	14.67
	-150+74μm (-100+200mesh)	39.43	28.00	0.92	14.30	40.48	28.11	44.83
	-74+38μm (-200+400 mesh)	19.41	28.10	1.05	13.09	20.00	15.79	20.20
	-38+25μm (-400+635 mesh)	9.76	27.30	1.68	10.97	9.77	12.69	8.51
	-25μm (-635 mesh)	20.79	26.80	2.37	7.13	20.43	38.26	11.79
	Head	100.00	27.28	1.29	12.58	100.00	100.00	100.00
8'	+150μm (+100 mesh)	1.50	26.50	0.49	20.42	1.44	0.56	2.51
	-150+74μm (-100+200mesh)	34.00	28.70	0.82	13.65	35.13	21.06	37.94
	-74+38μm (-200+400 mesh)	25.91	28.40	0.97	13.04	26.49	19.03	27.62
	-38+25μm (-400+635 mesh)	12.74	27.00	1.48	13.46	12.38	14.30	14.02
	-25μm (-635 mesh)	25.84	26.40	2.30	8.48	24.56	45.06	17.91
	Head	100.00	27.78	1.32	12.23	100.00	100.00	100.00
10'	+74μm (+200mesh)	24.29	28.00	0.79	19.08	24.58	14.11	33.60
	-74+38μm (-200+400 mesh)	34.24	28.20	1.00	14.56	34.89	25.12	36.14
	-38+25μm (-400+635 mesh)	12.06	26.70	1.60	13.78	11.64	14.22	12.05
	-25μm (-635 mesh)	29.40	27.20	2.15	8.54	28.90	46.55	18.20
	Head	100.00	27.68	1.36	13.79	100.00	100.00	100.00

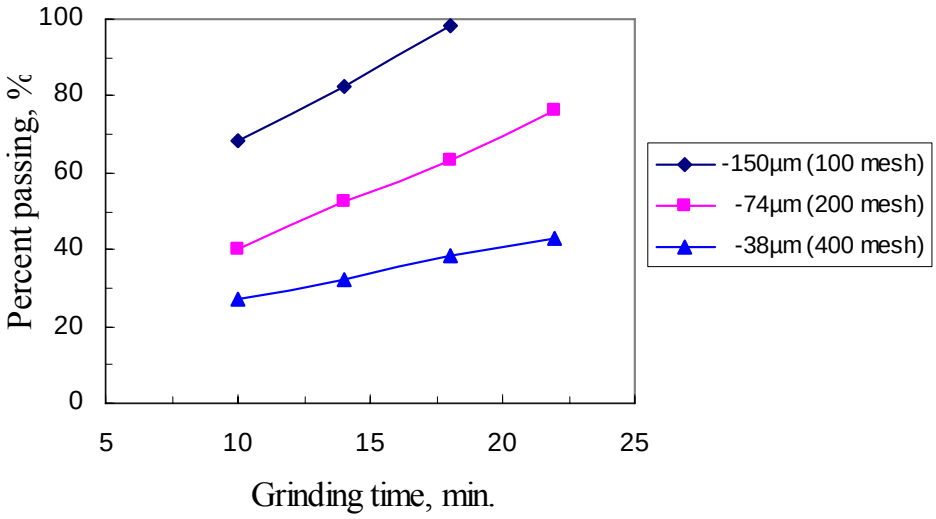

Figure 3 Size distribution as a function of grinding time for 1000 g batch

Based previous studies (Gu et al. 1999, Gu, 2002), the particle size for flotation was set to minus 150 μm (100 mesh) in order to achieve the satisfactory liberation phosphate particle form impurities such as dolomite, silica, etc. in dolomitic phosphate mineral sample for higher recovery of phosphate. According to grinding test results, 8 min. was chosen for 300 g batch and 16 min. for 1000 g batch.

Stirred-tank cell flotation test results

Dolomite flotation tests were carried out using a Denver 1.2 liter stirred-tank type flotation machine. In these flotation tests, effects of flotation pH and collector dosages were evaluated at the same impeller speed, aeration rate and solid percent of the flotation slurry.

Effect of flotation pH

Dolomite flotation tests were conducted in pH range from 4.5 to 5.9 using phosphoric acid as pH modifier. FAS-40A was used as dolomite flotation collector at the dosage of 2.0 kg/t of feed. The results are summarized in Table 8. Separation performances and the selectivity index of the dolomite flotation as a function of pH is plotted in Fig. 4. With the increase of pH, P_2O_5 recovery decreases. It indicates that more phosphate is reported to the float at higher pH. In the entire range of flotation pH, there is no much difference in P_2O_5 grade in the underflow of dolomite flotation. However, it can be seen that highest P_2O_5 and lowest MgO can be achieved around pH 5.4. With further increase of flotation pH, there is little effect on MgO content in the sink product, but increasing loss of P_2O_5 into the float. The selectivity index can also be used as a good evaluation criterion. The highest SI can be achieved at about pH 5.4.

Effect of collector dosage

A series of flotation tests were conducted to determine the optimum consumption of collector at pH 5.4 with the results shown in Table 9. The flotation performance and selectivity index as a function of FAS-40A dosage is plotted in Fig. 5. The Fig. 5 shows that with the increase of collector dosage, P_2O_5 grade has a slight increase, while MgO content decreases. After 2 kg/t, there is further decrease in MgO grade, but P_2O_5 loss increases. Selectivity index curve also indicates that best separation is obtained at 2 kg/t.

Table 8 pH effect on dolomite flotation using Denver D-12 machine and 1.2 liter cell

pH	Product	Wt.%	Grade, %		Recovery, %		SI
			P_2O_5	MgO	P_2O_5	MgO	
4.5	Float	3.4	20.23	4.44	2.56	10.63	24.33
	Sink	96.6	27.09	1.31	97.44	89.37	
	Feed	100.0	26.86	1.42	100.00	100.00	
4.9	Float	7.2	18.05	5.89	4.88	29.05	41.73
	Sink	92.8	27.27	1.12	95.12	70.95	
	Feed	100.0	26.61	1.46	100.00	100.00	
5.4	Float	10.7	17.54	6.29	7.04	48.60	54.70
	Sink	89.3	27.88	0.80	92.96	51.40	
	Feed	100.0	26.77	1.39	100.00	100.00	
5.9	Float	12.3	19.65	5.49	9.06	48.93	52.80
	Sink	87.7	27.68	0.80	90.94	51.07	
	Feed	100.0	26.69	1.38	100.00	100.00	

Operation conditions:

Collector dosage: 2 kg/t of feed;

Solid of slurry: 25%;

Impeller speed of flotation machine: 1100 rpm

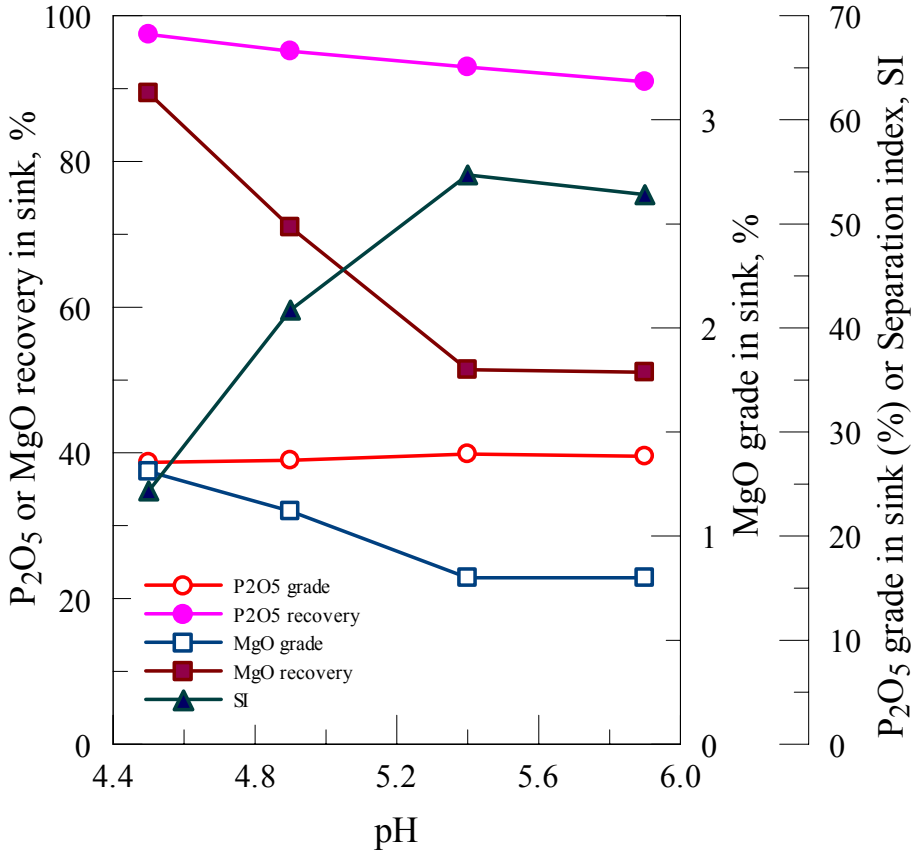

Figure 4 Dolomite flotation performance and selectivity index as a function of flotation pH

Table 9 Collector dosage effect on dolomite flotation using Denver D-12 machine and 1.2 liter cell

Collector kg/t	Product	Wt.%	Grade, %		Recovery, %		SI
			P_2O_5	MgO	P_2O_5	MgO	
1	Float	6.6	18.11	6.45	4.48	30.80	43.61
	Sink	93.4	27.23	1.02	95.52	69.20	
	Feed	100.0	26.63	1.38	100.00	100.00	
1.5	Float	8.3	17.69	6.38	5.46	37.47	48.22
	Sink	91.7	27.67	0.96	94.54	62.53	
	Feed	100.0	26.84	1.41	100.00	100.00	
2	Float	10.7	17.54	6.29	7.04	48.60	54.70
	Sink	89.3	27.88	0.80	92.96	51.40	
	Feed	100.0	26.77	1.39	100.00	100.00	
2.5	Float	13.1	19.31	5.33	9.51	49.87	53.03
	Sink	86.9	27.71	0.81	90.49	50.13	
	Feed	100.0	26.61	1.40	100.00	100.00	

Operation conditions:

pH: 5.4;

Solid of slurry: 25%;

Impeller speed of flotation machine: 1100 rpm

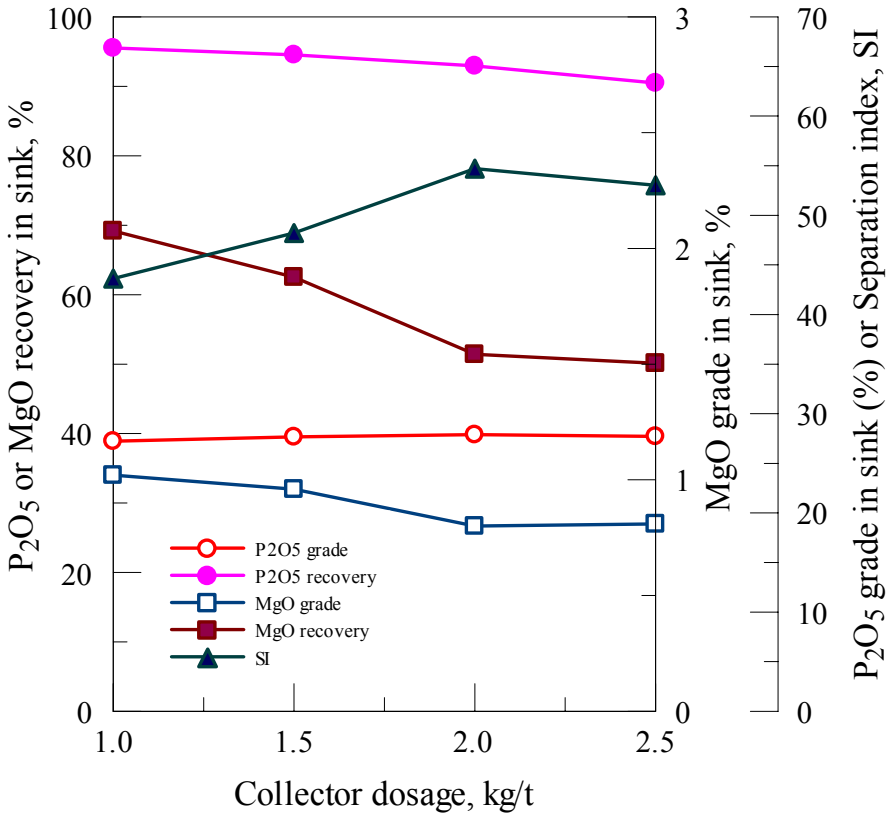

Figure 5 Dolomite flotation performance and selectivity index as a function of collector dosage

Modified packed column flotation test results

As described in previous section, five batches of 1000 grams milled sample are combined and added into the conditioning tank and diluted to the desired solid percentage. It was conditioned with phosphoric acid to adjust pH, then with fatty acid soap. The reagentized slurry is fed at about 3 ft. from the bottom of the modified packed column. Collector dosage, slurry pH, air flowrate and froth height are four parameters to be investigated. Operation conditions of four parameters are presented in Table 5. At each experiment condition, the float and sink are sampled for a given time interval. The samples are filtered, dried, weighed and analyzed. The weight percentage, analysis and recoveries of the sink product and calculated Selective Index, SI, of each run are summarized in Table 10.

Statistics analysis results

The analysis of the modified packed column flotation test results is carried out using the commercial statistic software package JMP (SAS Institute, Inc., Cary, NC). In dolomite flotation process, it can not just consider one performance, either MgO content, P_2O5 grade, or P_2O_5 recovery as a response to justify the effectiveness o the separation. For example, low MgO content in the product might be accompanied by low P_2O_5 recovery, and high P_2O_5 recovery is associated with high MgO content. In defining the selectivity index, several factors are taken into consideration, including P_2O_5 grade, P_2O_5 and MgO recoveries. Therefore, the selectivity index is chosen as a comprehensive response to evaluate the process.

In this study, the selectivity index is used as the response of the experiment input in JMP program. In running JMP program, “Stepwise” analysis option is selected. The stepwise regression procedure allows to select probabilities (p-value) for adding or deleting terms in the model. The p-value is chosen to be 0.10 for statistics analysis in this study. The program will automatically create a model using “forward” and “backward” procedures to select significant parameters and delete insignificant ones. The output of JMP includes the estimated coefficients, t-ratios and p-values, standard deviations, R^2 as well as an Analysis of Variance (ANOVA) table with lack-of fit information. The estimated coefficients, standard errors and t-ratios are presented in Table 11, and sum of squares and F-ratios in Table 12. Table 13 shows the Analysis of Variance (ANOVA).

Table 10 Results of modified packed column flotation

Run	Coded conditions				Natural conditions				Wt%	Grade, %		Recovery, %		SI
	pH	CL	IF	AR	pH	CL	IF	AR		P_2O_5	MgO	P_2O_5	MgO	
1	-1	-1	-1	-1	4.5	2	10	3.5	96.60	26.06	1.28	97.52	89.76	23.41
2	1	-1	-1	-1	5.5	2	10	3.5	94.80	26.86	1.15	96.05	81.56	32.22
3	-1	1	-1	-1	4.5	3	10	3.5	92.67	26.50	1.16	94.19	79.55	31.85
4	-1	-1	1	-1	4.5	2	20	3.5	96.20	26.08	1.26	97.02	86.61	27.05
5	-1	-1	-1	1	4.5	2	10	4.5	94.61	26.79	1.26	96.03	84.55	28.64
6	1	1	-1	-1	5.5	3	10	3.5	88.79	26.68	1.10	90.78	70.48	36.95
7	-1	1	1	-1	4.5	3	20	3.5	94.61	26.84	1.23	96.03	84.24	29.05
8	-1	-1	1	1	4.5	2	20	4.5	94.88	26.19	1.12	96.52	82.52	31.35
9	-1	1	-1	1	4.5	3	10	4.5	91.86	26.70	1.15	94.33	73.12	38.52
10	1	-1	1	-1	5.5	2	20	3.5	95.77	26.30	1.27	96.80	88.00	24.95
11	1	-1	-1	1	5.5	2	10	4.5	90.39	26.65	1.23	91.90	80.16	28.27
12	1	1	1	-1	5.5	3	20	3.5	90.84	26.88	1.11	92.92	73.93	36.6
13	-1	1	1	1	4.5	3	20	4.5	93.10	27.00	1.18	94.83	75.99	36.61
14	1	-1	1	1	5.5	2	20	4.5	92.89	26.38	1.29	94.08	84.82	25.27
15	1	1	-1	1	5.5	3	10	4.5	86.89	26.99	0.95	88.80	62.55	41.81
16	1	1	1	1	5.5	3	20	4.5	89.45	26.95	0.98	91.17	67.83	39.91
17	1	0	0	0	5.5	2.5	15	4	91.35	26.72	1.03	92.77	72.10	37.73
18	-1	0	0	0	4.5	2.5	15	4	92.49	26.71	1.14	93.95	78.04	33.3
19	0	1	0	0	5	3	15	4	90.99	26.77	1.12	92.47	73.82	35.82
20	0	-1	0	0	5	2	15	4	93.05	26.72	1.18	94.57	79.81	32.19
21	0	0	1	0	5	2.5	20	4	92.78	26.81	1.22	94.17	80.49	30.97
22	0	0	-1	0	5	2.5	15	4	91.71	26.84	1.14	93.32	77.02	33.68
23	0	0	0	1	5	2.5	20	4.5	91.39	27.00	1.16	92.98	76.54	33.86
24	0	0	0	-1	5	2.5	20	3.5	92.89	26.91	1.14	94.44	79.42	32.57
25	0	0	0	0	5	2	20	4	93.78	26.70	1.25	95.23	82.12	30.43
26	0	0	0	0	5	2	20	4	92.98	26.81	1.20	94.58	80.35	31.66

Table 11 Estimated coefficients, standard deviation, t-ratios and p-values

Term	Estimate	Std. Error	t-ratio	Prob>|t|
Intercept	32.49	0.46	70.90	<0.0001
pH	1.33	0.55	2.41	0.0260
CL	4.10	0.55	7.44	<0.0001
AR	1.64	0.55	2.98	0.0076
pH×CL	1.19	0.58	2.03	0.0565
pH×AR	-1.20	0.58	-2.06	0.0537
CL×AR	1.03	0.58	1.77	0.0936

Table 12 Sum of squares, F-ratios and p-values

Term	DF*	SS**	F-ratio	Prob>F
pH	1	31.81	5.83	0.0260
CL	1	302.33	55.38	<0.0001
AR	1	48.64	8.91	0.0076
pH×CL	1	22.52	4.12	0.0565
pH×AR	1	23.09	4.22	0.0537
CL×AR	1	17.02	3.12	0.0936

* Degree of freedom;

** Sum of squares.

Table 13 ANOVA table with selectivity index as responses

Source	DF	SS	MS	F-ratio
Model	6	445.41	74.23	13.5974
Error	19	103.73	5.46	Prob > F
Total	25	549.14		<.0001

From the output of the JMP program as shown in Table 13, DF is the degree of freedom, SS is the sum of squares and MS is the mean square. The F-ratios are calculated by comparing the sum of square (SS) of each factor with the error mean square. The statistic analysis data in Table 11 shows that statistically significant factors include flotation pH, collector dosage, air flowrate and interactions of pH with collector, pH with air flow rate and collector with air flow rate. It is interesting to note that froth height is not a significant factor between 15 and 20 inches in this case. This is probably because a sparger is used to generate fine bubbles in this study, which produce a quite stable froth layer. Based on the statistic analysis results, the reduced model in terms of the actual factor levels is:

$$Y = 32.48+1.33\times pH+4.10\times Collector+1.64\times Air+1.19\times pH\times Collector- 1.20\times pH\times air+1.03\times collector\times air \quad (5)$$

By using the coding algorithm [$X_i^* = 2((X_i\text{-midpoint}_i)/\text{range}_i)$], the model in terms of actual factor levels rather than the coded factor levels is:

$$Y = -9.74+9.96\times pH-32.08\times Collector+16.98\times Air+4.76\times pH\times Collector -4.8\times pH\times air+4.12\times collector\times air \quad (6)$$

The coefficient of determination (R^2) and adjusted coefficient of determination ($R^2_{adj.}$) are 0.81 and 0.75 respectively. A comparison of observed responses and those predicted by the reduced model are shown in Table 14 and Fig. 6. The results shows that the predictive model for SI values describes the actual SI values relatively well for various operation conditions.

Table 14 Experimental central composite design matrix showing observed and predicted responses

Run	Coded conditions				Natural conditions				Observed	Predicted
	pH	CL	IF	AR	pH	CL	IF	AR		
1	-1	-1	-1	-1	4.5	2	10	3.5	23.41	26.43
2	1	-1	-1	-1	5.5	2	10	3.5	32.22	29.11
3	-1	1	-1	-1	4.5	3	10	3.5	31.85	30.19
4	-1	-1	1	-1	4.5	2	20	3.5	27.05	26.43
5	-1	-1	-1	1	4.5	2	10	4.5	28.64	30.05
6	1	1	-1	-1	5.5	3	10	3.5	36.95	37.63
7	-1	1	1	-1	4.5	3	20	3.5	29.05	30.19
8	-1	-1	1	1	4.5	2	20	4.5	31.35	30.05
9	-1	1	-1	1	4.5	3	10	4.5	38.52	37.93
10	1	-1	1	-1	5.5	2	20	3.5	24.95	29.11
11	1	-1	-1	1	5.5	2	10	4.5	28.27	27.93
12	1	1	1	-1	5.5	3	20	3.5	36.6	37.63
13	-1	1	1	1	4.5	3	20	4.5	36.61	37.93
14	1	-1	1	1	5.5	2	20	4.5	25.27	27.93
15	1	1	-1	1	5.5	3	10	4.5	41.81	40.57
16	1	1	1	1	5.5	3	20	4.5	39.91	40.57
17	1	0	0	0	5.5	2.5	15	4	37.73	33.81
18	-1	0	0	0	4.5	2.5	15	4	33.3	31.15
19	0	1	0	0	5	3	15	4	35.82	36.58
20	0	-1	0	0	5	2	15	4	32.19	28.38
21	0	0	1	0	5	2.5	20	4	30.97	32.48
22	0	0	-1	0	5	2.5	15	4	33.68	32.48
23	0	0	0	1	5	2.5	20	4.5	33.86	34.12
24	0	0	0	-1	5	2.5	20	3.5	32.57	30.84
25	0	0	0	0	5	2	20	4	30.43	28.38
26	0	0	0	0	5	2	20	4	31.66	28.38

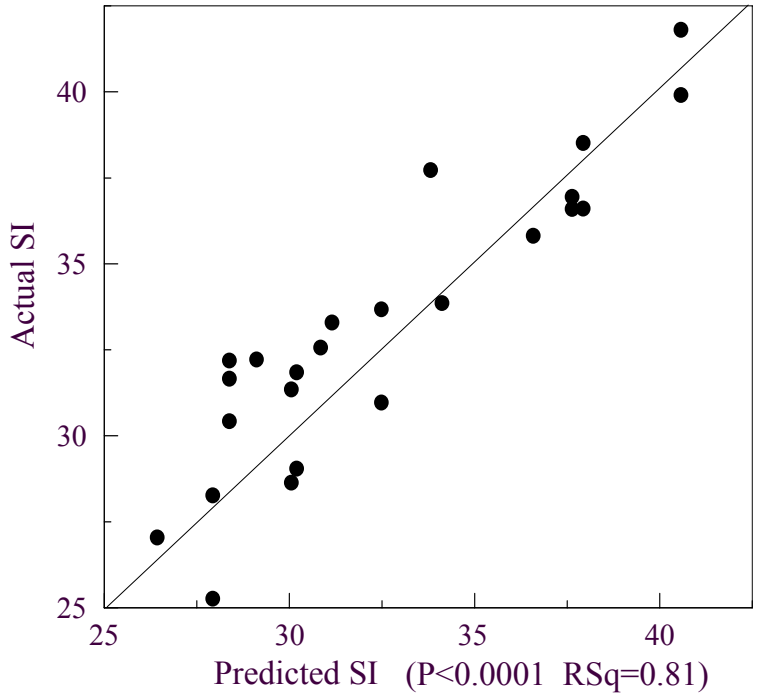

Figure 6 Comparison of the observed responses and predicted responses with reduced model

From Eq. 5, it can be observed that there are some interactions between pH and collector dosage, pH and air flow rate, and air flow rate and collector dosage. Interactive effects of different operation parameters are plotted in Fig. 7, 8 and 9. Those figures indicate that the highest separation selectivity index can be obtained at high values of pH, collector dosage and air flow rate. The best separation performance is achieved at around pH 5.5, which is coincident with the conclusions made by other investigators (Smani, et al. 1975, El-Shall, 2004, Anazia and Hanna, 1988, Abramov et al., 1993, Elgillani and Abouzeid, 1993, El-Shall, et al., 1996, Prasad et al., 2000, Gu et al. 1999, Peng and Gu, 2005). Further increase of pH will reduce the effect of phosphate depression and deteriorate the separation process by increasing P_2O_5 loss into the float. This leads to low separation selectivity which has been demonstrated in stirred-tank cell tests in this study and also reported elsewhere (Gu, 2002). It is not surprising that the best separation selectivity index is observed at collector dosage of 3.0 kg/t of feed in this set of column flotation tests. Increasing collector dosage might reduce MgO content in the underflow phosphate concentrate, but also at the cost of high P_2O_5 loss into the float. Compared with the stirred-tank cell tests, it can also be noted that column flotation consumes more collector than stirred-tank cell flotation.

At low pH, the selectivity index increases sharply with the increase of air flow rate. With further increase of the flotation pH, the magnitude of the selectivity index increase becomes smaller. At low collector dosage, the air flow rate has little effect on the selectivity. With the increase of the collector dosage, high air flow rate can improve the selectivity index.

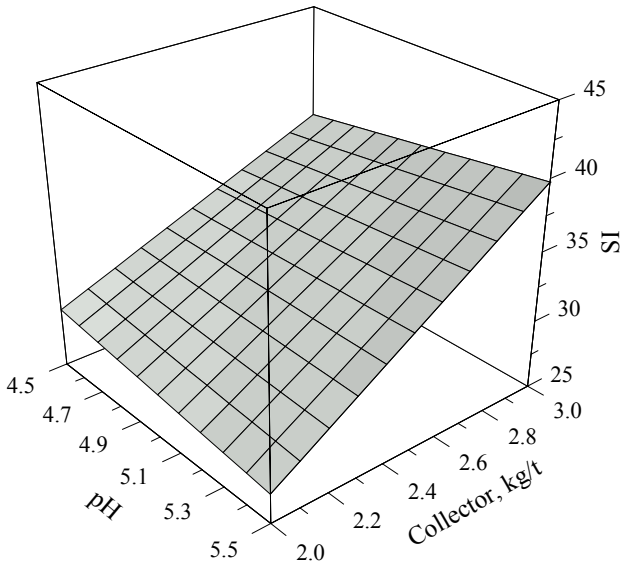

Figure 7 Interactive effect of pH and collector dosages with the selectivity index as separation responses

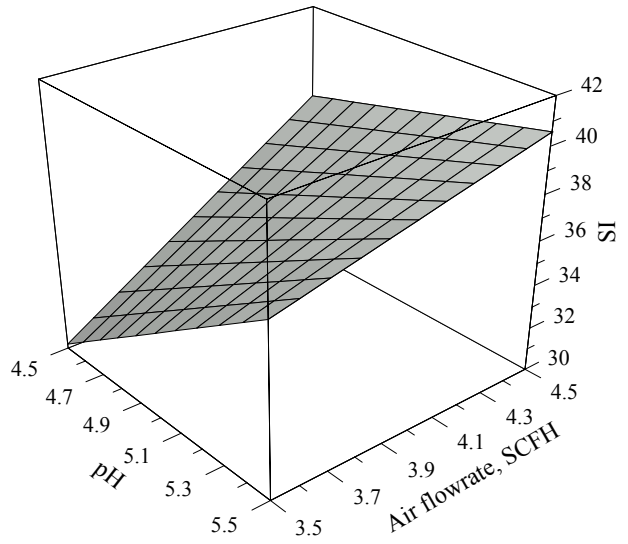

Figure 8 Interactive effect of pH and air flow rate with the selectivity index as separation responses

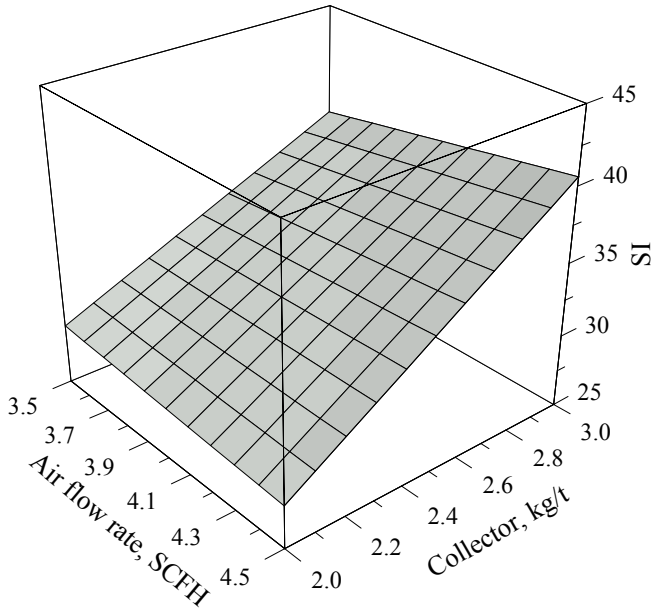

Figure 9 Interactive effect of air flow rate and collector dosages with the selectivity index as separation responses

Correlation between grade and recovery

Comparisons of the relationships between P_2O_5 recovery and P_2O_5 grade, MgO grade and P_2O_5 grade as well as P_2O_5 recovery and MgO grade in the underflow phosphate concentrate of dolomite flotation are plotted in Fig. 10, 11 and 12 respectively. Fig. 10 illustrates that the P_2O_5 recovery decreases with P_2O_5 grade increase. When dolomite particles are floated, some of phosphate particles are also floated with dolomite particles due to the entrapment of phosphate particles in froth, imperfect selectivity in the separation, interlocked particles, etc. Generally, increasing the amount of the float material can improve the P_2O_5 grade in the sink product. Such P_2O_5 grade improvement in the sink is achieved at the expense of P_2O_5 loss into the float.

Fig. 11 presents the correlation between MgO and P_2O_5 grade in the underflow of the dolomite flotation using modified packed flotation column. Although MgO and P_2O_5 grade are not well linearly related with each other, the trend shows that P_2O_5 grade increases with the decrease of the MgO content in the underflow product. Low MgO content in the underflow product means that more dolomite is reported to the float. Therefore, the P_2O_5 grade can be improved because of less dolomite left in the underflow. Figure 12 indicates that P_2O_5 recovery decreases with the decrease of MgO content.

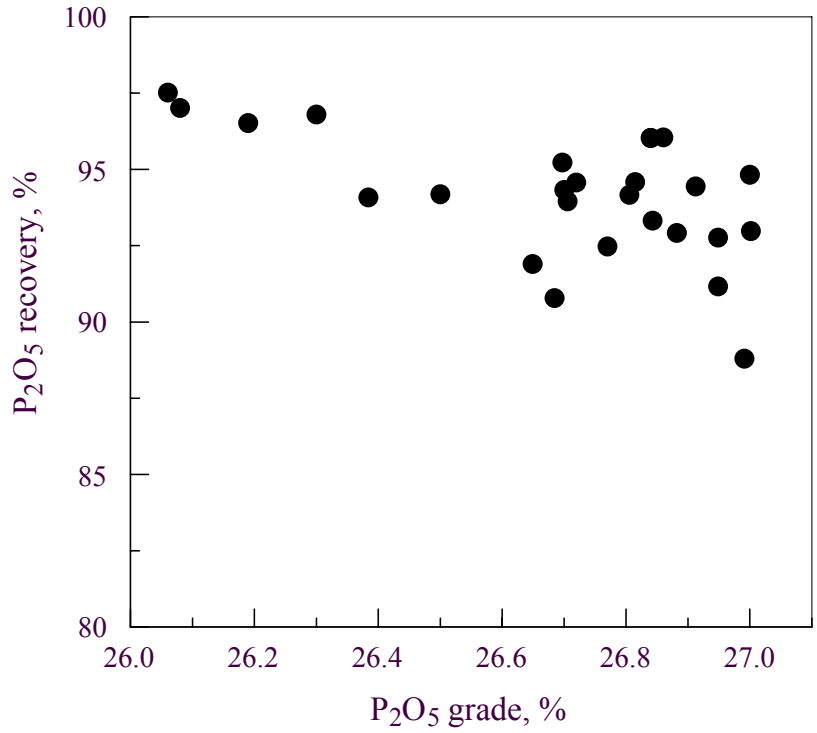

Figure 10 Relationship between P_2O_5 grade and P_2O_5 recovery in the sink product of dolomite flotation

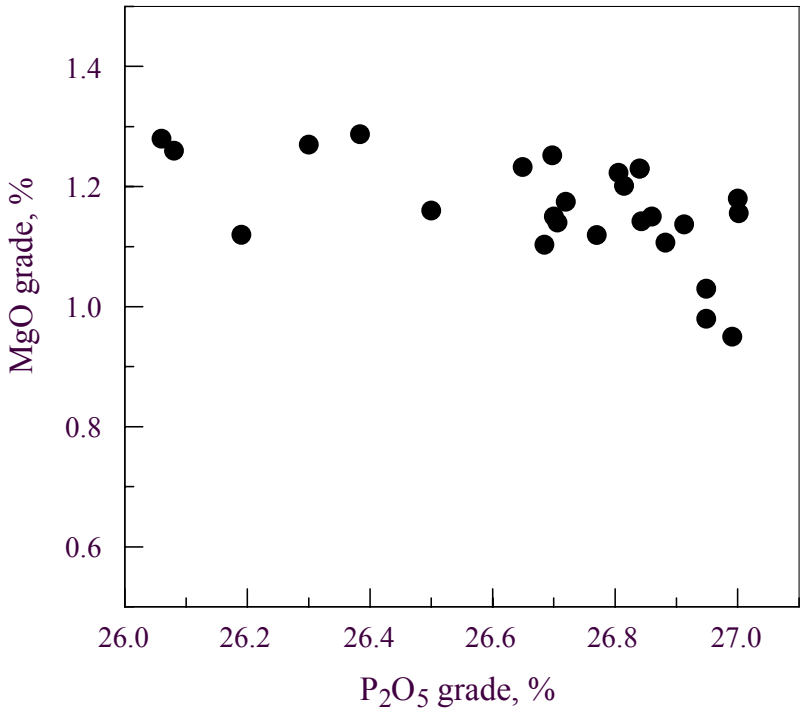

Figure 11 Relationship between P_2O_5 grade and MgO recovery in the sink product of dolomite flotation

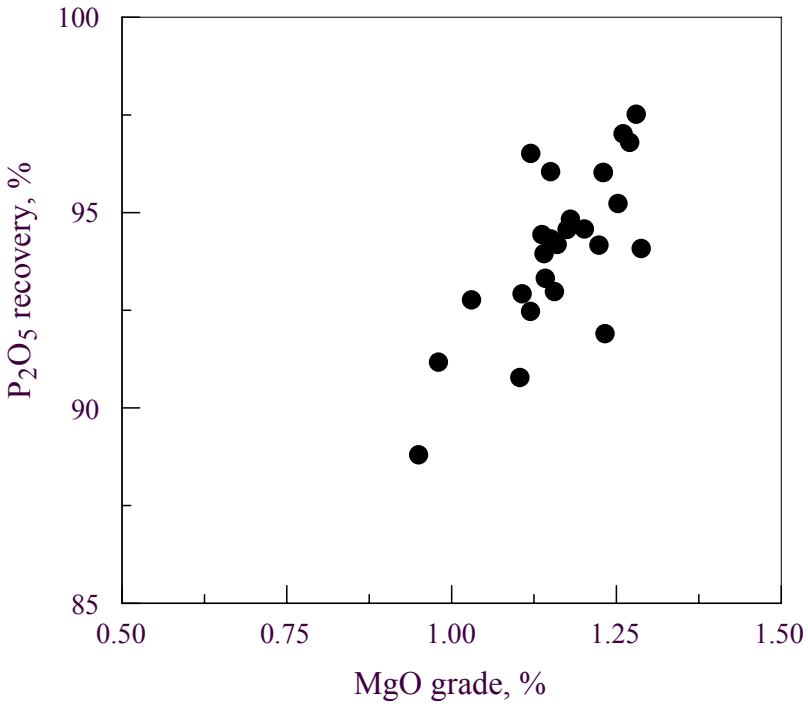

Figure 12 Relationship between MgO grade and P_2O_5 recovery in the sink product of dolomite flotation

Silica amine flotation

Under the operation conditions of pH 5.5, collector dosage 3.0 kg/t of feed, air flow rate 2.2 l/min. (4.5 SCFH) and froth height 15 cm, the underflow of the modified packed column after dolomite flotation was collected for silica amine flotation. The collected sample was first sized at 38μm (400 mesh). Applying double reverse flotation technology, the plus 38μm fraction was conditioned with fatty acid amine as collector and kerosene as collector aid. After conditioning, the slurry was subjected to silica flotation in Denver machine with 1.2 liter cell to reject silica into the float tailings. The underflow of silica flotation was combined with the minus 38μm fines to form a composite phosphate concentrate. The flowsheet and material balance are given in Fig. 13 and Table 15. It can be seen that the final composite phosphate concentrate contains 30.35% P_2O_5, 1.03% MgO and 4.88% acid insoluble. The overall P_2O_5 recovery is 87.14%.

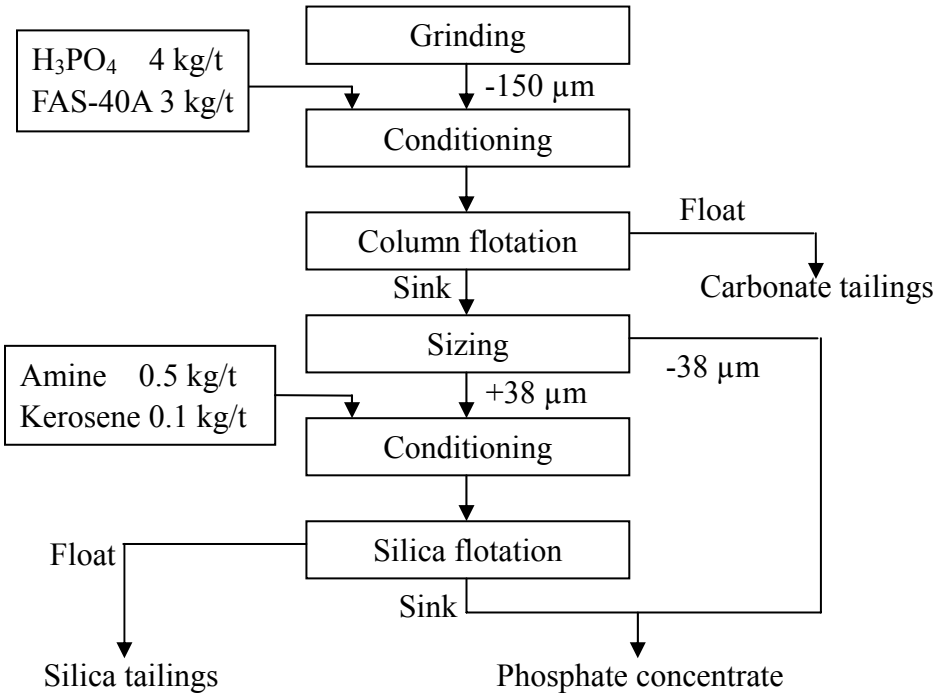

Figure 13 Flotation flowsheet of double reversed dolomitic phosphate flotation: dolomite flotation in modified packed flotation column and silica flotation in stirred-tank flotation cell.

Table 15 Material balance of dolomite flotation followed by silica amine flotation

Product	Wt. %	Grade, %			Recovery, %		
		P_2O_5	MgO	A.I.	P_2O_5	MgO	A.I.
Dolomite float	13.54	22.43	4.01	3.47	11.61	41.03	3.28
Silica float	11.35	2.88	0.07	89.63	1.25	0.60	71.10
Silica flot. sink	55.23	30.85	0.82	3.80	65.13	38.39	14.67
-38 μm of dolo.	19.88	28.97	1.33	8.14	22.01	19.88	14.95
Head	100.0	26.16	1.32	14.36	100.0	100.0	100.0
Composite product	75.11	30.35	1.03	4.88	87.14	58.37	25.88

CONCLUSIONS

Based on the stirred-tank cell and modified packed column flotation tests on Florida dolomitic phosphate pebble sample, following conclusions can be made:

(1) Fatty acid FAS-40A can be used as dolomite collector for dolomite flotation in acidic pH using phosphoric acid as pH modifier and phosphate depressant.

(2) Denver D-12 stirred-tank type machine with 1.2 liter cell can produce a rougher phosphate concentrate containing 26.8% P_2O_5 and 0.8% MgO at 93% P_2O_5 recovery. The flotation conditions are pH 5.4, 2.0 kg/t FAS-40A, 0.75 L/min air flow rate and 1100 rpm impeller speed. About 48.6% of dolomite can be removed to the float. With further increase of pH and/or collector dosage, more dolomite could be removed, but accompanied by more phosphate loss.

(3) Modified packed flotation column can be utilized to separate dolomite from phosphate. The underflow of dolomite flotation contains 26.9% P_2O_5 and 0.95% MgO can be obtained at the P_2O_5 recovery of 88.8%. The separation result of modified packed flotation column is not as good as that stirred-tank flotation cell in terms of MgO grade and P_2O_5 recovery in the underflow in this study. It can also be noted that flotation column requires higher collector consumption in order to achieve similar results of stirred-tank cell flotation. Further study is needed to determine the optimum operation conditions for dolomite column flotation.

(4) Due to low proportion of dolomite mineral particles in the phosphate sample tested and in froth layer, it is difficult to generate a stable froth layer at the top of the original packed column. Therefore, a sparger is added to produce fine size bubbles for facilitating the collision between dolomite particles and bubbles as well as stabilizing the froth layer.

(5) In the reduced model developed from experiment design statistics analysis by JMP, there is no froth height term, which might relate to low proportion of dolomite mineral in the phosphate sample for flotation and utilization of a sparger for production of fine size bubbles. The fine size bubbles generated from a sparger has stabilized the froth layer despite of low content of dolomite particles in the froth.

(6) The MgO grade in the DPP feed sample for this study is lower than expected, only 1.3 to 1.5%. The changes in the separation results are not very sensitive to the changes of the operation parameters of the modified packed flotation column.

REFERENCES

Abromov, A. A., Abromov, Al. Al., Onal, G., Atak, S., and Celik, M. S., 1993, "Mechanism of Reverse Flotation of Calcareous Phosphate Ores", Beneficiation of Phosphates: Theory and Practice, El-Shall, H., Moudgil, B., Wiegel, R., eds., SME, Littleton, CO, pp.281-288.

Anazia, I., and Hanna, J., 1988, "Innovative Process for Beneficiation of Dolomite Phosphate Ores", Int. J. Mineral Processing, Vol. 23, No. 3-4, pp.311-314.

Baumann, A. N., and Snow, R. E., 1980, "Processing Techniques for Separating MgO Impurities from Phosphate Products", In Proceedings, 2nd International Congr. Phosphorus Compounds, April, pp. 269-280.

Elgrilani, D. A., and Abouzeid, A. Z. M., 1993, "Flotation of Carbonates from Phosphate Ores in Acidic Media", Int. J. Mineral Processing, Vol. 38, pp.235-256.

El-Shall, H., and Zhang, P., Khalek, N. A., and El-Mofty, S., 2004, "Beneficiation technology of phosphates: challenges and solutions", Minerals and metallurgical Processing, Vol. 21, No. 1, pp.103-111.

El-Shall, H., Zhang, P. and Snow, R., 1996, "Comparative Analysis of Dolomite/Francolite Flotation Techniques", Minerals and Metallurgical Processing, Vol. 13, No. 3, pp. 135-140.

El-Shall, H., Cheng, Y. H., Abdel-Khalek, N. A., and Gupta, S., 1999, "A Parametric Study of Column Flotation of Florida Phosphates", Beneficiation of Phosphates: Advance in Research and Practice", Zhang, P., El-Shall, H., Wiegel, R., eds., SME, Littleton, CO, pp. 75-86.

Gruber, G. A., Zheng, S. B., and Hwang C. L., 2001, "A Pilot-Scale Demonstration of the IMC/CLDRI/FIPR Flotation Process for Florida High-MgO Pebble", Final report submitted to Florida Institute of Phosphate Research, publication No. 02-133-178.

Gu, Z. X., 2002, "Fine Particle Flotation for Florida Dolomitic Phosphate Pebbles", Master Thesis, West Virginia University, Morgantown, WV.

Gu, Z. X., Gao, Z. Z., and Hwang C. L., 1999, "Development of New Technology for Beneficiation of Florida Dolomitic Phosphate Resources", Final report submitted to Florida Institute of Phosphate Research, publication No. 02-129-167.

Gu, Z. X., Gao Z. Z., and Zheng S. B., 1999, "Beneficiation of Florida Dolomitic

Phosphate Pebble with a Fine Particle Flotation Process", Beneficiation of Phosphates: Advance in Research and Practice", Zhang, P., El-Shall, H., Wiegel, R., eds., SME, Littleton, CO, pp.155-162.

Lu S., and Sun K., 1999, "Development of Phosphate Flotation Reagents in China", Beneficiation of Phosphates: Advance in Research and Practice, Zhang, P., El-Shall, H., Wiegel, R., eds., SME, Littleton, CO, pp.21-26.

Moudgil, B. M., and Chanchani, R., 1985, "Flotation of Apatite and Dolomite Using Sodium Oleate as the Collector", Minerals and Metallurgical Processing, Vol. 2, No. 1, pp.13-19.

Prasad, M., Majunder, A. K., and Rao, T. C., 2000, "Reverse Flotation of Sedimentary Calcareous/Dolomitic Rock Phosphate Ore-An Overview", Minerals and Metallurgical Processing, Vol. 17, No. 1, pp.49-55.

Peng, F. F., and Gu, Z. X., 2005, "Processing Florida Dolomitic Phosphate Pebble in a Double Reverse Fine Flotation Process", Minerals and Metallurgical Processing, Vol. 22, No. 1, pp.23-30.

Smani, S., Cases, J. M., and Blazy, P., 1975, "Beneficiation of Sedimentary Moroccan Phosphate Ore", Part 1, 2, 3 and 4, Trans. SME-AIME, Vol. 258, pp 168-182.

Stephen, M.J., 2005, "Phosphate Rock", Metals and Minerals, Minerals Yearbook, Vol. 1, pp.122-124.

Zhang, P., 1993, "Phosphate Beneficiation-Trends of 90's," "Beneficiation of Phosphate: Theory and Practice." El-Shall, H., Moudgil, B., Wiegel, R., eds., SME, Littleton, CO, pp.399-425.

.

Appendix 8: Development of a Novel Fine Particle Centrifuge

FINAL REPORT

Contract Title and Number:	Period of Performance:
Crosscutting Technology Development at the Center for Advanced Separation Technologies (DE-FC26-02NT41607)	Starting Date: 6/1/04 Ending Date: 10/31/06

Sub-Recipient Project Title:	Report Information:
"Development of a Fine Particle Centrifuge"	Type: Final Report Number: -- Period: --
Principal Investigators:	Date: 12/1/06
Gerald Luttrell and Roe-Hoan Yoon Todd Burchett and Serhat Keles	Code: VA006
Contact Address:	Contact Information:
146 Holden Hall Virginia Polytechnic Institute & State University Blacksburg, VA	Phone: (540)231-4508 Fax: (540)231-3948 E-Mail: cast@vt.edu
Subcontractor Address:	Subcontractor Information:
No subcontracts issued.	Phone: Fax: E-Mail:

ABSTRACT

The solid-solid separation processes employed by modern coal preparation plants require large amounts of process water. After cleaning, the unwanted water must be removed from the surfaces of the particles using mechanical dewatering equipment. Coarse particles can be readily dewatered using simple screening systems, while finer particles require more complicated unit operations such as centrifuges and filters. Unfortunately, the processes used to dewater fine particles are inherently inefficient and expensive to operate and maintain. To overcome these problems, a novel centrifugal filter has been developed by researchers at Virginia Tech. Preliminary test data suggest that this new technology can reduce the moisture content of fine coal products by approximately 30-50% as compared to existing dewatering processes. The objective of this project is to construct a continuous prototype unit and to conduct a detailed experimental investigation of this new technology.

TABLE OF CONTENTS

INTRODUCTION

Background

Dewatering processes are used in coal preparation plants to remove excess surface moisture from the clean coal products. Coarser particles can be readily dewatered using simple screening systems, while finer particles require costly unit operations such as centrifuges and filters (Osborne, 1988). Moisture that is not removed by these processes reduces the heating value and increases the cost of transporting the clean coal. Excess moisture can also create unacceptable handling problems for both the coal producer and downstream consumers by plugging chutes, bins, and rail cars. In colder regions, coal handling problems can be particularly severe during winter months because of freezing.

The dewatering of fine coal (<0.15 mm) is particularly difficult due to the large surface area of fine particles (Leonard, 1991). At present, there are no mechanical dewatering processes that can inexpensively reduce the surface moisture of fine coal to a level that is acceptable for most industrial consumers. This shortcoming typically forces coal producers to discard the fine coal into refuse impoundments. Recent estimates for the U.S. coal industry suggest that approximately 2 billion tons of fine coal have already been discarded in abandoned ponds and 500-800 million tons are in active ponds. In addition, U.S. preparation plants discard 30-40 million tons of additional fresh fine coal to ponds each year. This activity represents a loss of valuable natural resources, loss of profit for coal producers, and the creation of a potential environmental hazard.

Hyperbaric Centrifugation

In light of difficulties associated with the removal of moisture from fine coal, researchers at the Center for Advanced Separation Technologies (CAST) have been developing a new suite of advanced technologies for fine coal dewatering. One of the most promising of these is a process known as hyperbaric centrifugation (Yoon and Asmatulu, 2002). A schematic of a prototype batch laboratory-scale hyperbaric centrifuge is provided in Figure 1. The test unit consists of a rotating filter drum that is perforated and lined with a suitable filter cloth (or mesh). Feed slurry placed within the drum forms a compact filter cake along the wall of the filter chamber by the centrifugal force. Compressed air is then injected into the rotating assembly further increasing the pressure drop across the filter cake. The combined action of the centrifugal forces and air pressure makes it possible to achieve higher filtration rates and lower equilibrium cake moistures than can be obtained using conventional centrifuge technologies or pressure filters.

In order to demonstrate the potential of hyperbaric centrifugation, Yoon and Asmatulu (2002) conducted several preliminary test runs with the batch laboratory-scale test unit. The tests were conducted using fine coal slurry samples that had been thickened to 60-70% solids via sedimentation and prefiltration. The variables examined in the course of this test work included drum rotation speed, air pressure, cake thickness, spin time, and the use/non-use of dewatering aids. The cake thickness, which varied in the 10-20 mm range, was measured after each test run.

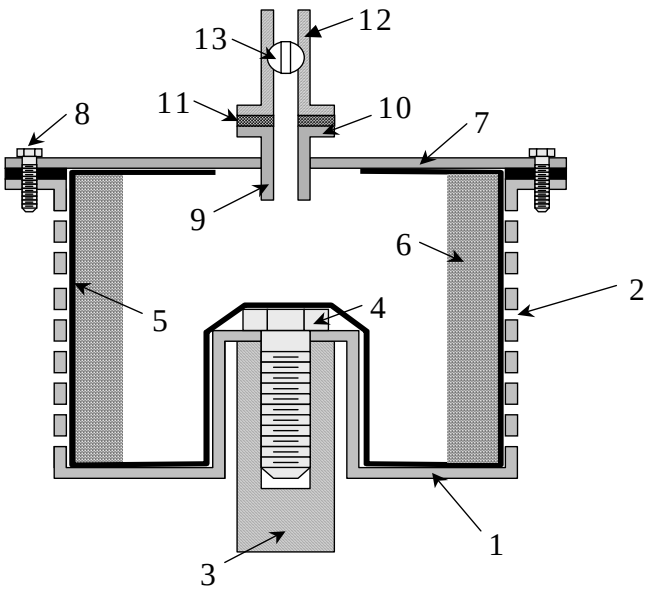

1 – rotating assembly
2 – perforated cylinder
3 – mounting shaft
4 – mounting bolt/nut
5 – filter cloth (or mesh)
6 - thickened slurry/cake
7 – pressure lid
8 – lid clamping bolts
9 – compressed air inlet
10 – rotating seal face
11 – rotating pressure seal
12 – stationary inlet
13 – air control valve

Fig. 1. Schematic of a batch hyperbaric centrifuge (Yoon and Asmatulu, 2002).

As shown in Table 1, the use of compressed air to create a pressure drop across filter cake made a substantial difference in the final cake moisture for the coal sample obtained from the Pittsburgh seam (0.6 mm x 0). The tests were conducted using air pressures of 50, 100 and 200 kPa and a centrifugal force of approximately 2,000 times that of gravity (G). The tests were also conducted with and without dewatering aid. In general, cake moisture decreased substantially from the baseline value of 36.5% with an increase in spin time and with a higher air pressure. At the shortest spin time of 30 sec, the moisture was decreased from 18.3% to 13.2% by increasing pressure from 50 to 200 kPa. At the longest spin time of 120 sec, the moisture was further reduced from 15.1% to just 9.1% by increasing the pressure from 50 to 200 kPa. While the product moistures were very low even without the dewatering aid (particularly at high air pressures), the use of dewatering air did provide an incremental reduction in all moisture values by about 3 percentage points.

Table 1. Results obtained on a Pittsburgh coal sample at different air pressures and spin times and with/without dewatering aid

Spin Time (seconds)	Cake Moisture (%wt)					
	50 kPa		100 kPa		200 kPa	
	No Reagent	Aid 2 lb/ton	No Reagent	Aid 2 lb/ton	No Reagent	Aid 2 lb/ton
0	36.5	36.5	36.5	36.5	36.5	36.5
30	18.3	14.9	14.2	11.1	13.2	10.1
60	16.3	13.6	12.9	10.5	10.6	8.2
120	15.1	12.8	10.6	8.6	9.1	7.3

Table 2. Results obtained on a deslimed Microcel™ flotation product at 2,500 G and varying air pressures

Spin Time (sec)	Cake Moisture (%wt)			
	Air Pressure (kPa)			
	None	50	150	250
0	41.1	41.1	41.1	41.1
30	27.5	12.2	10.0	9.1
60	26.2	10.9	8.0	7.1
90	25.9	8.9	7.1	6.1
120	25.4	8.0	6.3	4.6
150	25.0	7.6	6.0	3.9

Table 2 shows the results of another series of tests conducted using a sample of fine coal from the Middle Fork pond reclaim facility located near Carbo, Virginia. In this case, the sample was deslimed at 400 mesh before feeding to the laboratory hyperbaric centrifuge operated at a 2,500 G. As shown, single-digit moisture values could be obtained with this particular sample for several combinations of air pressure and spin time. At the highest gas pressure of 250 kPa, single-digit moisture values were obtained even at a relatively short spin time of just 30 sec. At lower gas pressures of 50 and 150 kPa, longer spin times of 90 and 60 sec, respectively, were required to obtain single-digit moisture values. These results are considered to be very impressive when compared to the relatively high baseline moisture value of 41.1%.

Project Objectives

The availability of a low-cost mechanical dewatering device that can efficiently remove moisture from fine coal will greatly benefit the U.S. coal industry. In light of this need, researchers at Virginia Tech have developed a novel filter centrifuge that can reduce the moisture contents of various fine coals to approximately 30-50% lower levels than can be achieved using the currently available dewatering methods. The new filter centrifuge is based on using a combination of gas (air) pressure and centrifugal force to increase the driving force for dewatering fine particles. This is important in removing water from the fine capillaries present in a cake, which is critical in reducing cake moistures. In light of this development, the specific objectives of this project were (i) to construct a small-scale continuous prototype unit for laboratory test purposes, (ii) to evaluate the effects of key operating and design variables, and (ii) to demonstrate the capabilities of the new process using fine coals from several different coal preparation plants.

EXPERIMENTAL

Task 1 – Equipment Design/Construction

Batch tests conducted to date indicate that increase in pressure drop by means of a compressed air can substantially improve the performance of a basket-type centrifugal filter. To further develop this concept, a continuous (or semi-continuous) centrifuge was designed and constructed as part of this project. Initially, the small-scale test unit was designed to operate at a target capacity of approximately 10 lb/hr. The unit was equipped with a variable speed drive so that the centrifugal force can be varied from 200 to 1000 G. The dewatering chamber was designed to operate at air pressures of up to 50 psig.

Task 2 – Equipment Testing

A variety of experimental test runs were conducted to evaluate the performance of the novel hyperbaric centrifuge. Important operating and design variables evaluated in this effort include feed rate, gas pressure, rotation speed, coal type, and feed particle size distribution. A simple parametric study was used to evaluate the effects of the important operating variables. These include feed solids rate (0-10 lb/hr), feed solids content (10-40%), rotation speed (100-500 rpm), and gas pressure/flow (0-60 psig). The effects of coal type, quality and size distribution were also be examined by conducting tests with coal samples collected from several different processing plants. In each series of experiments, tests were performed with and without compressed air, so that the improvement created by increased pressure drop can be quantified.

Task 3 – Engineering Design

After completing the tests with the continuous pressurized centrifugal filter, a prototype full-scale unit will be designed. This task will be carried out in cooperation with a team of engineers from Decanter Machine Company, who is the major supplier of screen bowl centrifuges. Once an acceptable unit has been designed, a preliminary cost-benefit analysis will be conducted to determine whether the prototype unit should be constructed as a follow-up to this project. Decanter will provide the necessary funds for the design and construction of the full-scale prototype unit that can be tested at several different industrial sites. Because of the funding cycle imposed by the CAST initiative, this particular task will be largely completed and reported at a later date using second-year funding.

RESULTS AND DISCUSSION

Task 1 – Equipment Design/Construction

The objective of this task was to design and construct a prototype of the hyperbaric filter centrifuge. The most difficult part of this task was to design a system that could accept dilute coal slurry and introduce compressed gas without disturbing the structure of the filter cake. Preliminary experiments showed that the filter cake cannot be disturbed while being dewatered without losing air pressure. In addition, the filter cloth used in the batch unit could not be used in a continuous unit because of blinding and excessive wear that would occur during cake removal. To overcome this problem, a two-stage process was designed. The first stage uses a thickening unit (i.e., paste thickener) to efficiently separate the water from feed solids (Figure 2). This system ensures that a high coal recovery is maintained. The thickened underflow is then pumped into a rotating centrifuge unit (Figure 3). The rotating section consists of a pressure chamber lined with a fine (0.1 mm) wedge-bar screen panel. For wear resistance, the panel was designed using trapezoidal tungsten carbide bars placed in parallel along the inside of the pressure chamber (Figure 4). The bar spacing (0.1 mm) is small enough to retain thickened coal slurry, but large enough to allow water to pass without blinding. This design makes it possible to introduce feed directly into the pressure chamber without the need to use a filter cloth or other fragile filter medium. The screen panel and cake scraper must be fabricated at near zero tolerance to ensure a tight seal is formed during pressurization.

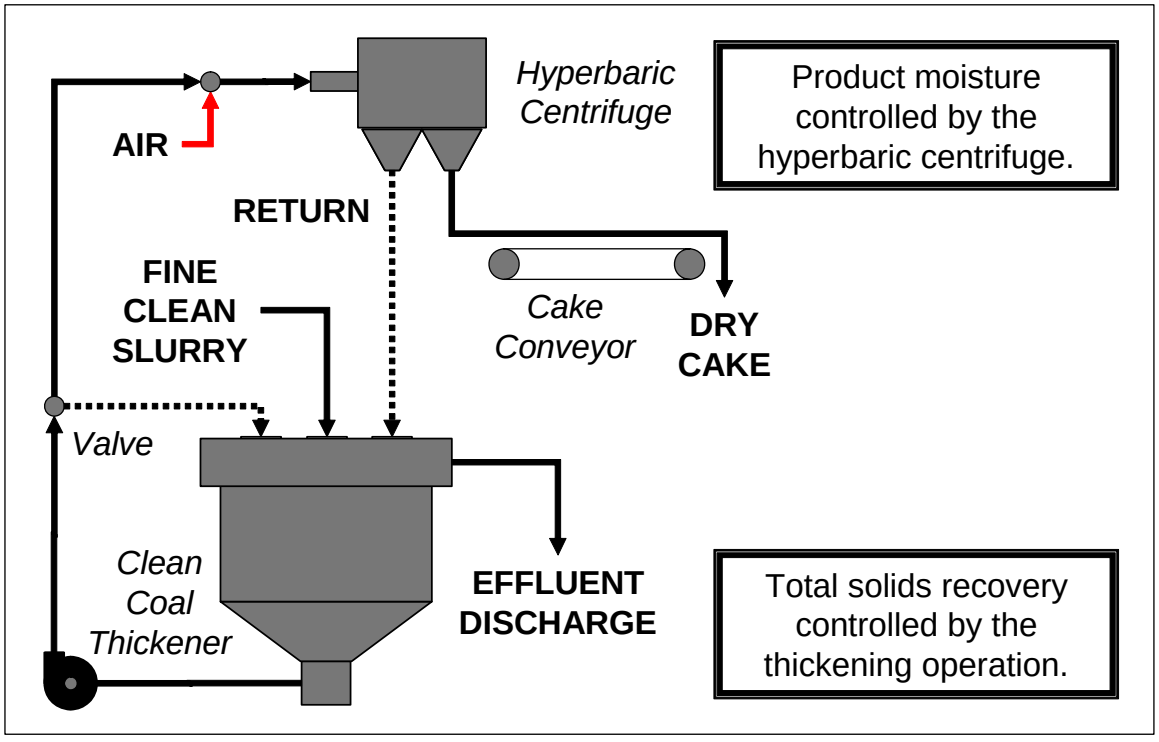

Figure 2. Hyperbaric filter centrifuge processing circuit.

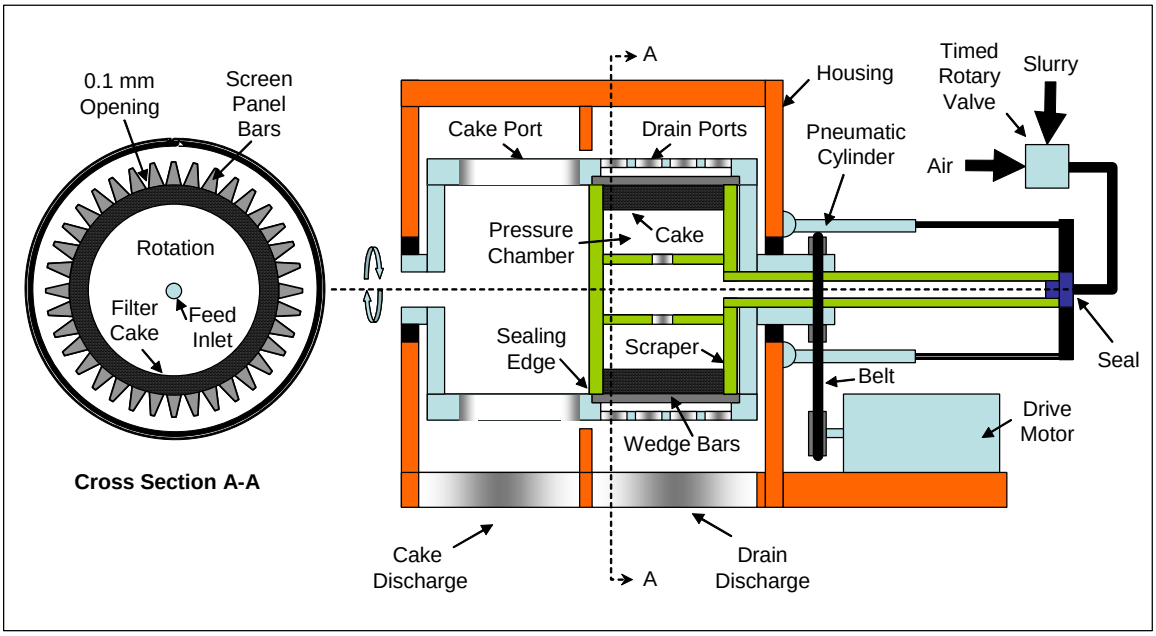

Figure 3. Simplified schematic of the prototype hyperbaric filter centrifuge.

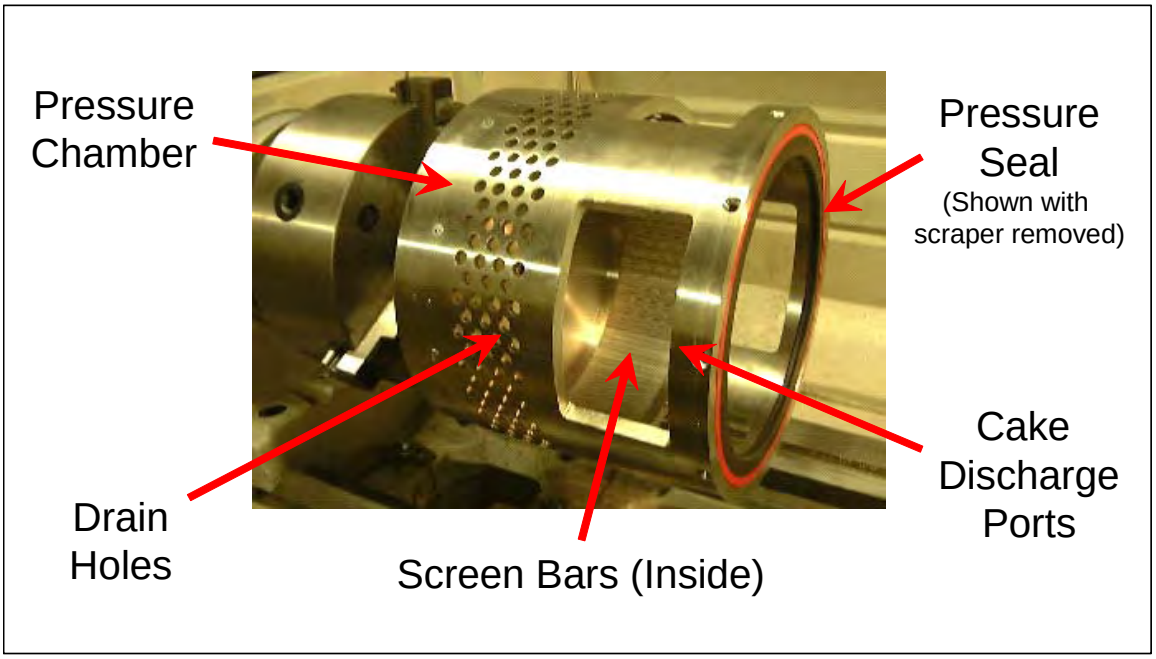

Figure 4. Key components of the rotating centrifuge pressure chamber.

Figure 5 shows the sequence of processing steps employed by the hyperbaric centrifugal filter. In this design, the rotating pressure chamber is mounted along the central axis of a hollow shaft. This shaft is driven by a variable speed motor. A second hollow shaft is located within the drive shaft to allow feed and air to enter the pressure chamber. The second shaft is also connected to two sets of end plates that serve to seal the pressure

chamber on one end and to discharge the cake on the other. During operation, thickened feed solids are pumped into the pressure chamber until the unit is filled (Figure 5a). Feed to the unit is then stopped and air is introduced until the desired pressure is achieved (Figure 5b). The chamber is held under pressure for a period of time sufficient to complete the drying cycle and obtain the target moisture content. As shown in Figure 2, the small amount of solids and water that pass through the 0.1 mm openings during feeding and dewatering is recycled back to the thickener to ensure that no coal is lost. After releasing the air pressure, a pneumatic ram is used to activate the scraper that pushes the dewatered cake off the screen and through discharge ports cut into the side walls of the pressure chamber (Figure 5c). The edges of the scraper are fabricated from nickel Teflon to provide an excellent seal and to serve as a replaceable wear element. After discharge is competed, the scraper returns to its original position and the entire cycle of dewatering is repeated.

The cake discharge system was considered to be the most critical element in the design. The cake is discharged using a pusher/scraper equipped with a Teflon pressure seal to minimize leakage (see Figure 6). The seal is designed as a wear component that can be easily accessed and replaced. In addition, the spacing bars had to be fabricated with a very tight tolerance (i) to prevent the excessive loss of solids though the screen and (ii) to provide a good seal against the wall of the pressure chamber. The bars used to construct the unit were obtained from a centrifuge manufacturer who

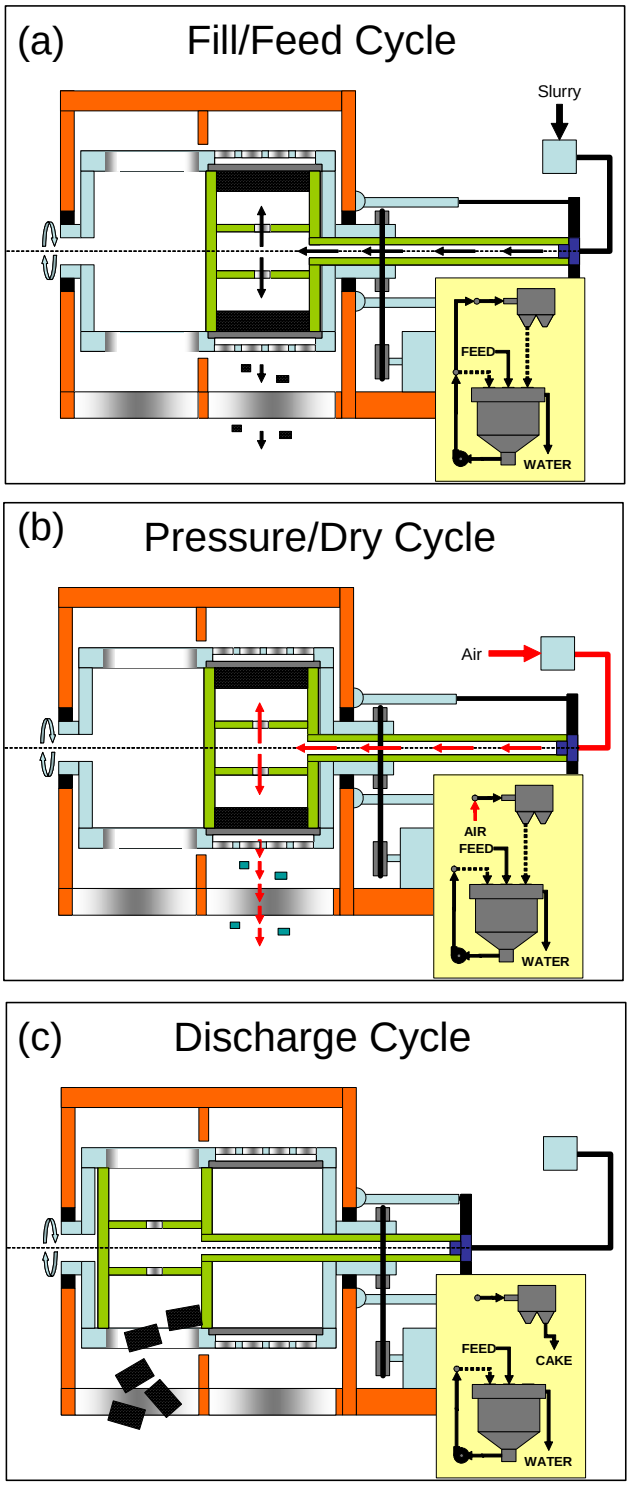

Figure 5. Process steps utilized by the hyperbaric filter centrifuge.

obtains prefabricated parts pressed from tungsten carbide (Figure 7). This makes the bars highly wear resistant and ensures that the same screen opening is maintained. A photograph of the assembled prototype hyperbaric centrifuge is provided in Figure 8.

Figure 6. Photo of Teflon pressure seal (red) and tungsten carbide spacer bars (back). (Shown with scraper removed.)

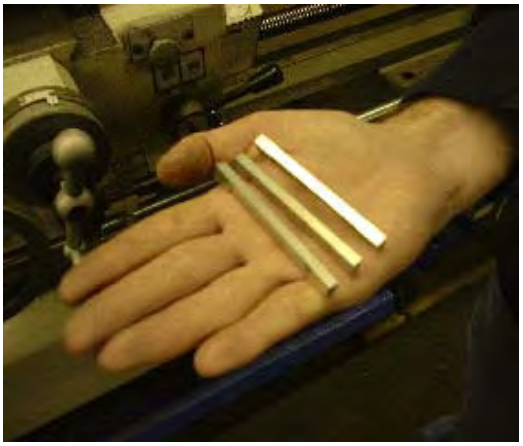

Figure 7. Photo showing the tungsten carbide spacer bars prior to installation inside the rotating pressure chamber.

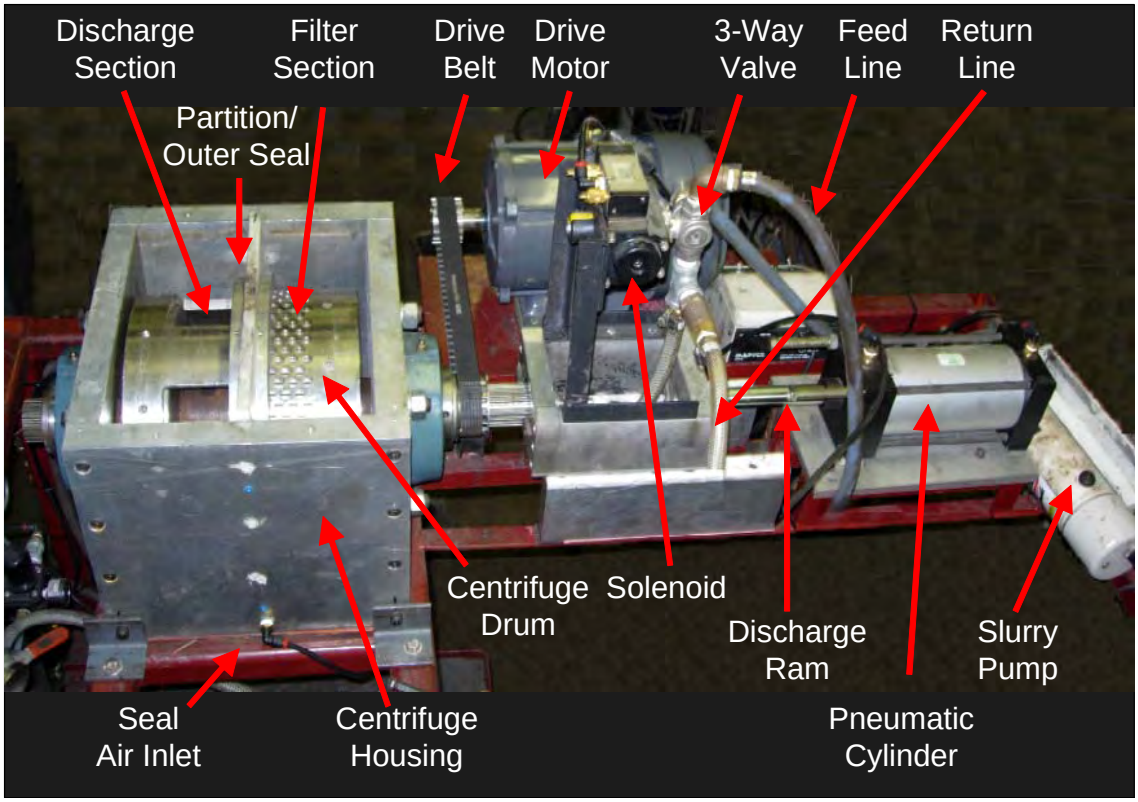

Figure 8. Photograph of the HFC with identification labels for key components.

Task 2 – Equipment Testing

Laboratory Batch Tests

Several tests were performed using a batch version of the hyperbaric filter centrifuge to verify the findings obtained in earlier studies carried out by Yoon and Asmatulu (2000). Table 3 provides a summary of the test results obtained using the batch unit as a function of drying time. The tests were conducted with and without air pressure (0 and 20 psig) and with and without rotation (0 and 346 Gs). In addition, the tests were performed using two types of filter medium (i.e., a tightly woven filter cloth and a thin synthetic filter mesh). As shown, the moisture dropped by several percentage points as the drying time increased from 30 to 120 sec for both the filter cloth and filter mesh tests. However, the moistures obtained using the filter cloth were generally lower than those obtained using the filter mesh by up to 1 percentage point. The lower moisture was believed to be due to higher losses of ultrafine coal that passed more readily through the larger openings in the filter mesh. On the other hand, an increase in air pressure from ambient conditions (0 psig) to 20 psig substantially lowered the moisture contents of the filter cakes. For the filter cloth, the moisture was reduced from 17.9% to 12.4% after the addition of air pressure for the longest cycle time of 120 sec. For the filter mesh, the moisture content dropped from 18.4% to 14.8% under the same test conditions. Due to motor restrictions, the rotational speeds used in this program were not sufficient to produce the higher gravitation forces (e.g., 500 Gs). Therefore, the moisture reductions obtained in this test program were not as great as those shown in previous research.

Table 3. Comparison of batch data obtained using filter cloth and filter mesh medium.

Cycle Time (sec)	Centrifugal Force (Gs)	Filter Cloth Moisture Content (%)		Filter Mesh Moisture Content (%)	
		0 psig	20 psig	0 psig	20 psig
30	346	19.8	15.2	20.1	16.3
60	346	18.7	13.8	19.7	15.7
90	346	18.3	13.0	19.1	15.4
120	346	17.9	12.4	18.4	14.8

Prototype Batch Tests

An initial series of shakedown tests were conducted to assess the mechanical functionality of the prototype test unit. During a typical production cycle, the basket (see Figure 9) is rotated at speeds up to 1000 RPM using a variable speed motor and drive belt (see Figure 10). Slurry from the feed tank is pumped into a distributor pipe located within the center of the shaft of the rotating basket. The basket is constructed using wedge-shaped tungsten carbide bars spaced at 0.1 mm intervals. All particles larger than the bar spacing are

Figure 9. Rotating drum assembly for the hyperbaric centrifuge.

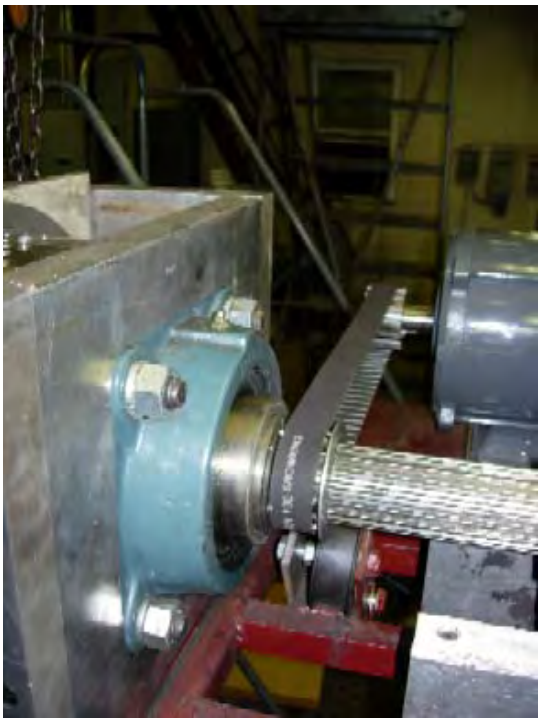

Figure 10. Motor, drive belt and shaft assembly for the hyperbaric centrifuge.

retained along with most of the fines (via entrapment in the cake). The feeding cycle is continued until a desired cake thickness is achieved. The feed flow is then diverted back to the feed tank via an automated three-way valve (see Figure 11). Compressed air is then introduced into the filter chamber to create a differential pressure across the cake. The combined force of the centrifugal field and air pressure drives out nearly all of the surface moisture and some ultrafine solids through the spacing between the basket bars. This effluent stream is passed back to the feed tank where the solids are concentrated by flocculation and recycled back to centrifuge to maintain a high recovery of solids. After this pressure drying cycle, the air pressure is released and the cake is discharged by a pneumatically driven scraper. The entire operation requires 30-120 seconds, depending on the range of operating conditions selected, feed particle size distribution, and target moisture level. The entire sequencing of the feeding, drying and discharge cycles is fully automated and controlled using a programmable logic controller (see Figure 12).

Unfortunately, the first test run showed that the design of the outside seal in the partition separating the effluent collection section from the dewatered cake section was inadequate. The problem allowed water to drip inadvertently into the cake collection chute, thereby artificially increasing the moisture content of the final product. A new seal design is currently being constructed as a means of eliminating this technical problem. In the interim, a limited number of preliminary tests were performed by operating the test unit in batch mode. In this mode, contamination of the dewatered product by water leaking around the seal was prevented by manually collecting the dewatered cake by hand.

Figure 11. Valve system for the introduction of feed slurry and air.

Figure 12. Electronic control panel for the new hyperbaric centrifuge.

The first batch test was performed using a very fine coal sample from a flotation circuit installed at a pond reclaim site. The baseline test, which was conducted using only the centrifugal field and no air pressure, provided a dewatered product with a moisture content of 16.9% by weight. The same test run using both the centrifugal field and air pressure to maximize moisture removal further reduced the moisture content to 9.1%.

Another series of shakedown tests conducted with a significantly coarser coal obtained from a plant flotation circuit gave a baseline moisture content of 11.0% when no air was added. The addition of air substantially reduced the moisture content of the cake down to a very low value of 1.9%. This exceptionally low moisture is believed to be due to the simultaneous removal of both moisture and ultrafine solids from the cake after the addition of air. Therefore, the moisture rejection obtained in “batch” mode would probably not be achieved in practice due to the recycling of fines that occurs when the unit is operated in “continuous” mode. Therefore, additional test work is necessary to fully assess the technical capabilities of the prototype unit.

Prototype Continuous Tests

After successfully completing the batch prototype tests, a new drum seal was constructed and the parts needed to run the unit in continuous mode were fabricated and installed. The problem which allowed water to drip inadvertently into the cake collection

chute was eliminated by the new seal design. The design of the feeding mechanism was also upgraded to allow the unit to run as a continuous unit. The batch unit mainly consisted of a pressurized rotating filter basket and a feed tank which is kept mixed all the time. The loss of ultrafine coal particles through the screen section of the rotating drum was the biggest issue with the batch unit. Preliminary tests indicated that up to 50% of the solids were reporting to the effluent for some fine feed coal samples.

Several series of shakedown tests were conducted in batch mode with the newly fabricated drum seal. The coal samples used in these tests were obtained from screen-bowl centrifuge feeds at existing coal preparation plants. The first set of tests were conducted at a constant fill time of 15 sec and air injection times of 0 (no air), 15 and 120 sec. The rotation speed was held constant at 1,100 rpm. A baseline moisture content of 15.6% was obtained when no air was injected. This value was reduced to 10.3% by injecting air for 15 sec and further reduced to 6.7% after 120 sec of pressurized air injection. Based on these promising results, a second set of test runs were conducted using a fresh coal sample from the same industrial plant site. The tests were conducted using a 15 sec fill time and air injection times of 5, 10, 30, 60 and 120 sec. Three sets of tests were performed at rotation speeds of 1000, 1250 and 1500 rpm. The test results, which are summarized in Table 4, show that the moisture dropped from just over 20% at the lowest air injection time and rotation speed to below 11% at the largest air injection time and rotation speed. The data are plotted in Figure 13 for comparison. This plot shows that an increase in air injection time from 5 to 120 sec incrementally improved the moisture removal by about 5 percentage points for the lowest rotation speed of 1000 rpm. The incremental improvement was somewhat (i.e., about 3 percentage points) for the higher rotation speeds of 1250 and 1500 rpm. Unfortunately, a

Table 4. Batch test results obtained using the hyperbaric centrifuge (15 sec fill time).

Air Time (sec)	Rotation Speed (rpm)	Rotation Force (g's)	Moisture Content (%)	Cake Weight (gms)
5	1000	142	20.1	16.5
10	1000	142	20.2	18.51
30	1000	142	14.7	22.79
60	1000	142	18.3	31.5
120	1000	142	15.0	33.95
5	1250	222	13.3	7.18
10	1250	222	14.5	14.43
30	1250	222	14.2	18.31
60	1250	222	13.9	20.71
120	1250	222	13.9	25.62
5	1500	319	13.3	14.89
10	1500	319	13.9	12.66
30	1500	319	13.3	15.09
60	1500	319	13.2	14.69
120	1500	319	10.9	17.87

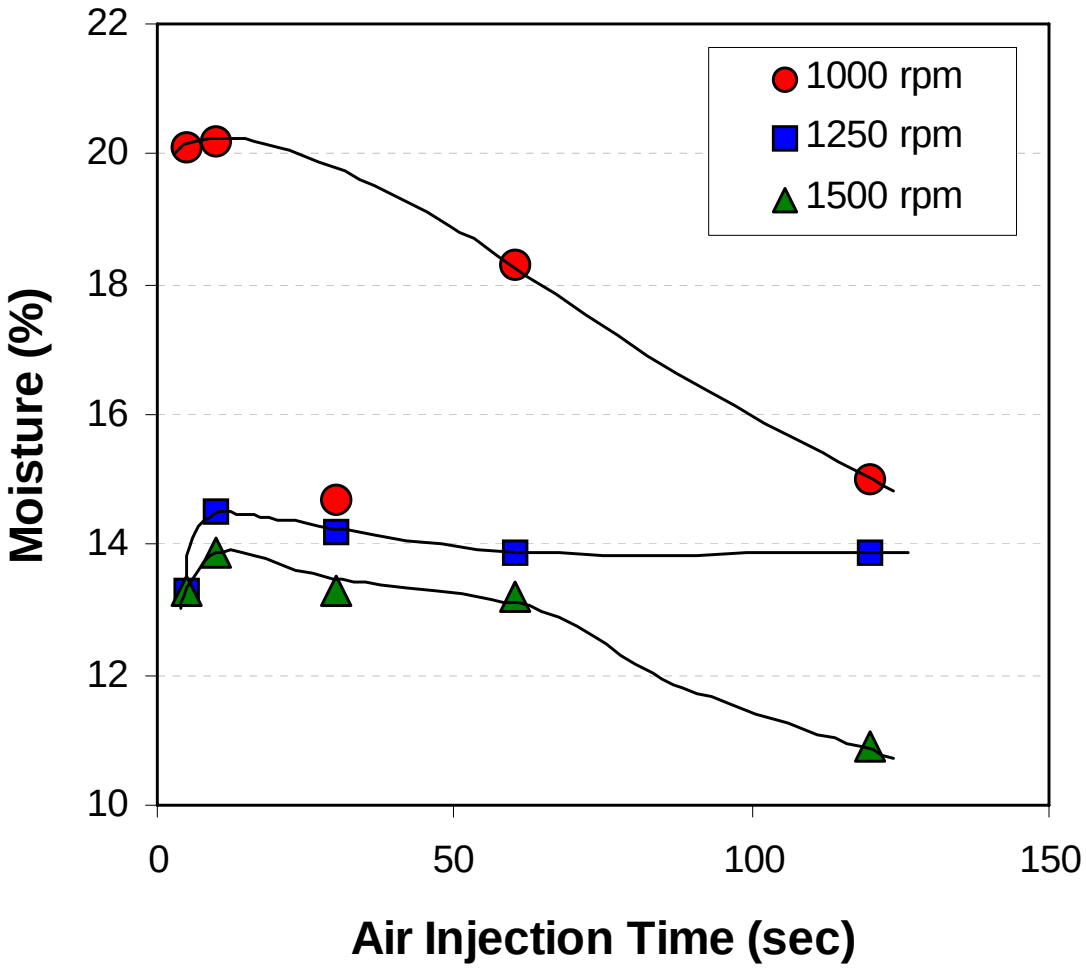

Figure 13. Batch test results obtained using the hyperbaric centrifuge (15 sec fill time).

baseline test (with no air injection) was not run due to plugging of the feed line that occurred when no air was introduced.

One problem with the previous set of tests is that the total time of centrifugation increased as the air injection time increased. Therefore, it was not possible to distinguish whether the reduction in moisture observed in Figure 13 was due to a longer period or air injection or a longer period of centrifugation. To overcome this problem, a third set of shakedown tests was conducted in which the machine was rotated for the same total duration with and without the addition of air. A freshly acquired coal sample from the same preparation plant site was again used in these experiments. The test runs were conducted at the highest rotation speed (1500 rpm – 390 g's) centrifugation times of 5, 10, 30, 60 and 120 sec. The tests were repeated with and without injecting air for each of centrifugation time. In addition, the feed time was increased from 15 to 30 sec in this particular series of tests to increase the amount of solids retained within the unit. The results of these tests are summarized in Table 5. A comparison of the data is also provided in Figure 14.

Table 5. Batch test results obtained using the hyperbaric filter centrifuge (30 sec fill time, 1500 rpm rotation speed – 390 g's).

Air Injection Used?	Rotation Time (sec)	Moisture Content (%)	Cake Weight (gms)
No	5	12.6	77.15
No	10	11.2	94.37
No	30	10.8	95.73
No	60	10.2	104.6
No	120	9.6	96.89
Yes	5	10.6	116.62
Yes	10	10.3	86.91
Yes	30	9.6	130.96
Yes	60	8.3	72.4
Yes	120	9.7	109.83

The test data indicate that the injection of air provided an incremental reduction in moisture removal of only about 1 percentage point. However, all of the moisture values obtained in this series of tests is already very low (around 12% total moisture or less). In fact, the values obtained with air injection at centrifugation drying times of 30 sec or greater are all single-digit values. These results suggest that either (i) the coal sample used in these tests contains very little fines or (ii) a large amount of the fines were lost through the screen section in the batch tests. Previous laboratory tests indicate that the differences in moisture obtained with and without air injection are much greater for cakes containing larger amounts of fine particles. Therefore, a much larger difference in moisture is expected once the continuous circuitry (i.e., integrated thickener) is operating and a proper circulating load of fines is maintained within the prototype. Continuous mode tests will be performed using the prototype during the next reporting period in order to verify this hypothesis.

Task 3 – Engineering Design

As indicated previously, the objective of this task is to complete the design for a production-scale proof-of-concept pressurized centrifugal filter. Most of the required work has not yet been completed since the second year funding for this portion of the project was provided under a separate CAST initiative and is still underway. However, to assist in the engineering design activities, a theoretical model has been developed under this task to develop a better understanding of the underlying mechanisms of dewatering by hyperbaric centrifugation. To simplify this analysis, the model system has been assumed to consist on a bed of settled particles initially submerged in water (Figure 15). This system can be readily described by the radii between the rotational axis of the centrifuge and the water level (r_w), cake surface (r_s), and bowl wall (r_b). The bed of particles is assumed to be comprised of a series of straight capillaries that radiate outward through the filter cake, an assumption that is

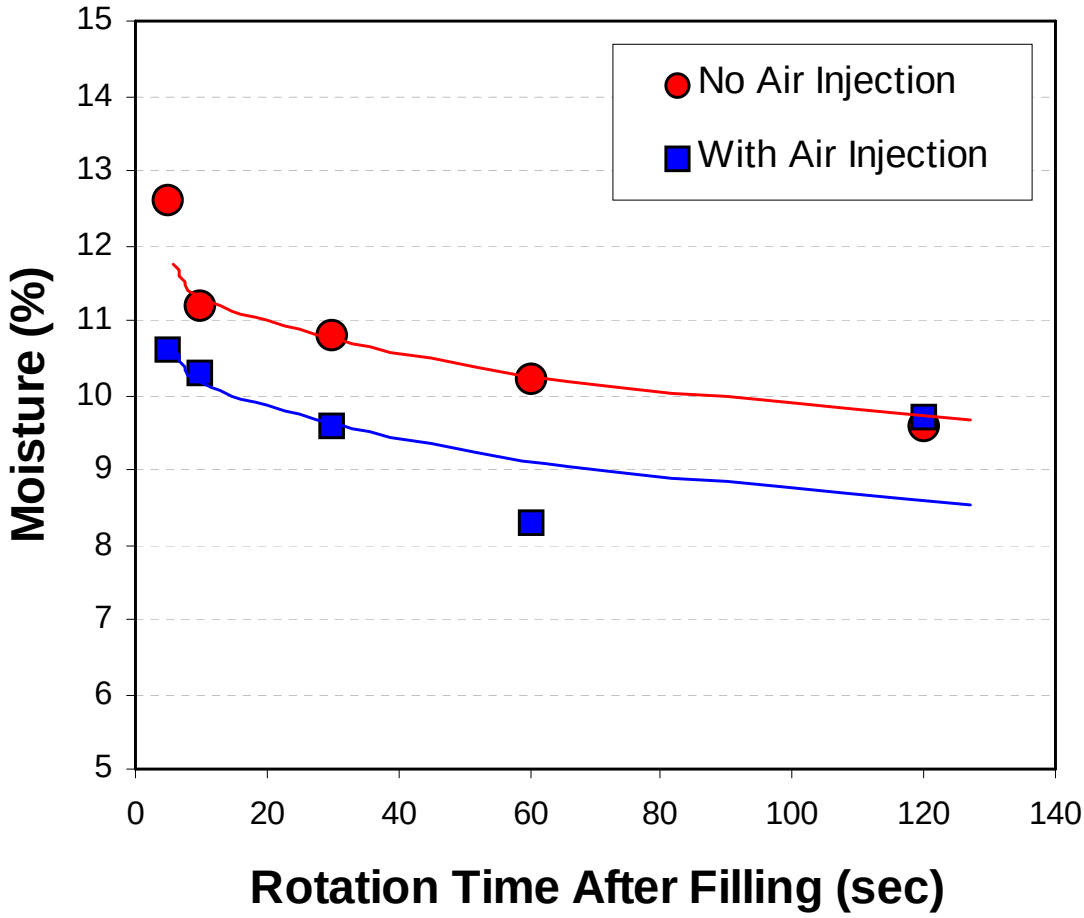

Figure 14. Batch test results obtained using the hyperbaric filter centrifuge (30 sec fill time, 1500 rpm rotation speed – 390 G's).

commonly used in elementary studies of filtration phenomenon. The analysis also assumes that the resisting and driving forces that control the dewatering must be equal at the equilibrium moisture content. This assumption makes it possible to neglect hydrodynamic flow resistance since no flow occurs under equilibrium conditions. The influence of the filter medium on dewatering is also not considered in this elementary analysis.

In light of the stated assumptions, the primary force resisting the dewatering of the cake is the capillary pressure. In the case where $r_w<r_s$, the liquid level is above the cake surface and the capillary pressure (P_{cap}) is given by the well-known equation:

$$P_{cap} = \frac{2\gamma \cos\theta}{r_c} \qquad [1]$$

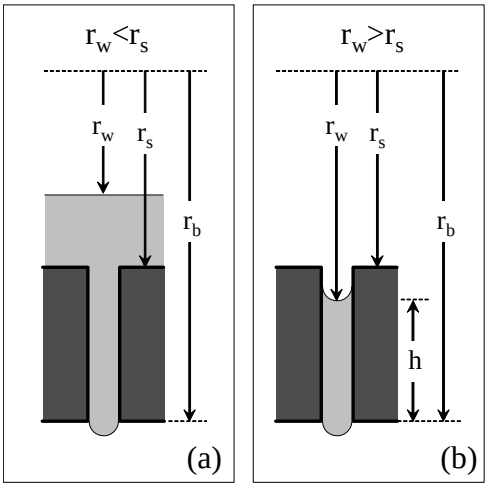

Figure 15. Geometry for capillary pressure when (a) $r_w<r_s$ and (b) $r_w>r_s$.

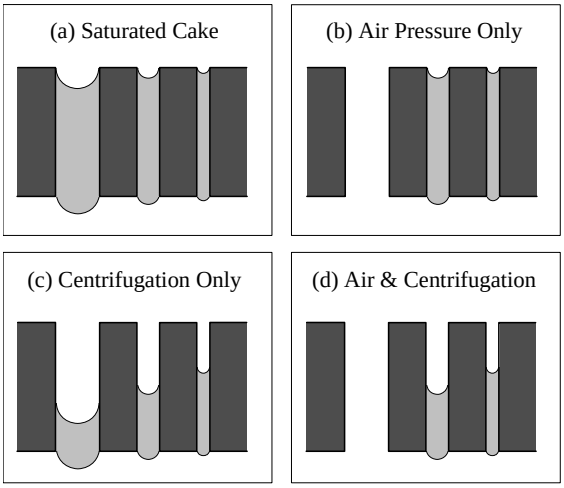

Figure 16. Response of various sizes of capillaries to different driving forces.

where γ is the interfacial surface tension, θ is the contact angle, and r_c is the capillary radius. For $r_w>r_s$, the cake is not fully saturated. This geometry introduces a second three phase contact that increases the resisting capillary pressure to a value given by:

$$P_{cap} = \frac{4\gamma \cos\theta}{r_c} \qquad [2]$$

The equilibrium moisture can now be calculated when compressed gas is the only driving pressure. In this case, equilibrium requires that $P_{gas} = P_{cap}$, i.e.:

$$P_{gas} = \frac{4\gamma \cos\theta}{r_c} \qquad [3]$$

After starting with a saturated cake (Figure 16a), this expression indicates that all water is forced from capillaries for which $P_{gas}>P_{cap}$. Water is removed entirely from all of the larger capillaries until gas breakthrough occurs and gas pressure is lost. Unfortunately, water remains in the smaller capillaries for which $P_{gas}<P_{cap}$ (Figure 16b). For a specified gas pressure, there is no reduction in the height of liquid (h) in capillaries smaller than the critical capillary radius defined by Eq. [3]. As a result, not all of the water can be removed from the cake capillaries using gas pressure as the only driving force.

When the centrifugal field is the only driving force, then the equilibrium requires that $P_{hyd} = P_{cap}$. For any distance r from the rotational axis, the hydrostatic pressure differential (P_{hyd}) created by the centrifugal field can be calculated by integration of:

$$P_{hyd} = \rho \int_{r_w}^{r_b} r\omega^2 dr = \frac{\rho\omega^2 r_b^2}{2}\left[1 - \left(\frac{r_w}{r_b}\right)^2\right] \quad [4]$$

where ρ is the fluid density and ω is the angular velocity, Since the height of water in the capillary (h) is equal to r_b-r_w and $h/r_b << 1$, Eq. [4] can be simplified to:

$$P_{hyd} = \frac{\rho\omega^2 r_b^2}{2}\left[1 - \left(1 - 2\frac{r_w}{r_b}\right)\right] = \rho\omega^2 r_b h \quad [5]$$

By combining Eqs. [2] and [5], we obtain:

$$h = \frac{4\gamma\cos\theta}{\rho\omega^2 r_b r_c} \quad [6]$$

This expression shows that the height of water in capillaries of all different sizes is reduced proportionally in accordance with capillary radius (Figure 16c). This response is in sharp contrast to the case in which only gas pressure is used and water is removed only from capillaries for which $P_{gas}>P_{cap}$. On the other hand, the driving force for additional water removal by centrifugation disappears for all capillaries when the water height (h) reaches the value dictated by Eq. [6]. As a result, not all of the water can be removed from the capillaries using centrifugation as the only driving force.

Now consider the case in which both gas pressure and centrifugation are combined for improved dewatering. Equilibrium for this case requires that $P_{hyd} + P_{gas} = P_{cap}$, which dictates that:

$$h = \frac{1}{\rho\omega^2 r_b}\left[\frac{4\gamma\cos\theta}{r_c} - P_{gas}\right] \quad [7]$$

In this case, the height of water in all of the capillaries predicted by Eq. [6] is further reduced by the gas pressure (P_{gas}). More importantly, the gas pressure removes water completely from capillaries for which $P_{gas}>P_{cap}$ (Figure 16d). As stated previously, this is not possible using centrifugation alone once the volume of water in the capillary is so small that $P_{hyd} < P_{cap}$. Likewise, the centrifugal force removes water from smaller capillaries that cannot be removed by gas pressure alone. Therefore, the combined influence of gas pressure and centrifugal force provide a synergistic effect for cake dewatering.

SUMMARY AND CONCLUSIONS

In order to improve the removal of moisture from fine coal streams, a project was initiated to construct and test a new dewatering technology known as a hyperbaric centrifuge. Previous tests conducted with a batch laboratory unit suggest that this new technology can reduce the moisture content of fine coal products by up to 50% compared to existing mechanical systems. In this project, work focused on the design of a pilot-scale continuous prototype of this technology. The selected design consisted of a two-stage process capable of achieving low product moistures while maintaining nearly complete recoveries of fine coal. To date, several laboratory tests were conducted using a batch fed unit to verify the extent of moisture removal that can be achieved using this approach. However, initial tests showed that several improvements in the design were needed to correct problems with the mechanical seal that allowed water to contaminate the dewatered cake. After correcting this and several other minor mechanical problems, several additional shakedown tests were carried out while operating the prototype unit in continuous mode. This mode of operation required the integration of a thickening unit into the test circuitry. This modification made it possible to improve fines recovery by circulating fines previously lost through the screen back to the circuit feed. Data obtained from these tests indicated that the new technology can indeed achieve extremely good removals of moisture from fine coal. The data also indicate that the moisture reduction was significantly better at higher rotation speeds and with higher gas injection pressures. Future work conducted during the next phase of this project will be performed (i) to demonstrate the capabilities of this new technology at a larger scale and (ii) to obtain scale-up data for the engineering design of a production scale unit.

REFERENCES

1. Leonard, III, J.W., 1991. Coal Preparation, Fifth Edition, Society for Mining, Metallurgy, and Exploration, Inc., Littleton, Colorado, 1991.

2. Osborne, D.G., 1988. Coal Preparation Technology, London: Graham & Trotman, 600 pp.

3. Yoon, R.-H. and R. Asmatulu, 2002. Methods of Improving Centrifugal Filtration, U.S. Patent Application Serial No. 09/531,373, filed March 21, 2000; U.S. Patent No. 6,440,316, Acc. 27 August 2002.

4. Yoon R.-H. and R. Asmatulu, MCT Patent Application Serial No. PCT/US02/11318, filed April 12, 2002.

Appendix 9: New Strategies for Dewatering of Coals

TECHNICAL PROGRESS REPORT

Contract Title and Number:	Period of Performance:
Establishment of the Center for Advanced Separation Technologies (DE-FC26-01NT41091)	Starting Date: 9/17/01 Ending Date: 5/31/05

Sub-Recipient Project Title:

New Strategies for dewatering of coals

Principal Investigator: M. S. Seehra
Co-investigators: A. Manivannan
M. Bachlechner

Contact Address:
Physics Department
West Virginia University
Morgantown, WV 26506-6315

Subcontractor Address:

No subcontracts issued.

Report Information:
Type: Final
Number: 04
Period: 3/03 to 08/05
Date: 08/23/05
Code: WV00 4-Final

Contact Information:
Phone: 304-293-3422 x1473
Fax: 304-293-5732
E-Mail: mseehra@wvu.edu

Subcontractor Information:
Phone:
Fax:
E-Mail:

DISCLAIMER

ABSTRACT

In this work, use of conventional microwaves at 2.45 GHz to dewater fine coal slurries was investigated. Initially, using milligram quantities of coal slurries, thermogravimetric analysis (TGA) was employed to determine the process of dewatering by thermal heating. Secondly, using gram quantities of fine coal slurries, a conventional microwave oven was used to determine the efficiency of dewatering by selective microwave heating. X-ray diffraction of the 'before' and 'after' microwave treated coal slurry showed that the coal carbon and ash is not affected by microwave treatment. Finally, a conventional microwave oven was modified to feed coal on a conveyor-belt to simulate a potential commercial unit. Appropriate microwave shielding and remote control operation of the unit was also done. Experiments with the conveyor-belt system using kg quantities of samples showed about 83% efficiency (relative to the theoretical limit) to dewater fine coal slurries by microwave heating without significantly heating coal carbon or ash. Computational studies were performed to better understand the intricate coal-water interactions .

TABLE OF CONTENTS

LIST OF FIGURES

EXECUTIVE SUMMARY

The objective of this project was to investigate alternative methods to dewater coal, particularly fine coal slurries, which are difficult to dewater by conventional methods (filtration, centrifugation, thermal drying). Thermal drying of coals is not an efficient process since hot air heats both coal and water. Consequently, dewatering using selective heating by conventional microwaves at 2.45 GHz was undertaken as the primary focus of this project. The basis for this choice is the fact that water absorbs 120 times more microwaves than coal [1,2]. Some initial computational studies to understand the intricate coal-water interactions were carried out by Dr. M. Bachlechner.

Using different coal slurries, experiments were first performed on gram quantities of samples with TGA (Thermogravimetric analysis), DSC (Differential Scanning Calorimetry) and XRD (X-ray diffraction) to understand the effect of microwave heating on water, coal carbon and ash in coal slurries. The microwave source for all our work was a conventional, store-bought microwave oven (800 Watts). These experiments showed that dewatering by microwave heating is indeed an efficient process approaching near 80% of the maximum theoretical efficiency. Therefore, a laboratory scale microwave dewatering unit with a conveyor-belt feed system was designed to simulate a potential commercial unit, with appropriate microwave shielding and remote control operation. In this unit, 83% efficiency (relative to the maximum theoretical limit) for dewatering of fine coal slurry was obtained. Our cost estimate to remove 10% moisture from coal slurry at 0.04$/kWh using microwave heating is about $3/ton of the slurry. This research is the basis of the M.S. Thesis of Mr. Aashish Kalra who carried out the experiments, with assistance from Dr. A. Manivannan, and under the guidance of Professor M.S. Seehra.

EXPERIMENTAL

To make this project industrially relevant, we acquired four samples of coal in kg quantities from a preparation plant owned/operated by Consol Inc. These samples were sent to Galbraith Laboratories (Knoxville, TN) for proximate and ultimate analysis, which are given in Appendix I. The most relevant sample for dewatering studies is coal #1which is the sample sent to settling ponds (referred as 'Ponds coal' in the report), and it contains 52.5% moisture, 26.6% carbon and 15.2% ash. Most of the experiments described below were carried out on this sample since the 'coal before processing' and 'coal sent to power plants' contain only minute amounts of moisture.

During the initial task of the experiments, we measured the moisture loss due to thermal heating using thermogravimetric analysis (TGA) on the sample ponds coal and also measured heat capacity of the sample using DSC (Differential Scanning Calorimetry). For the investigation of selective heating using microwave radiation, we did experiments of gram quantities of coal. These experiments were carried out with a conventional microwave oven (GE Model JES838SH001) with maximum power of 800 Watts. To measure the power used in the experiments, a power meter was inserted in the circuit between the power outlet and the microwave oven. In the first set of experiments, the sample was heated for 10-seconds intervals followed by measuring the weight of the

samples and recording the power used. In the other experiments, the interval was changed to 30-seconds.

In the second stage of experimentation, we designed a laboratory-scale microwave dewatering unit with a conveyor-belt feed system to simulate a potential commercial unit. Pictures of this laboratory dewatering unit are shown in Fig. 1 and schematic diagram of this unit is shown in Fig. 2.

Figure 1. Pictures of the Laboratory scale microwave dewatering unit are shown. (A) the complete unit covered with the microwave shielding is shown. (B) close up of the unit without the shield showing the microwave and the feeding belt.

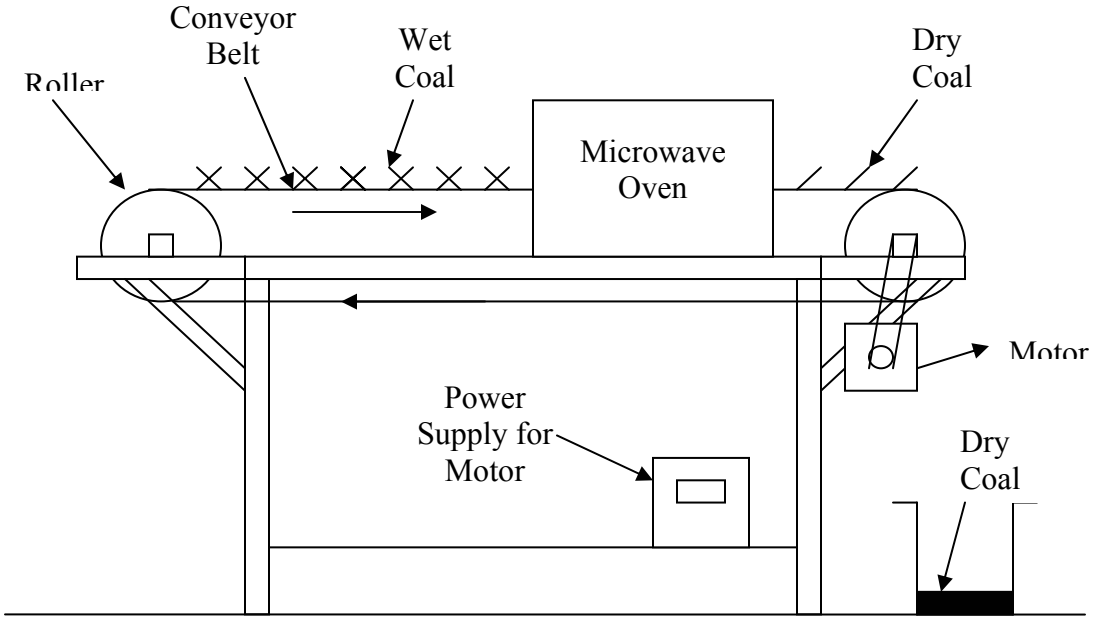

Figure 2. The schematic view of the laboratory scale microwave dewatering unit

The microwave-dewatering unit consists of a store-bought 800 watt microwave oven whose two opposite sides were opened up for feeding a conveyor-belt. The conveyor-belt is fed by two motor driven rollers mounted at the end of the table. The feed-speed is controlled by the rotation speed of the rollers. Due to the potential radiation hazard from an open microwave oven, we have used a commercial shield for safeguarding the system as well as allow a visual view of the system during operation. A portable microwave detector was used to check for any leaks of the microwaves outside the apparatus. Since the operator of the system must be protected from any microwaves, an electrical circuit was designed to control the operation of the system from a distance. A basic design of this electrical system for the microwave unit is shown in Fig. 3 and for the control system in Fig. 4. The main consideration in this design is that with the remote control switch, power to the microwave oven and the conveyor-belt motor can be controlled.

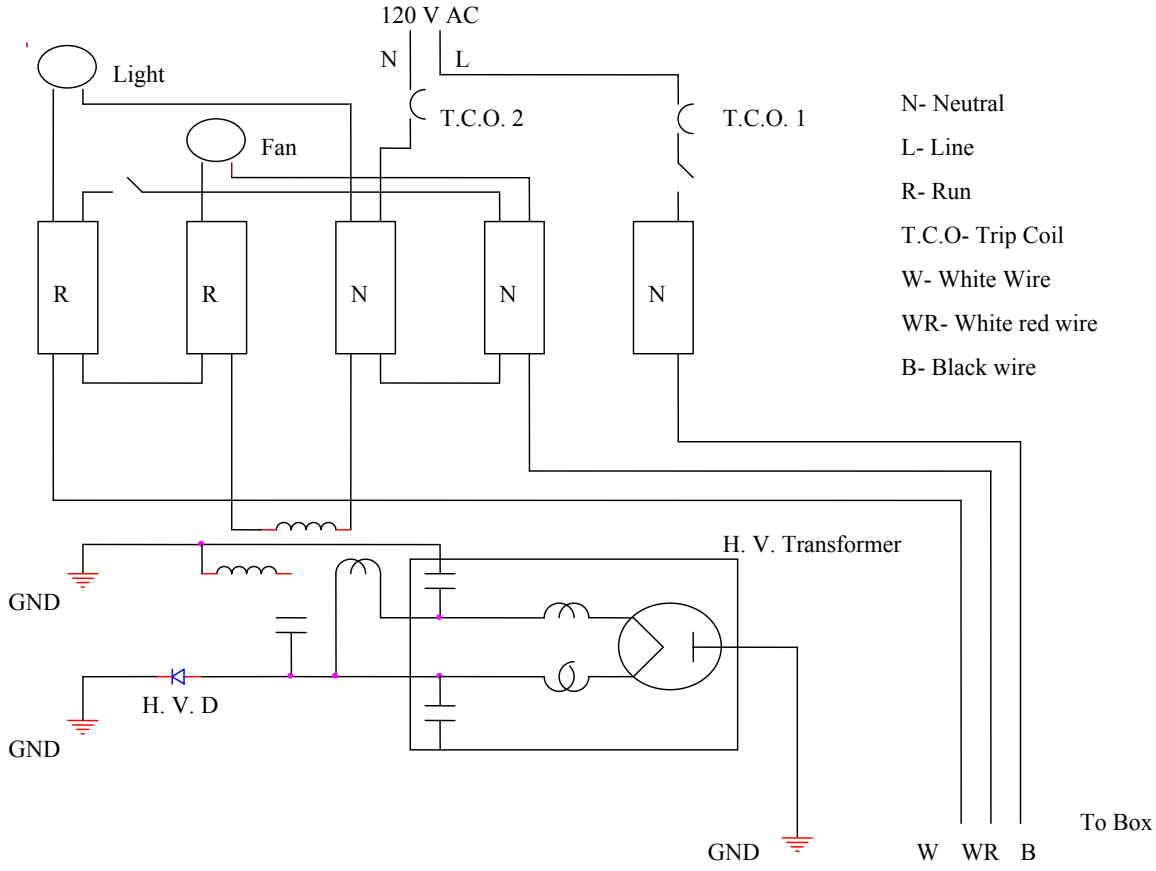

Fig. 3. The basic design of the electrical system used in the laboratory scale microwave dewatering unit.

RESULTS AND DISCUSSION:

During the initial task, we measured the moisture loss using thermogravimetric analysis (TGA) on the Ponds coal and also measured heat capacity of the sample using DSC (Differential Scanning Calorimetry). The results of the TGA experiments are shown in Fig. 5 for different heating rate and those of the DSC experiments in Fig. 6. The weight loss in Fig. 5 is primarily due to loss of moisture since most of this loss

occurs for T ≤ 100°C, and it agrees with the % moisture given in Appendix I. These experiments were done under 'thermal' heating, using in-house Mettler 3000 TGA system and DSC-30 system.

Using the TGA data for different heating rates, we calculated the activation energy for the mass loss using the Flynn Wall method [3]. The activation energy was found to be 8.9kcal/mol which is very close to the value of activation energy of the dewatering process (9kcal/mol).

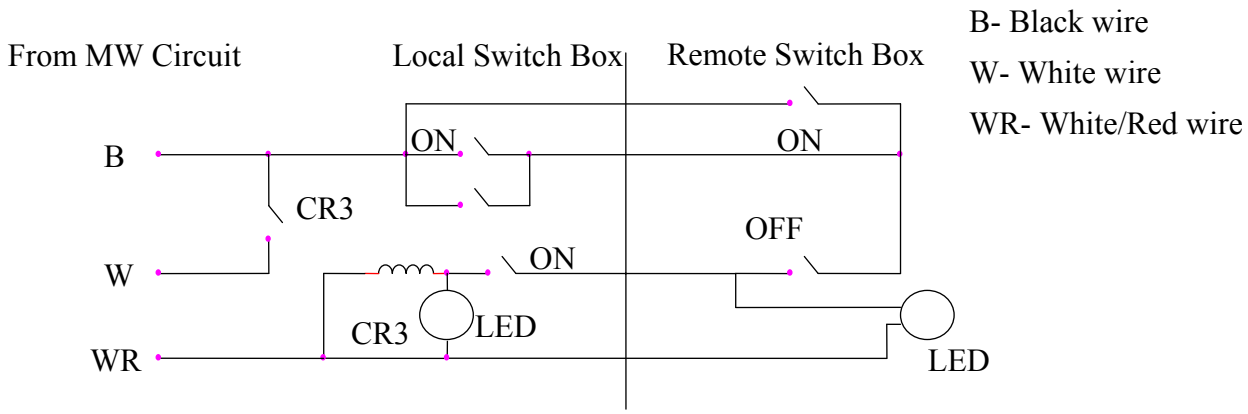

Fig. 4. The electric system used for the remote controlled operation of the laboratory scale microwave dewatering unit.

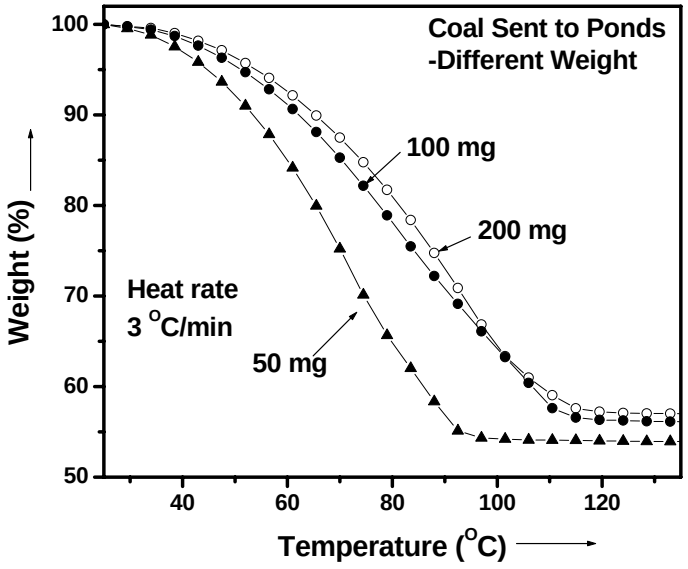

Fig. 5. Results from the TGA on the Ponds coal. The Y axis shows the % weight loss vs. temperature in °C. The results shown are for three different sample sizes of 50mg, 100 mg and 200mg.

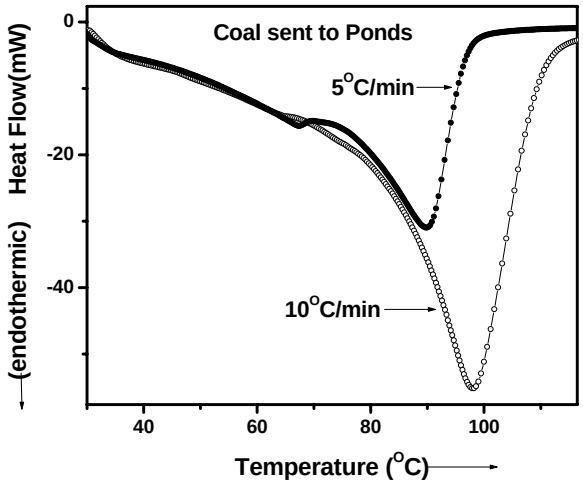

Fig. 6. The results from the DSC experiments are shown for two different heating rates.

The results from the microwave dewatering using the conventional microwave oven are shown in Fig. 7 and 8. The samples were placed on a flat Styrofoam plate as a thin layer so that maximum use of the power could be exploited. There is no visual indication of any water being absorbed by the Styrofoam plate. The data shown in Fig. 7 is for samples of mass 50, 100, 150 and 200 gms.

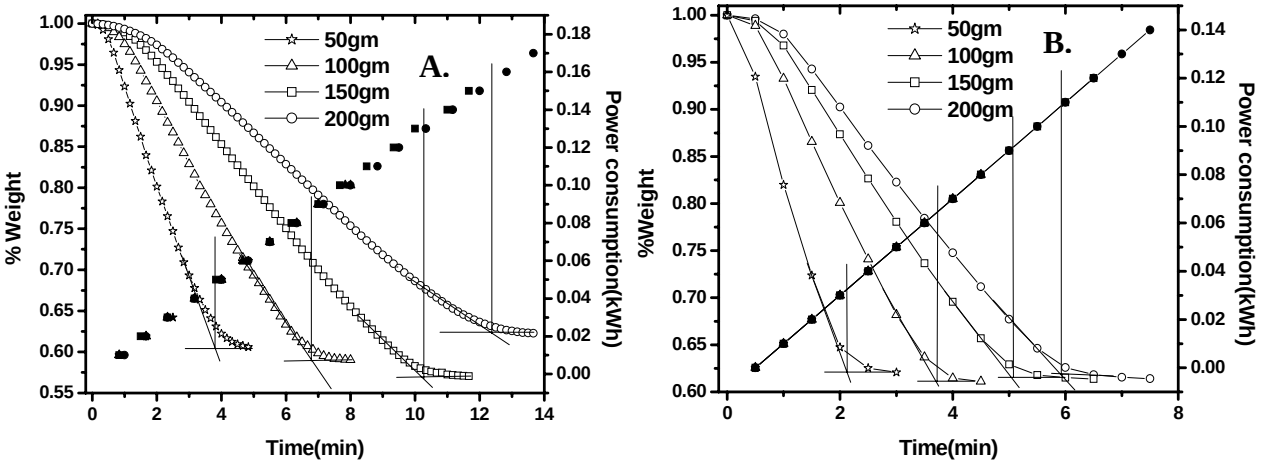

Fig. 7. Weight loss (left scale and open symbols) and power consumed (right scale and closed symbols) as a function of time in the microwave dewatering of a wet coal for four different masses. In the experiment (A) the samples are heated for 10-seconds (B) samples heated for 30-seconds interval, the sample is then taken out for weight measurements outside the microwave oven, the same sample is then put in the oven for the next data point.

From Figs 7 (a, b), we obtained the power needed to essentially eliminate all moisture (inflexion points in the figures) which are near 53% weight loss. This power is plotted against the mass of the sample used in Fig 8. The linear relation obtained is according to expectations, with the intercepts at zero mass yielding the power not utilized by the coal sample (power lost to the plate, coal and unused power). The slope dP/dm ≅ 1.33 x 10^{-3} kWh/gm for 10-seconds heating and dP/dm ≅ 9.8 x 10^{-4} kWh/gm for 30-second heating. Assuming the same dewatering rate for larger masses of wet coal, we calculate that 1kWh of power should be able to vaporize 0.75 kg of water for 10-second heating and 1.02 kg of water for 30-second heating.

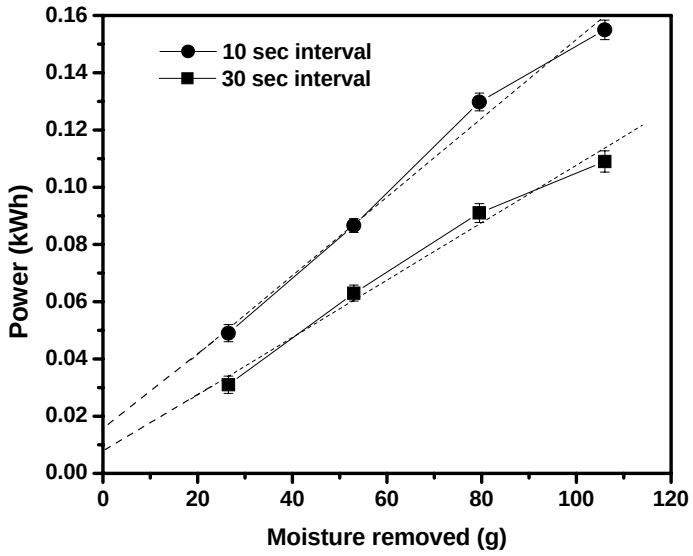

Fig. 8 Power used for dewatering is plotted against the initial mass of the sample with 53% moisture for two heating intervals. The dotted lines are drawn to estimate the slopes dP/dm

In order to determine whether microwave heating has in any way affected the coal or ash in the sample, we used X-ray diffraction of the 'before' and 'after' sample from the experiments in Fig. 7. The x-ray diffraction patterns (Fig. 9) show no significant change in the lines due to ash signifying that chemical phases in the ash are not affected by microwave heating. The broad background peaks near 2θ≈ 25° is due to coal carbon, indicating that carbon is still intact after microwave treatment. This is an important advantage of microwave dewatering vis-à-vis thermal drying of coals

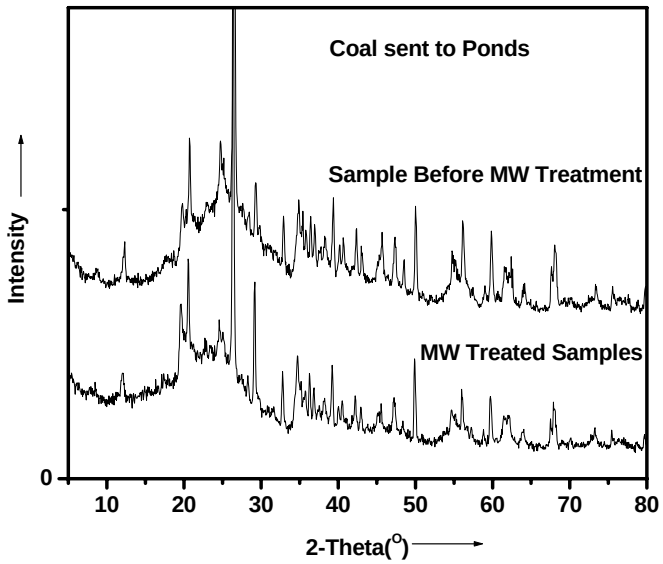

Fig. 9. X-ray diffraction patterns to determine the effect of microwave on coal and ash present in the coal.

Theoretical Estimate:

Energy H needed to convert m gms of water at room temperature (25^{o}C) to steam at 100^{o}C is given by

$$H = m\{(100-25)(4.18)+2256\} \text{ Joules}$$
$$= 2.5692\ m \text{ kilojoules} \qquad \text{---------- (1)}$$

For m = 1 kg, Eq. 1 gives H = 2.5695 x 10^6 J. Since 1kWh =3.6 x 10^6 J, this gives H = 0.71 kWh for one kg of water. Conversely 1kWh of power is able to vaporize 1.40 kg of water. In Figs 5and 6, the initial flat region of the curves is most likely due to the power used to heat the water from 25^{o}C to 100^{o}C whereas the sharp slope indicates conversion to steam. If we neglect the former contribution, then H = 2.256 x 10^6 J for 1 kg of water or conversely one kWh of power is able to vaporize 1.02kg of water. Comparing the experimental values and the theoretical values, we get an efficiency of about 73% for the dewatering process using microwave. The significance of this is that by using microwave power, the efficiency of dewatering obtained in our experiments is quite close to the theoretical limit. Thus most of the power is being used to dewater the coal, with only negligible loss of power to coal or surroundings. These experiments suggest dewatering of coals by microwave heating is extremely efficient and hence a practical possibility.

For further investigating these results, we did experiments using the microwave dewatering conveyor belt unit using larger sample sizes. Known amounts of samples were spread evenly over the conveyor belt which was fed through the microwave unit at a fixed speed. The amount of moisture lost was noted as the difference between the initial weight and the final weight and also by running TGA on ‘before’ and ‘after’ microwave

treated samples. A power meter was inserted in the line to know the amount of energy being used for the dewatering process. For the variables in our experiments, it was determined that the optimum belt speed is about 12 in/min (see Fig. 10).

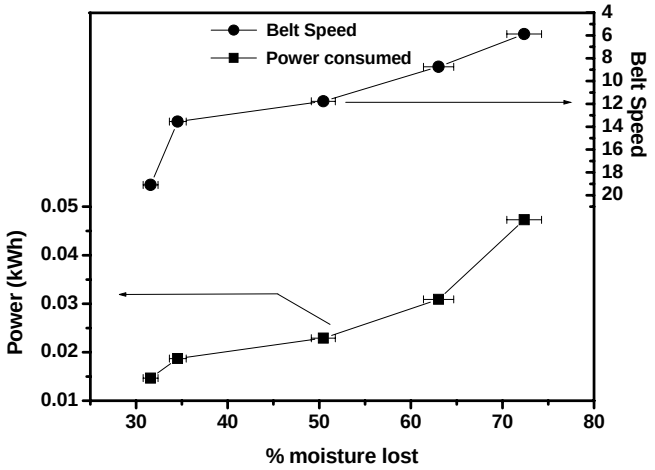

Fig. 10. Power consumed and belt speed vs. % moisture lost used to determine the optimum belt speed

For this belt speed we determined that 1.16 kg water/kWh could be removed. Comparing this value with the theoretical value of 1.4kg water/kWh we get an efficiency of 83%. This increase in efficiency from the previous experiment may be due to the fact that larger quantity samples are used thus reducing the lost power and the samples are more spread out on the conveyor belt.

Cost Estimate: We next estimate the cost of dewatering a ton (10^6gms) of coal having 10% moisture (10^5gms). Assuming one kWh is consumed to eliminate 1.4 kg of water, this would require 71.4 kWh for one ton of coal. At 0.04 $/kWh, yields the cost of dewatering to be about $3/ton of coal with 10% moisture. This estimate reflects only the cost of power used at the rate indicated.

Computational Studies (Dr. Bachlechner)

In the molecular-dynamics-simulation method, substances are described atomistically. Every atom is treated as classical particle the motion of which follows Newton's second law, m a = F (m is the mass of an atom, a is its acceleration, and F is the net force acting on the atom). The forces causing the motion are interactions between the atoms. The quality of the simulations is determined by the quality of the interaction model imposed on the atoms. In this technique, the second-order differential equations of motion for the trajectories of each particle are solved numerically by implementing the corresponding finite difference equations [4,5]. After specifying initial conditions and boundary conditions, the positions, r_i, and velocities, dr_i /dt, at any time t are used to

obtain new positions and velocities at time t + δt by integrating over the time interval, δt. For our molecular-dynamics simulations we use the velocity-Verlet algorithm [4,5].

In the present model of the coal/water interface we distinguish between three types of atoms, which seems to be enough if these atoms are assigned additional attributes. The oxygen atom and the two hydrogen atoms that make up a water molecule are numbered in sequence so that simple algebra allows to extract the information whether two or three atoms are within the same molecule or not. The atoms making up the amorphous carbon describing coal are appended to the end of the list of atoms.

In order to calculate interatomic forces, we introduce the following types of pair interactions [5]: Within the same molecule H-O; between different molecules O-O, H-H, and O-H; between carbon and water C-O. Three-body interactions within a water molecule assure the bond angle of 109.47° for the bonds H-O-H. It has been shown by Walther et al [6]. that such a model can be used to describe the density profile of water around a carbon nanotube.

To analyze the computational system we have developed tools to investigate interatomic distances between or within any type of atoms, pair distribution functions between or within any type of atoms, bond-angle distributions for the tetrahedral bond angle, and displacements of individual atoms, different atom types, as well as groups of atoms in given regions.

CONCLUSIONS:

Experiments performed in this work for dewatering of fine coal slurries using conventional microwave heating at 2.45 GHz have shown that efficiency of dewatering approaching the theoretical limit is possible with this technique. A laboratory scale conveyor belt unit simulating a commercial system was constructed and tested with appropriate shielding and remote control. This helped to demonstrate a possible commercial application. Adoption of such an approach for industrial application depends upon the economics of the coal market, a subject beyond the scope of this work.

PUBLICATIONS/PRESENTATIONS

1. Poster presentations of this work were made during 2005 at West Virginia University and at the Annual Meeting of the CAST in Blacksburg, VA.
2. This work is to form M.S. Thesis of Aashish Kalra, expected to be completed by December 2005. A paper based on this work is expected to be published in the near future.

REFERENCE:

1. D. P. Lindroth: "Microwave drying of fine coal", USBM Report of Investigations 9005, Minneapolis (1985).
2. V. S. Babu, L. Farinash and M. S. Seehra: "Carbon in diesel particulate matter: structure, microwave absorption and oxidation", J. Mater. Res. 10 (1995), 1075-1078.
3. Joseph H. Flynn and Leo A. Wall, "A quick, direct method for the determination of activation energy from thermogravimetric data", Polymer Letters, Vol. 4 (1966), pp. 323-328
4. M.P. Allen and D.J. Tildesley, Computer Simulation of Liquids. Clarendon Press, Oxford (1987).
5. O. Teleman, B. Jönsson, and S. Engström, "A Molecular Dynamics Simulation of a Water Model with Intramolecular Degrees of Freedom", Mol. Phys. 60 (1), 193-203 (1987).
6. J.H. Walther, R. Jaffe, T. Halicioglu, and P. Koumoutsakos, J. Phys. Chem. B 2001, 105, 9980-9987

Appendix- I

Table 1. Analysis of different coal samples

SAMPLE ID	ANALYSIS	AS RECEIVED		DRY BASIS	
SAMPLES SENT TO PONDS	Loss on Drying	52.53	%		
	Carbon	26.59	%	56.01	%
	Hydrogen	6.50	%	1.31	%
	Nitrogen	<0.5	%	<0.5	%
	Sulfur	1.42	%	2.99	%
	Chlorine	230	ppm	485	ppm
	Ash	15.23	%	32.08	%
	Oxygen (by diff)	50.24	%	7.56	%
SAMPLES MAGNETICALLY SEPARATED	Loss on Drying	16.88	%		
	Carbon	3.44	%	4.14	%
	Hydrogen	1.49	%	<0.5	%
	Nitrogen	<0.5	%	<0.5	%
	Sulfur	0.33	%	0.40	%
	Chlorine	160	ppm	193	ppm
	Ash	68.03	%	81.85	%
	Oxygen (by diff)	26.69	%	14.07	%
COAL AS MINED	Loss on Drying	0.71	%		
	Carbon	62.74	%	63.19	%
	Hydrogen	4.57	%	4.52	%
	Nitrogen	1.10	%	1.11	%
	Sulfur	4.46	%	4.49	%
	Chlorine	489	ppm	493	ppm
	Ash	18.29	%	18.42	%
	Oxygen (by diff)	8.79	%	8.22	%
COAL SENT TO POWER PLANT	Loss on Drying	1.12	%		
	Carbon	75.74	%	76.60	%
	Hydrogen	5.46	%	5.40	%
	Nitrogen	1.37	%	1.39	%
	Sulfur	3.17	%	3.21	%
	Chlorine	637	ppm	644	ppm
	Ash	6.21	%	6.28	%
	Oxygen (by diff)	7.99	%	7.07	%

Appendix 10: Novel Bioleaching Technology Assisted by Electrolytic Processes

Technical Report

	Period of Performance:
Contract Title and Number:	
Establishment of the Center for Advanced Separation Technologies (DE-FC26-01NT41091)	Starting Date: 10/1/02 Ending Date: 09/30/06

Sub-Recipient Project Title: Bioleaching Assisted by Electrolytic Processes	Report Information: Type: Final Number: Period: 5/1/02 to 5/31/05 Date: 5/30/05 Code: WV001
Principal Investigators: Eung Ha Cho Co-investigators: Ray R-K Yang	
Contact Address: Department of Chemical Engineering West Virginia University P. O. Box 6102 Morgantown, WV 26506-6102	Contact Information: Phone: 304-293-2111 x –2433 Fax: 304-293- 4139 E-Mail: Eung.Cho@mail.wvu.edu
Subcontractor Address: No subcontracts issued.	Subcontractor Information: Phone: Fax: E-Mail:

DISCLAIMER

EXECUTIVE SUMMARY

Three sulfide minerals, chalcopyrite, sphalerite, and pyrite, were leached using a bioleaching mode and an electrobioleaching mode. The former mode was used to leach the minerals with the bacterium *A. ferrooxidans* in a bioreactor. In the latter mode, the leaching of the minerals was performed in a combination of a bioreactor and an electrochemical cell. In this set-up, a solution was drained from the bioreactor by gravity to the cathode compartment where the Fe(III) content was reduced to Fe(II) before the solution was pumped back to the bioreactor. The idea is that an increase in Fe(II) concentration, which is a nutrient of the bacteria, by electrochemical reduction of Fe(III) would increase the bacterial population and in turn would accelerate the leaching of the mineral.

It has been found that the electrobioleaching of chalcopyrite is superior to the bioleaching with respect to the fact that leaching conversion is higher and a high level of Fe(II) can be maintained. However, the electrobioleaching of sphalerite does not show an improvement over bioleaching. The electrobioleaching of pyrite is similar to that of chalcopyrite, and this has potential to be used in applications such as coal desulfurization and pretreatment of refractory gold ore in heap leaching.

Table of Contents

LIST OF FIGURES

LIST OF TABLES

CHAPTER 1 INTRODUCTION

Bioleaching of sulfide minerals using the bacteria *Acidithiobacillus ferrooxidans* has been recognized as a promising method as it applies to leaching of low-grade, mixed-sulfide ore in a heap leaching or a dump leaching environment. Numerous papers have been published during the 1980s and 1990s, many of them at technical conferences, providing a wealth of background information on this subject. The mixed sulfide ore commonly contains sulfide minerals of iron, copper, and zinc. This bioleaching method presents many potential advantages over conventional pyrometallurgical techniques because it can be applied to all ore grades and to waste materials produced by conventional ore dressing. Also, it is an environmentally sound technique as it does not give rise to atmospheric pollution and has a low energy requirement. However, a general problem with the bioleaching method is that the leaching rate is so low that it takes a long period of time (1 -2 yrs) to complete the heap or dump leaching operation. This slow rate has been the major restriction to wider commercialization of this biotechnology.

According to statistics published in the early 1980s [(1)], about 18% of copper production in the United States is estimated to derive from in-situ, dump and heap leaching. Since the amount of low-grade ore of sulfide minerals is continually increasing, the necessity for application of this bioleaching technology has increased accordingly.

The leaching rate can be enhanced by applying direct current potentials to the bioleaching system.[(2)] The sulfide mineral is anodically polarized and is thus dissolved in the anodic compartment of an electrochemical cell. It was found [(2)] that the leaching conversion of sphalerite or pyrite increased by 3 – 4 times, in an 80 day leaching period, by application of anodic potential, which was characteristic of each mineral. It was also found that the leaching conversion of the minerals was further increased upon additional application of *A. ferrooxidans*.

Bacteria leaching can be enhanced by increasing bacterial population. *A. ferrooxidans*, the bacteria most widely used in bioleaching of sulfide minerals, was grown in an electrolytic bioreactor containing ferrous medium. [(3)] Passage of current through the medium reduced the bacterially generated ferric iron to ferrous iron, increased the cell concentration by 3.7 times and also increased the ferrous oxidation rate by 1.5 times at 29°C, compared with conventional cultivation techniques.[(3)] It was found from a similar study [(4)] that the bacterial growth rate increased at more negative potential in the range from 0 to -0.6 volts versus the glass reference electrode.

The present study is to adopt this mode of process in which *A. ferrooxidans* population is increased electrolytically or by reducing ferric to ferrous cathodically, and therefore enhancing the leaching of sulfide minerals. The objective of this project is to explore this new system as applied to bioleaching the sulfide minerals and particularly to determine its adaptability on each of sulfide minerals: chalcopyrite, sphalerite, and pyrite.

CHAPTER 2 THEORY

When sulfide minerals are leached in a bacteria-cultured solution with *A. ferrooxidans*, there are three categories of reactions that are closely related in determining their leaching rates. The mechanisms of these categories of the reactions are well reviewed in the literature. [5] The first category is oxidation reactions of ferrous ion and elemental sulfur. *A. ferrooxidans* needs these reactions to grow and also catalyzes them. The bacteria grow in the presence of ferrous ion and/or elemental sulfur (nutrients) under acidic (pH < 3.0) conditions. The reactions are:

$$4Fe^{2+} + O_2 + 4H^+ = 4Fe^{3+} + 2H_2O \quad (1)$$

$$2S + 3O_2 + 2H_2O = 2H_2SO_4 \quad (2)$$

It is noteworthy that reaction 1 is inhibited by the presence of some minerals. It was reported [6] that the presence of pyrite and coal inhibited the bacterial iron oxidation (reaction 1) to a great extent. Similar phenomena were observed with sphalerite. [7] This inhibition seems to have much influence on the leaching mechanisms in the present study.

The second category is the indirect leaching reactions, which are the leaching reactions of sulfide minerals with ferric ions that are produced by the bacterial catalysis (reaction 1). The indirect reactions are:

$$FeS_2 + 2Fe^{3+} = 3Fe^{2+} + 2S \quad (3)$$

$$CuFeS_2 + 4Fe^{3+} = Cu^{2+} + 5Fe^{2+} + 2S \quad (4)$$

$$ZnS + 2Fe^{3+} = Zn^{2+} + 2Fe^{2+} + S \quad (5)$$

The third category is the direct leaching reactions. These are the leaching reactions of sulfide minerals which are catalyzed by the bacteria. The direct reactions are:

$$FeS_2 + 15/4O_2 + 0.5H_2O = Fe^{3+} + 2SO_4^{2-} + H^+ \quad (6)$$

$$CuFeS_2 + 4.25O_2 + H^+ = Cu^{2+} + Fe^{3+} + 2SO_4^{2-} + 0.5H_2O \quad (7)$$

$$ZnS + 2O_2 = ZnSO_4 \quad (8)$$

Contribution of each category to the leaching rate varies from mineral to mineral. It is reported [5] that sphalerite is mainly oxidized by the indirect leaching mechanism while chalcopyrite and pyrite are mainly oxidized by the direct

leaching mechanism. It is expected that the different leaching behaviors of the two types of sulfide minerals may reveal different responses in the present study.

There is an additional factor that must be considered in understanding the leaching mechanisms in the present research. The leaching is limited by the presence of a diffusion barrier that is produced during the leaching reaction. As can be seen from reactions 3 through 5, elemental sulfur is formed. The sulfur layer sometimes becomes a protective layer that limits the diffusion rate. It was reported [8] that the sulfur layer formed during the leaching of chalcopyrite with ferric sulfate became a complete protective layer with no crack and that further leaching should be carried on by a solid state diffusion mechanism through the sulfur layer. In the case of sphalerite leaching, a different mechanism is envisioned. It was reported [9] that in the initial stages of sphalerite leaching (~13 - 16% of leaching conversion), the leaching rate followed the shrinking core model. This suggested that the sulfur layer did not act as a protective layer; however, leaching beyond this initial state fit a model in which the rate is controlled by diffusion through the sulfur layer, suggesting that the sulfur layer does act like a protective layer. These mechanisms may impact the leaching behaviors of the sulfide minerals in the present study.

CHAPTER 3 EXPERIMENTAL

3.1 Sample Preparation

Lump samples (5 – 10 cm) of sphalerite (ZnS), pyrite (FeS_2), and chalcopyrite ($CuFeS_2$), were obtained from Ward's Mineral (Rochester, NY). The samples were crushed by a jaw crusher to about 1 cm in size, manually sorted to remove conspicuous low-grade particles, crushed again by a roll crusher, and screened to produce a 150 - 200 mesh (75 – 100 microns) size fraction. This fraction was further treated to remove fines by decantation. The produced fraction of particles was slurried with about 500 mL of water in a one-liter beaker. The slurry was agitated by a swirling motion. When the agitation was stopped, the larger particles were allowed to settle, and the suspended fines were decanted. This procedure was repeated until only small amounts of fines could be seen in the agitated liquid. This fraction was air dried and used for leaching experiments.

Chemical analyses were conducted to determine the purity of each of the minerals. A one-gram sample was taken from each prepared size fraction, dissolved in boiling aqua regia, and filtered. The filtrate was properly diluted and analyzed for metal concentrations with an atomic absorption spectrophotometer. The metal concentrations were converted to purity of each mineral. Also, the percent of impurities were surmised from the metal concentrations by assuming that all the metals exist as metal sulfides. The results are summarized in Table 1.

Table 1. Chemical Analysis Results for Mineral Samples

Mineral	Purity (%)	Impurities (%)			
		sphalerite	chalcopyrite	pyrite	acid-insoluble
Sphalerite	86.02	-	0.13	0.53	13.32
Chalcopyrite	78.7	3.47	-	7.02	10.81
Pyrite	95.53	0.16	0.09	-	4.22

3.2 Culture History and Procedure

3.2.1 *Culture Origination*

A test tube containing a culture of the organism *Acidithiobacillus ferrooxidans* (ATCC 13598) was received and its initial propagation was as follows:

1. The contents of the test tube (~15 mL) were divided equally amongst 3 125 mL Erlenmeyer flasks.

2. A sterilized medium solution was filtered and added to each flask in a 5:1 ratio, resulting in each flask containing ~30 mL.

3. The flasks were sealed with sterile cotton.

4. The flasks were then transferred to an incubator where they were maintained at 26°C and shook at 250 rpm in a random-orbit shaker.

All glassware used was dry sterilized at a temperature 160 - 180°C for at least 45 minutes. The filtering apparatus, for the medium solution, was a Nalgene Model 300-4000, and the filter paper was Millipore TCMF (pore size = 0.22 μm & diameter = 47 mm). The filtering apparatus and filter paper were steam sterilized and dried prior to use under the following cycle: sterilization at 120°C for 20 min and drying at 160°C for 30 minutes. All work took place in a laminar flow hood, which was cleaned with 70% ethanol and allowed to equilibrate prior to use.

A medium solution was prepared with part A and part B.

Part A:

0.8 g ammonium sulfate	$(NH_4)_2SO_4$
2.0 g magnesium sulfate heptahydrate	$MgSO_4 \cdot 7H_2O$
0.4 g potassium phosphate dibasic	K_2HPO_4
5.0 mL ATCC Trace Mineral Supplement	ATCC # MD-TMS
1.0 N sulfuric acid	H_2SO_4

All ingredients were dissolved in ~600 mL of deionized water and the pH was adjusted to 2.3 using the sulfuric acid.

Part B:

Twenty grams of ferrous sulfate 7-hydrate ($FeSO_4 \cdot 7H_2O$) was dissolved in 200 mL of deionized water.

Finally, parts A and B were combined and the volume was brought up to 1.0 L using deionized water.

3.2.2 *First & Second Subcultures*

1. Two of the three initial 125 mL flasks were selected for subculture. The contents (by volume) of each was determined and then equally divided in half.

2. The four portions were each then transferred to their own sterile 500 mL flask.

3. Filtered medium was added to each of the 4 500-mL flasks in a ratio of 5:1.

4. Each flask was sealed with sterile cotton and returned to the incubator (26°C and 250 rpm).

5. After 7 days, one of the four initial 500-mL flasks was chosen and its volume was determined.

6. Portions of equal size were then removed from this flask and transferred to new sterile 500-mL flasks, so that the result was 4 flasks of equal volume. The original flask was labeled P (for parent) and the other three were labeled C1, C2, and C3.

7. Medium solution was then added to each flask to bring the total volumes to the levels as follows:

P(100)	100 mL
C1(150)	150 mL
C2(200)	200 mL
C3(250)	250 mL

8. The flasks were then sealed with sterile cotton and returned to the incubator.

3.2.3 *Subsequent Subcultures*

To ensure the viability of the culture, the following procedure was used over the next few weeks:

1. From the flask to be cultured, 10 mL was removed and transferred to a fresh flask, resulting in a pair of flasks, with the second being the child of

the first.

2. The volume of each was brought up to the initial volume of the parent and they were labeled. For example, the C1(100) flask became C1(100)-1 and C1(100)-1s.

3. The flasks were then sealed with sterile cotton and returned to the incubator.

Ultimately, the total volume was standardized to 250 mL, and a schedule of 14 days between subculture was adopted. After the viability of the culture was ensured, the culture procedure was changed slightly and accomplished as follows:

1. From the flask to be cultured, 2 10-mL portions were removed and transferred to fresh flasks. The volume was brought up to 250 mL using filtered medium and the labeling system was as follows: flask C2-4s became C2-5s1 and C2-5s2.

2. The flasks were then sealed with gas-permeable stoppers and returned to the incubator.

3.3 Bioleaching Apparatus

The bioreactor used in this study was fabricated of 4.8 mm thick, clear acrylic sheets. The base was 4 inches square and designed to hold 1 liter with sufficient head space. The top was left open to allow access for the stirrer and air bubbler. The solution was stirred with an overhead stirrer with an rpm setting high enough to ensure a well mixed environment. The impeller was coated with a vinyl-ester resin (Dow Derakane 411-350) to prevent interference with the reaction. To ensure that ample oxygen was available, dry-grade, compressed air was bubbled into the solution at a rate of approximately 7.1 mL/min. The solution was comprised of about 250 mL of a bacterial culture (7 days old) solution and 750 mL of *A. ferrooxidans* culture medium which contained 15g of $FeSO_4 \cdot 7H_2O$, 10 mL of trace mineral solution (ATCC Catalog MD-TMS), and was adjusted to pH 1.5 using 1.0 N sulfuric acid. Then, 20 g of the mineral (pyrite, chalcopyrite, or sphalerite) was added to initiate the bioleaching reaction.

The electrobioleaching apparatus was more complicated. The apparatus consisted of a bioreactor and an electrochemical cell, as shown in Figure 1. The bioreactor was identical to the one mentioned previously except for a tap hole (23 mm diameter) drilled on one of the side panels. The tap hole was used to allow

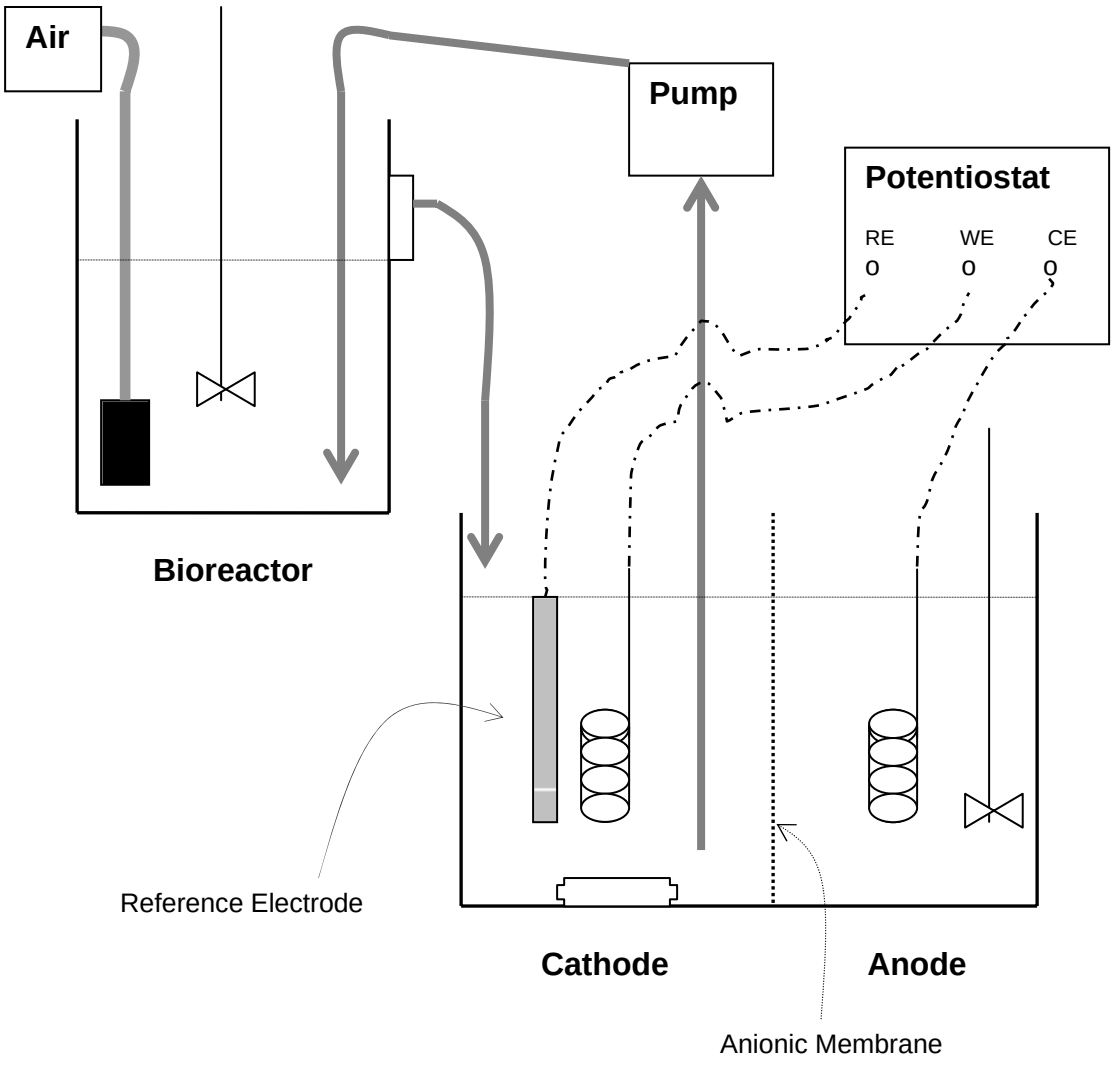

Figure 1. Schematic of experimental set-up for electrobioleaching mode.

the solution to flow back to the cathode compartment of the cell by gravity. The position of the tap hole was made so that the bottom of the hole coincided with the 1 liter mark in the reactor. The operation of the bioreactor in the electrobioleaching mode was basically the same as for the bioleaching mode outlined previously.

The electrochemical cell was also fabricated of 4.8 mm thick, clear acrylic sheets. The overall dimensions were 20 cm long, 10 cm wide, and 15 cm high. The cell was fabricated in two halves, with a flange on the open end of each half. A membrane along with two rubber gaskets were sandwiched between the two halves. The halves were then bolted together with fiberglass nuts and bolts. This clam-shell design allowed easy access to the membrane and the gaskets. The membrane (Ionics AR204-SZRA-412) was an anionic-exchange membrane designed to allow the passing of anions, but not cations. It was chosen to prevent ferric and ferrous ions from leaving the cathode compartment. The catholyte was stirred using a magnetic spin bar, while the anolyte was stirred using an overhead impeller, which has been coated with a vinyl-ester resin (Dow Derakane 411-350) to prevent interference.

Solution was pumped from the bottom of the cathode compartment to the bottom of the bioreactor using a peristaltic pump at a rate of approximately 1.55 mL/sec. Then the liquid level in the bioreactor rose, which caused the solution to be drained via gravity. When the experiment was started, the cathode contained 1 liter of 0.045 M ferric sulfate solution adjusted to pH 1.5 using 1 N sulfuric acid. The anode contained 1 liter of 0.2 M sodium chloride solution at natural pH. The current required to reduce the ferric iron in the cathode was supplied by a Perkin-Elmer Model 283 Potentiostat/Galvanostat. The working and counter electrodes were made of platinum-iridium (90% platinum, 10% iridium) mesh gauze, while the reference electrode was a saturated calomel electrode.

3.4 Experimental Procedures

The beginning of an experiment for the bioleaching mode was marked by the addition of mineral sample to the bioreactor. Twenty grams of the mineral sample was added to a mixture of 250 mL of subculture solution and 750 mL of 0.072 molar ferrous ion solution whose pH had been adjusted to 1.5 using 1.0 N sulfuric acid. The experiment was initiated when the reactor contents were agitated by an overhead stirrer. Air was blown into the reactor through a diffuser at a rate of 7.1 mL/min. On the third (or fourth) day and every 3 or 4 days thereafter, liquid samples were withdrawn from the bioreactor, filtered and analyzed for ferrous iron, total iron and zinc or copper. Five milliliters was pipetted for each ferrous and total iron analysis, 10 mL for copper, and 1 mL for zinc analysis. Fifteen minutes prior to sampling, the speed of the overheard stirrer was slowed. This was done to allow the solid mineral to settle out of solution, which in turn, kept it from being removed from the reactor.

Figure 1 shows a schematic of the experimental set-up for the electrobioleaching mode. The experiment for this mode was initiated and

conducted the same way as the bioleaching mode for the first seven days. On the seventh day, one liter of each, catholyte and anolyte, was prepared and charged to their respective compartments. The catholyte was 0.045 M ferric sulfate solution at pH 1.5. The anolyte was 0.2 M sodium chloride solution at natural pH. Ferric sulfate was chosen for the catholyte because the ferrous ion in solution would eventually be converted to ferric ion by bacterial catalysis and this situation could be simulated from the beginning.

When the catholyte and anolyte were charged to their compartments, the catholyte and the bioreactor solution were circulated for two hours. This circulation was needed to homogenize the two solutions. At the end of two hours liquid samples were withdrawn from the bioreactor and analyzed for ferrous iron, total iron, and zinc or copper. At this point, the potentiostat was turned on and reduction was begun at the cathode. Current was applied for 4 to 5 hours. At the end of the reduction period, another sample was taken from the bioreactor and analyzed for ferrous iron. By knowing the change in ferrous iron concentration and the coulombs supplied, current efficiency was determined. After this sampling, the circulation and reduction were stopped. The reduction was conducted at a current ranging from 40 to 100 mA in potentiostatic (constant voltage) mode, during which the potential was manually adjusted. The potentials were varied from 0.2 to 0.05 V for chalcopyrite and pyrite and 0.2 to -0.078 V for sphalerite, all against the saturated calomel electrode.

The electrochemical reduction was conducted whenever ferric concentration was more than 0.01 M. The reduction was performed four or five times during the entire leaching period of 40 days for pyrite and chalcopyrite, while it was done virtually daily (excluding weekends) for sphalerite. The sampling for metal ions was repeated every 3 or 4 days. Also, samples were taken from the anode compartment occasionally and analyzed for total iron and metal ions. The concentration build-up at the anode compartment was attributed to the leakage of solution through the anionic membrane and/or its gaskets.

Metal ions (copper and zinc) were analyzed with an atomic absorption spectrophotometer. These values were used to calculate the leaching conversions of chalcopyrite and sphalerite as a function of time. However, this method was not suitable for determining the leaching conversion of pyrite, because the background ion in the leach solution was soluble iron and the leaching product was also soluble iron. Furthermore, the mass balance on soluble iron was complicated by the precipitation of ferric iron as jarosite. Thus, the leaching conversion of pyrite was only estimated by recovering the unleached pyrite sample at the end of the experiment. The leach slurry was filtered and the solids were dried. Then the dry solids were leached with 200 mL of HCl (2 + 3), a mixture of 40 vol% of concentrated HCl and 60 vol% of deionized water for two hours at room temperature. The slurry was filtered, dried, and the solids were considered to be the unleached pyrite mineral.

Analyses for ferrous and total iron were made by utilizing a titration method that was derived from ASTM D2492-84, which is designed to analyze sulfur forms (pyritic sulfur and sulfate sulfur) from coal. Ferrous ion, after the solution was acidified, was titrated with potassium dichromate using barium

diphenylamine as an indicator. The end point was achieved when the color changed to violet, and was easily detected. Total iron was analyzed the same way except for pretreatment of the solution. Ferric ion in the solution was reduced to ferrous, using stannous chloride, before titration for total iron with potassium dichromate. Ferric concentration was determined by subtracting ferrous concentration from the total iron concentration.

The precipitation of ferric ion during the leaching of chalcopyrite and sphalerite, probably as jarosite, was calculated as a function of time. The precipitation was calculated by subtracting the total iron available in solution from the total iron that should be available in solution, if there were no precipitation. What is available includes number of moles of soluble total iron in the bioreactor for bioleaching mode, or in the bioreactor, and both the cathode and anode compartments, for the electrobioleaching mode. It also includes the moles of soluble iron removed when samples were taken in both modes of operation. The total iron which should be available, with zero precipitation, is the number of moles of initial total soluble iron (in the solutions) plus those coming from the leaching conversion, particularly for chalcopyrite. However, in the precipitation calculations, the number of moles of iron coming from the possible leaching of impurity minerals (see Table 1) was not considered. This might not cause a significant error in the calculations for sphalerite because the impurity minerals are small in amount (see Table 1). However, in the case of chalcopyrite, the error level may not be trivial because a significant amount of the impurity (pyrite) was present (see Table 1).

CHAPTER 4 RESULTS AND DISCUSSION

4.1 Chalcopyrite Leaching

Figure 2 compares the leaching conversion of chalcopyrite between the bioleaching and electrobioleaching modes. The two experiments were conducted concurrently for 41 days. It can be seen in Figure 2 that the leaching rates are very low for both methods. The mineral is leached by less than 2% in 41 days, realizing that it is a reflection of the leaching which has been observed in the past.[8] It can also be seen that despite the small leaching conversions, there is a clear distinction between the two modes of operation. The conversion observed in the electrobioleaching mode is 1.55% in 41 days, which is more than the conversion in bioleaching mode by 52%. This is a significant improvement.

The improvement can be analyzed using Figures 3 and 4. Figures 3 and 4 show the variations with time of the concentrations of Fe(II), Fe(III), and total iron for the bioleaching and electrobioleaching modes, respectively. There seems to be little or no inhibition effect of microbial oxidation of Fe(II) in the presence of chalcopyrite because Fe(II) ion starts being oxidized right after the initiation of the bioleaching, which can be seen in Figures 3 and 4. Figure 2 shows that the conversions start deviating from each other at 20 days. This reaction time coincides with when the Fe(II) concentration dropped to almost zero as can be seen in Figure 3. It is expected that the bacterial activity henceforth is greatly reduced or becomes lukewarm, so that the leaching may take place through oxidation with Fe(III). In the case of electrobioleaching mode, however, the leaching may take place mostly by the bacterial catalysis because Fe(II) concentration becomes much higher than in the bioleaching mode, as seen in Figures 3 and 4. These results, when combined with those shown in Figure 2 suggest that the direct leaching or the microbial catalysis of chalcopyrite takes place faster than the indirect leaching or the leaching with Fe(III) ion. Compared with the fast rate of the microbial catalysis of chalcopyrite, the bio-oxidation reaction of Fe(II) (reaction 1) may take place rather slowly. The rate of the reaction (reaction 1) is about 0.0028 mole/day, as can be seen from Figure 3, which is slow enough to be offset by the electrochemical reduction rate of the electrobioleaching, maintaining a good level of Fe(II) concentration throughout the leaching reaction (see Figure 4). The electrochemical reduction of Fe(III) during the electrobioleaching of chalcopyrite is depicted in Figure 4. The reduction of Fe(III) was made four times with a total electricity of 4840 coulombs. This electricity produced 0.0337 moles of Fe(II) with a current efficiency of 67.2%. The leakage through the anionic membrane resulted in a 12.2% loss of soluble iron and a 10% loss of cupric ion over the 41 day period.

Figure 5 reveals the precipitation of soluble iron during the leaching of chalcopyrite under both the bioleaching and the electrobioleaching modes of operation. There is a marked difference in precipitation between the two modes. The precipitation is 27.3% in the former mode, while it is only 4.5% in the latter.

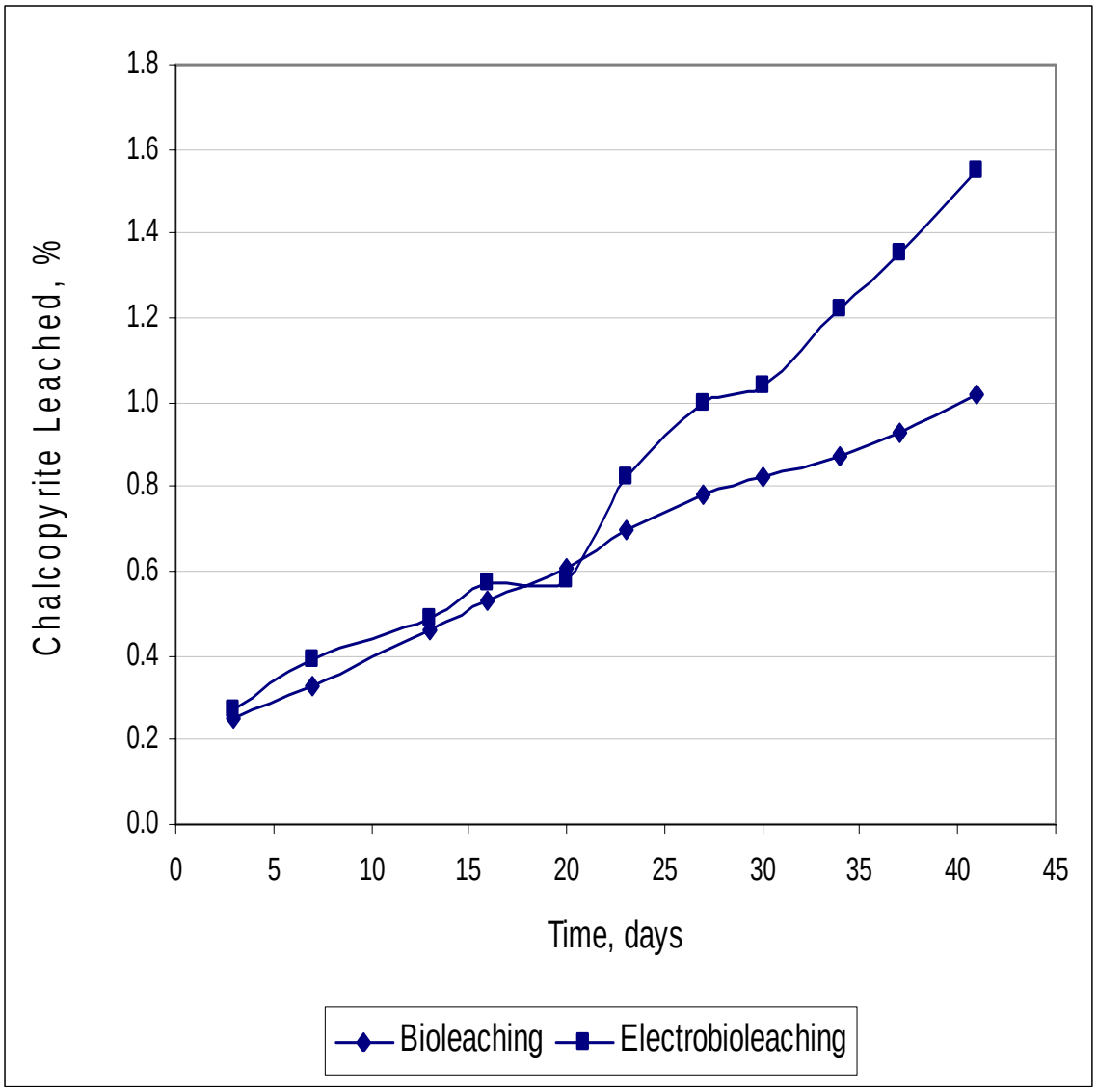

Figure 2. Leaching conversion of chalcopyrite in bioleaching and electrobioleaching modes.

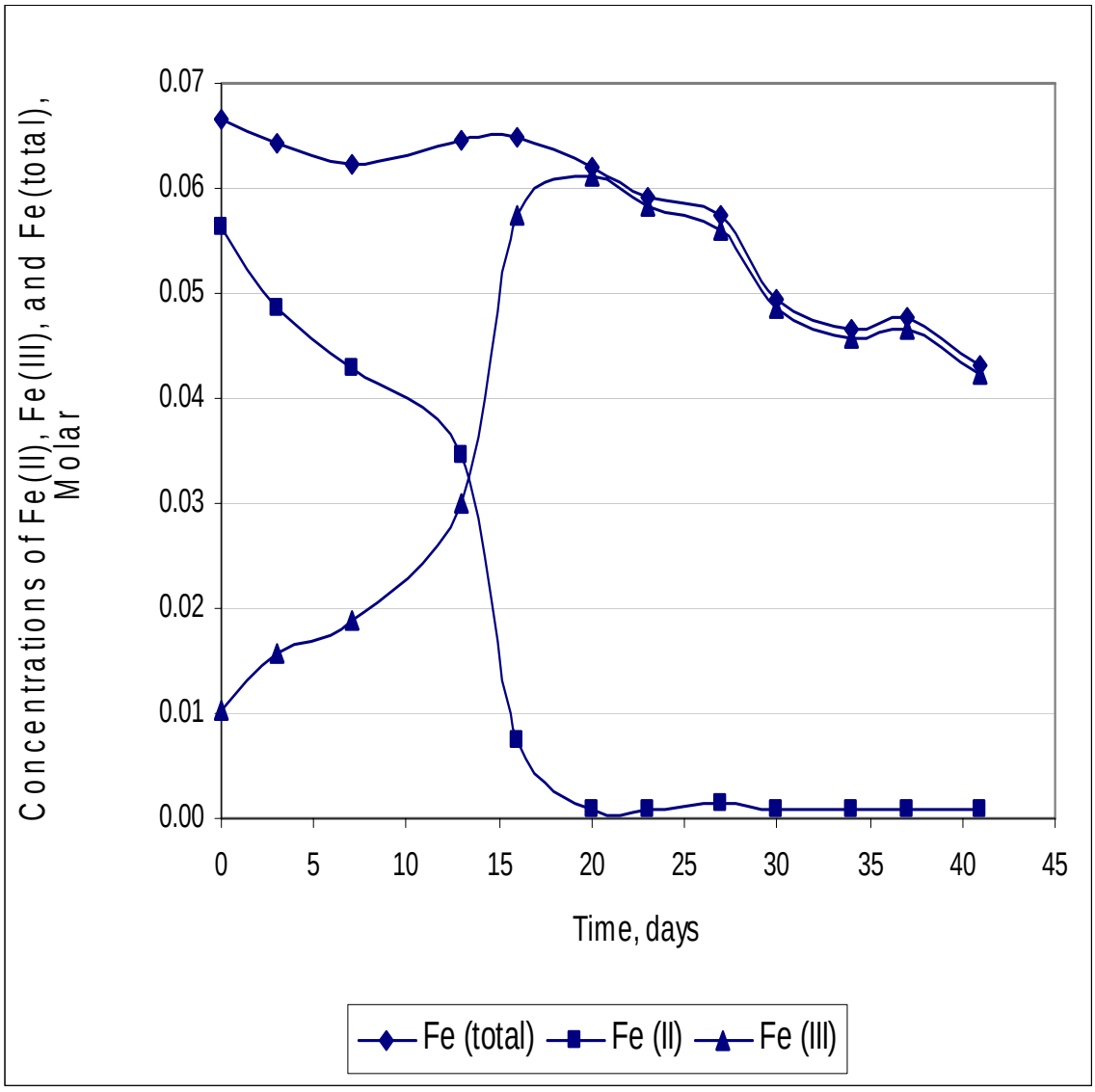

Figure 3. Concentrations of Fe(II), Fe(III), and Fe(total) during chalcopyrite leaching in bioleaching mode.

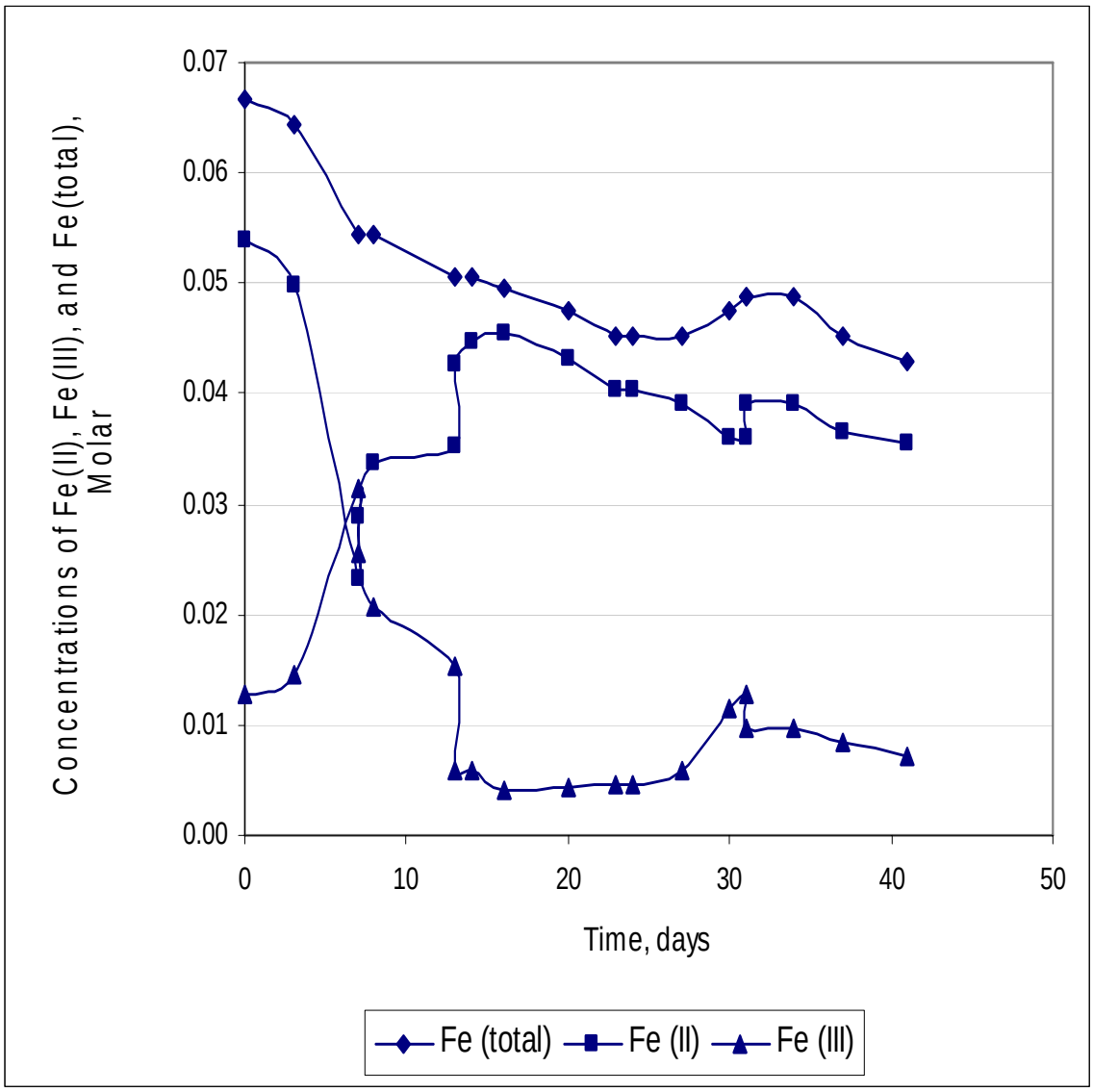

Figure 4. Concentrations of Fe(II), Fe(III), and Fe(total) during chalcopyrite leaching in electrobioleaching mode.

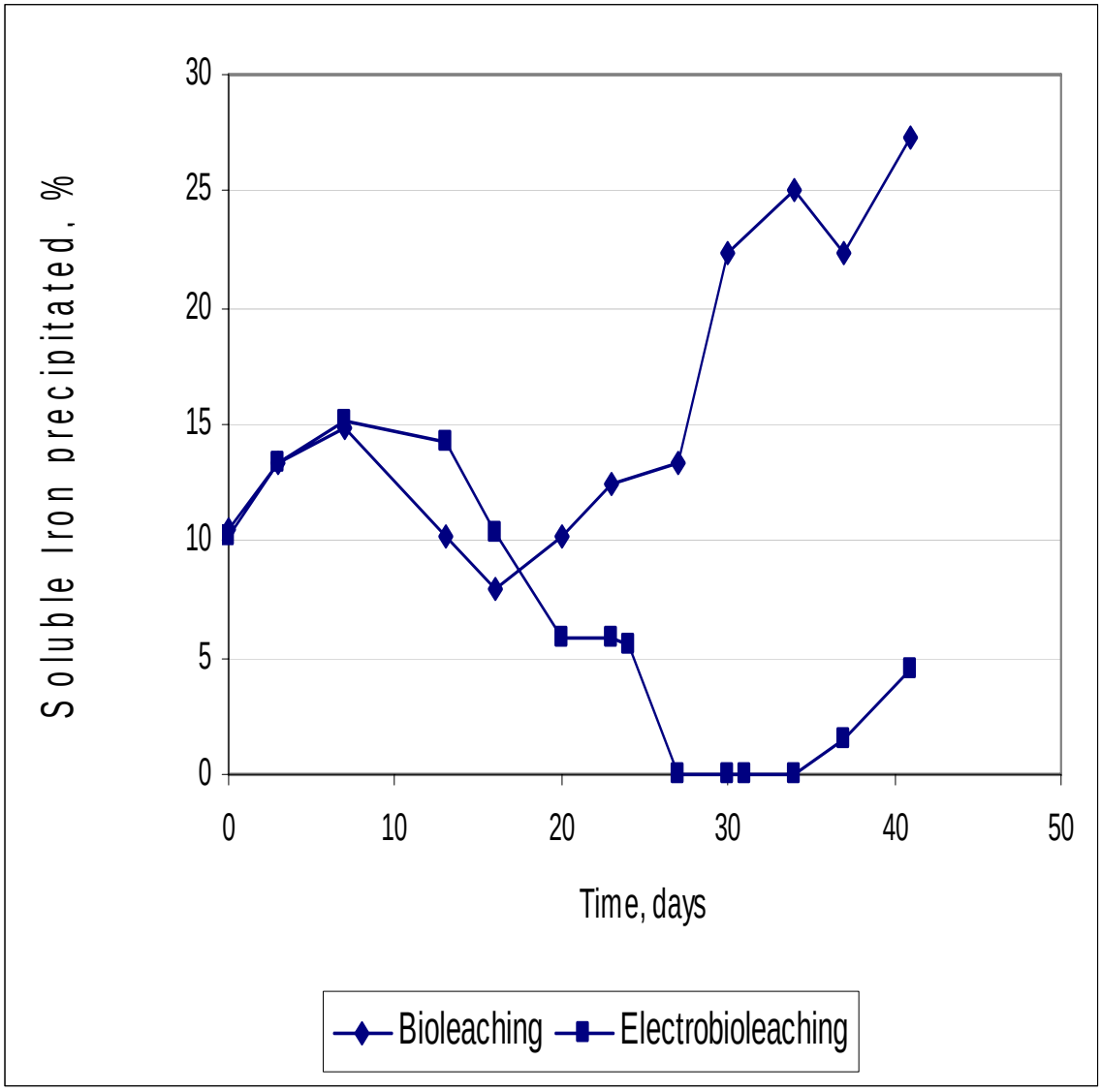

Figure 5. Precipitation of soluble iron during chalcopyrite leaching in bioleaching and electrobioleaching modes.

This is undoubtedly due to the difference in Fe(III) concentration (see Figures 3 and 4). This precipitation may not be influenced by the variation of solution pH. The pH varied from an initial value of 1.5 to the vicinity of 2 at the end of the experiment for the leaching of all the sulfide minerals throughout this study. pH variation within this range would not influence the precipitation of jarosite.[10]

Fe(III) ion would precipitate much more easily than Fe(II). The large difference in iron precipitation between the two modes, as shown in Figure 5, is due to the large difference in Fe(III) concentration. Large amounts of precipitation in the bioleaching mode depletes Fe(III) concentration and thus retards the leaching rate. However, this would not happen when operating in electrobioleaching mode if proper electrochemical reduction continues. Thus, a projection is possible; that is, the gap in the leaching conversion between the two modes is likely to be significantly widened as the leaching proceeds. It is concluded then that the electrobioleaching mode of operation is more suitable than the bioleaching mode.

Two experiments were conducted to leach chalcopyrite and sphalerite with only Fe(III) ion. The experiments were conducted in the bioreactor with a 20 g mineral sample in a 1-liter solution of 0.053 molar Fe(III). No bacteria culture was used in the solution. The results are shown in Figure 6. One can see that the leaching rate of chalcopyrite with Fe(III) is slightly lower than that observed in Figure 2, especially in the early stage (less than 7 days), which might result from both direct and indirect leaching mechanisms.

The contributing factors of the direct and indirect leaching rates may be estimated as follows: The leaching of chalcopyrite with ferric sulfate follows the diffusion model through the product layer of elemental sulfur. [8] The rate equation is given by [11]

$$1-\frac{2}{3}x-(1-x)^{2/3}=\frac{2kVc}{r_o^2\sigma}t \qquad (9)$$

where: x = leaching conversion
c = concentration of Fe(III)
k = rate constant
V = chalcopyrite molar volume
σ = stoichiometric factor, 4 in this case (see reaction 4)
r_o = average radius of chalcopyrite particle
t = reaction time

Equation 9 can be rewritten as

$$1-\frac{2}{3}x-(1-x)^{2/3}=kKc \qquad (10)$$

where, $K=\frac{2Vt}{r_o^2\sigma}$

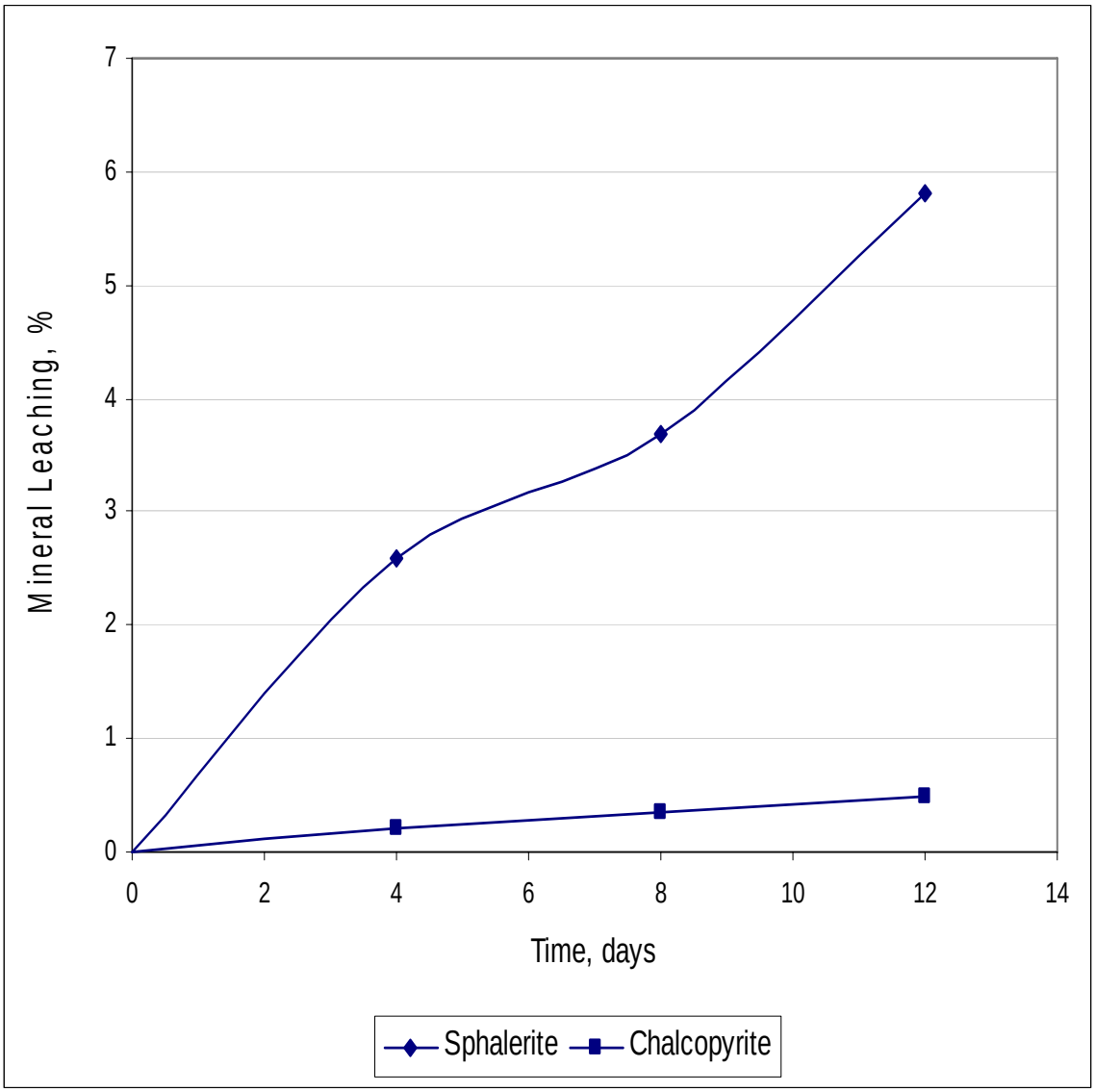

Figure 6. Leaching of chalcopyrite and sphalerite in 0.053 M ferric solution.

The leaching conversion is 0.38% at 0.053 M and at 12 days as shown in Figure 6. Then $k_1 Kc = 1.609 \times 10^{-6}$ and $k_1 K = 3.04 \times 10^{-5} \frac{liter}{mole}$ where k_1 is the rate constant for the indirect reaction. The leaching conversion under the combined mechanisms is 0.428% at the average concentration of Fe(III), 0.0189 M and 12 days as shown in Figures 2 and 3 for the bioleaching mode. Then, $(k_1 + k_2)Kc$ is 2.036×10^{-6} and $(k_1 + k_2)K = 1.077 x 10^{-4} \frac{liter}{mole}$ where k_2 is the rate constant of the direct reaction. Since K is the same in both cases, it can be determined that $k_2 = 2.52\ k_1$. The estimation is that the rate constant of direct leaching by microbial catalysis, in the early stages, is 2.52 times as high as that of indirect leaching. This is in good agreement with the leaching mechanisms mentioned previously.

4.2 Sphalerite Leaching

Figure 7 shows the leaching conversion of sphalerite in the bioleaching and electrobioleaching modes. It is observed that the leaching conversion in electrobioleaching mode is slightly higher than in bioleaching mode during the initial stage (up to 15 days), significantly higher in the middle stage (15 to 40 days), and then becomes virtually the same in the final stage (beyond 40 days). This comparison may be analyzed using the data as given in Figures 8 and 9, which show how the concentrations of soluble iron forms vary with time.

It is seen in Figure 8 that the Fe(II) concentration is maintained at a plateau-like state before dropping to virtually nil. This type of inhibition is believed to be rare and the behavior is not well understood at this moment. The plateau portion, up to 28 days, may be considered as an incubation period where the population or the catalysis of the bacteria is not large enough to oxidize Fe(II) (reaction 1). Then the cascading portion, after 28 days, is the breaking point of the incubation. It is considered that an extra contribution is made besides the sustained Fe(II) in breaking the incubation. It must be another bioreaction, or the sulfur oxidation reaction (reaction 2) that energizes the growth of the bacteria. The elemental sulfur is produced by the leaching of the mineral with Fe(III) (reaction 5). Since the leaching conversion of sphalerite reaches 2.8% after 28 days, the elemental sulfur produced amounts to 0.005 mole. This elemental sulfur might help to break the incubation.

Another crucial aspect of Figure 8 is that the oxidation rate of Fe(II) is 0.016 mole/day, which is 5.7 times faster than that for chalcopyrite. Thus, after the collapse of incubation, all the soluble iron exists as Fe(III) because the disappearance rate of Fe(II) (reaction 1) is faster than the production rate of Fe(II) (reaction 5). The incubation portion is also visible in Figure 9 in the case of the electrobioleaching mode. A dip, at 7 days, of Fe(II) is not due to microbial oxidation of Fe(II). It is rather because the solution was diluted with the catholyte. It is seen in Figure 9 that the collapse of incubation occurs between 22 and 27 days. This is earlier than what is observed in bioleaching mode.

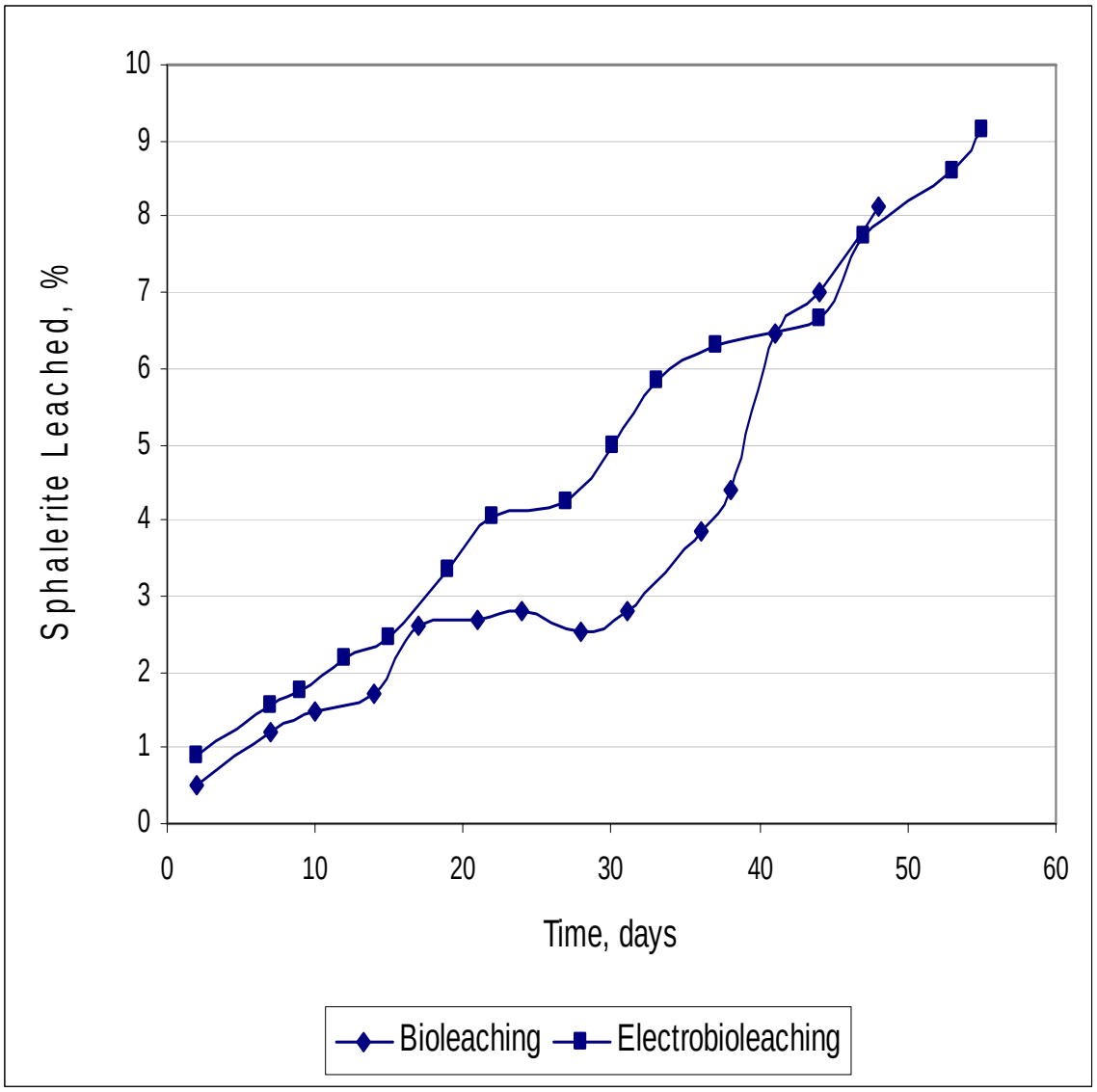

Figure 7. Leaching conversion of sphalerite in bioleaching and electrobioleaching modes.

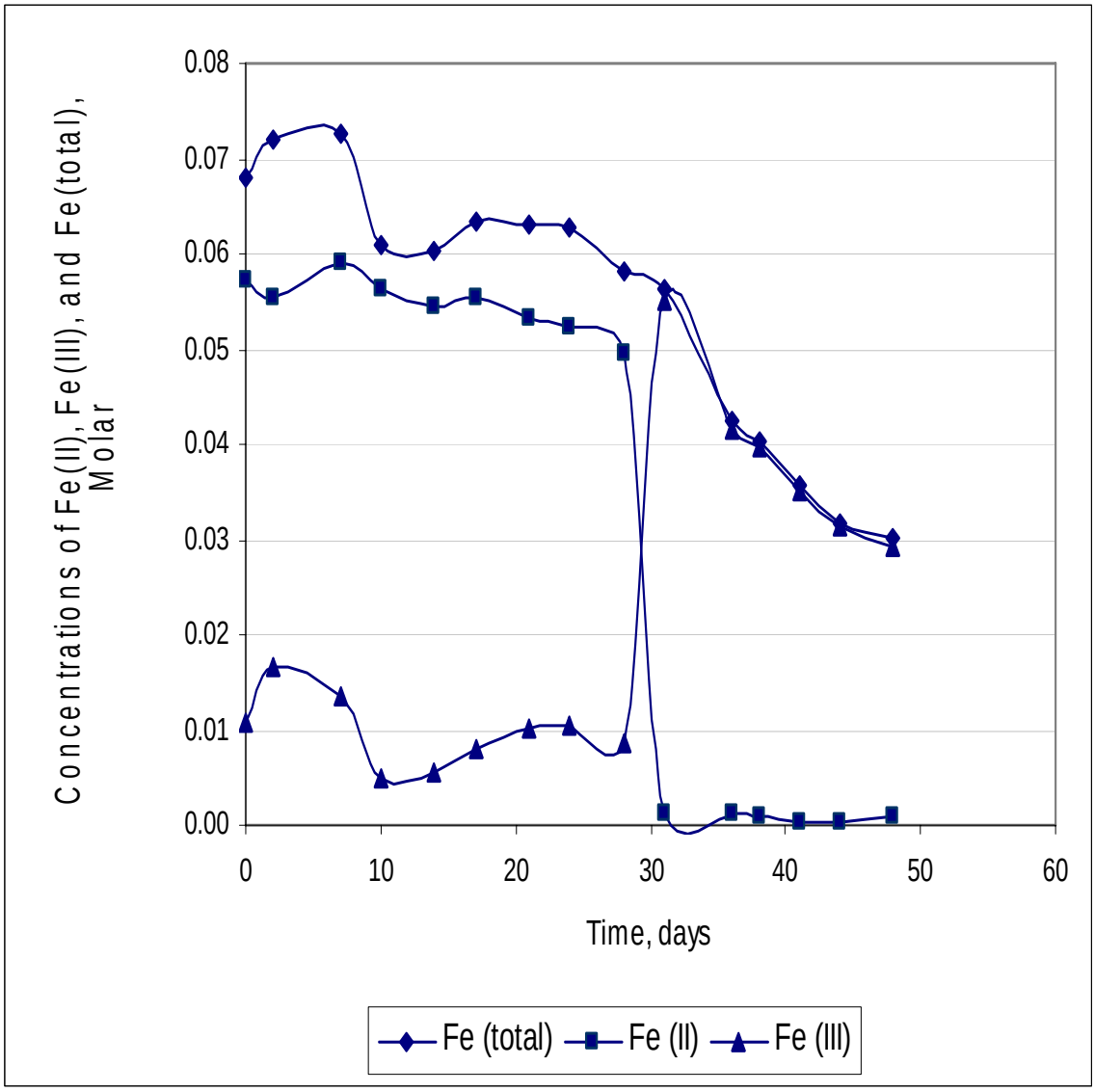

Figure 8. Concentrations of Fe(II), Fe(III), and Fe(total) during sphalerite leaching in bioleaching mode.

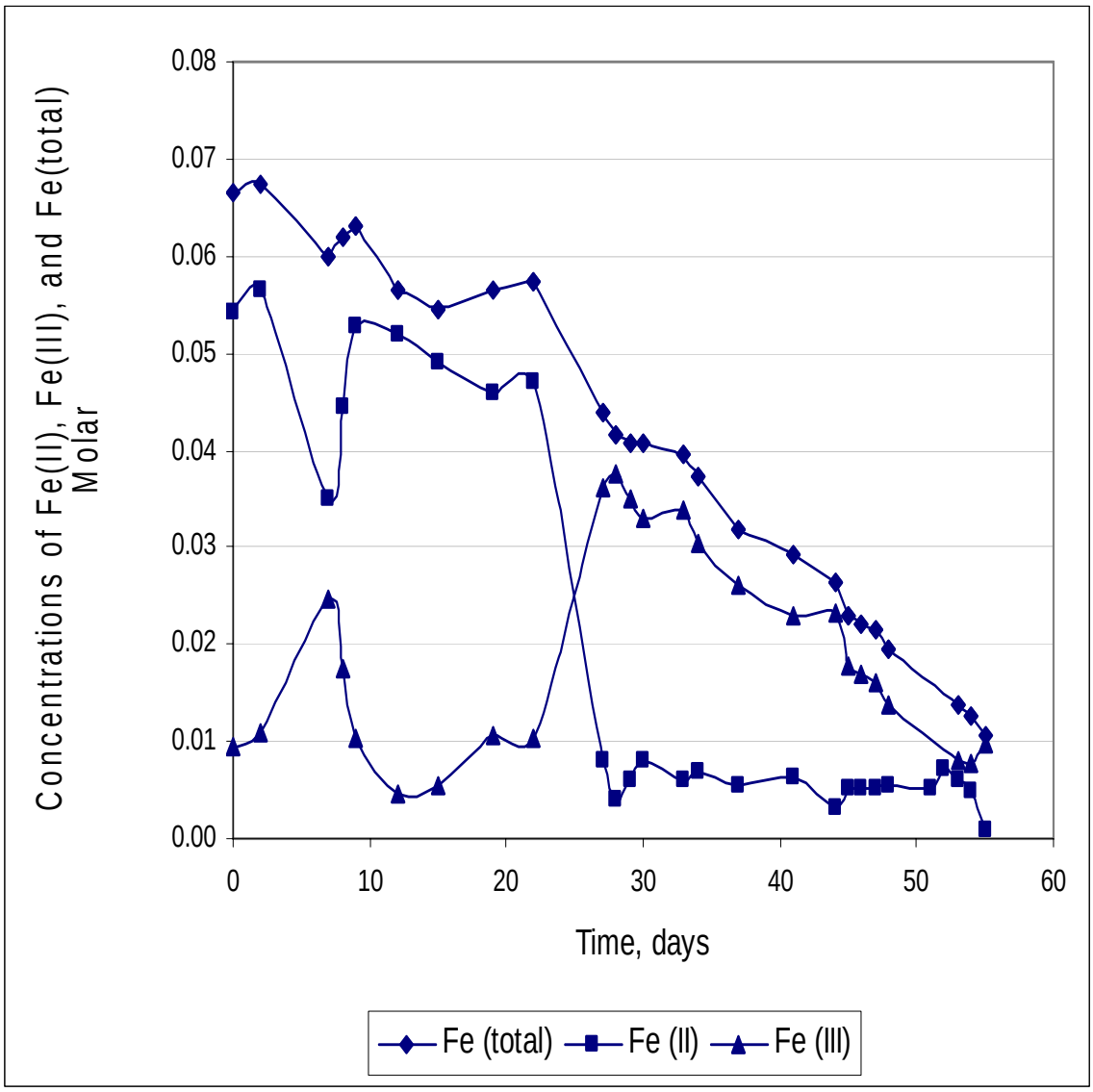

Figure 9. Concentrations of Fe(II), Fe(III), and Fe(total) during sphalerite leaching in electrobioleaching mode.

During the period up to 22 days, an amount of electricity is used to produce 0.029 molar of Fe(II) concentration. This electrical production of Fe(II) must help to shorten the incubation period from 28 to 22 days. As can be seen in Figure 9, the oxidation rate of Fe(II) at the incubation breaking point is 0.0156 mole/day which is virtually the same as that for bioleaching mode, and is 5.6 times larger than that for leaching chalcopyrite in electrobioleaching mode. This fast rate maintains a predominant concentration level of Fe(III), as seen in Figure 9, between 30 and 55 days, despite the continuous production of Fe(II) electrochemically, suggesting that the bio-oxidation rate of Fe(II) (reaction 1) is much higher than that of reaction 5.

The higher leaching conversion with the electrobioleaching mode in the middle stage, as shown in Figure 7, may be due to the fact that the combined effect of Fe(III) and microbial catalysis is larger than that for the bioleaching mode. The equality of the leaching conversion in the final stage may also be due to the equality of the combined effect of Fe(III) and microbial catalysis. The overall picture is that the leaching conversion did not improve much while the system was strenuously promoted by producing much Fe(II) ions in the electrobioleaching mode. This suggests that the indirect leaching reaction (reaction 5) takes place faster than the microbial catalysis reaction (reaction 8). This finding is reflected in the literature.[5]

The precipitation of soluble iron during the leaching reactions in the two modes of operation is shown in Figure 10. One can see from this figure that the precipitation is almost the same for the bioleaching and electrobioleaching modes. This may be because the time-average concentrations of Fe(III) are almost at the same level throughout the leaching. One important observation from Figure 10 is that the precipitation reaches almost 60% in 55 days at the leaching conversion of only 8.2%. This large loss of reagent may result from the mechanism in which once the incubation effect of the Fe(II) oxidation collapses, the oxidation of Fe(II) is accelerated by the microbial catalysis, and, as such, the produced Fe(III) is subject to precipitation. In the case of electrobioleaching mode, the situation is not much different. Fe(III) was reduced daily to Fe(II). However, once the incubation effect of the Fe(II) oxidation collapses, the microbial oxidation rate of converting Fe(II) to Fe(III) is overwhelmingly higher than the combined rate of electrochemical reduction and indirect leaching (reaction 5). This situation maintains the Fe(III) concentration in predominance which, in turn, causes the massive precipitation of the ferric ion. It is concluded then that the electrobioleaching mode is not better than the bioleaching mode. Furthermore, the bioleaching of sphalerite does not have salient advantages over chemical leaching with Fe(III) because iron precipitation would be smaller while achieving as much leaching conversion in the latter method.

The electrochemical reduction of Fe(III) to Fe(II) was conducted and the results are shown in Figure 9. The concentrations are the ones measured right after the electrochemical reduction took place. The reduction of Fe(III) was made using a total electricity of 20103 coulombs. This electricity produced 0.168 moles of Fe(II) from which the current efficiency was found to be 80.4%. This electricity is 4.2 times as much as was used in the electrobioleaching of chalcopyrite. As

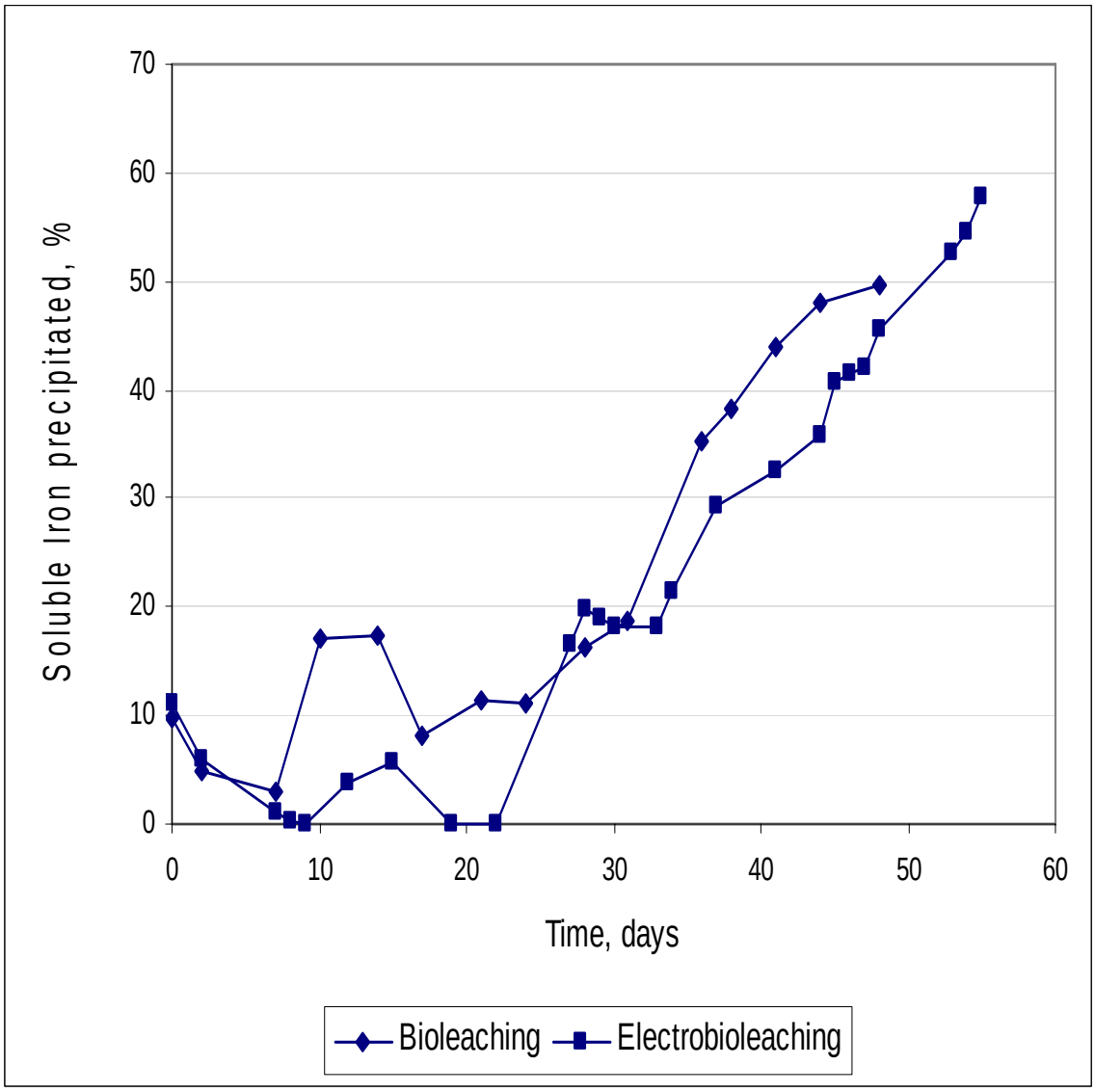

Figure 10. Precipitation of soluble iron during sphalerite leaching in bioleaching and electrobioleaching modes.

yet, the effect of microbial catalysis is lower than that of chalcopyrite leaching, as indicated by the differentials in leaching conversion between the two modes of operation (see Figures 2 and 7). The leakage of ions through the anionic membrane and/or rubber gaskets was determined. Over the 55-day period, the loss of soluble iron was 13.5% and the loss of zinc ion was 9.6%. This is similar to what was observed in the chalcopyrite leaching experiments.

The contribution made by each leaching mechanism (indirect and direct) in the early stages can be estimated using the data in Figures 6 and 7. The leaching conversion was 5.8% with 0.053 molar Fe(III) at 12 days, as shown in Figure 6, while it was 1.61% with 0.01 molar Fe(III) at 12 days, as shown in Figure 7. The former represents the indirect leaching mechanism and the latter represents the combination of the indirect and direct leaching mechanisms. The leaching of sphalerite with ferric sulfate follows the shrinking core model in the early stages.[9] The equation for the shrinking core model can be written as [12, 13]

$$1-(1-x)^{1/3}=\frac{k'Vc}{r_o}t \qquad (11)$$

where: x = leaching conversion
c = concentration of Fe(III)
k' = rate constant
V = chalcopyrite molar volume
r_o = average radius of chalcopyrite particle
t = reaction time

Equation 11 can be rewritten as

$$1-(1-x)^{1/3}=k'K'c \qquad (12)$$

where $K'=\frac{Vt}{r_o}$ and is the same for the two cases. By substituting the values previously mentioned into Equation 12, k_1'K' was found to be 0.372 liter/mole where k_1' is the rate constant for the indirect reaction (reaction 5). Also, (k_1'+k_2')K' was found to be 0.539 liter/mole where k_2' is the rate constant for direct reaction (reaction 8). Further calculations show that k_2' = 0.45k_1'. This is in meaningful contrast with that for chalcopyrite leaching. The rate constant of the bioleaching reaction of chalcopyrite (reaction 7) is more than twice than that of the rate constant of the chemical reaction (reaction 4). However, in the case of sphalerite, it is only 45% of the chemical reaction rate constant. This inequality of reaction rates has been delineated previously in this subsection.

4.3 Pyrite Leaching

As mentioned previously, the leaching conversion of pyrite could not be

determined. However, the values with the two modes were estimated by recovering unleached pyrite samples at the end of the experiments. The values were 11.5% for electrobioleaching mode and 8.1% for bioleaching mode. The ratio of the two is 1.42, which is somewhat smaller than what was found in the case of chalcopyrite leaching (1.52).

Figures 11 and 12 show the concentration variations with time of Fe(II), Fe(III) and Fe(total) during the leaching reactions using both bioleaching and electrobioleaching modes, respectively. Comparisons among Figures 3, 8, and 11 can distinguish the patterns with which Fe(II) concentration varies with time for the leaching of the three minerals. As can be seen in Figure 11, Fe(II) concentration drops initially and then is maintained at approximately the same level for 14 days, before dropping to small values. The plateau-like region may be due to the incubation effect of Fe(II) oxidation in the presence of pyrite. It can be seen that this effect with pyrite somewhat resembles that of sphalerite.

Comparison among Figures 4, 9, and 12 distinguishes the patterns with which Fe(II) concentration varies with time for the leaching of the three minerals in electrobioleaching mode. It can be seen, in Figure 12, that the incubation effect seen in Figure 11, is eliminated by the electrochemical reduction of Fe(III). It can also be seen that the pattern for pyrite, as shown in Figure 12, is almost identical to that of chalcopyrite (see Figure 4). This suggests that the leaching mechanisms of pyrite are based on those of chalcopyrite, especially in terms of the relationship between the leaching rates of the direct and indirect reactions, as well as the relationship between Fe(II) production and disappearance (reactions 3 and 1). This also suggests that the electrobioleaching of pyrite is viable for wider applications. The reduction was made three times for the entire period using 6241 coulombs to reduce 0.0526 moles of Fe(III) with a current efficiency of 81.3%.

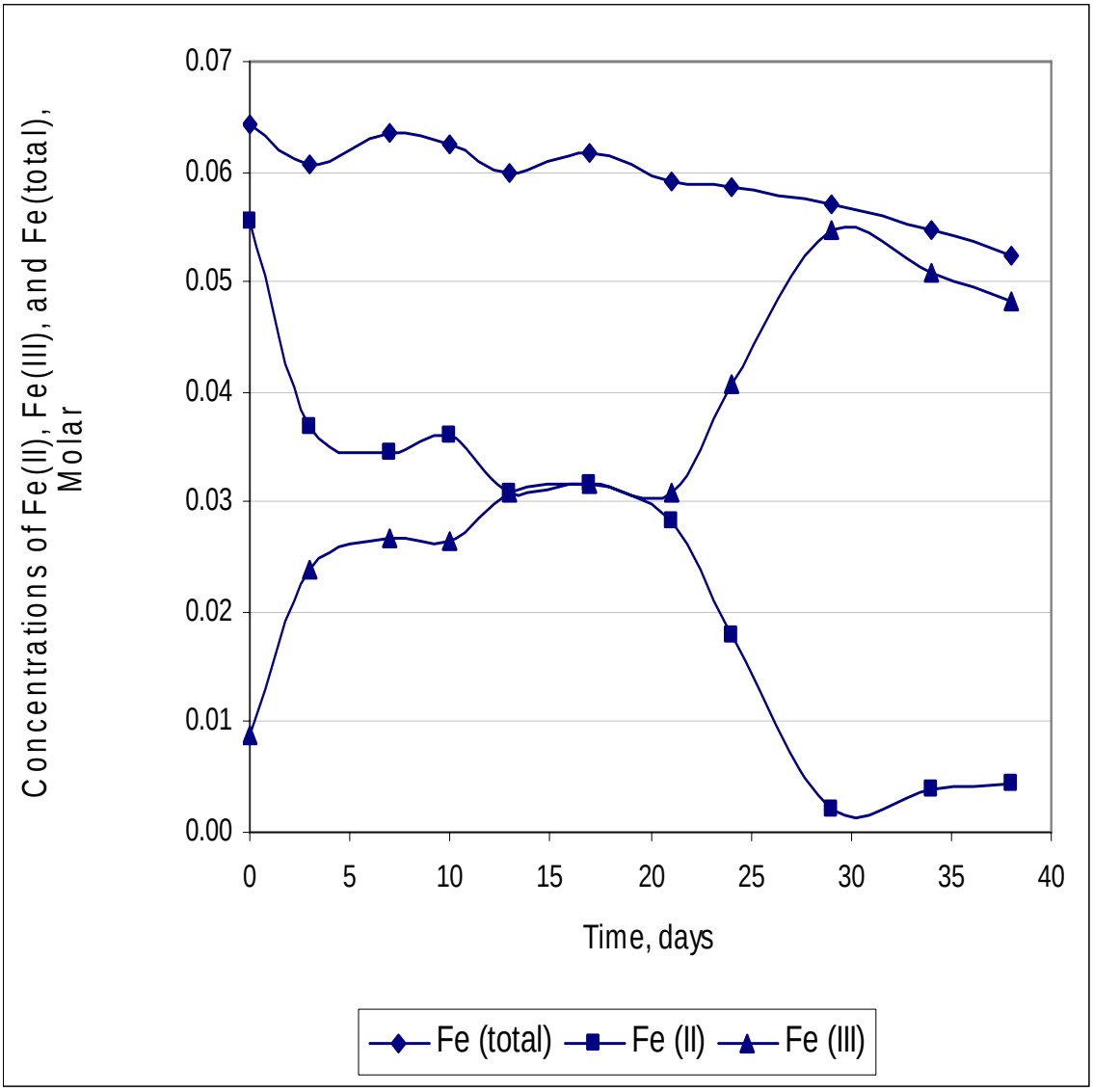

Figure 11. Concentrations of Fe(II), Fe(III), and Fe(total) during pyrite leaching in bioleaching mode.

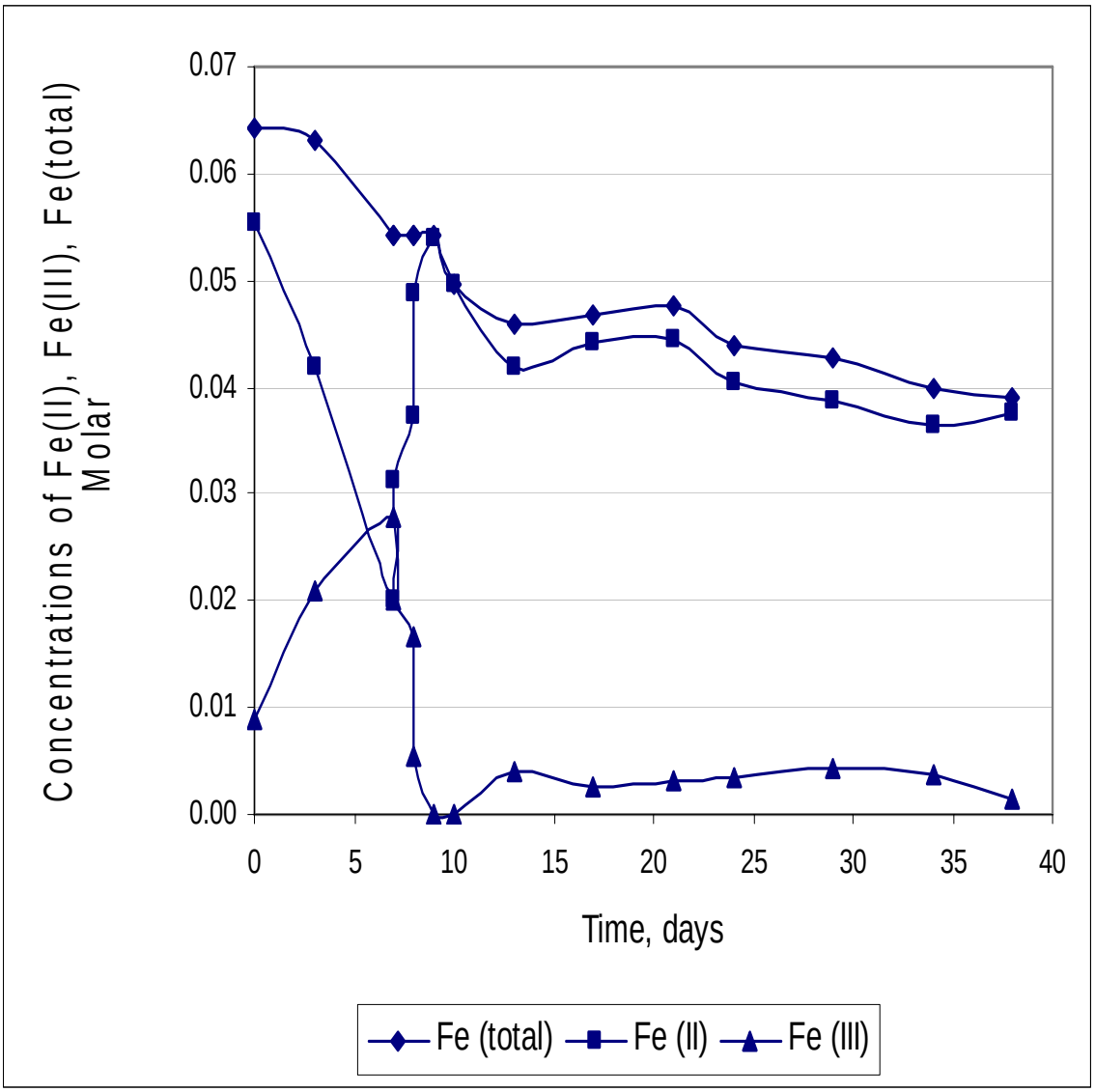

Figure 12. Concentrations of Fe(II), Fe(III), and Fe(total) during pyrite leaching in electrobioleaching mode.

CHAPTER 5 CONCLUSIONS

The electrobioleaching of chalcopyrite has advantages over the bioleaching of the mineral with respect to the fact that the leaching conversion is higher by 52%, while the total soluble iron precipitation is much lower, 4.5% versus 27.3%. The bioleaching rate is predominantly higher than the chemical leaching rate using only Fe(III). In addition to this, high levels of Fe(II) can be maintained by electrochemical reduction of Fe(III) which in turn minimizes the iron precipitation, and helps to grow the bacteria.

Nearly the opposite phenomena are observed for the electrobioleaching of sphalerite. This method of leaching is not an improvement over the bioleaching method. The microbial oxidation rate of Fe(II) to Fe(III) is much higher than the chemical leaching rate with Fe(III), which produces Fe(II). This mechanism tends to maintain a predominant level of Fe(III) concentration, which results in massive precipitation of iron, which in turn incapacitates the electrochemical reduction of Fe(III) to Fe(II).

The effect of electrobioleaching on pyrite is similar to that of chalcopyrite. The electrochemical reduction of Fe(III) to Fe(II) is pronounced and maintains a predominant level of Fe(II) concentration, which is the basis for accelerating the bioleaching of pyrite. The application of this electrobioleaching method on pyrite could be extended to applications like coal desulfurization and pretreatment of Carlin-type gold ore (refractory gold ore) in heap leaching.

BIBLIOGRAPHY

(1) M.E. Wadsworth, in Proceedings of 23rd Annual Conference of Metallurgists of Canadian Institute of Mining and Metallurgy, 1984, p.1.

(2) K.A. Natarajan, "Electrobioleaching of Base Metal Sulfides," Metallurgical Transactions B, February 1992, pp. 5-11.

(3) S.B. Yunker and J.M. Radovich, "Enhancement of Growth and Ferrous Iron Oxidation Rates of *T. ferrooxidans* by Electrochemical Reduction of Ferric Iron," Biotechnology and Bioengineering, 1986, vol. 28, pp. 1867-1875.

(4) Satoshi Nakasono, Norio Matsumoto and Hiroshi Saiki, "Electrochemical Cultivation of *Thiobacillus ferrooxidans* by Potential Control," Bioelectrochemistry and Bioenergetics, 1997, vol. 43, pp. 61-66.

(5) M. Boon and J.J. Heijinen, "Mechanisms and Rate Limiting Steps in Bioleaching of Sphalerite, Chalcopyrite and Pyrite with *Thiobacillus ferrooxidans*," in Proceedings of an International Biohydrometallurgy Symposium, Jackson Hole, Wyoming, August 22-25, 1993, Biohydrometallurgical Technologies vol. 1 – Bioleaching Process, edited by A.E. Torma, J.E. Wey, and V.I. Laksmanan, a publication of TMS, pp. 217-235.

(6) A. Malik, M.G. Dastidar, and P.K. Roychoudhury, "Factors limiting Bacterial Iron Oxidation in Biodesulphurization System," International Journal of Mineral Processing, 2004, vol. 73, pp. 13-21.

(7) A.E. Torma, C.C. Walden, and R.M.R. Branian, "Microbiological Leaching of Zinc Sulphide Concentrate," Biotechnology and Bioengineering, 1970, vol. 12, pp. 501-517.

(8) P.B. Munoz, J.D. Miller, and M.E. Wadsworth, "Reaction Mechanism for the Acid Ferric Sulfate Leaching of Chalcopyrite," Metallurgical Transactions B, June 1979, vol. 10B, pp. 149-158.

(9) J. Lochmann and M. Pedlik, "Kinetic Anomalies of Dissolution of Sphalerite in Ferric Sulfate Solution," Hydrometallurgy, 1995, vol. 37, pp. 89-96.

(10) J. E. Dutrizac, "Factors Affecting Alkali Jarosite Precipitation," Metallurgical Transactions B, December 1983, vol. 14B, pp. 531-539.

(11) Fathi Habashi, “Principles of Extractive Metallurgy,” vol. 1, p. 158, Science Publishers, New York, 1970.

(12) Zuo-Mei Jin, G. W. Warren, and H. Henein, “Reaction Kinetics of the Ferric Chloride Leaching of Sphalerite – An Experimental Study,” Metallurgical Transactions B, March 1984, vol. 15B, pp. 5-12.

(13) Eung Ha Cho, “Kinetics of Sodium Carbonate Leaching of Scheelite,” Journal of Metals, July 1988, vol. 40, no. 7, pp. 32-34.

Appendix 11: Coal Desulfurization Using Hypochlorite and Cupric Ion as a Catalyst – Feasibility Study

TECHNICAL REPORT

Contract Title and Number:	Period of Performance:
Establishment of the Center for Advanced Separation Technologies (DE-FC26-01NT41091)	Starting Date: 9/17/2001 Ending Date: 7/31/2005

Sub-Recipient Project Title:
Coal Desulfurization using Hypochlorite and Cupric Ion as a Catalyst – Feasibility Study

Report Information:
Type: Final
Number:
Period:
Date: 9/15/04
Code: WV005-FINAL

Principal Investigators: Eung Ha Cho
Co-investigators: Ray R-K Yang

Contact Address:
Department of Chemical Engineering
West Virginia University
P. O. Box 6102
Morgantown, WV 26506-6102

Contact Information:
Phone: 304-293-2111 x –2433
Fax: 304-293- 4139
E-Mail: Eung.Cho@mail.wvu.edu

Subcontractor Address:

No subcontracts issued.

Subcontractor Information:
Phone:
Fax:
E-Mail:

…

DISCLAIMER

ABSTRACT

Wet desulfurization of Pittsburgh No. 8 coal and Illinois No. 6 coal were conducted with sodium hypochlorite in the laboratory. Pittsburgh No. 8 coal was leached by hypochlorite at high pHs in one step process. The hypochlorite concentration varied from 0.2 to 0.6 molar; sodium hydroxide concentrations from 0.2 to 0.8 molar; and temperature was at the levels of 80 and 90°C. The desulfurization of Illinois No. 6 coal was conducted in three consecutive steps of pretreatment in concentrated ammonia at room temperature, leaching with hypochlorite at room temperature and hydrolysis in a sodium hydroxide solution at 90°C. In the leaching step, hypochlorite concentration varied from 0.2 to 0.8 molar.

In the early stages of this project, it was found that cupric ammine and hypochlorite could not be prepared in the same solution because ammonia used to solubilize cupric ions reacts with hypochlorite. Thus, all the subsequent work was conducted with leach solutions containing only hypochlorite without addition of cupric ammonia.

The desulfurization method of Pittsburgh No. 8 coal was found to reduce mainly pyritic sulfur. More than 70% of pyritic sulfur removal was achieved at the optimum conditions of 0.4 molar hypochlorite, 0.4 molar sodium hydroxide and 90°C. The desulfurization method for Illinois No. 6 coal was capable of reducing significant amounts of organic sulfur. The removal of organic sulfur achieved a 37.8% reduction at the optimum operation of leaching at 0.4 molar hypochlorite and room temperature followed by hydrolysis at 0.3 molar sodium hydroxide and 90°C. The chlorine content in the coal produced by the chlorination during leaching was kept below the threshold value of 0.3% at the optimum conditions of the desulfurization method for each coal.

TABLE OF CONTENTS

LIST OF FIGURES

LIST OF TABLES

CHAPTER 1

Introduction

Coal is a very complex material and its chemical composition varies widely. Of all the elements found in coal, sulfur is the single most important one which impedes the utilization of coal as a clean fuel. Many U.S. steam coals contain high percentages of sulfur which must be reduced as air pollution regulations become increasingly more stringent. According to Clean Air Acts of 1976 and 1990, sulfur dioxide emission from coal-fired power plants should be limited to 1.2 lb/MBTU, which can be translated to a total sulfur content in normal coal below 0.8 wt%.

Coal has three sources of sulfur: pyritic, organic and sulfate sulfur. The distribution of these sulfur contents and the total sulfur vary greatly from coal to coal produced in the U.S.. The total sulfur varies in the range of 2-4wt% and the organic sulfur and pyritic sulfur contents are almost equally partitioned in many coals. The sulfate sulfur content is usually very small with its content being lower than 0.2%.

Pyritic sulfur refers to ferrous disulfide (FeS_2). Much of the pyritic sulfur can be removed by physical separation methods such as gravity separation and froth flotation processes. The froth flotation process can remove up to 50% pyritic sulfur. However, the limitation of physical cleaning methods is that very fine pyrite particles are disseminated in the coal particles and those that are not exposed to the surface and not liberated are not amenable to physical separation.

Organic sulfur is part of, and chemically bonded to the coal matrix and it cannot be removed unless the chemical bonds holding it are broken. Meyers (Meyers, 1977a) summarized the structure of the organic sulfur in the coal to include mercaptans (RSH), sulfides (R – S – R'), disulfides (RS – S – R') and thiophenes where R and R' stand for hydrocarbon groups. For mercaptans, R stands for aliphatic groups. The structure of dibenzothiophene is characterized by:

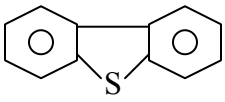

It is reported that certain forms of organic sulfur are amenable to removal by hypochlorite (Brubaker and Stoicos, 1985).

Many chemical methods were developed in the past; however, none has been commercialized. The Meyers process (Meyers, 1977b) uses ferric chloride solutions to remove pyritic sulfur. However, it requires rigorous operating conditions. It used six one-hour leachings with one-molar ferric chloride at 100°C to achieve more than 95% pyritic sulfur removal. Organic sulfur is generally much more difficult to remove than pyritic sulfur. A solvent of p-cresol was identified as a chemical to reduce organic sulfur (Meyers, 1977c). It is reported that a leach with p-cresol for 3 hours at 200°C achieved the average organic sulfur reduction of 47 wt. % for Indiana No. 5 seam coal.

The Chlorinolysis process was developed by Hsu et al. (Hsu et al., 1977). Chlorine gas and methyl chloroform were utilized to leach pyritic and organic sulfur at 74°C. Methyl chloroform was used to solubilize bubbled chlorine gas. The coal matrix was chlorinated during the leaching. The chlorine content in the coal reached up to 25% in two hours. The coal was effectively dechlorinated by treating it with steam at a temperature of 500°C. This process could remove up to 70% of organic sulfur and 77% of pyritic sulfur, and 76% of total sulfur.

Cho (Cho, 1989) conducted a similar study in a system where Sewickley seam coal was leached in a 0.1-N hydrochloric acid solution through which chlorine gas was bubbled. The results showed that most of the pyritic sulfur and approximately 40% of the organic sulfur were removed at room temperature. It was observed that the chlorine content in the leach coal reached up to 31%.

A similar desulfurization scheme with sodium hypochlorite (Brubarker and Stoicos, 1985), was utilized and removed substantial amounts of organic sulfur but not much pyritic sulfur from Illinois No. 6 coal. Further treatment with sodium carbonate at 80°C (hydrolysis) reduced the organic sulfur additionally. The organic sulfur was reduced by 62% when different coals were leached and subsequently hydrolyzed for one hour each, and this treatment was repeated. The pyritic sulfur was reduced by only 23% under the same treatment. Another interesting result of this leaching scheme was that hypochlorite chlorinated the coal matrix only slightly, or much less severely, than aqueous chlorine. It was observed that the chlorine levels in the coal ranged between 2 and 2.7%.

The disadvantage of the use of aqueous chlorine in the Chlorinolysis process is that it chlorinates the coal matrix extensively and that treatment at a high temperature (500°C) is needed to restore the chlorinated coal. The cost of this treatment is high so that the entire desulfurization process with aqueous chlorine would not be feasible for commercialization. However, Brubaker and Stoicos (Brubaker and Stoicos, 1985) have proven that desulfurization with hypochlorite does not readily chlorinate the coal structure, while it can reduce the organic sulfur as well as the aqueous chlorine process.

The objectives of this study are:

(1) To explore a proper desulfurization method by which Pittsburgh No. 8 coal and Illinois No. 6 coal can be leached effectively with hypochlorite;
(2) To determine the effects of parametric conditions such as hypochlorite concentration, pH and temperature on the desulfurization;
(3) To determine the optimum operating conditions in consideration of the maximum sulfur reduction and minimum coal loss by hypochlorite oxidation;
(4) To determine the technical feasibility for commercialization of this technology by considering the leaching conditions and sulfur reductions.

CHAPTER 2

Theory

2.1 Chlorine Solution Chemistry

Sodium hypochlorite solution is not stable at low pHs due to the equilibrium reactions of chlorine (Garrels, 1965):

$$HClO = H^+ + ClO^- \qquad K = 3.3 \times 10^{-8} \qquad (1)$$

$$HClO + Cl^- + H^+ = Cl_{2\,(aq)} + H_2O \qquad K = 2.3 \times 10^{3} \qquad (2)$$

$$Cl_{2\,(g)} = Cl_{2\,(aq)} \qquad K = 0.02 \qquad (3)$$

$$Cl_{2\,(aq)} + Cl^- = Cl_3^- \qquad K = 0.2 \qquad (4)$$

where K is the equilibrium constant at 25°C. At high pH (>10), hypochlorite ClO^- is predominant. Hypochlorous acid, HClO, will become dominant when pH decreases. At pH 7.5, the two species have the same concentration. Below 7.5, aqueous chlorine will form and escape as gaseous chlorine. So sodium hydroxide should be added to the hypochlorite solution to maintain high pH and stabilize the original hypochlorite concentration.

2.2 Hypochlorite Leaching

Some of the organic sulfur in coal may exist as carbon sulfide and disulfide. These sulfides react with hypochlorite to produce sulfonyl chloride ($RSOCl^-$) as shown (Hsu et al., 1977):

$$R - S - R' + 2ClO^- = RSClO^- + R'ClO^- \qquad (5)$$

$$RS - S - R' + 2ClO^- = RSClO^- + R'SClO^- \qquad (6)$$

R and R' stand for the hydrocarbon groups and S refers to sulfur. The sulfonyl chloride is further oxidized to sulfonate or sulfate:

$$2RSClO^- + H_2O + 3ClO^- = 2RSO_3H + 5Cl^- \qquad (7)$$

$$RSClO^- + 3H_2O = RCl + 6H^+ + SO_4^{2-} + 5e \qquad (8)$$

Reactions (7) and (8) are electrochemical reactions and their corresponding anodic reactions are:

$$RSClO- + 2H2O = RSO3H + 3H+ + Cl- + 3e \qquad (9)$$

$$RSClO^- + 3H_2O = RCl + 6H^+ + SO_4^{2-} + 5e \qquad (10)$$

And the cathodic reaction is:

$$ClO^- + 2H^+ + 2e = Cl^- + H_2O \qquad E^0 \text{ (at 25ºC)} = 1.72 \text{ eV} \qquad (11)$$

Pyritic sulfur also can be leached with hypochlorite. The anodic reaction is:

$$FeS_2 + 11H_2O = Fe(OH)_3(s) + 2SO_4^{2-} + 19H^+ + 15e$$

$$E^0 \text{ (given in cathodic reaction at 25ºC)} = -0.4 \text{ eV} \qquad (12)$$

Then the overall reaction is:

$$2FeS_2 + 15ClO^- + 7H_2O = 2Fe(OH)_3(s) + 15Cl^- + 4SO_4^{2-} + 8H^+ \qquad (13)$$

$$\Delta G^o \text{ (at 25ºC)} = -1466.6 \text{ kcal/mole}$$

The magnitude of ΔG^o suggests that the overall reaction is thermodynamically very spontaneous under normal conditions.

The second step of the desulfurization is the hydrolysis step in which further removal of the organic sulfur and dechlorination will take place. In this step, the leach coal will be treated in a solution containing sodium hydroxide around 90°C. The following reactions may take place in the hydrolysis step:

$$RCl + OH^- = ROH + Cl^- \qquad (14)$$

$$RSO_3H + H_2O = ROH + 2H^+ + SO_3^{2-} \qquad (15)$$

2.3 Coal Oxidation with Hypochlorite

It is known that coal can be oxidized with hypochlorite, resulting in its weight loss. It is reported that sodium hypochlorite oxidizes Illinois No. 6 coal. The oxidation yields several products, depending on the pH and the kind of the coal (Mayo and Kirshen, 1979; Chakrabartty, 1978; Mayo, 1975). The products vary from black, high-molecular weight, bicarbonate-soluble acids to the benzene polycarboxylic acids and carbon dioxide. For example, at pH 13, 96% of the coal was dissolved and 80% of the dissolved carbon was found as the high-molecular-weight acids (Mayo and Kirshen, 1979). Between pH 9 and 11, the production of soluble acids was lower while that of CO_2 was higher. Below pH 9 more coal structure was destroyed — simple, oxidation-resistant benzene and aliphatic carboxylic acids were the principle organic products in the solution. According to Chakrabartty (Chakrabartty, 1978), Mayo and Kirshen studied the oxidation of Illinois No. 6 coal with hypochlorite. It was found that in one experiment, 80% loss of the original carbon was accounted for as follows: 13.6% in undissolved residue, 59.4% in colored acids soluble in aqueous bicarbonate, 7.1% in lighter colored acid readily soluble in water and 19.9% in

carbon dioxide. The colored acids had an average molecular weight of 900 g and the water soluble acids had a molecular weight of about 200 g.

CHAPTER 3

Experimental Methods

3.1 Materials

Pittsburgh No. 8 coal and Illinois No. 6 coal were used in this study. Pittsburgh No. 8 coal was obtained from the Fair Fax Mine #3, Anker Energy, Morgantown, WV. Illinois No. 6 coal (IBC 101) was obtained from the Illinois Geological Survey. A bulk Pittsburgh No. 8 coal sample was crushed and screened to produce a 65 ×150 mesh fraction. This fraction was floated by the conventional froth flotation techniques. The concentrate was dried and used in this study. Illinois No. 6 coal (IBC 101) sample was also crushed and screened to produce a 65 ×150 mesh fraction. This fraction was used for leaching experiments directly without further treatment by froth flotation because the original coal already has a low ash content. These fractions were analyzed and the results are given in Table 1.

Table 1. Analytical Results of Untreated Coal

	Pittsburgh No. 8	IBC 1
Ash (%)	8.18	8.02
Pyritic sulfur (%)	0.82	0.33
Organic sulfur (%)	1.60	3.33
Sulfate sulfur (%)	0.02	0.10
Total sulfur (%)	2.44	3.76
Total acid (mmol/g)	0.47	3.14
Chlorine content (%)	0.06	0.03
Moisture content (%)	1.25	4.67

Hypochlorite solutions to be used for the leaching experiments were prepared by diluting the hypochlorite stock solution which was purchased from a chemical supplier. The purchased chemical was 2.14 molar hypochlorite concentration and pH 12.3 - 12.6. This stock solution was kept in a refrigerator to minimize the loss due to evaporation.

3.2 Experimental Apparatus

The leaching experiments for Pittsburgh No. 8 coal and the hydrolysis experiments for Illinois No. 6 coal were conducted in a one-liter reactor placed in a constant-temperature paraffin-oil bath (Figure 1). The reactor has four necks. The central neck was equipped with a stirrer connected to a variable-speed motor. The stirring speed was 500 rpm for all the experiments. One of the side necks was fitted with a reflux condenser which was used to prevent excessive evaporation at high temperatures. The third neck was equipped with a thermometer which was used to measure the temperature of the solution. And the last one was used for charging the coal sample and/or pipetting solution to analyze its chlorine concentration.

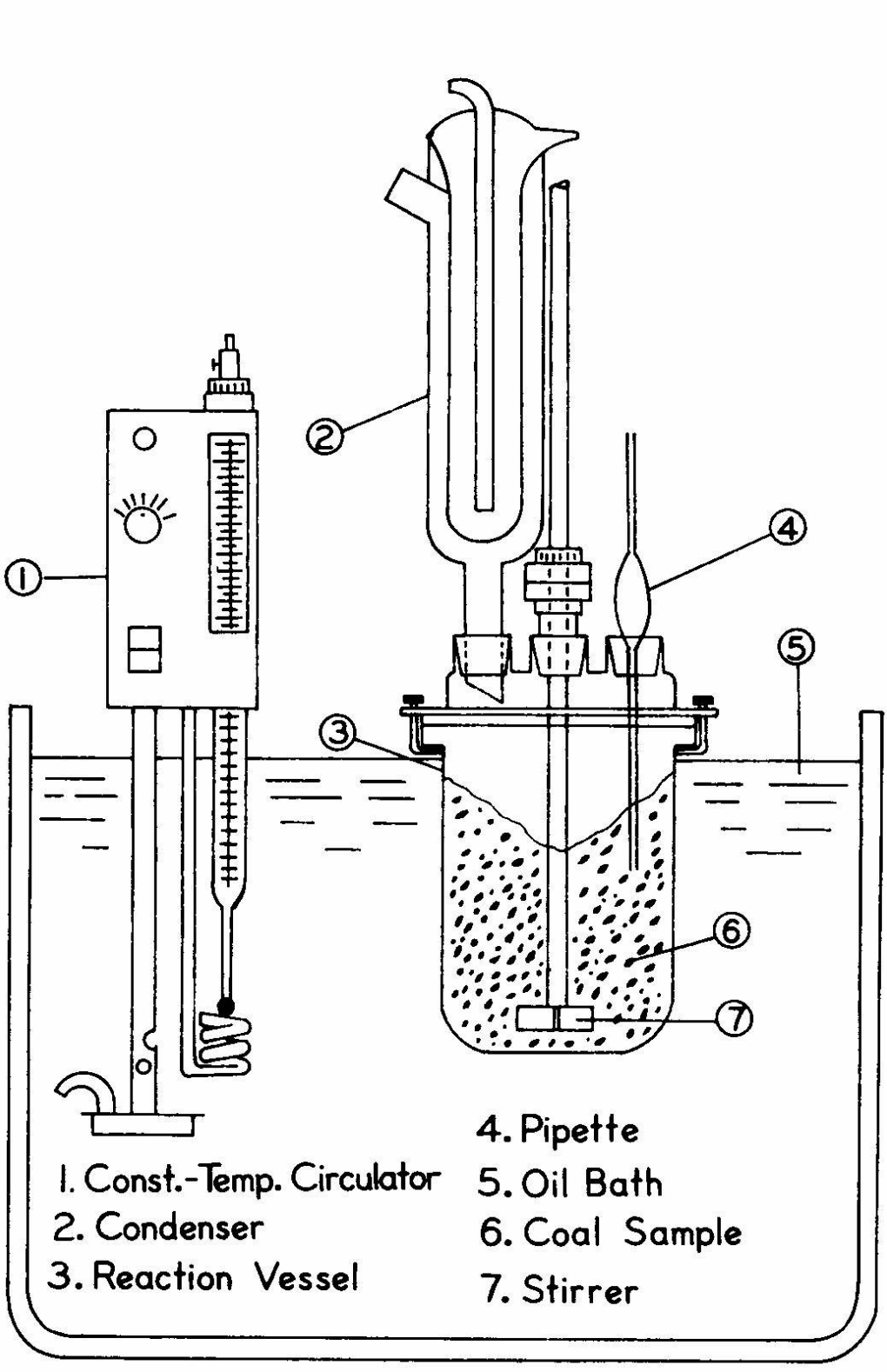

Figure 1. Schematic diagram of leaching apparatus.

3.3 Experimental Procedures

3.3.1. Pittsburgh No. 8 Coal:

A 500-ml hypochlorite solution at the desired concentration was charged into the reactor. When the leach solution reached the desired temperature, twenty grams of coal sample was added to the reactor. The leaching continued for 2 hours. After leaching, the coal slurry was filtered on Whatman No. 1 filter paper. The filtered coal was dried naturally in air for overnight, weighed and analyzed for total sulfur, pyritic sulfur, sulfate sulfur, chlorine content and ash content. Leaching conversions of pyritic sulfur and organic sulfur were determined using these data.

3.3.2. Illinois No. 6 Coal:

It was found that the procedures taken for the leaching of Pittsburgh No. 8 coal was not suitable for leaching Illinois No 6 coal, mainly due to the excessive loss of Illinois No. 6 coal during leaching. Thus, an alternate method was explored and adopted to leach this coal more effectively. The method consisted of three steps of ammonia pretreatment, leaching with hypochlorite at room temperature and hydrolysis at high pH and high temperature.

Twenty grams of coal was pretreated at room temperature with 50 ml of a concentrated ammonia hydroxide solution in a 250-ml beaker. The coal was stirred on a magnetic stirrer at a stirring speed fast enough to keep the particles in suspension. The coal was stirred for one hour, filtered through Whatman No. 1 paper and dried under an infrared lamp. The dried coal was then leached at room temperature with a 100 ml hypochlorite solution in a 250-ml beaker. The coal was stirred for one hour, then filtered and dried in the same way as in the pretreatment. About 2 grams of the dried coal was taken for analyses for total sulfur, pyritic sulfur, chlorine content and ash content. The remaining coal sample was then hydrolyzed.

The hydrolysis was conducted in the reactor shown in Figure 1. A 500 ml sodium hydroxide solution was charged to the reactor and when the temperature reached 90°C, the leach coal was added to start hydrolysis. After hydrolysis for one hour, the coal was filtered on Whatman No. 1 paper and dried in the same way as in the pretreatment. About 2 grams of the dried coal was taken to be analyzed for total sulfur, pyritic sulfur, chlorine content and ash content. This is the end of the first cycle. The second cycle was performed in order to reduce more of the sulfur content by repeating the leaching and hydrolysis processes. The leaching was conducted with the dried coal which resulted from the hydrolysis step of the previous cycle. All the procedures were the same as in the first cycle.

3.4 Experimental Conditions

Table 2 encompasses the experimental conditions applied. The conditions were designed to determine their effects on the coal desulfurization.

Table 2. Experimental Conditions

	Pittsburgh No. 8	IBC 101
Leaching temperature, °C	50, 60, 70, 80, 90	Room temperature
Hypochlorite concentration in leaching solution, M	0.2, 0.3, 0.4, 0.6	0.2, 0.4, 0.6, 0.8
Sodium hydroxide concentration in leaching solution, M	0.2, 0.3, 0.4, 0.8	0, 0.1
Leaching time, hr	2	1
Sodium hydroxide concentration in hydrolysis, M	N/A	0.1, 0.3

3.5 Analyses

Total sulfur was analyzed according to ASTM method D3177-84, (Eschka Method). A weighed sample was well mixed with Eschka mixture and burned in a furnace at 800°C. All the sulfur transformed into sulfate and was dissolved into hot water. And the sulfate was precipitated as barium sulfate, which was filtered, burned in a furnace and weighed. Total sulfur was also analyzed by an elemental analyzer. The elemental analyzer was a Flash 1112 instrument, manufactured by ThermoQuest. Most of the Illinois No. 6 coal samples were analyzed by this method. Both methods were reliable in analyzing the total sulfur content. For example, the untreated Illinois No. 6 coal was analyzed for total sulfur by both methods at virtually the same level of 3.76%.

Pyritic sulfur was analyzed according to ASTM method D2492-84. Coal was leached with hydrochloric acid (2+3) solution (2 volumes of concentrated HCl and 3 volumes of water) to remove non-pyritic iron and the left-over pyrite was again leached with nitric acid (1+7) solution (1 volume of concentrated HNO_3 and 7 volumes of water). The solubilized iron was determined by Perkin-Elmer Atomic Absorption Spectroscopy, which was stoichiometrically converted to pyritic sulfur.

Sulfate sulfur was analyzed according to ASTM method D2492-84. Sulfate sulfur was extracted together with non-pyritic iron using hydrochloric acid (2+3) solution and was precipitated as barium sulfate. The precipitate was filtered, burned in a furnace and weighed.

Organic sulfur was calculated by subtracting the combination of pyritic sulfur and sulfate sulfur from the total sulfur.

Ash content in coal was analyzed according to ASTM method D2795-85 and moisture content was analyzed according to ASTM method D3173-87.

Chlorine content in the coal was analyzed according to ASTM method D2361-85, (Eschka Method). A slight modification of the ASTM method was made. In this analytical method, nitrobenzene was not used but the precipitate of AgCl was filtered before Ag-containing solution was titrated with potassium thiocyanate. A 5-ml indicator solution of ferric ammonium sulfate was added to the filtrate instead of 8 to 10 drops suggested by the ASTM method. This modification was made for better detection of the color change at the end point.

Chlorine concentration of the hypochlorite solution was analyzed according to ASTM method D2022-64. Solid potassium iodide was added to the chlorine-containing solution and dissolved. The solution was acidified by adding concentrated acetic acid. The aqueous chlorine oxidizes the iodide to iodine, which was titrated by sodium thiosulfate solution using starch as an indicator.

The concentration of the total acidic groups on the coal surface was analyzed in order to particularly explain the drastically different leaching behaviors between Pittsburgh No. 8 coal and Illinois No. 6 coal. The method adopted by Luo (Luo, 1994) was used for the determination of total acidic groups on the coal surface. The coal sample was contacted with barium ion in a solution. The barium ion exchanged with the H^+ ion in the carboxylic and phenolic groups to form precipitates on the coal surface. The H^+ ions were produced. The following reactions were involved:

$$2RCOOH(s) + Ba^{2+} = (RCOO)_2Ba(s) + 2H^+ \quad (16)$$

$$2ArOH(s) + Ba^{2+} = (ArO)_2Ba(s) + 2H^+ \quad (17)$$

where the (s) denotes a solid species at the coal surface, RCOOH is carboxylic acid group and ArOH stands for phenolic group. The total acidic groups are taken as the combination of carboxylic and phenolic groups. The H^+ ions produced according to reactions 16 and 17 were titrated with sodium hydroxide solution.

For determination of the total acidic group content on coal, one gram of as-received or oxidized coal sample was transferred into a 200 ml plastic bottle. Before transferring the sample, the bottle was purged with nitrogen, and while still purging, 100 ml of 0.3 N $Ba(OH)_2$ solution was pipetted into the bottle. The bottle was then sealed and agitated at room temperature on a shaker for 16 hours. The contents of each bottle with nitrogen purging was vacuum-filtered using No. 1 Whatman filter paper. Immediately after this filtration step, 25 ml of the filtrate was pipetted into the titrator cup, which already contained 30 ml of 0.3 N HCl and 10 ml of CO_2-free distilled water, and this solution was titrated with 0.2 N NaOH using m-cresol purple as the indicator. A blank titration was also performed so that the content of total acidic groups in the coal (in meq/g coal) could be calculated. These procedures determined the concentrations of $Ba(OH)_2$ in the blank test and the test with coal sample. The difference in concentrations of $Ba(OH)_2$ in these two tests determined the concentration of the total acidic groups.

CHAPTER 4

Results And Discussion

In the early stages of this research, many preliminary experiments were conducted to find ways to effectively leach the sulfur components from Pittsburgh No. 8 and Illinois No. 6 coals. It was found that Pittsburgh No. 8 coal could best be leached with a one step process at high temperatures. Pretreatment with ammonia solution or hydrolysis at high temperature and high pH was not found particularly effective. Thus, only the leaching step was applied to Pittsburgh No. 8 coal in this study. In the case of Illinois No. 6 coal, all the consecutive steps of pretreatment, leaching and hydrolysis were found to be necessary for effective reduction of sulfur content. Thus, all these steps were applied to the desulfurization of Illinois No. 6 coal in this study.

It was observed that the coal weight was reduced through leaching or hydrolysis particularly for Illinois No. 6 coal. Weighing the coal sample before and after treatment was not used to determine the weight loss because very fine particles produced from each step could not be recovered through filtration. This was because the filtration rate was so low that a part of the slurry solution was decanted in order to speed up the filtration. The loss of coal was determined by comparing the ash contents in the coal. The assumption was that coal ash was not dissolved through each step. Also, the weight loss of coal due to the sulfur reduction was considered to be negligible. The calculation was based on a proportionality relationship. The loss was extrapolated into an x-y plot where y axis is weight loss and x axis is ash content of the leach coal. It ranges from y = 0 when x is the same as that of the original coal to y = 100% when x = 100%. For example, when the ash content of the leach coal is 10% and the ash content of the original coal is 8%, the weight loss would be the product of the slope of the line (100/(100-8)) and the x axis value (10 -8):

$$\frac{100}{100-8} \times (10-8) = 2.17\%$$

Throughout all the leaching experiments for Pittsburgh No. 8 coal and Illinois No. 6 coal, sulfate sulfur content was found to be very small (less than 0.01%); thus, sulfate sulfur was not included in the calculation for organic sulfur content.

4.1 Pittsburgh No. 8 Coal

Three series of experiments were conducted; namely, those for temperature effect, pH effect and concentration effect. It was found throughout all the experiments that the loss of coal due to oxidation with hypochlorite was negligible.

Hypochlorite leaching was conducted at 50, 60, 70, 80 and 90°C. No solid sodium hydroxide was added to the hypochlorite solution for this series of experiments. Table 3 presents the leaching results.

**Table 3. Effect of Temperature on the Desulfurization of Pittsburgh No. 8 Coal ([OCl^-] = 0.49 molar, pH 12.6, 2 hours)*

Temperature, °C	50	60	70	80	90
TS, %	1.86(23.8)	1.78(27.0)	1.70(30.0)	1.66(32.0)	1.55(36.5)
PS, %	0.25(70.0)	0.24(70.7)	0.22(73.2)	0.22(73.2)	0.18(78.0)
OS, %	1.61(----)	1.54(3.8)	1.48(7.5)	1.44(10.0)	1.37(14.4)
Cl, %	0.71	0.72	0.79	1.30	1.35

*Values in parentheses are reduction percentages.

The reduction percentage values obtained through the leaching process are given in parentheses and were calculated based on the amount of total sulfur, pyritic sulfur or organic sulfur in the original coal. Table 3 shows that the reduction in total sulfur (TS), pyritic sulfur (PS) or organic sulfur (OS) increases as the temperature increases. The total sulfur was reduced by 36.5% at 90°C. This is the highest reduction value in this series. The reduction values in total sulfur are mainly attributed to the reductions in pyritic sulfur not by those in organic sulfur. The pyritic sulfur content was reduced by 70% at 50°C and 78% at 90°C. However, very small amounts of organic sulfur were reduced. The organic sulfur was reduced by 14.4% at 90°C, which is the maximum reduction in this series. Table 3 also shows that the chlorine content in the leach coal increases with increasing temperature. The chlorine content reaches 1.35% at 90°C. This is well above the generally accepted threshold value of 0.3% chlorine in coal (Wandless, 1957).

The temperature effect on the leaching rate of pyritic sulfur is generally very small, which suggests that the leaching may be limited by a diffusion process such as pore diffusion inside the coal particle. It seems that most of the organic sulfur (e.g., 80%) is not amenable to leaching by hypochlorite. This suggests that the organic sulfur structures in Pittsburgh No. 8 coal mainly are those which are intrinsically difficult to be leached out by hypochlorite.

Since the reduction in sulfur forms is at maximum at 90°C as shown in Table 3, this temperature was used for all the subsequent series of experiments for the Pittsburgh No. 8 coal. The next series was conducted particularly in order to reduce the chlorine content in the leach coal by adding various amounts of solid sodium hydroxide, i.e., by changing the pH of the hypochlorite solution. The results are given in Table 4.

Table 4. Effect of pH on the Desulfurization of Pittsburgh No. 8 Coal (90°C, [OCl^-] = 0.4 molar, 2 hours)*

pH	11.47	12.46	13.01	13.14	13.23
NaOH, M	0	0.035	0.2	0.4	0.8
TS, %	1.94 (20.5)	1.73 (29.1)	1.58 (35.2)	1.56 (36.1)	1.68 (31.1)
PS, %	0.53 (35.4)	0.34 (58.6)	0.24 (70.8)	0.24 (71.1)	0.30 (63.7)
OS, %	1.41 (11.8)	1.39 (13.1)	1.34 (16.2)	1.32 (17.3)	1.38 (13.6)
Cl, %	1.75	1.51	0.56	0.30	0.37

* Values in parentheses are reduction percentages.

The pH was varied from 11.47 to 13.23 as shown in Table 4. It is seen that the chlorine content decreases from 1.75 to 0.3% as pH increases from 11.47 to 13.14. However, further increase in pH from 13.14 to 13.23 increases the chlorine content from 0.30 to 0.37%. These results show that there is a minimum value of the chlorine content at pH 13.14, or at 0.4 molar sodium hydroxide. The data in Table 4 show that at pH 13.14, the reduction of TS, PS and OS is at maximum or the sulfur contents are at minimum. This may be explained by two reaction mechanisms that take place simultaneously during the leaching process: one is the leaching reaction and the other is hydrolysis. The leaching rate of the sulfur forms would increase with decreasing pH because decreasing pH would increase the rate of the cathode reaction of hypochlorite dissociation (Equation (11)). However, the hydrolysis (Equations (14) and (15)) increases as pH increases. This hydrolysis in turn increases the reduction in the sulfur forms and decreases chlorine content. The decrease in sulfur reductions as pH increases from 13.14 to 13.23 may be explained by a mechanism in which the hydrolysis levels off above pH 13.14 but the leaching rate decreases as mentioned previously. However, the increase in chlorine content as pH increases from 13.14 to 13.23 cannot be explained by this mechanism and is not well understood at this time.

Using the optimum values of pH 13.14 and temperature 90°C previously determined, a series of experiments was conducted to determine the effect of hypochlorite concentration. The concentration was varied from 0.2 to 0.6 molar and the results are given in Table 5.

Table 5. Effect of Hypochlorite Concentration on the Desulfurization of Pittsburgh No. 8 Coal (90°C, pH 13.14, 2 hours)*

Conc., M	0.2	0.3	0.4	0.6
TS, %	1.75 (28.3)	1.62 (33.6)	1.56 (36.1)	1.71 (29.9)
PS, %	0.29 (64.2)	0.31 (62.4)	0.24 (71.1)	0.22 (73.1)
OS, %	1.51 (5.8)	1.36 (14.9)	1.32 (17.3)	1.54 (3.8)
Cl, %	0.18	0.23	0.30	0.60

* Values in parentheses are reduction percentages.

The data given in Table 5 exhibit the same trend as the effect of pH shown in Table 4. The sulfur reductions increase as the hypochlorite concentration increases from 0.2 to 0.4 molar, but decreases as it increases further. The reduction in pyritic sulfur is an exception. The deterioration of desulfurization with application of higher hypochlorite concentration (0.6 molar) may be due to the rigorous chlorination of coal at the high concentration level. The chlorine content with the 0.6 molar hypochlorite leaching rises to 0.6% which is twice as much as that with 0.4 molar hypochlorite leaching.

The leaching behaviors of the sulfur forms in this series or as a whole may be explained by a mechanism in which hypochlorite ions are adsorbed on the coal surface, followed by sulfur reduction and chlorination of the coal matrix. The surface concentration of the adsorbed hypochlorite at 0.6 molar may be greater than that at 0.4 molar. This higher surface concentration of the species can chlorinate the coal structure more rigorously than that at 0.4 molar, as can be seen from the chlorine analysis. Thus, the remaining surface concentration of hypochlorite may be lower than that at 0.4 molar, leading to deterioration of the desulfurization.

4.2 Illinois No. 6 Coal

In the early stages of leaching of Illinois No. 6 coal, the coal was leached at 0.4 molar hypochlorite at room temperature without addition of solid sodium hydroxide. It was found that the temperature of the leach slurry went up significantly above room temperature, indicating that the coal was dissociated by oxidation during leaching. The filtrate was a black solution. According to Mayo and Kirshen (1979), the black solution contains oxidation-resistant benzene and aliphatic carboxylic acids as the principle organic products. Bubbles that were believed to be carbon dioxide were seen on top of the leach solution. Also the dried and filtered coal appeared to be much harder than before. Ash analysis showed that the ash content in the leach coal increased significantly, indicating that the coal was oxidized and lost its weight. For example, in one experiment, 20 grams of coal was leached in a 100 ml solution of 0.4 molar hypochlorite, an initial pH of 11.41 at room temperature. Soon after adding the coal into the hypochlorite solution, the temperature went up continuously to 39°C in 30 minutes. Bubbles were produced violently in the beginning of the reaction. After one-hour leaching, the coal was filtered and dried, and the pH of the filtrate was found to have decreased to 7.20. The ash content of the leach coal was analyzed to be 10.88%. This ash content was translated into the weight loss of 3.11% using the method mentioned previously.

Next, ammonia pretreatment was tested in an effort to reduce the oxidation of Illinois No. 6 coal with hypochlorite. Ammonia pretreatment was applied prior to leaching and hydrolysis by Brubaker and Stoicos (Brubaker and Stoicos, 1985). In one experiment of this study, 20 grams of coal was pretreated in a 50-ml concentrated ammonia hydroxide solution (14.8 molar) at room temperature for 1 hour. Then the coal was filtered and washed thoroughly with distilled water. This pretreated coal was leached in a 100-ml solution of 0.4 molar hypochlorite and initial pH 11.41. These conditions were the same as those of direct leaching without pretreatment that was mentioned previously. The temperature of the coal slurry during the leaching went up to 39°C in 30 minutes, which was the same temperature rise as in the previous test. After one-hour leaching, the coal was filtered and dried, and the pH of the filtrate was found to decrease to 7.94, which was higher than that in the previous case. The ash content of the leach coal was analyzed to be 9.54%. This ash content was translated into the weight loss of 1.65%, which was smaller than that in the previous test. The observation of the pH decrease and weight loss through the leaching of the two different treatment methods may lead one to believe that the ammonia pretreatment reduces the oxidation of Illinois No. 6 coal somewhat in the subsequent hypochlorite leaching step. However, as mentioned previously, the Pittsburgh No. 8 coal did not lose its weight through leaching with hypochlorite even at 90°C. The temperature of the leach slurry did not rise. No bubbles were observed on top of the slurry and the color of the leach solution did not change. Also, the ash content of the leach coal did not change from that of the untreated coal.

These data prove that the role of ammonia in the pretreatment was to reduce the weight loss of Illinois No. 6 coal in the subsequent leaching step with hypochlorite. However, the ammonia pretreatment was not necessary for Pittsburgh No. 8 coal because the coal did not lose its weight through leaching with hypochlorite. It is speculated that the acidic groups on the coal surface such as phenolic and carboxylic groups may play a role in coal oxidation. Comparison of the total acid concentrations between the two coal samples reveals

that the Illinois No. 6 coal has much higher concentration than that of the Pittsburgh No. 8 coal as shown in Table 1. It is also speculated that the coal oxidation has much to do with the total acidic groups existing on the coal surface. However, the investigation over the coal oxidation with hypochlorite was beyond the scope of the present study. There was circumstantial evidence to reinforce this speculation. As mentioned previously, the Illinois No. 6 coal was less oxidized somewhat in the leach step with hypochlorite after the coal had been pretreated with ammonia. The concentration of the total acidic group on the Illinois No. 6 coal was found to be reduced from 3.14 to 2.74 mmol/g coal or by 12.7% through the ammonia pretreatment. Thus, the ammonia pretreatment was applied to all the subsequent experiments with Illinois No. 6 coal.

Unlike the desulfurization of Pittsburgh No. 8 coal, Illinois No. 6 coal was leached and then hydrolyzed. This was due to the fact that Illinois No. 6 coal could not be leached at high temperature because of the problems connected with severe weight loss. Thus, Illinois No. 6 coal was leached at room temperature and the leach coal was subsequently hydrolyzed at 90°C, and these two steps were repeated once in the second stage. Twenty grams of leach coal was produced each time by reacting it in 100 ml of 0.6 molar hypochlorite without addition of sodium hydroxide at room temperature. Then three hydrolysis experiments were conducted using this leach coal to determine the optimum conditions especially in terms of the concentration of the hydrolysis reagents. The results are provided in Table 6.

Table 6. Effect of Reagents on the Hydrolysis of Illinois No. 6 Coal (90°C, 1 hour)

Concentration, M	Na_2CO_3, 0.3	NaOH, 0.1	NaOH, 0.3
TS after leaching, %	3.15	3.15	3.15
Cl after leaching, %	1.58	1.58	1.58
TS after hydrolysis, %	3.14	2.97	2.68
Cl after hydrolysis, %	0.233	0	0.092
Ash after hydrolysis, %	15.58	10.98	15.43
Wt loss after hydrolysis, %	8.22	3.22	8.06

It can be seen that all the hydrolysis conditions reduce the chlorine content from 1.58% to below its threshold value. The hydrolysis with 0.3 molar sodium carbonate is not effective because it can not reduce the total sulfur content. Thus, this reagent hydrolysis was discarded. The hydrolysis at 0.3 molar sodium hydroxide seems more effective than that at 0.1 molar sodium hydroxide because the total sulfur content at the former condition is significantly lower than that at the latter condition. Thus, all the subsequent hydrolysis experiments were conducted using 0.3 molar sodium hydroxide. This condition was particularly selected although the coal weight loss amounted to 8.06% as opposed to 3.22% at 0.1 molar sodium hydroxide. The underlying judgment was that this much coal weight loss should be tolerated for the additional reduction in total sulfur by 0.29%.

Table 7 presents data from two experiments conducted to determine the effect of sodium hydroxide concentration in the leach solution. One experiment was conducted at 0.6 molar hypochlorite without addition of solid sodium hydroxide and the other experiment was conducted at the same hypochlorite concentration and 0.1 molar sodium hydroxide.

Table 7. Effect of Sodium Hydroxide Concentration in the Leach Solution on the Leaching of Illinois No. 6 Coal ([OCl^-] = 0.6 molar, room temperature)

Sodium hydroxide concentration, M	0	0.1
pH of the leaching solution	11.63	12.59
TS, %	3.15	3.07
Cl, %	1.58	3.44
Ash, %	10.45	14.14
Weight loss, %	2.64	6.65

It is seen that the inclusion of solid sodium hydroxide in the leach solution at the level of 0.1 molar yields worse results in terms of chlorine content, ash content and weight loss. Thus, no solid sodium hydroxide was added to the leach solution for all the subsequent leaching experiments.

The next series of experiments was conducted to determine the effect of hypochlorite concentration in the leach solution. For each concentration, two cycles of experiments were conducted. Coal was leached and hydrolyzed in the first stage and the hydrolyzed coal was leached and hydrolyzed again under the same conditions in the second stage. The results are given in Table 8 for the first stage.

Table 8. Effect of Hypochlorite Concentration on the Desulfurization of Illinois No. 6 Coal in the First Stage*

Concentration	TS, %	PS, %	OS, %	Cl, %	Ash, %	Wt loss, %
Leaching 0.2 M [ClO^-]	3.33 (11.4)	0.25 (24.2)	3.08 (7.5)	0.29	8.47	0.49
Hydrolysis 0.3 M [OH^-]	2.74 (27.1)	0.26 (21.2)	2.48 (25.5)	0	15.25	7.86
Leaching 0.4 M [ClO^-]	3.35 (10.9)	0.29 (12.1)	3.06 (8.1)	1.26	9.54	1.65
Hydrolysis 0.3 M [OH^-]	2.89 (23.1)	0.23 (30.3)	2.67 (19.8)	0	14.40	6.94
Leaching 0.6 M [ClO^-]	3.15 (16.2)	0.30 (9.1)	2.86 (14.1)	1.58	10.45	2.64
Hydrolysis 0.3 M [OH^-]	2.68 (28.7)	0.23 (30.3)	2.45 (26.4)	0.09	15.43	8.06
Leaching 0.8 M [ClO^-]	2.74 (27.1)	0.28 (15.2)	2.47 (25.8)	4.52	13.54	6.00
Hydrolysis 0.3 M [OCl^-]	2.53 (32.7)	0.25 (24.2)	2.28 (31.5)	0.19	15.41	8.31

* Values in parentheses are reduction percentages.

The values in Table 8 reflect four separate leaching/hydrolysis experiments with increasing hypochlorite concentration followed by a hydrolysis treatment at 0.3 molar sodium hydroxide. The values in each box reflect actual remaining material in the coal and the calculated reduction percentage in parenthesis. For example, TS of Illinois coal was originally 3.76% (Table 1), and following leaching with 0.2 molar hypochlorite, 3.33% TS remained in the coal, reflecting a reduction of 11.4% TS. When the coal was hydrolyzed, 0.59% was extracted, leaving a remaining TS of 2.74%. This reveals a 27.1% reduction form the original amount.

It is seen from the table that the reduction in total sulfur increases with increasing hypochlorite concentration in the leach solution. The reduction of TS increases from 11.4% to 27.1% when the hypochlorite concentration increases from 0.2 to 0.8 molar. The total sulfur is reduced further through hydrolysis. It is reduced by 15.7% more by hydrolysis when the coal was leached at 0.2 molar hypochlorite and by 5.6% more when the coal was leached at 0.8 molar hypochlorite.

For the pyritic sulfur reduction, it seems that there is no effect from either changing the hypochlorite concentration or the hydrolysis. The pyritic sulfur reduction was by 21% on the average. On the other hand, the organic sulfur reduction seems to follow a pattern similar to that of the reduction of total sulfur reduction. The largest organic sulfur reduction occurred when the coal was leached at 0.8 molar hypochlorite and then hydrolyzed. The organic sulfur was reduced from the original amount of 3.33% to 2.28% with a 0.8 molar hypochlorite leaching followed by 0.3 molar NaOH hydrolysis. This is a 31.5% reduction which is a significant reduction considering that organic sulfur is generally very difficult to be leached.

When it comes to chlorination of coal (Cl%) with hypochlorite, there seems to be no problem. Leaching with hypochlorite raised the chlorine content to a high level up to 4.52%, but hydrolysis lowers the level far below the threshold value as can be seen in Table 8.

The weight loss increases as the hypochlorite concentration increases in the leaching step. The weight loss was 0.49% when the coal was leached at 0.2 molar hypochlorite, and increased to 6.00% when the coal was leached at 0.8 molar hypochlorite. However, additional weight loss is caused by the subsequent hydrolysis, and the weight loss seems to be at the same level around 7-8%, irrespective of hypochlorite concentration in the leaching.

Table 9 provides the data for the desulfurization results after the second-stage leach and hydrolysis. Comparison of the data for the total sulfur reduction between the first and the second stages (Tables 8 and 9) reveals that the desulfurization in the second stage is not as effective as that in the first stage. It is also seen that the total sulfur reduction increases by increasing hypochlorite concentration from 0.2 to 0.4 molar, yields a maximum value of 39.6% at 0.4 molar, and then decreases as hypochlorite concentration increases further. This phenomenon was detected in the first stage; however, it was not as pronounced as in the second stage. This mechanism may be due to the more rigorous chlorination at higher hypochlorite concentrations as explained previously for the leaching of Pittsburgh No.8 coal (see Table 5). Table 9 also shows that the pyritic sulfur was not additionally reduced by the second-stage desulfurization.

Table 9. Effect of Hypochlorite Concentration on the Desulfurization of Illinois No. 6 Coal in the Second Stage*

Concentration	TS, %	PS, %	OS, %	Cl, %	Ash, %	Wt loss, %
Leaching 0.2 M [ClO^-]	2.80 (25.5)	0.22 (33.3)	2.58 (22.5)	0.98	13.77	6.25
Hydrolysis 0.3 M [OH^-]	2.67 (29.0)	0.19 (42.4)	2.49 (25.2)	0	14.46	7.00
Leaching 0.4 M [ClO^-]	2.70 (28.2)	0.23 (30.3)	2.47 (25.8)	2.89	15.67	8.32
Hydrolysis 0.3 M [OH^-]	2.27 (39.6)	0.20 (39.4)	2.07 (37.8)	0.09	15.97	8.67
Leaching 0.6 M [ClO^-]	2.57 (31.6)	0.25 (24.2)	2.32 (30.3)	4.07	16.15	8.84
Hydrolysis 0.3 M [OH^-]	2.53 (32.7)	0.24 (27.3)	2.29 (31.2)	0	16.21	8.90
Leaching 0.8 M [ClO^-]	2.60 (30.9)	0.22 (33.3)	2.38 (28.5)	7.04	18.28	11.15
Hydrolysis 0.3 M [OCl^-]	2.48 (34.0)	0.23 (30.3)	2.26 (32.1)	0	18.41	11.30

* Values in parentheses are reduction percentages.

The organic sulfur reduction seems to follow the same pattern as that for the total sulfur reduction. The largest organic sulfur reduction occurred when the coal was leached at 0.4 molar hypochlorite and hydrolyzed. This is contrasted with the first stage because the largest organic sulfur reduction in the first stage comes at 0.8 molar hypochlorite. The organic sulfur at 0.4 molar in the second stage is reduced from 3.33% to 2.07%, or by 37.8%. This reduction is a significant accomplishment since organic sulfur is considered to be a refractory sulfur source in coal. Table 9 shows the optimum hypochlorite concentration for the desulfurization of Illinois No. 6 coal is 0.4 molar. This concentration results in the maximum organic sulfur reduction and the coal weight loss by 8.67% which is not exorbitant for this desulfurization method using a strong oxidation reagent of hypochlorite.

CHAPTER 5

Conclusions

1. The desulfurization of Pittsburgh No. 8 coal with hypochlorite is effective with one step of leaching at 90°C while that of Illinois No. 6 coal requires three consecutive steps of pretreatment with ammonia at room temperature, leaching with hypochlorite at room temperature and hydrolysis at 90°C for effective leaching.

2. The desulfurization method for Pittsburgh No. 8 coal can reduce mainly pyritic sulfur from 0.82% to 0.24% or by 71.1% at the optimum condition of 0.4 molar hypochlorite and 0.4 molar sodium hydroxide in the leach solution.

3. The desulfurization method with Illinois No. 6 coal can reduce significant amounts of organic sulfur. Organic sulfur was reduced from the original amount of 3.33% to 2.07% or by 37.8% reduction with the optimum operation of leaching at 0.4 molar hypochlorite at room temperature followed by the hydrolysis at 0.3 molar sodium hydroxide and 90°C.

4. The chlorination of the coal structure was observed during the desulfurization of both coals. However, the chlorine content in the Pittsburgh No. 8 coal was controlled at the minimum level of 0.3% which is the threshold value. The chlorine content in the Illinois No. 6 coal was reduced far below the threshold value through hydrolysis at each stage.

5. Weight loss of Illinois No. 6 coal due to oxidation occurs when reacting with hypochlorite. The weight loss was by 8.67% at the optimum conditions of leaching and hydrolysis. However, no weight loss of Pittsburgh No. 8 coal was detected.

6. This desulfurization method has merits as a feasible technology for some special commercial processes. It has merits on Pittsburgh No. 8 coal because this one-step operation can emulate the Meyers Process which utilizes multiple stages of rigorous leaching. Also, this desulfurization method has merits on Illinois No. 6 coal because it can achieve significant organic sulfur reduction at moderate conditions. However, more research work is necessary on a larger scale such as bench scale or pilot plant scale before this technology is implemented for a commercial process.

BIBLIOGRAPHY

Brubaker, R. B. and Stoicos, T., 1985, "Precombustion Coal Desulfurization with Sodium Hypochlorite," *Proceeding of the First International Conference on Processing and Utilization of High Sulfur Coal*, Oct. 13-17, Columbus, Ohio, edited by Y. A. Attia, pp. 311-326.

Chakrabartty, Sujit K, 1978, "Oxidation of Coal by Alkaline Sodium Hypochlorite," *ACS Symposium Series*, 71 (Org. Chem. Coal), 100-7.

Cho, E. H., 1989, "Coal Desulfurization with Aqueous Chlorine," *Met. Trans. B*, vol. 20B, Oct., 567-571.

Garrels, R. M., 1965, "Solutions, Minerals and Equilibrium," Freeman, Cooper and Company, San Francisco, p. 407.

Hsu, G. C., Kalvinskas, J. J., Ganguli, P. S. and Gavalas, G. R., 1977, "Coal Desulfurization by Low-Temperature Chlorinolysis," *Coal Desulfurization*, edited by Wheelock T. D., ACS Sym. Series 64, pp.207-217.

Luo, Qiuliang, 1994, "Coal Oxidation and Calcium Loading on Oxidized Coals," Master of Science Thesis, West Virginia University.

Mayo, Frank R, 1975, "Application of Sodium Hypochlorite Oxidations to the Structure of Coal," *Fuel*, 54(4), 273-5.

Mayo, Frank R. and Kirshen, Norman A., 1979, "Oxidation of Coal by Aqueous Sodium Hypochlorite," *Fuel*, 58(10), 698-704.

Meyers, R. A., 1977 a, "*Coal Desulfurization*," Marcel Dekker, New York, p.18.

Meyers, R. A., 1977 b, "*Coal Desulfurization*," Marcel Dekker, New York, p.65.

Meyers, R. A., 1977 c, "*Coal Desulfurization*," Marcel Dekker, New York, p.224.

Wandless, A. M., 1957, "British Coal Seams: A Review of the Properties with Suggestions for Research," *J. Inst. Fuel*, 30, 545-8.

Appendix 12: Development of Electrochemical Sensor for On-Site Monitoring of Heavy Metal Ions in Coal Processing And Utilization

TECHNICAL PROGRESS REPORT

Contract Title and Number:	Period of Performance:
Establishment of the Center for Advanced Separation Technologies (DE-FC26-01NT41091)	Starting Date: 9/17/01 Ending Date: 09/30/06

Sub-Recipient Project Title:	Report Information:
Development of Electrochemical Sensor for On-site Monitoring of Heavy Metal Ions in Coal Processing and Utilization	Type: Final Number: Period: 9/17/01-12/31/04
Principal Investigators: A. Manivannan and M. S. Seehra	Date: 2/7/05 Code: WV003-FINAL
Contact Address: Physics Department West Virginia University Morgantown, WV 26506-6315	Contact Information: Phone: 304-293-3422 x1429 Fax: 304-293-5732 E-Mail: amanivan@wvu.edu
Subcontractor Address: No subcontracts issued.	Subcontractor Information: Phone: Fax: E-Mail:

Disclaimer

This report was prepared as an account of work sponsored by an agency of the United States Government. Neither the United States Government nor any agency thereof, nor any of their employees, make any warranty, express or implied, nor assume any legal liability or responsibility for the accuracy, completeness, or usefulness of any information, apparatus, product, or process disclosed, or represents that its use would not infringe privately owned rights. Reference herein to any specific commercial product, process, or service by trade name, trademark, manufacturer, or otherwise does not necessarily constitute or imply endorsement, recommendation, or favoring by the United States Government or any agency thereof. The views and opinions of authors expressed herein do not necessarily state or reflect those of the United States Government or agency there of.

Abstract

In this work, electrochemistry based on boron-doped-diamond (DDD) electrodes was investigated for the quantification of Hg, Cd and Pb in the ppb-ppt range in laboratory prepared solutions. For Hg, the rotating disk electrode technique and the standard addition method allowed reliable quantification of mercury in the 0.005 – 50 ppb range in practical samples of KCl impinger solutions prepared from flue gas released by a pilot-scale coal-fired combustion facility. For the simultaneous detection of Cd and Pb in laboratory solutions at the ppb range, some mutual interference was detected which could be handled by developing three-dimensional calibration curves. However, testing of Cd and Pb in practical samples has not yet been done. In future work, we will focus on the development of a portable sensor for Hg quantification.

Table of Contents **Page No.**

Executive Summary

The goal of this project was to develop electrochemical techniques using highly boron-doped diamond (BDD) films as electrodes for the quantification of Hg, Cd and Pb in solutions in the ppb-ppt range. A specially designed O-ring-type three-electrode cell was used for the measurements, with saturated calomel electrode (SCE) as the reference electrode and a platinum wire as the counter electrode. All solutions used were prepared with analytical grade reagents.

Electrochemical experiments for the simultaneous measurements of micromolar-level concentrations of Pb and Cd in solutions were carried out using differential pulse anodic stripping voltammetry (DPASV). Cd was found to strip at -0.85 V versus SCE and Pb at -0.65 V versus SCE. Although these peaks are sufficiently apart for clear detection of Cd and Pb, some mutual interference was detected which could be taken into account with the aid of three-dimensional calibration plots. Additional details of these investigations can be found in Manivannan et. al., 2004a,b.

For the quantification of mercury, differential pulse voltammetry (DPV) experiments were performed in nitrate, thiocyanate and chloride media, with emphasis on the chloride medium because practical samples usually contain chloride impurities. To overcome the problem of calomel formation in chloride medium, purposely-added gold (3 ppm) was co-deposited on the BDD surface during DPV detection. Using these procedures, linear calibration plots of peak differential current versus concentration were obtained in the three media for the ppb range, which could be used for determining mercury in unknown samples. These initial results and the chemistry involved are described in two publications [Manivannan et al 2002 and 2004a,b].

For detecting mercury in solutions in the 0.005 – 50 ppb range, we used a rotating disk electrode (RDE) technique with rotation speed = 2000 rpm. The RDE technique was found to improve the detection level because of the improved hydrodynamic flow of the electrolyte at the electrode surface. These calibration curves were then employed to detect mercury in ten real samples prepared from flue gas released by a pilot-scale coal-fired combustion facility at the National Energy Technology Laboratory (Pittsburgh). To check the validity of our results, Hg in the same samples was also determined by the CVAAS (cold-vapor atomic absorption spectrometry). An excellent one-to-one correlation was obtained for

the results obtained by the two methods. These studies have shown that BDD mounted in a RDE system together with gold co-deposition is able to detect mercury with sufficient sensitivity for practical analysis of environmental samples. Further details of these studies are presented in a recent paper (Manivannan et al 2005) and a M.S. thesis (Ramakrishnan, 2004). Electrical characterization of the BDD films used in our work is described in another paper (Manivannan et al 2003). Our future work in this area will focus on the development of a portable instrument.

Experimental

Most of the experiments reported here were carried out on a free-standing BDD film purchased from Harris International Inc. The electrical and magnetic characteristics of this film have been described in a recent paper (Manivannan et al, 2003). For the rotating disk electrode (RDE) experiments, a 6 and 2 mm diameter disk of this film was mounted in a Pine Instrument RDE body (Fig. 1). The BDD electrodes were pre-cleaned in dilute HCl at 1 V vs. SCE (Saturated Calomel Electrode) for 5 min before each experiment.

Figure. 1. Rotating Disk Electrode on a Pine Instrument Rotator

For the basic experiments, a specially designed O-ring-type three-electrode electrochemical cell was used with SCE as the reference electrode and a platinum wire as a counter electrode (Fig. 2). The solutions used in the experiments were prepared from analytical grade reagents. Potentiostats made by Hokuto-Denko (Model HZ-3000) and Bioanalytical Labs (Model BAS-100) were used in the electrochemical measurements. To test the viability of the technique developed here, ten samples (impinger solutions) were obtained from the 500-lb/h coal-fired combustion facility located at NETL (National Energy Technology Laboratory), Pittsburgh, through the courtesy of Dr. Granite. Concentrations of mercury so determined were compared with the concentrations determined on the same samples by CVAAS (Cold-Vapor Atomic Absorption Spectrometry). Further details of these procedures are given in a recent paper (Manivannan et al 2005).

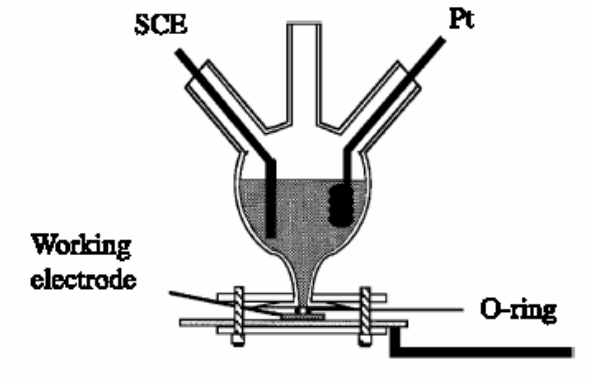

Figure 2. Schematic diagram of the electrochemical cell.

Results and Discussion

We focused primarily on the results obtained in the chloride media since the practical (field) samples always contain some chloride. Results on the nitrate and thiocyanate media are given in the recent paper (Manivannan et al, 2005) and in the M.S. thesis (Ramakrishnan, 2004). In Fig. 3, we show the DPV (Differential Pulse Voltammetry) scan for 2 – 14 ppb Hg^{2+} concentration in 1 M KCl (pH = 1), with 3 ppm gold solution added. The peak at 0.23 V vs. SCE is assigned to the one-electron oxidation of Hg^0 to Hg^+, whereas the second peak at 0.32 V is attributed to the one-electron oxidation of Hg from mercury-gold alloy (Manivannan et al 2005).

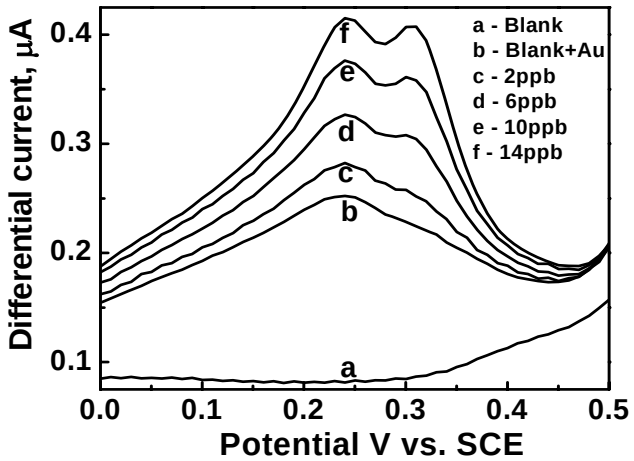

Figure 3. DPV scans for 2 ppb to 14 ppb Hg^{2+} concentrations in 1 M KCl (pH=1). A 3-ppm gold standard solution was added; deposition time = 30 sec; deposition potential = –0.1 V vs. SCE. (slope: 1.6 ± 0.09 µA ppb^{-1}; Intercept: 0.04 ± 0.009 µA).

With the RDE technique (rotation speed = 2000 rpm), the DPV scan obtained are shown in Fig. 4. In this case, the only dominant peak is the one near 0.32 V vs. SCE. We believe that the near absence of the peak at 0.23 V vs. SCE in Fig. 4 is due to the formation of a more uniform mercury-gold as a result of the rotation of the electrode. This probably makes the process of one-electron stripping from surface mercury a less significant phenomenon. Thus the RDE technique provides a significant advantage because from the practical point of view, it is easier to deal with one peak rather than two. The peak current for ppb concentrations after subtracting the background from blank, is plotted against the mercury concentration in Fig. 5, yielding an excellent linear curve. This linearity forms the basis for the quantification of Hg in this work.

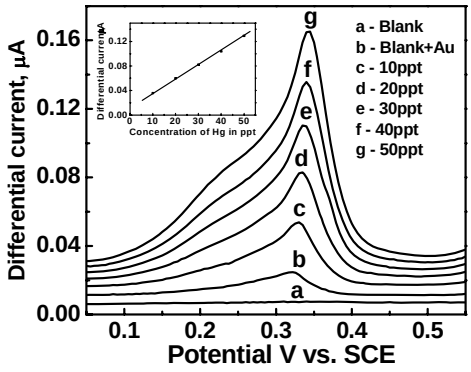

Figure 4. DPV scans for 10 ppt to 50 ppt Hg^{2+} concentrations in 1 M KCl (pH=1). A 1.5 ppm gold standard solution was added; deposition time = 60 sec; deposition potential = – 0.1 V vs. SCE, rotating disk electrode (diameter, 2 mm); rotation speed = 2000 rpm. (slope: 2.3±0.03 μA ppb^{-1}; Intercept: -0.01±0.001 μA).

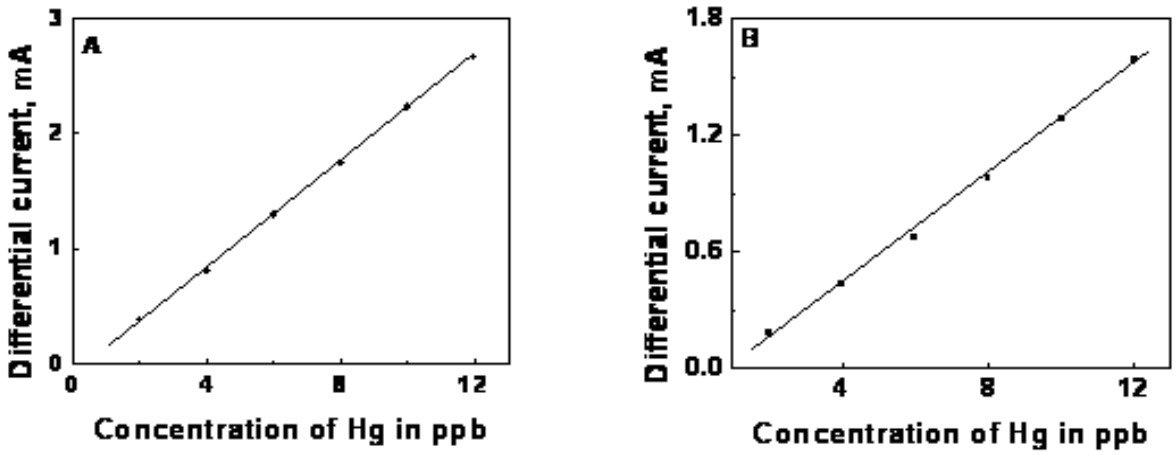

Figure 5. Calibration plots obtained from the DPV scans for 2 to 12 ppb Hg^{2+} concentrations in 1 M KCl (pH = 1) using a rotating disk electrode setup mounted with a diamond electrode using a Hokuto-Denko Model HZ-3000 potentiostat (A) (slope: 0.2±0.002 μA ppb^{-1}; Intercept: -0.1±0.02 μA) and a portable potentiostat PalmSens (B) (slope: 0.1±0.004 μA ppb^{-1}; Intercept: -0.1±0.03 μA) respectively. A 3 ppm gold solution was added in each case. Rotation speed = 2000 rpm; deposition time = 60 sec; deposition potential = -0.1 V vs. SCE; scan rate = 100 mV/sec.

To check the reproducibility of the calibration curve, we carried out successive measurements on the same electrode. The results are shown in Fig. 6. Although the curves are linear, the slopes are different for the different runs. The reason for this difference in slopes is somehow related to the surface structure of the BDD electrode and this issue will be investigated in our future work. However, we can still use the calibration curves to accurately determine mercury in unknown samples by using the standard addition method described below.

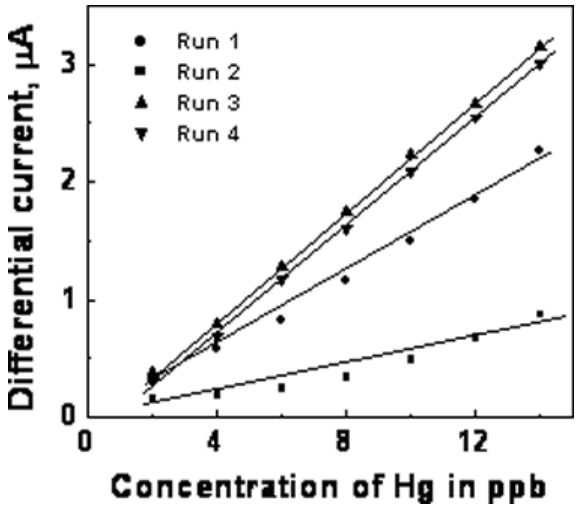

Figure 6. Four consecutive DPV calibration plots for 2-14 ppb of mercury concentrations in 1 M KCl (pH=4). A 3 ppm gold standard solution was added; deposition time = 60 sec; deposition potential = –0.1 V vs. SCE; rotation speed = 2000 rpm. Runs 3 and 4 were performed consequently on the same day.

In Table 1, we have listed ten impinger samples obtained from the coal-fired NETL plant. For these samples, mercury concentrations were determined both by the standard edition method and by CVAAS and these values are listed in Table 1. In the standard edition method, we simply add known concentrations of mercury to the unknown sample and plot the peak current vs. Hg concentration added (Fig. 7). Assuming linearity, only two additions are necessary to draw a straight line, although we did three additions. The intercept on the x-axis for zero current yields the Hg concentration in the unknown. The numbers in Table 1 were obtained using this procedure. Finally, to represent the correlation between the two set of determination of Hg in these samples, we plotted in Fig. 8 the Hg concentration determined by the CVAAS method and the standard edition method. The fact that most of the points fall on the solid line (Fig. 8) representing one-to-one correspondence between the two methods over two decades of concentrations provides significant reliability of the method developed in this work. Of course, if the slopes of the successive calibration curves were completely reproducible, then the standard edition method would be unnecessary and the calibration curve could be used directly for Hg determination. This issue will be addressed in our future work, along with developing a portable sensor.

Sample	Standard Addition Method (ppb)	CVAAS Method (ppb)
1	0.53	0.41
2	0.25	0.39
3	0.43	0.41
4	0.045	0.02
5	0.20	0.21
6	0.30	0.18
7	0.09	0.09
8	0.12	0.12
9	1.97	1.94
10	0.0053	0.0044

Table 1. Comparison of DPV results by standard addition method and CVAA analysis on KCl impinger samples obtained from a pilot-scale combustion facility collected during coal burning.

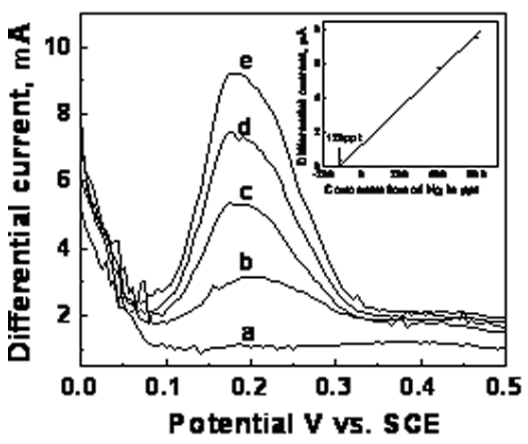

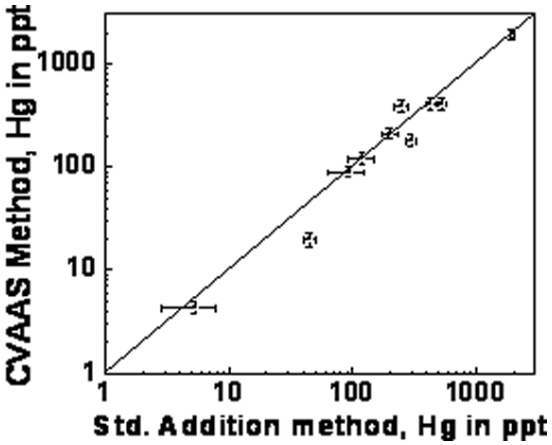

Figure 7. (left) DPV peak currents and calibration plot (inset) for sample 8 using the standard addition method. A 3-ppm gold solution was added. (a) Sample with 3-ppm gold only, (b) 200 ppt of Hg, (c) 400 ppt of Hg, (d) 600 ppt of Hg. Other conditions are: deposition time = 60 sec; deposition potential = -0.1 V vs. SCE scan rate = 50 mV/sec; rotation speed = 2500-rpm. (slope: 9.4±0.5 μA ppb^{-1}; Intercept: 1.7±0.3 μA).

Figure 8. (right) Comparison plot of the concentrations determined by the standard addition and CVAA methods (Table I). The solid line represents a one-to-one correlation between the two methods.

We also carried out a number of experiments for the simultaneous detection of Pb and Cd with the BDD electrodes using DPASV (Differential Pulse Anodic Stripping Voltammetry). In Fig. 9, we show the DPASV curves of Pb and Cd for different concentrations. Comparing these results with those from Pb and Cd alone, it was observed, Pb and Cd affect each other when simultaneously present (Fig. 10). In a recent publication, (Manivannan et al, 2004) we have provided details of this effect. We have also developed a model and three dimensional calibration curves to take into account this Pb/Cd interaction so that concentrations of Pb and Cd could be determined accurately. However, the method has not yet been applied to any determinations in the unknowns, analogous to our experiments with Hg. Such studies might be carried out in future.

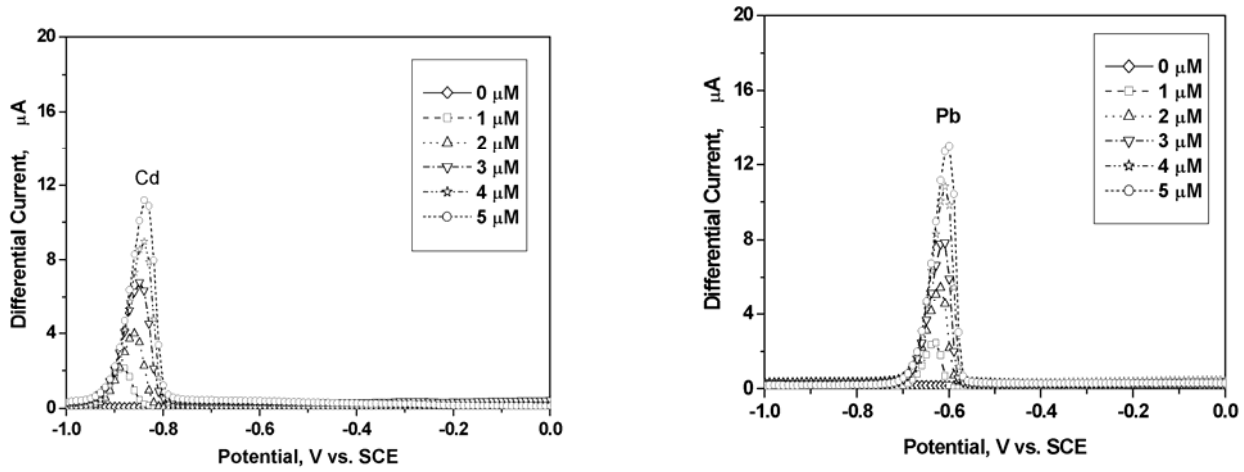

Figure 9. DPASV curves for the stripping of Cd and Pb deposited from solutions containing 1-5 μM $Cd(NO_3)_2$ and $Pb(NO_3)_2$ in 0.2 M acetate buffer (pH = 5.0) respectively; the deposition time was 2 minutes at –1.0 V vs. SCE.

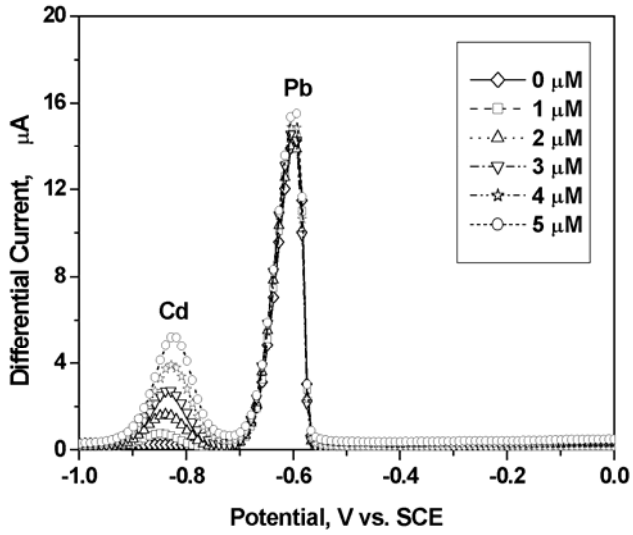

Figure 10. DPASV curves for the stripping of Cd and Pb from solutions containing $Cd(NO_3)_2$ in 0.2 M acetate buffer with 5 μM $Pb(NO_3)_2$; the deposition time was 2 minutes at –1.0V vs. SCE.

Conclusions

For the detection of Hg, reliable linear calibration curves were obtained in the 0.005-50 ppb range using the rotating disk electrode technique. These calibration curves were then used in the standard edition method to determine Hg concentrations in ten KCl impinger solutions prepared from flue gas by a pilot-scale coal-fired combustion facility. A reliable one-to-one correspondence of Hg concentrations determined by this technique and CVAAS provides assurance for the correctness of the procedures developed here.

For the detection of other heavy elements such as Cd and Pb simultaneously in a solution, some mutual interaction between Cd and Pb was indicated. Although the problem can be handled by developing three-dimensional calibration curves, the technique still needs to be tested on unknown samples.

The overall conclusion from these studies is that the electrochemistry using BDD electrodes has the potential of commercial applications. However, a portable and reliable detector still needs to be developed, and tested. This problem is the focus of our research in the new project which was initiated recently.

References

1. A. Manivannan, R. Kawasaki, D. A. Tryk and A. Fujishima, "Interaction of Pb and Cd during anodic stripping voltammetric analysis at boron-doped diamond electrodes", Electrochimica Acta 49, 3313-3318 (2004).
2. A. Manivannan, M. S. Seehra, D. A. Tryk and A. Fujishima, "Electrochemical detection of ionic mercury at boron-doped diamond electrodes", Analytical Letters 35, 355-368 (2002).
3. A. Manivannan, M. S. Seehra and A. Fujishima, "Detection of mercury at the ppb level in solution using boron-doped diamond electrode", Fuel Process. Technol. 85, 513-519 (2004).
4. Latha Ramakrishnan, M.S. Thesis entitled, "Trace Detection of Mercury using Boron-Doped Diamond Electrodes", West Virginia University (2004).
5. A. Manivannan, L. Ramakrishnan, M. S. Seehra, E. Granite, J. E. Butler, D. A. Tryk and A. Fujishima, "Mercury detection at boron doped diamond electrodes using a rotating disk technique", Journal of Electroanalytical Chemistry, 2005 (7 pages) in press.

6. A. Manivannan, S. Underwood, E. H. Morales and M. S. Seehra, “Magnetic and electrical conduction of heavily boron-doped diamond”, Materials Characterization 51, 329-333 (2003).

Student Endeavors

Latha Ramakrishnan, M.S. Thesis entitled, “Trace Detection of Mercury using Boron-Doped Diamond Electrodes”, Department of Physics, West Virginia University (2004).

Publications

1. Manivannan, R. Kawasaki, D. A. Tryk and A. Fujishima, “Interaction of Pb and Cd during anodic stripping voltammetric analysis at boron-doped diamond electrodes”, Electrochimica Acta 49, 3313-3318 (2004).
2. Manivannan, M. S. Seehra, D. A. Tryk and A. Fujishima, “Electrochemical detection of ionic mercury at boron-doped diamond electrodes”, Analytical Letters 35, 355-368 (2002).
3. Manivannan, M. S. Seehra and A. Fujishima, “Detection of mercury at the ppb level in solution using boron-doped diamond electrode”, Fuel Process. Technol. 85, 513-519 (2004).
4. Latha Ramakrishnan, M.S. Thesis entitled, “Trace Detection of Mercury using Boron-Doped Diamond Electrodes”, West Virginia University (2004).
5. Manivannan, L. Ramakrishnan, M. S. Seehra, E. Granite, J. E. Butler, D. A. Tryk and A. Fujishima, “Mercury detection at boron doped diamond electrodes using a rotating disk technique”, Journal of Electroanalytical Chemistry, 2005 (7 pages) in press.
6. Manivannan, S. Underwood, E. H. Morales and M. S. Seehra, “Magnetic and electrical conduction of heavily boron-doped diamond”, Materials Characterization 51, 329-333 (2003).

Conference Presentations

1. A. Manivannan, D. A. Tryk, and A. Fujishima, "Diamond Electrodes for Trace Metal Detection" 6th International Mini Symposium on Diamond Electrochemistry and Related Topics, March 5-6, 2002, Sanjo Kaikan, The University of Tokyo, Tokyo, Japan.
2. A. Manivannan, D.A. Tryk, M.S. Seehra, and A. Fujishima, "Trace Mercury Determination by Anodic Stripping Voltammetry for on-line Monitoring", Air Quality IV conference held in Washington D.C. September (2003)
3. A. Manivannan, M.S. Seehra, and A. Fujishima, "Mercury Monitoring using Diamond Sensor Electrodes", Pittsburgh Coal Conference Conference, Pittsburgh, September (2003)
4. A. Manivannan, D.A. Tryk, M.S. Seehra, and A. Fujishima, "Boron Doped Diamond Electrodes for Trace Metal Detection", 203rd meeting of the Electrochemical Society, Paris, France April (2003)
5. A. Manivannan, M.S. Seehra, E. Granite and A. Fujishima, "PPT Level Detection of Mercury using Diamond Rotating Disk Electrodes", 21st Pittsburgh Coal Conference Conference, September 13-17 Osaka, Japan (2004)

Appendix 13: Evaluation of Coal Cleaning Efficiency Using Transponder-Based Density Tracers

FINAL REPORT

Contract Title and Number:	Period of Performance:
Establishment of the Center for Advanced Separation Technologies (DE-FC26-01NT41091)	Starting Date: 9/17/01 Ending Date: 9/30/06

Sub-Recipient Project Title:
"Evaluation of Coal Cleaning Efficiency Using Transponder-Based Density Tracers"

Principal Investigators:
Gerald Luttrell and Roe-Hoan Yoon
Chris Wood and Chris Barbee

Contact Address:
146 Holden Hall
Virginia Polytechnic Institute & State University
Blacksburg, VA

Subcontractor Address:
No subcontracts issued.

Report Information:
Type: Final Report
Number: --
Period: --
Date: 12/1/06
Code: VA005

Contact Information:
Phone: (540)231-4508
Fax: (540)231-3948
E-Mail: cast@vt.edu

Subcontractor Information:
Phone:
Fax:
E-Mail:

DISCLAIMER

ABSTRACT

Density tracers are widely regarded as one of the most powerful diagnostic tools for evaluating the performance of heavy medium circuits. Unfortunately, the full capabilities of density tracers are often not realized in practice due to problems that occur during the retrieval step. To overcome this problem, an advanced electronic monitoring system has been developed to automatically identify and count the density tracers as they pass through a coal cleaning circuit. This technique, which relies on recent technological breakthroughs in transponder technology, improves the reliability of the tracer data by eliminating statistical errors associated with lost tracers. This development also makes it possible for efficiency tests to be performed very rapidly by a single person in an extremely cost-efficient manner. It is estimated that the average U.S. coal preparation plant could easily benefit by $500,000 or more annually by preventing coal losses that are detectable using this new technology.

TABLE OF CONTENTS

INTRODUCTION

Background

Heavy medium separators, which include static heavy medium baths and centrifugal heavy medium cyclones, are widely used by the coal preparation industry to upgrade run-of-mine coals in the plus 0.5 mm size range. In the U.S. alone, heavy medium circuits are used by more than 80% of all preparation plants and account for an annual production of nearly 250 million tons of clean coal. Because of the high tonnages treated by the heavy medium circuits, a small improvement in separation efficiency can have a large impact on plant profitability. For example, a modest two percentage-point increase in the efficiency of heavy medium circuits in the U.S. would produce an additional 4.5 million tons of saleable coal from the same tonnage of mined coal. At a market price of $30/ton, the recovered tonnage represents additional annual revenues of more than $135 million for the total U.S. coal industry and more than $500,000 for an average preparation plant.

Partition Curve Analysis

The performance of heavy medium separators is typically assessed using a partition curve. This curve, which may also be known as an efficiency or Tromp curve, is a plot of particle specific gravity (SG) versus an experimental partition factor (P). The partition factor represents the statistical probability that a feed particle of a given SG will report to the refuse stream (see Figure 1). The partition factor can be calculated using:

$$P = \frac{Cc}{Ff} = \frac{(f - t)c}{(c - t)f} \tag{1}$$

in which C is the concentrate mass rate, F is the feed mass rate, and f, c and t are the assays values for the feed, concentrate and tailings, respectively (dry basis). Since the right-hand side of this expression contains only assay values, no actual measurements of mass flow rates are required to calculate the partition factor.

The partition curve can be used to identify the specific gravity of separation, which is commonly referred to as the cutpoint. The cutpoint is defined as the specific gravity (SG_{50}) at P=0.5. Particles of this specific gravity have an equal chance of reporting to either the clean coal or refuse streams. In addition, the characteristic shape of the partition curve can provide useful insight. For example, Figure 1(a) shows an ideal separation curve represented by a step function that shifts from 0 to 1 at the cutpoint. Unfortunately, an ideal curve is not realistically achievable in real-world processes due to the inherent misplacement of particles created by turbulence and other production related demands. Less efficient separations would be represented by an “S”-shaped transition function with a non-zero slope at the cutpoint. As such, the partition curve shown in Figure 1(c) is less efficient than that shown in Figure 1(b). For convenience, the slope of the partition curve is often reported as an Ecart probable (Ep) given by:

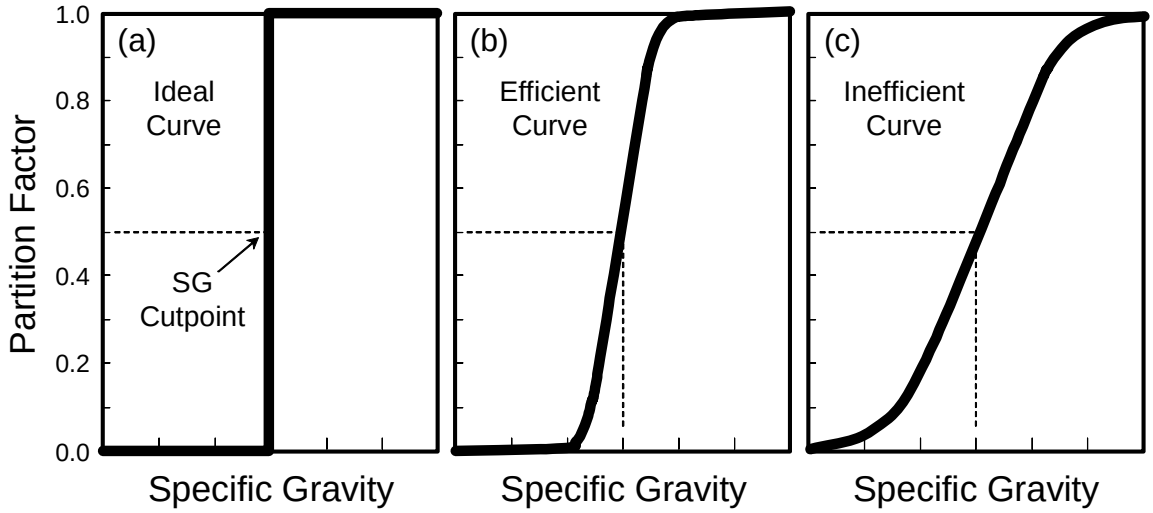

Fig. 1. Generalized partition curves for (a) ideal, (b) efficient and (c) inefficient separations.

$$Ep = \frac{SG_{75} - SG_{25}}{2} \tag{2}$$

in which SG_{75} and SG_{25} are the specific gravities at P=0.75 and P=0.25, respectively. Note that the separation efficiency increases as the Ep value decreases (i.e., small Ep values are desirable).

The tails of a partition curve also provide useful insight into separator performance. For an unbiased unit, the partition curve will be reasonably symmetrical since particles are misplaced by purely random processes in direct proportion to the deviation from the cutpoint. As shown in Figure 2(a), a curve of this type will have a low density tail that closes out at P=0 and a high density tail that closes out at P=1. An offset partition curve suggests that the process data is biased by some characteristic of the separator, e.g., short-circuiting. A curve that does not close out at zero (Figure 2(b)) indicates gross bypass of low density solids to the high density stream. This type of curve may occur if the volumetric flow to a spiral is reduced so that lighter particles can no longer be retained in the high velocity flow along the outer wall. Likewise, a curve that does not close out at one (see Figure 2(c)) indicates gross bypass of high density solids to the low density stream. This type of curve may be created by beaching/sanding along the inside of a spiral that would force heavy minerals toward the outer wall. In either case, the direct bypass of very light and/or very heavy particles should be minimized to prevent an unnecessary decline in the recovery or grade of the concentrate. An offset partition curve is often due to improper equipment selection, mechanical failures, or excessive production rates. In industrial plants, the misplacement may be corrected using multistage circuits that have been properly configured to address the bypass problem.

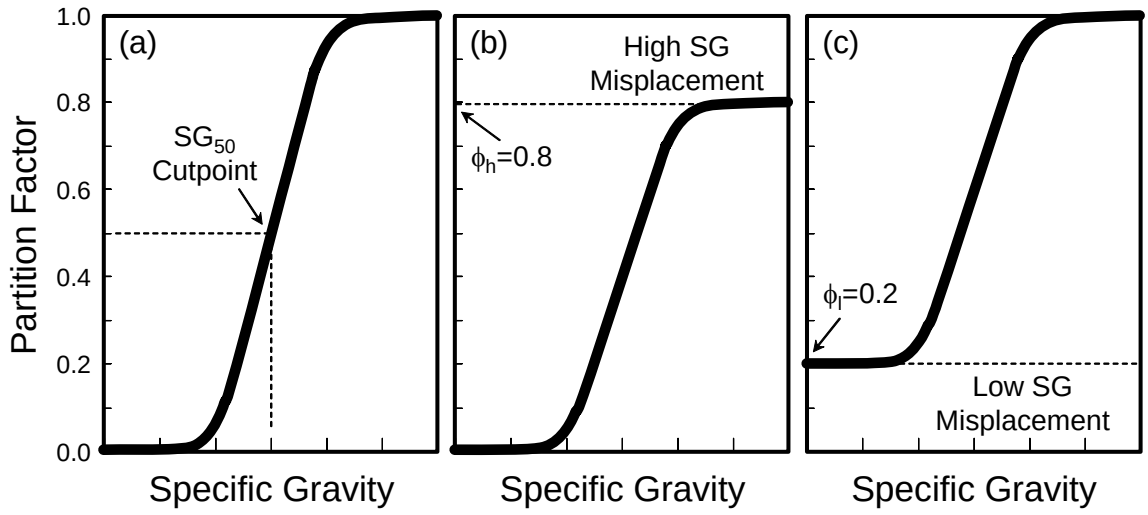

Fig. 2. Generalized partition curves showing (a) no bypass, (c) high-density bypass and (c) low-density bypass.

Several empirical expressions have been used to mathematically fit partition curve data. These equations include various types of transition functions that belong to the sigmoid family of curves. One of the most common of these is the Whiten (1972) equation given by:

$$P = \frac{1}{1+\exp\{(SG_{50} - SG)/Ep\}} \quad . \tag{3}$$

If the tails of the curve do not close at 0 and 1, then the values obtained from Equation (3) can be adjusted using:

$$P^* = \phi_l + (1-\phi_l)\phi_h P \tag{4}$$

in which ϕ_h and ϕ_l are the high and low bypass coefficients, respectively (see Figure 2). This equation provides a powerful tool for mathematically comparing the fitting coefficients that describe the characteristic shapes of different partition curves.

The data required to construct a partition curve is typically obtained from plant samples that have been subjected to laboratory float-sink analysis. Float-sink tests use heavy organic liquids to segregate particles into very narrow specific gravity classes. Grains of low-density coal (SG=1.3) can be readily separated from heavier minerals such as shale (SG>2.5) using this technique. Unfortunately, this type of characterization technique is relatively costly and requires a substantial amount of time (sometimes weeks) in order to obtain the required data. Also, the toxic fumes from the volatile organic liquids also have the potential to create serious heath problems for laboratory workers and a release hazard to the environment if not properly handled. As a result, many of these liquids have been banned in some industrialized nations.

Density Tracers

Density tracers are another method that can be used to construct partition curves for dense medium separators (Ayat and Leonard, 1986). Density tracers are cubic plastic blocks that incorporate high-density fillers to create synthetic particles with densities of 1.2 SG or higher with an accuracy of ±0.005 SG. The blocks are typically introduced into the feed of a density separator to mimic the behavior of coal particles. During a typical test, a large number of tracers (usually more than 500) of different densities are added to the feed stream and allowed to pass through the dense medium separator. The tracers report to either the high-density (refuse) or low-density (clean coal) streams as dictated by the characteristics of the separator. The tracers are brightly colored so that they can be manually retrieved by personnel from the drain-and-rinse screens that are just downstream from the dense medium separator. Tracers that report to the low-density product are recovered and counted separately from those that report to the high-density product (see Figure 3). A simple mathematical procedure is then followed to develop an efficiency (or partition) curve for the density separator. Since this procedure eliminates the need for sample collection and laboratory analysis, the partitioning data obtained using tracers are generally more accurate than data derived using conventional sampling and float-sink procedures. More importantly, the partition curve can be obtained in a matter of minutes, compared to several weeks when conventional float-sink tests are used. The cost of a full-scale sampling campaign to obtain similar data would be many times more expensive than a density tracer test. Because of these advantages, density tracers are regarded as one of the most powerful diagnostic tools for evaluating heavy medium circuits.

Unfortunately, the full capabilities of density tracers are often not realized in industrial practice due to problems that occur during the retrieval step. The retrieval process may require a dozen or more workers to be placed at the drain-and-rinse screens to collect all of the tracer blocks in complex heavy medium circuits. In addition, the tracers are often buried in the particle bed on the drain and rinse screens, particularly if the plant circuits are heavily loaded. If this occurs, many of the tracers can be lost and are never counted. For example, Figure 4 shows the result obtained from a plant evaluation in which 20 tracers of various densities between 1.52 and 1.72 SG were added to a heavy medium cyclone circuit. The black- and grey-filled boxes represent tracers that were collected from the clean coal and refuse streams, respectively. The unfilled boxes represent tracers that were

Fig. 3. Determination of a partition curve using density tracers (Courtesy of Partition Enterprises).

lost during the collection procedure. The lost blocks introduce uncertainty into the computations used to determine the circuit efficiency. To minimize this problem, manufacturers of density tracers tend to produce blocks that are larger than most of the coal particles in the feed stream so they can be more readily spotted during the test. Although the larger tracers are easier to locate and collect, these blocks often separate differently than smaller coal particles. Field studies have shown that the larger tracers separate at a lower overall cut-point and are more prone to become "hung" in heavy medium cyclones than smaller coal particles. As such, these problems greatly limit the capabilities of density tracers for trouble-shooting the performance of heavy medium circuits in U.S. plants.

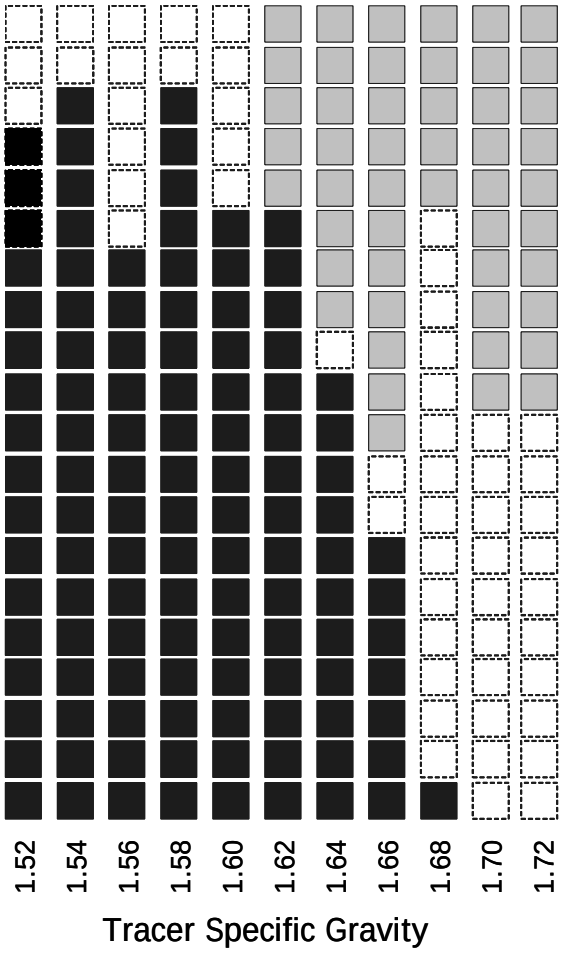

Fig. 4. Illustration of problems resulting from the loss of tracers during manual retrieval (black=reported to clean; grey=reported to refuse).

Electronic Density Tracers

The technical problems associated with counting density tracers can be overcome by imbedding an electronic tag (known as a transponder) within each block so that it can be remotely detected. Transponders are electronic devices that act as coupled transmitters-receivers. During operation, a stationary interrogator (called a reader) sends out an electronic signal to the remote transponder (called a tag). The tag receives the signal and then responds back to the reader to establish its presence and/or identity. Transponder technology was initially developed as a means of identifying aircraft in World War II. Friendly aircraft would respond to secret preprogrammed interrogation codes and automatically indicate to radar operators that they were not a threat. Transponders are still used on commercial aircraft to convey the height and identity of aircraft on airport radar displays.

Transponder technology has continued to grow at a rapid pace during the past decade as a result of continued advances in microelectronics. Numerous types of transponder systems are now commercially available for use in electronic tagging. The different technologies vary widely in terms of price (varying from a few cents to more than $1,000 per unit) and performance (reading range and reliability). For the general public, the most recognized application of transponders is in the area of electronic article surveillance (EAS).

EAS systems are used to electronically detect goods that are removed from a retail store without being purchased (see Figure 5). The systems comprise a tag attached to the goods and a sensor mechanism. Magnetic and radio frequency versions of these transponders are very cheap and are generally attached permanently to the goods or their packaging. The retailer simply neutralizes the tag when the items have been legitimately purchased. Microwave tags are significantly more expensive and are removed by the store personnel using a special tool when the item has been purchased. At present, EAS systems make use of use of single-bit transponders that only allow the presence of the tag to be established since they do not have sufficient data capabilities to convey the identity of the tagged item. These commercial systems, which are available from many competing suppliers, are estimated to represent a market share of approximately 6,000 million tags per year at a cost of $0.10-$0.15 each.

Fig. 5. Low-cost tag consisting of a single chip and antenna for tracking of shipped packages.

More recently, technological advances have made it possible to manufacture low-cost transponders that broadcast both the presence and identity of tagged items. These multi-bit tags can provide a coded data string back to the reader so that its unique identity can be established. These tags can operate in either active or passive modes. Active tags require an onboard power supply (such as a battery), whereas passive tags do not require an onboard energy sources since they are powered by the energy of the interrogation signal provided by the reader. In a passive system, the reader is more complex because it provides the signal stability, the energy of the system, and the receiver selectivity to read the weak return signal. Also, the maximum working distance between the reader and tag is usually limited to less than about 1 meter. The advantage of a passive system is that the tags are compact, very durable, and much less expensive. Such a tag would consist of only a simple integrated circuit attached to a printed antenna. Several manufacturers have recently suggested that passive electric field tags in a read-only mode may soon be commercially manufactured for less than $0.10 per unit when produced in high volume.

The passive multi-bit tags are ideally suited for the electronic identification of density tracers. In this type of an application, the read-only transponders would be encased within plastic blocks of different densities. Each tag would have a unique binary code programmed into the silicon chip so that the properties of the block (e.g., density, size, shape, etc.) would be known. Antenna for the readers would be placed at strategic locations downstream from the heavy medium separator. An illustration of such a setup is shown in Figure 6. When the

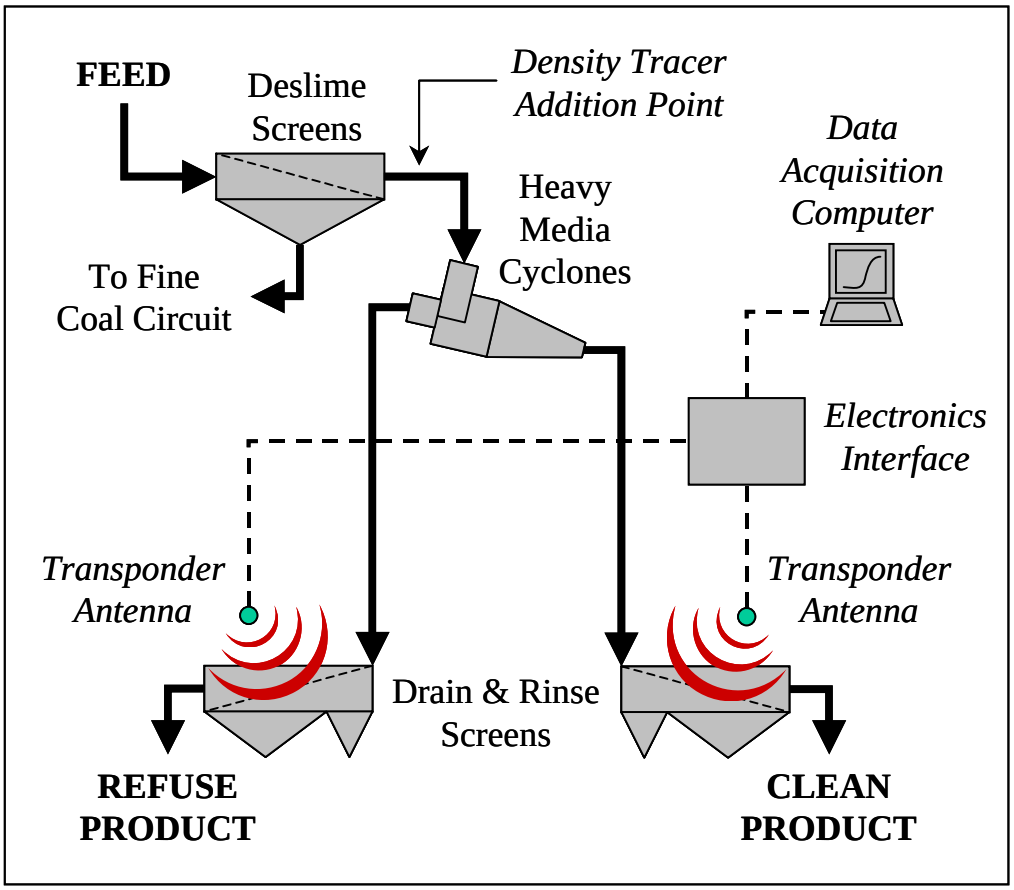

Fig. 6. Layout of a transponder-based density tracer system for monitoring the efficiency of a heavy medium cyclone circuit.

tracers pass by the antenna, the tag would become energized and an identification signal would be transmitted back to each reader. The returned signal would be converted to digital code and recorded by a central computer. The data would be compared with a database maintained on the central computer to establish the unique identity of the tagged item. In this case, the permanent memory of read-only tags would be preprogrammed at the factory or, if required, programmed by the user in the field. Similar applications of these types of transponder systems include animal tracking, vehicle control, personnel access, production control, ski passes, event timing, golf ball recovery, and document authentication.

Project Objectives

The primary objective of this project was to develop a new type of density tracer that can be automatically counted using an electronic tagging system. This approach, which makes use of recent advances in transponder technology, eliminates statistical errors associated with lost tracers. This development also makes it possible for efficiency tests to be performed very rapidly by a single person in a cost-efficient manner. To achieve this

objective, two phases of technical work were conducted. In the first phase, the hardware and software systems required to develop the transponder-based system were procured and configured for this application. This phase of work included the manufacture of density tracers with embedded electronic transponder tags and the construction of stationary readers for identifying and counting the tagged tracers. Electronic interfaces and graphical software were also developed to convert the tracer counts into efficiency curves for use by plant personnel. The prototype system was then tested and evaluated in the laboratory using a simulated circuit. In the second phase of work, the electronic monitoring system was relocated to an industrial site for field-testing and evaluation under actual plant conditions. After completing this phase of work, a preliminary cost analysis was performed to estimate the expenses associated with the construction of a commercial electronic density tracer system.

EXPERIMENTAL

Task 1 - Transponder Evaluation

A detailed study was conducted to compare the capabilities of several commercially available transponder systems. The primary factors to be considered in the evaluation of the tags included storage capability, user programmability, transmission-receiver signal reliability, interference filtering, physical size, and mechanical durability. In addition, the costs associated with the procurement and construction of both the reader and tags was considered prior to selecting an appropriate system. Details related to the evaluation are discussed in the "Results and Discussion" section of this report.

Task 2 - Transponder Procurement

After completing the initial evaluation of transponder systems, two commercial readers systems and several types of tags were purchased from suitable vendors. Once the components were received and assembled, shakedown tests were conducted to verify that the performance specifications of the transponders could be duplicated under controlled laboratory conditions. Other items purchased included a computer for data acquisition and control, appropriate input-output cards, and suitable software for the user interface.

Task 3 - Preparation of Density Tracers

After developing a basic identification system, a partial set of density tracers were manufactured using the transponder technology. Factor-programmed tags were encased directly within each tracer block to identify both the size and density of the block. For preliminary testing, several 32 mm cubic blocks were manufactured with embedded tags. As described later within this report, these prototype blocks were used to conduct trial runs of the proposed counting system in a laboratory environment. After completing these tests, a second set of transponder-based density tracers were manufactured for use in follow-up laboratory tests and final field trials. These additional blocks were manufactured using a narrower SG increment of 0.02 SG for blocks between 1.46 and 1.76 SG. Additional tagged blocks were also prepared for 1.32 and 2.00 SG to ensure that the tails of the partition curve could be well defined and that no gross misplacement of coal or rock occurred.

Task 4 - Testing and Evaluation

Several series of laboratory trials were conducted to determine the capabilities and limitations of the transponder-based system for counting the density tracers. These trails were performed by randomly dropping the tagged density tracers on a moving conveyor belt loaded with different amounts of mined material. These tests were used to determine the extent of interference that may be present in the relatively weak transmission signals from tracers buried to different depths by different types of solid materials. This information was important in determining the required strength of the energizing fields and optimal locations of the reader antenna.

Task 5 - Software Development

This task involved the development of required software for the transponder-based density tracer system. This activity included the preparation of a suitable user interface, programming of the required computation algorithms, and the completion of required logic interfaces between the transponder system and computer. The user interface was designed to provide a direct graphical readout showing the process efficiency curve and pertinent performance indicators (e.g., SG cutpoint and Ep) that can be used by plant operators to evaluate the circuit performance and estimate coal losses.

Task 6 - Field Testing

Final testing of the proposed system was conducted at an industrial test site provided by a local coal preparation plant operator. As described later, detailed procedures for the setup of the system and assessment of the test data were specifically tailored for the test site. However, because of the preliminary nature of this work, the plant trials were limited to testing of relatively simple circuits with a minimal number of drain-and-rinse screens. This limitation was necessary because of the small number of reader antenna (only four) and associated hardware that could be purchased under the modest project budget. The test circuit was also selected so that the tagged density tracers can be easily recovered by plant personnel and reused in additional test runs.

RESULTS AND DISCUSSION

Task 1 - Transponder Evaluation

A detailed study was conducted during the past reporting period to compare the capabilities of several commercially available transponder systems. The technical factors considered in the evaluation included transmission mode/frequency, storage capacity, programmability, detection range, interference susceptibility, physical size/density, and mechanical durability. Smaller tags are more attractive since they are easier to incorporate within the tracer blocks and are less likely to cause variations in the absolute density of an individual tracer block. However, the initial evaluation of commercially available systems showed that detection distance decreases with transponder size (i.e., the read range is very short for a very small transponder). Therefore, as a compromise between size and read range, transponders incapable of providing a minimum read range of at least 15 cm (6 inches) and tags larger than 32 mm (1.25 inches) were not considered for this application. In addition, component cost was viewed as one of the primary considerations in the development of the prototype system. Since the tracer blocks will not be recovered, the tags must be available at a price that will allow them to be disposable.

In addition to size and cost, the choice of transmission frequency is perhaps the most important consideration in the selection of a transponder system. At present, commercial systems are available that operate in three general frequency ranges (see Table 1). The frequency must be carefully matched to the conditions of the given application. In the current application, the transponder tags will be placed within density tracers of tight density tolerances and small dimensions (e.g., 16 mm tracer cubes). The tracers will be introduced into the density separation circuit, which could include unit operations such as centrifugal pumps, dense medium concentrators, vibrating screens, and an array of sumps, pipes, chutes, or bins. The tracers will eventually report to either the clean coal or refuse conveyor belts, where they may be buried within several inches of damp coal or rock. Each step in the process introduces a different challenge to being monitored by the transponder technology.

Two types of transponder systems were considered for use in this application, i.e., induction and electromagnetic. Induction systems typically operate in the 125-134 kHz and 13.56 MHz frequency range. These devices are called “induction” transponders since the energizing field and data stream are transmitted by means of inductive coupling (much like a transformer). During operation, the antenna of the reader generates a magnetic field that supplies energy by inducing a voltage in the coil of the tag. Data transmission is

Table 1. Transmission frequencies for commercial transponder systems.

Category	Transmission Frequency	
I	Low (LF) and High (HF)	30kHz – 300 MHz
II	Radio (RF) and Ultra High (UHF)	300 MHz – 3 GHz
III	Microwave (MF)	>3 GHz

accomplished by changing one parameter of the transmitting field (i.e., amplitude, frequency, or phase). The transmitted signal field strength is strongly dependent on the separation distance (d) between the tag and the antenna. The field is generally proportional to $1/d^3$ to $1/d^4$, depending on the orientation of the tag with respect to the reader transmitter loop. Therefore, the working range of these tags must be kept very short (usually within 20-30 cm).

Electromagnetic (or radio frequency) transponders operate in the 400 to 1000 MHz frequency range. These devices make use of conventional electromagnetic wave propagation to transmit data, commands, and power (for passive tags). During operation, the interrogator transmits an electromagnetic wave that passes outwards with a spherical wave front. The energy propagates through the atmosphere (or other material) by exciting electrons that, in turn, radiate energy at the same frequency. The process continues as newly excited electrons radiate other nearby electrons in an expanding progression. Tags placed within the field are immersed in the propagating wave and collect some of the energy as it passes. The amount of energy available at any particular point is related to the distance between the tag and transmitter (d). The field is proportional to $1/d^2$, which makes the working distance of these devices significantly greater than that of induction based systems.

Signal interference is an issue that must be addressed when developing a transponder-based monitoring system. Electromagnetic waves are similar to light waves and behave in a similar manner. These waves can be reflected off radio conductive surfaces, refracted between dissimilar dielectric medium, and diffracted around sharp edges. These phenomena have the potential to substantially degrade the transmission signal between the tag and reader. In general, electromagnetic systems involve shorter wavelengths than induction systems and, as such, are much more prone to interference.

Reflection occurs when electromagnetic waves rebound off conductive surfaces such as metal, water, etc. When a transmitted wave meets at some point with an opposite reflected wave, a signal cancellation (or null) can occur, resulting in a no read situation. On the other hand, the signal strength may be intensified if the two waves meet at some point in phase. Unfortunately, nulls are much more prevalent than enhancements. The use of multiple antennae configured at 900 MHz can reduce, but cannot eliminate, the adverse effects of these problems associated with wave reflection.

Refraction and diffraction are also important considerations. Refraction is a measure of the ability of electromagnetic waves to penetrate (or pass through) a substance. This ability depends largely on the electrical conductivity of the materials involved. For example, the particulate solids contained in run-of-mine coals have low electrical conductivities and are expected to pass electromagnetic waves. On the other hand, water has a high electrical conductivity and will tend to reflect and absorb electromagnetic energy. Thus, the presence of moisture is a concern for electromagnetic systems. Refraction is caused by the change in velocity of an electromagnetic wave when it crosses a boundary between one propagating medium and another. If this crossing is at an angle, then one part of the wave front will change speed before the other, thereby changing the direction of the wave. Both of these phenomena may interfere with the transmission process.

Table 2 provides an overview of some of the commercial distributors of transponder systems that were directly contacted in conjunction with this project. A description of the capabilities and limitations associated with each distributor is included for comparison. This initial review suggests that the most promising distributors appear to be Intersoft and Texas Instruments.

Task 2 - Transponder Procurement

Based on the preliminary assessment of commercially available systems, two transponder identification development kits were purchased for use in this project. The first kit was purchased from Intersoft. The kit included a reader board, several miniature glass-encased tags (6 and 9 mm), and a 5 x 10 cm rectangular gate antenna. The system was powered by a standard 9-volt battery. The second kit was purchased from Texas Instruments. This system included a reader board, a 14 cm (5.5 inch) long rod type antenna, and an assortment of miniature tags (e.g., molded plastic and glass encased). This system required the additional purchase of an external regulated power supply to power to the reader module. Several miscellaneous components, such as wiring, connectors, electrical boxes, etc., were

Table 2. Comparison of commercial providers of transponder systems.

Manufacturer	Description of Capabilities
Balogh	Staff has considerable experience in new industrial applications, but product line appears to be too costly for density tracer applications.
BioMark	Company focuses on animal tagging/identification and offered little flexibility in terms of developing other applications.
Checkpoint Systems	Company is developing low-cost tags for electronic article surveillance (EAS), but size limitations with their products are a concern.
Intermec	High-end products do not currently appear to be cost-effective for use in disposable density tracers.
Intersoft	The company offers an inexpensive product line and can provide low-cost product development kits for new applications.
Matrics	This group deals exclusively with 900 MHz frequencies that could not function in a moist environment due to interference problems.
RFID Inc.	Company recognized that a 135 MgHz frequency would be best suited for density tracers, but communication with technical staff is difficult.
Texas Instruments	This group currently offers tags with the most capabilities and a reasonable price. The density consistency of their tags is a concern.
Trolley Scan	Products from this company were found to be incapable of meeting the required size specifications for density tracer applications.

purchased from local suppliers.

After working with both systems, it was determined that the Texas Instruments system was best suited for the density tracer application. In addition to being very robust and highly flexible, this particular system was the most affordable of the candidate systems. Therefore, a complete Texas Instruments TIRIS system was purchased, which included the components listed in Table 3. A schematic layout for the components is provided in Figure 7. The system included a reader board, an assortment of molded plastic and glass-encased tags, and a short (14 cm long) rod-type antenna. To improve signal strength and read range, a high power module was also purchased as a separate item to increase the input power the reader module. Also, an additional set of glass-encased tags (ten 23 mm and ten 32 mm) and four larger gate antenna (101 x 41 cm) were also purchased from Texas Instruments for the

Table 3. Transponder system components purchased from Texas Instruments.

Part Number	Component Description
RI-CTL-MB2A RS232	Control Module
RI-RFM-007B	Hi-Performance Reader Module
RI-ANT-G04E	Gate Antenna (4)
RI-TRP-RRHP	23 mm Read Only Transponder
RI-TRP-RR2B	32 mm Read Only Transponder
RI-ACC-AT12	Antenna Tuning Indicator
IHC24-2.4	International Power 24VDC power supply

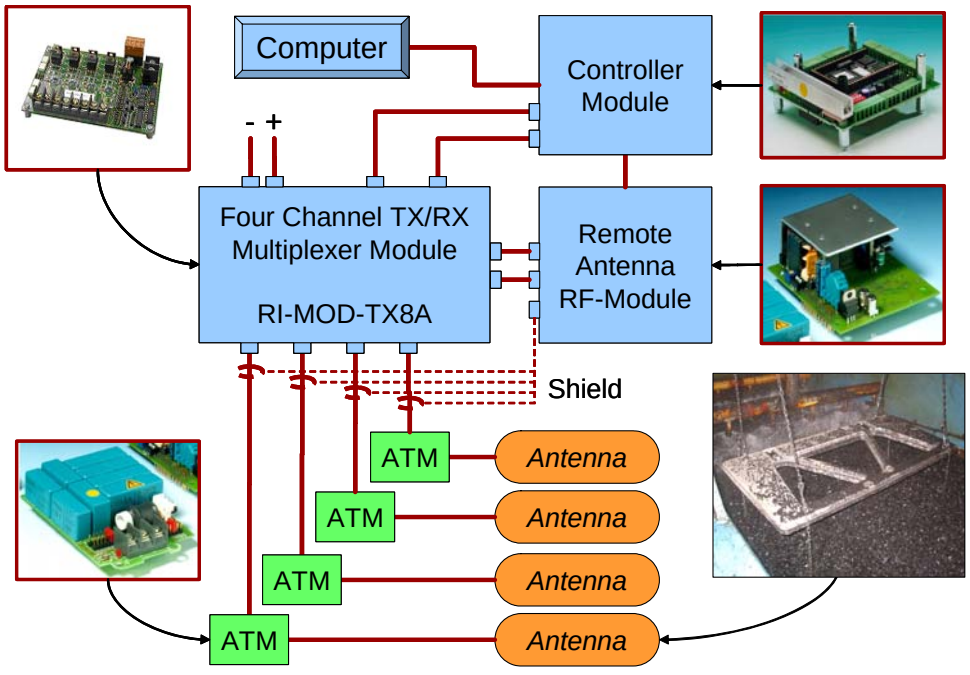

Fig. 7. Transponder system components purchased from Texas Instruments.

prototype system.

Several series of experiments were performed to evaluate the capabilities of an off-the-shelf detection system manufactured by Texas Instruments. Laboratory tests conducted using static (stationary) tracers indicated that this low-cost system could reliability detect tags embedded in density tracers, but some severe limitations existed in terms of effective read range (maximum allowable distance between the antenna and transponder tag). For example, a convenient location for the placement of the reader antenna would be on the clean coal belt and the refuse belt. In order for this location to be a viable option, a read range that is at least as deep as the load on the belt (45-60 cm) is required. While many factors influence the read range, the most important consideration is the power of the interrogation system. Because these transponders are activated passively, they draw all of their power from the magnetic field created by the interrogation antenna. The available voltage falls off as 1/distance^3 and the power falls off as 1/distance^6. Other factors influencing the power requirement include the tag power demand, tag quality factor (Q), tag tuning, tag antenna aperture, and reader antenna aperture.

The magnetic field used for activation of the transponder is related to the type of antenna(s) used to transfer power to the transponder and transmit data back to the reader. The size of the antenna determines how far the magnetic flux lines are emitted from the reader antenna. The larger the antenna the further the flux lines will extend into the region being monitored. The read range for a low frequency, inductively coupled, passive system is approximately one to two times the reader's antenna diameter. Larger antennas will yield a larger read area, but caution must be taken because the increased reception may lead to a worse signal-to-noise ratio at the receiver. The antenna needs to be tuned to resonate at the operating frequency in order for the maximum energy to be transferred to the transponder. The resonant frequency (f_r), in a LC circuit, is described by:

$$f_r = \frac{1}{2\pi\sqrt{LC}} \tag{5}$$

in which L is the inductance and C is the capacitance. The TI-RIS reader requires an antenna with an inductance of 26 to 27.9 µH. The antenna used in this system has an inductance of 24.4 µH. In order to bring the inductance up to 27 µH, a 0.0047 µF capacitor is put in parallel with the antenna. In addition to being tuned to the resonant frequency, the antenna should have a Q factor of 100. (Q is defined as the ratio of the effective impedance caused by the inductance of the coil at the frequency of transmission to the resistance in the antenna wire). The Q factor can be calculated using:

$$Q = \frac{2\pi f_r L}{R} \tag{6}$$

in which R is the resistance. Since Q effectively represents the ratio of stored energy to dissipated energy, a higher Q indicates that a larger amount of energy can be extracted from the reader's field. In the current configuration, L = 27 µH, f_r = 134 kHz, and R = 0.22. This combination provides an acceptable Q factor of 105.

For this application, smaller (23 mm) transponders are needed so that they can be embedded in density tracers that have sizes similar to the coal being treated. A ferrite rod can be used to focus the magnetic flux lines into the transponder's antenna. This is common in applications where the aperture of the antenna is less than 1 cm. Another factor that can affect the read range is noise. Depending on the type of signal modulation that is employed the signal can be corrupted by electronic noise in the environment. The FSK (frequency shift keying) employed by the TI transponder is better than ASK (amplitude shift keying) at being immune to surrounding noise. In addition to the system design, there are also several environmental factors that affect the read range. The orientation of the transponder, movement of the transponder, and metal in the proximity are examples of application specific factors that also affect the read range.

Task 3 - Preparation of Density Tracers

For initial evaluations, a partial set of density tracers were manufactured using the transponder technology. This work involved the placement of 40 factory-programmed tags encased within tracer blocks to uniquely identify both the size and density of the block. The 32 mm cubic blocks were manufactured by Partition Enterprises in Australia using twenty 23 mm and twenty 32 mm tags. These prototype blocks were used to conduct trial runs of the proposed counting system in a laboratory environment. The prototype density tracers for this project were cast by mixing a low-density resin base (such as epoxy) with sufficient high-density filler (such as zinc oxide) to attain the desired target SG upon complete drying/curing. A small transponder tag with a unique digital code was placed inside each block during the casting process. A reddish-colored pigment (or dye) was added to the resin to make the block easier to see by eye during manual collection. A proprietary manufacturing methodology developed by Partition Enterprises, Australia, was used to ensure that the filler and pigment was homogeneously distributed and the mixture was free of entrained air voids.

The manufacturing of density tracers with an acceptable density tolerance was one of the major challenges that had to be addressed in this project. Ideally, the electronic tracers should have a density tolerance of at least $\pm$0.01 SG. The presence of the glass-encased transponder complicates the manufacturing process since the block is no longer homogeneous (i.e., the mass and volume of the transponder must also be considered). Mathematically, the composite density of the tracer block (ρ) can be calculated using:

$$\rho = \rho_t \phi_t + \frac{1-\phi_t}{\left(\frac{1-m_f}{\rho_r} + \frac{m_f}{\rho_f}\right)} \tag{7}$$

in which m_f is the mass fraction of high-density filler, ϕ_t is the volume fraction occupied by the transponder tag, and ρ_t, ρ_r, and ρ_f are the densities of the transponder tag, dried resin, and filler, respectively. Using this relationship as a guide, a set of test blocks was prepared to evaluate the precision of the manufacturing procedures. The densities of the blocks were experimentally measured using a density balance, i.e.:

Table 4. Measured SG values for manufactured density tracer blocks.

	Measurement 1			Measurement 2			
Target SG	Weight in Air (gms)	Weight in Water (gms)	Block SG	Weight in Air (gms)	Weight in Water (gms)	Block SG	Avg +/- from target SG
1.80	54.69	24.4	1.8055	54.69	24.39	1.8050	-0.005
1.80	55.04	24.49	1.8016	55.04	24.61	1.8087	-0.005
1.78	53.48	23.52	1.7850	53.48	23.44	1.7803	-0.003
1.78	54.17	23.92	1.7907	54.2	23.86	1.7864	-0.009
2.00	60.66	30.37	2.0026	60.63	30.33	2.0010	-0.002
2.00	62.27	31.24	2.0068	62.26	31.16	2.0019	-0.004

$$SG = \frac{W_A}{W_A - W_W} \tag{8}$$

in which SG is the specific gravity of the block, W_A is the block weight when suspended in air, and W_W is the block weight when suspended in water. The results obtained from these measurements are summarized in Table 4. All of the test blocks achieved the required tolerance specification of less than $\pm$0.01 SG, and all but one achieved a tolerance comparable to that typically obtained for conventional density tracers (i.e., $\pm$0.005 SG).

Another issue that must be considered for the electronic density tracers is abrasion. During use, the outer surfaces of tracer blocks are often chipped away as the blocks pass through the plant circuitry. The loss of volume has minimal effect on conventional density tracers since the blocks are homogenous throughout. However, this is not true for the case of electronic density tracers. Since the embedded transponders are typically of a higher density than the surrounding resin, the tracer blocks become slightly denser as the surface is eroded

Table 5. Calculated variation in density after loss of block volume.

Target SG	Density Tracer SG Versus Percentage Volume Loss			
	1%	5%	10%	20%
1.400	1.400	1.401	1.402	1.404
1.500	1.500	1.501	1.502	1.504
1.600	1.600	1.601	1.601	1.603
1.700	1.700	1.701	1.701	1.703
1.800	1.800	1.800	1.801	1.802
1.900	1.900	1.900	1.901	1.902
2.000	2.000	2.000	2.001	2.001
2.100	2.100	2.100	2.100	2.101
2.200	2.200	2.200	2.200	2.200

away. To assess the impact of this problem, the change in block density was calculated using Equation (7) for different starting densities and for total volume losses of 1, 5, 10 and 20%. The results summarized in Table 5 indicate that a gain of less than 0.004 SG units is expected for blocks of low density (1.4-1.5 SG) even when up to 20% of the total block volume is lost. The net increase in density drops to just 0.003 SG units at intermediate densities (1.6-1.7 SG) and is essentially negligible for higher densities (>2.0 SG). These calculations suggest that the loss of block volume caused by normal abrasion/chipping should not be a serious problem for the transponder-based density tracers.

Task 4 - Testing and Evaluation

Several series of laboratory trials were conducted using the prototype tracers. This work was performed (i) to develop a protocol for how the transponders would be installed within the plastic blocks of different densities, (ii) to confirm that the plastic polymer used in manufacturing the tracers would not inhibit the transponder activation or return signal, and (iii) to determine whether the required tolerances on density could be maintained after embedding the transponders. Particular emphasis was placed on identifying factors that would optimize the read range, improve accuracy, and reduce interference during the detection of the tracer blocks (Sorrells, 2000).

The preliminary evaluation of the tagged tracer blocks was conducted using a test platform that allowed the location of the transponders within the reader field to be accurately recorded. The reader, control module, and antenna were installed on the test apparatus (Figure 8). The transponders were placed on a graduated grid (Figure 9) so that the perimeter of the detection limits (read range) could be established. The detection limit tests were performed by placing the transponder tags in three different orientations (i.e., 0, 45 and 90 degrees) relative to the axis of the reader antenna.

The results obtained from the orientation tests are plotted in Figure 10. The data clearly indicate that the selected transponder tags could indeed be detected by the reader system. The tags provided a maximum read range of approximately 62 cm (24.5 inches). However, the read range was found to be strongly dependent on the orientation of the transponder tag. The 90

Fig. 8. Test platform constructed to establish the tag detection limits (read range).

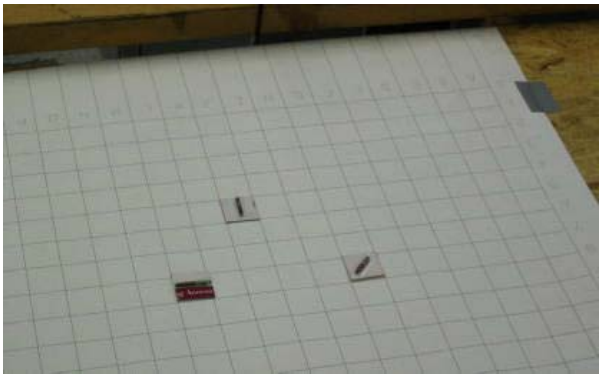

Fig. 9. Rectangular grid used to quantify detection limits and tag orientation.

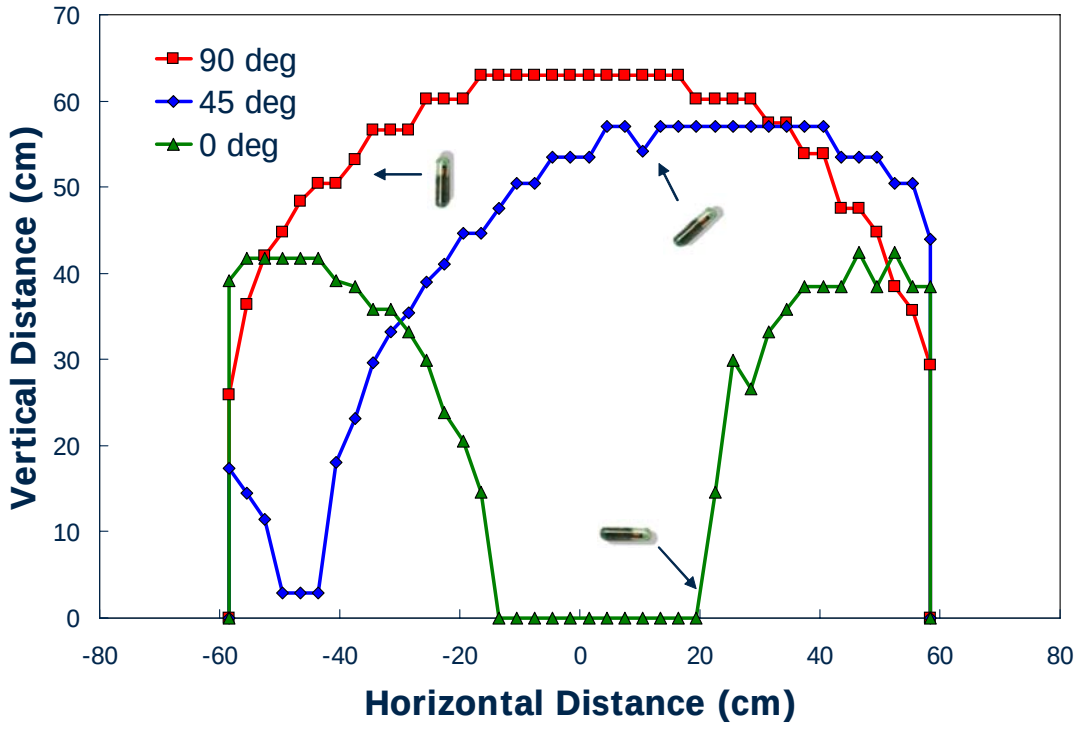

Fig. 10. Vertical and horizontal read range for tags placed in different orientations.

degree (standing) orientation provided the strongest signal when placed directly in front of the reader antenna. The signal diminished at the boundaries to each side of the transponder. In contrast, the 0 degree (flat) orientation provided good signals when the antenna was located to each side of the transponder, but was essentially invisible (no detection was possible) when placed directly ahead of the antenna.

This work performed with the test platform suggests that two antenna, oriented at right angles to each other, may be required to ensure that all possible orientations of the embedded transponder tags will be accurately identified as they pass by the detection point. On the other hand, it was also believed possible that the random motion of the tracer blocks over drain-and-rinse screens, conveyors, etc., could be adequate to ensure proper orientation and detection. To test this possibility, a pilot-scale test circuit was constructed using two conveyor belts that constantly circulated the transponder tracers past the reader antenna (Figure 11). In this case, the reader antenna was placed 56 cm (22 inches) above the surface of the belting material. This experimental setup made it possible to determine how the transponder movement and other spatial factors such as belting material type, coal bed thickness, conveyor framing location, etc., affected the transponder readings.

Fig. 11. Pilot-scale conveyor used to evaluate tracer orientation and read range.

The static tests conducted with stationary blocks indicated that transponder orientation strongly influenced the read range. On the other hand, the dynamic tests conducted by passing blocks on a belt conveyor through the antenna field indicated that the transponders could be detected regardless of block orientation (provided they were kept in motion). In fact, the tests conducted with the pilot-scale circuit demonstrated that all tracer blocks could be accurately identified as they passed below the antenna on the conveyor belt. Therefore, the problem of orientation experienced with the stationary static tracers does not appear to be a problem for actual practice. The dynamic tests did, however, show that problems could occur with duplicate readings when two blocks passed under the antenna in close proximity to each other. The reader system is designed to forward the transponder identification (ID) number to the computer only when the ID is different that the one last read. If multiple transponders are in the field for a sufficiently long period of time, one tag can be read and then the other, therefore allowing the first one to be read again. To overcome this problem, each tracer block required a unique ID number so that it can be compared with the data file log and counted only once by the computer software.

In light of the promising results obtained with using the prototype system, a complete set of uniquely tagged density tracer blocks were manufactured for use in the field trails. Twenty blocks equipped with embedded transponder tags were manufactured for each SG value between 1.46 and 1.76 SG in increments of 0.02 SG. In addition, twenty additional

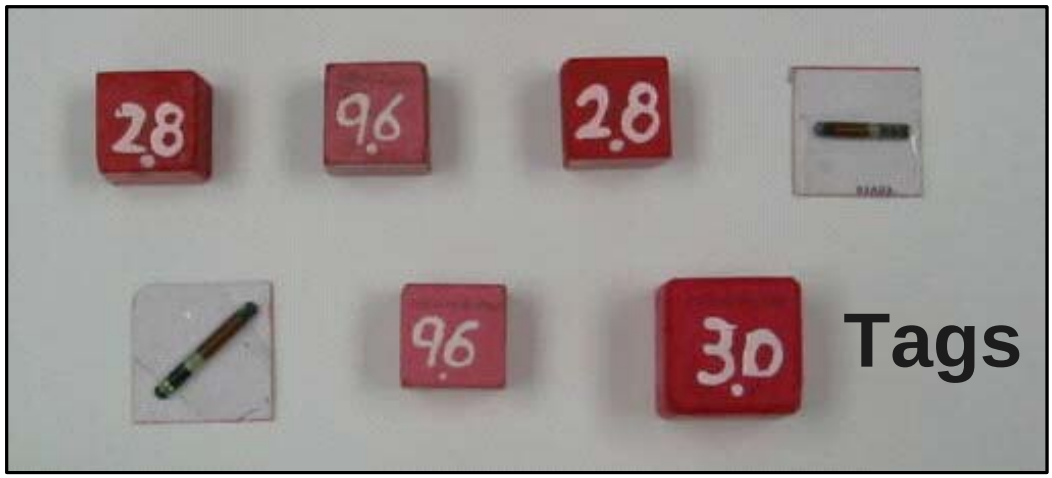

Fig. 12. Sizes of transponder-based density tracers prepared for this project.

blocks of 1.30 and 1.90 SG were also manufactured so that the tails of the partition curves could be well established. Unlike the prototype blocks that were 32 mm cubes, the newer blocks were manufactured slightly smaller (i.e., 22 mm cubes) so as to better represent the size of coal particles that would be expected to be present in the field trails. A photograph showing some of the manufactured blocks is provided in Figure 12.

Task 6 – Software Development

Considerable work was required to develop the data acquisition software for the transponder-based density tracer system. This activity included the construction of a suitable user interface, programming of the computation algorithms, and the completion of required logic interfaces between the transponder system and computer. The user interface was designed to provide a direct graphical readout showing the process efficiency curve and pertinent performance indicators (e.g., SG cutpoint and Ep). This information can be directly used by plant operators to evaluate the on-line circuit performance and estimate coal losses. A Visual Basic program interfaced with the reader hardware was developed to capture and record the tracer identification numbers. Once the collection step was completed, the data was processed using Excel VBA and Excel SOLVER for reporting of the final results. A COM interface was also written in Visual Basic to control the acquisition of data from the antenna array. This program automatically cycles through the four antennas to record the location where each transponder was read. Proper tuning of the antenna array was found to be extremely important in achieving the optimum read range for the transponder-based tracers.

The pilot-scale test circuit provided a convenient opportunity to evaluate the data acquisition system used to tally the tags and to generate the user report. Two software packages were evaluated for this task. The first program was DASYLab (Data Acquisition System Laboratory). This program is attractive because it has the power to handle several inputs and outputs simultaneously. The problem with this package was that it required very

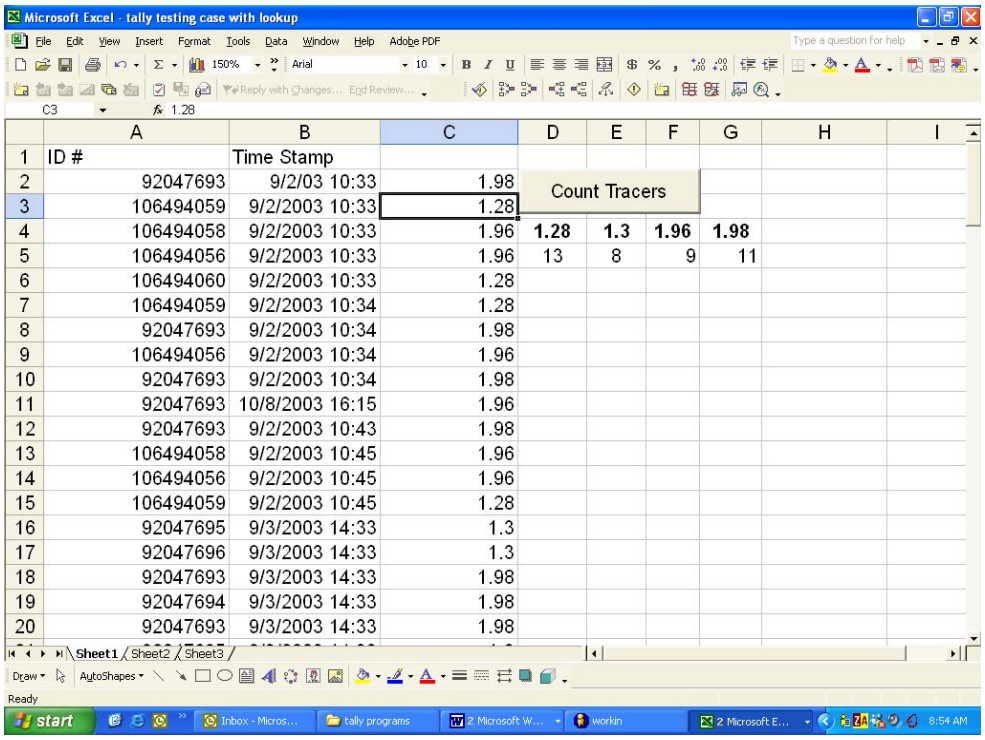

	A	B	C	D	E	F	G	H	I
1	ID #	Time Stamp							
2	92047693	9/2/03 10:33	1.98						
3	106494059	9/2/2003 10:33	1.28						
4	106494058	9/2/2003 10:33	1.96	**1.28**	**1.3**	**1.96**	**1.98**		
5	106494056	9/2/2003 10:33	1.96	13	8	9	11		
6	106494060	9/2/2003 10:33	1.28						
7	106494059	9/2/2003 10:34	1.28						
8	92047693	9/2/2003 10:34	1.98						
9	106494056	9/2/2003 10:34	1.96						
10	92047693	9/2/2003 10:34	1.98						
11	92047693	10/8/2003 16:15	1.96						
12	92047693	9/2/2003 10:43	1.98						
13	106494058	9/2/2003 10:45	1.96						
14	106494056	9/2/2003 10:45	1.96						
15	106494059	9/2/2003 10:45	1.28						
16	92047695	9/3/2003 14:33	1.3						
17	92047696	9/3/2003 14:33	1.3						
18	92047693	9/3/2003 14:33	1.98						
19	92047694	9/3/2003 14:33	1.98						
20	92047693	9/3/2003 14:33	1.98						

Fig. 13. Data screen used in the identification of tagged density tracers.

specific formats for reading signals from devices. The TI tag has an identification number that exceeds the character limits of the DASYLab input. Therefore, this package was abandoned in favor of the WinWedge software. WinWedge serves as a pipeline that transfers the data from the reader into another program on the computer. In this case, the data was transferred using DDE (Dynamic Data Exchange) routines to the Excel spreadsheet program for data manipulation and plotting. Figure 13 shows a snapshot of the computer screen after a set of test runs.

Task 7 – Field Testing

Final testing of the proposed system was conducted on-site at an industrial coal preparation plant. The test site was selected so that the tagged density tracers could be easily recovered by plant personnel and reused in additional test runs. Because of the preliminary nature of this work, the plant trials were limited to testing of a relatively simple heavy medium cyclone circuit with a minimal number (only four) drain and rinse screens. This limitation was necessary because of the small number of reader antenna (only four) and associated hardware purchased using the modest project budget. For reference, a schematic layout of the electronics and antenna system around the plant heavy medium cyclone circuitry is provided in Figure 14.

During testing, the four antennas were suspended above the drain and rinse screens using chains. The use of chain connectors allowed for easy installation, adjustment and removal of the antennas. Two antennas were required for each drain and rinse screen in order

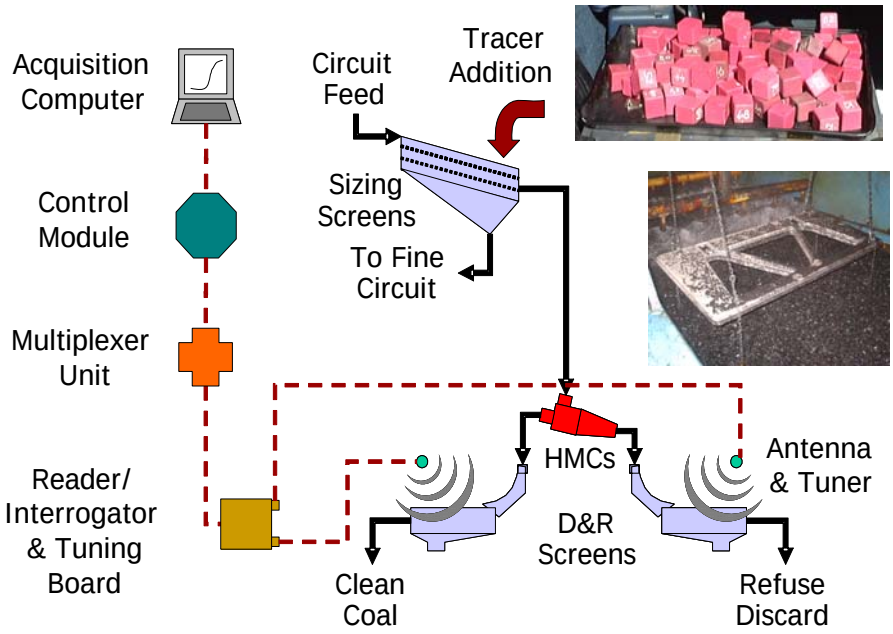

Fig. 14. Layout used in the field testing of the density tracer counting system.

to fully cover the width of the 1.8 m wide (6 ft wide) screens. In order to be sure of no interference between the antennas, one antenna was placed close to the end where the material comes onto the screen and one was positioned near the end where the material was discharged (Figure 15). For the end closest to the feed end of the screens, the chains holding the antennas were supported from C-clamps attached to the underside of the plant floor structure (Figure 16a). Since there was not any floor structure above the antennas near the discharge end of the screen, the chains holding these antennas were attached to temporary support structure constructed from PVC piping (Figure 16b).

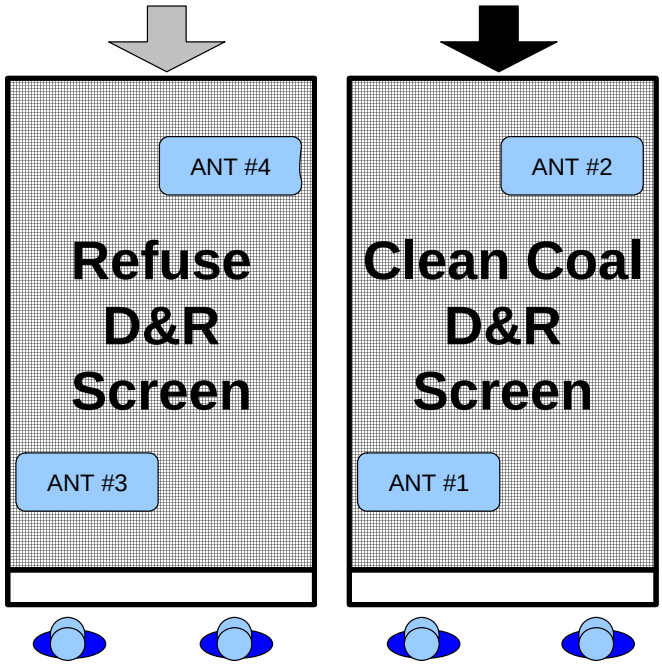

Fig. 15. Antenna layout above D&R screens (two persons per screen used for collection).

After installing the antenna and electronics, two series of full-scale test runs were conducted to assess the performance of the automated system for detecting and counting transponder-based tracers. The plant operating conditions for the test runs are summarized in Table 5. For first full-scale test, the antennas were mounted at

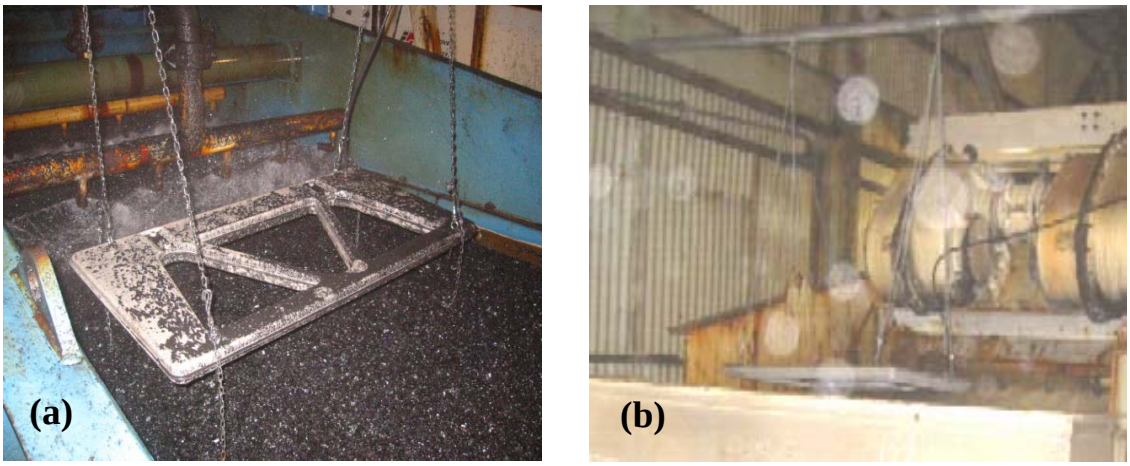

Fig. 16. Antenna mounting to (a) plant structure and (b) temporary PVC piping.

approximately 30 cm (12 inches) off the surface of the screen deck and about 18 cm (7 inches) from the screen edge. The tracer blocks were added into the process stream at a point where the feed to the fine heavy medium cyclone circuit comes off the upstream deslime screens. The tracers were manually introduced by hand into the feed stream at 5 second intervals. A hand-held antenna was used to electronically log the exact time that each tracer block added. For verification of the detection system, the tracer blocks were manually recovered by two persons stationed at the discharge end of each screen (see Figure 15).

Table 6 summarizes the test data obtained from the first series of in-plant tests using the electronic density traces. As shown, a total of 378 density tracers with densities ranging from 1.3 to 1.9 SG were added to the feed stream. In this case, 95% of the tracers added to the feed stream were collected by hand. The unusually high recovery rate of tracers by hand was probably due to the large number of workers used to collect the tracers (i.e., two persons were stationed at each 1.8 m wide screen). In most cases, tests conducted with conventional density tracers in

Table 6. Plant conditions for the tracer test runs.

	Run #1	Run #2
Plant Feed Rate (tph)	571	547
Plant Clean Coal Rate (tph)	142	213
Fine HMC SG PLC Setpoint	1.55	1.55
Fine HMC SG Cup Reading	1.65	1.66
Coarse HMC SG PLC Setpoint	1.55	1.56
Coarse HMC SG Cup Reading	1.60	1.60
Fine HMC pressure (psi)	19	19
Diameter (cm / inches)	76 / 30	76 / 30
Vortex finder (cm / inches)	30 / 12	30 / 12
Apex (cm / inches)	23 / 9	23 / 9
Number of Antenna	4	4
Antenna Height (cm / inch)	30 / 12	23 / 9
Antenna Edge (cm / inch)	8 / 3	0 / 0
Tracer Addition Interval (sec)	5	15

Table 7. Data obtained from manual and electronic counting of density tracers.

SG	Feed	Clean		Refuse		Total		Collected (%)		Partition	
		Hand	EDT	Hand	EDT	Hand	EDT	Hand	EDT	Hand	EDT
1.30	21	19	14	0	0	19	14	90	67	0.00	0.00
1.46	21	20	14	0	0	20	14	95	67	0.00	0.00
1.48	21	20	19	0	0	20	19	95	90	0.00	0.00
1.50	21	19	16	0	0	19	16	90	76	0.00	0.00
1.52	21	20	18	0	0	20	18	95	86	0.00	0.00
1.54	21	18	16	0	0	18	16	86	76	0.00	0.00
1.56	21	21	19	0	0	21	19	100	90	0.00	0.00
1.58	21	21	15	0	0	21	15	100	71	0.00	0.00
1.60	21	18	14	0	0	18	14	86	67	0.00	0.00
1.62	21	18	15	0	0	18	15	86	71	0.00	0.00
1.64	21	19	14	2	2	21	16	100	76	0.10	0.14
1.66	21	11	8	10	7	21	15	100	71	0.48	0.48
1.68	21	1	1	20	19	21	20	100	95	0.95	0.95
1.70	21	0	0	20	16	20	16	95	76	1.00	1.00
1.72	21	0	0	20	16	20	16	95	76	1.00	1.00
1.74	21	0	0	21	12	21	12	100	57	1.00	1.00
1.76	21	0	0	20	12	20	12	95	57	1.00	1.00
1.90	21	0	0	21	19	21	19	90	90	1.00	1.00
Sum	378	225	183	134	103	359	286	**95.0**	**75.7**	--	--

Hand – manual collection, EDT – electronic density tracer system

U.S. plants exhibit block losses of 15-25%, with losses exceeding 40% in some heavily loaded circuits (see Table 7). Unfortunately, the electronic detection system developed in this project detected only 76% of the blocks added to the feed stream (see Table 6).

The low detection of the electronic tracer blocks was believed to be related to two separate issues. The first issue involved the location of the antennas. Diagnostic tests indicated that tracer blocks which passed near the very corners of the screens were being completely missed by the antenna array. This problem was corrected by relocating the antenna so that the end of each antenna was directly over the edge of each screen. The

Table 8. Examples of typical density tracer losses for industrial preparation plants.

Plant Circuit	Tracers Collected from Clean	Tracers Collected from Refuse	Total Tracers Recovered	Total Tracers Added	Total Tracers Lost	Percent Tracers Lost
A	191	96	287	360	73	20.3
B	127	112	239	325	86	26.5
C	161	197	358	440	82	18.6
D	81	178	259	440	181	41.1
E	129	57	186	240	54	22.5

antennas were also lowered 8 cm (3 inches) to a distance of 23 cm (9 inches) above the screen deck to further improve the readability. The second issue related to poor detection involved a problem of tracer coincidence. Diagnostic tests showed that only one identification number was read when two transponders passed under an antenna at the same point in time. To eliminate this problem, the length of time between the addition of one tracer block and another was increased from 5 to 15 seconds.

A second test run was conducted using the new antenna positions and longer time spacing between tracer block additions. The test data from the second test run is provided in Table 8. In this case, the number of tracer blocks added to the feed stream was substantially reduced from 378 to 65. The reduction was considered reasonable to be necessary in order to minimize the losses of tracer blocks collected by hand. As shown, 64 of 65 blocks (98.5%) were detected and counted by the electronic system during the second test run. In comparison, 60 of 65 (92.3%) blocks were collected manually by hand in the same test run. The electronic system was superior to the manual counting method despite the fact that two workers were placed at each 1.8 m (6 ft) wide screen in an attempt to ensure that the maximum possible blocks were collected by hand. The very high detection rate for the electronic system indicates that the modifications to the antenna location and changes to the timing of block additions greatly improved the system reliability.

Figure 17 shows the partition curve obtained using the electronic density tracers. For comparison, the data are plotted for both the manual counting (hand collection) and electronic transponder counting methods. The Whiten formula was used to provide a best-fit regression curve through the data points obtained using the electronic tracers. The fitted data show that the plant heavy medium circuit was operating at a specific gravity cutpoint (SG_{50})

Table 9. Data obtained from manual and electronic counting of density tracers.

SG	Feed	Clean		Refuse		Total		Collected (%)		Partition	
		Hand	EDT	Hand	EDT	Hand	EDT	Hand	EDT	Hand	EDT
1.30	5	4	5	0	0	4	5	80	100	0.00	0.00
1.56	5	5	5	0	0	5	5	100	100	0.00	0.00
1.58	5	4	5	0	0	4	5	80	100	0.00	0.00
1.60	5	5	5	0	0	5	5	100	100	0.00	0.00
1.62	5	4	4	0	0	4	4	80	80	0.00	0.00
1.64	5	4	5	0	0	4	5	80	100	0.00	0.00
1.66	5	4	4	1	1	5	5	100	100	0.20	0.20
1.68	5	1	1	4	4	5	5	100	100	0.80	0.80
1.70	5	0	0	5	5	5	5	100	100	1.00	1.00
1.72	5	0	0	5	5	5	5	100	100	1.00	1.00
1.74	5	0	0	4	5	4	5	80	100	0.80	1.00
1.76	5	0	0	5	5	5	5	100	100	1.00	1.00
1.90	5	0	0	5	5	5	5	100	100	1.00	1.00
Sum	65	31	34	29	30	60	64	**92.3**	**98.5**	--	--

Hand – manual collection, EDT – electronic density tracer system

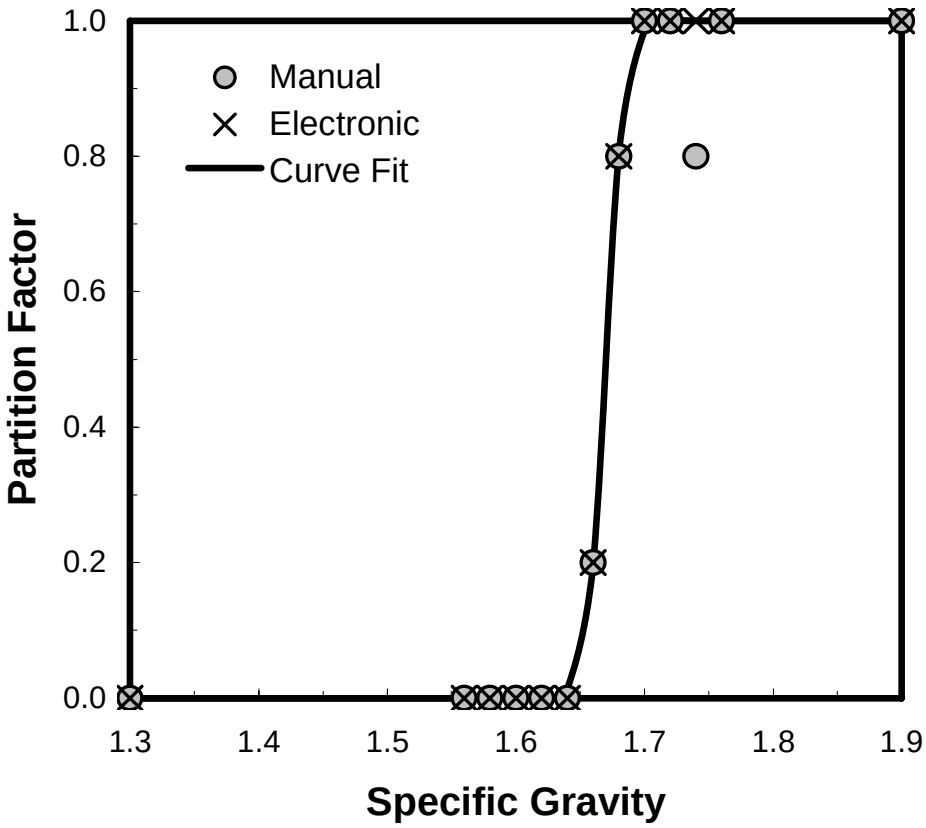

Fig. 17. Partition curve obtained using density tracers.

of 1.67 SG. The sharpness of the separation, as measured by the Ecart probable error (Ep), was found to be 0.008. This very good efficiency number, combined with the fact that the ends of the curve close at low and high SG values, indicated that no gross misplacement of either coal or rock occurred for this particular test run. More importantly, the automated system was able to numerically quantify these key indicators of circuit performance in just a matter of minutes using only a single person.

In light of the successful test work, an economic analysis was performed to estimate the total cost of the electronic density tracer system developed under this project. A summary of the total capital costs required to purchase the necessary hardware components is provided in Table 7. As shown, the total equipment cost for the reader and antenna systems was determined to be $3,596 (which includes the laptop computer and required software). The total cost for the purchase of transponder tags and the manufacture of 414 density tracer blocks was $2,948. Therefore, the total hardware cost for the system was about $6,500. As such, the total cost of the assembled system, including construction labor, is expected to be less than $10,000.

Table 10. Estimated equipment cost for the electronic density tracer system.

Quantity	Description	$/Unit	$ Total
1	481-1033-ND (Series 2000 High Performance Remote Antenna RFM)	$239.07	$239.07
1	481-1035-ND (RFID 2000 CONTROL MODULE RS232 RI-CTL-MB2A-03)	$227.51	$227.51
1	481-1037-ND (Series 2000 4 Channel TX/RX Multiplexer)	$165.21	$165.21
4	481-1034-ND (RFID 2000 ANT TUNING-MOD 134.2K)	$89.10	$356.40
4	481-1045-ND (Series 2000 Gate Antenna Large)	$202.49	$809.96
1	381-1082-ND Fan	$12.81	$12.81
5	PT06E12-3S(SR)-ND* Plug w/sockets (power cord)	$18.48	$92.40
5	PT02E-12-3P-ND Recept w/pins (power cord)	$10.62	$53.10
1	Plug w/pins PT06E10-6P(SR)-ND* (data cord)	$16.43	$16.43
1	Recept. w/pins PT00E-10-6P-ND (data cord)	$22.63	$22.63
175 ft	Belden 9207 Twin-axial Wire	$0.43	$75.25
1	Power Supply AC-DC 24VDC	$75.00	$75.00
1	Miscellaneous Hardware (Electrical box, chain, clamps, etc.)	$250.00	$250.00
1	Computer and Software	$1,200.00	$1,200.00
		Subtotal	**$3,595.77**
414	481-1007-ND (23 mm glass type transponder RO)	$2.12	$877.68
414	Manufacture of Tracers (Charge by Partition Enterprises, LLC)	$5.00	$2,070.00
		Subtotal	**$2,947.68**

SUMMARY AND CONCLUSIONS

Field tests were carried out to evaluate the capabilities of the proposed electronic detection system for counting density tracers. The test runs were performed by passing density tracers embedded with passive transponders through a heavy medium cyclone circuit at an industrial plant site. Several problems were encountered during the initial test run that resulted in poor detection levels for the electronic tracers. These problems, which included improper antenna heights and excessively rapid tracer introduction, were corrected by simple changes to the radio equipment and test protocols. After making these modifications, very accurate counts of the transponder-based tracers were achieved. In the final test run, 98.5% of the electronically tagged tracer blocks were detected by the automated counting system. This level of detection was superior to the 92.3% collection rate achieved using manual (hand) collection. The superior performance was particularly impressive considering that two employees were used per 1.8 m width (6 ft width) of screen to ensure that very high manual collection rates were maintained. The manual collection rate is normally much lower in actual practice since (i) fewer personnel are normally available for collecting the density tracers and (ii) few plant sites are as ideally suited for block collection as the one employed for this test work. The estimated capital cost for the construction of the transponder-based system (including tracer blocks) was estimated to be less than $10,000 U.S.

REFERENCES

1. Ayat, M.G. and Leonard, J.W., 1986. “A Novel Tracing Technique for the Coal Preparation Industry,” SME Annual Meeting, New Orleans, Louisiana, March 2-6, 1986, Preprint No. 86-33.

2. DASYLab, “Book 1: User Guide” and “Book 2 Module Reference Guide,” DASYTECH USA, A National Instruments Company, NH, 1991-2001.

3. Scher, Bob, “Antenna Considerations for Low Frequency RFID Applications,” http://www.rfidusa.com/rfid_antenna_consid.html.

4. Sorrells, Peter, 2000 “Optimizing Read Range in RFID Systems,” *EDN Magazine*, December 7, 2000, pp. 173-184.

5. Texas Instruments, Series 2000 Reader System, RI-RFM-007B, Reference Guide

6. Whiten, W.J., 1972. “Simulation and Model Building for Mineral Processing,” PhD Thesis, Univeristy of Queensland, Australia, 213 pp.

7. WinWedge, “RS-232 User Guide,” TAL Technologies, PA, www.taltech.com.